The stability field of ferropericlase with respect to oxygen fugacity in the Earth's mantle and the origin of superdeep diamonds

DISSERTATION

zur Erlangung des akademischen Grades einer Doktorin
der Naturwissenschaften (Dr. rer. nat.)
in der Bayreuther Graduiertenschule für Mathematik und
Naturwissenschaften (BayNAT)
der Universität Bayreuth

vorgelegt von

Caterina Melai
aus *Camposampiero (Italien)*
Bayreuth, 2023

This doctoral thesis was prepared at the department of Bayerisches Geoinstitut at the University of Bayreuth from October 2017 until March 2023 and was supervised by Prof. Dr. Daniel Frost and Dr. Tiziana Boffa Ballaran.

This is a full reprint of the thesis submitted to obtain the academic degree of Doctor of Natural Sciences (Dr. rer. nat.) and approved by the Bayreuth Graduate School of Mathematical and Natural Sciences (BayNAT) of the University of Bayreuth.

Date of submission: 02.03.2023

Date of defence: 29.03.2023

Acting director: Prof. Dr. Hans Keppler

Doctoral committee:

Prof. Dr. Dan Frost (reviewer)

Prof. Dr. Alan B. Woodland (reviewer)

PD. Dr. Catherine A. McCammon (chairman)

Prof. Dr. Marc Hirschmann

Table of contents

Abstract

Although rare, some inclusions in so called superdeep diamonds appear to originate below the lithospheric mantle, raising questions as to how they form under these conditions and, therefore, how the deep carbon cycle operates. Ferropericlase, (Mg,Fe)O, makes up ~20 vol% of the lower mantle and is found in ~50% of superdeep diamonds. Although it is often argued that such diamonds come from the lower mantle, ferropericlase can in principle form at shallower depths from SiO_2-poor materials. In addition to Fe^{2+}, synthetic and natural ferropericlase also contains Fe^{3+}. At room pressure the Fe^{3+}/Fe_{tot} ratio of ferropericlase varies strongly with oxygen fugacity (fO_2), reaching a minimum where ferropericlase is in equilibrium with iron metal and a maximum where it coexists with spinel ferrite (Fe_3O_4-$MgFe_2O_4$) solid solution. Ferropericlase inclusions in diamonds also show evidence for the exsolution of a spinel-ferrite phase.

To interpret the fO_2 at which these inclusions formed and to understand why spinel-ferrite exsolution occurs, experiments were performed to measure ferropericlase Fe^{3+}/Fe_{tot} over a range of fO_2, up to its coexistence with spinel-ferrite, and at higher pressures up to 30 GPa, where it coexists with recently discovered mixed-valance Fe and Mg-oxides. Once the fO_2 rises above a certain threshold, all samples contain nanocrystalline topotaxial exsolutions of spinel-ferrite, that exsolve during quenching. Characteristics of the Mössbauer spectra make it possible to determine the original ferropericlase Fe^{3+}/Fe_{tot} ratio from the contribution of the exsolution and to reconstruct the high temperature composition. Using these results and measurements made using electron energy loss spectroscopy, a thermodynamic model has been developed that

describes the entire range of ferropericlase compositions in the system Mg-Fe-O between 1atm and up to 30 GPa.

A poorly constrained parameter in this thermodynamic treatment is the compressibility of the spinel-ferrite phase. To resolve this, X-ray diffraction experiments were performed in a diamond anvil cell on single crystals of pure $MgFe_2O_4$, as well as on an intermediate composition. The compressibility changes non-linearly with Mg-content across the solid solution, may be due to an interruption of Fe^{2+}-Fe^{3+} electron hopping by introducing Mg cations into the spinel structure.

The resulting thermodynamic model indicates that the ferropericlase Fe^{3+}/Fe_{tot} ratio in equilibrium with spinel ferrite increases slightly with pressure. Above 10 GPa, however, after the phase transformation of spinel ferrite to the high-pressure oxide, $[Fe^{2+}, Mg]_2Fe^{3+}{}_2O_5$, the Fe^{3+}/Fe_{tot} ratio declines rapidly reaching values at 30 GPa, that would exclude some ferropericlase inclusions in diamonds from being formed in the lower mantle, since they have Fe^{3+}/Fe_{tot} ratios up to 0.12. Using this model, the ferropericlase Fe^{3+}/Fe_{tot} ratio in equilibrium with diamond and $(Mg,Fe)CO_3$ magnesite can be calculated, defining a redox buffer, with the acronym FDM, that imposes an effective limit on the possible fO_2 at which ferropericlase inclusions in diamond can form. The ferropericlase Fe^{3+}/Fe_{tot} ratio at FDM also decreases with pressure, indicating that only a few of the ferropericlase inclusions found in diamonds so far could have formed at the top of the lower mantle and if so, they must have formed at relatively oxidising conditions from carbonate minerals or melts. Many of the other inclusions have maximum formation depths in the transition zone. A few of the most oxidised inclusions could have only formed in the upper mantle and only from more oxidised precursors, implying that ferropericlase inclusions are formed through reduction of carbonates at depths mainly shallower than the lower mantle. Interestingly the FDM fO_2 curves for ferropericlase inclusions with Fe/(Fe+Mg) ratios > 0.5 intersect the stability of $[Fe^{2+}, Mg]_2Fe^{3+}{}_2O_5$, implying that this, or an

$[Fe^{2+}, Mg]_3Fe^{3+}_2O_6$ high-pressure oxide, could be trapped in diamond at near lower mantle conditions.

In a separate study performed during a three-month research visit to Tohoku University the nitrogen contents and nitrogen stable isotope ratios of several hydrous minerals and diamond were measured, after high pressure and temperature equilibration with a fluid produced by the decomposition of glycine ($C_4H_5NO_2$). Phlogopite, antigorite, lizardite and montmorillonite were equilibrated at 3 GPa and 500 °C. The recovered samples incorporated N contents between 0.35 and 2.14 wt% which were enriched in ^{15}N compared to the glycine starting material. This suggests that the passage of N-bearing fluids through hydrous mineral-bearing assemblages in subduction zones could cause N isotope fractionation in the mantle. Diamonds were also synthesised from graphite in the presence of an Fe-Ni-S catalyst and glycine at 13 GPa and 1700 °C. N was found to partition evenly between diamond and the coexisting metallic catalyst but the diamond became depleted in ^{15}N compared to the glycine starting material. This implies that, during diamond growth processes, coexisting fluids should become progressively ^{15}N enriched.

Zusammenfassung

Obwohl sie selten sind, scheinen einige Einschlüsse in so genannten supertiefen Diamanten ihren Ursprung unterhalb des lithosphärischen Mantels zu haben, was die Frage aufwirft, wie sie unter diesen Bedingungen entstehen und wie der tiefe Kohlenstoffkreislauf funktioniert. Ferroperiklas, (Mg,Fe)O, macht ~20 Vol.- % des unteren Erdmantels aus und ist in ~50 % der super-tiefen Diamanten zu finden. Obwohl oft behauptet wird, dass solche Diamanten aus dem unteren Erdmantel stammen, kann sich Ferroperiklas prinzipiell auch in geringerer Tiefe aus SiO_2-armen Materialien bilden. Synthetische und natürliche Ferroperiklase enthalten neben Fe^{2+} auch Fe^{3+}. Bei Raumdruck schwankt das Fe^{3+}/Fe_{tot} -Verhältnis von Ferroperiklas stark mit der Sauerstoffflüchtigkeit (fO_2) und erreicht ein Minimum, wenn Ferroperiklas im Gleichgewicht mit metallischem Eisen steht, und ein Maximum, wenn es mit Spinellferrit (Fe_3O_4-$MgFe_2O_4$) koexistiert. Ferroperiklas-Einschlüsse in Diamanten zeigen ebenfalls Anzeichen für die Entmischung einer Spinell-Ferrit-Phase.

Um den fO_2-Wert zu interpretieren, bei dem sich diese Einschlüsse gebildet haben, und um zu verstehen, warum es zu Spinell-Ferrit-Entmischungen kommt, wurden Experimente durchgeführt, in denen das Fe^{3+}/Fe_{tot}-Verhältnis von Ferroperiklas über einen Bereich von fO_2 bis zu seiner Koexistenz mit Spinell-Ferrit gemessen wurde, sowie bei höheren Drücken bis 30 GPa, wo er mit kürzlich entdeckten Fe- und Mg-Oxiden mit gemischter Wertigkeit koexistiert. Sobald der fO_2-Gehalt einen bestimmten Schwellenwert überschreitet, enthalten alle Proben nanokristalline topotaxiale Ausscheidungen von Spinell-Ferrit, die sich beim Abschrecken entmischt haben. Anhand der Merkmale der Mössbauer-Spektren lässt sich der Beitrag der Entmischungen zum

ursprünglichen Ferroperiklas Fe^{3+}/Fe_{tot}-Verhältnis bestimmen und die Hochtemperaturzusammensetzung rekonstruieren. Anhand dieser Ergebnisse und der Messungen mittels Elektronenenergieverlustspektroskopie wird ein thermodynamisches Modell entwickelt, das den gesamten Bereich der Ferroperiklas-Zusammensetzung im System Mg-Fe-O zwischen 1atm und 30 GPa beschreibt.

Ein nur unzureichend bekannter Parameter in dieser thermodynamischen Beschreibung ist die Kompressibilität der Spinell-Ferrit-Phase. Um dies zu klären, wurden Röntgenbeugungsexperimente in einer Diamant-Stempelzelle an Einkristallen aus reinem $MgFe_2O_4$ sowie an einer Zwischenzusammensetzung durchgeführt. Die Kompressibilität ändert sich nichtlinear mit dem Mg-Gehalt im Mischkristall, was auf eine Unterbrechung des Fe^{2+}-Fe^{3+}-Elektronenübergangs durch die Einführung von Mg-Kationen in die Struktur zurückzuführen sein könnte.

Das daraus resultierende thermodynamische Modell zeigt, dass das Fe^{3+}/Fe_{tot}-Verhältnis von Ferroperiklas im Gleichgewicht mit Spinellferrit mit dem Druck leicht zunimmt. Oberhalb von 10 GPa jedoch, nach der Phasenumwandlung von Spinellferrit in das Hochdruckoxid $[Fe^{2+}, Mg]_2Fe^{3+}{}_2O_5$, nimmt das Fe^{3+}/Fe_{tot} -Verhältnis rasch ab und erreicht bei 30 GPa Werte, die die Bildung einiger Ferroperiklas-Einschlüsse in Diamanten im unteren Erdmantel ausschließen würden, da sie Fe^{3+}/Fe_{tot} -Verhältnisse von bis zu 0.12 aufweisen. Anhand dieses Modells kann das Ferroperiklas-Fe3+/Fetot-Verhältnis im Gleichgewicht mit Diamant und $(Mg,Fe)CO_3$-Magnesit berechnet werden, wodurch ein Redoxpuffer mit dem Akronym FDM definiert wird, der eine wirksame Grenze für den möglichen fO_2-Wert darstellt, bei dem sich Ferroperiklaseinschlüsse in Diamant bilden können. Das Ferroperiklas- Fe^{3+}/Fe_{tot} -Verhältnis bei FDM nimmt ebenfalls mit dem Druck ab, was darauf hindeutet, dass sich nur wenige der Ferroperiklas-Einschlüsse in Diamanten im obersten Bereich des unteren Mantels gebildet haben könnten, und wenn, dann

müssen sie sich unter relativ oxidierenden Bedingungen aus Karbonatmineralen oder Schmelzen gebildet haben. Viele der anderen Einschlüsse haben ihre maximale Bildungstiefe in der Übergangszone. Einige der am stärksten oxidierten Einschlüsse könnten sich nur im oberen Erdmantel und nur aus stärker oxidierten Vorläufern gebildet haben, was darauf hindeutet, dass Ferroperiklas-Einschlüsse durch Reduktion von Karbonaten in Tiefen gebildet werden, die grösstenteils geringer sind als die des unteren Erdmantels. Interessanterweise schneiden die FDM-fO_2-Kurven für Ferroperiklaseinschlüsse mit Fe/(Fe+Mg)-Verhältnissen > 0.5 die Stabilität von $[Fe^{2+}, Mg]_2Fe^{3+}{}_2O_5$, was darauf hindeutet, dass dieses oder ein $[Fe^{2+}, Mg]_3Fe^{3+}{}_2O_6$-Hochdruckoxid in Diamant bei Bedingungen nahe dem unteren Mantel eingeschlossen sein könnte.

In einer separaten Studie, die während eines dreimonatigen Forschungsaufenthalts an der Universität Tohoku durchgeführt wurde, wurden die Stickstoffgehalte und die stabilen Stickstoffisotopenverhältnisse mehrerer wasserhaltiger Minerale und von Diamant nach einer Äquilibrierung unter hohem Druck und bei hoher Temperatur mit einer durch die Zersetzung von Glycin ($C_4H_5NO_2$) erzeugten Flüssigkeit gemessen. Phlogopit, Antigorit, Lizardit und Montmorillonit wurden bei 3 GPa und 500 °C äquilibriert. Die gewonnenen Proben enthielten N-Gehalte zwischen 0.35 und 2.14 Gew.-%, die im Vergleich zum Glycin-Ausgangsmaterial mit ^{15}N angereichert waren. Dies deutet darauf hin, dass der Durchgang von N-haltigen Flüssigkeiten durch wasserhaltige Mineralparagenesen in Subduktionszonen eine N-Isotopenfraktionierung im Mantel verursachen könnte. Diamanten wurden auch aus Graphit in Gegenwart eines Fe-Ni-S-Katalysators und Glycin bei 13 GPa und 1700 °C synthetisiert. Es wurde festgestellt, dass sich der Stickstoff gleichmäßig zwischen Diamant und dem koexistierenden metallischen Katalysator verteilt, der Diamant jedoch im Vergleich zum Glycin-Ausgangsmaterial an ^{15}N verarmt ist. Dies deutet darauf hin, dass während des Diamantwachstums koexistierende Flüssigkeiten zunehmend mit ^{15}N angereichert werden.

Chapter 1

Introduction

Diamonds are important carriers of information from the Earth's deep interior. In recent decades a series of minerals have been found sealed as inclusions in diamonds from different cratonic settings (e.g. Russia, Australia, Africa and Canada) that appear to come from the convecting mantle i.e. to have a sublithospheric origin. The unique unreactive containment of the diamond host makes it possible for minerals that would only be expected to form at particular depths in the deep mantle, to be transported to the surface without undergoing chemical exchange. In fact, residual pressure on the inclusions from the diamond host has even made it possible for high pressure mineral structures to be preserved if the inclusions remain closed (Nestola et al. 2017, 2018). Some inclusions, based on their chemical compositions, have been proposed to come from the lower mantle (Kaminsky 2012 and references therein). The lower mantle, which extends from 660 km to 2891 km depth, comprises more than half (e.g. ~56%) of the total volume of our planet and has to date been mainly investigated through seismological observations, theoretical calculations and high pressure-high temperature (*HP-HT*) experiments. Despite the lower mantle making up so much of the Earth's interior and likely playing a central role in Earth's geodynamic processes, as well as being its largest geochemical reservoir, its composition and structure are not well known. If inclusions in diamonds could be unequivocally linked to the lower mantle or to specific levels in the lower mantle, then this could reveal not only information on the composition

and mineralogy at these depths but also on diamond forming processes that are part of the deep volatile cycle of the Earth. One of the first minerals to have been identified as a potential lower mantle inclusion in sublithospheric diamonds was ferropericlase $(Mg,Fe)_{1-x}O$ (Scott Smith et al. 1983; Wilding et al. 1991; Harte and Harris 1994; Sobolev et al. 1999; Harte et al. 1999; Davies et al. 1999, 2004; Stachel et al. 2000; Zdgenizov et al. 2001; Kaminsky et al. 2001, 2009a; Hayman et al. 2005; Tappert et al. 2005a, 2009a; Donnelly et al. 2007; Stachel and Harris 2008; van Rythoven and Schulze 2009; Kaminsky 2012; Harte and Hudson 2013), where the x accounts for the fact that iron is present in both Fe^{2+} and Fe^{3+} oxidation states. Experimental studies have shown that in addition to bridgmanite, ferropericlase is likely to be one of the major minerals in the lower mantle, making up for 16-20 % of its volume, if the bulk composition of the lower mantle is similar to that of the upper mantle (Ringwood 1991; Kesson et al. 1998; Hirose 2002; Irifune et al. 2010). Ferropericlase frequency as an inclusion in sublithospheric diamonds, its significant range in iron content and its variation in ferric iron content, which may be linked to a spinel ferrite exsolution assemblage that it sometimes contains (Harte et al. 1999; Anzolini et al. 2019, 2020; Wirth et al. 2014; Kaminsky et al. 2015a; Palot et al. 2016; Nestola et al. 2016a), naturally raise questions as to how ferropericlase may have formed and what processes may exist in the mantle to cause these variations. Experimentally, understanding the phase relations of ferropericlase with respect to pressure, *P*, temperature, *T*, and oxygen fugacity (fO_2) conditions, can provide us with insight into the deep diamond formation process, during which the inclusions last equilibrated with the mantle. Furthermore, the study of subsequent mineral exsolution within the inclusions might provide information on the *P*-*T* path of exhumation.

If the inclusions in a diamond can provide sufficient information to decipher where in the Earth the diamond formed, then the diamond itself can provide further constraints on a very important topic: the deep-volatile cycle. The isotopic composition of the diamond can inform us on where the carbon originated and therefore of the likely pathway or cycle of carbon in the Earth. However,

diamond can also potentially give information on the cycle of nitrogen, which is the most common impurity in diamond. The origin of nitrogen in the interior and its cycle are poorly explored but have important implications for the subduction process and the formation of the atmosphere (Busigny et al. 2003; Goldblatt et al. 2009; Halama et al. 2010, 2014; Busigny and Bebout 2013; Johnson and Goldblatt 2015; Wordsworth 2016; Yoshioka et al. 2018; Mysen 2019).

In this introductory chapter, the relevance of the inclusion in diamond to our understanding of the Earth interior will be presented, with special attention to ferropericlase. Leading up to that, the reader will be introduced to the ground knowledge of how we understand the Earth's interior to be and how that information has been acquired. Both for diamond formation processes and ferropericlase Fe^{3+} content, fO_2 plays a crucial role, therefore an insight to oxygen fugacity and our understanding of how it varies within our planet is provided. The controversial origin of ferropericlase inclusion in diamonds is then extensively discussed presenting a compilation of the existing knowledge acquired to this day. Finally, nitrogen and its deep cycle into the Earth's interior is here summarized to frame the work that has been done during a three months visit to Tohoku University in Japan.

1.1 Earth's interior: what do we know

One of the biggest challenges scientists face when investigating the Earth's interior is the lack of samples that can allow the direct observation of what the inner layers of our planet are made of. Mantle xenoliths are fragments of the mantle brought to Earth's surface during volcanic eruptions. They are common in alkalic and potassic mafic magmas as well as in kimberlite pipes. The deepest mantle xenolith rock samples are found in kimberlitic magmas but come from depths of less than 300 km (Beyer and Frost 2017). Furthermore, mantle xenoliths come from the conductively cooling lithospheric mantle and have generally undergone phases of partial melting and

metasomatism since being part of the underlying convecting asthenosphere (Anderson and Bass 1984, Haggerty 1995, Frost et al. 2008). Mafic and ultramafic magmas form from melting of the asthenosphere mantle but interpreting the composition of the mantle from which they came from is complicated by the melting processes itself, as most melts are an assimilation of individual partial melts from varying depth and lithologies.

On the other hand, sublithospheric diamond inclusions have the potential to sample regions of the asthenospheric upper mantle, transition zone and even possibly the lower mantle (e.g. Kaminsky 2012 and references therein). Such inclusions not only provide information on what the mantle is made from at greater depths but because they last equilibrated with the mantle as the diamond formed, they also record conditions prevailing during the diamond forming process. A key parameter in this respect is the oxygen fugacity, which is important for understanding the nature of the carbon-bearing liquids from which the diamonds formed. However, despite being metaphorically regarded as "messengers from the interior of the Earth" the diamond "messages" are never so plain and clear, and require thorough experimental investigation to be correctly deciphered (Kaminsky 2012 and references therein). Experiments are required, for example, to determine the depths at which such inclusions may have formed. Even before this, however, some knowledge of the likely structure of the interior and what its deeper layers may be composed of is required in order to have any idea of where such inclusions may have originated.

Geophysical methods have played a fundamental role in painting a more complete picture of our planet's interior (Figure 1.1). Remote sensing of Earth's inaccessible interior has allowed properties, such as density, electrical conductivity, and the velocities of seismic waves produced by earthquakes, to be determined as a function of depth both as global averages and on a regional basis (Dziewonski and Anderson 1981, Kennett and Engdahl 1991, Kennet et al. 1995). Using travel-time curves of the time taken for seismic waves to arrive at a seismometer as a function of

distance from the earthquake, Bullen (1942) proposed a spherically symmetric 'shell model' of the Earth's interior. The model shows the Earth to be composed of layers with distinguishing velocity features, namely the crust, the upper mantle (UM), transition zone (TZ), lower mantle (LM), outer and inner core. The large catalogue of body-wave travel times and normal mode observations was later compiled to obtain spherically symmetrical (1D) Earth models of P and S velocity and also density as a function of depth, such as the preliminary reference Earth model (PREM, Dziewonski and Anderson 1981), IASP91 (Kennett and Engdahl 1991) and AK135 (Kennet et al. 1995). In these models the interior was separated into depth intervals, similar to those defined by Bullen, each separated by seismic discontinuities, the depths of which were determined from studies of reflected and converted seismic waves. A central task of modern mineral physics has been to invert the information on seismic velocities and discontinuities into a mineralogical model of the interior.

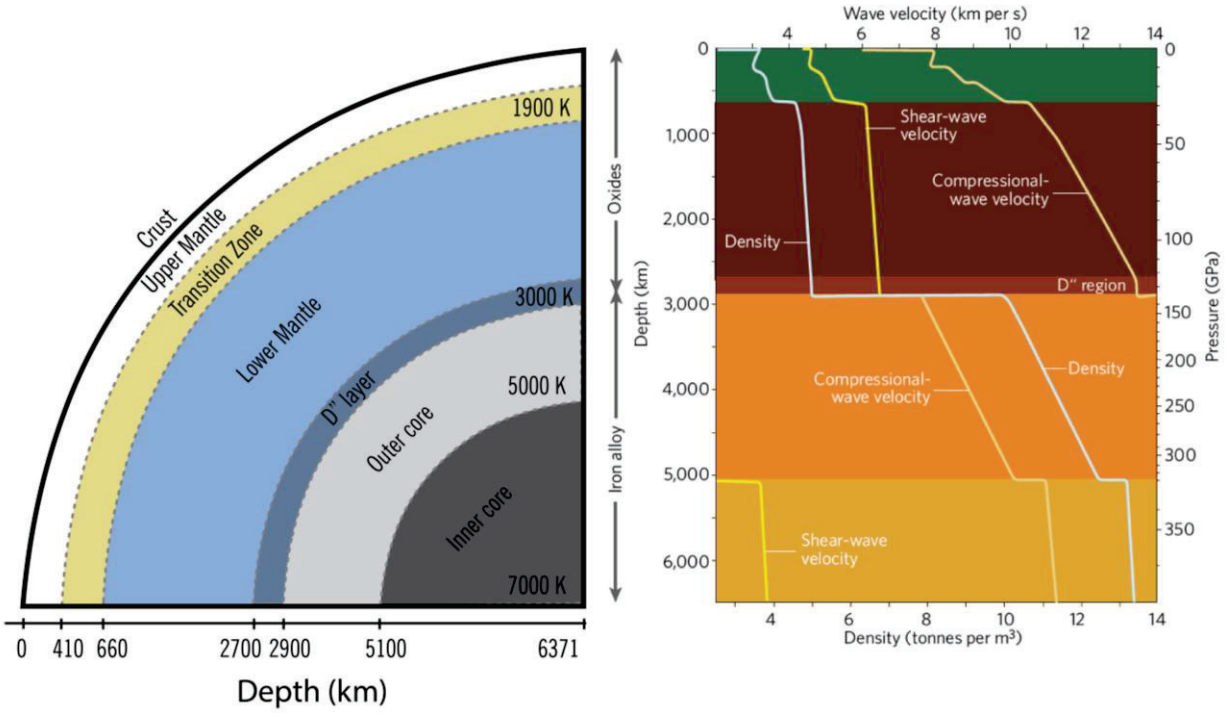

Figure 1.1 : Density and velocity profile of Earth (Dziewonski and Anderson 1981). Figure modified after Romanowicz (2008).

This requires two types of experimental data: petrological information on the mineralogy that the mantle is likely to have as a function of depth and bulk composition and information on the variation with pressure and temperature of the elastic properties of minerals that can be used to forward calculate the variation of density and seismic wave velocities of a given phase assemblage with depth (Ita and Stixrude, 1992; Stixrude and Lithgow-Bertelloni, 2012). The comparison of such mineral physics predictions with models like PREM can be used to confirm whether mantle properties are consistent with a particular average bulk composition at a particular depth (Anderson and Bass 1984; Ita and Stixrude 1992).

A reasonable assumption for the composition of the mantle at depth is that it is the same as that of the upper mantle, reflected by primitive mantle xenoliths found at the surface. As xenoliths are sections of the lithospheric mantle that have undergone melt extraction and metasomatism, however, Ted Ringwood came up with the pyrolite composition for the primitive asthenospheric mantle consisting of one part of basalt and four parts of harzburgite (Ringwood 1962). Many experimental studies have examined the mineralogy of the pyrolite composition throughout the mantle (Ringwood 1991; Kesson et al. 1998; Hirose 2002; Irifune et al. 2010). At lower mantle conditions, the major phases that form are orthorhombic Mg-silicate perovskite or bridgmanite $(Mg,Fe,Al)(Si,Al)O_3$ (~80 volume %), cubic ferropericlase $(Mg,Fe)_{1-x}O$ (~13 volume %), and cubic calcium-silicate perovskite $CaSiO_3$ (~6 volume %). Recent studies that use mineral physics model to calculate seismic velocities expected for these minerals at depth (Figure 1.2) indicate that measured seismic velocities at least at the top of the lower mantle are consistent with the lower mantle having a pyrolite composition (Kurnosov et al. 2017; Tsuchiya et al. 2020). In fact, one of the best approaches to model the velocities of the mantle is to describe both the thermodynamic stability and the elastic properties of each mineral in an assemblage with the same consistent set of parameters. In this way data from different sources (e.g. X-ray diffraction equation of state,

ultrasonic measurements, Brillouin spectroscopy, phase equilibria, calorimetric data) can be combined to provide redundancy in the refined data set (Stixrude and Lithgow-Bertelloni 2005).

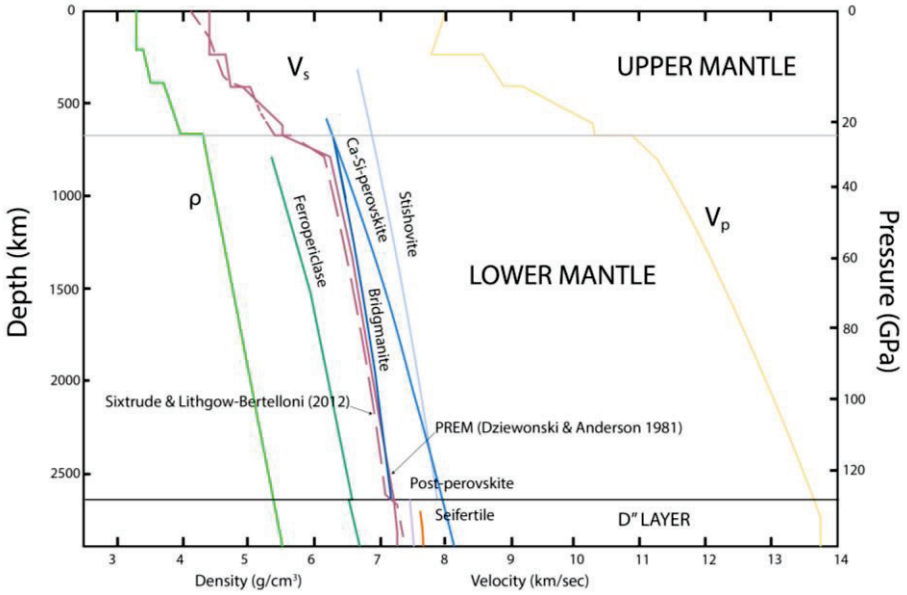

Figure 1.2: Pyrolite mantle seismic wave velocity and density profiles as a function of depth. Compressional wave velocities (Vp) are shown in yellow while shear-wave velocities (Vs) in purple and the density (ρ) of pyrolite in g/cm^3 in green. The velocities of the major lower-mantle minerals also are reported for comparison. This image has been modified after Kaminsky 2017.

Such models for mantle mineralogy indicate that in the lower mantle the Mg_2SiO_4 component, which dominates the mineralogy of the upper mantle and transition zone, breaks down into an MgO component in ferropericlase and an $MgSiO_3$ component in bridgmanite. On this basis a lower mantle origin was proposed for ferropericlase inclusions in diamonds because it would not be stable in a pyrolite assemblage at lower pressure conditions (Harte and Harris 1994; Harte et al. 1999; Kaminsky 2012; Harte and Hudson 2013). Other inclusions with the same chemistry as expected for bridgmanite and $CaSiO_3$ perovskite in the lower mantle have also been found in diamonds and, although controversial, in some studies it has been proposed that the high pressure structures of these minerals are preserved by the residual pressure provided by the diamond host (Nestola et al. 2018). The structure of ferropericlase, however, does not change at high pressure and although ferropericlase would not be stable in a pyrolite assemblage at shallower depths than

the lower mantle, it could form from other compositions that were isolated from the mantle. For this reason, it makes sense to examine other compositional aspects of ferropericlase that could provide information on the conditions under which it was formed.

1.2 Oxygen fugacity and redox state

Oxygen fugacity *(f*O_2*)* is a thermodynamic state function that is typically used in petrology as a scale to describe the redox state of an environment, i.e. how oxidizing or reducing it is. As the redox state influences the proportions of elements in different oxidation states, it can affect the phase relations, melting properties, coexisting gas compositions and transport properties in the Earth (e.g. Frost and McCammon 2008; Stagno and Fei 2020). Oxygen fugacity is the effective partial pressure of O_2, but it is more useful to consider it as a measure of the chemical potential of oxygen in reactions where reagents and products contain the same elements with different oxidation states (Eugster 1957). It is a measure of the free energy change between the oxidized and the reduced portions of, for example, a mineral assemblage in a rock or experimental charge (Frost 1991). It is a common misconception that *f*O_2 is describing the behaviour of some amount of free oxygen present in the system. Even in systems containing oxidized fluids the proportion of free O_2 is vanishingly small and *f*O_2 is instead describing the oxygen reactivity in mineral assemblages or how easily oxygen can be passed from one variably valent element to another.

The oxidation state of the Earth's mantle can be related to the *f*O_2 through mineral equilibria and it is commonly measured using equilibria involving Fe^{3+} and Fe^{2+} components, as iron is by far the most abundant element with a variable oxidation state preserved in rocks. While Fe^{2+} substitutes for Mg^{2+} in minerals, Fe^{3+} generally enters smaller or interstitial cation sites that can require charge balance if another 3+ cation is not being replaced. This can lead to further effects such as, for example, the dehydrogenation of amphiboles (e.g. Phillips et al. 1988; Dyar et al.

1992) and in some minerals can lead to the creation of cation vacancies (e.g. Hazen and Jeanloz 1984). The formation of vacancies in this way can result in transport properties, such as electrical conductivity, diffusivity and rheology, becoming sensitive to fO_2 (Cline et al. 2018).

Considering the redox equilibrium:

$$2FeO + ½\ O_2 = Fe_2O_3 \quad (1)$$

where the iron oxides are components in mineral phases A and B, then the fO_2 can be calculated from the condition of equilibrium:

$$logfO_2 = 2\frac{\Delta G^{o}_{P,T}}{RTln(10)} + 2log\frac{a^{A}_{Fe_2O_3}}{(a^{B}_{FeO})^2} \quad (2)$$

where $\Delta G^{o}_{P,T}$ is the standard state Gibbs free energy of the pure end member reaction at the P and T of interest, R is the gas constant, $a^{A}_{Fe_2O_3}$ is the activity of the Fe_2O_3 component in phase A and a^{B}_{FeO} is the activity of the FeO component in phase B. This relation might intuitively suggest that a high fO_2 corresponds to a high activity, i.e. concentration, of Fe_2O_3 in phase A. At room and relatively low pressures (< 3 GPa) this is the case and at an fO_2 compatible with the formation of iron metal, for example, mantle minerals and melts contain very small concentrations of Fe_2O_3 (Frost and McCammon 2008 and references therein). However, in the deeper mantle, the formation of denser crystal structures that can stabilize Fe_2O_3-bearing components results in changes in $\Delta G^{o}_{P,T}$ that allow significant Fe_2O_3 concentrations to be present in minerals at low fO_2 (McCammon 2005a, 2005b). In fact, due to the energetically favourable coupled substitution of Al and Fe^{3+} into the crystal structure of the lower mantle mineral $(Mg,Fe)(Si,Al)O_3$ bridgmanite, this mineral can contain over 50 % of its iron as Fe_2O_3, i.e. $Fe^{3+}/Fe_{tot} > 0.5$, even in equilibrium with metallic iron (McCammon et al. 1997, 2004b, 2005a; Lauterbach et al. 2000; Frost et al. 2004). As metallic iron stability implies the lowest fO_2 at which either Fe_2O_3 or FeO can be stable in mineral phases, then the requirement for bridgmanite to have such a high Fe^{3+}/Fe_{tot} ratio at these conditions would drive the charge disproportionation reaction:

$$3\,FeO \quad = \quad Fe_2O_3 \quad + \quad Fe \qquad (3)$$
$$\text{bridgmanite} \quad \text{bridgmanite} \quad \text{alloy.}$$

This means that although upper mantle rocks appear to contain on average less than 0.3 wt % Fe_2O_3 (Canil and O'Neill 1996; McCammon 2005a), the lower mantle may contain approximately 4 wt. % Fe_2O_3 (Figure 1.3).

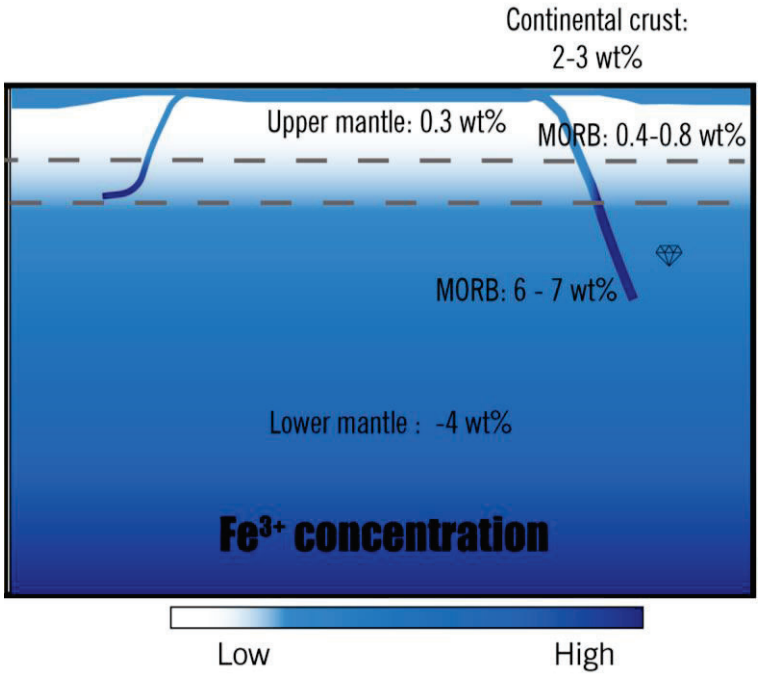

Figure 1.3: The Fe^{3+} concentration in the Earth's mantle is here expressed as weight % Fe_2O_3. The composition of subducted slabs is simplified to that of mid-ocean ridge basalt (MORB). This image was modified after McCammon 2005b.

1.3 Redox buffers

As can be seen in equations (1) and (2), if the iron components of a redox equilibrium are pure end-members, then their activities would be unity and the fO_2 becomes dependent only on $\Delta G^{o}_{P,T}$, which for any equilibrium will change only with P and T. This is the basis of a redox buffer, which comprises a mixture of pure phases from both sides of such an equilibrium. This mixture imposes a fixed value of fO_2 for a given P and T.

Redox buffers can be used to constrain the fO_2 in experiments by employing double capsules, where an H_2O saturated buffering assemblage is placed in an outer capsule, usually made of gold, and transfers the fixed fO_2 to the inner capsule, usually made of platinum, by the diffusion of H_2 through the inner capsule wall. As shown in Figure 1.4, the *T* dependences of the redox buffer fO_2 values are sub-parallel to each other. The same occurs for the pressure dependences. In order to remove the *P* and *T* effects from absolute fO_2 values it is common practice to express values of oxygen fugacity relative to a reference buffer, e.g. ΔFMQ = -2 indicates an oxygen fugacity that is 2 log units below the fayalite-magnetite-quartz, FMQ, buffer. This provides a framework with recognizable markers that are to a large extent independent of the specific *P* and *T*. The most commonly employed solid-state redox buffering equilibria used in petrology are (Frost 1991):

IW:
$2\,Fe + O_2 = \text{“FeO”}$
iron wüstite

WM :
$\text{“FeO”} + ½\,O_2 = Fe_3O_4$
Wüstite magnetite

QIF:
$Fe + SiO_2 + O_2 = Fe_2SiO_4$
iron quartz fayalite

FMQ:
$3Fe_2SiO_4 + O_2 = Fe_3O_4 + 3\,SiO_2$
fayalite magnetite quartz

Ni-NiO:
$2\,Ni + O_2 = 2\,NiO$

MH:
$4\,Fe_3O_4 + O_2 = 6\,Fe_2O_3$
magnetite hematite

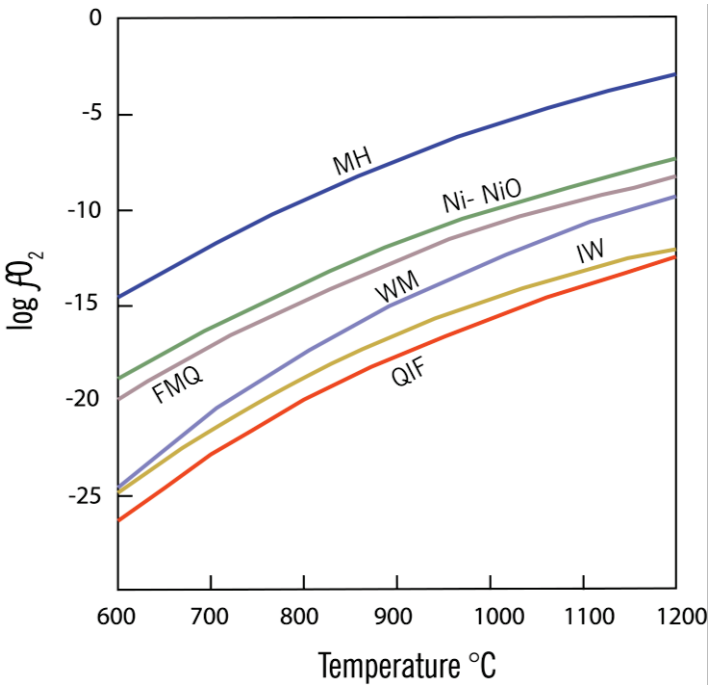

Figure 1.4: Log fO_2 of the buffer equilibria plotted against temperature at 1 bar. This image was modified after Wood et al. 1990.

1.4 The redox state of present-day mantle

The fO_2 of a mantle assemblage, such as a xenolith, can be determined with an equilibrium similar to equation (2) and using the activities of ferric and ferrous iron components in the different mineral phases. This requires calibrations of the standard state Gibbs free energy for the particular equilibrium and activity composition relations for the minerals in question (O'Neill and Wall 1987; Nell and Wood 1991; Ballhaus et al.1991). Using such an oxythermobarometer and employing iron components in the minerals spinel, orthopyroxene and olivine in upper mantle xenoliths it has been possible to show that upper mantle rocks exhibit oxygen fugacities in the range ΔFMQ ±2 (Brandon and Draper 1996; Rohrbach et al. 2007; Frost and McCammon 2008; Kelley and Cottrell 2009; Malaspina et al. 2010; Stagno and Fei 2020). Local variations in fO_2 are likely caused by processes such as partial melting, mantle metasomatism and potentially the incorporation of recycled oxidized material during subduction (Rohrbach and Schmidt 2011; Berry et al. 2013). At pressures above 2 GPa (60 km) spinel-peridotite assemblages transform to garnet-peridotite and an oxythermobarometer employing an equilibrium involving garnet, olivine and orthopyroxene can be used to determine the fO_2 of xenoliths that come from between approximately 60 and 250 km. Such measurements indicate a general trend of decreasing fO_2 with increasing depth (Ballhaus and Frost 1994; Woodland et al. 2006; Frost and McCammon 2008; Foley 2008; 2011; Stagno and Fei 2020). This arises due to the volume change of the oxythermobarometer equilibrium as a smaller molar volume is achieved by putting ferric iron into garnet compared to ferrous iron into olivine and orthopyroxene (Frost and McCammon 2008; Stagno and Fei 2020). At depths of 200 - 250 km mantle fO_2 values are mainly in the range ΔFMQ -2 to -4 (Frost and McCammon 2008; Stagno and Fei 2020).

Mantle fO_2 is driven down with pressure by the negative volume change of the reaction as ferric iron enters garnet. Although there are no mantle rocks from depths significantly deeper than 250

km, mantle fO_2 cannot continue to decrease at higher pressures because eventually an fO_2 is reached where Ni-Fe alloy will start to precipitate from the mantle silicates (O'Neill and Wall 1987; Rohrbach et al. 2007; Frost and McCammon 2008). At these conditions, projected to be at a pressure of approximately 10 GPa or just over 300 km depth, average mantle fO_2 should become buffered at values in the range from IW to ΔIW -1, as shown in Figure 1.5. As described previously, for a pyrolitic lower mantle, experiments have shown that the energetically favourable substitution of ferric iron into $(Mg,Fe)(Al,Si)O_3$ bridgmanite results in bridgmanite Fe^{3+}/Fe_{tot} ratios greater than 0.5 in equilibrium with metallic iron (Frost et al. 2004). This should ensure that, at least in the top of the lower mantle, the fO_2 should also be below IW, with Fe-Ni metal forming through charge disproportionation as in Equation 3. Experimental results show that for a pyrolitic lower mantle where the bulk O/Fe ratio is the same as the upper mantle, ~ 1 wt.% metal with a composition of 88 wt.% Fe, 10 wt.% Ni and 1 wt.% S would be present coexisting with bridgmanite having approximately 50 % of its iron in the ferric state (Frost et al. 2004; Frost and McCammon 2008).

We can delimit the range of fO_2 at which diamonds can form in the mantle, with the lower end being the conditions where Fe-Ni metal becomes stable and the upper end where diamonds would be oxidized to form carbonate. At upper mantle pressure this maximum fO_2 is determined by the so called EMOD buffer:

$$\underset{\text{Enstatite}}{MgSiO_3} + \underset{\text{Magnesite}}{MgCO_3} = \underset{\text{Olivine}}{Mg_2SiO_4} + \underset{\text{Diamond}}{C} + O_2 \qquad (4)$$

The fO_2 of this equilibrium and equivalent equilibria that become stable at higher pressures are indicated by the gold curve in Figure 1.5.

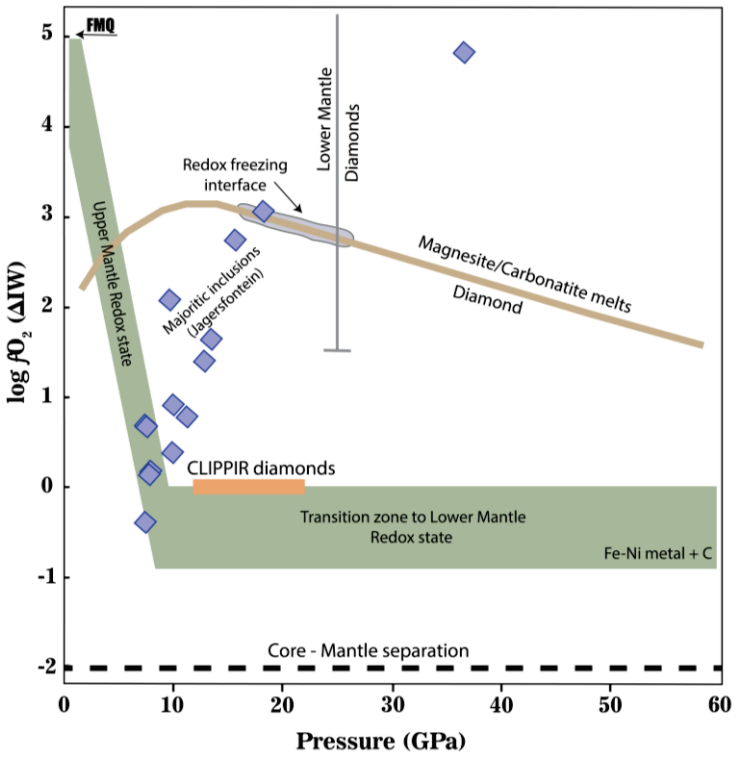

Figure 1.5: Log fO_2 (relative to IW buffer) as a function of pressure for a pyrolitic mantle assemblage with an Fe/O content typical for the top of the lower mantle (green shaded region). The gold curve indicates the fO_2 at which diamond would be oxidized to carbonate minerals or melts. The orange box displays the estimated fO_2 of metal-bearing "CLIPPIR" (Cullinan-like, large, inclusion-poor, pure, irregular, resorbed) diamonds (Smith et al. 2016a). The grey vertical line shows the range of fO_2 from ferropericlase inclusions in diamonds (Kaminsky et al. 2015). The blue diamond symbols show the fO_2 estimated from majorite inclusions in diamonds (Kiseeva et al. 2018). The gold curve indicates the fO_2 at which diamonds and carbonate (magnesite) are in equilibrium with a mantle mineral assemblage (Stagno 2019). This image was modified after Stagno and Fei 2020.

This curve has been determined through experimental studies in which diamonds and solid carbonate coexist along with silicate minerals of the transition zone and lower mantle (see Stagno 2019 and references therein). The range of fO_2 over which diamonds can form reaches a maximum of ΔIW +3 to -1 at the base of the upper mantle (~14 GPa) but is projected to contract at higher pressures.

At depths greater than 250 km the only natural samples available from the mantle are inclusions in diamonds. Sublithospheric, or superdeep, diamonds are identified principally when their inclusions are judged to reflect assemblages expected in the deeper mantle. One of the most reliable index minerals in this respect is majoritic garnet, as the substitution of Al for Si and Mg in these garnets only occurs at pressures significantly above 200 km and can be calibrated as a function of depth (Collerson et al. 2010; Kiseeva et al. 2018; Thomson et al. 2021). However, ringwoodite, $CaSiO_3$ walstromite, ferropericlase, jeffbenite (Nestola et al. 2016b), Fe-Ni alloys, carbides and majoritic garnets have all be used to argue for a superdeep origin (Scott Smith et al.1984; Harte and Harris 1994; Harris et al. 1997; Harte et al. 1999; McCammon 2001; Kaminsky et al. 2001, 2013, 2015a,b; Hayman et al. 2005; Brenker et al. 2005, 2007; Wirth et al. 2007, 2009; Walter et al. 2008, 2011; Harte 2010, Harte and Richardson 2012; Kaminsky 2012; Pearson et al.2014; Nestola 2017). As shown in Figure 1.5, Cullinan-like, large, inclusion-poor, pure, irregular, resorbed (CLIPPIR) diamonds that contain Fe-Ni alloys can be safely considered to form at conditions close to IW. It is feasible to draw similar conclusions about the fO_2 conditions under which the other inclusions were formed by analysing their Fe^{3+}/Fe_{tot} ratio and calibrating oxy-thermobarometry equilibria using high pressure experiments. Assumptions have to be made, however, on the compositions of other minerals that the inclusions may have been in equilibrium with before the entrapment occurred, because many inclusions are monomineralic and if they are not, there is a strong likelihood that they would have reacted after capture due to changes in *P* and *T* condition during exhumation. As shown in Figure 1.5 this was attempted for a series of majorite-garnet inclusion by Kiseeva et al. (2018). The results show an increasing trend in fO_2 with pressure, rising to a value that is clearly outside of the range where diamond should be stable. The thermodynamic data for the oxy-thermobarometry equilibrium used were only estimated in the mentioned study, however, as to date no high pressure experimental study exists through which to calibrate a majorite-garnet oxythermobarometer. Figure 1.5 also shows the range of fO_2 estimated

from ferropericlase inclusions in diamonds. This trend also extends well out of the diamond stability field, an issue that is examined extensively in this thesis.

1.5 The formation of diamonds

Sublithospheric or superdeep diamonds comprise only around 6 % of all diamonds (Stachel and Harris 2008; Walter et al. 2011; Kaminsky 2012; Pearson et al. 2014; Smith et al. 2016; Nestola 2017; Nestola et al. 2018). The remaining 94% are of a "shallow" origin of less than 250 km in the Earth (Richardson et al. 1984; Stachel and Harris 2008). Shallow diamond formation is favoured by high pressures, > 5 GPa, and relatively low temperatures, 900-1300 °C (Stachel and Harris 2008; Stachel and Luth 2015; Nimis 2022), therefore, regions with very low geothermal gradients such as the geologically old parts of continental lithospheric mantle keels (i.e. cratons), are the main locations of diamond formation. Cratons are composed of crustal basement rocks, such as granites and gneisses that are more than ~1.5 billion years old and the lithospheric mantle roots beneath them can extend to depths of more than 250 kilometres, creating the perfect environment for diamond nucleation. Diamonds that form within these continental roots are known as lithospheric diamonds and are carried up to the surface, as with all diamonds, by rare high-Mg potassic magmas i.e. kimberlites and lamproites (Gurney et al. 2010). In Figure 1.6 it can be observed how as a consequence of relaxed geotherms, the graphite-diamond transition is raised to shallower depth within subcratonic lithosphere, creating a diamond stable window where cratonic roots extend down into the diamond stability field ~ 120-250 km depth (Stachel and Harris 2008).

There are essentially two redox reactions that could in principal produce diamonds in the lithospheric mantle (Rosenhauer et al. 1977; Eggler and Baker 1982; Luth 1993): (*i*) the reduction of CO_2 or carbonate components dissolved in either melts or fluids (Shirey et al. 2019 and

references therein); (*ii*) the oxidation of reduced carbon in the form of methane or other higher hydrocarbons (Thomassot et al. 2007; Matjuschkin et al. 2020).

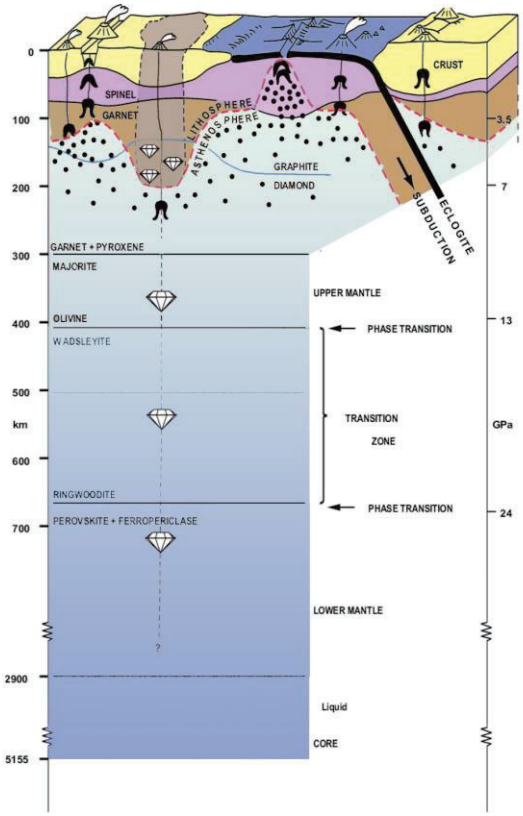

Figure 1.6: Detailed view of Earth's crust, mantle, and core from the top down. Modified after Stachel et al. 2005

The problem, however, is that for diamonds to form simply in either of these ways, some other component has to either accept or provide oxygen. In many studies it is assumed that different oxidation states of iron fulfil this role (e.g. Rohrbach and Schmidt 2011) but as pointed out by Luth and Stachel (2014), most diamonds represent carbon concentrations that are too large for iron in the surrounding mineral or melt phases to have provided the complementary redox reaction, regardless of whether this involves oxidation or reduction. Instead, Luth and Stachel (2014) propose that diamonds precipitate on cooling of C-O-H fluids without involving redox reactions with external components. This implies a reaction such as:

$$CH_4 + CO_2 = 2H_2O + 2C \qquad (5)$$

that would be expected to shift to the right on cooling as fluids penetrate the conductively cooling lithospheric mantle and travel up the thermal gradient.

For sublithospheric diamonds there is no comparable thermal gradient for them to form along, unless that occurs on the underside of subducting lithosphere. The presence of carbonate inclusions in some sub-lithospheric diamonds (Brenker et al. 2007; Walter et al. 2008; Kaminsky et al. 2009; Wirth et al. 2009; Kaminsky 2012) indicates that despite fO_2 being expected to decrease with pressure in the upper mantle, it is still possible for diamonds to form at higher fO_2 conditions. This is thought to be possible, for example, if the local redox environment is perturbed by the influx of carbonate-bearing material from a subducting slab. This mechanism creates an fO_2 increase in small mantle domains within "redox fronts" around subducting lithosphere (Rohrbach and Schmidt 2011; Palyanov et al. 2013). The diamond forming mechanism proposed for this scenario is reduction by oxidation of iron components, either FeO or Fe in alloys, so called redox freezing (Rohrbach and Schmidt 2011). Thomson et al. (2016) demonstrated that carbonate melts from the originally basaltic section of a subducting slab, would be reduced on entering the overlying mantle. The problem arises again, however, as to whether mantle iron components would have sufficient buffering capacity to produce superdeep diamonds, which still represent a large localized concentration of carbon (Luth and Stachel 2014). It is also not clear whether the carbon isotopes of superdeep diamonds are compatible with such a carbonate origin. Mixing between slab derived carbonates and mantle derived CH_4-bearing fluids would be a possible alternative.

Not all superdeep diamonds contain carbonates, however. The iron-rich alloys found in CLIPPIR diamonds, which are known to be superdeep because they also contain majorite-garnet (Smith et al. 2016), are consistent with diamond formation close to the IW buffer as expected for an average mantle at these conditions. Smith et al. (2016) found thin fluid jackets of CH_4 and films of CH_4+H_2 around the metallic inclusions in CLIPPR diamonds. This observation is consistent with preserved

methane recovered in synthetic diamonds grown in molten Fe-Ni alloys as a result of hydrogen inadvertently dissolved in the metallic liquid (Smith and Wang 2016). Smith et al. (2016) reported for the first time measurable CH_4 in mixed-habit diamonds from Zimbabwe. The observation of these inclusions confirms that natural diamond formation is not restricted to formation involving carbonates (Navon et al. 1988; Luth 1993; Navon 1999; Cartigny et al. 2001a; 2001b) but that CH_4 bearing fluids percolating through the lithosphere possibly play an important role.

1.6 Ferropericlase: does it indicate lower mantle origin?

As stated previously, ferropericlase, (usually referred to as magnesiowüstite when Fe/[Fe+Mg] > 0.5), is the second most abundant phase (~20 vol%) in Earth's lower mantle, according to the pyrolite model (Ringwood 1991; Kesson et al. 1998; Hirose 2002; Irifune et al. 2010). However, in superdeep diamonds, ferropericlase makes up ~50 % of the inclusion population and is more frequently found than bridgmanite, considered to be the most abundant lower mantle mineral.

Oxides along the ferropericlase-magnesiowüstite solid solution have the rock-salt NaCl-type (B1) structure ($Fm\bar{3}m$ space group) consisting of interpenetrating fcc (face-centered-cubic) lattices that generate an alternating framework of both Mg^{2+}/Fe^{2+} cations and O^{2-} anions in octahedral coordination (Wicks and Duffy 2016). The complexity of this solid solution comes through the substitution of Fe^{3+}. The Fe-oxide end-member, wüstite, is non-stoichiometric due to Fe^{3+} substitution, and it is described with the general formula $Fe_{1-x}O$, where at 1 bar x is in the range 0.04-0.15, which corresponds to an Fe^{3+}/Fe_{tot} ratio between approximately 0.1 and 0.36 (Hazen and Jeanloz 1984). Non-stoichiometry characterizes the whole solid solution, however, and fper is also able to incorporate Fe^{3+} even at high- Mg contents (see paragraph 1.7).

When ferropericlase was first found in association with $(Mg,Fe)SiO_3$ within a single diamond from the Koffiefontein kimberlite, South Africa, the assemblage was considered to indicate a lower

mantle origin of the host diamond (Scott Smith et al. 1984). On this basis, similar inclusions have been thought to have a lower mantle origin and have been extensively reported from South Australia (Scott Smith et al. 1984; Tappert et al. 2009a); Brazil (Wilding 1991; Harte and Harris 1994; Harte et al. 1999; Hayman et al. 2005; Stachel and Harris 2008; Kaminsky et al. 2009a, 2001; Kaminsky 2012; Harte and Hudson 2013), Canada (Davies et al. 1999, 2004; Tappert et al. 2005a; Donnelly et al. 2007; van Rythoven and Schulze 2009), Russia (Sobolev et al. 1999; Zdgenizov et al. 2001) and West Africa (Stachel et al. 2000).

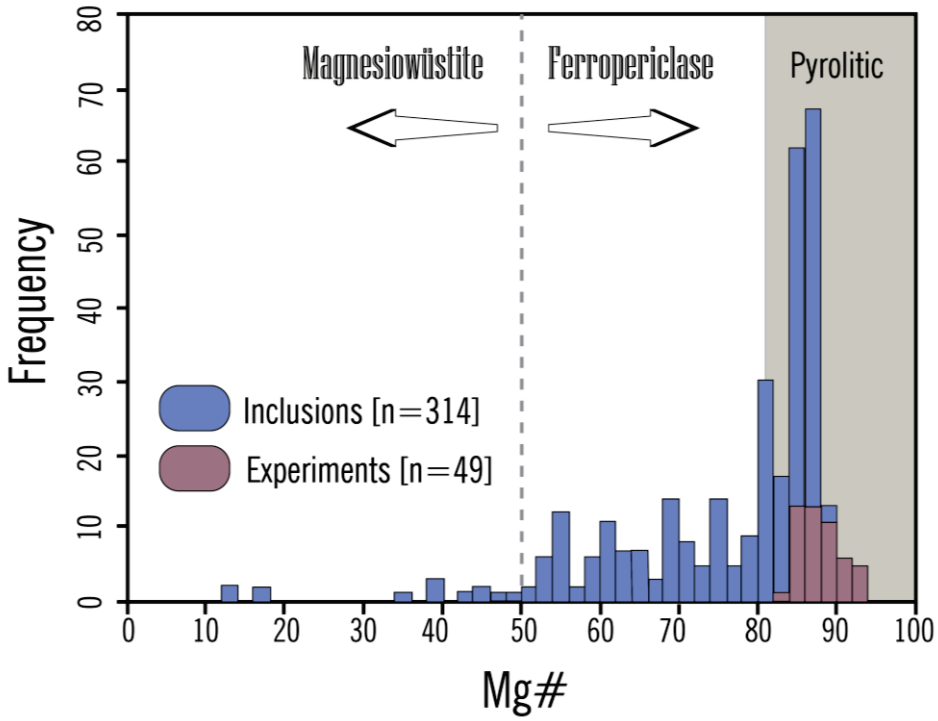

Figure 1.7: Mg# of (Fe,Mg)O inclusions in diamonds from localities worldwide are plotted in terms of frequency of finding for the specific composition. Selected experimental studies in pyrolite and fertile lherzolite KLB-1 compositions are also plotted to highlight the vast compositional range of the Fper with respect to the expected pyrolytic Mg value. Figure modified after Kiseeva et al. 2022

As shown in Figure 1.7, ferropericlase inclusions also cover a wide compositional range. Fe-Mg partitioning in the lower mantle does result in ferropericlase becoming more iron-rich with depth (Badro et al. 2003). Experimental results in pyrolitic systems indicate plausible Mg/ (Mg + Fe) ratios in the range 0.73–0.90 (e.g. Kesson and Fitz Gerald, 1992; Irifune et al. 2010). Although

natural samples occupy a much wider range in FeO content (0.36-0.90), the highest frequency in inclusions occurs for compositions that would be expected for the top of the lower mantle. Some rare samples extend to an Mg/ (Mg + Fe) ratio of 0.16 (Zedgenizov et al. 2014), i.e. close to the wüstite end-member. This extreme range in Fe-contents has led to propose in some studies a diamond origin in the D″ region of the base of the mantle (Harte et al. 1999). Nonetheless, critical voices, such as Gurney (1989) and later Stachel et al. (1998), have pointed out that the occurrence of ferropericlase inclusions is not an unequivocal indicator of a lower mantle origin as it is stable at *P-T* conditions throughout the Earth. It was proposed, for example, that ferropericlase parageneses could be explained by locally reducing conditions and low silica activity at shallower mantle depths (i.e. in the stability field of olivine), where the reduction of magnesite could result in an olivine-ferropericlase-diamond paragenesis (Stachel et al. 1998; 2000). Stachel et al. (2000) reported, for example, a contacting pair of ferropericlase and olivine inclusions. Brey et al. (2004) countered previous experimental arguments that the Na or Cr contents of ferropericlase were consistent with a lower mantle origin (Kesson and Gerald 1992), by showing that these could be achieved at upper mantle or transition zone conditions. Brey et al. (2004) argued for an origin in upper mantle or transition zone rocks through reduction of carbonates in otherwise highly depleted rocks such as dunites. This scenario was tested experimentally by Bulatov et al. (2019), who reported the simultaneous crystallization of ferropericlase and diamond during reduction of carbonate–silicate melts saturated in olivine at upper mantle conditions.

The Ni contents of ferropericlase inclusions decrease with increasing Fe content (Figure 1.8). When Fe-Ni metal is projected to form in the upper mantle at approximately 300 km depth, the Ni concentration would be expected to be initially high (60 mole %) but to decrease with increasing depth as more Fe metal reduces as the fO_2 decreases (Frost and McCammon 2008).The highest ferropericlase Ni contents appear to be broadly consistent with what would be expected for ferropericlase inclusions in the top portion of a metal saturated pyrolite lower mantle (Urakawa

1991; Irifune et al. 2010). If the inclusions were formed at even greater pressures, then Ni would be expected to become more lithophile compared to Fe (Li and Agee 1996), so it is unlikely that the Ni-content of ferropericlase would then decrease, as in Figure 1.8, in the lower mantle, even if Fe-Mg partitioning with bridgmanite causes the ferropericlase Fe-content to increase. Instead, Thomson et al. (2016) proposed that variable extents of oxidation of Fe-Ni metal by incoming carbonate melts in an otherwise ultramafic transition zone can explain the range of Fe and Ni contents in ferropericlase inclusions.

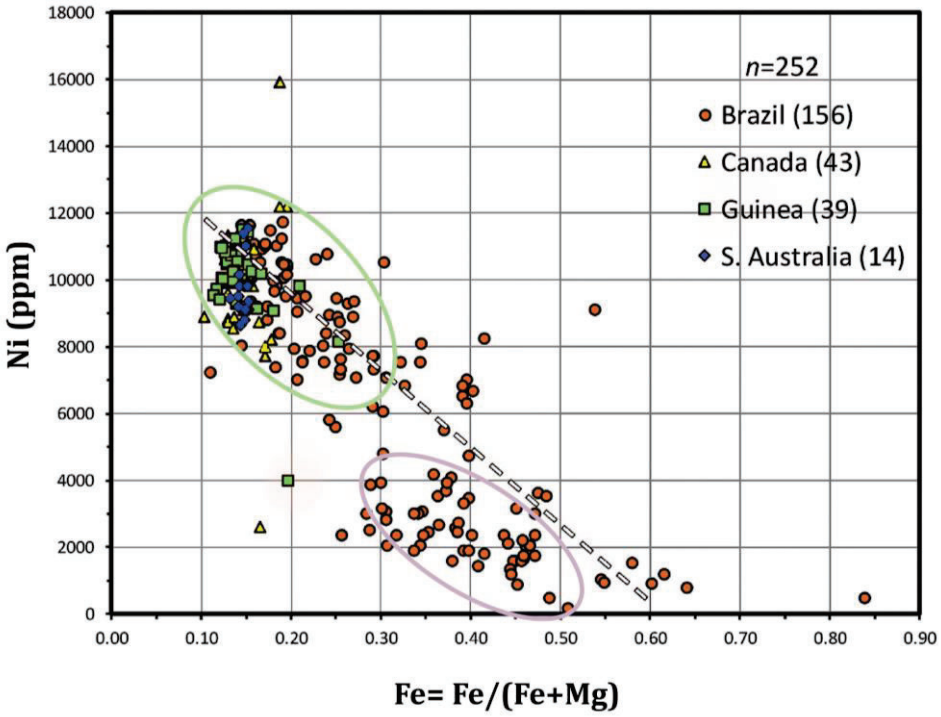

Figure 1.8: Relationship between the Fe and Ni content in ferropericlase inclusions in diamond. The white dashed trendline is taken from Kaminsky et al. (2020) , however, the dataset may be better described by two possible clusters of Ni concentrations. These are highlighted by the two coloured ellipses. This Figure was modified after from Kaminsky et al. 2020.

It is important to be able to understand the formation conditions of such inclusions as they provide some of the only direct evidence for the passage of carbon bearing fluids and melts in the deep mantle. Although several studies point to the possibility of ferropericlase inclusions being formed at depths shallower than the lower mantle, there is no geobarometer that can be used to demonstrate this categorically. Some of the best evidence comes from Stachel et al. (2000) who report touching

olivine and ferropericlase inclusions, however, these could still have formed during prograde reactions between bridgmanite and ferropericlase. In this thesis the stability of ferropericlase in the MgO-FeO-Fe_2O_3 system has been explored at high *P* and *T*, with the aim of constraining the formation conditions of ferropericlase inclusions.

1.7 Ferric iron content in (Mg,Fe)O

At room pressure the periclase-wüstite solid solution, which is referred to here for simplicity as ferropericlase or fper, regardless of the Fe/(Fe+Mg) ratio, has been studied quite extensively in the MgO-FeO-Fe_2O_3 system (Brynestad and Flood 1958; Katsura and Kimura 1964; Speidel 1967; Valet et al. 1975; Hilbrandt and Martin 1998) and significant literature also exists, particularly in the FeO-Fe_2O_3 subsystem, describing efforts to characterize the defect structure that accompanies ferric iron substitution (e.g. Roth 1960; Koch and Cohen 1969; Greenwood and Howe 1972; Burgmann 1975; Catlow and Fender 1975; Andersson and Sletnes 1977; Lebreton and Hobbs 1983; Hazen and Jeanloz 1984; Vallet and Carel 1989; Schweika et al. 1995;Welberry and Christy 1997; Dimitrov et al.1999, 2000; Welberry et al. 2014; Gavarri and Carel 2018). The substitution of ferric iron in fper is charge balanced through the creation of metal cation vacancies (V), and results in non-stoichiometry that can be described by the formula

$$\mathrm{Mg_z Fe^{2+}_{1-z-3x} Fe^{3+}_{2x} V_x O}.$$

At room pressure the $Fe^{3+}/\sum Fe$ ratio of fper varies strongly with oxygen fugacity, reaching a minimum where fper is in equilibrium with iron metal (Srecec et al. 1987; O'Neill et al. 2003) and a maximum where it coexists with spinel phases along the magnetite-magnesioferrite (Fe_3O_4-$MgFe_2O_4$) solid solution (Brynestad and Flood 1958; Katsura and Kimura 1965; Speidel 1967; Hilbrandt and Martin 1998). The addition of MgO to $Fe_{1-x}O$ in equilibrium with iron metal drives

the fper $Fe^{3+}/\sum Fe$ ratio down, whereas when $Fe_{1-x}O$ is in equilibrium with magnetite-magnesioferrite the $Fe^{3+}/\sum Fe$ ratio goes up as MgO is added (Jung et al. 2004).

McCammon (1993) performed the first rigorous study on the effect of pressure on Fe^{3+} incorporation in $Fe_{1-x}O$ in equilibrium with iron metal. The results show that the Fe^{3+}/Fe_{tot} ratio decreases strongly with pressure at 1000 °C, from approximately 0.1 at room pressure to less than 0.02 above 8 GPa. McCammon et al. (1998) also found that the Fe^{3+}/Fe_{tot} ratio of fper with Mg/(Mg + Fe) = 0.2 at conditions of the Re-ReO_2 buffer decreased to less than 0.1 by 18 GPa, compared to room pressure where an interpolation from the data of Speidel (1967) would imply a value closer to 0.4 at the same fO_2. Subsequent studies seem to confirm a general decrease in the $Fe^{3+}/\sum Fe$ ratio of fper with pressure when using the same buffer, with values for lower mantle conditions in the range between 0 and 0.2 Fe^{3+}/Fe_{tot}, depending on the Mg/(Mg+Fe) ratio and fO_2 (Bolfan-Casanova et al. 2002; Frost and Langenhorst 2002; McCammon et al. 2004a, 2004b; Otsuka et al. 2010, 2013). Otsuka et al. (2013) used the results of high-pressure experiments to calibrate an equation for the Fe^{3+} content of fper as a function of MgO-content, pressure, temperature and fO_2. Such an expression can in principal be used to estimate the fO_2 at which fper inclusions in diamonds were formed, but as will be shown in the next section, the reliability of this expression is questionable.

Several studies have also noted that fper inclusions in diamonds can contain nano- to micro-size exsolutions of magnetite-magnesioferrite spinel phases, here and after referred to as spft (Harte et al. 1999; Wirth et al. 2014; Kaminsky et al. 2015; Nestola et al. 2016; Palot et al. 2016; Anzolini et al. 2019,2020). Wirth et al. (2014), for example, found nano-meter scale coherent spft exsolutions in $(Mg_{0.35}Fe_{0.65})O$ fper diamond inclusions. Most of the exsolution was too small to be analysed accurately but crystals with a size approaching 100 nm could be analysed and had the stoichiometry, $(Mg_{0.42}Fe_{0.56}Mn_{0.02})[Fe_{1.94}Al_{0.03}Cr_{0.03}]O_4$, which is close to the mid position of the

magnesioferrite-magnetite solid solution. Wirth et al. (2014) recognised that this exsolution of spft, at some point after the inclusion had been captured in the diamond lowered the Fe^{3+}/Fe_{tot} ratio of the fper to a value of 0.07. From an estimate of the volume of the spft exsolution they were able to reconstruct the original fper Fe^{3+}/Fe_{tot} ratio as being between 0.11 and 0.14. Kaminsky et al. (2015) suggested that the Fe^{3+}/Fe_{tot} ratios determined by means of Mössbauer spectroscopy for fper grains present in lower mantle may be too low because it does not include the presence of spft clusters which appear to be a common feature in fper inclusions. These authors suggest that approximately 0.021 needs to be added to the Fe^{3+}/Fe_{tot} ratio determined using Mössbauer spectroscopy. Spft exsolution from fper has also be observed in a number of experiments, principally performed at room pressure and also in this case the bulk Fe^{3+}/Fe_{tot} ratio was calculated adding together the fper and spft Mössbauer contributions taking into account their relative abundance (Longo et al. 2011).

Aside from the necessity to correct fper Fe^{3+}/Fe_{tot} ratios for exsolved spft phases, the question remains as to the conditions at which the exsolution occurs and whether this reflects changes in *P* or *T*, or possibly even fO_2, after the inclusions were captured. The coexistence of two Fe^{2+}-Mg solid solutions i.e. fper and spft, raises the possibility of being able to perform either barometry or thermometry on the assemblage. However, although both fper and spft are well studied solid solutions, virtually nothing is known on how Fe and Mg partition between these phases.

1.8 Thermodynamic modelling of the MgO-FeO-Fe_2O_3 system

Modelling the thermodynamic properties of phases that make up inaccessible regions of the Earth's interior is a powerful tool to better understand and constrain their composition and *P-T* stability fields. In addition to complementing phase equilibria experiments, thermodynamic modelling allows the interpretation and extrapolation of the experimental results to conditions beyond the

investigated *P-T* range accessible in the laboratory. Furthermore, it allows results at different pressures to be connected through a consideration of the volume changes of reactions and it enables data from different types of experiments and measurements to be incorporated into a single model that can then incorporate significant redundancy.

Several studies have examined the fO_2 dependence of non-stoichiometry in $Fe_{1-x}O$ wüstite (Darken and Gurry 1945; Brynestad and Flood 1958 ; Burgmann 1975; Lebreton and Hobbs 1983; Hazen and Jeanloz 1984; Janowski et al.1989; Gavarri and Carel 2019). As the substitution of Fe^{3+} has to be balanced with the creation of metal cation vacancies, the stoichiometry of wüstite can be described in a similar way to fper in the last section i.e.:

$$Fe^{2+}_{1-3x}Fe^{3+}_{2x}V_xO$$

However, X-ray and neutron diffraction studies (Roth 1960; Schweika et al. 1995) have shown that Fe^{3+} can both replace Fe^{2+} in the octahedral sublattice and occupy normally vacant interstitial sites, which are in tetrahedral coordination with oxygen. Therefore, the general formula becomes:

$$^{VI}[Fe^{2+}_{1-3x}Fe^{3+}_{2x-t}V_{x+t}]^{IV}(Fe^{3+}_t)O$$

where t is the amount of Fe^{3+} at the tetrahedral site, which has a site multiplicity of 2. The value of t for different bulk compositions is not well constrained (Hazen and Jeanloz 1984) but it would seem that at room pressure between 1/2 and 1/4 of the Fe^{3+} may be in the tetrahedral sites in quenched wüstite. Fper samples quenched from high *P-T* experiments have also been shown to contain some proportion of tetrahedral Fe^{3+} from analysis of Mössbauer spectra (Otsuka et al. 2010). Furthermore, satellite X-ray diffraction reflections indicate that vacancies tend to order around tetrahedral Fe^{3+} to form defect clusters, which can themselves organise into long-range ordered structures (Hazen and Jeanloz 1984). It is not known, however, to what extent the formation of tetrahedral interstitials is favoured by rapid cooling during quenching.

There are a number of studies that have used thermogravimetric and wet chemical methods to determine the Fe^{3+} content of wüstite as a function of fO_2 and T at room P (Brynestad and Flood 1958; Valet et al. 1975 ; Burgmann 1975). Several thermodynamic models have been proposed that have focused on describing the relationship between fO_2 and Fe^{3+} content in wüstite based on given expressions for the configurational entropy. If an oxidation equilibrium such as:

$$2Fe^{2+} + 0.5O_2 = 2Fe^{3+} + V + O^{2-} \quad (6)$$

is considered then applying a mass action law gives:

$$K = \frac{\left(X_{Fe^{3+}}\right)^2 \left(X_V\right)}{\left(fO_2\right)^{0.5} \left(X_{Fe^{2+}}\right)^2} \quad (7)$$

where X_V is, for example, the mole fraction of vacancies on octahedral sites. There are many ways that this equation could be evaluated, however, depending on how ordering of vacancies and Fe^{3+} cations are treated or whether Fe^{3+} cations are considered to also enter tetrahedral sites. Valet et al. (1975), for example, considered that local charge balance required a $2Fe^{3+}$ V association resulting in K depending on either X_V or $X_{Fe^{3+}}$ but not both. Burgmann (1975) considered 14 different variations of such a model but concluded that no single formulation would result in a value of K that could describe the entire range of fO_2 versus Fe^{3+} content for wüstite at room pressure. Equations proposed by Brynestad and Flood (1958) and Valet et al. (1975) show the same is true for fper, where particular formalisms work for only certain ranges of MgO content.

Later efforts to model the stability of wüstite and fper have put less emphasis on a detailed understanding of the configurational entropy and have instead focused on modelling the Fe^{3+} incorporation using an expression for the excess Gibbs energy, $\Delta_m G^{ex}$. This procedure is equivalent to inserting activity coefficients into equation 7 (Jung et al. 2004; Hidayat et al. 2015). Jung et al. (2004) considered fper to be a solid solution involving single site mixing of MgO, FeO and $FeO_{1.5}$ components. They optimised a very large data set of structural, thermodynamic and

phase equilibrium data to obtain a model for the entire MgO-FeO-Fe_2O_3 system at room pressure. As thermodynamic data for the MgO and FeO end-members are well constrained, their main contribution to the thermodynamics of fper was to determine the pure end-member Gibbs energy expression and excess Gibbs energy terms for mixing involving $FeO_{1.5}$. Jung et al. (2004) describe the excess Gibbs energy for fper through a sum of binary mixing terms with no ternary mixing terms i.e.:

$$\Delta_m G^{ex} = X_1X_2\alpha_{12} + X_1X_3\alpha_{13} + X_2X_3\alpha_{23} \quad (8)$$

where the subscripts 1, 2 and 3 refer to FeO, MgO and $FeO_{1.5}$ respectively and α_{12}, α_{13} and α_{23} are binary interaction energies equivalent to forming two moles of (1-2), (1-3) or (2-3) nearest neighbour pairs, respectively from (1-1) (2-2) and (3-3) nearest neighbours. Each α term is expanded as a polynomial e.g.:

$$\alpha_{12} = \sum_{i\geq 0}\sum_{j\geq 0} q_{12}^{ij} X_1^i X_2^j \quad (9)$$

where q_{12}^{ij} are empirical coefficients that describe the non-ideal interactions (Pelton 2001). Jung et al. (2004) use a "Toop-type" approximation for fper mixing where $FeO_{1.5}$ is the so-called asymmetric component (Pelton 2001). In this way α_{23}, describing MgO-$FeO_{1.5}$ interaction, would be written,

$$\alpha_{23} = \sum_{i\geq 0}\sum_{j\geq 0} q_{23}^{ij}(1-X_3)^i X_3^j \quad (10)$$

i.e. $X_2 = (1-X_3)$, rather than $(1-X_1-X_3)$, which has the overall effect of strengthening the dependence of $\Delta_m G^{ex}$ on X_3 i.e. on $FeO_{1.5}$. For fper, Jung et al. (2004) refined the terms $q_{FeO,MgO}^{00}, q_{FeO1.5,FeO}^{10}$ and $q_{FeO1.5;MgO}^{02}$ and took the terms $q_{\mathrm{FeO,FeO_{1.5}}}^{00}$ and $q_{\mathrm{FeO,FeO_{1.5}}}^{10}$ from a previous refinement of the Fe-O system (Degterov et al. 2001), to give the combined expression:

$$\begin{aligned}\Delta_m G^{ex} = {} & X_{\mathrm{FeO}}X_{\mathrm{FeO_{1.5}}}q_{\mathrm{FeO,FeO_{1.5}}}^{00} + X_{\mathrm{FeO}}X_{\mathrm{FeO_{1.5}}}\left(1-X_{\mathrm{FeO_{1.5}}}\right)q_{\mathrm{FeO,FeO_{1.5}}}^{10} + \mathrm{X_{FeO}X_{MgO}q_{FeO,MgO}^{00}} \\ & + \left(\mathrm{X_{FeO_{1.5}}}\right)^2\mathrm{X_{MgO}q_{FeO_{1.5},MgO}^{10}} + \mathrm{X_{MgO}X_{FeO_{1.5}}}\left(1-\mathrm{X_{FeO_{1.5}}}\right)^2\mathrm{q_{FeO_{1.5},MgO}^{02}}\end{aligned} \quad (11)$$

Figure 1.9a shows the phase relations calculated at 1300 °C and room pressure in the study of Jung et al. (2004) and the blue line defines the conditions at which ferropericlase reaches saturation in Fe^{3+} and coexists with spft. Although the model of Jung et al. (2004) fits the available data reasonably well there are some inconsistencies and in some aspects the constraints are poor.

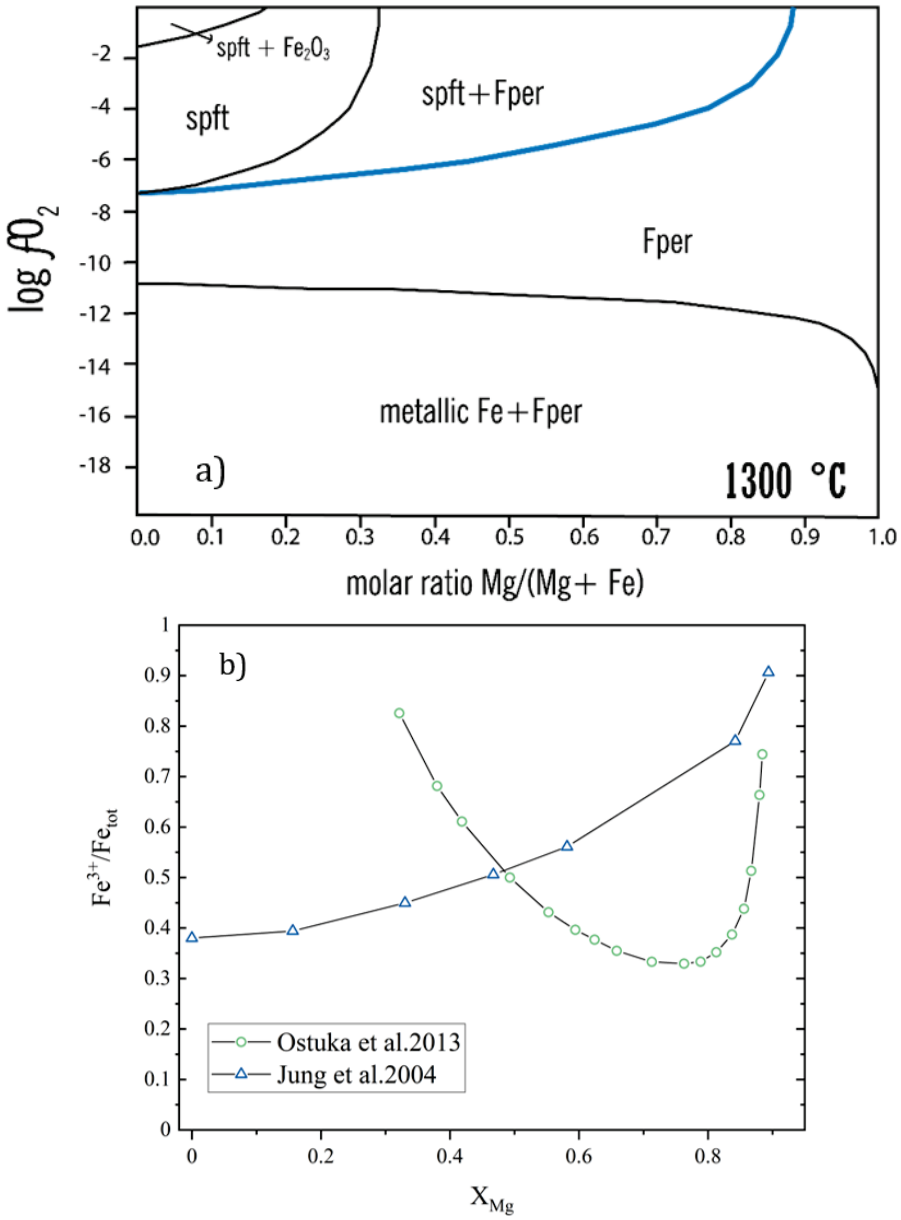

Figure 1.9: a) Calculated phase diagram of the MgO-FeO-Fe_2O_3 system at 1300 °C from the work of Jung et al. 2004 The solid blue line defines the conditions at which ferropericlase reaches saturation in Fe^{3+} and coexists with spft. **b)** The Fe^{3+}/Fe_{tot} curves have been here calculated along the field of coexistence with spft (blue line in A) from the model of Jung et al. 2004 (blue triangles) and Otsuka et al.2013 (green circles)

For example, the data of Speidel (1967) and Valet et al. (1975) on fO_2 versus fper Fe^{3+}/Fe_{tot} for Mg/(Mg+Fe) > 0.89 are not well fit by the model. This could be because the thermogravimetric methods used to determine the Fe^{3+}/Fe_{tot} ratio become increasingly inaccurate as Fe_{tot} decreases or it could be a result of an over simplistic description of the fper configurational entropy. There are no measurements of the Fe^{3+}/Fe_{tot} ratio of fper at conditions where it coexists with spft. This is because the phase relations were not directly measured in most previous experiments. Instead the fields of fper, fper + spft and spft were inferred from changes in slope of the fO_2 versus Fe^{3+} content of the recovered experimental assemblages (Brynestad and Flood 1958; Katsura and Kimura 1964; Speidel 1967), i.e. individual phases were not measured for their Fe^{3+} contents in the recovered assemblages, only the bulk Fe^{3+} was determined. Only one study (Hilbrandt and Martin 1998) has measured Fe-Mg contents of coexisting fper and spft but even then, only the Fe_{tot} content of fper was measured. Mössbauer spectroscopy has not been used extensively for room pressure measurements on fper, and the measurements that do exist do not extend to Fe^{3+}/Fe_{tot} ratios above 0.2 . Measurements of the Fe^{3+}/Fe_{tot} ratio of fper in equilibrium with spft would place excellent constraints on the thermodynamics of Fe^{3+} substitution into fper, however, as this not only would define the Fe^{3+} maximum but also the thermodynamic properties of the fper solid solution would be well constrained at these conditions through equilibria involving both phases. Since this boundary also determines the conditions at which spft would exsolve from fper, in order to understand this process it would be important to be able to determine the fO_2, Fe^{3+}/Fe_{tot} ratio of fper and MgO- content of coexisting spft at this boundary as a function of P and T.

A more recent study from Otsuka et al. (2013), has analysed high P and T data on fper Fe^{3+} contents determined at buffered fO_2 conditions and calibrated a quite simple equation to describe the Fe^{3+} mole fraction as a function of fO_2, P, T and total Fe mole fraction X_{Fe}:

$$Fe^{3+} = C(X_{Fe}^4 fO_2)^m exp\left[-\left((1-X_{Fe})E_{Mg}^* + X_{Fe}E_{Fe}^* + PV^*\right)/RT\right] \qquad (12)$$

This expression treats the fO_2 dependence as a free parameter m, which is found to be 0.114 (3), a value closer to what would be expected if Fe^{3+} is dominantly in tetrahedral sites. The values C=2.6 (1) x10^{-3} and E^*_{Mg}= -35 (3) kJ/mol and E^*_{Fe} = -98 (2) kJ/mol are terms which linearize the reaction enthalpy in terms of X_{Fe}. V^* is the volume change, refined to be 2.09 (3) cm^3/mol and R is the gas constant equal to 0.008314 kJ/mol K. The fO_2 is in Pa. Otsuka et al. (2013) used data on the fper Fe^{3+} content from studies covering conditions from room pressure up to 24 GPa but only data with Mg/(Fe+Mg) > 0.5 (Speidel 1967; Dobson et al.1998; Bolfan-Casanova et al. 2002; Frost and Langenhorst 2002; O'Neill et al. 2003; McCammon 2004a; McCammon et al. 2004b; Otsuka et al. 2010). Figure 1.9b shows the Fe^{3+}/Fe_{tot} ratio of fper calculated along the boundary of spft coexistence from the model of Jung et al. (2004). Using the fO_2 calculated for this boundary and shown in Figure 1.9a, the Fe^{3+}/Fe_{tot} ratio of fper is also calculated using the model of Otsuka et al. (2013) and shown in Figure 1.9b. Even though this model does use some room pressure data it is quite inconsistent with the model of Jung et al. (2004) at these limiting Fe^{3+} contents. This raises questions as to how reliably the model of Otsuka et al. (2013) can be extrapolated and interpolated. Nevertheless, Otsuka et al. (2013) and Kaminsky et al. (2015) used the expression (12) to determine the fO_2 of various fper inclusions in diamonds by assuming conditions of the top of the lower mantle. The spread of the resulting fO_2 values from the analysis performed of Kaminsky et al. (2015), who used fper Fe^{3+} estimates that were amended to account for the effects of spft exsolution, is from FMQ to approximately ΔIW + 1.5. This is strange because as shown in Figure 1.5 this range extends far above the field where diamonds should be stable.

In summary, the only model capable of describing the composition of fper across its entire stability field (Jung et al. 2004), is only calibrated at room pressure. Even this model lacks constraints on the composition of fper where it coexists with spft as there are no direct analyses of coexisting compositions that include the fper Fe^{3+}/Fe_{tot} ratio. The model of Otsuka

et al. (2013) calculates only the Fe^{3+} content of fper for a given set of conditions and X_{Fe} and cannot be used directly to calculate these specifically at conditions where spft coexists. At room pressure this model deviates strongly from that of Jung et al. (2004) in its prediction of the Fe^{3+} content of fper at oxygen fugacities where fper coexists with spft. Predictions of the fO_2 recorded by fper inclusions in diamonds using the model of Otsuka et al. (2013) at conditions of the top of the lower mantle extend to values that are far above the diamond stability field.

1.9 The magnetite-magnesioferrite solid solution

As shown in Figure 1.9a at high fO_2 the fper stability field is bounded by coexistence with spinel ferrite (spft) phases along the Fe_3O_4-$MgFe_2O_4$ magnetite-magnesioferrite join. The AB_2O_4 spinel structure consists of a cubic ($Fd\bar{3}m$) close-packed oxygen array with cations in tetrahedral (T) and octahedral (M) coordination (Hill et al. 1979). Their crystal chemistry can be described by the general formula $^{IV}(A_{1-x}B_x)^{VI}(A_xB_{2-x})O_4$, where x defines the inversion parameter describing the fraction of B-type cations (in this case Fe^{3+}) in the tetrahedral site and hence the degree of cation ordering. Two ordered configurations can be found in spinels, one with x = 0 (normal spinel) and one with x = 1 (inverse spinel), whereas complete disorder is achieved when x = 2/3. The ordering/disordering process between tetrahedral and octahedral sites in the spinel structure is non-convergent since it does not give rise to a change in symmetry. Magnetite and magnesioferrite form an inverse spinel solid solution, i.e. all or most of the Fe^{3+} is in the tetrahedral site. O'Neill et al. (1992) reported that the inversion parameter for magnesioferrite decreases to 0.72 with increasing temperature to 1100 °C at 1bar, similarly to magnetite (Jung et al. 2004). Non-ideality of the magnetite-magnesioferrite solid solution has been studied by Jamieson and Roeder (1984) using Fe-Mg partitioning with coexisting olivine solid solution at room pressure and 1300 °C with the assumption that the olivine solid solution is ideal and the spinel solid solution is regular and single-sited.

They found the solid solution to fit an asymmetric model with Margules interaction parameters of

$W^{\mathrm{spft}}_{\mathrm{Mg-Fe}} = 2 \pm 2$ kJ/mol and $W^{\mathrm{spft}}_{\mathrm{Fe-Mg}} = 7 \pm 4$ kJ/mol.

1.10 High pressure Fe_3O_4-$MgFe_2O_4$ post spinel phases

Although the stability field of fper is bounded by the spft solid solution at room pressure, many recent studies have identified an array of breakdown products from spft at pressures above approximately 8 GPa (Andrault and Bolfan-Casanova 2001; Schollenbruch et al. 2009; 2011; Lavina et al. 2011; Yamanaka et al. 2015; Uenver-Thiele et al. 2017a; 2017b;). There is evidence that some of these high-pressure phases may have also exsolved from fper inclusions in diamonds (Anzolini et al. 2020) and in fact McCammon et al. (1998) proposed that the apparent decrease in the amount of Fe^{3+} fper hosted by fper at high pressure may result from phase transitions of spft phases. Defining the fper stability field at high pressures and temperatures will, therefore, involve boundary reactions at high fO_2 conditions with post spft phases or post spft breakdown products.

The first high pressure post-magnetite observation was made at room-temperature, where an unquenchable transition was observed above 21 GPa to a phase often denoted as *h*-Fe_3O_4 (e.g. Mao et al. 1974; Huang and Bassett 1986; Pasternak et al. 1994; Fei et al. 1999; Lazor et al. 2004). Fei et al. (1999) found the *h*-Fe_3O_4 phase to remain stable down to approximately 24 GPa at 550 °C and proposed for this phase an orthorhombic $CaMn_2O_4$- type structure. Dubrovinsky et al. (2003), however, was able to refine the structure of the spft high-pressure polymorph using a $CaTi_2O_4$-type structural model. Schollenbruch et al. (2011) proposed that magnetite already transformed to a new structure at approximately 10 GPa but were unable to characterise the high-pressure phase. However, Lavina et al. (2011) reported the discovery of a new orthorhombic iron-oxide with Fe_4O_5 ($Fe_2^{2+}Fe_2^{3+}O_5$) stoichiometry (O5 phase) at 10 GPa and 1527 °C, which turned out to be just the first of a range of new high pressure iron-oxide phases with different

stoichiometries. Woodland et al. (2012) were then able to reinterpret the observations of Schollenbruch et al. (2011) to show that the transformation of magnetite that they observed at 10 GPa and 700-1400 °C was actually to an assemblage of Fe_4O_5 and Fe_2O_3 hematite. This was followed by the discovery of an Fe_5O_6 ($Fe_3^{2+}Fe_2^{3+}O_6$) phase produced at similar conditions as those for Fe_4O_5 (Lavina and Meng 2015), an Fe_7O_9 ($Fe_3^{2+}Fe_4^{3+}O_9$) at 24-26 GPa and 1600-1700 °C (Sinmyo et al. 2016) and an Fe_9O_{11} ($Mg_{0.87}Fe_{4.13}^{2+}Fe_4^{3+}O_{11}$) produced at 12 GPa and 1300 °C. (Ishii et al. 2018). Diamond anvil cell experiments by Hikosaka et al. (2019) appear to indicate that Fe_4O_5 and Fe_5O_6 may remain stable to approximately 40 GPa. A number of further iron-oxides and high pressure Fe_3O_4 phases have since been discovered at conditions compatible with the deeper lower mantle (Bykova et al. 2016; Khandarkhaeva et al. 2021).

Myhill et al. (2016) showed experimentally that Fe_4O_5 would first be formed from a mixture of Fe_3O_4 and $Fe_{1-x}O$ at pressures close to 8 GPa. They also performed thermodynamic calculations to obtain a consistent model for Fe_4O_5 formation and examined its stability with respect to fO_2. As shown in Figure 1.10, the field of $Fe_{1-x}O$ is first predicted to expand with respect to fO_2 at pressures up to 8 GPa, where the high fO_2 boundary is with Fe_3O_4, but then to narrow at higher pressures as the Fe_4O_5 and Fe_5O_6 phases become stable. Recent work by Woodland et al. (2023) has shown that Fe_5O_6 is also formed from Fe_3O_4 and $Fe_{1-x}O$ at almost identical conditions to Fe_4O_5. In terms of the Earth's mantle and inclusions in diamonds the most plausible phases to potentially be present are those with larger Fe^{2+}/Fe^{3+} ratios that are more likely to coexist with fper, thus we would expect Fe_5O_6 and Fe_9O_{11} to be potentially more important in the Earth than Fe_4O_5 or Fe_7O_9.

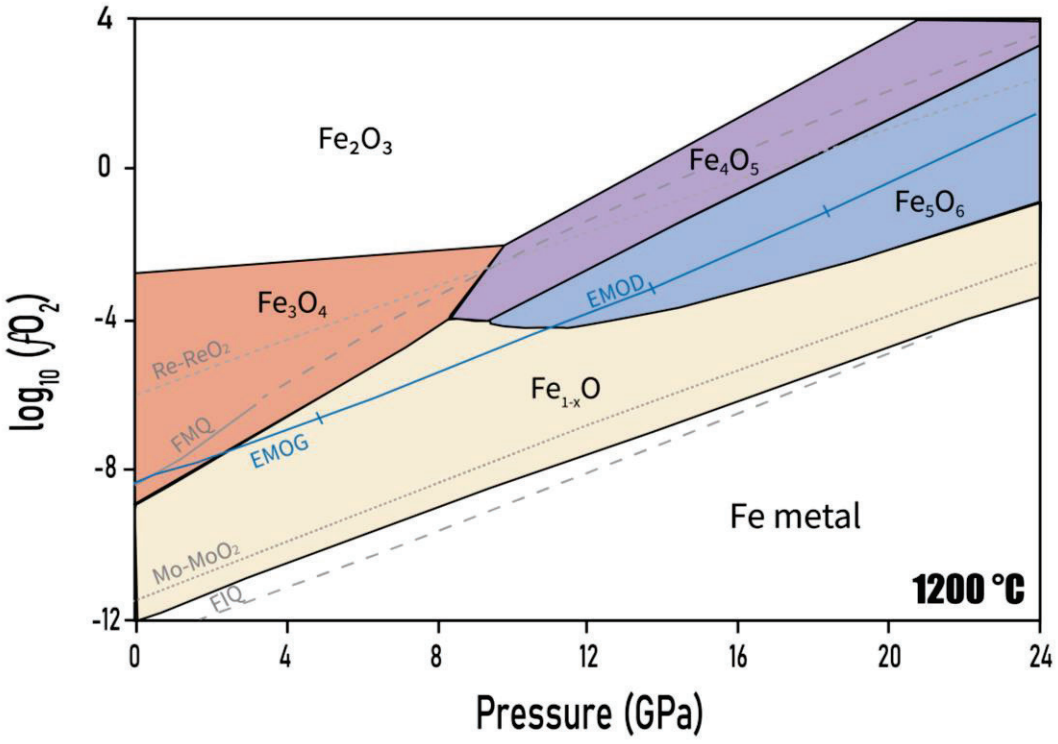

Figure 1.10: Phase stabilities in the Fe–O system as a function of log fO_2 and pressure calculated at 1200 °C, modified after Myhill et al. (2016). The stabilities of the different iron oxides are compared with curves calculated for the Re–ReO_2, Mo–MoO_2, EMOD (enstatite + magnesite = olivine + diamond), FMQ (fayalite = magnetite + quartz) and QIF (quartz + Fe = fayalite) oxygen buffers (Holland and Powell 2011; Holland et al. 2013). The metal–metal oxide buffer equilibria are calculated using the1 bar data from Barin (1989), with estimates for the *PVT* equations of state taken from the literature (Myhill et al. 2016).

The first study to examine the stability of $MgFe_2O_4$ magnesioferrite at high pressure identified an isochemical transition to the same high-pressure structure as proposed for *h*-Fe_3O_4 (Andrault and Bolfan-Casanova 2001). The phase transformation was found to be completed by 25 GPa upon laser heating at > 2000 K. Levy et al. (2004) performed a thermodynamic analysis and proposed that this so called *hp*-$MgFe_2O_4$ would be unstable at lower temperatures with respect to an assemblage of MgO and Fe_2O_3. Soon after the discovery of Fe_4O_5 an isostructural $Mg_2Fe_2^{3+}O_5$ end-member was identified at 15 GPa and 1550 °C, implying that a complete Fe^{2+}-Mg solid solution likely exists for this O5 stoichiometry (Boffa Ballaran et al. 2015). Uenver-Thiele et al.

(2017a) examined the high-pressure stability of magnesioferrite and found that it indeed breaks down to an assemblage of Fe_2O_3 and MgO between 8-10 GPa and 900-1200 °C.

The phase boundary of this transformation was found to be in very good agreement with the predictions of the Holland and Powell (2011) thermodynamic database, implying that changes, for example, in the state of cation ordering in $MgFe_2O_4$ with pressure have no significant effect on its high-pressure phase relations. At higher temperatures (>1200 °C), however, the breakdown reaction involved the formation of a phase with unquenchable structure (UQ in Figure 1.11) coexisting with Fe_2O_3. The fine-grained nature of the back-transformed and mixed assemblage made it difficult to determine the stoichiometry but it could be either $Mg_4Fe_2O_7$ or $Mg_5Fe_2O_8$. At pressures above 13 GPa the $Mg_2Fe_2O_5$ phase is recovered together with Fe_2O_3 and it is observed to become stable at lower temperatures with increasing pressure (up to 18 GPa) at the expenses of the MgO plus Fe_2O_3 field.

Uenver-Thiele et al. (2017b) also studied the phase relations of an intermediate spft composition $Mg_{0.5}Fe^{2+}_{0.5}Fe^{3+}_2O_4$, as shown in Figure 1.11, which broke down to an assemblage of $Mg_2Fe_2O_5$ and Fe_2O_3 at pressures just above10 GPa and 1000-1600 °C. Further reactions then took place to form $(Mg,Fe)_3Fe_4O_9$ towards higher temperatures and *hp*-$Mg_{0.5}Fe_{0.5}Fe_2O_4$ at pressures above 14 GPa (Uenver-Thiele et al. 2017b). Further work examining the Fe-Mg partitioning between the O5 solid solution and olivine indicate that the O5 phase does not partition Si and that Fe^{2+}-Mg mixing in O5 may be relatively ideal (Uenver-Thiele et al. 2018). The results also show a linear dependence with Mg-content of the molar volume along the O5 solid solution.

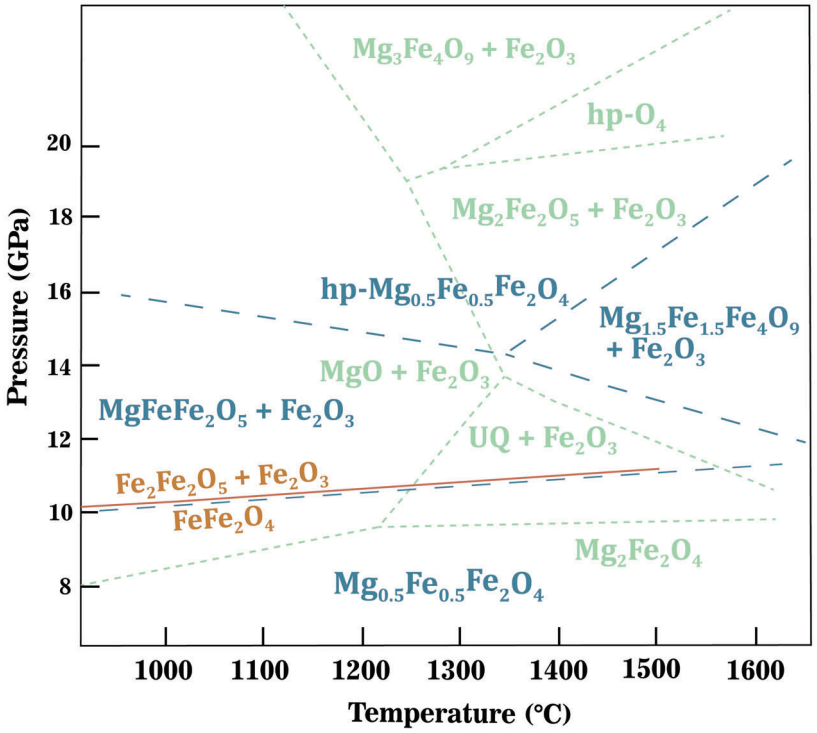

Figure 1.11: High pressure and temperature phase relations of $MgFe_2O_4$ (in green; Uenver-Thiele et al. 2017a), $Mg_{0.5}Fe_{0.5}Fe_2O_4$ (in blue; Uenver-Thiele et al. 2017b) and Fe_3O_4 (in brown; Schollenbruch et al. 2011; Woodland et al. 2012), modified after Uenver-Thiele et al. (2017b).

As stated previously, the Fe_5O_6 stoichiometry (O6 phase) is closer in composition to $Fe_{1-x}O$ than Fe_4O_5. Recently, however, Woodland et al. (2023) investigated the stability of phases along the compositional join Fe_5O_6-$Mg_3Fe_2O_6$ and found the solid solution to be incomplete and to extend to an $Mg/(Fe^{2+}+Mg)$ ratio of only 0.27 at 1400 °C and 10 GPa. An $Mg_{0.5}Fe^{2+}_{2.5}Fe^{3+}_2O_6$ phase was found to breakdown to an assemblage of the O5 phase and fper below approximately 1200 °C at 10 GPa and approximately 1000 °C at 16 GPa, providing one of the few observations of a post spft product coexisting with fper. If the O6 stoichiometry is not stable at higher Mg-contents this still leaves the possibility that an $(Mg, Fe^{2+})_5Fe^{3+}_4O_{11}$ phase (O11 phase) coexists with fper, as it is known to have at least some Mg-solubility (Ishii et al. 2018). Woodland et al. (2023) found evidence that this phase may be stable between 9 and 14 GPa between 800 and 1500 °C.

1.11 Equations of state terms of FeO-MgO-Fe_2O_3 phases

To determine the high-pressure phase relations of fper and the conditions at which it coexists with more oxidised phases or iron metal, information on the *P-V-T* equations of state (EoS) of the phase components involved are required. MgO has been extensively studied (Jamieson 1982; Duffy et al. 1995; Dewaele et al. 2000; Speziale et al.2001; Jacobsen et al.2008; Tange et al. 2009; Dorogokupets 2010). Campbell et al. (2009) determined the EoS of $Fe_{1-x}O$ synthesised with coexisting iron metal at high pressures and temperatures, which should render a stoichiometry as near as possible to pure FeO. Isothermal compressibility experiments by Hazen (1981) and Fei (1996) indicate little effect of stoichiometry on the compressibility of $Fe_{1-x}O$, although there is some indication that the thermal expansion of $Fe_{1-x}O$ may increase with x (Haas and Hemingway 1992). Dorogokupets et al. (2017) have assimilated a large amount of data on gamma iron into a *P-V-T* EoS.

Several studies have investigated the compressibility of Fe_3O_4 and $MgFe_2O_4$ (Mao et al. 1974; Wilburn and Bassett 1977; Finger et al. 1986; Nakagiri et al. 1986; Olsen et al. 1994; Gerward and Olsen 1995; Haavik et al. 2000; Andrault and Bolfan-Casanova 2001; Levy et al. 2004; Reichmann and Jacobsen 2004; Lazor et al. 2004; Rozenberg et al. 2007; Gatta et al. 2007; Greenberg et al. 2009). The results, however, provide a wide range of bulk moduli, K_{T0}, with values $155 < K_{T0} < 222$ GPa for magnetite and $170.5 < K_{T0} < 233$ GPa for magnesioferrite. Moreover, no data on samples with mixed compositions along the magnetite-magnesioferrite solid solution are present in the literature.

Bulk modulus values for the high-pressure Fe-O phases Fe_4O_5 and Fe_5O_6 have been determined (Woodland et al. 2012; Lavina et al. 2011; Lavina and Meng 2015) but no data exists currently for any of the Mg endmembers. As shown in Figure 1.12, if these are plotted as a function of the molar volume normalised to the number of O atoms in the formula, then they plot quite well

along a line joining hematite and wüstite. The bulk modulus for Fe_3O_4, determined in what is probably the most reliable study of Gatta et al. (2007), shows the largest deviation by about 5 GPa. This relationship could be used to estimate bulk modulus values for Fe-O phases that have not yet been determined such as Fe_7O_9 or Fe_9O_{11}. Interestingly this would predict the bulk modulus of an $FeO_{1.5}$ fper component to be 180 GPa, but given the large number of cation vacancies that would be expected in this structure this is certainly likely to be an overestimate.

In Figure 1.12b the Fe^{3+}/Fe_{tot} for the phases are plotted as a function of the volume normalised with respect the number of oxygen atoms. When Fe_7O_9 and Fe_9O_{11}, are added a clear linear trend is observed for the high-pressure phases likely reflecting their construction from different proportions of similar trigonal prism and octahedral polyhedra (Bykova et al. 2015). Magnetite with its larger tetrahedral sites plots clearly off this trend, heralding its decomposition at high pressure. The $FeO_{1.5}$ component of wüstite also plots significantly to higher volumes implying that increasing pressure would be expected to drive Fe^{3+} out of wüstite. The diagram also heralds phase transitions in Fe_2O_3 that have been found at pressures above 40 GPa (Bykova et al. 2015).

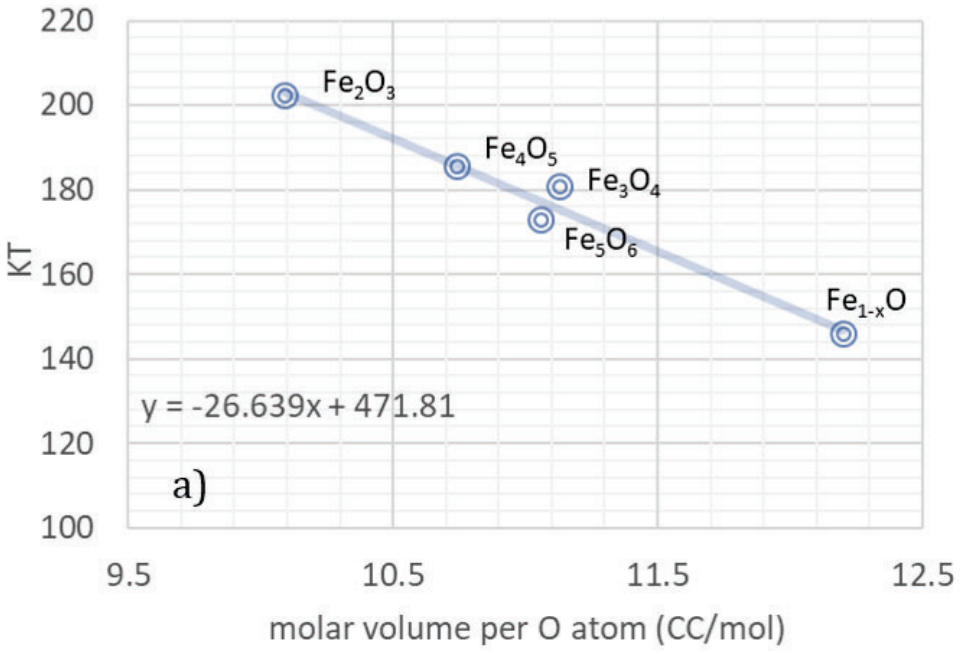

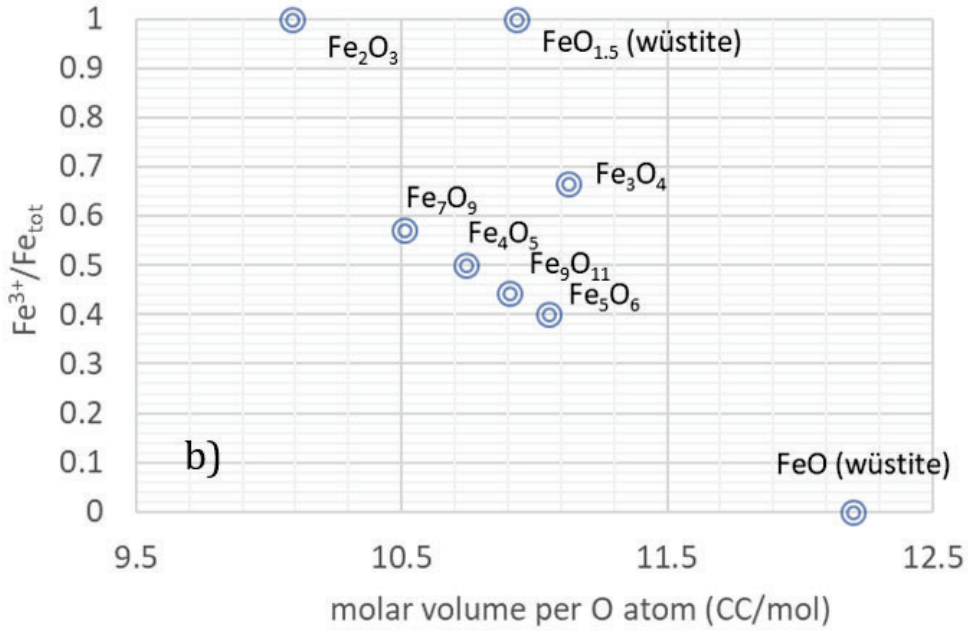

Figure 1.12: a) Isothermal bulk moduli of Fe-O phases plotted as a function of molar volume normalised to the number of O atoms. A clear linear trend is observed with magnetite being the largest outlier. **b)** The Fe^{3+}/Fe_{tot} is plotted against the volumes normalised to the number of O atoms.

1.12 Earth's missing nitrogen

Although nitrogen is one of the predominant elements in the atmosphere and biosphere, based on a comparison with other volatile elements, it is possible that these surface reservoirs account for only 25-30% of the total planetary inventory of nitrogen (Goldblatt et al. 2009; Palya et al. 2011; Busigny and Bebout 2013; Johnson and Goldblatt 2015). The interpretation of this N deficit can be summarized in three schools of thought: (i) there is a hidden reservoir in the silicate mantle taking up the majority of the N budget (Johnson and Goldblatt 2015; Yoshioka et al.2018); (ii) N was preferentially incorporated into Earth's metallic core during core-mantle segregation (Roskosz et al. 2013; Speelmanns et al. 2018); (iii) Nitrogen was lost early through volatility and processes such as impact erosion (Tucker and Mukhopadhay 2014). In terms of the first mechanism, however, our understanding of N in the mantle is hampered by the overall large uncertainty (50–

100%) in the global N subduction flux both today and in the past (Johnson and Goldblatt 2015), a lack of understanding of the processes controlling N during subduction and its later redistribution and poor knowledge over how N is partitioned during such present and past geological processes.

A significant amount of knowledge concerning mantle N geochemistry comes from diamonds, which make up ≥ 90 % of the mantle nitrogen database (Stachel et al. 2022 and references therein). Nitrogen is ubiquitous in both natural and laboratory-grown diamonds and due to the age of mantle diamonds, that span a time period from 4000 to 200 Ma (Gurney et al. 2010), they potentially allow temporal constraints to be placed on the internal N cycle (see Cartigny et al. 2014 for a review). N is the dominant impurity in the diamond lattice (Kaiser and Bond 1959) and is present as either single substitution atoms (C centres) or in the form of aggregates (A and B defects). The A nitrogen centre involves a pair of nitrogen atoms jointly replacing a single carbon atom, whereas the B defect is an aggregate of nitrogen atoms tetrahedrally arranged around a vacancy (Kaminsky and Khachatryan 2004 and references therein). Depending on nitrogen concentrations, diamonds are divided into Type I, nitrogen containing, and Type II, containing less than 1ppm of N (Robertson et al. 1934). The majority (~98%) of natural diamonds correspond to type Ia with N concentrations up to 3000-5000 ppm (Cartigny 2005; Deines et al. 1993; Mikhail et al. 2014a; Mikhail and Howell 2016) (Figure 1.13a). When it comes to sublithospheric diamonds, the nitrogen content is low, with reported values of N concentration in a lower mantle diamond having a median of 17 ppm nitrogen (Harte 2010; Smith and Kopylova 2014 and references therein) (Figure 1.13b). This would seem to be an indicator that N is not deeply recycled into the mantle but it could also be an indication for a change in N partitioning with depth (Roskosz et al. 2013; Smith and Kopylova 2014; Speelmanns et al. 2019) The substantial nitrogen content in type I diamonds means that nitrogen is often considered to be 'compatible' in diamond (Stachel and Harris 2009). This will depend,

however, on whether diamond growth is an equilibrium process and on the form N takes in the diamond growth medium (Mikhail et al. 2014a; Stachel et al. 2022; Cartigny et al. 2014), which could be molecular nitrogen (N_2), ammonium ions (NH_4^+) and even metallic nitrides (Thomassot et al. 2007; Smith and Kopylova 2014). Mikhail and Howell 2016 give an extensive discussion on the matter. There remains a pressing need to better understand how *P*,*T*, mineralogy and melt/fluid compositions affect the speciation of nitrogen under a range of mantle conditions relevant to diamond formation and even more crucial is to unravel what processes are involved in the N cycle that may influence the availability of N in the deep mantle.

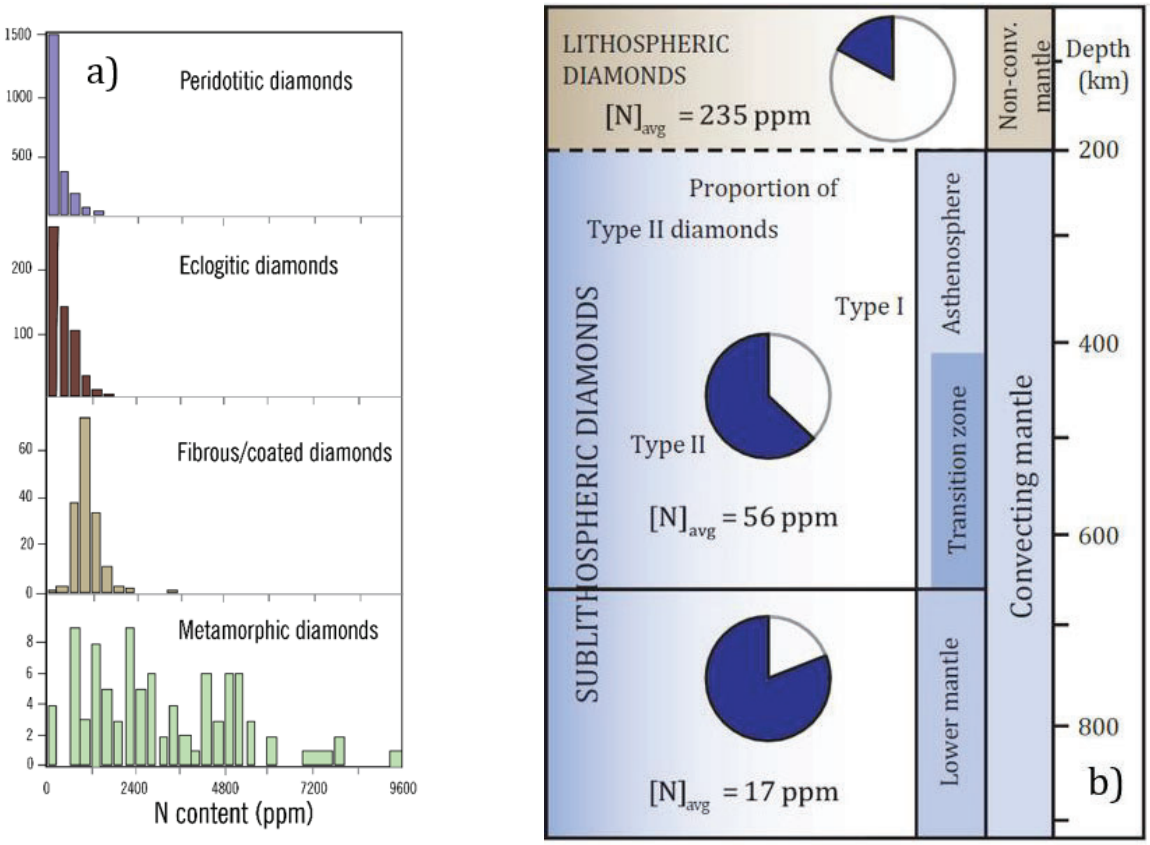

Figure 1.12: a) Comparative histograms of nitrogen content in diamonds, modified after Cartigny 2005; **b)** Schematic mantle section summarizing the average nitrogen content and type of diamond based on N concentration with depth. The averages for the diamonds are calculated compiling the data from Stachel and Harris 2009; Hayman et al. 2005; Tappert et al. 2005, 2009a; Bulanova et al. 2010; Hutchison et al. 1999; McDade and Harris 1999; Stachel and Harris 1997; Deines et al. 1991; Davies et al.1999; Stachel et al. 2002; Palot et al. 2012. This figure was modified after Smith and Kopylova 2014.

1.12.1 The nitrogen isotopic imbalance

Further constraints on the N processes in the mantle come from the distribution of the N stable isotopes and the observation that there is a significant imbalance between the large amount of isotopically heavy N that appears to be subducted, compared to the relatively small amount of isotopically light N that is outgassed from the mantle at mid ocean ridges (Javoy et al. 1984, 1986; Javoy 1997). Variations in the isotopic composition of nitrogen are expressed in the usual δ-notation in permil: $\delta^{15}N_{sample} = [(^{15}N/^{14}N)_{sample}/(^{15}N/^{14}N)_{standard}-1]x1000$, where the standard is atmospheric N_2. Surface material recycled into the mantle is expected to have a positive $\delta^{15}N$ value, distinct from the negative values measured in most mantle samples. In fact, as sampled by diamonds and MORB, N in the mantle is depleted in ^{15}N relative to the atmosphere ($\delta^{15}N \approx -5\pm2$ ‰) whereas N in sedimentary rock and residual MORB have positive $\delta^{15}N$ values generally up to +10 ‰ (Figure 1.13). If the mantle were the source of surface N, which is then isotopically fractionated between the air and crustal reservoirs formed from organic material, then the mantle value should lie somewhere between atmospheric ($\delta^{15}N = 0$ ‰) and crustal N values ($\delta^{15}N = +5$ ‰). Javoy (1997) proposed a solution to this imbalance by arguing that the Earth's surface N budget was established through the accretion of a positive $\delta^{15}N$ late veneer, whereas an earlier accreted deep Earth primordial N reservoir had a very negative $\delta^{15}N$, similar to that of enstatite chondrites ($\delta^{15}N \sim -20$‰). The upper mantle $\delta^{15}N$ has then been established through mixing between recycled heavy N from the surface and very light N from the primordial mantle. This was seen as the only mechanism by which mantle N could remain light, in spite of the subduction flux of heavy N (Javoy 1997). However, the discovery that deep mantle plume sources appear to have positive $\delta^{15}N$ (Dauphas and Marty 1999), led to the idea that subduction in the Proterozoic and Phanerozoic brought positive $\delta^{15}N$ material into the deep mantle but that more reducing conditions at the surface in the Archean resulted in earlier subduction bringing material with negative $\delta^{15}N$

into the shallower mantle (Marty and Dauphas 2003). While a temporal change in the $\delta^{15}N$ of subducted material might potentially be linked to the gradual oxidation of the surface, there appears to be no evidence for such a change in the diamond record, at least back to 3.5 GPa (Stachel et al. 2022), and it does not seem to be consistent with measurements made on actual Archean sediments (Cartigny and Marty, 2013). A recent study linking N isotopes and $N_2/^3He$, argues that subduction may have had a limited influence on the mantle N concentration and isotopic ratio (Labidi and Young 2022), with recent analyses of N fluxes into subduction zones being argued to be in balance with the arc degassing flux (Libidi et al.2020; Labidi and Young 2022). It seems hard to explained the range of $\delta^{15}N$ in diamonds, which spans from −39.4 to +16.9 ‰ (Stachel et al. 2022), without some subduction recycling being involved, but it is possible that the recycled N flux sampled by diamonds was actually small or that it only affected the lithosphere. It is also possible that at least some of the $\delta^{15}N$ range recorded by diamonds results from N isotope fractionation within the mantle.

A complete understanding of the origin and development of the deep Earth's N cycle requires knowledge of how and how much N may enter the mantle and how it is then internally distributed through partitioning processes. Our understanding of these aspects is limited, however. Estimates for the size of the N subduction flux is based on nitrogen concertation measurements of only a few key rock types (Javoy 1997; Tolstikhin and Marty 1998; Johnson and Goldblatt 2015; Bebout et al. 2016; Zerkle and Mikhail 2017; Hirschmann 2018). Experimental studies on mineral-fluid-melt N partitioning (Roskosz et al. 2006; Mysen and Fogel 2010; Mallik et al. 2018; Mysen 2018, Pöter et al. 2004; Jackson et al. 2021, Förster et al. 2019) exist over a relatively small range of conditions and there is very limited knowledge of how factors such as pH and fO_2 influence N speciation and partitioning (Mikhail and Sverjensky 2014; Zerkle and Mikhail 2017).

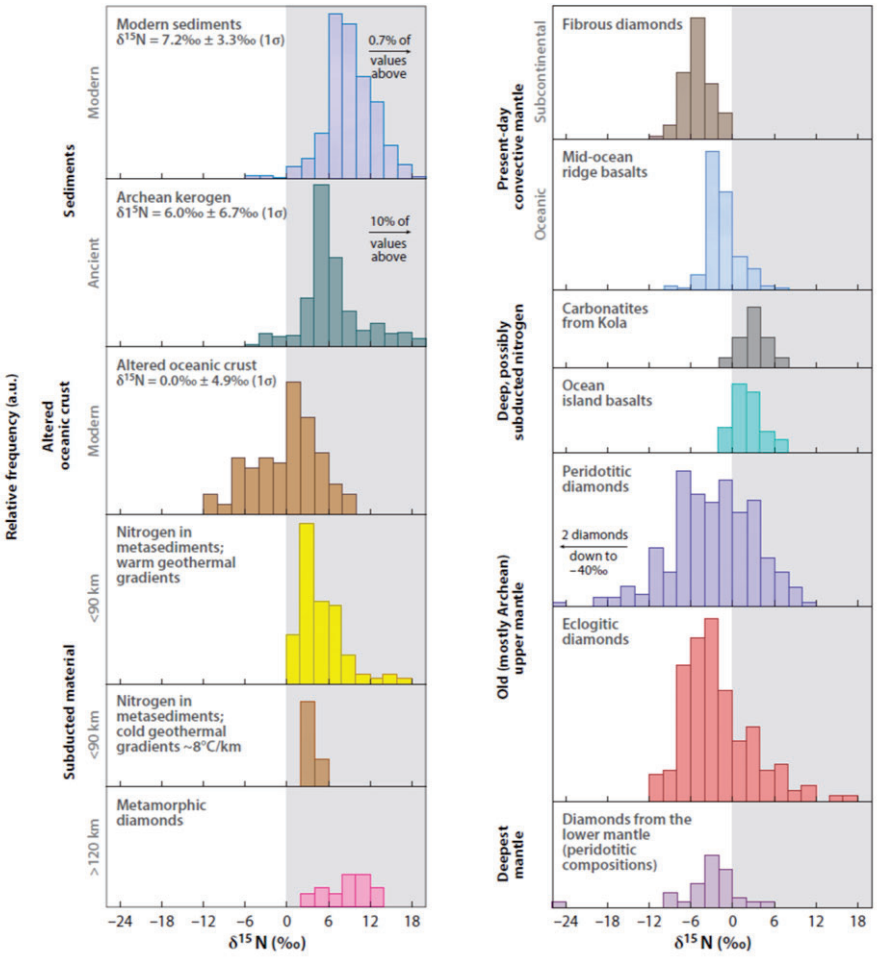

Figure 1.13: Crustal/sedimentary N is enriched in ^{15}N compared to the atmosphere. During sediment subduction, devolatilization would preferentially release ^{14}N, further enriching subducted material in ^{15}N as observed for metamorphic diamonds further demonstrating that N can survive at depth >3 GPa (Cartigny et al. 2001a,2004; Busigny et al. 2011). N isotopes are fractionated only a few ‰ during incorporation in diamond, as it can be observed by the isotopic similarity of fibrous/coated diamond and MORB (Tomassot et al. 2009). Eclogitic diamonds show negative $\delta^{15}N$, similar to peridotitic and lower mantle diamonds (Palot et al. 2012) implying that they cannot directly come form subducted carbon. This figure was modified after Cartigny et al. 2014.

1.12.2 The nitrogen cycle

N is cycled within the Earth system in two ways: a fast, biologic cycle (e.g. Kelly 2000; Sigman et al. 2019); and a slow, geologic one (e.g. Boyd 2001; Holloway and Dahlgren 2002; Kerrich et al. 2006; Thomazo and Papineau 2013). Atmospheric di-nitrogen (N_2) is massively cycled by

biological activity and enters the rock cycle as organic matter matures, releasing the ammonium ion (NH_4^+). Having similar charge and ionic radius as potassium (K), the ammonium ion substitutes K and, to a lesser extent, sodium and calcium in minerals such as clays and micas (Busigny and Bebout 2013). Micas are the dominant host of K in metasediments and the potassium-nitrogen correlation has been extensively used to argue that white micas are likely the main hosts of N at these conditions (e.g. Bebout et al. 2013; Busigny et al. 2003; Halama et al. 2010). Nitrogen can also be incorporated into altered oceanic crust (AOC) by hydrothermal and/or microbial alteration with N concentration in a range of 1.3- 18.2 ppm (e.g. Busigny et al. 2005, 2019; Li et al. 2007; Bebout et al. 2018). The N concentrations of subducting sediments varies strongly depending mainly on the organic content, from as low as ~10 ppm in sandstones, carbonates and cherts, to as high as ~2400 ppm in the organic-rich sediments (e.g. Sadofsky and Bebout 2004; Li and Bebout 2005; Busigny and Bebout 2013). Once entrained in oceanic sediments and crust, N is carried into subduction zones, where it is either released back to the surface after metamorphic devolatilization, stored in mantle wedge serpentinites by the infiltration of slab-derived fluids or carried into the deeper mantle past the subduction barrier (e.g. Hilton et al. 2002; Bebout et al. 2013; Pagé et al. 2018). Released volatilized N either oxidizes to N_2 and escapes via arc volcanism or is incorporated into intrusive igneous rocks (Figure 1.14). Results from some recent studies (e.g. Halama et al. 2010; 201; Cannaò et al. 2020) imply that part of the sedimentary N could be re-captured by the meta-basaltic component of the subducting slab during prograde metamorphism. Li et al. (2021) reported natural evidence for N re-fixation during early stages of subduction in natural pillow-shaped blueschists from Northeast China.

Nitrogen that is not returned to the surface becomes entrained in mantle circulation and could be subsequently sampled by plume related magmas (e.g. Dauphas and Marty 1999; Hilton et al. 2002). The isotopic signature of i.e. back-arc basin basalts glasses (Sano et al. 2001) is of $\delta^{15}N$ values between -2.7 and +1.9 ‰, implying mantle origin of the nitrogen (Hilton et al. 2002). Thus,

subduction-zone N recycling may have had an impact on the long-term evolution of Earth's reservoirs (i.e. Sano et al. 2001; Marty and Dauphas 2003; Mallik et al. 2018; Bekaert et al. 2021). Mallik et al. (2018) estimated that 45-75 % of subducted N may enter the deep mantle. Part of this estimate, however, used Rb as a proxy for N in partitioning calculations due to the similar ionic radius of Rb^+ and NH_4^+. While this may be reasonable, it does not allow for possible effects of fO_2 on partitioning relations.

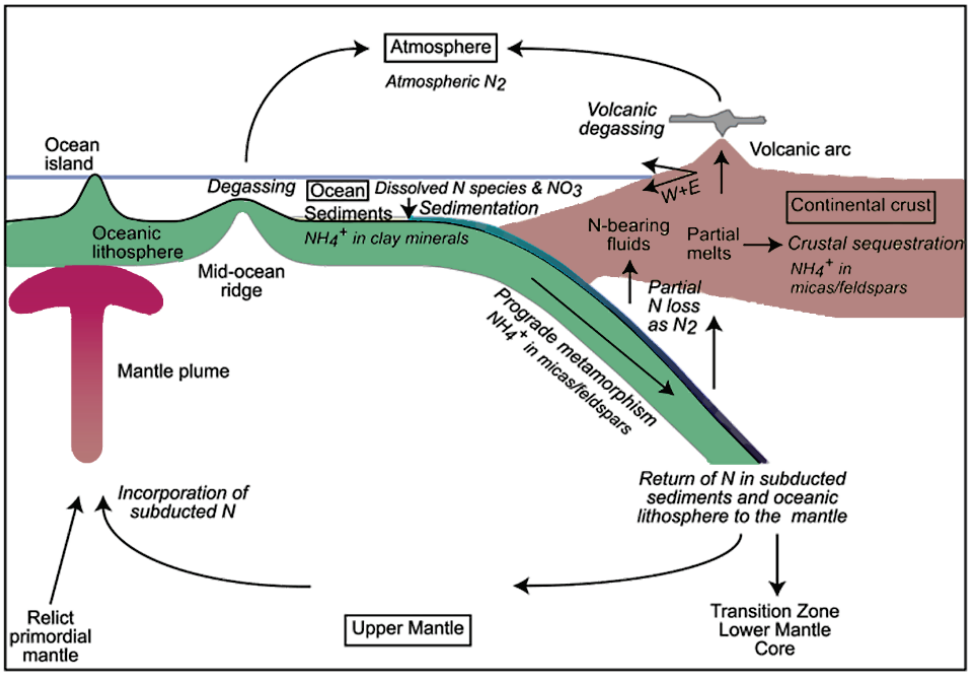

Figure 1.14 : Schematic representation of the geological nitrogen cycle (based on Bebout et al. 2013a,b; Cartigny and Marty 2013). W + E = Weathering and erosion

1.13 Aims of the thesis

As described above, ferropericlase is not only one of the most important minerals in the lower mantle but also forms one of the inclusions most frequently found in superdeep diamonds. The ferric iron content of ferropericlase inclusions can in principle be used to interpret the formation conditions of super deep diamonds and reveal the nature of the material from which they formed. However existing models for the ferropericlase Fe^{3+}/Fe_{tot} ratio cannot describe its composition over the required range of conditions. Furthermore, exsolution of spinel ferrite phases is frequently reported for ferropericlase inclusions in diamonds but conditions at which this occurs are unknown. In order to provide the necessary information for constraining the behaviour of the $MgO\text{-}FeO\text{-}Fe_2O_3$ the following objective have been considered:

- To determine the effect of composition on the compressibility of phases along the spinel ferrite solid solution, as such data are required for thermodynamic modelling of phase boundaries between ferropericlase and spinel ferrite.
- To determine the Fe^{3+}/Fe_{tot} of ferropericlase at fO_2 conditions up to those where it coexists with either spinel ferrite phases or higher-pressure mixed valence Fe and Mg oxides as well as to determine the coexisting Fe and Mg contents of ferropericlase and coexisting spinel ferrite and higher-pressure oxides, in order to interpret the conditions at which exsolution occurs in diamond inclusions.
- To characterise the spinel exsolution in ferropericlase and their effect on its unit-cell volume in order to test whether it can be used to conveniently determine the Fe^{3+}/Fe_{tot} ratio as suggested by Dobson et al. (1997).
- To derive a thermodynamic model that can be used to described the composition and phase relations of ferropericlase up to conditions of the lower mantle in order to interpret the

conditions at which diamonds containing ferropericlase inclusions formed and to constrain the precursor materials.

Moreover, during a three month visit to Tohoku university in Japan experiments were performed in order to study isotopic fractionation between N-rich fluids created by the breakdown of glycine and either hydrous mineral or diamonds. Although this investigation is only preliminary, it was designed to develop a methodology through which nitrogen isotope fractionation experiments might be performed. These data are important for examining whether variations in N isotopes in samples derived from the mantle originate from different sources that are within or have been returned to the mantle or from fractionation processes operating in the mantle.

Chapter 2

Methods

The methods employed in the various aspects of the work in this thesis are described in this chapter. These include sample preparation methods as well as high temperature and high pressure and temperature synthesis techniques and analytical methods. In the following paragraphs, for each technique a general theoretical background is presented followed by subsections where the particular procedures adopted are described in detail. Descriptions of experimental results and characterization are included only where they relate to method developments.

2.1 Synthesis of the starting materials

The starting material employed in Chapter 3 was provided by a collaborator and the details concerning the synthesis can be found in Uenver-Thiele et al. (2017b).

Starting materials for the experiments in Chapter 4 and 5 were prepared from a stoichiometric mixture of reagent grade oxides, carbonates, and metal powders. Attention was payed to always dehydrate water-sensitive oxides (e.g. Fe_2O_3 and MgO) in air at 1000 °C overnight before the weighing process, to ensure higher precision. Oxides were ground together in an agate mortar under ethanol for one hour to produce a fine-grained homogeneous mixture. Mixed powders were then pressed into pellets and sintered in a furnace at 1 atm with a heating cycle up to 500 °C for decarbonation. The pellets were reduced overnight at 1100 °C and 1 atm in the gas mixing furnace at 2 log units

below the fayalite-magnetite-quartz buffer ($\Delta\log fO_2$ = - 2 FMQ) to ensure initial low proportions of ferric iron. The proportion of carbon monoxide to carbon dioxide ($CO:CO_2$) required to achieve a particular oxygen fugacity was determined using look-up tables that are based on the equilibrium,

$$2CO + O_2 \rightleftharpoons 2CO_2 \quad (1)$$

In order to study the Fe^{3+} content in ferropericlase, the Mg-content of (Mg, Fe)O was varied from 0.86 to 0 mol% and in some cases hematite was also added to promote the formation of a coexisting Fe^{3+}-rich oxide. PtO_2 powder was also added to the starting powder as a sliding redox sensor, meaning that Pt alloys with Fe in the starting material during the experiment and the Fe content of the Pt-Fe alloy depends on the fO_2 at the experimental conditions. The fO_2 can be determined using chemical analyses of ferropericlase and Fe-Pt alloy performed after the experiment is recovered (Woodland and O'Neill 1997). All the starting materials prepared are reported in Table 2.1.

Table 2.1: Compositions of the ferropericlase starting materials are reported in wt %. The proportion of hematite is calculated relative to the weight of the reduced ferropericlase composition to which it was added, as for the PtO_2 redox sensor.

Fper stoichiometry	Cr_2O_3	NiO	Na_2O	MnO	FeO	MgO	total	Added Fe_2O_3	Added PtO_2
$(Mg_{0.86}Fe_{0.14})O$	0.50	1.30	0.05	0.20	13.71	84.24	100	20 wt%	4 wt%
$(Mg_{0.50}Fe_{0.50})O$	0.50	1.30	0.05	0.20	48.98	48.98	100	20 or 5 wt%	4 wt%
$(Mg_{0.30}Fe_{0.70})O$	0.50	1.30	0.05	0.20	68.57	29.39	100	20 wt%	4 wt%
$(Mg_{0.05}Fe_{0.95})O$	0.50	1.30	0.05	0.20	93.05	4.90	100	20 or 10wt%	4 wt%
FeO	0.50	1.30	0.05	0.20	97.95	0	100	5 wt%, none	4 wt%
1 atm experiments									
$(Mg_{0.15}Fe_{0.85})O$	0.50	1.30	0.05	0.20	84.03	13.99	100	none	4 wt%
$(Mg_{0.80}Fe_{0.20})O$	0.50	1.30	0.05	0.20	19.59	78.36	100	none	1 wt%

For the diamond synthesis experiment described in Chapter 6, Fe-Ni-S alloy was prepared from a mixture of pure Fe metal, Ni metal and sulfur. Sulfides are the most abundant inclusions in lithospheric diamonds (Harris 1992) and superdeep CLIPPR diamonds (Smith et al. 2016). Many experiments have been performed to investigate the effects of different metal catalyst compositions on diamond formation (see D'Haenens-Johansson et al. 2022 and Pal'yanov et al. 2005 for an extensive review). Diamonds have been crystallized from liquid metallic alloys by supersaturation at 15 GPa when the sulfur content of the liquid ranged from 5 to 15 wt.% (Zhimulev et al. 2012, 2016, 2018; Chepurov et al. 2009). A stoichiometry of $Fe_{0.58}Ni_{0.30}S_{0.12}$ was finally selected finding a reasonable compromise between the natural composition reported by Smith et al. 2016 for natural samples, and experimental reports of diamond formation in the Fe-Ni-S-C system (Zhimulev et al. 2012; Bataleva et al. 2016; Litvin et al. 2002; Pal'yanov et al. 2005, 2006, 2007; Sato and Katsura 2001). Particular attention was paid in selecting experimental results where spontaneous nucleation of diamond was observed. That is because, no diamond seed was utilized in our study.

2.2 Gas-mixing furnace

In Chapter 3, results are described from a series of experiments performed at ambient pressure (1 atm) employing the starting material showed in Table 2.1.

The experiments were run at high temperature (up to 1450 °C) under controlled oxygen fugacity conditions using a gas-mixing furnace at the BGI. In this apparatus, a pellet is placed in a Fe-saturated platinum basket that ensures no Fe loss from the sample during the experimental run. The basket is hung on the sample holder made out of thick Pt rods and enveloped in an alumina tube (Figure 2.1). The Pt-basket is wired to the sample holder by means of a thin platinum wire. Electrically induced melting of the thin wire allows fast quenching (i.e., drop-quench) at the end of the experiments, with the basket containing the sample falling rapidly into the sample holder at

the bottom of the furnace. The furnace box is made of an alumina refractory ceramic fibre tube surrounded by three SiC heating elements.

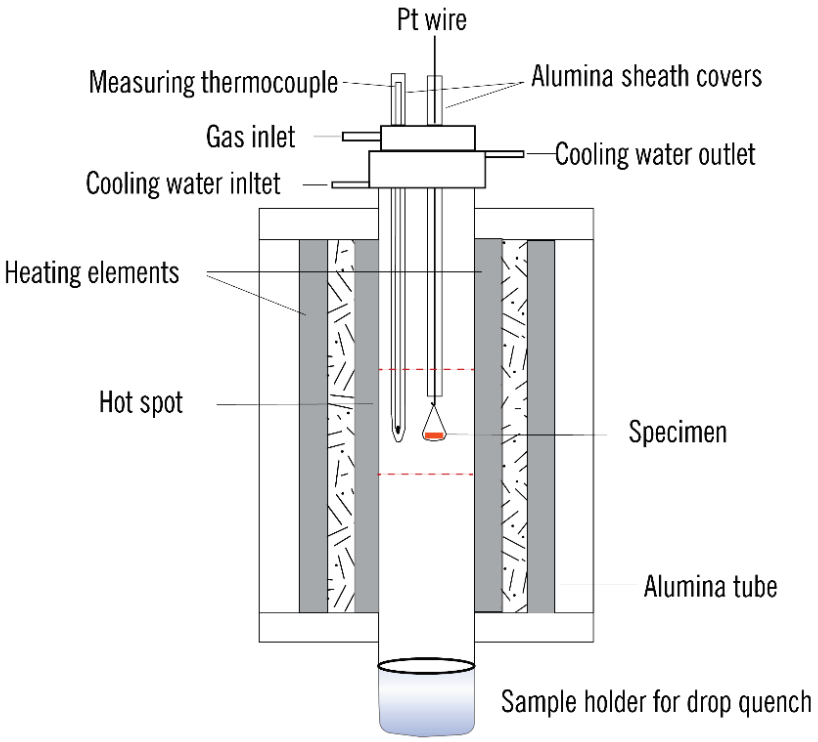

Figure 2.1: Schematic diagram of the vertical furnace for the equilibration experiments (modified after Chen et al. 2021).

The two main parameters that are controlled in these experiments are temperature and oxygen fugacity fO_2. Temperature is monitored using a type S thermocouple Pt-$PtRh_{10}$. Caution was taken to place the samples in the "hot spot", located at approximately 35 cm from the top, that is the spot in the furnace chamber in which the temperature peaks and its value is more stable over time. Moreover, several calibrations have led to the quantification of the ΔT between the temperature of interest and the real temperature at the hot spot. This can vary between - 30 °C at 1000 °C to -60°C at 1300 °C. For each run, the temperature was corrected accordingly. Oxygen fugacity is controlled by the proportion of CO and CO_2 mixture. The fO_2 is expressed as a difference to a redox buffer (i.e., fayalite-magnetite-quartz). Experimental conditions, log fO_2, and gas mixtures for each experiment are reported in Table 4.3 in Chapter 4.

2.3 High pressure experimental methods

In order to simulate the conditions of the Earth's interior, laboratory equipment has been developed and perfected over the past decades following the principle of pressure (*P*) generation expressed as $P = \frac{F}{A}$ where *F* is the applied force and *A* is the area on which the force is applied. According to this relation, high-pressure conditions can be achieved through either the reduction of the surface area, or the increase of the force. Different experimental devices use different combinations of these parameters and make it possible to investigate the whole range of *P-T* conditions existing in the Earth (Figure 2.2).

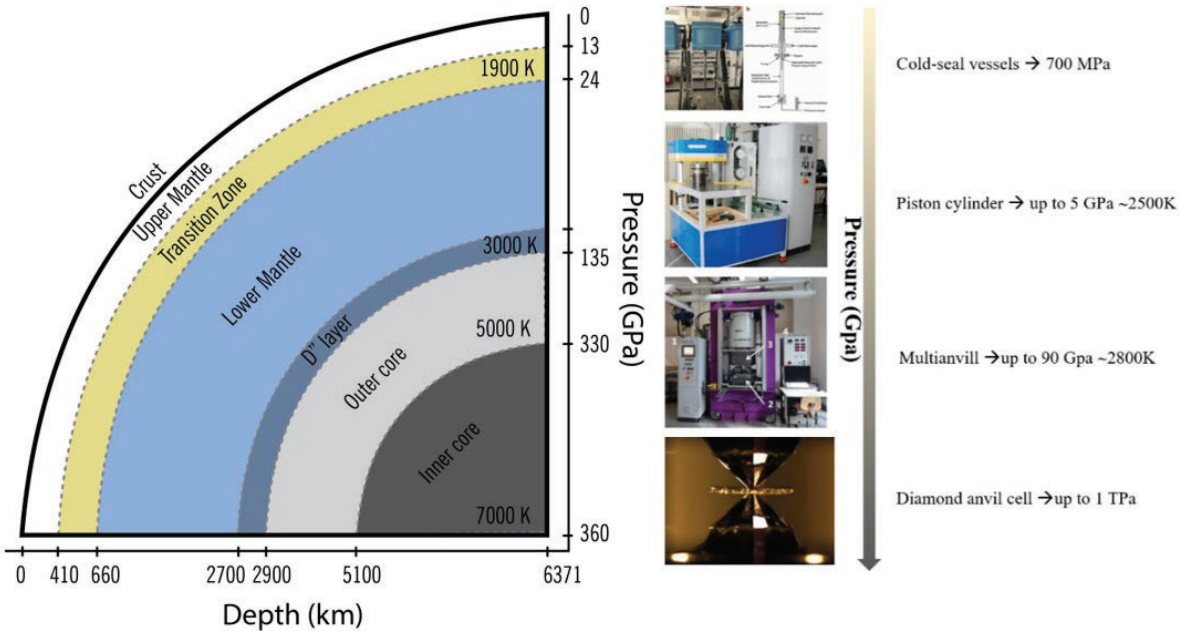

Figure 2.2: Cartoon sketch of Earth's interior along with pressure distribution with depth and the most appropriate experimental tool to simulate the desired conditions.

In the following section, the high-pressure (*HP*) and high-temperature (*HT*) techniques involved in the preparation of the samples in this study are presented.

2.3.1 Multi-anvil apparatus

The majority of the *HP-HT* experiments were conducted in 1000-tonne (Hymag), 1200-tonne (Sumitomo) and 5000-tonne (Zwick) presses with a 6-8 Kawai-type split-sphere guide blocks at the BGI. Moreover, one experiment in Chapter 5 was performed in the IRIS-15 Voggenreiter LPH 1500-840/200 press. Some of the experiments reported in Chapter 6 were performed in a 1500-tonne Kawai type multi-anvil press at Tohoku University in Sendai, Japan. A general description of the multi-anvil apparatus is provided here whereas each chapter includes details specific to the individual aspects of the work.

The split-sphere multi-anvil design was introduced by Kawai et al. (1970), and is comprised of a set of six outer hardened steel sphere-split shaped anvils (first stage anvils) that compress an inner cubic space in which a set of eight corner-truncated tungsten carbide (WC) cubes (second stage anvils) is placed. The two stages of anvils are compressed inside a hydraulic press. A uniaxial force is produced by raising the oil pressure inside the press that is then focused onto smaller and smaller surfaces using the anvil stages. The second stage anvils compress a ceramic pressure medium in the form of an octahedral assembly. The sample is contained inside the octahedral pressure medium and pyrophyllite gaskets are placed between the second stage anvils (Figure 2.3a) which seal in the high-pressure region while supporting the truncations and allowing the anvils to advance and decrease the volume of the assembly. Both the pressure medium and the gaskets flow as they are loaded, with the pressure medium being also extruded into the gasket region. At high temperatures stresses within the assembly are relaxed as it flows, creating quasi-hydrostatic conditions at the sample (Fig 2.3b).

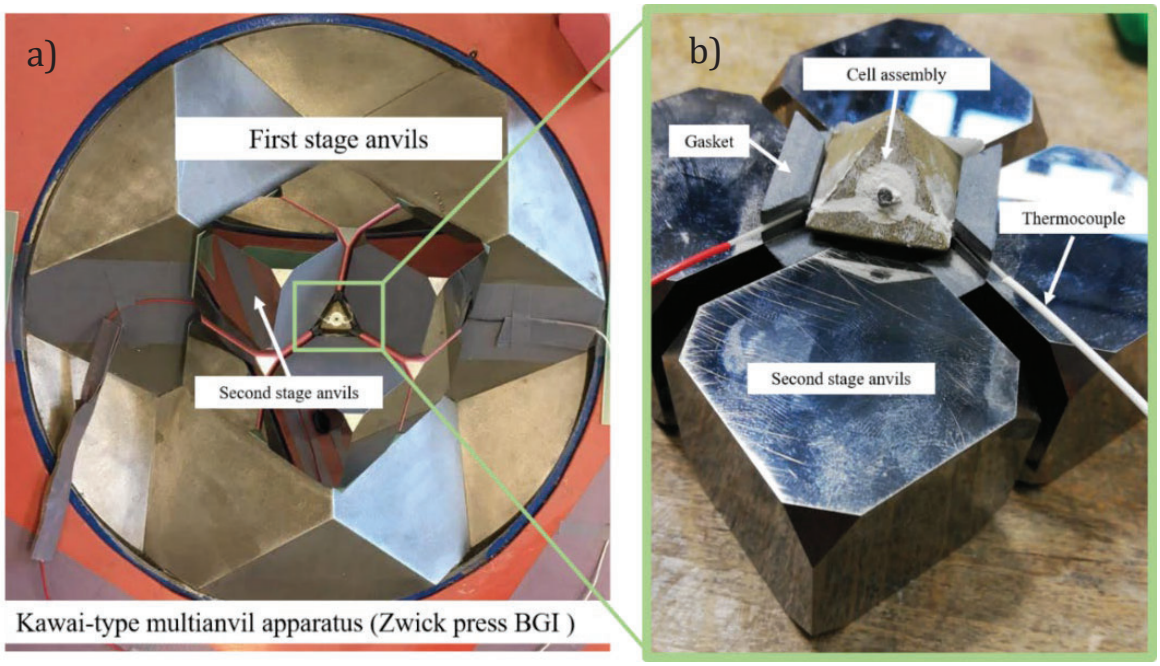

Figure2.3: Setup for a multi-anvil experiments **(a)** Kawai-type split-sphere first stage anvils from the 5000-tonne Zwick press at BGI, with 7 of the 8 second stage anvils showing the cell assembly located in the middle. **(b)** Second stage anvils with cell assembly, gaskets and thermocouple.

By varying the force exerted by the hydraulic press, the truncation edge length (TEL) of the second stage anvils, and the octahedral edge length (OEL) of the pressure medium, different pressures can be achieved. The press load versus sample pressure calibrations employed in this study were those routinely used at BGI, and are based on mineral phase transitions as described in Keppler and Frost (2005) (Figure 2.4). For the experiment performed at 30GPa on the IRIS-15 Voggenreiter LPH 1500-840/200 press, the pressure calibration is reported by Ishii et al. (2016).

For pressures between 6 and 12 GPa, 18-mm edge length Cr_2O_3-doped MgO octahedra were employed as pressure media, which were compressed using WC cubes with 11 mm corner truncations (18/11 assembly). Experiments performed at higher pressure were done using 18/8 and 7/3-type assemblies at 16 to 20 and 25 GPa respectively. It was possible to perform experiments up to 20 GPa using 18/8 assembly by conducting the experiments on the Zwick 5000-tonne press (Figure2.3a) at BGI.

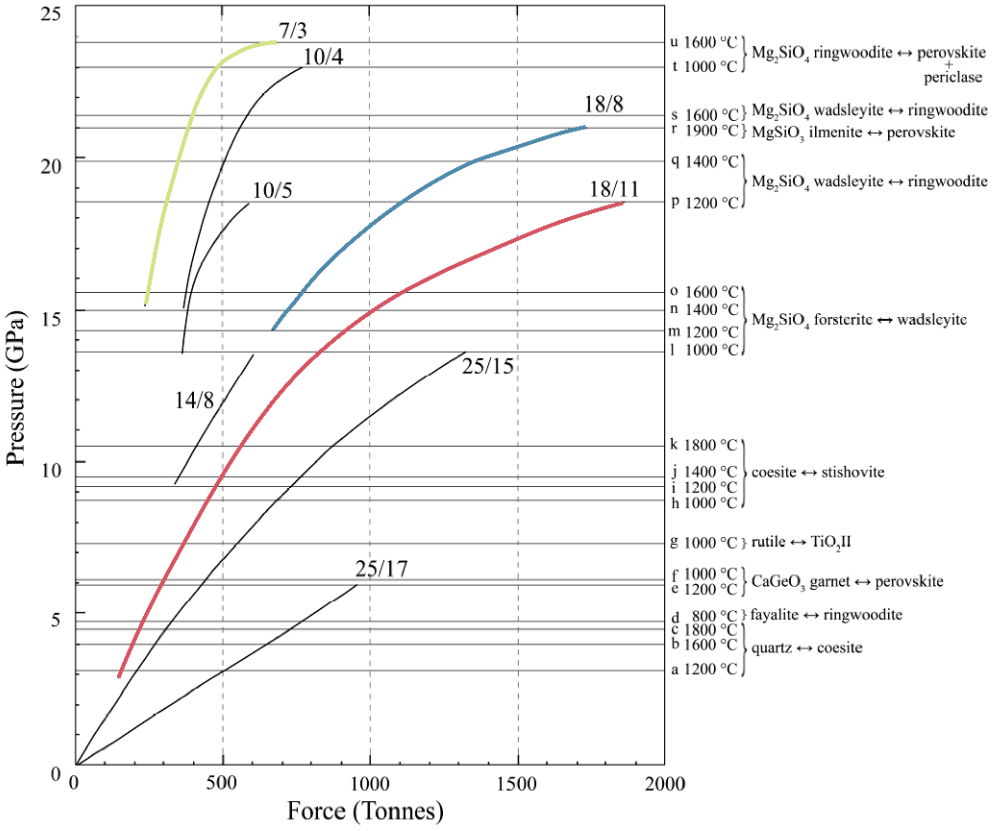

Figure 2.4: Pressure calibration curves used in the present work (modified after Keppler and Frost 2005). Major phase transformations used for the calibrations are shown at the right side of the figure, and the additional details and references can be found in Keppler and Frost (2005). The highlighted curves represent the assemblies employed in the present work.

The Cr_2O_3-doped MgO octahedra contain a cylindrical $LaCrO_3$ or graphite (C) heater depending on the temperature and pressure of interest, which is enveloped by an outer ZrO_2 sleeve (Figure 2.5) acting as a thermal insulator (Keppler and Frost 2005). The connection between the heater and the WC anvils is provided by a molybdenum (Mo) or graphite ring and disk placed on the top and bottom of the assembly, respectively (Figure 2.5). Depending on the size of the octahedra utilized, the size of the capsules varies from 1 mm ø × 1 mm for the 7/3 -type, to 2 mm ø × 3.5 mm for the 18/11-type and 4 mm ø × 4 mm for the 25/15-type multi-anvil assemblies.

For all the performed runs, type D thermocouple ($W_{97}Re_3$-$W_{75}Re_{25}$) was employed for temperature monitoring. The thermocouple wires (0.25 mm thick) are guided through a 4-hole alumina tube to create a junction just above the sample container. Coils made of copper or thin alumina tubes are

used to protect the thermocouple wire through the assembly. For the 7/3 assembly, thermocouple wires (0.08 or 0.13 mm thick) are inserted longitudinally through the wall of the furnace, with the hot junction at the midpoint of the heater. For those experiments in which the thermocouple failed, temperature was estimated from the power-temperature relationship determined in previous runs. Moreover, Hernlund et al. (2006) calculated that in the 18/11 standard BGI assembly the temperature gradient is about 50 °C over the entire length of the capsule, and this factor was also taken into account. This gradient is likely to be larger in the smaller assemblies.

All experiments followed the standard procedure of cold pressurizing with subsequent heating to the target temperature with a 100 °C /min rate. Isobaric quenching of the experiments was achieved by turning off the power to the furnace, after which the sample was slowly decompressed. The cooling rate was approximately 200-250 °C /s.

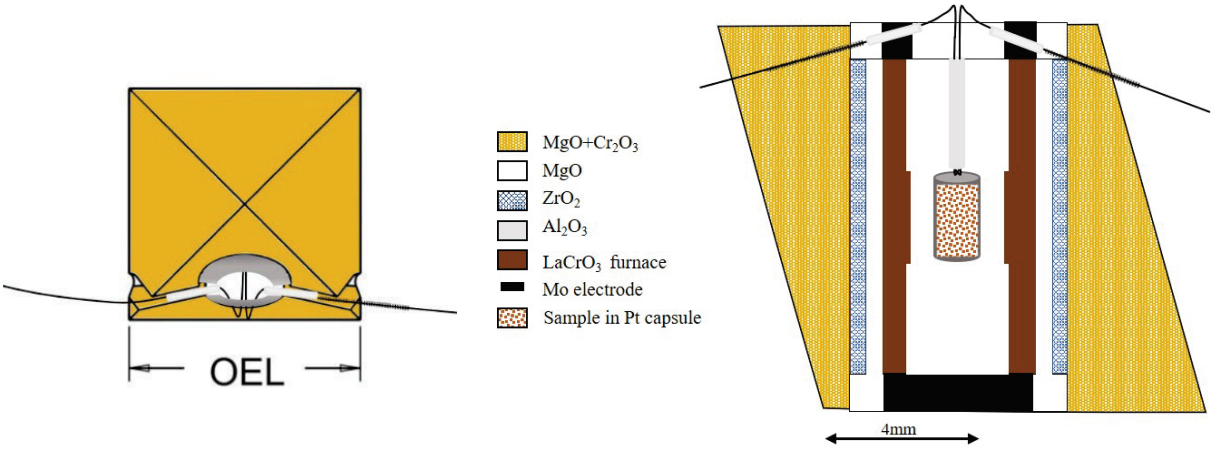

Figure 2.5.: Schematic setup of the 18/11 assembly type used for the low-pressure sample synthesis. The sample capsule (2 mm outer diameter) is placed together with the heater and the thermocouple inside an octahedrally shaped MgO pressure medium. The edge length of the octahedra is 18 mm.

2.3.1.1 Experiment at 30 GPa on the IRIS press

A single experiment was run at 30 GPa in the IRIS-15 Voggenreiter LPH 1500-840/200 press at the BGI. For this experiment 1.5 mm truncated TF05 WC (Ishii et al. 2016) anvils and a cell

assembly with dimensions of 5.7 mm (Figure 2.6) was employed. Two samples were placed, one above and one below the thermocouple junction. Each sample was 0.35 mm long and was located in a dense Al_2O_3 tube as capsule holder. Dimensions of the Al_2O_3 tube are 0.6 mm outer diameter and 0.25 mm inner diameter. In this specific setup, a 25 µm thick Rhenium (Re) foil heater was used and the thermocouple wires were inserted in the radial direction through the wall of the furnace with the junction located in the middle of the assembly.

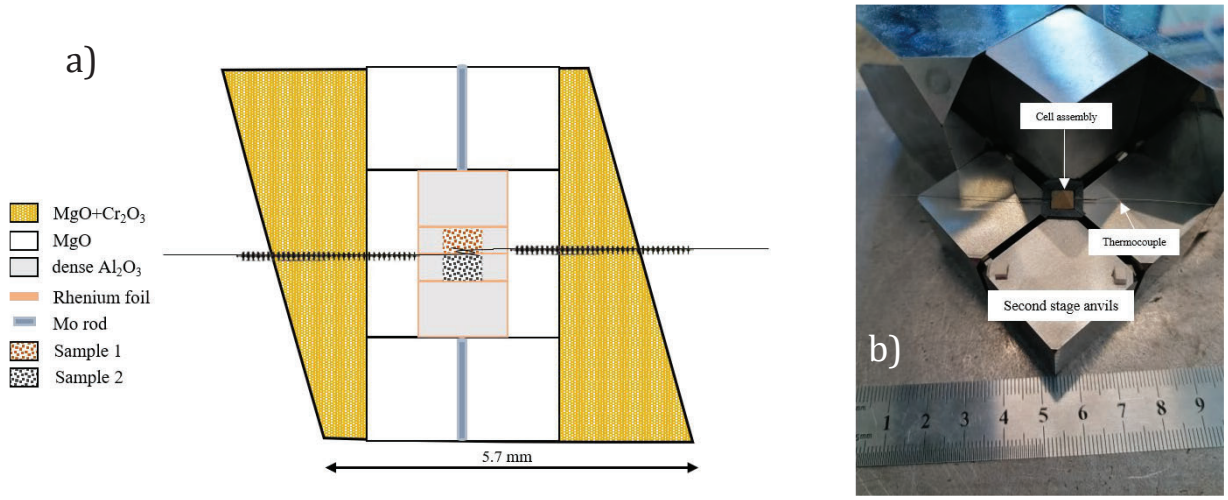

Figure 2.6: a) Schematic setup of the 5.7/1.5 modified assembly used for the 30 GPa experimental run. **b)** Second stage anvils with cell assembly, gaskets and thermocouples are shown as well to display the change of dimension in the setup.

2.3.1.2 Magnesioferrite single crystal synthesis

For the investigation of the magnesioferrite compressibility (Chapter 3), $MgFe_2O_4$ single crystals were produced using a pre-synthesized magnesioferrite powder. The synthesis details can be found in Uenver-Thiele et al. (2017b). The recovered magnesioferrite, $MgFe_2O_4$, had a unit-cell parameter of a = 8.3875(1) Å (Uenver-Thiele et al. 2017b). The high-pressure experiment was performed using an 18/11 Cr_2O_3-doped MgO octahedral pressure assembly. The starting material was loaded into a Pt capsule together with a thin layer of PtO_2 to maintain oxidizing conditions during the experiment. The capsule was then seal welded. The experiment was performed at 5 GPa

and 1300 °C for 8 hours. Heating was achieved with a graphite furnace and the temperature was monitored by a W_3/Re_{97}-W_{23}/Re_{75} thermocouple with no pressure correction applied to the electromotive force (emf). The run product (experiment S7645) consisted of black cubic-shaped single crystals with dimensions varying between 20 and 150 μm .

2.3.1.3 Nitrogen partitioning experiments and capsule designs

In the frame of the project described in Chapter 6, two different set of experiments were performed in order to investigate the behavior of nitrogen and its isotopes. A set of equilibration experiments was run on hydrous minerals and a diamond synthesis experiment was performed to investigate diamond-metallic melt N partitioning. Here, details of the different capsule designs are presented.

For the equilibration experiments, an Au-tube capsule was utilized and the powdered samples were loaded together with glycine ($C_2H_5NO_2$) (i.e., the nitrogen source) and a thin SiO_2 layer (Figure 2.7a). The SiO_2 layer allows the physical separation of the hydrous mineral from the residual C produced by the glycine decomposition, after the experiment so that they can be analysed separately. The experiments were performed at 3 GPa and 500 °C, where glycine breaks down according to $3C_2H_5NO_2 \rightarrow 6H_2O + NH_3 + 12C + N_2$. Fluid calculations using the Deep Earth Water model of Huang & Sverjensky (2019) at 3 GPa and 500°C confirm this speciation.

For diamond synthesis experiment, the Fe-Ni-S alloy powder was loaded into an MgO single-crystal capsule together with graphite (C) and glycine (Figure 2.7b). The filled single-crystal capsules were wrapped in a second capsule made of Pt-foil.

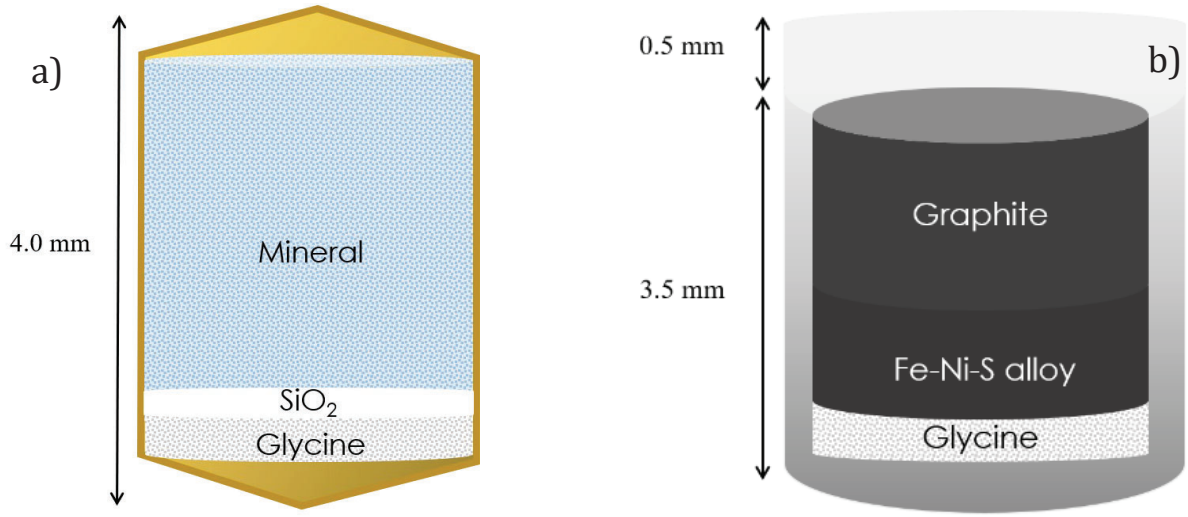

Figure 2.7: Schematic representation of the capsule designs used in the experiments described in Chapter 6. **(a)** The design used in the equilibration of hydrous minerals with glycine and **(b)** the MgO single-crystal capsule in which the diamond synthesis experiment was run.

2.4 Single crystal compressibility experiments

In Chapter 3, the $MgFe_2O_4$ single crystals synthesized in the multi-anvil press were used to study the compressibility of this spinel structured ferrite. In order to investigate the equation of state (EoS) of this mineral, the sample was loaded in a diamond anvil cell.

2.4.1 Diamond anvil cell technique

The diamond anvil cell (DAC) technique allows materials to be studied at pressures that now routinely exceed hundreds of GPa, through spectroscopic, X-ray diffraction and elastic-inelastic scattering techniques. This technique was first introduced by Weir et al. (1959) and through technical developments achieved in the subsequent years, the instrument is now capable of generating pressures up to 1 TPa, much higher than any static compression device (Yagi et al. 2019 and references therein).

The operating setup of the DAC comprises two opposing diamonds with the sample inserted in a pressure chamber drilled into a metal gasket that is compressed between the polished surface tips, culets, of the conically shaped diamond anvils (Figure 2.8). In this way, by decreasing the pressurized area down to surfaces of few tens of micrometres, pressures that exceed the Earth's core pressure can be achieved. Higher pressures are achieved using smaller culet surface areas but, at the same time, the sample dimensions also have to decrease. The diamond anvils are glued on to tungsten carbide seats that transfer the load achieved by tightening screws that join the two interlocking parts of the DAC body. The anvil culets compress a metallic gasket, commonly made of rhenium metal, that is pre-indented to a thickness of ~ 50 μm and drilled to create a sample chamber hole. The sample is placed inside the gasket hole, which is then filled with either a pressurised inert gas (e.g., Ne, Ar, He etc.), a liquid, or a solid (e.g., KCl, NaCl, MgO as a sandwich-like assembly), that acts as a pressure transmitting medium.

There are two main DAC designs employed in the HP-community. In the piston-cylinder design, the diamond seats are placed on opposing inner surfaces of two perfectly interlocking inner and outer cylinders. As force is applied to the DAC, the sliding piston and cylinder relationship helps to maintain the axial alignment of the diamond culets. The Merrill-Bassett design (Miletich et al., 2000; Bassett, 2009) comprises two plates to which the opposing diamond seats are attached. The plates are aligned through guide pins on one of the plates, which pass through holes on the opposing plate, resulting in a less sturdy alignment compared to the piston cylinder design.

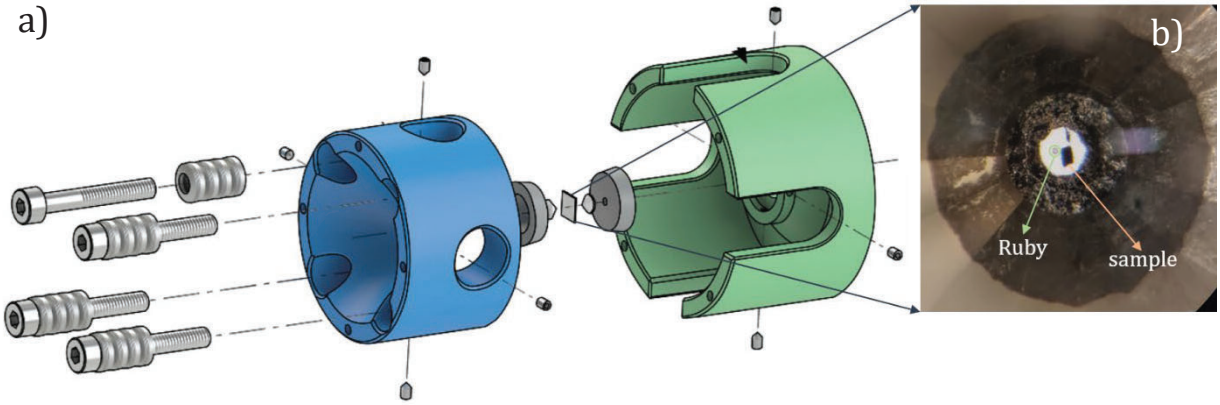

Figure 2.8: a) BX90 diamond anvil cell design modified after Kantor et al. (2012). **b)** An image of the magnesioferrite single crystal loaded in the cell together with the ruby chip can be observed in the enlarged image of the diamond cullet.

The diamond anvil cell used in this study is a BX90 type (Kantor et al. 2012) that is a screw-driven piston-cylinder-type DAC with symmetrical 90° axial openings. It was used with 400 μm culet diamonds with Boehler-Almax design (Boehler & De Hantsetters, 2004). The diamonds were fixed to cylindrical tungsten carbide seats with conical support and an opening angle of 90° using superglue. The alignment was performed using the optical interference fringes generated through contact of the culets of opposing anvils. A rhenium gasket (Re) with original thickness of 250 μm was pre-indented up to 11 GPa to a thickness of approximately 65 μm. The pressure achieved during the pre-indentation process was determined using the Raman shift of the diamond peak. Pressure determination using the diamond Raman procedure, described for example in Akahama & Kawamura (2006), relies on the correlation between the wavenumber of the Raman band with the normal stress of the culet surface. The analytical expression for quasi-hydrostatic pressure determination (Akahama & Kawamura, 2006) is,

$$P(GPa) = K_0 \left(\frac{\Delta_v}{\Delta_0}\right)\left[1 + \frac{1}{2}(K'_0 - 1)\left(\frac{\Delta_v}{\Delta_0}\right)\right] \quad (2)$$

where Δv is the measured wavenumber of the high frequency edge, v_0 is the edge frequency at ambient pressure (v_0 =1334 cm^{-1}), K_0 = 547 GPa and K'_0 = 3.75 are, respectively, the bulk modulus and the bulk modulus pressure derivative of a hydrostatically compressed elastic material, with properties calibrated to describe the relationship between the Raman frequency and the normal stress at the diamond anvil culet.

A hole of 250 μm diameter was made in the centre of the pre-indented gasket with a laser drilling apparatus, to provide the sample chamber (Figure 2.8) After cleaning all the cell components with ethanol, the gasket was placed on the top of one diamond and fixed with one small piece of putty. Details concerning sample loading are described in Chapter 3.

2.4.1.1 In-situ pressure determination

The fluorescence R_1 line of the ruby crystal inserted into the DAC sample chamber (Figure 2.8) was used to determine the pressure in-situ before and after each single-crystal X-ray diffraction measurement. The fluorescence bands were measured with a Raman micro-spectrometer equipped with a red He-Ne laser (λ= 632.8 nm) with 20 mW laser power. The spectrometer was centred at 694 nm to measure the ruby fluorescence lines at ambient pressure and was then progressively centred at higher wavenumbers according to the increasing pressure. Before every measurement, a ruby at ambient pressure conditions was measured as a reference. Fluorescence spectra for the ruby in the DAC were collected before and after every single-crystal X-ray diffraction experiment in order to detect possible pressure changes during the measurements.

The application Origin 2017G was used to fit the fluorescence spectra with two Lorentzian profiles for the fluorescence lines R_1 and R_2. Pressure was then calculated using the calibration reported by Dawaele et al. (2008) according to the relation:

$$P = \frac{A}{B} * \left[\left(1 + \frac{\Delta\lambda}{\lambda_0}\right)^B - 1\right] \quad (3)$$

where λ_0 is the position of the R_1 line at ambient conditions and $\Delta\lambda$ the shift in the R_1 line of the ruby inside the DAC. The A and B parameters are 1920 GPa and 9.61 respectively and were determined by calibration of the R_1 ruby fluorescence lines against the ambient-temperature equations of state of iron, cobalt, nickel, zinc, molybdenum and silver (Dawaele et al. 2008).

2.5 Single crystal X-ray diffraction

In the present work, selected single crystals were investigated by single crystal X-ray diffraction (XRD) both at room pressure and at high pressure in the diamond anvil cell. Different instruments were employed in the analytical process depending mainly on the size of the investigated sample. In the following paragraphs, the diffractometers used to characterize the magnesioferrite (mfr) and the $Mg_{0.5}Fe^{2+}_{0.5}Fe^{3+}_2O_4$ (Fe50) single crystals are described in detail.

2.5.1 Area detector diffractometer

An Oxford Diffraction Xcalibur diffractometer was used equipped with a Sapphire2 CCD area detector (90-92 mm diagonal, 1024 x 1024 pixels) and a ceramic X-ray tube with MoKα radiation (λ = 0.70784 Å) monochromated using a graphite crystal and operated at 50 kV and 40 mA. The crystal quality was initially tested by short intensity data collections, from which the orientation matrix was obtained (see also Section 2.6). This information was then used to conduct a more accurate analysis of peak shapes and line widths using a single-crystal diffractometer equipped with a point detector (see Section 2.5.2). Full intensity data collection for structural refinement was finally performed on a good-quality crystal in air. The crystal was mounted to the tip of a glass capillary and complete redundant intensity data (redundancy of 5) were collected using ω scans

with a width of 0.5° and a default time of 10 to 20 s in a 2θ range between 2 and 78°. The elevated redundancy helped identifing outlier reflections.

The data collection for the sample in the DAC was performed up to 2θ = 60° with a scan width of 0.5°, a longer acquisition time of 45 s, and a detector distance of 70 mm. After every data collection, a movie around the phi axis was recorded with 2° steps for shape determination, in order to apply an analytical absorption correction (Angel 2004). The cell was not tilted or reversed during the data collection.

2.5.2 Point detector diffractometer

In order to determine the lattice parameters of the investigated samples with high accuracy, a Huber four-circle diffractometer with a Eulerian cradle goniometer was employed equipped with a point detector. A collimated X-ray beam (MoKα radiation operating at 50 kV and 40 mA) helped to maximize the signal to noise ratio during the measurement and the point detector allowed a precise and accurate determination of the position of the reflections. The Huber diffractometer was driven by the SINGLE software described in Angel and Finger (2011). Every reflection was centered at eight equivalent positions in order to eliminate experimental aberrations such as crystal offset and incorrect zero positions of 2θ, ω, χ, and ϕ circles (Angel et al. 2000). Eight-position centering was performed on 16 reflections for both samples in air with the crystals mounted on a glass fiber. Vector-least-square analysis of the centered reflections was used to determine the unit-cell lattice parameters of the investigated samples (Shoemaker and Bassi 1970; Tichy 1970). The room-pressure unit-cell lattice parameters determined for the two samples are reported in Table 3.1 in Chapter 3.

Due to the small size of the magnesioferrite crystal (60 x 40 x 20 μm^3) it was necessary to perform the in-situ single-crystal X-ray diffraction measurements in a DAC using a Huber four-circle

Eulerian cradle diffractometer equipped with a high-brilliance rotating anode X-ray source FR-E+ SuperBright, which used MoKα radiation (λ = 0.70784 Å) operated at 45 kV and 55 mA (Figure 2.9).

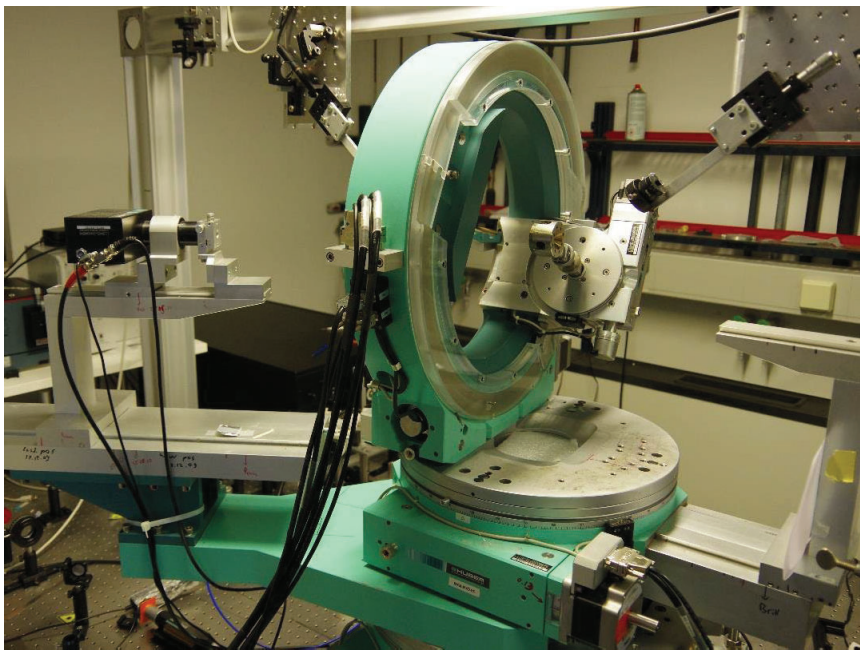

Figure 2.9: Eulerian cradle four-circle diffractometer in combination with the Brillouin spectroscopy setup at BGI. The diffractometer has a high-brilliance rotating anode and a point detector allowing for measurements of small single-crystals.

In this machine, multilayer VaryMax^{TM} optics were used to focus the X-ray beam at a distance of 800 mm from the sample (Trots et al.2011). The detector consisted of a YAP:Ce scintillator coupled to a photomultiplier, amplifier, and two discriminators. The advantage of this diffractometer with respect to the conventional Huber diffractometer described above, comes from the brightness of the rotating anode, which gives rise to an increase of the reflection intensities up to 80 times (Trost et al. 2011, Pamato 2014). In this way it was possible to measure small single crystals with dimensions of less than 60 μm. At each pressure point, 16 reflections were centered with the eight-position centering method previously described (King and Finger 1979). In this machine, the $K\alpha_1/K\alpha_2$ ratio is not constant due to the presence of the focusing mirrors, and the data is collected allowing the machine to fit the ratio for all the reflections. In the case of the

sample in this study, the last three pressure points showed some peak broadening and were therefore collected with a fixed $K\alpha_1$ /$K\alpha_2$ ratio of 0.3. After the data collection, each reflection was individually fitted using the software WinIntegrStp 372 (Angel 2003). The software allows the integration of single-crystal intensity data using pseudo-Voight functions. Table 3.3 in Chapter 3 reports all pressure points and cell parameter collected in this study.

2.6 Single crystal structural refinements

Single crystal intensity data were integrated with the CrysAlisPro 171.37.39 software (Rigaku, Oxford Diffraction). An initial peak search allows all possible reflections in the measured frames to be identified. The software itself proceeds with an automatic integration and indexing procedure to search for the most likely unit-cell lattice parameters and for the orientation of the investigated crystal with respect to the diffractometer axes. Once the orientation matrix and the correct unit-cell lattice parameters have been obtained, an automatic integration, which also accounts for the contribution of the background, is run over all collected frames, so that the intensity of each reflection is calculated. During this integration, Lorentz and polarization corrections as well as an empirical absorption correction are included. Outlier rejection for $m\bar{3}m$ Laue class was selected, Friedel mates were used as equivalents and a F-lattice filter was applied. For the collected sample, the shape of the sample was taken into account by manually drawing the individual faces around the image of the crystal acquired with a movie. Using the Clark and Reid (1995) analytical formulation, shape optimization was applied for absorption correction.

After the finalization of the data integration procedure, very good R_{int} values were obtained, which indicate the discrepancy between equivalent reflections, according to the following expression:

$$R_{int} = \frac{\sum|F_o^2 - F_o^2(mean)|}{\sum F_o^2} \quad (4)$$

Where F_0^2 represents the observed intensity.

For the dataset collected with a DAC, a numerical absorption correction was performed using the Absorb6.0 package. This package, written by Angel (2004), is integrated into the CrysAlisPro absorption correction software and performs path length calculations over a Gaussian grid of unequally spaced points in order to calculate the difference between the paths of the incident and diffracted beams. To determine the shape of the sample, faces are manually drawn around the sample to estimate its shape. After inserting the sample thickness and specifying whether it is positioned on the incident or the diffracted side of the diamond anvil cell, the absorption correction runs during the integration procedure described above. After finalizing the integration process with the CrysAlisPro software, an *hkl*-file containing a list of intensities with respective Miller indices and errors is obtained, which are used to calculate the squared structural factors for the structural refinements. The observed reflection conditions were consistent with the $Fd\bar{3}m$ space group, therefore a structure solution and refinement based on F^2 were performed with the SHELX97 program package (Sheldrick 2008) in the ShelXle (Hübschle et al. 2011) graphical user interface using this space group. Scattering factors for neutral species (Ibers and Hamilton 1974) were employed for Mg, Fe and O, all sites were considered to be fully occupied, and all displacement parameters were refined anisotropically. Moreover, the occupancies of Mg and Fe were refined without chemical constraints both at the tetrahedral and at the octahedral sites. Finally, an instruction-file (.cif), containing all the information about the crystal model, was created.

The goodness of the refinement procedures can be checked considering several parameters. The weighted discrepancy index that defines the quantities minimized during the structural refinement ($wR2$) is defined considering the intensity values:

$$wR2 = \sqrt{\frac{\sum w(F_o^2 - F_c^2)^2}{\sum w(F_o^2)^2}} \tag{5}$$

Where w stands for weight (e.g. relative intensities of the peaks), F_0 represents the observed and F_c the calculated structural factors larger than $4\sigma(F)$. The weighting scheme in ShelX is simplified to:

$$w = \frac{1}{\sigma^2(F_o^2) + (aP)^2 + bP} \tag{6}$$

Where *a* and *b* are parameters chosen by the program and

$$P = \frac{2F_c^2 + Max\ (F_o^2, 0)}{3} \tag{7}$$

The residual R index is calculated to describe the reflection-by-reflection disagreement between the observed and calculated one:

$$R1 = \frac{\sum\left||F_o| - |F_c|\right|}{\sum|F_o|} \tag{8}$$

The goodness-of-fit parameter (GooF) is an indicator for the distribution of the difference between the calculated and the measured intensities to the distribution expected from the weight of the refinement and should lie close to 1.

$$GooF = \sqrt{\frac{\sum w(F_o^2 - F_c^2)^2}{n - m}} \tag{9}$$

Where *n* describes the number of data points and *m* the number of refined parameters. Further details on the structural refinement for the crystals with compositions along the magnetite-magnesioferrite join are reported in Chapter 3 in paragraph 3.2.3.

2.7 Equations of state (EoS)

The volume variation of a solid material with pressure and temperature is described by its equation of state (EoS) (e.g., Angel.2000). Equations of state also define the elastic properties of the investigated material and therefore not only provide fundamental thermodynamic data but also

give insights into the interatomic interactions within the solid state. These interactions resist the externally applied compressive stresses and also control the thermal expansion.

An EoS allows the derivation of elastic parameters such as the bulk modulus, defined as

$$K = -V\left(\frac{\delta P}{\delta V}\right)_T \tag{10}$$

and its pressure derivatives

$$K' = \left(\frac{\delta K}{\delta P}\right)_T \tag{11}$$

$$K'' = \left(\frac{\delta^2 K}{\delta P^2}\right)_T \tag{12}$$

There is no absolute thermodynamic basis to define the correct form of the EoS of solids, hence all equations of states that have been developed are based on assumptions. The validity of these assumptions can only be judged in terms of whether the derived EoS reproduces the experimental data.

The Birch-Murnaghan EoS (BM-EoS) is the most common equation of state used in geoscience to fit compressibility data, and it is preferred to the earlier Murnaghan EoS (Murnaghan 1937), which is only valid for compression smaller than 10% (Angel 2000). The BM-EoS is a finite strain EoS based on the assumption that the strain energy of a solid under compression can be expressed as a Taylor series in the finite Eulerian strain ε. The Eulerian finite strain of an elastically isotropic body is defined by considering the coordinates of a particle in the final or strained condition.

The Birch-Murnaghan Eos (Birch 1947) is based upon the Eulerian strain, f_E:

$$f_E = \frac{1}{2}\left[\left(\frac{V_0}{V_P}\right)^{\frac{2}{3}} - 1\right] = -\varepsilon \tag{13}$$

The resulting relationship between pressure and volume at a reference temperature, which in this study was 298 K, is expressed as follows:

$$P(V) = 3K_0 f_E(1+2f_E)^{\frac{5}{2}}(1+\frac{3}{2}(K'-4)f_E+\frac{3}{2}(K_0K"+(K'-4)(K'-3)+\frac{35}{9})f_E{}^2). \quad (14)$$

The program EoSfitGUI (Angel et al. 2014) has been used to fit the pressure- volume data collected in Chapter 3 using a BM-EoS. The program is based on a least-square fitting aimed at minimizing the weighted sum of the squares of the differences between the observed and calculated pressures at a given volume, according to the expression:

$$\chi_w^2 = \frac{1}{n-m}\sum w_i \left(P_{obs,i} - EoS(V_{obs,i}, T_{obs,i})\right)^2 \quad (15)$$

Where n is the number of data points with weight w_i and m is the number of refined parameters. A visual diagnostic tool to determine at which order term to truncate the Taylor expansion of the strain energy and hence which bulk modulus derivative, such as K' and K'', should be refined, is provided by the F-f_E plot. This plot expresses the normalized pressure F versus the Eulerian strain f_E. The normalized pressure for a Birch-Murnaghan EoS can be calculated using the following equation:

$$F = \frac{P}{3f_E\,(1+2f_E)^{5/2}} \quad (16)$$

When the P-V data are transformed into and F-f_E plot, a direct indication of the compressional behaviour is obtained. If the data points all lie on a horizontal line of constant F, then K' is equal to 4 and the data can be fitted with a second-order truncation of the Birch-Murnaghan EoS. On the other hand, if the data points plot as an inclined straight line, the slope of the line provides the value of K' according to the relation

$$slope = \frac{3K_0(K'-4)}{2} \quad (17)$$

and the data can be adequately described by a third-order truncation. In both cases, K'' has an implied value based on the values of K_0 and K' and can be calculated using the following equation:

$$K" = \frac{-1}{K_0}\left[(3-K')(4-K')+\frac{35}{9}\right] \quad (18)$$

If the data are described as a parabolic curve, they need to be fitted with a fourth-order equation of state which requires four variables (V_0, K_0, K' and K'').

In Chapter 3, the results of EoS fittings are shown in Table 3.1 and displayed in Figure 3.4 and 3.5.

2.8 Analytical Techniques

After recovering the capsules from the multi-anvil experiments, all synthesized samples were mounted in epoxy resin, sectioned and polished for analysis with a scanning electron microscope (SEM), electron probe microanalysis (EPMA), X-ray powder diffraction (XRD), or Mössbauer spectroscopy (MS). Before SEM and EPMA measurements, the samples were coated with a ~12 nm thick carbon layer to avoid electrical charging of the surface under the electron beam. All the analytical techniques used are described in the following sub-sections and some more specific details can be found in the respective chapters.

2.8.1 Scanning electron microscopy

Scanning electron microscopy (SEM) was firstly used on all the recovered samples to obtain magnified, high special resolution images and to identify the crystallized phases by semi-quantitatively determining the mineral compositions. In the SEM, a focused electron beam is produced by an electron gun and scanned across the polished specimen. Interactions between the electron beam and the sample produce different signals such as secondary electrons (SE), backscattered electrons (BSE) and Auger electrons (Figure 2.9). Secondary electrons are emitted from the near-surface regions of the sample as a result of inelastic interactions between the primary electron beam and the sample, and provide information on the sample's surface topography. Backscattered electrons originate through elastic interactions between the beam and the sample.

BSE are strongly dependent on the average atomic number of the target phase and therefore can provide an image that varies in brightness depending on the atomic number of the analyzed material. Moreover, inner shell electrons are ejected through interaction with the electron beam. When outer shell electrons fall back to fill the resulting empty shells, characteristic X-ray radiation is emitted. These characteristic energies depend on the electronic configuration of the elements in the sample and can be recorded in so called energy dispersive mode, providing a qualitative chemical composition of the individual phases.

Preliminary energy-dispersive X-ray spectroscopy (EDS) measurements of sample compositions and high-quality images were collected using a GEMINI LEO 1530 scanning electron microprobe operating at 21 kV, 14 mm working distance, and using a Si (Li) detector from Oxford INCA. This provided an overview of the crystallized phases in the run product, the crystallite sizes, and qualitative compositions. Data acquisition and post-processing was performed with the AZtec software from Oxford Instruments.

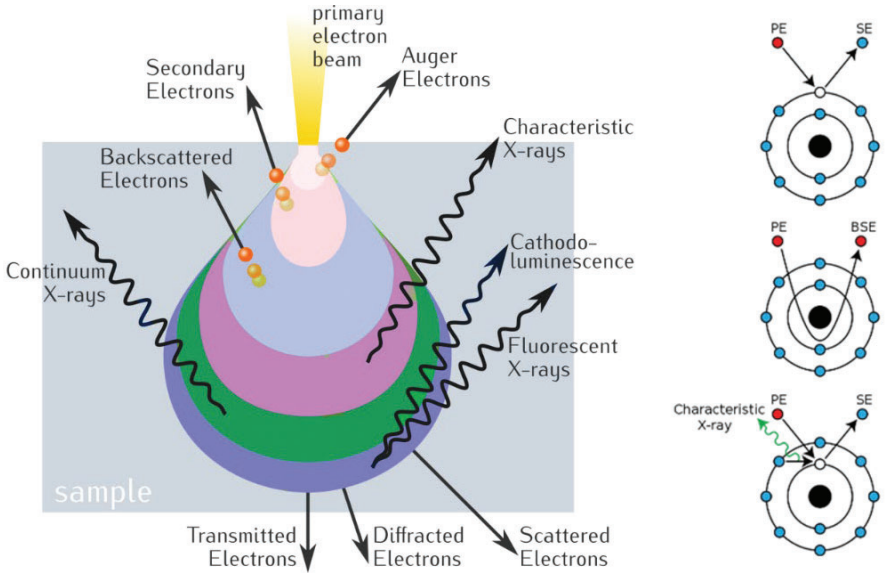

Figure 2.9: Schematic illustration of the interaction volume with the electron beam (PE). High energy back scattered electrons provide information from a larger sample volume than secondary electrons. Characteristic X-rays used for chemical analyses arise from an even larger volume (image modified after vaccoat.com).

2.8.2 Electron probe micro-analyzer

In order to acquire an accurate quantitative composition of the major elements in the different samples, electron microprobe measurements were performed. The JEOL JXA-8200 electron microprobe (EPMA) equipped with five wavelength-dispersive spectrometers at BGI was used to determine the composition of all the synthesized samples.

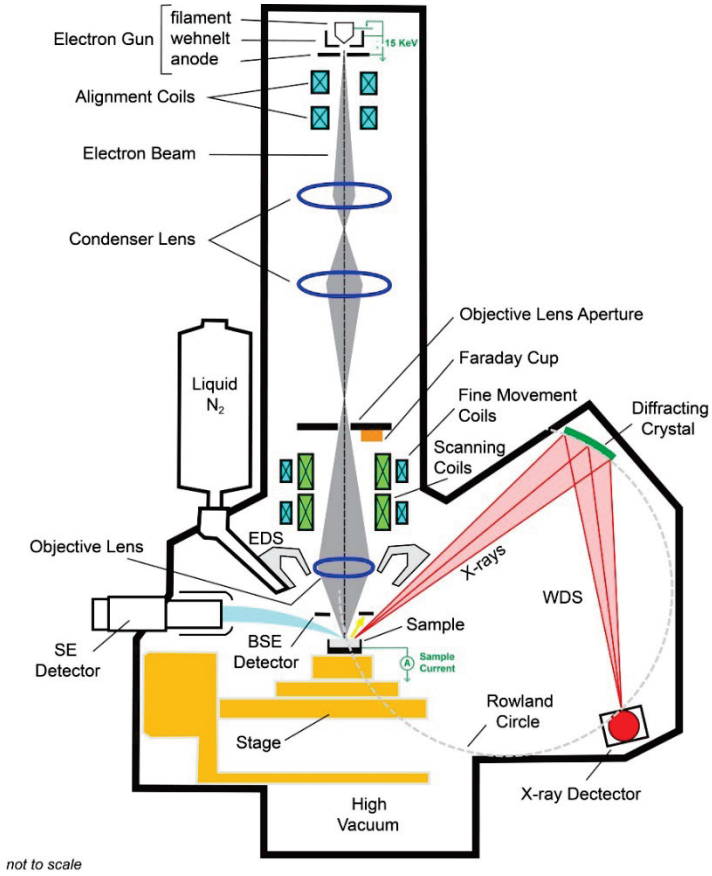

Figure 2.10: Configuration of an electron microprobe (source: UCLA.org).

The principle behind the electron microprobe is fundamentally the same as the SEM described in the section above and its main components are shown in Figure 2.10. Similar to the SEM, the sample is bombarded by an accelerated and focused electron beam generated by a tungsten filament. The interaction between the beam and the sample yields both derivative electrons and X-rays. Accurate quantitative elemental analyses come from the intensity of characteristic X-rays that are emitted depending on elemental abundancies in the analyzed phases. Characteristic X-ray

can be analyzed either by an energy dispersive spectrometer (EDS) or in wavelength dispersive mode using spectrometers with different diffracting crystals.

In this thesis, wavelength-dispersive spectroscopy (WDS) was employed to obtain precise quantitative analyses of experimental samples. WDS uses two main components: one or more diffracting crystals of known *d*-spacing and an X-ray detector. According to Bragg equation ($n\lambda = 2d\sin\theta$) the diffracting crystal is used to both discriminate X-rays and to focus them to an X-ray detector. By rotating the crystal relative to the point source of X-rays, the value of θ is changed and different X-ray wavelengths are thus diffracted to the detector. The X-ray source (i.e., the sample), the diffracting crystal, and the detector lie on the circumference of an imaginary circle (Rowland circle). The diffracting crystal is curved with the same circumference and by moving it and the detector along the same Rowland circle ensures the same focusing geometry at the detector. The different crystal spectrometers such as synthetic LiF (lithium fluoride), TAP (thallium acid phthalate) and PET (pentaerythritol) crystals that have known *d*-spacings allow the intensity and the position of the spectral lines to be compared with those emitted by standard materials (Reed,2005).

In EPMA analysis, a matrix correction is applied in order to obtain true concentrations, including atomic number, absorption and fluorescence correction. There are two main types of models used for matrix correction: a ZAF (atomic number-absorption-fluorescence) correction, which is a generalized algebraic procedure that assumes a linear relation between concentration and X-ray intensities; a phi-rho-Z (e.g., PRZ "mass depth" or Rho-Z, the function that describes the relative intensity of X-ray generation with mass depth, is call Phi) which is a method that uses the depth distribution of the generated characteristic X-rays, where the atomic number (Z) effect and the absorption (A) effect are simultaneously taken into account. A full description of the EPMA principle and instrumentation can be found in Reed (2005).

2.8.3 Powder X-ray diffraction

Powder X-ray diffraction (XRD) allows phase identification as well as the determination of unit-cell lattice parameters and, using Rietveld analysis, crystal structures. The method employs the Bragg equation: $n\lambda = 2d\sin\theta$, which relates the wavelength λ of the incident radiation, the lattice spacing within crystalline materials (d) with the angle (θ) of the scattered X-ray beam. The diffraction geometry is shown in Figure 2.11, where an incident beam is being diffracted from two successive (*hkl*) planes, where d_{hkl} is the interplanar spacing.

$AB + BC = 2d_{hkl}sin\theta$ defines the path difference for beams from successive planes. The path difference between two X-ray beams diffracted from two equivalent *hkl* planes is an integral number *n* of the wavelength. In a polycrystalline sample containing sufficient crystallites, the Bragg equation is satisfied simultaneously for the different *d* spacings, as long as the crystallites are randomly distributed in the sample.

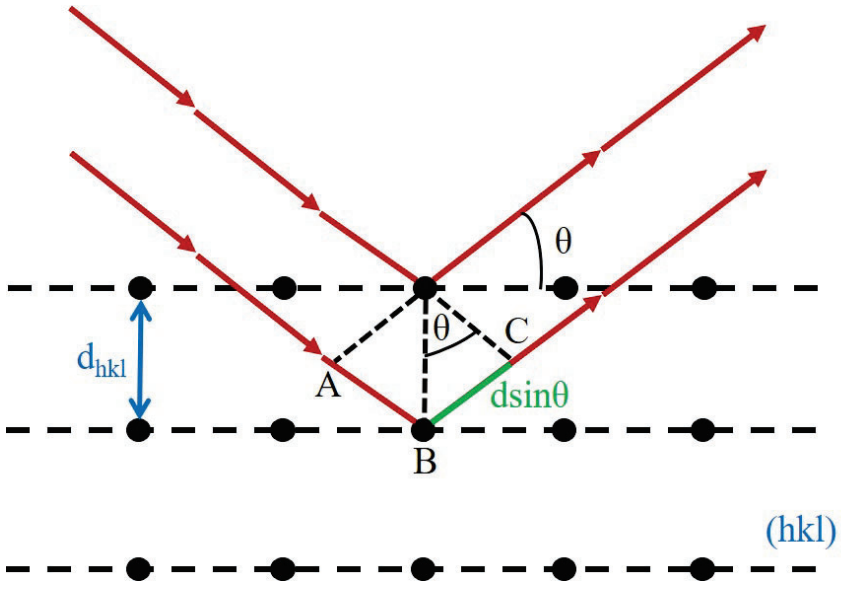

Figure 2.11: The conditions for a Bragg reflection diffracted from a plane (*hkl*) with a *d*-spacing d_{hkl} at a scattering angle of θ. The path difference between the two beams "reflected" from the successive plane is AB+BC, which is an integral number of λ. Image has been modified from Putnis (1992)

A Bruker D8 DISCOVER micro focused X-ray diffractometer equipped with a micro-focus source (IμS) using CoKα radiation and operated at 40 kV and 500 μA, was employed with a two-dimensional solid-state detector (VÅNTEC500). The X-ray beam is collimated to a minimum spot size of 50 μm diameter by an IFG polycapillary X-ray mini-lens. The detector is a 2 - dimensional large-area detector that allows the collection of a large reciprocal space up to high diffraction angles. Data collections were performed in a 2θ range between 25° and 85° for a total measurement time of 3600 s. The collected X-ray patterns were integrated using the DIFFRACEVA-V3.1 package and compared to the "Crystallography Open Data" database.

XRD measurements in this study were also performed employing the Philips X'Pert PRO diffractometer using monochromatic CoKα (λ = 1.78897 Å) radiation selected with a focusing monochromator (i.e., a symmetrically cut curved Johansson Ge (111) crystal) and equipped with a Philips X'celerator detector. Silicon (NIST SRM 640c) was added as an internal standard. Data were collected between 10° and 120° 2θ at 40 kV and 40 nA.

Unit-cell lattice parameters were determined using the general structure analysis system (GSAS) software package and the EXPGUI interface (Toby 2001; Larson and von Dreele 2004). Unit-cell lattice parameters of the phases obtained with the Bruker D8 DISCOVER micro focused X-ray diffractometer are provided in Table A.5.1 in the Appendix of Chapter 5. Unit-cell lattice parameters obtained from the Philips X'Pert PRO diffractometer are reported in Table 4.3 in Chapter 4.

2.8.4 Mössbauer Spectroscopy

Mössbauer spectroscopy (MS) is a convenient and reliable analytical method for the precise determination of iron oxidation state, coordination and magnetic characteristics. In the present work, MS was used for determining the Fe valence state in the samples discussed in Chapters 3 to

5. The foundations of the Mössbauer (Mössbauer, 1958) methodology are described in detail in Bancroft (1973) and Gütlich et al. (1978) and reviewed in McCammon (1995, 2000), McCammon et al. (2004), and Dyar et al. (2006).

This technique is based on the Mössbasuer effect which is the recoilless resonant emission and absorption of γ-rays (quanta of photon radiation) by atomic nuclei. During the nearly recoil-free emission and absorption of γ-photons, the energy of the absorbed and emitted photon is nearly identical. A nucleus confined within a solid emits and absorbs γ-rays without energy loss, which would otherwise occur due to the recoil of an isolated nucleus. In a solid, the recoil momentum is transferred to the surrounding crystal lattice, resulting in a strong resonance at the same energy level. The absorption/emission energy range is restricted to the full-width half maximum (FWHM) of the nuclear transition, as dictated by the Heisenberg uncertainty principle, and it is related to the lifetime of the nuclear excited state. For this reason, this effect can be exploited for very sensitive measurements of the chemical environment of target atoms given the extremely narrow natural linewidth of the transition. Therefore, by probing the chemical environment of atomic nuclei, Mössbauer spectroscopy allows the determination of the coordination and oxidation state of atoms.

A radioactive source is used to produce γ-rays that are transmitted through the sample. Part of the gamma rays get absorbed and re-emitted by the atoms in the target material, while the others pass through the sample with no interaction and are collected by a detector located behind the sample. The resulting spectrum, therefore, presents dips, rather than peaks, in the count rate at the discrete energies where photons were absorbed. The capacity of an atom to absorb and emit gamma rays is at certain discrete, quantized energies, and so the source must emit radiation that is at the right energy for the isotope of interest. In the case of ^{57}Fe, a source of ^{57}Co with a half-life of 271.8 days is conventionally used. The Co isotope decays, via electron capture (β-decay), to an excited state of ^{57}Fe* with an excitation energy of 136.3 keV. From this state, ^{57}Fe* decays to its ground state

through a series of γ-photon emissions. Approximately 9% of the excited ^{57}Fe decays directly into the ground state, while the remaining 91% first relaxes to a 14.4 keV energy level before reaching the ground state. The characteristic radiation at 14.4 keV are distinctive for the free Fe atom (Dyar et al. 2006). The emission of gamma rays comprises 11% of the total emitted radiation and has a life time of ~141 ns (Figure 2.12). The ^{57}Co radioactive parent is commonly included in a Rh matrix to prevent ^{57}Co magnetic interactions.

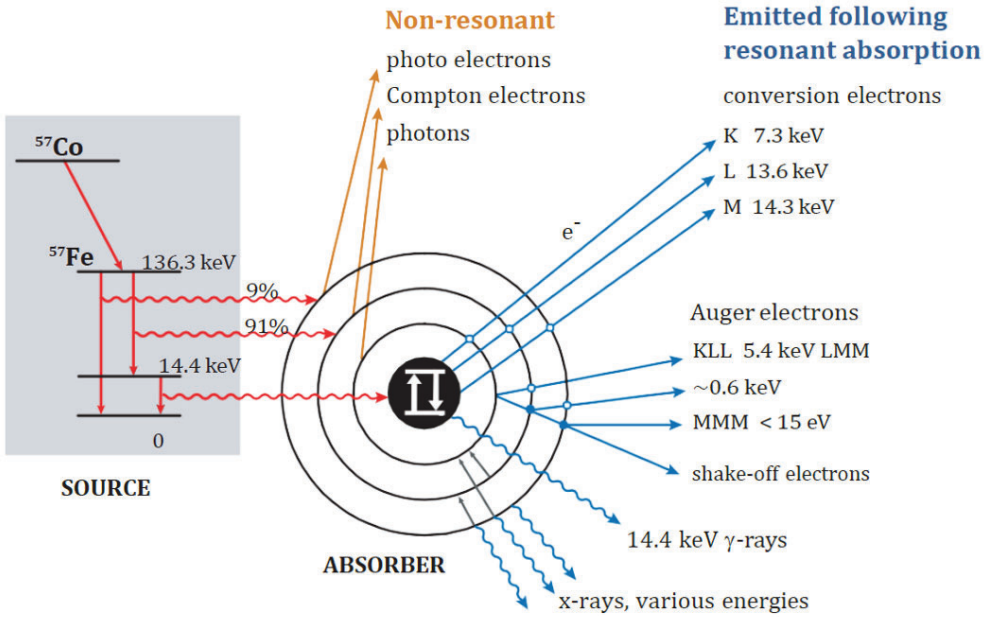

Figure 2.12: The nuclear decay scheme for ^{57}Co→^{57}Fe and various backscattering processes for ^{57}Fe that can follow resonant absorption of an incident gamma photon, modified from Dyar et al. (2006). ^{57}Co has a 270-day half-life and decays primarily to the 136.3-keV level of ^{57}Fe. 9% of the time, deexcitation is directly to the ground state with emission of a 136.3-keV gamma photon. Otherwise, decay is to the 14.4-keV state and then to the ground state with a half-life of 97.7×10−9 s. Of the 14.4 keV transitions, ~11% result in emission of a gamma ray, whereas the remaining 89% result in transfer of the transition energy to an atomic electron. As the Fe atom must undergo some electronic rearrangement to accommodate the vacancy that results, emission of characteristic X-rays and possibly Auger electrons may occur.

The nuclear energy levels are modified by the nuclear electronic environment, creating several characteristics in the spectrum that are described by the so-called hyperfine parameters. These

parameters are products of fixed nuclear and variable electronic properties and are used to identify both the coordination and redox state of Fe. A typical Mössbauer spectrum consists of sets of dips, usually in doublets or sextets, with each set corresponding to an iron nucleus in a specific environment in the sample. Different sets of dips depend on the environment experienced by the Fe nucleus. The nuclear environment itself depends on factors such as the number of electrons (Fe^0, Fe^{2+}, Fe^{3+}), number of coordinating anions, symmetry of the site, and presence/absence of magnetic ordering. For this reason, the resulting spectra of a sample consists of a superimposition of doublets and sextets.

In order to characterize the different effects on the resulting spectrum due to the electronic environment of the Fe nucleus, the hyperfine parameters are used. Hyperfine parameters are defined as: isomer shift (IS)/center shift (δ or CS), quadrupole splitting (QS), and magnetic hyperfine coupling/ hyperfine splitting (B_{hf}) (Figure 2.13). The local environment around Fe atoms in the source and the absorber are not the same and this leads to an offset from the zero-velocity position in the transmission spectrum (CS). As a consequence, the CS parameter is generally reported relative to an α-Fe standard absorber, and reveals important information such as valence, spin and coordination state of the examined atom in the sample. The center shift is extremely sensitive to the oxidation state of the sample; it decreases with increasing s-electron density around the nucleus which also depends on the type and bond length of ligands coordinated to the Fe atoms. A quadrupole splitting (QS) occurs due to the interaction of the nuclear quadrupole moment of the atom with the electric field gradient around the nucleus, resulting in a splitting of the excited state into two different excited levels. This is caused by the asymmetric electronic charge distribution of an atom that produces an electric field gradient around the nucleus. For ^{57}Fe nucleus the excited state is split in two sublevels which appear as two distinct absorption lines (doublet) in a Mössbauer spectrum. In a doublet, QS is defined as the difference between the two transition energies or rather the separation between the two component peaks. QS is sensitive to oxidation

state and site geometry. For magnetic phases, the nuclear energy levels are usually split into a sextet due to the Zeeman-effect. This defines the magnetic hyperfine splitting that follows the selection rules for magnetic dipole transitions where six transitions are allowed, resulting in a sextet in the Mössbauer spectrum. The excited state of ^{57}Fe split into four energy levels for a total of six possible transitions that form six absorption line dips in the Mössbauer spectrum. This parameter gives information about the magnetic structure of the investigated material.

The combination of the hyperfine interactions (i.e., CS and QS) provides characteristic information about the oxidation state and site occupancy of Fe in the investigated sample (Figure 2.13 B). The absolute values of hyperfine parameters are specific for a certain redox state and coordination of an Fe atom, and they can coexist in experimental products. This leads to overlapping of the signals that have to be appropriately deconvoluted by considering the relative abundance of the different phases.

a)

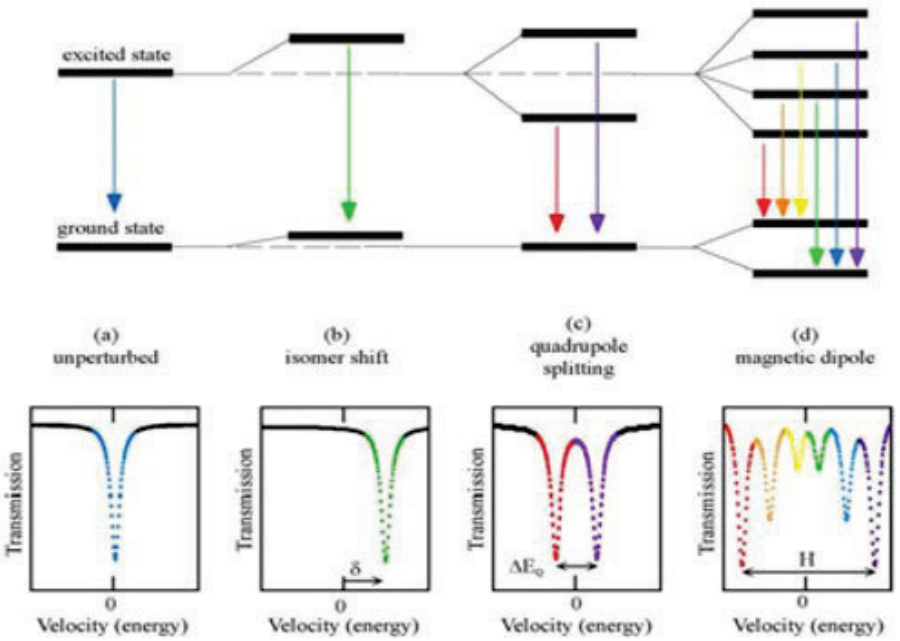

b)

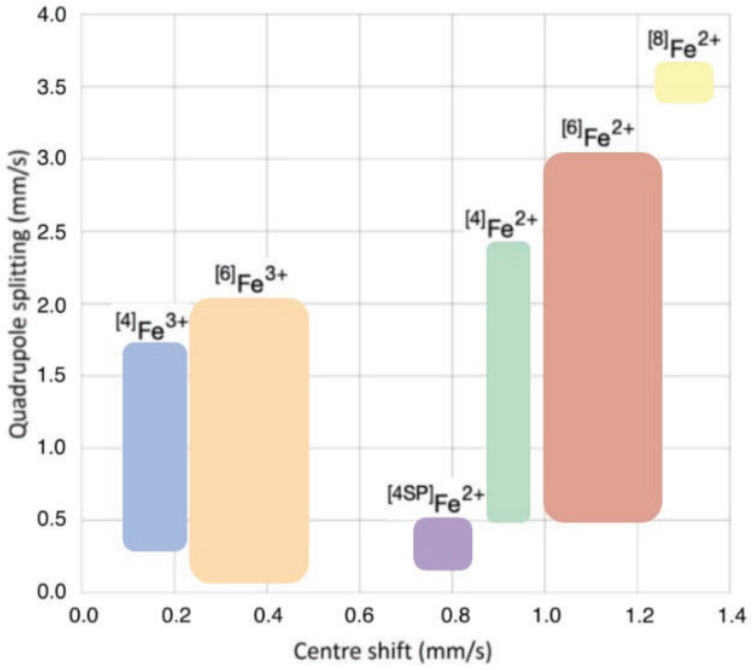

Figure 2.13: **(a)** Schematic illustration of the hyperfine parameters. Figure modified from (McCammon 2000) **(b)** Room temperature center shift vs quadrupole splitting data for common rock-forming minerals (after McCammon, unpublished, based on data from Burns and Solberg 1990).The region with CS in the range 0.5-0.9 mm/s is poorly constrained and usually assigned to $Fe^{2.5+}$, representing the delocalization of electrons between Fe^{2+} and Fe^{3+}.

In the present work, the samples recovered from multi-anvil experiments described in Chapter 5 were polished to a thickness varying between 250 and 200 μm, depending on the iron content of the sample, calculated to be the thickness giving an ideal Mössbauer signal (Long et al. 1983). A Pb-foil with a hole was used to reduce the beam size on the sample to a diameter of 1 mm. The samples investigated in Chapter 4 on the other hand, were prepared as powder samples and loaded in sample holders with diameter of 12 mm. The optimum powder weight was calculated based on the Fe content and electronic absorption coefficients.

Powdered samples were analysed using a conventional Mössbauer source (nominal 1.85 GBq over 5mm diameter), whereas polished samples were measured with a Mössbauer point source (nominal 370 MBq over 500μm diameter) at room temperature conditions. Cumulative spectra were acquired using a proportional counter, and multichannel scaling mode with 512 channels was used

with a constant acceleration over a velocity range. The energy of the gamma rays was Doppler-shifted with velocities ranging from +5 to -5 mm/s and +12 to –12 mm/s by moving the source relative to the sample in constant acceleration mode. The velocity scale was calibrated relative to α-Fe foil. The resulting spectra were fitted using a pseudo-Voigt line shape and a 1st order polynomial baseline with MossA 1.01f software package (Prescher et al. 2012). All spectra were fitted with the smallest number of adjustable parameters needed to obtain a statistically good fit. A full transmission integral was used to account for the thickness effect of the point source. Note that Mössbauer spectra could only be collected for bulk assemblages due to the large beam size. Some of the spectra showing a strong magnetic component were fit using the NORMOS program written by R.A. Brand (distributed by Wissenschaftliche Elektronik GmbH, Germany) given that it provides a more rigorous modelling of the magnetic field distribution, therefore allowing a more realistic fit. Extensive descriptions of the fitting procedure and resulting hyperfine parameters for all the samples investigate using MS can be found in Chapters 4 and 5.

2.8.5 Synchrotron Mössbauer Source spectroscopy

The Synchrotron Mössbauer Source (SMS) at the Nuclear Resonance Beamline (ID18) at the European Synchrotron Facility (ESRF) in Grenoble, France, allows phase specific, high spatial resolution and low acquisition time measurements to probe the electronic and magnetic properties of iron. SMS is dedicated to the excitation of nuclear levels by synchrotron radiation and is based on pure nuclear reflection of an iron borate crystal ($^{57}FeBO_3$). The sources of radiation and optical elements are optimized to provide an intense, highly monochromatic, collimated, and stable X-ray beam of small cross-section at the Mössbauer transition energy of 14.4 keV. In contrast to radioactive sources, the beam emitted by the SMS is fully resonant and fully polarized, has high brilliance and can be focused to a 10 μm × 10 μm spot. The SMS spectrum of sample Fe50 (Chapter 3) was collected at the ID18 beamline (Rüffer and Chumakov 1996) using the nuclear

monochromator as described by Potapkin et al. (2012). Before and after collection of the sample spectrum, the linewidth was controlled via acquisition of a spectrum of $K_2Mg^{57}Fe(CN)_6$, which consists of a single line. The velocity scale was ±12 mm/s and was calibrated using 25 μm thick natural-enriched α-Fe foil. A Mössbauer spectrum of the sample was collected for 2 hours and fitted using pseudo-Voigt line shapes and a 1st order polynomial baseline with the MossA 1.01f software package (Prescher et al. 2012*).* Details of the fitting of the collected spectrum and the site occupancies can be found in Chapter 3, Figure 3.1.

2.8.6 Elemental analyzer isotope ratio mass spectrometer

The elemental analyser isotope ratio mass spectrometer (EA-irMS) is a bulk measurement technique that provides representative data for the average isotopic signal and elemental concentration in the sample of interest (Figure 2.14). As this is a bulk technique, phases have to be separated to get individual analyses. The bulk sample is weighted, placed into a tin capsule and lowered into a combustion furnace through an auto sampler carousel, where it is combusted at elevated temperatures (1020 °C). The latent heat associated with the oxidation of the tin capsule temporarily increases the combustion temperature up to 1800ºC, creating the conditions for the rock forming mineral to be combusted. Combustion takes place in an O_2 atmosphere in a quartz reactor to produce N_2+N_xO_y, and CO_2. All gas products are carried by He flow (130 mL/min). The reactor typically contains Cr_2O_3, as an oxidant and Co_3O_4 + Ag to bind sulphur and halogens. Removal of excess oxygen and reduction of the NO_x to N_2 takes place at 650 °C in a second quartz reactor that is packed with high purity Cu and CuO. The analyte is next carried through a chemical trap where water produced during combustion is removed and after that into the gas chromatograph (GC) where CO_2 and N_2 are separated (Figure2.14b). Before entering the irMS, all the analytical gases pass through the thermal conductivity detector (TCD) that determines the N, C and S

abundances by comparing the values to those of the reference material for which the elemental composition is known (histidine $C_6H_9N_3O_2$). The nominal error of elemental analyses is of the order of 0.1 wt%.

The EA system is then connected to the irMS, isotope ratio mass spectrometer, via an interface that limits the gas volume entering the ion source, and that also provides a means to introduce pulses of working gas and to dilute the sample gas with additional He. In the ion source of the mass spectrometer, gas molecules are ionised through interaction with the electron beam. The ions leave the source and are focused and accelerated via high voltage. The mass spectrometer itself is a sector-field instrument and ions pass through a magnetic field before reaching the Faraday cup detector. The strength of the magnetic field and the accelerating voltage determine the trajectory of the ions and therefore which ions will enter the Faraday cups. The use of multiple collectors allows the simultaneous measurement of ion intensity ratios. For nitrogen, three collectors are necessary in order to collect mass to charge ratios (*m/z*) of 28 ($^{14}N^{14}N$), and of 29 ($^{14}N^{15}N$), so that the isotope ratio can be calculated from the 29/28 values. Also, *m/z* =30 ($^{15}N^{15}N$) is monitored in order to observe the contribution of incomplete reduction of NO gas, whose mass number is 30 ($^{14}N^{16}O$). Each cup is connected to its own amplifier whose gain is defined by a precise, high ohmic resistor. Each amplifier has a different gain such that ion ratios at natural abundance levels will produce similar signals. The signals from each amplifier are recorded simultaneously every tenth of a second, digitised and recorded by irMS data system, this creates a chromatogram for ions of given *m/z*, the peak area being proportional to the number of ions detected.

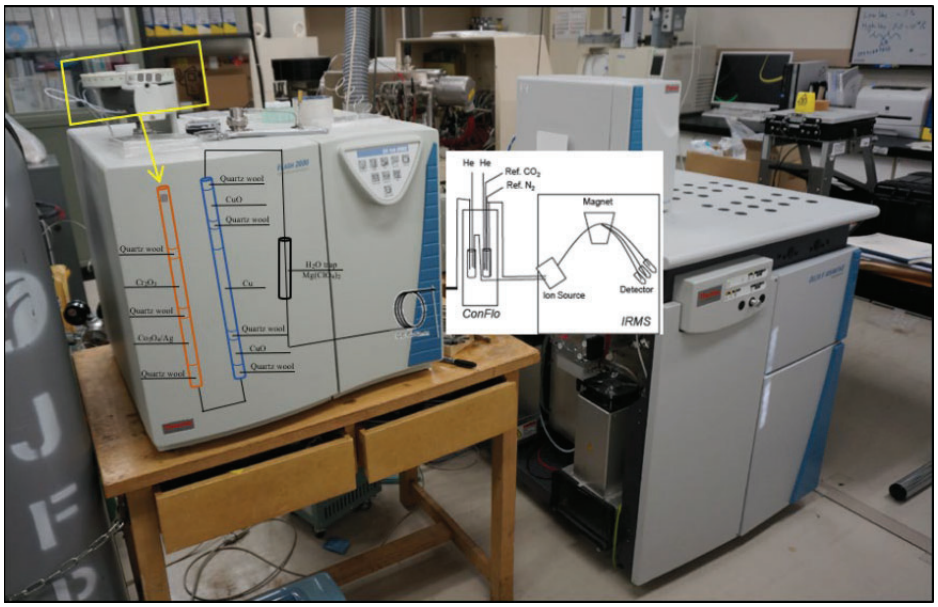

Figure 2.14: Schematic representation of EA-irMs (elemental analyser isotope ratio mass spectrometer)

It is important to monitor the stability of the measurement of the isotopic composition of the working gas prior to the sample measurements. The raw data from continuous flow IRMS are initially evaluated relative to the working gas and the hence reproducibility of this measurement determines the best reproducibility that can be achieved. This measurement is known as the "zero enrichment" or "on-off' test, and involves introducing 10 pulses of working gas into the instrument and recording the standard deviation of the δ-values, relative to the one pulse defined as a standard. The standard deviation in this machine for N_2 must be less than 0.06 ‰ before performing the real measurement. There are two types of calibration materials, primary materials used to define the δ-scale, and secondary ones which are natural or synthetic compounds that have been carefully calibrated versus the primary calibration materials. In the case of nitrogen, the primary calibration material is atmospheric nitrogen and the secondary one adopted in the present study is histidine ($C_6H_9N_3O_2$). Before the analysis of the experimental samples, several tin capsules loaded with histidine samples were loaded in the autosampler. Moreover, because the gases evolved from the tin capsules will combine with those from the samples and contribute to the measured δ-values, a

signal from a blank analysis is performed after each measured sample. The average peak area and δ-value of the blank measurement can be used to correct the data for the blank contribution. Variations in the isotopic composition of nitrogen are expressed in the usual δ-notation in permil: $\delta^{15}N_{sample} = [(^{15}N/^{14}N)_{sample}/(^{15}N/^{14}N)_{standard}-1]\times1000$, where the standard is atmospheric N_2. The results are presented in Chapter 6. Both nitrogen concentration and isotopic ratio have been collected, and the resulting data are reported in Table 6.2 , together with the calculated fractionation factor ($\Delta^{15}N = \delta^{15}N_{product} - \delta^{15}N_{reactants}$).

2.9 Focused Ion beam (FIB) device

In Chapters 4 and 5, TEM investigations of several ferropericlase samples are discussed. In order to perform the measurements, the samples have to be electron transparent. To prepare the sample for this nanoscale analyses, the FEI Scios DualBeam Focused Ion Beam (FIB) at the BGI was used. This instrument allows for an area of interest on the sample surface to be selected and then a cross section of this area in the form of a thin lamella to be extracted, that is sufficiently thin for TEM observation (Figure 2.15).

The dual nature of the instrument is provided by the two independent microscope columns, a focused ion beam and an electron beam, in the same machine. The two columns are positioned at 52° relative to each other, and the high-precision tilting stage allows the alignment of the sample perpendicular to both systems simultaneously. The electron column delivers the superior imaging quality of a Scanning Electron Microscope (SEM) while being less destructive than the ion beam imaging. Sample preparation capabilities of the machine are further extended by the presence of micro-manipulators and the gas injection systems (GIS) in the microscope chamber. The first allows in-situ manipulations such as lift-outs, rotations and transfers of microscopic sample parts during preparation, while the second enables both site-specific material deposition and material-

specific preferential milling by introducing reactive gases in the vicinity of the electron or ion probe during operation. The FIB milling technique occurs through sputtering of Ga^+ ions accelerated to 30 kV. The principles of FIB milling and detailed descriptions can be found elsewhere (e.g., Wirth 2004; Miyajima et al. 2010). In the following, specifics of the sample preparation procedure applied in this work are described.

Prior to insertion in the FIB apparatus, the samples were carbon coated to a thickness of about 20 nm to prevent electrical charging under the electron beam. For the preparation of the lamellae, the Ga^+ ion beam was operated at 30 kV and 1 nA, whereas the electron beam at 20 kV and 1.6 nA. Using the electron beam imaging system, the area of interest was identified and a protective platinum (Pt) layer of about 20 μm length and 2 μm width (Fig 2.15a) was deposited. A lamella of approximately 20 μm length and 10-13 μm height, was slowly and precisely milled from both sides of the coated area by a lower current Ga^+ ion beam, using a step-cut geometry (i.e., "regular cross section") with an ion beam current of 5 to ~30 nA (Figure 2.15b). Subsequently, the "cleaning-cross section procedure" was performed in order to thin down the sample (~10 pA ion beam current). For the following step, the sample was tilted to 7°, therefore allowing a plain view to undercut the milled area with a U-cut attained by ion beam perforation of the specimen along the side and the bottom edges (Figure 2.15c). The almost completely cut-free lamella was then attached to a needle with a Pt-deposited patch, and slow retraction performed with the needle micromanipulator allowed the full detachment of the FIB lamella. The TEM holder was then inserted into the FIB machine, and the lamella was attached to it with the aid of the deposition of a platinum patch on each side, and finally cut free from the needle (Fig 2.15d). As a last step, a slow and precise process of thinning on both sides was performed using the Ga^+ beam to obtain an approximately 100 nm thick lamella. The thinning process was performed at low kV (30 kV

and 0.05-0.30 nA) by tilting the sample by ±2.5° from the parallel position. The thinned lamella was finally "ion showered" to eliminate the implanted Ga^+ ions at 5 kV.

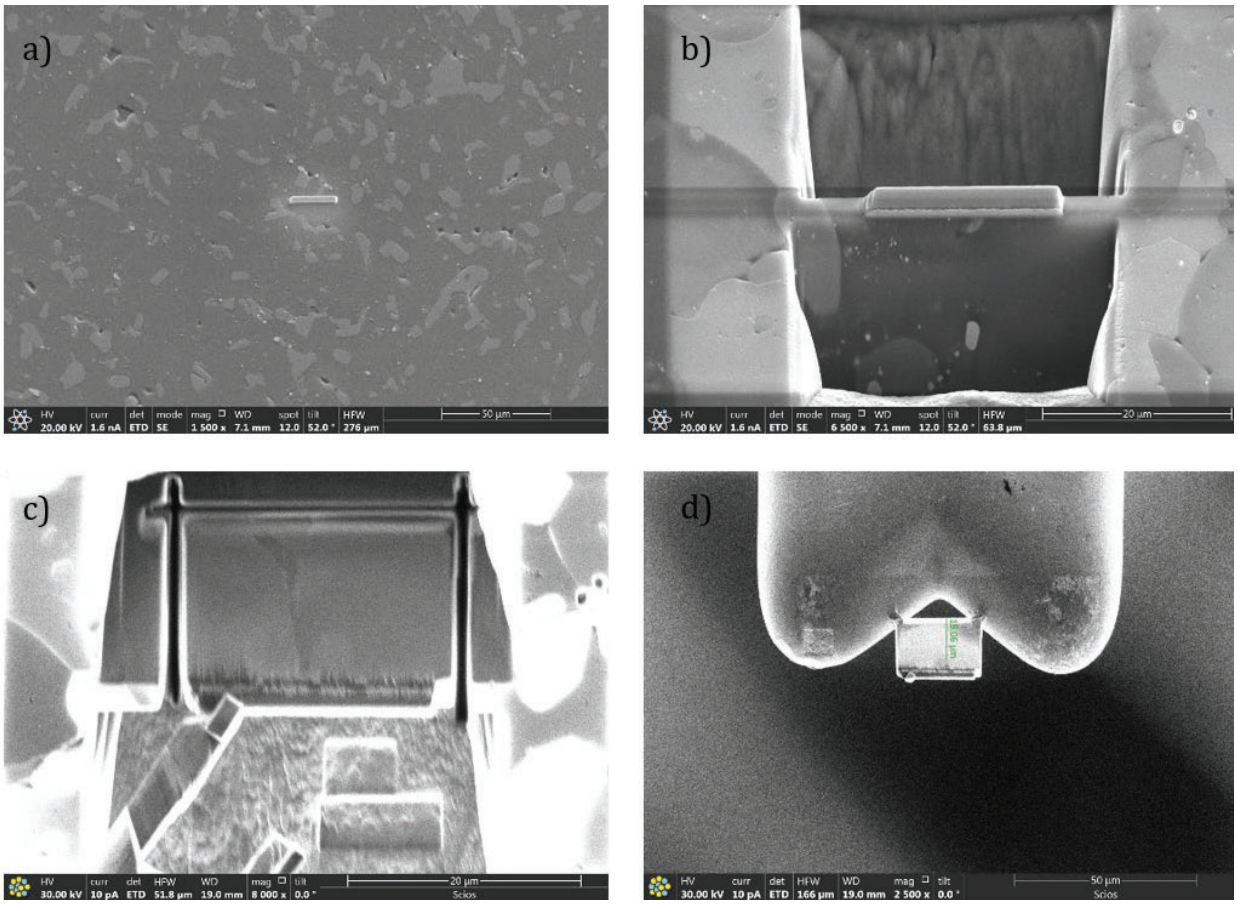

Figure 2.15: SE images showing a typical FIB lamella cutting procedure preformed in this case on sample Z2151B recovered from MA experiments.

2.10 Transmission electron Microscopy (TEM)

The nano-scale investigation of the samples of interest in the present study was performed using two Transmission Electron Microscopes (TEM): (1) ATEM, *FEI Titan G2 80-200* and (2) TEM, *Philips CM20FEG* equipped with an energy dispersive X-ray spectrometer (EDXS, *NORAN System, Thermo scientific and Brucker QUANTAX*) and an electron energy-loss spectrometer (EELS, *Gatan GIF Quantum® Model 963*) both installed at BGI.

As mentioned above (Section 2.9), samples are suitable for TEM investigation when they are thin enough to be transparent to an electron beam. This characteristic, coupled with the high image resolution of the TEM instrumentation, allows structural and chemical analyses down to the atomic level for many types of material (e.g., metals, glasses, polymers). The TEM provides morphologic, chemical, crystallographic and spectroscopic information on materials with atomic spatial resolution.

The TEM comprises essentially three components: (1) an electron gun that produces the electron beam, which is then focused onto the sample by the condenser system (e.g. electromagnetic lenses and apertures), (2) the image-producing system, made of the objective lens, the movable specimen stage, and the intermediate and projector lenses, that serves to focus the electrons passing through the sample to form a real, highly magnified image, and (3) the image recording system that converts the electron image into a form perceptible to the human eye. The image recording system consists of a fluorescent screen for viewing and focusing the image and a digital CCD camera for recording. Fundamental for this highly sensitive machine is the ultra-high vacuum, in the range of 10^{-7} to 10^{-9} Pa, that prevents the generation of an electrical arc, particularly at the TEM cathode.

The interaction between the incident beam and the specimen can be used for different purposes, such as nanoscale imaging (e.g., bright-field/dark-field imaging and STEM), crystal structure determination (e.g., SAED), chemical analysis (e.g., EDS), and oxidation state (e.g., EELS). The TEM can be operated in either TEM or STEM mode (Figure 2.16).

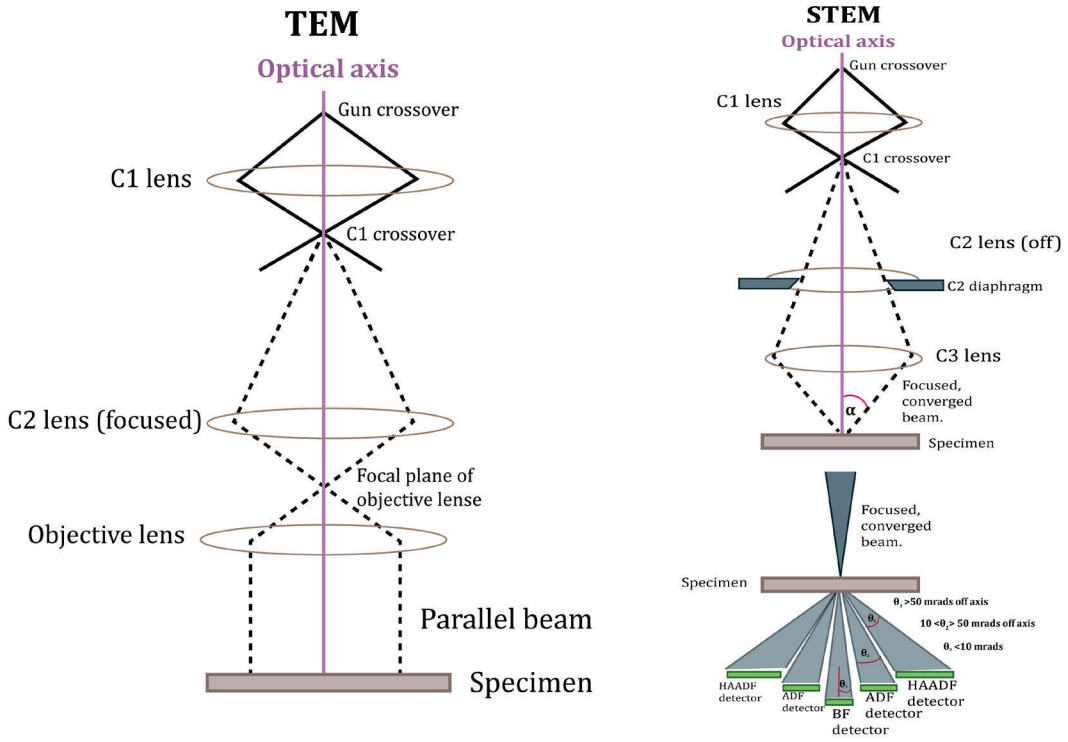

Figure 2.16 : Optics arrangement for TEM and STEM mode. In TEM mode, parallel electron beams are focused perpendicular to the sample plane. In STEM mode, the beam is focused at a large angle and is converged into a focal point. The transmitted signal is collected as a function of the beam location as it is rastered across the sample. There are multiple detectors for STEM imaging such as BF (bight field) for small angles (< 0-10 mrad); ADF (annular dark-field) for large angles (10-50 mrad) and HAADF (high-angle annular dark field) for angles > 50mrad.

In TEM mode, a parallel electron beam illuminates a wide region on the sample and the electrons transmitted through the specimen are detected by a CCD camera to produce a diffraction pattern or an image. The transmitted electrons can either directly pass through the specimen or scatter at different angles determined by the type of interaction with the material. An objective aperture at the back-focal plane below the specimen can be used to select either directly transmitted or scattered electrons to obtain a bright field (BF) or a dark field (DF) image respectively. The contrast in BF or DF images is mainly governed by diffraction (amplitude contrast) of the specimen, therefore, it can give valuable information about the crystal structure of the sample. DF images are especially useful to image and identify crystal defects.

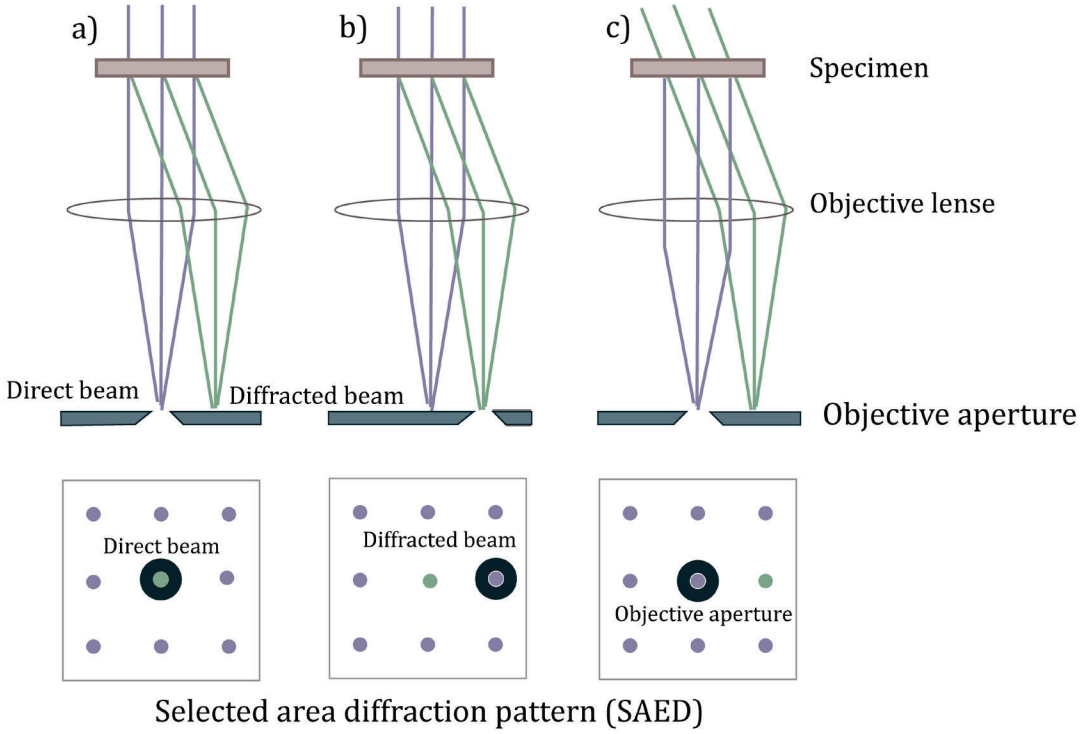

Figure 2.17: Schematic representation of imaging modes. **(a)** The images formed with the direct beam contribute to a bright field image. **(b)** If another diffraction spot is selected for the imaging, it is referenced as dark-field imaging. **(c)** In order to minimize the lens aberrations, the specimen can be tilted in order to center the selected diffracted spot. This technique is called centered dark-field imaging.

In STEM mode, the electron beam is converged to obtain a well-focused spot, which is scanned across a desired region of the sample and the scattered electrons are collected below the sample with the help of semi-conductor detectors to produce the images (Figure 2.16a). The detectors used in STEM mode to collect the scattered electrons have an annular shape, hence the name annular dark field (ADF) detectors. Depending on the scattering angles (in mrads) of the collected electrons, the resulting ADF images may contain diffraction as well as Z-number contrast. The electrons-nuclei interactions (the so-called Rutherford scattering) result in a high angle scattering that produces high angle annular dark field (HAADF) images (Pennycook and Varela 2011). In these images, due to the Z-dependence of contrast, the heavier atoms appear brighter than the lighter ones.

Measurements in this study were carried out using a 200 kV stationary electron beam with a spot size during the spectroscopy data acquisition of 0.2 nm. High-resolution TEM (HR-TEM) imaging of the synthetic ferropericlase samples was performed employing three detectors, the bright field (BF), dark field (DF) and high-angle annular dark-field (HAADF) detectors. The collection of these images allowed the observation of nanoscale exsolutions in the ferropericlase crystals that were not observable at the SEM scale and would therefore be overlooked. For the identification of the exsolved phases, selected area electron diffraction (SAED) patterns were collected. These are obtained when transmitted electrons are elastically scattered by the specimen according to Laue's law. A comprehensive description of these measurements and experimental results are reported in Chapters 4 and 5.

One of the most valuable contributions of the TEM to this project was the possibility to measure Fe^{3+}/Fe_{tot} ratios of specific areas of phases in the multiphase samples, using electron energy loss (EEL) spectroscopy. The principle behind this method is that it detects the change in kinetic energy of inelastically scattered electrons from a solid specimen providing structural and chemical information of the investigated matter with a spatial resolution down to the atomic level and an energy resolution between 0.1 and 1 eV (Egerton 2009; Egerton and Malac 2005). Approximately half of the electrons that hit the sample surface in the TEM pass through the specimen without losing any energy (i.e., they are elastically scattered), the remaining ones lose energy because of different interactions with the sample (i.e., they are inelastically scattered). An incident electron can lose its energy by exciting either atomic vibrations (phonons), collective oscillations of the free electron gas (plasmons) in the specimen, or it can transfer energy by exciting a core shell electron. In all these cases, the energy loss suffered by the incident electrons is characteristic to the elements and thus gives direct information about the composition of the specimen. The amount of lost energy can be measured by a magnetic prism located below the TEM image recording system (post column). Finally, a plot displaying how many electrons have lost a particular amount

of energy, creates the electron energy loss (EEL) spectrum (Figure 2.18a). Nonetheless, most electrons do not suffer any inelastic scattering. These produce the greatest contribution to the spectrum, giving rise to the so-called zero-loss peak (ZLP) located at ~ 0 eV, with a width that reflects the energy distribution of the electron source. This peak is located in the "low-loss" or "zero-loss" EELS spectrum region (<50eV), where some other features arising from inelastic scattering by conduction and valence electrons (e.g., plasmon excitation) can also be observed (figure 2.18b). At higher energies, the "core-loss spectrum" represents the inelastic scattering of the inner shell electrons of an atom. These characteristic spectral features, that appear as sharp edges with a more gradual decline, are defined as "ionization edges" and are comparable to X-ray absorption spectroscopy (XAS) absorption edges. K-edges and $L_{2,3}$-edges are ionization edges that appear at higher energy-loss and exhibit a particular shape that comprises sharp excitations at the onset of the absorption edge (e.g., white lines). It is well established that transition metal oxidation states are linked to the shape of the $L_{2,3}$ excitation edges (Egerton 2009; Hofer et al. 2016; Cave et al. 2006). They are characterized by sharp maxima just above the edge onsets, and represent transitions to empty *d* states. In general, the excitation edges shift to a higher energy-loss for a higher oxidation state. The Fe^{2+} L_3-edge has a sharp maximum at ~ 707.5 eV, whereas Fe^{3+} L_3-edge shows a maxima at ~709.5 eV. Metallic iron has an $L_{2,3}$-edge shape different from that of Fe^{2+} and Fe^{3+}, with broad asymmetrical L_3 and L_2 peaks. The crystallinity of the sample has little effect on the Fe $L_{2,3}$ shape because the spectra are dominated by quasi-atomic transitions, with only minor modification from the solid-state environment, i.e., between crystalline or amorphous states.

For the purpose of the present work, EELS spectra were collected at the Fe $L_{2,3}$ edges to investigate the Fe valence state of ferropericlase grains in areas where the oxide contained Fe^{3+}-rich exsolutions but also coexisted with other Fe^{3+}-rich oxides. For the samples studied in Chapters 4 and 5, a modification to the methodology of EELS data evaluation is described that was necessary

to account for Fe^{3+} in tetrahedral coordination found in the magnesioferrite exsolution. The details are explained specifically in Chapter 4.

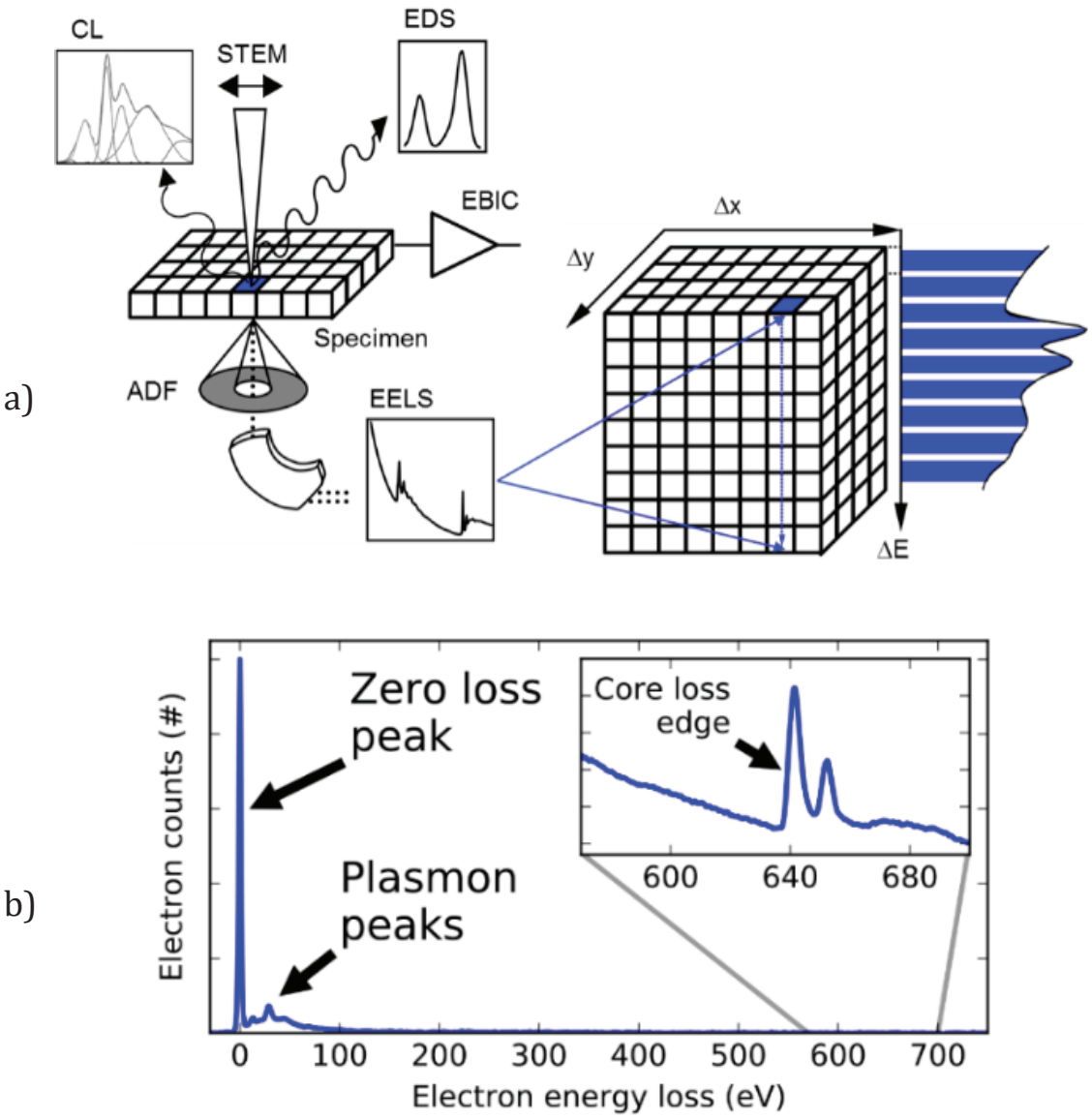

Figure 2.18: (a) A schematic illustration of the acquisition of an EELS spectrum imaging dataset. In STEM mode, a fine electron probe is scanned across the sample and an EELS spectrum is acquired at each scan point in parallel with the acquisition of a reference ADF image. **(b)** Example of an energy-loss spectrum and the core-loss edge. (image modified after www.gatan.com)

3. Compressibilities along the magnetite-magnesioferrite solid solution

3.1 Introduction

AB_2O_4 minerals with the spinel-type structure include aluminates, ferrites and chromites, that are found in metamorphic and igneous rocks of the Earth's crust and mantle. Besides their petrological importance as an indicator of the degree of partial melting (Dick and Bullen 1984), spinels are used extensively in geothermometry and oxybarometry, which has motivated significant studies on their thermodynamic properties and cation ordering (e.g. Jamieson and Roeder 1984; O'Neill and Wall 1987). The spinel structure consists of a cubic ($Fd\bar{3}m$) close-packed oxygen array with cations in tetrahedral (T) and octahedral (M) coordination (Hill et al. 1979). Their crystal chemistry can be described by the general formula $^{IV}(A_{1-x}\,B_x)^{VI}(A_x\,B_{2-x})O_4$, where x defines the inversion parameter describing the fraction of B-type cations in the tetrahedral site and hence the degree of cation ordering. Two ordered configurations can be found in spinels, one with $x = 0$ (normal spinel) and one with $x = 1$ (inverse spinel), whereas complete disorder is achieved when $x = 2/3$. The ordering/disordering process between tetrahedral and octahedral sites in the spinel structure is non-convergent since it does not give rise to a change in symmetry.

As Cr-Al spinels are typically only stable within the top 60 km (i.e. ~ 2 GPa) of the mantle (Robinson and Wood 1998) their elastic properties are not critical in the thermodynamic

description of their phase relations. The discovery of numerous mixed valence iron-oxides at pressures above approximately 6 GPa (Lavina et al. 2011; Lavina and Meng 2015), however, and the observation that these oxides form solid solutions with Mg (Uenver-Thiele et al. 2017a; 2017b) has renewed interest in thermodynamic calculations to understand the Fe-Mg-O phase diagram (Myhill et al. 2016; Uenver-Thiele et al. 2018). To determine thermodynamic parameters for such high-pressure oxides, the properties of the lower pressure precursor phases become important, which in the case of Fe-Mg-O oxides includes the inverse spinels along the binary join magnetite-magnesioferrite. Furthermore, it has been recognized that ferropericlase inclusions in sublithospheric diamonds, can contain exsolution of Fe_3O_4 magnetite - $MgFe_2O_4$ magnesioferrite spinels (Harte et al. 1999; Wirth et al. 2014; Kaminsky et al. 2015; Palot et al. 2016; Anzolini et al. 2020). Wirth et al. (2014), for example, found spinel exsolutions that were enriched in Fe compared to the surrounding ferropericlase and had a stoichiometry, $(Mg_{0.42}Fe_{0.56}Mn_{0.02})[Fe_{1.94}Al_{0.03}Cr_{0.03}]O_4$, very close to the magnesioferrite-magnetite solid solution, having a 50:50 mfr-mgt composition. This exsolution likely occurred from the initial Fe^{3+}- bearing ferropericlase as the pressure-temperature conditions within the diamond inclusions changed (Wirth et al. 2014; Anzolini et al. 2020). To produce thermodynamic models to understand the conditions at which this exsolution may have occurred, and hence learn something about the diamond transport history, requires knowledge of the equation of state (EoS) parameters along the magnetite-magnesioferrite solid solution.

Previous X-ray diffraction studies on magnetite-magnesioferrite spinels have been performed to investigate the state of cation ordering as a function of temperature and pressure (O'Neill et al. 1992; Antao et al. 2005a; Antao et al. 2005b). However, as pressures approach the limit of magnetite-magnesioferrite stability the elastic properties will have a much larger effect on their volumes than those resulting from cation ordering alone, particularly as the spinels become more ordered at higher pressures (Antao et al. 2005a; Turkin and Drebushchak 2005). Several studies

have investigated the compressibility of the end-members Fe_3O_4 and $MgFe_2O_4$ (Mao et al. 1974; Wilburn and Bassett 1977; Finger et al. 1986; Nakagiri et al. 1986; Olsen et al. 1994; Gerward and Olsen 1995; Haavik et al. 2000; Andrault and Bolfan-Casanova 2001; Levy et al. 2004; Reichmann and Jacobsen 2004; Lazor et al. 2004; Rozenberg et al. 2007; Gatta et al. 2007; Greenberg et al. 2009). The results, however, provide a wide range of bulk modulus, K_{T0}, with values $155 < K_{T0} < 222$ GPa for magnetite and $170.5 < K_{T0} < 233$ GPa for magnesioferrite (see references in Table 3.1.). Most of these previous studies were performed on powdered samples. In some cases, the phases themselves were poorly characterised, involved different states of cation ordering or contained further components. A few of the magnetite studies, however, have used single-crystal diffraction (Finger et al. 1986; Nakagiri et al. 1986; Reichmann and Jacobsen 2004; Gatta et al. 2007 in Table 3.1.). The results of these studies are in better agreement, suggesting that this technique may be more accurate than powder X-ray diffraction, likely because the broadening of reflections due to non-hydrostatic stresses can be monitored very carefully. The large discrepancies among the different studies result in uncertainties when calculating thermodynamic properties from the breakdown reactions of these phases. Moreover, no data on samples with mixed compositions along the magnetite-magnesioferrite solid solution are present in the literature (Table 3.1.).

Table 3.1: EoS parameters for sample mfr and Fe50 in the present study are reported together with the literature data for the magnetite-magnesioferrite solid solution. Pressure medium, pressure calibrant and analytical methods are indicated when available.

This study	**sample**	**V_0 (Å^3)**	**K_{T0} (GPa)**	**K'_T**	**P_{max}**	**P med**	**P calib**	**method**
Mfr (BM2)	$Mg_{0.96(1)}Fe_{0.04(1)}Fe_2O_4$	588.97 (8)	178.4 (5)	4	18.87	He	ruby	SXRD
Mfr (BM3)	$Mg_{0.96(1)}Fe_{0.04(1)}Fe_2O_4$	589.02 (9)	176 (2)	4.2 (2)	18.87	He	ruby	SXRD
Fe50 (BM2)	$Mg_{0.5\ (1)}Fe_{2.5(1)}O_4$	590.21 (5)	188.0 (6)	4	12.76	Ne	ruby	SXRD
Fe50 (BM3)	$Mg_{0.5\ (1)}Fe_{2.5(1)}O_4$	590.20 (5)	189 (3)	3.7 (5)	12.76	Ne	ruby	SXRD
Reference	**sample**	**V_0**	**K_{T0}**	**K'_T**	**P_{max}**	**P med**	**P calib**	**method**
Mao et al. (1974) (BM2)	Fe_3O_4	591.96	183 (10)	4	3.2	NaCl	NaCl	PXRD
Wilburn and Bassett (1977) (BM2)	Fe_3O_4	-	155 (12)	4	6.5	ME	ruby	PXRD
Finger et al.(1986)	Fe_3O_4	-	186 (5)	4[a]	4.5	ME	ruby	SXRD
	Fe_3O_4	-	183 (5)	5.6[a]	4.5	ME	ruby	SXRD
Nakagiri et al.(1986)	Fe_3O_4	591.54 (6)	181 (2)	5.5 (15)	4.5	ME	ruby	SXRD
Olsen et al. (1994)	Fe_3O_4	-	200 (20)	-	5.5	MA	NaCl	SP XRD
Gerward and Olsen (1995)	Fe_3O_4	-	215 (25)	7.5 (40)	25	-	-	SP XRD
Haavik et al (2000) (BM2)	Fe_3O_4	591.96	217 (2)	4	30	N_2	-	SP XRD
Haavik et al (2000) (BM3)	Fe_3O_4	591.96	222 (8)	4.1 (9)	30	N_2	-	SP XRD
Lazor et al. (2004)	Fe_3O_4	591.96	198.4	6.8	36	NaCl	NaCl	SP XRD
Reichmann and Jacobsen (2004)	Fe_3O_4	592.19 (3)	180 (1)	5.2 (4)	8.3	MEW	qtz	SXRD
Gatta et.al (2007) (BM2)	Fe_3O_4	591.4 (1)	180 (1)	4	11	MEW	ruby	SXRD
Gatta et.al (2007) (BM3)	Fe_3O_4	591.4 (1)	182 (4)	3.6 (8)	11	MEW	ruby	SXRD
Rozenberg et al.(2007)	Fe_3O_4	591.62 (7)	180.6 (1)	4.33 (13)	20	He	Sm^{2+}	PXRD
Gerward and Olsen (1995)	$MgFe_2O_4$	-	233 (40)	4.1 (2)	37	-		SP XRD
Andrault and Bolfan Casanova (2001) (BM2)	$MgFe_2O_4$	589.9	195 (17)	4	46	-	gold	SP XRD
Levy et al. (2004)	$MgFe_2O_4$	591.4 (1)	181.5 (13)	6.32 (14)	34	N_2	ruby	SP XRD
Greenberg et al. (2009) (BM2)	$MgFe_2O_4$	591.0 (2)	170.5 (8)	4	30	He	ruby	SP XRD
Greenberg et al. (2009) (BM3)	$MgFe_2O_4$	590.7 (2)	179 (2)	3.3 (2)	30	He	ruby	SP XRD

Notes= MEW = methanol: ethanol: water= 16:3:1, ME= methanol: ethanol=4:1; PXRD=powder x-ray diffraction; SXRD= single crystal XRD; SPXRD= synchrotron powder XRD; MA= Multianvill experiments; [a] assumed values; Standard deviations in the last digits are in parentheses.

The aim of this study is to constrain the compressibility of magnesioferrite as well as to investigate the compression behaviour of the magnetite – magnesioferrite solid solution. To this end, two single-crystals with the approximate stoichiometries $MgFe_2O_4$ and $Mg_{0.5}Fe^{2+}_{0.5}Fe^{3+}_{2}O_4$ were investigated employing single-crystal X-ray diffraction at ambient conditions and in diamond anvil cells at higher pressures. To obtain samples that were close to being fully ordered inverse spinels, single crystals were produced in high-pressure and high-temperature synthesis experiments, recovered and characterised before the compression experiments.

3.2 Experimental methods

3.2.1 Sample synthesis and characterization

$MgFe_2O_4$ single crystals were produced in a Kawai-type, 1200 tonne Sumitomo multi-anvil press at the Bayerisches Geoinstitut using pre-synthesized magnesioferrite powder. Details concerning the synthesis of the starting material can be found in Uenver-Thiele et al. (2017b). The high-pressure experiment was performed using a Cr_2O_3-doped MgO octahedral pressure assembly with an 18 mm edge length and WC cubes with 11 mm truncations. The starting material was loaded in a welded Pt capsule together with a thin layer of PtO_2 to maintain oxidizing conditions during the experiment. This ensured the presence of only Fe^{3+} in the synthesized crystals and minimized Fe loss to the capsule. The experiment was performed at 5 GPa and 1300 °C for 8 hours. Heating was achieved with a graphite furnace and the temperature was monitored by a W_3/Re_{97}-W_{23}/Re_{75} thermocouple with no pressure correction applied to the electromotive force. The run product (experiment S7645) consisted of black single crystals with cubic shapes having dimensions varying between 20 and 150 μm. A JEOL JXA-8200 electron microprobe (EMP) equipped with five wavelength-dispersive spectrometers at the Bayerisches Geoinstitut was used to determine the

composition of the synthesized sample. Four polished grains were mounted in epoxy for the measurement. Forsterite, andradite and Fe_2O_3 were used as standards for Mg, Fe and O respectively, and a ZAF algorithm was used for matrix correction. Measurements were performed in wavelength-dispersive mode with a 15kV accelerating voltage and 15 nA beam current. The analyses yielded a final stoichiometry of $Mg_{0.96(1)}Fe^{2+}_{0.04(1)}Fe^{3+}_2O_4$, i.e. close to the end-member $MgFe_2O_4$ composition and is referred to as mfr hereafter.

Single crystals of $Mg_{0.5}Fe^{2+}_{0.5}Fe^{3+}_2O_4$ were produced using an 800 tonne Walker type multi-anvil at the University of Frankfurt (Walker et al. 1990). The experimental set up and sample characterization are reported in Uenver-Thiele et al. (2017a). The synthesis was performed at 9 GPa and 1000 °C for 7 hours. The recovered sample (M650) contained several black crystals with sizes between 30 and 150 μm. Quantitative chemical analyses yielded a stoichiometry of $Mg_{0.50(2)}Fe^{2+}_{0.50(1)}Fe^{3+}_2O_4$ (Uenver-Thiele et al. 2017a). This sample is hereafter referred to as Fe50.

3.2.2 Synchrotron Mössbauer source (SMS) spectroscopy

SMS spectra on the Fe50 sample were collected at the Nuclear Resonance beamline ID18 (Rüffer and Chumakov 1996) of the European Synchrotron Radiation Facility (ESRF) in Grenoble, using the Synchrotron Mössbauer Source described by Potapkin et al. (2012). In this system, the source of radiation and optical elements are optimized to provide an intense, highly monochromatic, collimated and stable X-ray beam of small cross-section at the Mössbauer transition energy of 14.4 keV. In contrast to a radioactive source, the beam emitted by the SMS is fully resonant and fully polarized, has high brilliance and can be focused to a 10μm × 10μm spot. Before and after collection of the SMS spectrum of sample Fe50, the linewidth was controlled via acquisition of a spectrum of $K_2Mg^{57}Fe(CN)_6$, which consists of a single line. The velocity scale was ±12 mm/s

and was calibrated using 25 μm thick natural-enriched α-iron foil. The spectrum was collected for 2 hours and fitted using pseudo-Voigt line shapes and a 1st order polynomial baseline with the MossA 1.01f software package (Prescher et al. 2012).

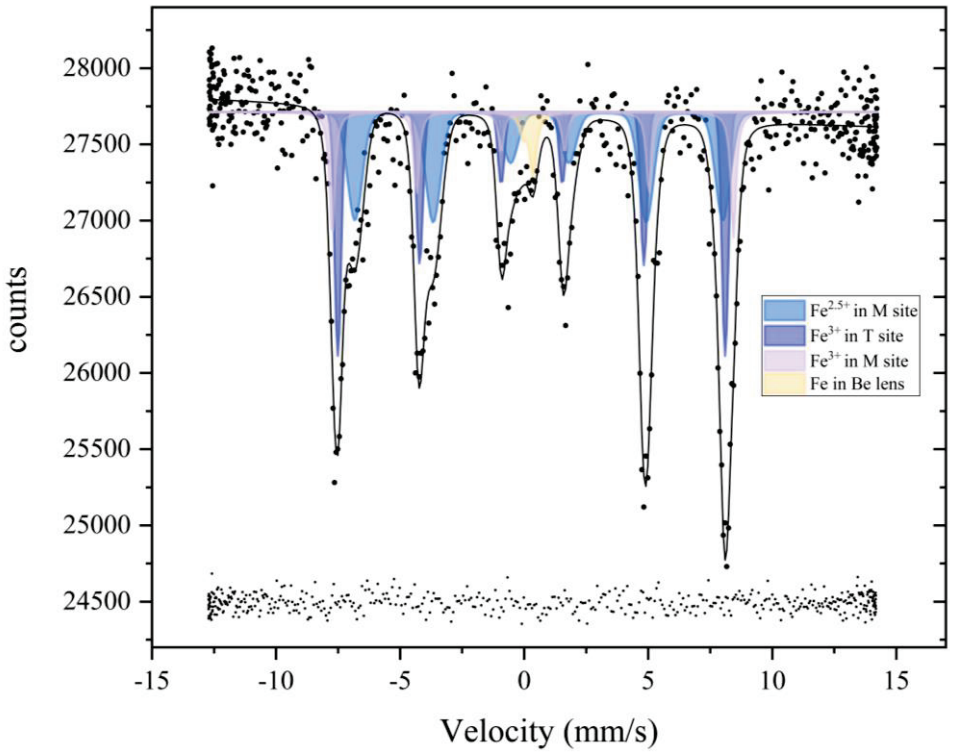

Figure 3.1: Synchrotron Mössbauer source (SMS) spectrum of sample Fe50 collected at ambient conditions. Solid circles: experimental data; solid grey line: full transmission integral fit of the magnetic sextet shown in shaded coloured areas: Fe^{3+} at the tetrahedral site (dark blue); Fe^{3+} at the octahedral site (purple); $Fe^{2.5+}$ at the octahedral site (light blue) and Fe contained in the Be window (yellow). The fitting residual is shown at the bottom of the figure.

The Mössbauer spectrum (Figure 3.1.) is dominated by three sextets with the following hyperfine parameters: i) centre shift (CS) = 0.30(2) mm/s (relative to α-Fe) and hyperfine magnetic field (BHF) = 48.4(1) T, which is characteristic of Fe^{3+} ions at the tetrahedral sites; ii) CS= 0.61(4) mm/s and BHF= 45.9(4) T, which can be assigned to an intermediate valence $Fe^{2.5+}$ at the octahedral sites; and iii) centre shift (CS) =0.35(5) mm/s and BHF=50.1(3) characteristic of octahedrally coordinated ferric iron (e.g. as typical for α-Fe_2O_3). A fourth component, observed in the SMS spectrum is due to Fe contained in the beryllium (Be) lenses and is fit with known

hyperfine parameters. The distribution of the iron species between tetrahedral (T) and octahedral (M) site is $^{T}Fe^{3+}$ =33%; $^{M}Fe^{3+}$= 21% and $^{M}Fe^{2.5+}$ =46% with the $^{M}Fe^{2.5+}$ component consisting of half $^{M}Fe^{3+}$ and half $^{M}Fe^{2+}$. No $^{T}Fe^{2+}$ component could be fitted to the Mössbauer spectrum, suggesting that, if present, it is less than 5%, which is of the order of the uncertainties on the peak areas in the fitting procedure. Using the Mg and Fe concentrations from the microprobe analyses, together with the different iron components from the Mössbauer spectrum, the Fe50 chemical formula can be written as: $^{T}[Mg_{0.17(10)}Fe^{3+}_{0.83(10)}]^{M}[Mg_{0.34(10)}Fe^{3+}_{1.09(10)}Fe^{2+}_{0.57(10)}]O_4$.

3.2.3 Single crystal X-ray diffraction in air

Reflections from numerous single crystals from the Fe50 sample were examined, but all showed evidence of twinning to some extent. A Fe50 crystal (M650x7) with dimensions of 50 x 60 x 70 μm^3 was finally chosen for which one of the twin components was sufficiently small. This allowed the integration of an adequate number of reflections belonging only to the larger twin to be used for the structural refinements. For the mfr sample it was possible to select a single crystal (S7645x8) with dimensions 70 x 70 x 80 μm^3, that was devoid of twinning. Full intensity data collections for structural refinements at ambient conditions were performed in air for both samples, glued onto the tips of glass capillaries. Complete redundant intensity data were collected using an Oxford Xcalibur diffractometer equipped with a Sapphire 2 CCD area detector and a ceramic X-ray tube with MoKα radiation (λ = 0.70784 Å) monochromated using a graphite crystal and operating at 50 kV and 40 mA. Several ω scans were performed with a width of 0.5° and a default time of 10 to 20 s in a 2θ range between 2 and 78°. The intensity data were integrated with the Crysalis Pro software (Rigaku, Oxford diffraction) and Lorentz and polarization corrections as well as a numerical absorption correction based on the crystal shape were performed. Before integrating the intensity data of the Fe50 crystal, the Crysalis Pro software was used to determine

the mutual orientation of the two twin components, which indicated a 60° rotation around [111], as expected for the spinel-type structure. The orientation matrices of the two twin components were then used to integrate the reflection intensities belonging to either one of the twin components, whereas overlapping reflections were neglected. This procedure resulted in 2848 reflections observed for the first twin component and 336 reflections observed for the second, therefore only data from the first component were used for the structural analysis. The observed reflection conditions were consistent with the $Fd\bar{3}m$ space group, therefore, a structure solution and refinement based on F^2 were performed with the SHELX97 program package (Sheldrick 2008) in the ShelXle (Hübschle et al. 2011) graphical user interface using this space group. Scattering factors for neutral species (Ibers and Hamilton 1974) have been employed for Mg, Fe and O, all sites were considered to be fully occupied and all atoms were refined anisotropically. Moreover, the occupancies of Mg and Fe were refined without chemical constraints both at the tetrahedral and at the octahedral sites. The magnesium and iron contents resulting from the refined occupancies are $^{T}[Mg_{0.02(3)}Fe_{0.98(3)}]^{M}[Mg_{0.44(3)}Fe_{1.56(3)}]O_4$ for the Fe50 sample and $^{T}[Mg_{0.11(3)}Fe_{0.89(3)}]^{M}[Mg_{0.92(3)}Fe_{1.08(3)}]O_4$ for the mfr sample, in agreement with the chemical formula obtained from microprobe analyses. Details of the structural refinements are provided in the attached crystallographic information files (CIF). Unit-cell parameters, inversion parameters and bond lengths are reported in Table 3.2. together with data from the literature.

Table 3.2: Unit-cell parameter (a_0), composition and temperature of synthesis of the individual crystals along with the bond length distances for both the tetrahedral (T-O) and octahedral (M-O) sites and the inversion parameters (x). For comparison, literature data for the end-members magnesioferrite and magnetite are also shown. The inversion parameter for the magnesioferrite was calculated using the linear relation with a_0 ($x = 81.34 - 9.598a_0$ (Å)) reported by O'Neill et al. (1992).

Present study	**sample**	**T (°C) of synthesis**	**a (Å)**	**x**	**x calculated**	**T-O (Å)**	**M-O (Å)**
S7645x8 (mfr)	$Mg_{0.96(1)}Fe_{0.04(1)}Fe_2O_4$	1300 (5 GPa)	8.3821 (2)	0.85-0.89	0.89	1.9060 (19)	2.0442 (10)
M650x7 (Fe50)	$Mg_{0.50(1)}Fe_{2.50(1)}O_4$	1000 (9 GPa)	8.3883 (3)	>0.83		1.898 (2)	2.0506 (13)
reference	**sample**	**T (°C) of synthesis**	**a (Å)**	**x**	**x calculated**	**T-O (Å)**	**M-O (Å)**
Antao et al. 2005b	$Mg_{1.0003}Fe_{1.9998}O_4$**	900	8.39704 (5)	0.841 (4)	0.745	1.888 (3)	2.060 (1)
	Same sample as above***		8.39705 (5)			1.918 (4)	2.043 (2)
Levy et al. 2004	$Mg_{1.02}Fe_{1.99}O_4$	1000 to 950 to 900	8.39389 (5)	0.802 (11)	0.775	n/a	n/a
Greenberg et al.2009	$MgFe_2O_4$	1200	8.3912 (7)	n/a	0.801	n/a	n/a
Antic et al. 2002	$MgFe_2O_4$	500	8.3886 (1)	0.82 (1)	0.826	1.861 (2)	2.071 (2)
Andreozzi et al. 2001	$Mg_{0.956}Fe_{2.044}O_4$	1200 to 800	8.3841 (3)		0.87	1.9099 (15)	2.0428 (8)
Nakatsuka et al. 2004	$Mg_{1.02}Fe_{1.99}O_4$	1200 to 700 to 300	8.3600 (4)	0.854 (6)	1.100	1.915 (1)	2.031 (1)
Bosi et al. 2009	Fe_3O_4	1200 to 900	8.3967 (3)	1.00		1.8872 (15)	2.0600 (8)
Fleet 1981	Fe_3O_4	natural	8.3941 (7)	n/a		1.888 (2)	2.0584 (9)
Finger et al. 1986	Fe_3O_4	~1550 (*)	8.3778 (5)	n/a		1.887 (4)	2.054 (2)
Gatta et al. 2007	Fe_3O_4	n/a	8.3950 (5)	n/a		1.885 (1)	2.0607 (8)
Haavik et al. 2000	Fe_3O_4	1100	8.3965 (7)	n/a		1.889 (1)	2.059 (1)
Nakagiri et al. 1986	Fe_3O_4	1050	8.3949 (3)	n/a		1.8873 (29)	2.059 (16)
Reichmann and Jacobsen 2004	$(Fe_{2.996}Al_{0.003}Ti_{0.001})O_4$	natural	8.39639 (14)	n/a		n/a	n/a

Notes: (*) temperature of synthesis was assessed from the work of Smiltens (1952) referenced in the methodology related paper by Harrison and Aragon (1978); ** data from the synchrotron; *** data from an in house diffractometer for the same sample as in **. The uncertainties are reported in parenthesis. The values in the x calculated column were obtained using the relationship between lattice parameter and inversion parameter reported by O'Neill et al (1992).

3.2.4 Diamond Anvil cell (DAC) preparation

For the high-pressure experiments, the mfr and the Fe50 crystals were one-side polished to final dimensions of 60 x 40 x 20 μm^3 and 70 x 55 x 16 μm^3, respectively. The crystals were loaded in two separate DACs equipped with Boehler-Almax diamonds with a culet size of 400 μm (Boehler and De Hantsetters 2004; Kantor et al. 2012). Samples were placed in the centre of a 250 μm hole that was drilled in pre-indented rhenium (Re) gaskets together with 10 μm diameter ruby spheres for pressure calibration. The two cells were loaded with different pressure transmitting media using the gas loading system installed at BGI (Kurnosov et al. 2008) and the pressure was increased to different target pressures. The cell with sample mfr was loaded with helium (He) at a starting pressure of 0.3 GPa and compressed in steps of ~1 GPa up to 18.87(5) GPa. Above this pressure, broadening (assessed at full width half maximum) of the sample reflections was observed (Figure 3.2.) and the experiment was concluded. The cell with sample Fe50 was loaded with neon (Ne) and unit-cell lattice parameters were obtained in a first run (RUN 1) up to 2.28(2) GPa. Above this pressure the gasket weakened and therefore a further loading, with the same crystal in Ne was performed. Unit-cell parameters were then collected up to a maximum pressure of 12.76(4) GPa (RUN 2), after which reflection broadening occurred. After each pressure increase, the pressure inside the cell was left to stabilize for at least one day to minimize pressure changes during measurements. A Raman micro-spectrometer equipped with a He-Ne laser (λ= 632.8 nm) with 20 mW laser power was used to measure the fluorescence bands of the ruby sphere inside the DAC before and after the X-ray diffraction measurements. As a reference, a ruby chip at ambient conditions was also measured after each measurement. Pressures were determined using the ruby fluorescence calibration reported by Dewaele et al. (2008).

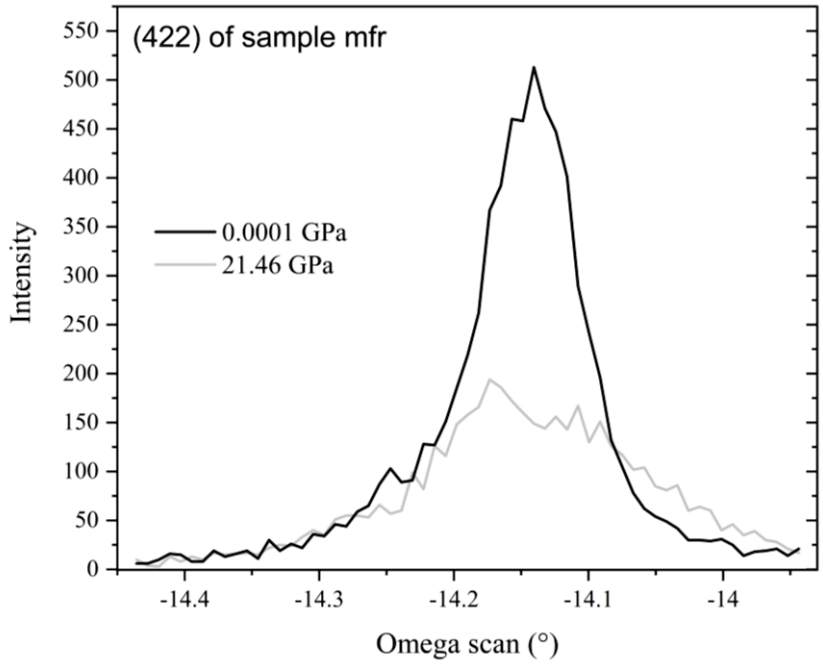

Figure 3.2: The (422) reflection of the mfr sample is shown both at 0.0001 GPa (black solid line) and 21.46 GPa (light-grey solid line). Due to the onset of peak broadening at full width half maximum, as a result of non-hydrostatic conditions, the experiment was concluded and this pressure point was excluded from the fitting procedure

3.2.5 High-pressure single crystal X-ray diffraction

High-pressure single-crystal diffraction for sample Fe50 was performed using a Huber four-circle diffractometer equipped with a Eulerian cradle goniometer, a point detector and a collimated diffracted beam from a conventional glass X-ray tube operating at 50 kV and 40 mA and producing MoKα radiation. Sample mfr was measured using a Huber four-circle Eulerian cradle diffractometer equipped with a point detector and using a high -brilliance rotating anode X-ray source with MoKα radiation operated at 55kV and 45mA and focused using multilayer VaryMax^{TM} optics (Trots et al. 2011). For both samples up to 16 Bragg reflections were centred using the eight-position centring method (King and Finger 1979). The centring procedure and the least-square refinement of the unit-cell parameters were performed using the SINGLE software

(Angel and Finger 2011). The resulting unit-cell edge and volumes measured at different pressures are reported in Table 3.3.

Table 3.3: Unit-cell parameters and unit-cell volumes (Å³) determined by means of high-pressure single-crystal X-ray diffraction for Fe50 sample (number M650x4) and the endmember mfr sample (number S7645x7).

M650x4 (Fe50)			**S7645x7 (mfr)**		
P (GPa)	**a (Å)**	**V (Å³)**	**P (GPa)**	**a (Å)**	**V (Å³)**
	RUN 1		0.00010	8.3821 (2)	588.93 (4)
0.00010	8.3883 (3)	590.23(7)	1.30 (6)	8.36293 (11)	584.89 (2)
0.50 (4)	8.3811 (2)	588.72 (5)	3.14 (5)	8.3357 (2)	579.21 (3)
1.58 (4)	8.3638 (2)	585.07 (5)	4.96 (5)	8.3094 (2)	573.74 (3)
2.28 (3)	8.3547 (3)	583.17 (6)	6.44 (5)	8.2885 (2)	569.41 (3)
	RUN 2		8.14 (5)	8.2648 (2)	564.55 (4)
0.00010	8.3883 (2)	590.23 (5)	9.15 (11)	8.2522 (2)	561.96 (5)
3.44 (12)	8.3424 (4)	580.59 (7)	12.21 (5)	8.2142 (2)	554.24 (5)
6.18 (9)	8.3028 (4)	572.37 (7)	14.03 (5)	8.1928 (2)	549.92 (4)
7.36 (5)	8.2881 (4)	569.34 (7)	15.87 (7)	8.1720 (3)	545.75 (5)
8.66 (5)	8.2712 (4)	565.86 (7)	17.25 (12)	8.1563 (4)	542.60 (7)
9.77 (5)	8.2565 (4)	562.84 (7)	18.87 (5)	8.1391 (4)	539.18 (7)
9.96 (9)	8.2548 (4)	562.50 (7)			
10.83 (7)	8.2459 (5)	560.67 (9)			
10.97(9)	8.2425 (5)	559.99 (9)			
11.90 (7)	8.2310 (10)	557.64 (11)			
12.76 (5)	8.2208 (10)	555.58 (11)			

Standard deviations are in parentheses

3.3 Results and discussion

3.3.1 Degree of order of the investigated samples

The cation distribution at the octahedral and tetrahedral sites obtained by means of single-crystal X-ray diffraction can be used to calculate the bond distances of these sites using the structure model proposed by Lavina et al. (2002) based on 295 spinel single-crystal analyses from the literature. This model was tested in order to confirm whether all Fe present at the tetrahedral site in the mfr sample is trivalent. The T-O bond distance according to (Lavina et al. 2002) can be obtained as :

$$\mathrm{T}-\mathrm{O}=\sum_{i}{}^{IV}X_i\,{}^{IV}D_i+k_1\,{}^{IV}Fe^{3+}$$

where ${}^{IV}X_i$ are the chemical species at the tetrahedral site, ${}^{IV}D_i$ are the cation oxygen bond distances of each specific atom at the tetrahedral site and k_1 is an empirical coefficient which accounts for the fact that the T-O distances are longer than expected when Fe^{3+} is present at that site. The cation-oxygen distances ${}^{IV}D_{Mg}$, ${}^{IV}D_{Fe^{2+}}$, and ${}^{IV}D_{Fe^{3+}}$, as well as the k_1 coefficient have been taken from Lavina et al. (2002). From the tetrahedral site occupancies determined in the mfr structural refinement, i.e. ${}^{IV}X_{Fe}=0.89(3)$ and ${}^{IV}X_{Mg}=0.11(3)$, it is possible to calculate two different T-O bond distances, one assuming that all iron at the tetrahedral site is ferric, yielding a T-O = 1.894 Å and the other assuming that the 0.04 Fe^{2+} atoms present in the mfr sample (see chemical formula based on EMP measurements) are all occupying the T site, yielding a T-O = 1.898 Å. Both values are similar, albeit smaller than the refined T-O bond distance T-O = 1.9060(19) Å (Table 3.2). The small difference between the two calculated T-O bond distances (well inside the model uncertainties) does not allow to differentiate between a full Fe^{3+} occupancy or the presence of minor amounts of Fe^{2+} at the tetrahedral site. Therefore, based on the Lavina et al. (2002) model, the mfr inversion parameter, *x*, could, in principle, vary between 0.85 and 0.89.

However, the mfr inversion parameter can also be calculated using the previously determined linear relationship between the inversion parameter and the unit-cell lattice parameter a_0, using the equation x = 81.34 - 9.598 a_0 (Å) (O'Neill et al. 1992). From this relationship, we obtain an inversion parameter of x= 0.89 (Table 3.2.) in excellent agreement with that obtained from the structural refinements, assuming all Fe at the tetrahedral site is ferric iron. Therefore, the mfr sample synthesised in this study has a high degree of order. Moreover, the degree of order of the mfr sample is higher after annealing at 5 GPa and 1300 °C than that of the magnesioferrite starting material (Uenver-Thiele et al. 2017a), which had x = 0.837 (according to its unit-cell lattice parameters) and was synthetized at 900 °C, at room pressure. This confirms that pressure favours cation ordering in these spinels, in agreement with the results reported by Turkin and Drebushchak (2005) and Antao et al. (2005a). In fact, the determined inversion parameter is in good agreement with parameters determined at a similar pressure and temperature by Antao et al. (2005a) for mfr (i.e. 0.906(8)).

For sample Fe50, the SMS spectrum (Figure 3.1.) showed the presence of 0.83 atoms per formula unit (apfu) of ferric iron at the tetrahedral site. This value is smaller than the refined Fe value of 0.98(3) obtained from the structural refinement, however, no Fe^{2+} can be detected at the tetrahedral site in the SMS spectrum, which therefore requires 0.17 apfu of Mg at the tetrahedral site to maintain a full site occupancy. Note also that the amount of Fe^{2+} at the octahedral site derived from the SMS spectrum is already 0.57(10) apfu, i.e. the entire Fe^{2+} content expected in the Fe50 sample, according to the chemical analysis. The difference between the cation distributions obtained from the SMS spectrum and from the single-crystal structure refinements are likely due to the resolution of the two methods, which can be assessed from the uncertainties, which are much larger for the SMS data. The T-O = 1.899 Å bond distance for the Fe50 spinel calculated using the Lavina et al. (2002) model from the SMS cation distribution [$^{IV}X_{Fe^{3+}} = 0.83(10)$ and $^{IV}X_{Mg} = 0.17(10)$], is in agreement with the tetrahedral bond length obtained from the structural

refinements (Table 3.2.), whereas the T-O = 1.887 Å calculated from the cation distribution from the structural refinement [${}^{IV}\mathrm{X}_{Fe^{3+}} = 0.98(3)$ and ${}^{IV}X_{Mg} = 0.02(3)$] is smaller than the observed value. Given that Lavina et al. (2002) report that their model appears to underestimate the T-O bond distance for ferrite spinels, even considering the empirical coefficient k_1, we can expect that the inversion parameter of sample Fe50 is larger than 0.83, confirming also that Fe50 is an almost completely inverse spinel, having a similar cation substitution as the mfr sample.

3.3.2 Crystal chemistry of the $MgFe_2O_4$ – Fe_3O_4 solid solution

The room pressure crystal chemistry of the samples in this study can be investigated through a comparison with literature data on magnetite-magnesioferrite samples and, in particular, with those used in previous compressibility studies (Table 3.2.). Unit-cell parameters for magnesioferrite from compressibility studies are quite varied and range from a = 8.3841(3) to 8.3970 (5) Å, with one outlier sample having a = 8.3600 (4) Å (Nakatsuka et al. 2004). These samples (Table 3.2.) have been synthesised at temperatures between 500 to 1200 °C, with some being quenched in a step-wise manner, which has thus affected the final degree of order that is probably the main cause of the unit-cell variation. The predictions by O'Neill et al. (1992) for the expected unit-cell parameters of fully ordered and disordered magnesioferrite are indicated in Figure 3.3a. The sample of Nakatsuka et al. (2004) (Table 3.2.) has a very small unit-cell parameter, not consistent with the other reported values, and lies well below the predicted fully ordered end-member. This may be caused by a degree of non-stoichiometry through the substitution of a maghemite γ-Fe_2O_3 component, which is expected to decrease the unit-cell parameter further (O'Neill et al. 1992). The mfr sample investigated in this study is at the lower end of the main cluster of values from the literature (a = 8.3821 (2) Å), and is, therefore, one of the most ordered samples examined to date, in line with the evidence presented in the previous section.

Reported magnetite end-member unit-cell parameters show a much smaller range in values, between 8.3941(7) Å and 8.3967 (3) Å, consistent with all the samples being ordered inverse spinel. As opposed to mfr, magnetite cation disorder cannot, to our knowledge, be quenched as it results only from the movement of an electron. Only the study of Finger et al. (1986) reports a significantly smaller value (a =8.3778 (5) Å), which is interpreted to be due to the presence of a γ-Fe_2O_3 maghemite component (Volenik et al. 1975), consistent with the high temperature synthesis from a liquid.

To investigate the behaviour of the magnetite-magnesioferrite solid solution, the unit- cell parameters (Table 3.2.) are plotted as a function of the molar $Mg/(Mg+Fe^{2+})$ fraction, X_{Mg}, in Figure 3.3a. A line has been drawn between the value obtained for mfr in this study and an average value (a = 8.3962 Å) for magnetite. The Fe50 sample investigate in this study lies on the linear trend between these most ordered samples. It should be noted, however, that it may be possible to produce a more ordered magnesioferrite sample, particularly at high pressures (Antao et al. 2005a), which would render a non-linear unit-cell relationship with Mg content, so there are no inferences from this line in terms of Vegards law.

The Mg/Fe^{2+} substitution in the close packed structure of spinels influences the tetrahedral, T-O, and octahedral, M-O, bond lengths (Figure 3.3b and 3.3c). In the ordered magnetite-magnesioferrite solid solution Mg substitutes for Fe^{2+} at the octahedral site, whereas only Fe^{3+} occupies the tetrahedral site. With increasing Mg content, the M-O bond length decreases due to the smaller radius of Mg with respect to Fe^{2+}. This decrease causes a small increase of the tetrahedral bond distance, due to the close interconnectivity of the spinel structure.

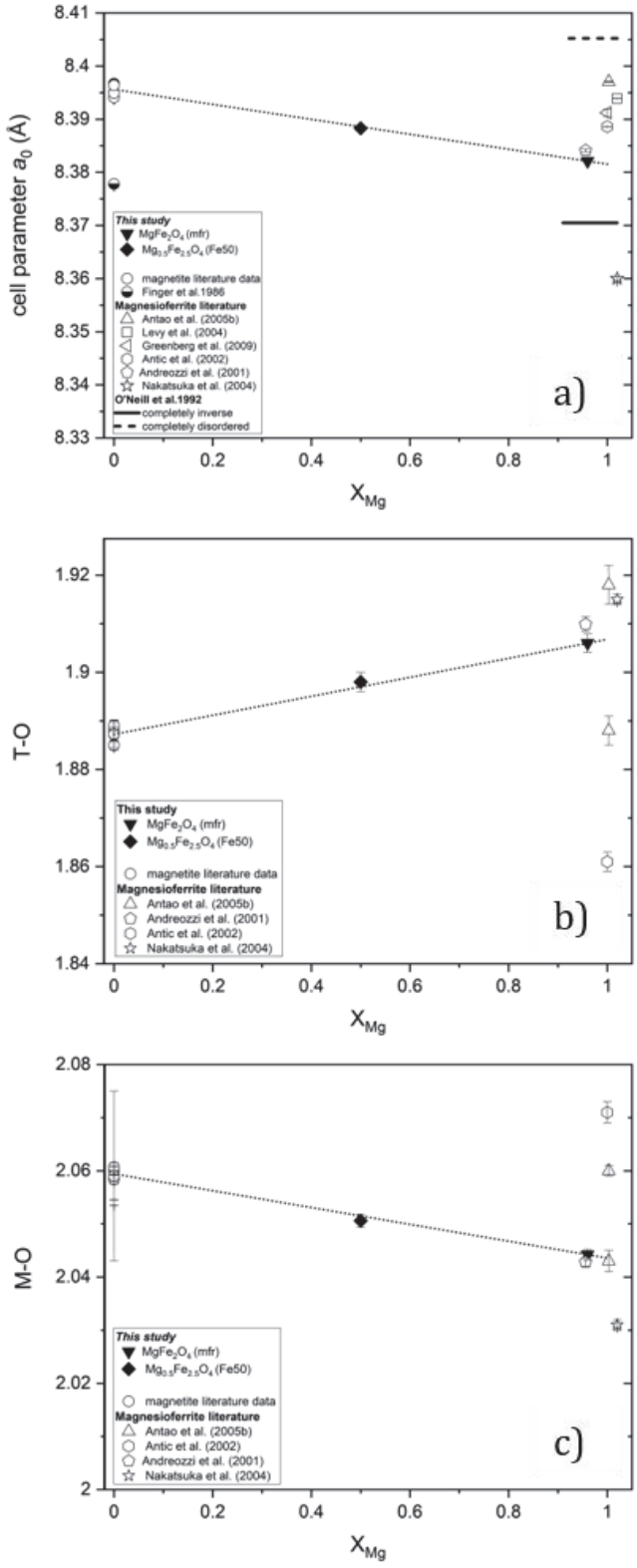

Figure 3.3: a) Variation of the unit-cell parameter (a_0) along the magnetite-magnesioferrite solid solution as a function of X_{Mg} (i.e. molar $Mg/(Fe^{2+}+Mg)$. Predicted fully ordered (solid line) and fully disordered (dashed line) magnesioferrite unit-cell parameters (O'Neill et al. 1992) are also reported. **b)** Tetrahedral, T-O bond length variation across the solid solution. **(c)** Octahedral, M-O bond length variation across the solid solution. Empty symbols refer to literature data (Table 3.2.): circles are magnetite samples (Bosi et al. 2009; Fleet 1981; Finger et al. 1986 (half filled circle); Gatta et al. 2007; Haavik et al. 2000; Nakagiri et al. 1986) and for the magnesioferrite end-member, the different studies are reported in the legend. Filled symbols are the samples investigated in the present study: the triangle is the near end-member mfr sample and the diamond the intermediate $Mg_{0.5}Fe_{2.5}O_4$ sample (Fe50). The dashed line in all the plots connects the magnesioferrite end-member in the present study with an average value for the cluster of magnetite end-member samples reported in the literature (see Results and discussion).

The magnetite samples reported in Table 3.2. have similar bond distance values, as expected due to their high degree of order. A line through the average of these values and the bond distances of

the mfr sample investigated in this study can be used to describe the linear behaviour of the most ordered magnetite-magnesioferrite solid solution. The M-O bond distance of the ordered Fe50 sample lies just slightly below this trend and the T-O bond length slightly above (Figure 3.3b and 3.3c respectively). This very slight shortening of the M-O distance compared to the linear trend may be related to the raised incompressibility of this intermediate sample, as discussed later. Cation disorder should decrease the M-O bond distances and increase the T-O bond distances even further, as Fe^{2+}/Mg enter the tetrahedral site and are replaced by Fe^{3+} at the octahedral site. This is clearly the case for the single-crystal $Mg_{0.956}Fe_{2.044}O_4$ sample studied by Andreozzi et al. (2001), which is slightly more disordered (x=0.87) than our mfr sample. Data for the other reported end-member magnesioferrite samples (Table 3.2.), however, do not appear to follow this behaviour (Figure 3.3B and 3.3C) and show in some cases an increase in M-O distance even though they report higher levels of disorder. These studies, however, have been performed on polycrystalline samples and it is likely that the large correlations between refined parameters during the Rietveld refinements resulted in a poorly constrained oxygen positions due to its low scattering factor. This is well illustrated in the study by Antao et al. (2005b) where different values for the M-O and T-O bond distances are reported for the same sample analysed with two different X-ray sources (Table 3.2.), despite the fact that the same unit-cell lattice parameter is obtained from the two techniques.

3.3.3 Compressibility of the $MgFe_2O_4$ – Fe_3O_4 solid solution

The decreasing trends of the unit-cell volumes with pressure for the mfr and Fe50 samples are shown in Figure 3.4. No evidence of a phase transition was observed in the pressure range investigated. The end-member magnesioferrite is clearly more compressible than the Fe50 sample. The normalized stress, F_E, versus Eulerian finite strain, f_E, plot (Angel 2000) is illustrated in Figure 3.5. Both data sets are well represented within uncertainties by horizontal straight lines indicating

that a second order truncation of the Birch-Murnaghan (BM) equation of state (EoS) (Birch 1947) is sufficient to describe the experimental *P-V* data. In this case only two EoS parameters are refined, the room pressure unit-cell volume, V_0, and the bulk modulus, K_{T0}, whereas the first pressure derivative of the bulk modulus, K', assumes the value of four. The quality of the *P-V* data, however, appears adequate to constrain the value of K', therefore, a third-order truncation of the BM EoS was also used, with three refined EoS parameters, V_0, K_{T0}, and K'. The results from fitting a BM2 and a BM3 EoS to the *P-V* data of both samples are reported in Table 3.1. The K' values of the BM3 EoS are identical to 4 within their uncertainties. K_{T0} is found to decrease significantly by approximately 10 GPa between the Fe50 (188.0±0.6 GPa BM2) and mfr (178.4±0.5 GPa BM2) samples (Figure 3.6.).

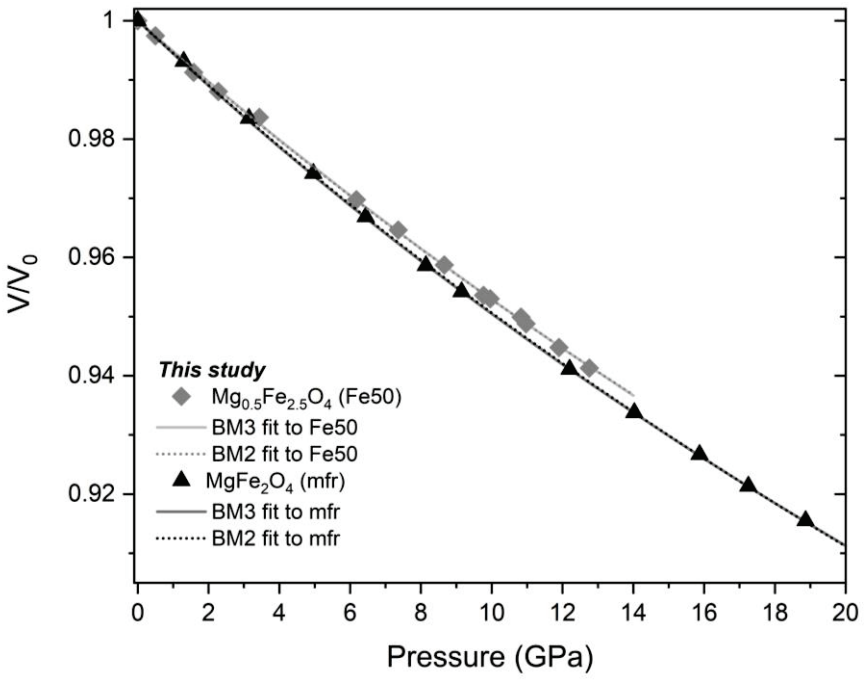

Figure 3.4: Variation of the unit-cell volume as a function of pressure for the magnesioferrite (mfr) end-member and the intermediate $Mg_{0.5}Fe_{2.5}O_4$ (Fe50) crystals examined in this study. The solid lines show the fit of the third-order Birch-Murnaghan EoS (BM3) of the P-V data. Dashed lines show the fit of the second-order Birch Murnaghan EoS (BM2). The standard uncertainties are smaller than the symbols.

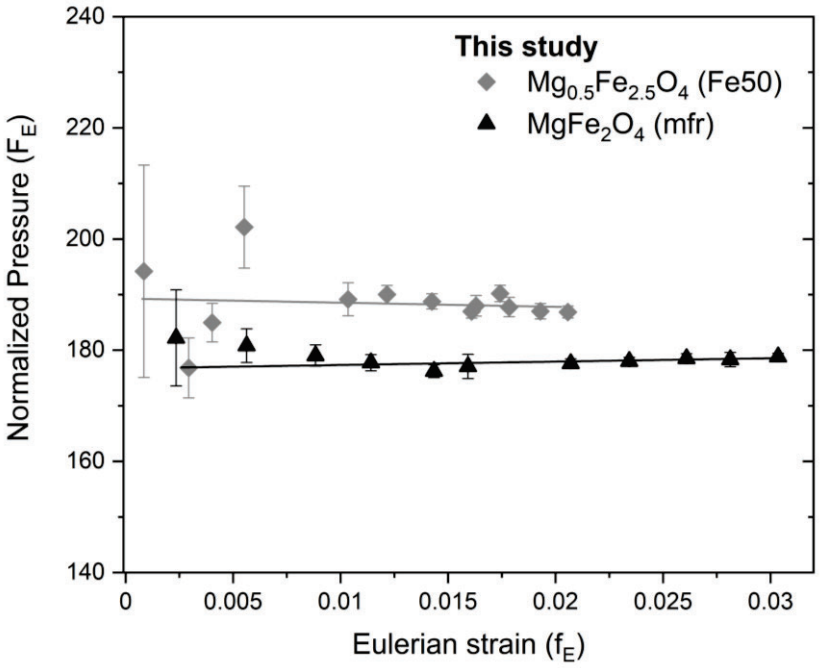

Figure 3.5: Normalized pressure F_E vs. the Eulerian strain f_E calculated for the P-V data collected in this study. Eulerian strain is defined as $[(V_0/V)^{2/3}-1]/2$and F_E, the normalized stress, as $[P/(3f_E)*(1+2f_E)^{5/2}]$ (Angel et al.2000). The solid lines are weighted linear regressions through the data points yielding intercept values of K_{T0} = 176 (2) GPa for the mfr near end-member magnesioferrite sample and K_{T0} = 189 (3) GPa for the Fe50 intermediate composition.

Data reported in the literature (Table 3.1.) for the end-members magnetite and magnesioferrite vary considerably between the different studies (Figure 3.6.). For the magnesioferrite studies, K_{T0} values range between 170.5 and 233 GPa and K' between 3.3 and 6.32 (Figure 3.6.). The reasons for this large difference among the reported data sets are probably multiple but likely include non-hydrostatic conditions and insufficient data coverage. A comparison between the inversion parameter x for the samples used in each study and the obtained EoS terms shows no obvious correlation. The very large K' in the study of Levy et al. (2004) probably results from non-hydrostatic conditions arising from the use of an N_2 pressure medium, which has been shown to become non-hydrostatic above approximately 6 GPa (Angel et al. 2007). The results of Greenberg et al. (2009) are very similar to those of this study up to approximately 20 GPa, however, their sample appears to become softer at higher pressures, leading to a low determined value of K' of 3.3. This can be seen in the F_E- f_E plot reported by Greenberg et al. (2009) which shows a kink

above 20 GPa. Although somewhat speculative one possible explanation for this would be the approach or commencement of a phase transition to a post-spinel phase, such as that observed by Andrault and Bolfan-Cassanova (2001). As magnesioferrite is anyway expected to break down at ~10 GPa and high temperatures (Uenver-Thiele et al. 2017b), the measurements in the current study should cover a sufficient range (up to ~19 GPa) to obtain suitable elastic properties for thermodynamic calculations of its stability field. Amongst various studies on magnetite compressibility, the study of Gatta et al. (2007) used a very similar methodology to that employed here and the results are in good agreement with several other studies on magnetite (Nakagiri et al. 1986; Rozenberg et al. 2007; Reichmann and Jacobsen 2004). As shown in Figure 3.6, the K_{T0} value obtained for the mfr sample (178.4 (5) GPa) is only slightly lower than the value of 180 (1) GPa for magnetite (Gatta et al. 2007) while the values of K' obtained by using a BM3 EoS are identical within the uncertainties. That the values of K_{T0} for the two endmembers are similar, with just a very small increase in K_{T0} between the Mg and Fe^{2+} endmembers, is consistent with studies on the normal spinels $MgAl_2O_4$ (193±1 GPa) and $FeAl_2O_4$ (193.9±1.7 GPa; Nestola et al. 2007, 2015) and $MgCr_2O_4$ (182.5±1.4 GPa) and $FeCr_2O_4$ (184.8±1.7 GPa; Nestola et al. 2014). The sample with mixed composition (Fe50) is stiffer than both end-members (Figure 3.7.), indicating that a simple linear relationship of bulk moduli along the most ordered magnesioferrite-magnetite solid solution cannot describe the intermediate compositions. This behaviour is unusual, as other normal spinels such as Fe_2SiO_4-Mg_2SiO_4 (Higo et al. 2006) and $MgAl_2O_4$-$FeAl_2O_4$ (Bruschini et al. 2018) show near monotonous changes in K_{T0} across significant sections of the solid solutions. A non-linear behaviour has been observed for the bulk modulus along the $MgAl_2O_4$ - $MnAl_2O_4$ join (Bruschini et al. 2015), however, the difference among the bulk moduli along the solid solution is less than 3 GPa (i.e. of the order of the uncertainties) and appears to be related to changes in the inversion parameter (Bruschini et al. 2015). The difference between the K_{T0} of the

Fe50 sample and its two endmembers is also greater than the differences between any of the studied Fe-Mg spinel endmembers.

One consideration is that although the magnetite is a fully ordered inverse spinel, the mfr and Fe50 samples retain some level of cation disorder (x=0.83-0.89). If the fully ordered mfr were stiffer, this might render a linear X_{Mg}-K_{T0} relationship among the samples. Studies at least on the normal spinel $MgAl_2O_4$, appear to indicate that there is no resolvable effect of varying cation ordering on K_{T0} (Nestola et al. 2007; Bruschini et al. 2018). This implies that the potential softening effect of putting Mg into the octahedral site is balanced by the hardening influence of Al entering the tetrahedral site. However, the magnesioferrite inverse spinel may behave differently. The increase in volume at room temperature on disordering, for example, is larger for magnesioferrite compared to $MgAl_2O_4$ spinel (O'Neill et al. 1992; Nestola et al. 2007).

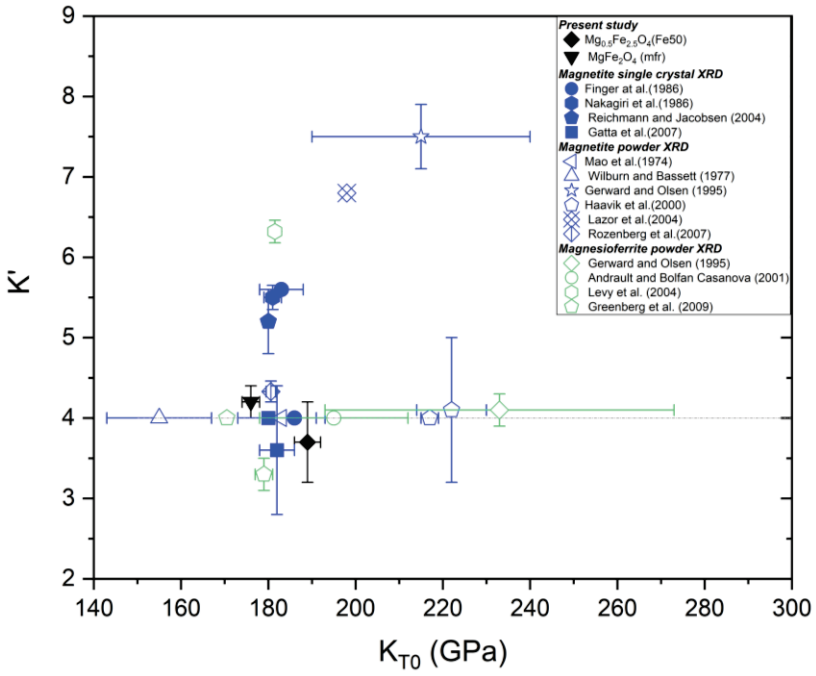

Figure 3.6: K_{T0} vs. K' plot showing the refined data of the studied samples and literature data on the magnetite-magnesioferrite solid solution. Black data points are the refined values for the two samples in the present study. Literature data are for magnetite (blue) and magnesioferrite (green). Filled symbols indicate data acquired using single-crystal X-ray diffraction. Empty symbols show data acquired with powder X-ray diffraction.

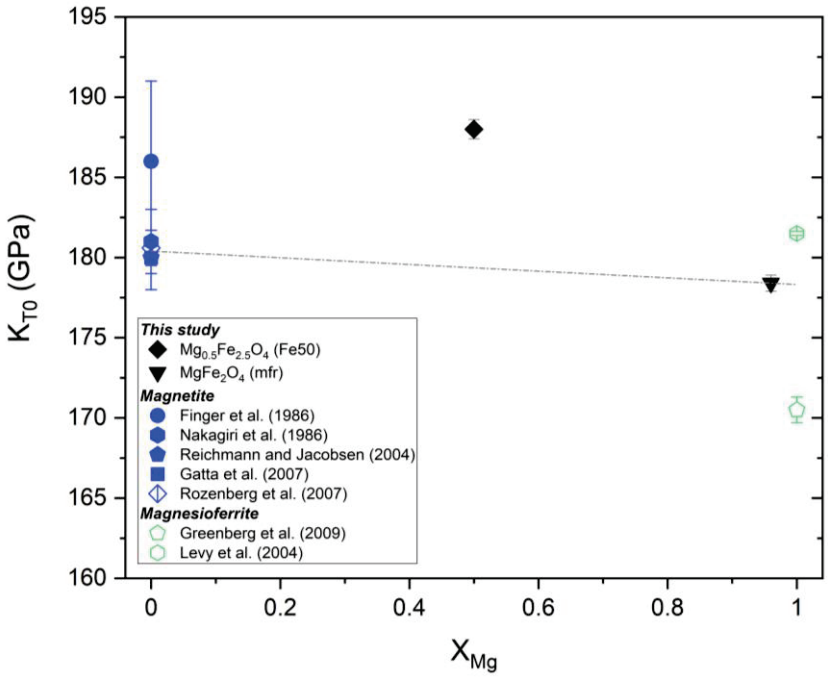

Figure 3.7: K_{T0} vs the Mg/(Mg+Fe^{2+}) ratio along the magnetite-magnesioferrite join. The dashed line joins the near-endmember magnesioferrite (mfr) K_{T0} value obtained in this study with the value for magnetite of 180 (1) GPa reported by Gatta et al. (2007). All K_{T0} values are for second order truncations of the Birch-Murnaghan equation of state.

Similarly, the softening effect of Mg entering the tetrahedral site may not be balanced by Fe^{3+} entering the octahedral site, as half of this site is already filled by Fe^{3+}. Density functional theory calculations on $MgAl_2O_4$ spinel (Núñez-Valdez et al. 2018), do predict a higher bulk modulus for a theoretically fully ordered inverse spinel, compared to normal ordered spinel. This effect is not predicted to be much larger, however, and is probably not sufficient to raise the mfr K_{T0} significantly to render a linear relationship between Mg substitution and K_{T0}.

The higher K_{T0} for the Fe50 sample implies that some type of Fe^{2+}-Mg interaction is causing the octahedral site to be stiffer than when it is dominated by either Mg-Mg or Fe^{2+}-Fe^{2+} neighbours. One way that this might occur is through an interruption of the electron hopping between Fe^{2+} and Fe^{3+}, which causes the averaged $Fe^{2.5+}$ valence observed in Mössbauer spectra of magnetite. If the presence of local Mg reduces the extent of hopping then the more localised Fe^{2+} 3d electron may increase the degree of covalency, and therefore the strength, of the Fe^{2+}-O octahedral bond. This

could decrease the compressibility. Once the X_{Mg}=0.5 composition has been reached a further increase in Mg may then dilute this effect. If this is the case, then the non-linear elastic behaviour with composition is likely to be a peculiarity of the magnetite-magnesioferrite solid solution. The polyhedral moduli in this system can be calculated using the ionic potential model of Bruschini et al. (2015), taking into account the state of cation ordering determined in this study, and can be used to obtain the bulk moduli (Bruschini et al. 2015) across the solid solution. However, this approach gives rise to end member bulk moduli that are greater than the experimentally determined values and predicts a linear dependence of the bulk modulus across the solid solution. This also implies that the effect of Fe^{2+} and Fe^{3+} cations on polyhedral compressibility of the spinel structure does not simply depend on their respective charge and ionic radii, as found for other spinel structures (Bruschini et al. 2015), but also on the specific types of metal-oxygen bonding.

A final aspect is to consider whether the change in incompressibility across the solid solution would result in a significant excess molar volume at high-pressure, which could potentially contribute to the degree of non-ideality of the solid solution. At 10 GPa, however, i.e. near the limit of high-pressure magnetite-magnesioferrite stability, the predicted excess molar volume is at most 0.07 cm^3/mol, which would not have a significant influence on the thermodynamics of mixing.

3.4 Summary

In this study, the crystal chemistry and room temperature compressibility of near endmember $MgFe_2O_4$ magnesioferrite and an intermediate $Mg_{0.5}Fe_{2.5}O_4$ inverse spinel composition have been examined by means of single-crystal X-ray diffraction performed in the diamond anvil cell. A high degree of cation order was achieved by synthesising the single-crystal samples at high-pressure and high-temperature conditions. The magnesioferrite sample synthesised at 5 GPa and 1300 °C had an inversion parameter of x=0.892(2), which is in good agreement with the high-pressure and

high-temperature determinations of Antao et al. (2005a), and indicates a significant decrease in high-temperature disordering with increasing pressure. The intermediate sample, synthesised at 9 GPa and 1000 °C, was nearly fully ordered (x> 0.83).

Compressibility data were collected up to 18.87 GPa for magnesioferrite and up to 12.76 GPa for $Mg_{0.5}Fe_{2.5}O_4$. Plots of the normalized stress versus the Eulerian finite strain indicated that a 2nd order truncation of the Birch-Murnaghan equation of state would provide a suitable fit to the data. This yielded V_0 =588.97 (8) Å^3 and K_{T0} = 178.4(5) GPa for magnesioferrite and V_0 =590.21 (5) Å^3 and K_{T0} = 188.0 (6) GPa for the $Mg_{0.5}Fe_{2.5}O_4$ composition. Using a 3rd order Birch-Murnaghan equation of state resulted in values of K' that were indistinguishable from 4, within the uncertainties. Measurements on magnetite using the experimental procedure of Gatta et al. (2007) reveal a K_{T0} = 180(1) with K' = 4.

The slightly higher K_{T0} for the Fe-end-member of the magnetite-magnesioferrite solid solution mimics the behaviour of the normal spinel joins $FeAl_2O_4$-$MgAl_2O_4$ and $FeCr_2O_4$-$MgCr_2O_4$ (Nestola et al. 2007; 2014; 2015). However, the significantly larger incompressibility of the intermediate $Mg_{0.5}Fe_{2.5}O_4$ composition has not been observed for other Fe-Mg spinels but likely results from stiffer octahedra, arising from some form of Fe^{2+}-Mg interaction. A smaller negative deviation from a linear compositional dependence of the octahedral M-O bond distance for the intermediate composition may be an indication for the stiffening of the octahedra, with respect to the end-members. A possible explanation, is that the substitution of Mg into the octahedral site interrupts the exchange (hopping) of the Fe^{2+} 3d electron with neighbouring Fe^{3+} cations. If this electron is then more localised on the Fe^{2+} site it may raise the covalency and, therefore, the strength of the Fe^{2+}-O bond, with a consequent increase of the incompressibility.

4. Ferropericlase stability and composition as a function of oxygen fugacity

4.1 Introduction

The ferric iron concentration of the (Mg,Fe)O periclase-wüstite solid solution has been studied quite extensively in the MgO-FeO-Fe_2O_3 system (Brynestad and Flood 1958; Katsura and Kimura 1965; Speidel 1967; Valet et al. 1975; Hilbrandt and Martin 1998; Otsuka et al. 2010) and significant literature also exists, particularly in the FeO-Fe_2O_3 subsystem, describing efforts to characterize the defect structure that accompanies ferric iron substitution (e.g. Koch and Cohen 1969; Vallet and Carel 1989; Schweika et al. 1995; Gavarri and Carel 2018). The substitution of ferric iron in (Mg,Fe)O is charge balanced through the creation of metal cation vacancies (V), and results in non-stoichiometry that can be described by the formula $Mg_zFe^{2+}_{1-z-3x}Fe^{3+}_{2x}V_xO$. At room pressure the Fe^{3+}/Fe_{tot} ratio of (Mg,Fe)O varies strongly with oxygen fugacity, reaching a minimum where the oxide is in equilibrium with iron metal (Srecec et al. 1987; O'Neill et al. 2003) and a maximum where it coexists with spinel phases along the magnetite-magnesioferrite (Fe_3O_4-$MgFe_2O_4$) solid solution (Brynestad and Flood 1958; Katsura and Kimura 1965; Speidel 1967; Hilbrandt and Martin 1998).

Since (Mg,Fe)O is the second most abundant phase in the lower mantle, its ferric iron content can influence transport properties such as electrical conductivity (Hansen and Cutler 1966; Wood and Nell 1991; Dobson et al. 1997; Potapkin et al. 2013), rheology (Terwillinger et al. 1970; Tremper

et al. 1974) and diffusion (Mackwell et al. 2005). Inclusions of (Mg,Fe)O are also found in diamonds and are often used as evidence for a sub-lithospheric provenience (Harte and Hudson 2013; Kaminsky 2012; Kaminsky et al. 2009, 2001; Stachel and Harris 2008; Hayman et al. 2005; Harte et al. 1999; Harte and Harris 1994; Wilding 1990; Stachel et al. 2000; Davies et al. 2004, 1999). Analyses of the ferric iron content of these inclusions can potentially be used to provide information on the oxygen fugacity of diamond formation processes, using constrains on its dependence on pressure, temperature and MgO content (Otsuka et al. 2013). Several studies also have noted that such inclusions can contain nano- to micro-level exsolutions of magnetite - magnesioferrite spinel phases (Harte et al. 1999; Anzolini et al. 2019; Palot et al. 2016; Nimis et al.2019; Wirth et al. 2014; Kaminsky et al. 2015; Nestola et al. 2016). The presence of these Fe^{3+}-rich exsolutions raises the question of whether they may provide information on the post entrapment history of the (Mg,Fe)O inclusions, which could be potentially investigated if the conditions at which this exsolution occurs were well constrained. To assess this, information is required on the phase relations between (Mg,Fe)O, which we refer to here as ferropericlase (fper), for simplicity, even when Fe > Mg, and Fe_3O_4-$MgFe_2O_4$, which we refer to here as spinel-ferrite (spft). Data are required on where the intervening boundary lies between these two phases with respect to the ferric iron content of fper and the Fe-Mg contents of the coexisting phases and how these vary with pressure and temperature. This information, however, is not well known even at room pressure conditions for the more Mg-rich fper compositions that are applicable to the mantle. This problem arises from two issues. Firstly, the room pressure phase relations and ferric iron contents of fper have been mainly determined using thermogravimetric or wet chemical methods. However, not only do these measurements become increasingly imprecise with higher Mg-contents but the phase fields of fper, fper + spft and spft are generally inferred through changes in slope of the ferric iron-fO_2 relationship (Brynestad and Flood 1958; Paladino 1960; Katsura and Kimura 1965; Speidel 1967). Only in very rare cases have the Fe-Mg contents of coexisting fper

and spft been directly analyzed (Hilbrandt and Martin 1998) and even then, only the bulk Fe content of (Mg,Fe)O was determined. This leads to inconsistencies between studies, that become apparent when attempts are made to combine them into a single thermodynamic model (e.g. Jung et al. 2004). Secondly, it is well documented that spft can form from fper during temperature quenching (Dobson et al. 1998; McCammon et al. 1998; Reichmann et al. 2000; Boiocchi et al. 2001; Longo et al. 2011). This has been far more documented for wüstite, where the exsolution of magnetite may be facilitated by the formation of clusters of octahedral cation vacancies around ferric iron occupying normally vacant tetrahedral interstitial sites (e.g. Koch and Cohen 1969; Hentschel 1970; Shen et al. 1983; Hazen and Jeanloz 1984; Stolen et al. 1996). Aggregation of these clusters through corner or edge sharing appears to occur on cooling (Nowotny and Rekas 1989; Schweika et al. 1995). An important aspect of this aggregation is that in an edge sharing cluster involving five tetrahedral ferric iron interstitials and sixteen octahedral vacancies, each vacancy is shared by no more than two tetrahedral Fe^{3+}, giving rise to a sublattice that is identical to magnetite (Catlow and Fender 1975; Dimitrov et al. 1999; Hazen and Jeanloz 1984).

Here, to clarify the stability field of fper at room pressure, which is essential for understanding its stability at higher pressure conditions, experiments have been performed to determine the Fe^{3+}/Fe_{tot} of fper as a function of fO_2 up to conditions where it coexists with the spft solid solution. A set of experiments with two bulk compositions ($Mg_{0.80}Fe_{0.20}O$ and $Mg_{0.15}Fe_{0.85}O$) chosen to reproduce the variation in diamond inclusions, were conducted using a gas mixing furnace, whereby the fO_2 was calculated from the inclusion of an Fe-Pt sliding redox sensor in the fper sample (Kessel et al. 2001). The Fe and Mg contents of coexisting fper and spft phases were measured and the results used to develop a thermodynamic model in the Fe-Mg-O system that describes the fper stability field with respect to both Fe-metal and spft. We show that, in most of the fper samples examined, a significant proportion of the original Fe^{3+} is present as a coherent exsolution of a spft, the presence of which creates problems

in determining the fper Fe^{3+}/Fe_{tot} using Mössbauer spectroscopy and has further effects on the unit-cell parameter of fper.

4.2 Experimental methods

4.2.1 Sample synthesis

Starting materials were prepared from a stoichiometric mixture of Fe_2O_3, MgO and minor amounts of NiO (1.3 wt%), Cr_2O_3 (0.5 wt%), MnO (0.2 wt%), and Na_2O (0.05 wt%) representative of naturally found Fper inclusions in diamond. Fe_2O_3 and MgO powders were fired overnight at 1000 °C to remove volatiles. Powders with two stoichiometries ($Mg_{0.80}Fe_{0.20}O$ and $Mg_{0.15}Fe_{0.85}O$) were weighed and ground together in an agate mortar under ethanol. Between 1 to 4 wt % PtO_2 powder was added as a sliding redox sensor (Table 4.1).

Table 4.1: Composition of the ferropericlase starting materials are reported in wt%. Added PtO_2 component is calculated relative to the weight of the ferropericlase composition to which it was added. PtO_2 was used as redox sensor.

Stoichiometry		**Cr_2O_3**	**NiO**	**Na_2O**	**MnO**	**FeO**	**MgO**	**total**	**Added PtO_2**
$(Mg_{0.80}Fe_{0.20})O$	(A)	0.50	1.30	0.05	0.20	19.59	78.36	100	2/1 wt%
$(Mg_{0.15}Fe_{0.85})O$	(B)	0.50	1.30	0.05	0.20	84.03	13.99	100	4 wt%

The starting powders were dried, pressed into pellets and then hung inside a CO-CO2 gas mixing furnace using a platinum wire cage. The samples were equilibrated in the furnace for 12 - 48 hours at 1300 and 1450 °C and at oxygen fugacities between -1 and +2 log units of the fayalite-magnetite-quartz oxygen buffer (ΔFMQ) (Table 4.2). After equilibration, the pellets were quenched in air by cutting the platinum wire.

The recovered samples were analyzed using a DISCOVER micro focused X-ray diffractometer and if they were found to consist only of fper they were returned to the gas mixing furnace and re-equilibrated at a slightly higher fO2. The recovered pellets then were mounted in epoxy resin and ground and polished for further chemical (EPMA) and X-ray analyses.

Table 4.2: Experimental conditions for 1 atm experiments performed in the gas-mixing apparatus. All the samples were held at T and fO_2 for 24hrs. The calculated fO_2 from the Pt-Fe redox sensor is also reported.

Run	Compo.	T (°C)	fO_2 ΔFMQ	$CO:CO_2$	Calculated fO_2	Run products
RPP1	(A)	1300	-1	85:15	-8.3	fper +Pt+ Ca-Si melt[#]
RPP2	(A)	1300	0	95:5	-7.2	fper +Pt + n-spft*+ Ca-Si melt[#]
RPP3	(A)	1300	2	98:2	-5.3	fper +Pt+ n-spft* + Ca-Si melt[#]
RPP4	(A)	1300	0	95:5	-7.0	fper +Pt+ n-spft*
RPP5	(A)	1300		100:0	-3.2	fper + spft + Pt
RPP6	(A)	1300		100:0	-3.1	fper + spft + Pt
RPP9	(A)	1450		100:0	-2.4	fper +Pt+ n-spft*
RPP10	(B)	1300	-1	85:15	-8.1	fper +Pt+ n-spft*
RPP11	(B)	1300	0	95:5	-7.1	fper + spft + Pt
RPP12	(B)	1300	-0.4	92:8	-7.5	fper +Pt+ n-spft*

Note: (*) magnetic phase observed in the Mössbauer spectra but not observed in the SEM or EPMA data collection. Run products are ferropericlase (fper), spinel-structured ferrite (spft); nm-sized spinel-structured ferrite (n-spft) and platinum alloy (Pt). (#)contamination in starting material

4.2.3 Chemical analyses

The polished pellet mounts were carbon coated for initial phase identification with a ZEISS LEO 1530 scanning electron microscope (SEM). Representative images of the samples are shown in Figure 4.1.

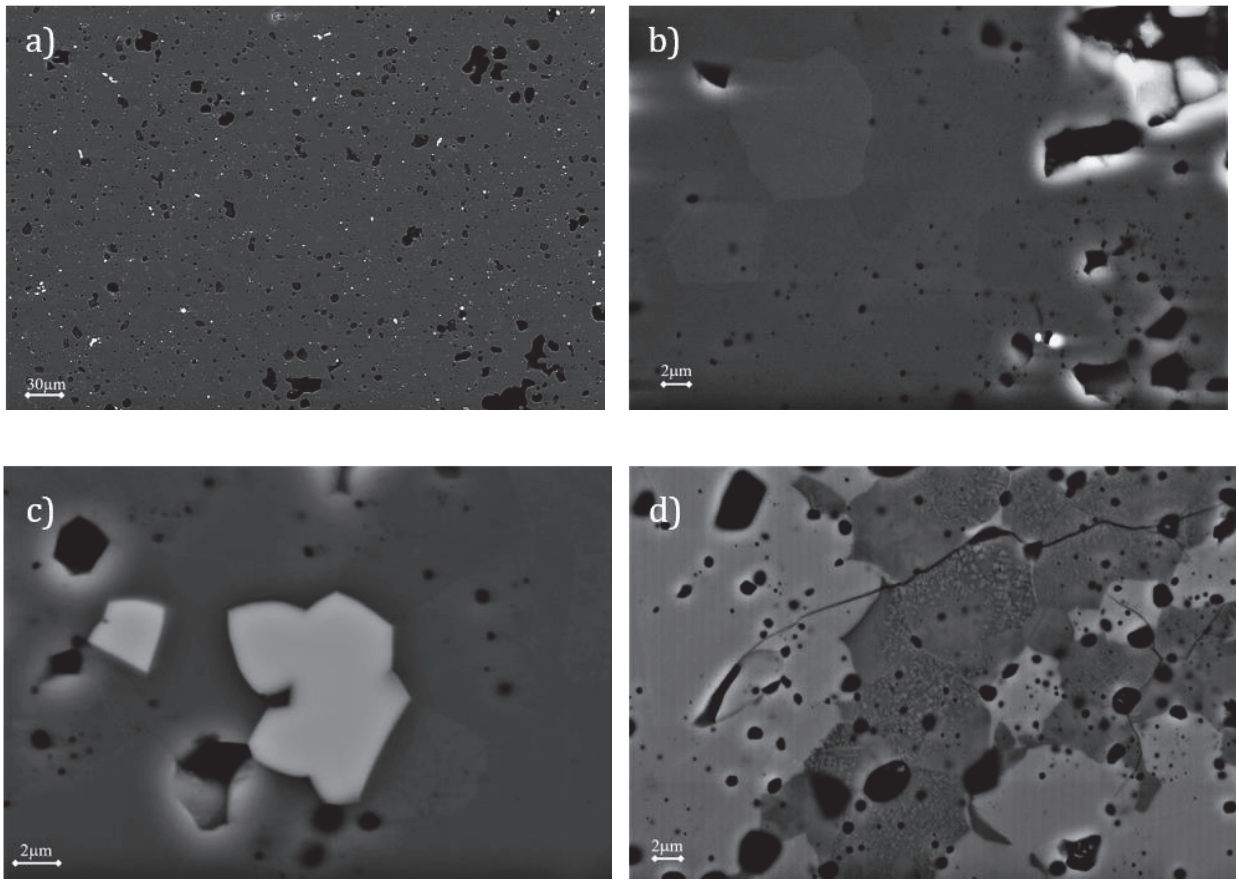

Figure 4.1: Back scattered electron images of experimental run products obtained at varying fO_2 conditions and from the two different bulk composition**: a)** Sample RPP1 synthesised at 1300 °C and ΔFMQ = -1. The gray homogeneous ferropericlase matrix coexist with brighter Pt-Fe alloys and no additional phase can be observed; **b)** Sample RPP4 synthesised at 1300 °C and ΔFMQ = 0 shows the presence of brighter inhomogeneous areas in the grey ferropericlase matrix; **c)** Sample RPP6 synthesised at 1300 °C and ΔFMQ = 2 can be observed to have ferropericlase (dark grey) coexisting with brigt spft crystals. Brighter inhomogenous areas can be observed in the ferropericlase matrix; **d)** Sample RPP11 synthesised at 1300 °C and ΔFMQ = 0 consists prevalentely of spft coexisting with only few grains of ferropericlase (darker regions). In the ferropericlase crystals, dendritic nanometer-sized spinel structured ferrite (n-spft) crystals can be observed

Further quantitative chemical analyses were carried out with a JEOL JXA-8200 electron microprobe analyzer (EPMA) equipped with five wavelength-dispersive spectrometers. Measurements were performed in wavelength-dispersive mode using a 15 kV accelerating voltage and 15 nA beam current. Matrix correction was performed using the ZAF algorithm (Goldstein et al.2003).

For oxide analyses the standards employed were olivine (Mg), andradite (Fe), albite (Na), nickel oxide (Ni), $MnTiO_3$ (Mn), Cr_2O_3 (Cr) and Fe_2O_3 (O). Iron, platinum and nickel metals were used as standards when analyzing the platinum-alloy redox sensor. The focused beam had a width between 1-2 μm. A minimum of 20 points were measured on each major phase in the sample. The resulting averaged compositions are reported in Table A.4.1.

4.2.4 Mössbauer spectroscopy (MS)

Mössbauer analyses were performed on powdered samples loaded in 12 mm diameter sample holders. The optimum powder weight was calculated based on the Fe content and electronic absorption coefficients (Rancourt et al. 1993). Measurements were performed using a conventional Mössbauer source, i.e. nominal 1.85 MBq^{57} over a 5 mm diameter (McCammon et al. 2021). The velocity scale was calibrated relative to an α-Fe foil with 25 μm thickness. The resulting spectra were fitted with a pseudo-Voigt line shape and a 1st order polynomial baseline in the MossA 1.01f software package (Prescher et al. 2012). Some of the spectra showing a strong magnetic component were first fit using the NORMOS program written by R.A. Brand (distributed by Wissenschaftliche Elektronik GmbH, Germany). After the magnetic field distribution was fitted, the samples were all re-fitted using the MossA program. The fitting procedure is described in detail in the results section and the resulting hyperfine parameters for all samples are reported in Table A.4.2.

4.2.5 Powder X-ray diffraction

Part of the sample pellets were finely ground and mixed with a Si standard (NIST SRM 640c) in order to collected X-ray diffraction patterns using a Philips X'Pert PRO powder XRD operating at 40 kV and 40 nA with monochromatic CoKα (λ = 1.78897 Å) radiation.

Table 4.3: Unit-cell lattice parameters for the run products of the 1atm gas-mixing furnace pellets determined by powder X-ray diffraction

run	phase	a (A)	V (A^3)	Molar Volume (cm^3/mol)
RPP1	fper	4.2288(1)	75.622(2)	11.385
RPP2	fper n-spft	4.2251(1) 8.448(5)#	75.424(3)	11.355
RPP3	fper n-spft (GSAS) n-spft	4.2178(1) 8.426(1) 8.424(3)#	75.028(2) 598.2(2)	11.296
RPP4	fper n-spft	4.2237(1) 8.426(8)#	75.347(2)	11.344
RPP5	fper spft (GSAS) spft n-spft	4.2098(1) 8.4101(4) 8.401(3)% 8.411(7)#	74.609(2) 594.85(8)	11.233
RPP6	fper spft (GSAS) spft n-spft	4.2088(1) 8.4020(5) 8.396(1)% 8.409(2)#	74.557(3) 593.13(11)	11.375
RPP9	fper n-spft (GSAS) n-spft	4.2115(1) 8.4133(4) 8.411(1)#	74.700(2) 595.52(8)	11.246
RPP10	fper n-spft (GSAS) n-spft	4.2721(1) 8.4065(3) 8.405(1)#	77.968(5) 594.08(7)	11.738
RPP11*	fper spft (GSAS)	4.2549(3) 8.3966(1)	77.03(2) 591.98(2)	11.597
RPP12	fper Spft (GSAS)	4.2708(1) 8.3970(1)	77.90(1) 592.07(4)	11.728

Note: Fe-Pt alloy was present in all XRD patterns; *the spft phase coexisting with fper dominates the XRD pattern, therefore no information on the exsolved nano spinel phase inside fper can be obtained from the XRD analysis; # unit-cell axis of exsolved n-spft phase was determined following the procedure described in the text; **%** unit-cell axis of spft coexisting with fper was determined following the procedure described in the main text

X-ray data were collected between 30° and 100° 2θ. Unit-cell parameters (Table 4.3) were determined for all samples from full-pattern refinements using the general structure analysis system (GSAS) software package and the EXPGUI interface (Toby 2001; Larson & von Dreele 2004).

4.2.6 Transmission electron microscopy (TEM)

Pellets RPP6, RPP10 and RPP11 were prepared for TEM analysis. A lamella of the RPP6 pellet, with dimensions of 20 × 13 μm, was cut from the initial mount using a focused ion beam (FIB) milling machine (*FEI Scios* DualBeam) following the procedure described in the Chapter 2, Section 2.9. Measurements were carried out using a 200 kV analytical TEM (*FEI Titan G2 80-200 S/TEM*, *Philips CM20FEG*) equipped with an energy dispersive X-ray spectrometer (EDXS, *Brucker QUANTAX*) and an electron energy-loss spectrometer (EELS, *Gatan GIF Quantum® Model 963*). The spot size of the stationary electron beam during the data acquisition was 0.2 nm. The TEM was employed in scanning mode (STEM) to acquire high-angle annular dark-field (HAADF), bright-field (BF) and dark-field (DF) images of microtextures present in the sample as well as selected area electron diffraction (SAED) patterns. Fe-$L_{2,3}$-edge electron energy-loss near-edge structure (ELNES) measurements were performed for sample RPP6 and RPP11 using a collection semi-angle of β = 2.7 mrad, an energy-dispersion of 0.1 eV per channel and 10–20 s integration time per read-out with an energy resolution of 0.8–0.9 eV, measured as the full width of the zero-loss peak at half-maximum. EELS spectra also were collected for the spft phases coexisting with fper in both samples. The EELS spectra were corrected for dark current and channel-to-channel gain variation of the detector. The program EELSA written by Clemens Prescher (http://www.clemensprescher.com/programs/eelsa) was used to subtract an exponential background extrapolated from the pre-edge region of the EELS spectra and to remove the multiple

inelastic scattering of the transmitted electrons by Fourier-ratio deconvolution with the low-loss valence spectra (Egerton 1996), collected from the same specimen regions. The determination of the Fe^{3+}/Fe_{tot} ratios using the procedure described by van Aken et al. (1998) and van Aken and Liebscher (2002), which involves evaluating a 2 eV-wide integration window around the $L_{2,3}$ edges and employs an empirically calibrated universal curve, was found to give inconsistent results. For the coexisting spft phase in sample RPP6, for example, which is nearly pure end-member magnesioferrite and, therefore, contains negligible Fe^{2+} (Table A.4.1), such a procedure gives a Fe^{3+}/Fe_{tot} ratio of ~ 0.70. This may be due to the fact that the spinel used as standard for the calibration of 100% of Fe^{3+} in the study of van Aken and Liebscher (2002) was franklinite, $ZnFe_2^{3+}O_4$, which is an ordered normal spinel, i.e. Fe^{3+} occupies mainly or exclusively (depending on the degree of order) the octahedral sites. On the other hand, magnesioferrite is an inverse spinel, i.e. Fe^{3+} is equally distributed between the tetrahedral and octahedral sites. The site-specific Fe $L_{2,3}$ ELNES of tetrahedral Fe^{3+} has a lower energy than the Fe $L_{2,3}$ ELNES of octahedral Fe^{3+} (Tatsumi et al. 2010) giving rise to large broadening of the EELS spectra, as already observed for the magnetite-rich spinels studied by van Aken and Liebscher (2002). This broadening very likely affects the resulting intensities calculated in the 2 eV integration windows used for the universal calibration curve (van Aken and Liebscher 2002). In this study, therefore, an alternative method has been used whereby only the Fe L_3 ELNES is fitted, after subtracting an arctan function to remove the contribution from transitions to unoccupied continuum states (van Aken and Liebscher 2002). To benchmark this procedure, the EELS spectra of the spft phase coexisting with fper in sample RPP11 (Table 4.2) were fitted using i) two Gaussian peaks centered at ~ 707.7 eV and ~ 709.7 eV to mimic the pre-peak and main peak of Fe^{3+}, respectively (see andradite ELNES in van Aken and Liebschen 2002), ii) two Gaussian peaks centered at ~708.3 eV and ~710.7 eV to mimic the main and weaker peaks of Fe^{2+}, respectively (see hedenbergite ELNES in van Aken and Liebschen 2002) and a small Guassian peak above 712 eV to take into account the complex feature

of the L_3 broad signal (Figure 4.2). The Gaussian peaks are constrained to have a similar full width at half maximum in order to reduce the strong correlations between them.

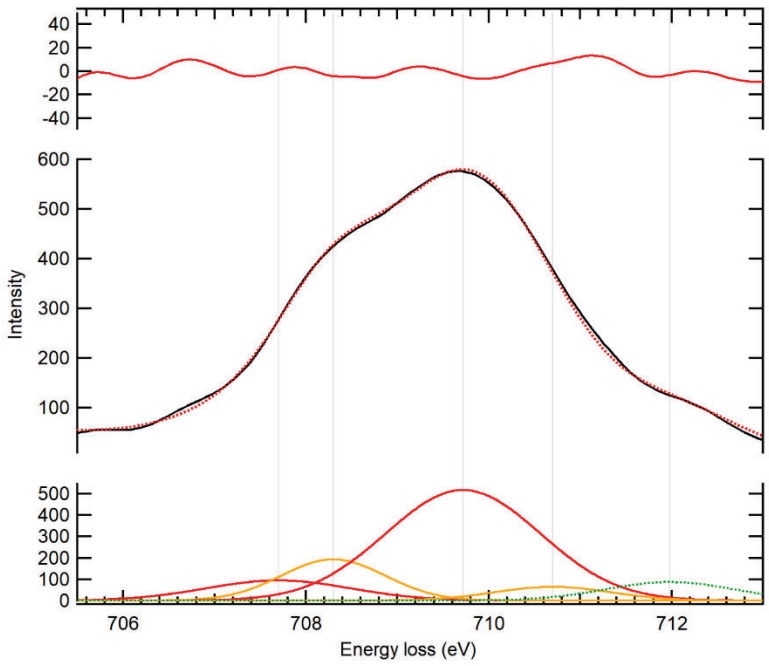

Figure 4.2: Fe L_3 electron energy-loss near-edge spectrum of the spinel phase coexisting with fper in sample RPP11. The two red Gaussian peaks represent the signal due to Fe^{3+}, whereas the two orange Gaussian peaks represent the signal due to Fe^{2+}. The green Gaussian peak is used to better fit the broad ELNES feature at higher energy and it is considered part of the background.

Using this method, we obtained an Fe^{3+}/Fe_{tot} ratio of 0.77 in excellent agreement with the spinel composition ($[Mg_{0.48}Fe^{2+}_{0.52}]Fe^{3+}{}_2O_4$; Table A.4.1) obtained by means of EPMA. The EELS spectra of sample RPP11 were fitted using the same number of Gaussian peaks. For sample RPP6, whose iron content is only 0.12 atoms per formula unit (Table A.4.1), the small peaks of the Fe^{3+} and Fe^{2+} signals at 707.7 eV and 710.7 eV could not be resolved, therefore only three Gaussian peaks (two for the Fe speciation and one for the background) were used (Figure A.4.1). The area of the Gaussian profiles were then used to determine the Fe^{3+}/Fe_{tot} ratios for RPP6 and RPP11 samples (Table 4.4).

Table 4.4: Fe^{3+}/Fe_{tot} ratios obtained for the fper samples investigated in this study by means of Mössbauer spectroscopy, as well as re-calculated taking into account the MS contribution of the ferric iron in n-spft exsolution and as obtained from the EELS analyses.

Run	Fe^{3+}/Fe_{tot} MS	Fper + n-spft	EELS value
RPP1	0.07 (2)		
RPP2	0.07 (2)	0.22 (5)	
RPP3	0.09 (3)	0.61 (11)	
RPP4	0.07 (2)	0.15 (11)	
RPP5	0.33 (8)	0.87 (9)	
RPP6	0.33 (8)	0.90 (10)	0.81 (5)
RPP9	0.12 (6)	0.83 (10)	
RPP10	0.13 (2)	0.33 (10)	
RPP11	0.25 (2)	0.66 (12)	0.40 (6)
RPP12	0.16 (3)	0.44 (10)	

4.3 Results

4.3.1 Phase relations

For both nominal compositions, $(Mg_{0.80}Fe_{0.20})O$ and $(Mg_{0.15}Fe_{0.85})O$, gas mixing experiments were performed to produce a series of samples at different oxygen fugacities until a level was reached where an assemblage containing both fper and spft was formed. For the former bulk composition this occurred at 1300 °C when a pure CO_2 atmosphere was used, whereas for the latter a 95:5 CO_2:CO mixture (nominal ΔFMQ = 0) was needed at the same temperature. In experiments performed at oxygen fugacities below these levels, SEM images show that the samples are comprised of fper with minor amounts of Pt-Fe alloy, which is found scattered throughout all samples in this study (Figure 4.1a). In experiments performed at ΔFMQ > 0, however, brighter and darker regions can be observed inside the fper crystals (Figure 4.1b). At the highest fO_2 conditions, regions of nominal fper composition can be seen to coexist with well crystallized grains

of spft that are generally larger than 5 μm (Figure 4.1c and 4.1d), and the fper can also be seen to contain sub-micron exsolutions of a brighter, more iron-rich phase, that are particularly visible in fper grains from the $(Mg_{0.15}Fe_{0.85})O$ composition (Figure 4.1d).

Chemical analyses of the well crystallized spft phases yielded compositions of $(Mg_{0.98(1)}Fe_{0.02(1)})Fe_{1.98(2)}O_4$ and $(Mg_{0.97(1)}Fe_{0.03(1)})Fe_{1.98(2)}O_4$ for sample RPP5 and RPP6 respectively (Table A.4.1) indicating that the spinel phase in these samples is almost an end-member magnesioferrite. For samples RPP11 the composition of spft is $(Mg_{0.48(2)}Fe_{0.52(2)})Fe_{1.98(2)}O_4$ (Table A.4.1). The chemical analyses of the Fe-Pt alloy show that it contains up to ~5 wt % Ni (Table A.4.1) at low fO_2, such Ni content decreases with increasing oxygen fugacity. Ni is found to partition more favourably into fper, whereas Cr prefers the coexisting spft phase and Mn switches preference from fper at the higher Fe-content to spft at lower Fe-contents, probably reflecting a higher oxidation state of Mn at the higher fO_2. Measured concentrations of Na in all phases are too low to draw conclusions.

4.3.2 TEM observations

TEM investigations were carried out on the $(Mg_{0.80}Fe_{0.20})O$ sample RPP6 and $(Mg_{0.15}Fe_{0.85})O$ samples RPP10 and RPP11 for which inhomogeneous areas were observed inside the fper crystals (Figure 4.1c and 4.1d). High-resolution STEM bright field images of sample RPP6 (Figure 4.3a) show a pronounced spotty contrast resulting from local distortions of the crystal lattice due to the presence of pervasive microstructure. Such microstructures are round in shape and have dimensions of ~ 20-25 nm. High-resolution STEM bright field images of the more Fe-rich samples RPP10 and RPP11, show large darker areas with dimensions up to 100 – 200 nm (i.e. Figure 4.3b). The selected area electron diffraction patterns (SAED) of fper (inset in Figures 4.3a and 4.3c) contain several spots that cannot be indexed with the unit-cell of fper (red circles), but that can be

indexed instead with the unit-cell of a spinel-type structure (white circles). This confirms that the microstructure seen inside the fper crystals results from nanometer sized spinel exsolution, which will be referred hereafter as n-spft to distinguish them from the spft phase coexisting with fper in samples synthetized at the highest oxygen fugacities (Table 4.2). The n-spft exsolutions are in topotaxial relation with the ferropericlase matrix giving rise to a perfect superposition of the unit-cell axis of the two materials at least for the order of reflections observed for sample RPP6 (Figure 4.3a inset). For sample RPP10 a small mismatch between the two reciprocal lattices starts to be visible for the 008 reflections of n-spft (Figure 4.3c), in agreement with the X-ray diffraction results discussed later. Moreover, for some grains of sample RPP10 it was possible to also observe strong satellite reflections around the *hk0* reflections of fper (Figure 4.3b, inset), suggesting that different types of defect clusters (Andersson and Sletnes 1977; Welberry et al. 2014) are also present in the structure of fper, together with the n-spft exsolution.

The Fe^{3+}/Fe_{tot} values (Table 4.4) determined from fitting the EELS spectra collected in regions where the n-spfr are present in the fper matrix are considered to represent the amount of ferric iron dissolved into fper before quenching. These values are much larger than those obtained from the MS signal of fper, but smaller, especially in the case of sample RPP11, than the re-calculated values determined taking into account the Fe^{3+} magnetic signal of the n-spft phase (see following section).

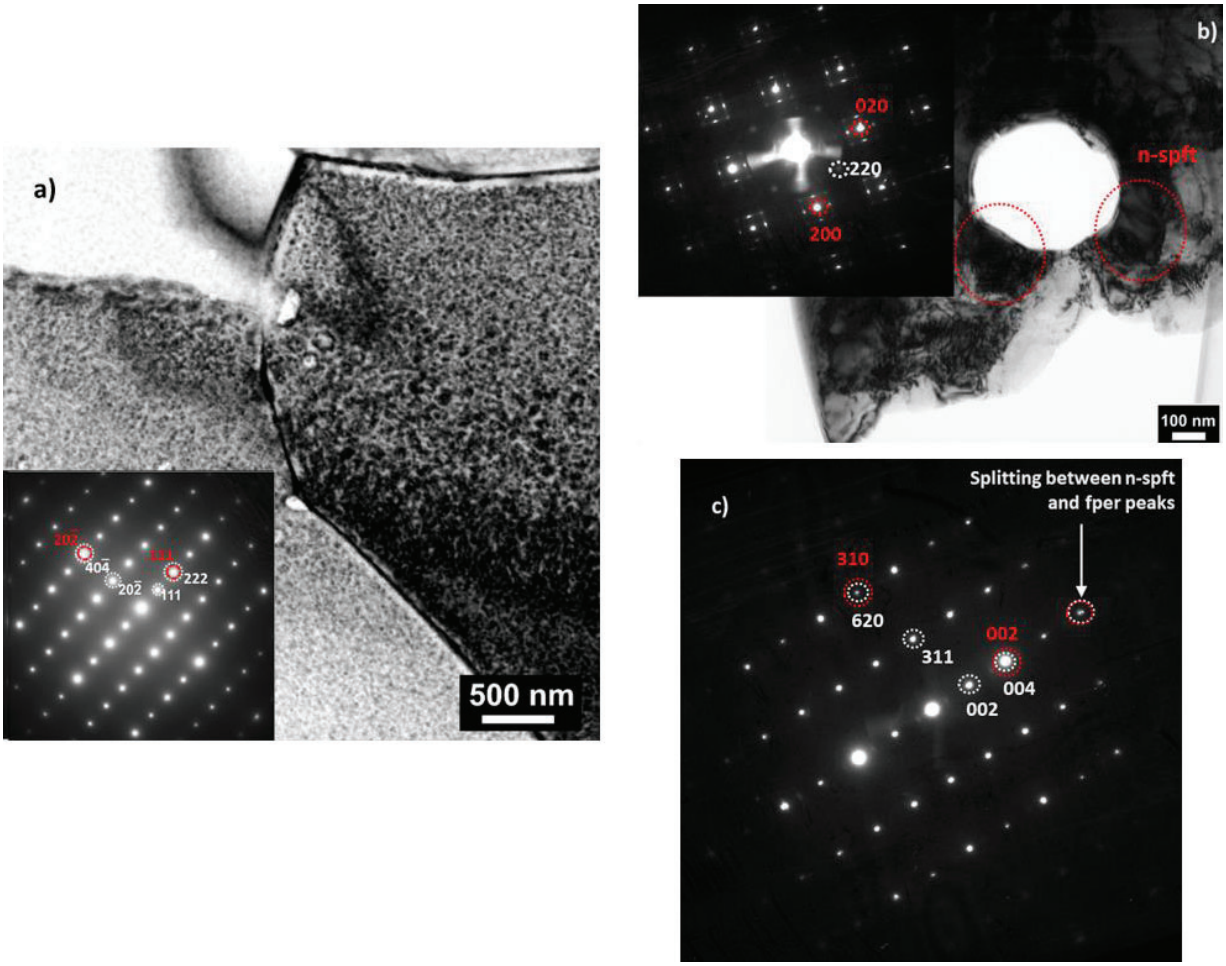

Figure 4.3: High-resolution STEM bright field images of **a)** sample RPP6 and **b)** sample RPP10 with corresponding selected area electron diffraction patterns**. c)** Electron diffraction pattern taken from the region indicated with n-spft in **b)** Sample RPP6 shows the presence of ~20 nm sized exsolutions distributed throughout all fper grains. The corresponding electron diffraction pattern consists of both reciprocal lattices of fper (in red) and of the exsolution (in white) which can be indexed using the spinel structure. The exsolution are topotaxial with fper and the unit-cell axis of n-spft appears to be the double of that of fper. Sample RPP10 shows large exsolutions (on the order of 100 nm in size), whose diffraction patterns also can be indexed with the spinel structure (white) in **c)** Note, however that splitting between the n-spft (white) and the fper (red) reflections can be seen for the *008* reflection. RPP10 fper areas where no large exsolutions are present show satellite reflections around the *hk0* reflections of fper, indicating the presence of defect clusters.

4.3.3 Fitting of the Mössbauer spectra

A selection of room temperature Mössbauer spectra (MS) is shown in Figure 4.4, whereas the MS of all other samples are reported in Figure A.4.2.

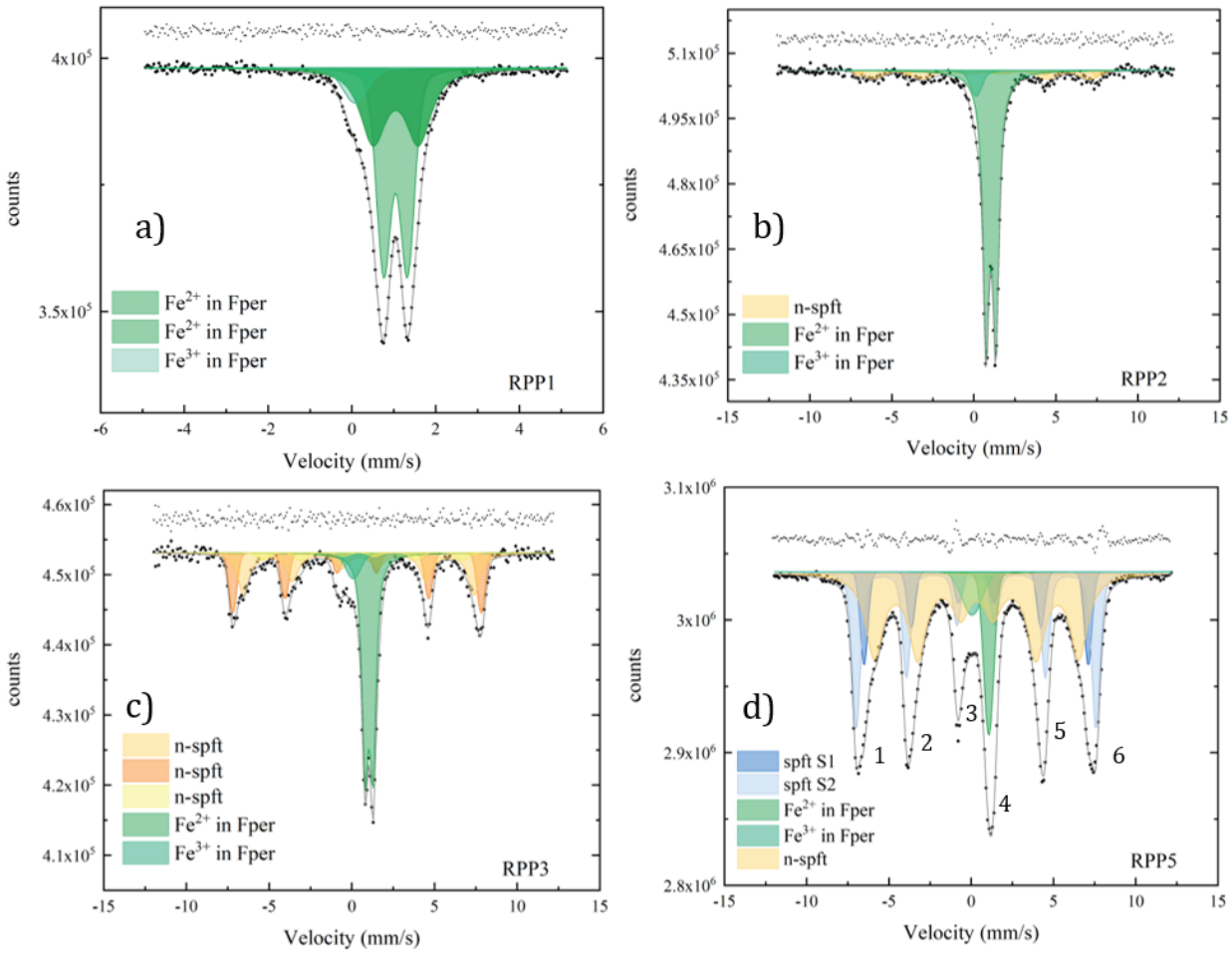

Figure 4.4: Representative room-temperature Mössbauer spectra **a)** for sample RPP1 only the fper signal is observable. The two doublets (dark green) correspond to Fe^{2+} in fper, whereas the singlet (light green) is Fe^{3+}; **b)** in sample RPP2 a magnetic component (yellow) that belongs to the exsolved n-spft is present together with fper; **c)** in sample RPP3 the n-spft exsolution has a much stronger magnetic component which has been fitted with three sextets; **d)** sample RPP5 presents a more complex spectrum, where the magnetic contribution belong to both the spft phase coexisting with fper (with S1 and S2 contribution, dark and light blue, respectively, see text) and the n-spft (yellow).

Only for sample RPP1, obtained from the $(Mg_{0.80}Fe_{0.20})O$ bulk composition equilibrated at the lowest fO_2 (Table 4.2), is it possible to fit the Mössbauer spectrum simply with a fper signal consisting of two quadrupole doublets for the Fe^{2+} and a singlet for the Fe^{3+} (Table A.4.2). The

center shift (CS) of Fe^{3+} indicates that it occupies the interstitial tetrahedral site of the fper structure (McCammon et al. 1998; McCammon 1995). Note that two doublets for ferrous iron have been used to obtain a statistically better fit, and to represent slightly different Fe^{2+} configurations, as in previous studies (McCammon et al. 1998; O'Neill et al. 2003; Longo et al. 2011; Bataleva et al. 2019; Kiseeva et al. 2022). The MS of all other samples contain a sextet absorption from a magnetic phase together with the fper signal. This sextet can be very weak and broad, as in the case of the Mössbauer spectrum from sample RPP2 equilibrated at a nominal Δ FMQ = 0 but increases significantly for samples equilibrated at higher oxygen fugacity (Figures 4.4 and A.4.2), although a macroscopic spft phase only coexisted with fper in samples RPP5, RPP6, and RPP11 (Table 4.2).

TEM data have indicated that fper grains from both compositions contain nano-scale exsolutions of n-spft, therefore, the magnetic component observed in the MS spectra in samples synthesized at oxygen fugacities below the spft field can likely be attributed to such exsolution. Nanocrystalline magnetite has been extensively studied due to the possibility of tuning its magnetic properties by reducing the grain size (Goya et al. 2003; Kalska-Szostko et al. 2006; Lak et al. 2013; Witte et al. 2016; Fock et al. 2018). Mössbauer measurements on magnetite with particle sizes less than 150 nm start to change in appearance, due to the increase of the surface to volume ratio (Hartridge et al. 1997; Goya et al. 2003; Castellanos-Rubio et al. 2019). The magnetic hyperfine fields of magnetite characterized by two sextets, S1 corresponding to Fe^{3+} at the tetrahedral site, with a magnetic hyperfine field (BHF) of ~ 48 T, and S2 corresponding to octahedral $Fe^{2.5+}$ at ~ 46 T, start to merge into a single sextet, which becomes broader, asymmetric and shifted to smaller values of BHF (Goya et al. 2003; Castellanos-Rubio et al. 2019). Castellanos-Rubio et al. (2019), for example, examined nanocrystalline wüstite samples that contained a coherently embedded exsolution of what they termed a magnetite-like phase. The corresponding Mössbauer spectrum contained a broad relaxed sextet with a relatively small

magnetic hyperfine field of ~35 T, a feature observed in several similar studies (Kalska-Szostko et al. 2006; Lak et al. 2013; Castellanos-Rubio et al. 2019). The same relaxed feature has also been observed for Mg-rich ferropericlase samples, presumably arising from nanocrystalline exsolution of magnesioferrite (Bhide and Tambe 1969). The sextets observed in the MS of our samples are consistent with such nano-magnetite signals. Magnetite samples with grain sizes < 10 nm undergo a collapse from the magnetic ordering to a superparamagnetic state at room temperature, with consequent contraction of the Mössbauer sextet into a central doublet (Hartridge et al. 1997; Goya et al. 2003; Morup et al. 1976; Fock et al. 2018; Hah et al. 2021), but the exsolutions observed in this study are larger than this (Figure 4.3) and therefore maintain their magnetic signature.

To reconstruct the composition of fper that existed during high temperature equilibration, the Fe^{2+} and Fe^{3+} components of the n-spft phase need to be added back to those that remained within the quenched fper structure. To this end, the magnetic sextet of samples RPP2, RPP3, RPP4 and RPP9 from the $(Mg_{0.80}Fe_{0.20})O$ bulk composition as well as that of RPP10 and RPP12 formed from the $(Mg_{0.15}Fe_{0.85})O$ bulk composition was empirically fit using up to three sextets depending on the intensity and the resolution of the signal. The intensity ratios of the magnetic components are defined by the parameter a12 and a13. The parameter a12 is the intensity ratio between the outer two lines (1 and 6) and the middle two lines (2 and 5), while a13 is the intensity ratio between the outer two lines and the inner two lines (3 and 4) (Figure 4.4d). The ideal values for these two ratios are 1.5 and 3, respectively. During the fitting of samples RPP2, RPP3, RPP4, RPP9, RPP10 and RPP12 these parameters were left free to vary resulting in a relatively small variation with respect to the ideal values (± 0.24 for a12 and ± 0.57 for a13). The hyperfine parameters for these components show hyperfine magnetic field values that vary between 37 T and 48 T. The resulting hyperfine parameters for n-spft are consistent with the fits reported in the literature for nano particles of ferrite spinels (Kalska-Szostko et al. 2006; Lak et al. 2013; Castellanos-Rubio et al. 2019).

For samples RPP5, RPP6 and RPP11, the MS are complicated by the fact that they contain both a macroscopic spinel phase (spft) coexisting with fper containing n-spft exsolution. It is in principle still possible to differentiate between the spft and n-spft components in the MS based on their different BHF values. The MS fitting, therefore, was first performed using the NORMOS program in order to ensure the appropriate fit of the magnetic signal of the spft and n-spft phases. Once the BHF parameters were defined, further fitting of the MS spectra was performed with the MossA 1.01f software package (Prescher et al. 2012) with the magnetic hyperfine field fixed to the values obtained with NORMOS. Note that the obtained BHF values of ~49 T and ~46 T for S1 and S2, respectively are indeed consistent with macroscopic spft (Evans and Hafner 1969; Castellanos-Rubio et al. 2019). Due to the large correlation between the different components, several constraints were applied during the fitting of the MS for these three samples. The position of the ferric iron singlet in fper was fixed to the CS position for tetrahedral ferric iron taken from the literature (McCammon et al. 1998; Otsuka et al. 2010), since no evidence for octahedral Fe^{3+} was found in the other samples, for which the CS position could be refined. For the spft sextet components, the intensity ratios of a12 and a13 were fixed to the ideal values (e.g. 1.5 and 3) to enable consistent results for all spectra and to avoid unrealistic values due to instabilities in the minimization process due to the large correlations between fitting parameters. An additional sextet was added for the n-spft exsolution with all parameters free to vary to account for the slow collapsing of the magnetic ordering, which needs to be accommodated by a change in the intensities of the different lines. The hyperfine magnetic field for this sextet for the MS of these three samples varies between 28 T and 36 T (Table A.4.2).

To account for the contribution of the n-spft component to the composition of fper that existed during high temperature equilibration, the valence state of the fitted sextets needs to be considered. Centre shift values of ~ 0.3-0.5(mm/s) define a Fe^{3+} valence state, whereas, values of ~ 0.6-0.7 (mm/s) indicate an $Fe^{2.5+}$ valence state. The samples from the $(Mg_{0.80}Fe_{0.20})O$ bulk composition

showed n-spft sextets with CS indicating only Fe^{3+} component (Table A.4.2), which is consistent with the expectation that the exsolving n-spft is likely to be almost end member magnesioferrite with negligible Fe^{2+} (Table A.4.1). In these cases, the Fe^{3+} intensity of the n-spft component was simply summed to that of the ferric iron component of fper. For the samples from the $(Mg_{0.15}Fe_{0.85})O$ bulk compositions, centre shifts indicating the presence of $Fe^{2.5+}$ are observed (Table A.4.2), therefore only half of the intensity for these sextets was considered for the calculation of the Fe^{3+} of the original fper at high temperature. The Fe^{3+}/Fe_{tot} of fper considering only the intensity of the Fe^{3+} singlet in fper, and with the back-calculated contribution of the n-spft are reported in Table 4.4. Although the re-calculation procedure gives rise to large uncertainties, it is clear that these values are more in agreement with those obtained from the EELS analyses (Table 4.4) and likely represent better the Fe^{3+} content of fper at high temperature.

4.3.4 X-ray powder diffraction

In agreement with the Mössbauer measurements and the TEM observations, the powder diffraction pattern of sample RPP1 consists of reflections belonging only to fper and Pt/Fe alloy, whereas the diffraction patterns of all other samples contain extra peaks which can be assigned to a spinel phase. For samples synthetized from the $(Mg_{0.80}Fe_{0.20})O$ bulk composition, most of the reflections of the spinel phase, no matter whether n-spft or coexisting spft phase, coincide with the fper reflections (Figure 4.5). This means that $a_{fper} \cong \frac{1}{2} a_{n-spft}$ in agreement with the TEM electron diffraction patterns (Figure 4.3a).

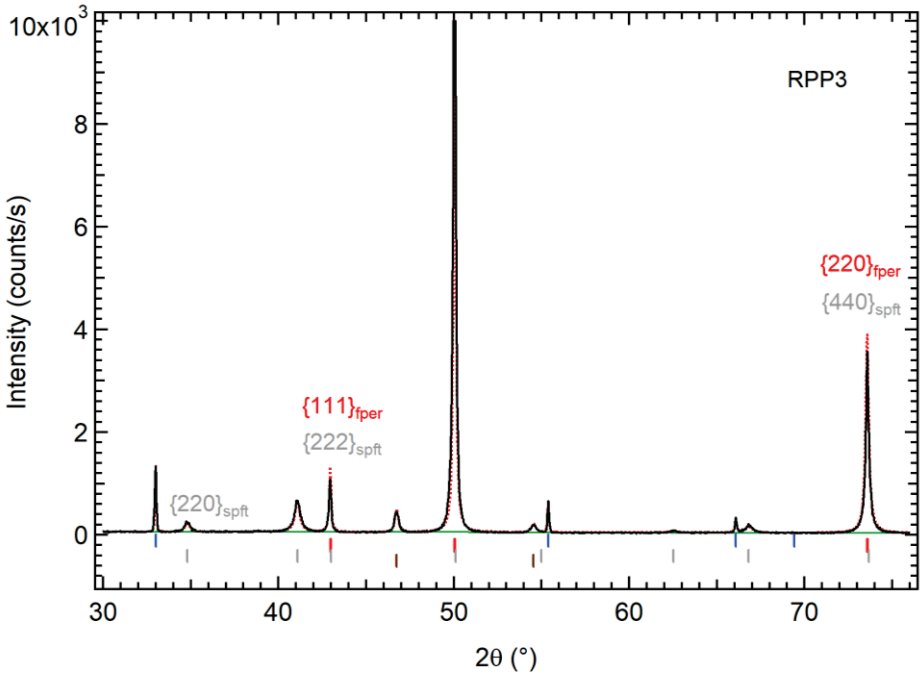

Figure 4.5: X-ray powder diffraction pattern collected at room temperature for sample RPP3. All reflections of fper are superimposed on those of n-spft, suggesting that the two unit-cell axes are one the half of the other. Si standard (blue ticks); fper (red ticks); n-spft (grey ticks); and Pt-Fe alloy (brown ticks).

The {220} and {311} reflections of the spinel phase have been used to qualitatively evaluate the grain size of the n-spft exsolutions inside the fper crystals. These reflections are not superimposed on the fper reflections and, being among the most intense, can be observed also for those samples (RPP2 and RPP4) which have been equilibrated at relatively low fO_2 (Table 4.2) and thus contain a smaller amount of n-spft exsolution (Figure 4.6a). With increasing fO_2 these two reflections become stronger and sharper as it is clearly visible in Figure 4.6b, where the diffraction patterns for samples obtained from the $(Mg_{0.80}Fe_{0.20})O$ bulk composition have been enlarged around the 2θ region of the {311} reflection.

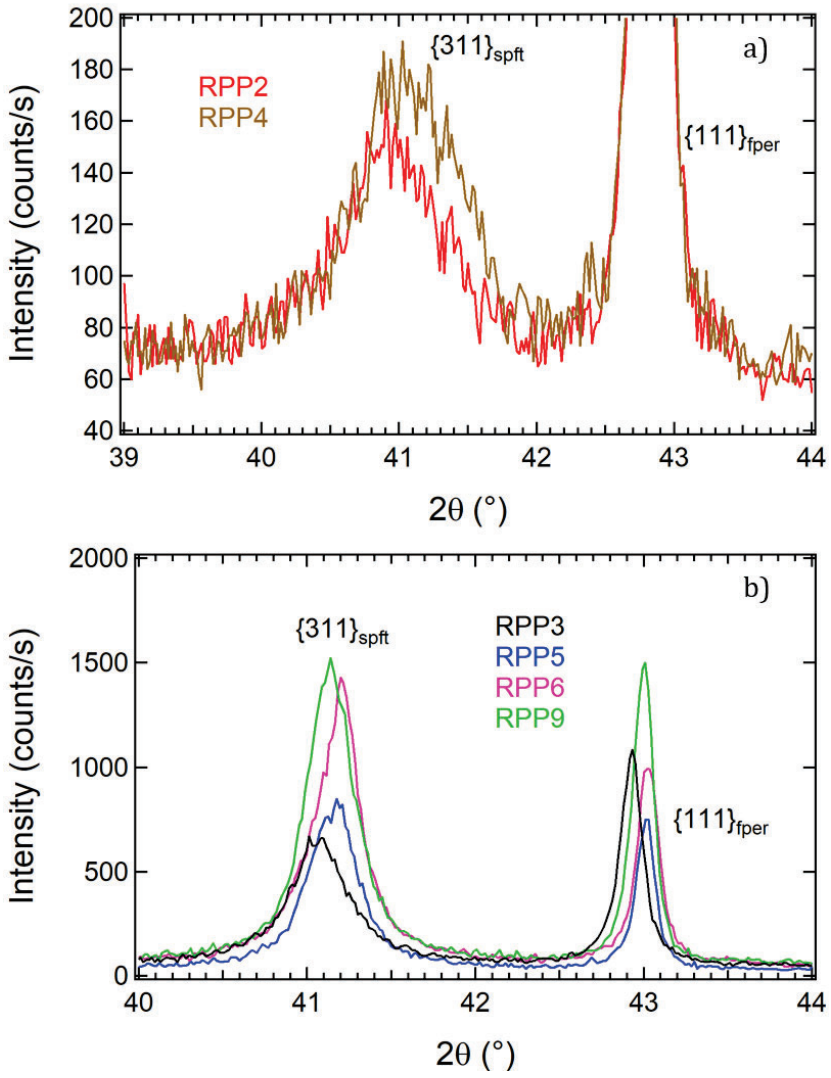

Figure 4.6: Details of the X-ray powder diffraction patterns collected for the samples synthetized from the $(Mg_{0.80}Fe_{0.20})O$ bulk composition in the 2θ region of the {311} reflection of the spinel phase. **a)** samples RPP2 and RPP4 synthetised at the lowest oxygen fugacities. The {311} reflection is very weak and broad but already visible. **b)** samples RPP3, RPP5 and RPP6 synthetised at higher oxygen fugacities and sample RPP9 synthetised at higher temperature. The {311} reflections becomes more intense likely due to the increasing amount of n-spft exsolutions.

The {220} and {311} reflections of samples RPP2, RPP3 and RPP9 were fitted using a Gaussian profile in order to obtain the full width at half maximum (FWHM) of the two powder diffraction peaks. The FWHM values, expressed in radians, calculated at the two different 2θ angles have been used to obtain an average grain size of the n-spft exsolution by means of the Scherrer equation (Scherrer 1912):

$$FWHM(2\theta) = \frac{0.94\lambda}{Lcos\theta} \quad (1)$$

where λ is the X-ray radiation wavelength and L is the average particle size. The instrumental broadening has been assumed to be negligible, given the broad features of the two reflections and the high-resolution of the diffractometer used, which can be assessed from the sharp Si standard peaks having a FWHM (33.15°) = 0.004 rad (Figure 4.5). Moreover, the positions of the Gaussian profiles have been used to determine the unit-cell axis of the n-spft phase (Table 4.3). For samples RPP5 and RPP6 the {220} and {311} reflections are a convolution of both spft and n-spft diffraction peaks giving rise to an asymmetric signal (Figure 4.6b). For these samples, therefore, two Gaussian profiles have been used to fit each of the two peaks. As expected the FWHM of one of the two Gaussians is quite sharp (~ 0.06 – 0.07 rad) and it has been assigned to the macroscopic spft phase coexisting with fper, whereas the second Gaussian profile is very broad and thus may be assigned to the contribution of the n-spft exsolution. The calculated grain sizes vary from 10-12 nm for samples RPP2 and RPP4 up to 30-32 nm for sample RPP9. The average grain size of the n-spft exsolution in sample RPP6 is ~ 20 – 22 nm, in excellent agreement with the results obtained from the high-resolution STEM images (Figure 4.3a). For this composition, the order of increasing grain size (Figure 4.7) follows broadly the trend of increasing fO_2 and of increasing proportion of n-spft exsolution according to magnetic signal in the MS (Figure 4.4).

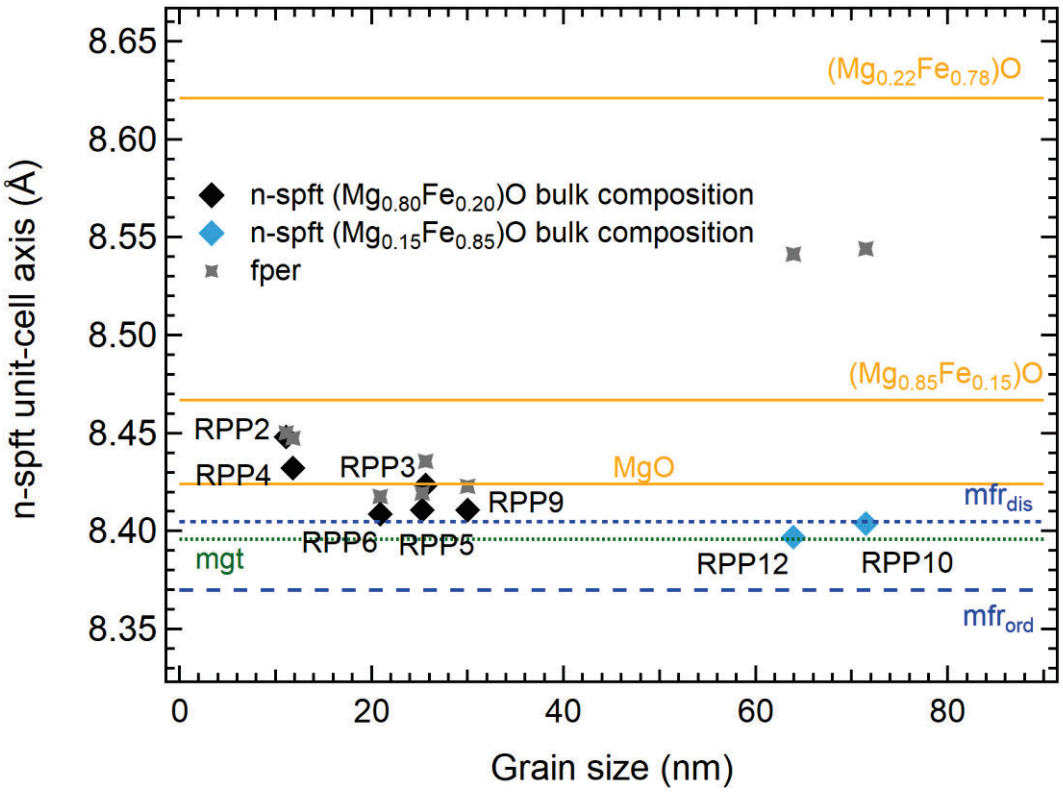

Figure 4.7: Relation between the unit-cell axis of the n-spft exsolutions present in the fper crystals synthetized in this study and their grain sizes. For samples derived from the $(Mg_{0.80}Fe_{0.20})O$ bulk composition, the n-spft unit-cell axis is closely correlated to the fper lattice and it is larger than expected for magnetite-magnesioferrite spinels. On the other hand, for samples derived from the $(Mg_{0.15}Fe_{0.85})O$ bulk composition, the difference between n-spft unit-cell axis and the fper lattice is much larger.

The Gaussian positions used to fit the spinel {220} abd {311} X-ray diffraction peaks have been used to calculate the unit-cell axes of both the spft and n-spft phases (Table 4.3). For samples RPP3 and RPP9, the a-axis values obtained from the Gaussian fit are identical within uncertainties to that obtained from the GSAS refinements (Table 4.3). For samples RPP5 and RPP6, however, it is clear that the GSAS refinement values are an average between the contribution from the spft phase coexisting with fper and the n-spft exsolution (Table 4.3). The spft phase coexisting with fper in samples RPP5 and RPP6 is magnesioferrite containing a negligible amount of Fe^{2+} (less than 0.02 apfu) (Table A.4.1). The lattice parameters obtained from the Gaussian fits (Table 4.3)

suggest that such spft have a high-degree of disorder, according to the relationship between unit-cell axis and inversion parameter reported by O'Neill et al. (1992). The n-spft lattice parameters on the other hand are all larger than expected for magnesioferrite and magnetite (Figure 4.7) and appear closely correlated to the fper unit-cell axes (reported as doubled values in Figure 4.7), which in turn are smaller than expected given their chemical compositions (Table A.4.1). This behaviour may be the result of a combination of different reasons: i) the large a-axis values of n-spft may be due to the nanoparticle nature of these exsolutions (Kurian et al. 2018); ii) the small a-axis values of fper may be due to changes in the actual Mg/(Mg+Fe) ratio driven by the exsolved n-spft phase. Such chemical changes cannot be characterized by means of EPMA since the analysis is giving a bulk composition, i.e. fper + n-spft; iii) the small a-axis values of fper may be due to the presence of Fe^{3+} which is the major iron component in these samples (Table 4.4); iv) the oxygen sublattices of n-spft and fper are coherent across the grain boundaries to reduce lattice strains. Note however, that changes in Mg/(Mg+Fe) ratio alone, for example, cannot explain the very small unit-cell parameter of fper for samples RPP5 and RPP6 without taking into account both the Fe^{3+} and the lattice relaxation effects since the *a*-axis of fper is even smaller than pure MgO in these samples, in spite of the presence of Fe^{2+} and Fe^{3+} documented by the Mössbauer spectra (Figure 4.4d and Figure A.4.2b).

The diffraction pattern collected for samples synthesized from the $(Mg_{0.15}Fe_{0.85})O$ bulk composition show a clear separation between the fper and spft reflections (Figure 4.8) likely because the fper unit-cell is in this case more different than the half of the spft spinel unit-cell axis. Moreover, contrary to what was observed for samples synthetized from the $(Mg_{0.80}Fe_{0.20})O$ bulk composition, the spft reflections are much more intense and sharper (Figure 4.9). The {220} and {311} reflections of samples RPP10 and RPP12 have been fitted using a Gaussian profile, however, given that the breadth of these peaks is not much larger than that of the Si standard, the instrumental broadening has been taken into account.

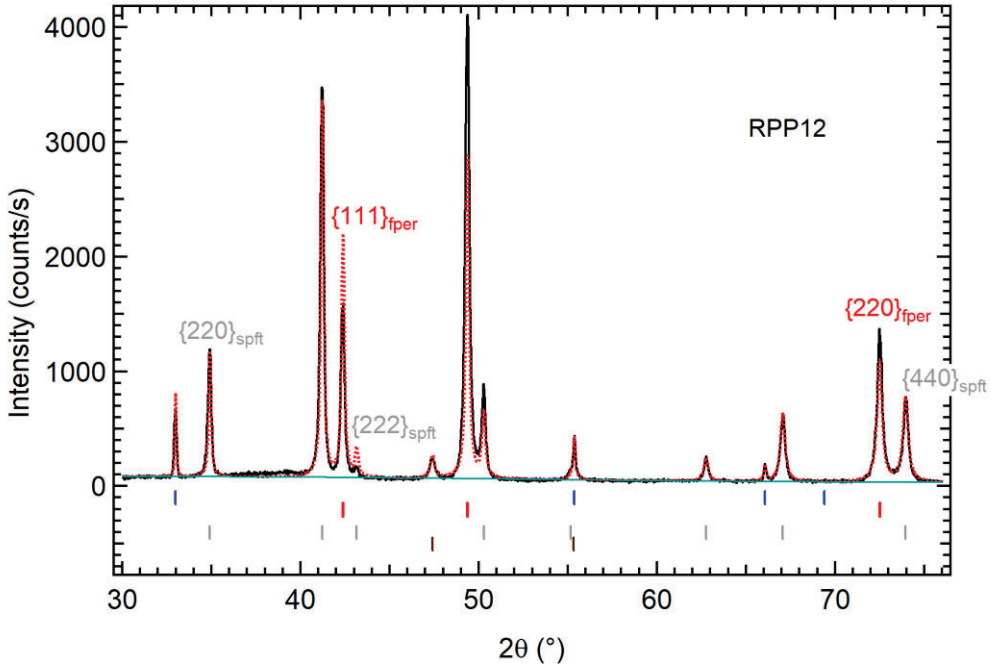

Figure 4.8: X-ray powder diffraction pattern collected at room temperature for sample RPP12. The reflections of fper and of n-spft are clearly well separated

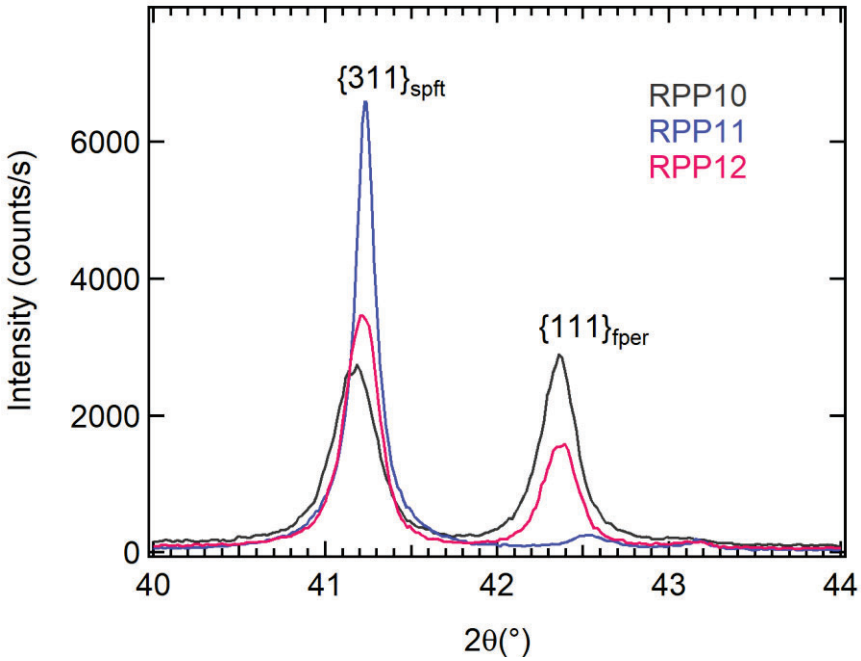

Figure 4.9: Details of the X-ray powder diffraction patterns collected for the samples synthetized from the $(Mg_{0.15}Fe_{0.85})O$ bulk composition in the 2θ region of the {311} reflection of the spinel phase. The {311} reflections is very intense and sharp even for those samples (RPP10 and RPP12) for which only the n-spft is present. The diffraction pattern of RPP11 is dominated by the spft phase coexisting with fper whose peaks are weak in comparison.

The $FWHM_{n\text{-}spft}$ has been therefore calculated according to (Warren 1990):

$$FWHM^2_{n-spft} = FWHM^2_{meas} - FWHM^2_{Si} \quad (2)$$

where $FWHM^2_{meas}$ is the breadth of the Gaussian profiles fitting the {220} and {311} reflections and $FWHM^2_{Si}$ is the breadth of the Gaussian profile fitting the {111} reflection of the Si standard. This approach is not exactly correct, since the shape of the diffraction profiles are not simply Gaussian, however, it gives the lowest estimate for the grain sizes of these exsolutions. The diffraction pattern of sample RPP11 is dominated by the spft phase coexisting with fper as is visible in Figure 4.9 where the {111} reflection of fper is hardly visible. For this reason, it was not possible to determine the grain size of the n-spft in this sample. The resulting grain sizes of the n-spft exsolution in samples RPP10 and RPP12 are much larger than those obtained for samples synthesized from the $(Mg_{0.80}Fe_{0.20})O$ bulk composition (Figure 4.7), in agreement with the STEM images (Figure 4.3b). Moreover, as already discussed, the fper lattice is not closely related to the n-spft lattice, with $a_{fper} > \frac{1}{2} a_{n-spft}$ (Figure 4.7), although such difference is barely visible in the electron diffraction pattern (Figure 4.3c)

In order to constrain the effect of Fe^{3+} substitution on the molar volume of fper, the unit cell parameters of the samples investigated in this work are compared with those reported from a number of previous studies (Dobson et al. 1998; Hamada et al. 2021; Jackson et al. 1978; Jacobsen et al. 2002; Matsui et al. 2012; McCammon et al. 1998; O'Neill et al. 2003) in Figure 4.10. Most of the available data are for the wüstite end-member which have been summarized and fitted by McCammon and Liu (1984) and are not shown in Figure 4.10 for clarity. The molar volumes of the FeO and $Fe_{2/3}O$ end members have been obtained from the relationship between the unit-cell axis and the composition Fe_xO of the wüstite samples reported by McCammon and Liu (1984) and are 12.256 and 10.953 cm^3/mol, respectively. O'Neill et al. (2003) provided lattice parameters and Mössbauer data for fper samples that were produced in equilibrium with iron metal and, therefore,

have the lowest possible equilibrium room pressure Fe^{3+}/Fe_{tot}. The best fit to these data using the FeO end-member molar volume reported above and an MgO end member molar volume of 11.250 cm^3/mol (Jacobsen et al. 2002; Matsui et al. 2012) requires a small excess volume term, $V^{ex} = X_{MgO}X_{FeO}\left[0.301 * X_{FeO} + 0.146 * X_{MgO}\right]$ cm^3/mol. To fit the all fper data reported in Figure 4.10 with these three end-members, the only remaining parameters that could be refined are excess volume terms involving $Fe_{2/3}O$. However, these excess terms provide very little improvement in the least square fits of all data and have been therefore ignored at this stage.

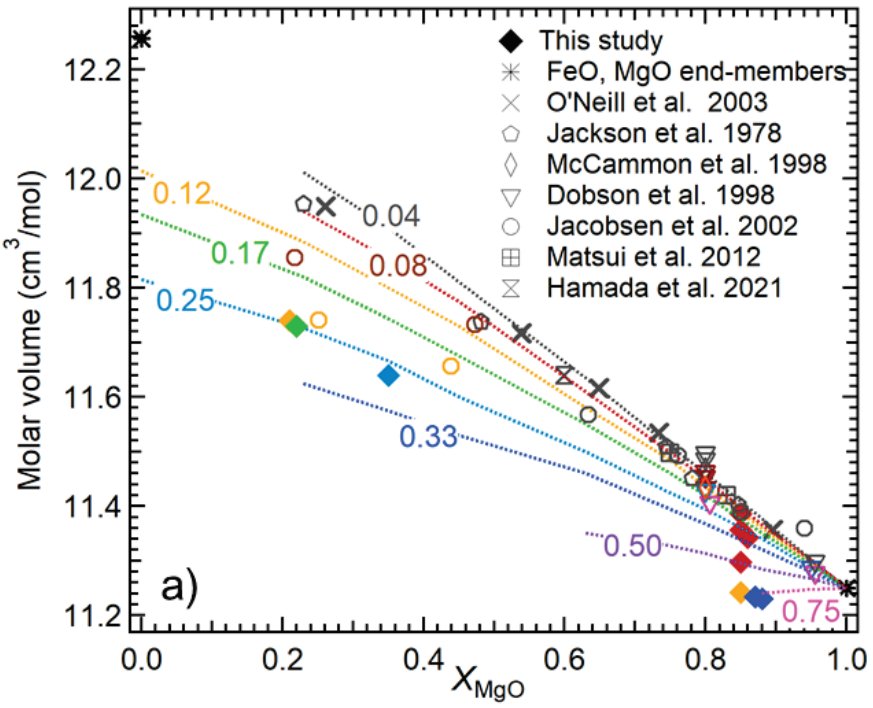

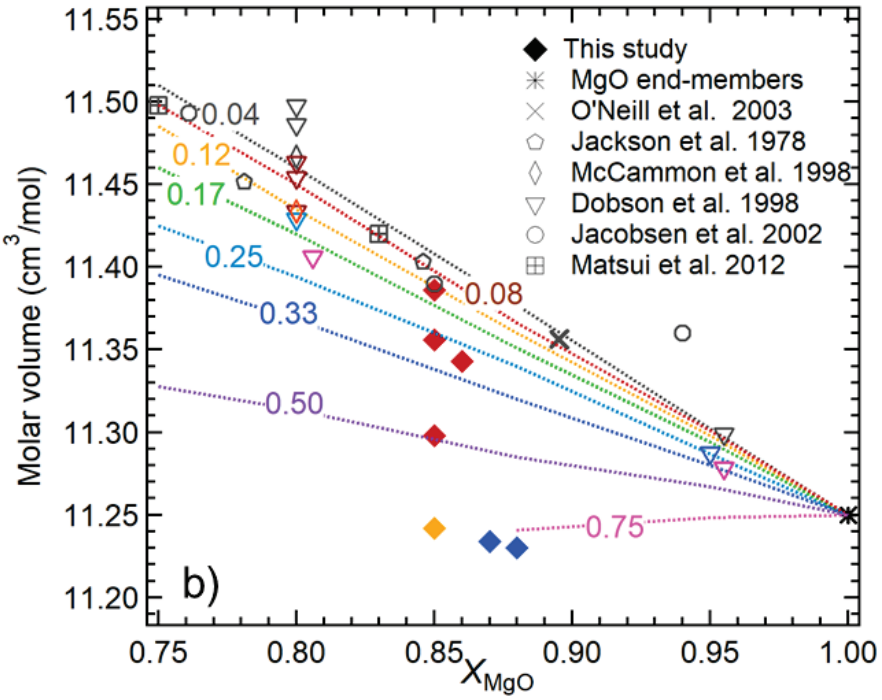

Figure 4.10: **a)** Molar volume of fper as a function of its MgO content, X_{MgO}, with coloured contours indicating the Fe^{3+}/Fe_{tot} ratios, reported for each curve. The samples investigated in this study and those reported in the literature have reported Fe^{3+}/Fe_{tot} ratios similar to those indicated by the contour colours. The colours of the data from this study correspond to the MS fper measurements and do not include the n-spft component. **b)** An enlargement of the Mg-rich samples region.

Plots of the resulting model, i.e. from a linear combination of the FeO and $Fe_{2/3}O$ volumes, fitted just from the wüstite data, an MgO end-member and a V^{ex} term for MgO-FeO mixing, are shown as dashed curves for different Fe^{3+}/Fe_{tot} contents in Figure 4.10. This is not to imply that this model is correct but it is used here only as a reference frame to discuss the existing data. The majority of the room pressure fper data plot below the model curves for the corresponding Fe^{3+}/Fe_{tot} ratio, with the divergence generally increasing with Fe^{3+}/Fe_{tot} ratio. For the majority of these fper data obtained at room pressure the fper Fe^{3+}/Fe_{tot} ratio has been determined using Mössbauer spectroscopy and many of the studies even report the appearance of spft exsolution in the spectra and SEM images (Reichmann et al. 2000; Jacobsen et al. 2002), similar to the samples in this study. The strong deviation from the model curves, that is particularly apparent in the data

collected in the present work at X_{MgO} = 0.85 (Figure 4.10b), results from the fact that the electron microprobe analyses used to determine X_{MgO} are also measuring a contribution from near end-member magnesioferrite n-spft exsolution, but the Fe^{3+}/Fe_{tot} ratio plotted is for fper only, as this should be the amount influencing the X-ray diffraction patterns of the recovered fper crystals. This exsolution causes the iron-content of the sample to appear higher in the EPMA analyses, whereas in reality, upon exsolution of n-spft, the fper itself shifts in composition towards higher MgO contents. As a result, the samples from this study with the highest fper Fe^{3+}/Fe_{tot} ratio have molar volumes that are very close to pure MgO. The fact that the Mössbauer spectra of these samples show that there is still some Fe^{2+} in the fper structure, however, suggests that coherent n-spft exsolution also causes some contraction in the fper unit cell in order to reduce lattice strains.

The high Fe^{3+}/Fe_{tot} ratio for samples synthesized by Dobson et al. (1998) at 5 GPa plot consistently higher than the model curves (Figure 4.10b). The Mössbauer spectra of these samples show no evidence for n-spft exsolution and indicate that the Fe^{3+} of fper is in tetrahedral coordination, as observed in this study. The model proposed by Dobson et al. (1998), which cannot be extrapolated below the proposed lower limit in X_{MgO} of 0.8, indicates a strongly non-linear dependence of the unit cell volume on the Fe^{3+}/Fe_{tot} ratio, implying significant excess volume terms. To fit these high-pressure data to our three end-member model requires large positive asymmetric excess volume terms for MgO-$Fe_{2/3}O$. Once it is recognized that the majority of the other fper samples synthesized at room pressure are likely affected by n-spft exsolution, this may be the most reasonable model which would be consistent with the fact that quite large MgO-$Fe_{2/3}O$ excess Gibbs free energy terms are required to fit the room pressure phase relations, as discussed in the next section. Based on these results, however, it appears that X-ray diffraction alone is not sufficient to accurately characterize the Fe^{3+}/Fe_{tot} ratio content in fper.

4.3.5 Experimental fO_2 determination and thermodynamic modelling of the fper stability field

To achieve the objective of determining the compositions of coexisting fper and spft solid solutions, existing measurements in the Fe-Mg-O and Fe-O systems are combined with the new observations to obtain a consistent thermodynamic model.

The fO_2 is calculated, in the first place, by using a Pt-Fe-Ni alloy sliding redox sensor obtained by adding Pt powder to the pellets (Woodland and O'Neill 1997), through the equilibrium:

$$2Fe_{(alloy)} + O_2 \leftrightarrow 2\ FeO_{(fper)} \quad (3)$$

using the expression:

$$\log(fO_2) = \frac{\Delta G^0_{P,T\ (3)}}{\ln(10)\,RT} + 2\log\left(a_{FeO}^{fper}\right) - 2\log(a_{Fe}^{alloy}) \quad (4)$$

Where $\Delta G^0_{P,T(3)}$ is the standard state Gibbs free energy of equilibrium (3) and a_i^j is the activity of component i in phase j. As spft was present in certain experiments, fO_2 can also be determined using the equilibrium:

$$3Fe_{(alloy)} + 2O_2 \leftrightarrow Fe_3O_{4(spft)} \quad (5)$$

with an expression analogous to equation (4) and also from the equilibrium:

$$4FeO_{(fper)} + O_2 \leftrightarrow 4FeO_{1.5(fper)} \quad (6)$$

We refined terms to describe the activity composition relations of fper using the constraint that the oxygen fugacity determined using the three equations is the same for a given experiment. To do this we used standard state Gibbs free energies of formation from Holland and Powell (2011), including the Landau expressions for the spft phases, but for Fe-metal and the FeO and $FeO_{1.5}$ end members of fper the equations refined in the Fe-O model of Hidayat et al. (2015) were used instead. The activity of Fe in Fe-Pt alloys was calculated using the Margules interaction parameters determined by Kessel et al. (2001). These are combined with data from Lu et al. (1995) and Ono

et al. (1977) to obtain a Fe-Pt-Ni ternary asymmetric Margules model (Mukhopadhyay et al. 1993), so that a small correction for a minor amount of Ni in the alloy (Table A.4.1) can be considered.

A simple single site mixing model has been used for magnetite-magnesioferrite with asymmetric Margules terms. To make the data internally consistent we first used our fper solution model, described in the following, to fit the fper-olivine Fe-Mg partitioning data of Wiser and Wood (1991). In this way, a single symmetric Margules parameter for olivine, W_{Fe-Mg}^{ol}, of 2.6 kJ/mol, has been obtained. This value is identical to that obtained by O'Neill et al. (2003). We then used this value with the olivine-spft Fe-Mg partitioning data of Jamieson and Roeder (1984) to obtain the two interaction terms for spft given in Table A.4.3.

Mixing models for fper are potentially very complex as Fe^{3+} can substitute onto either octahedral or tetrahedral sublattices and vacancies may be locally ordered, as described previously. There is very little useful information for sublattice occupancies and defect clustering, however, on which to base a more realistic mixing model because most observations have been made on quenched samples for which changes in cation distribution have almost certainly occurred during quenching.

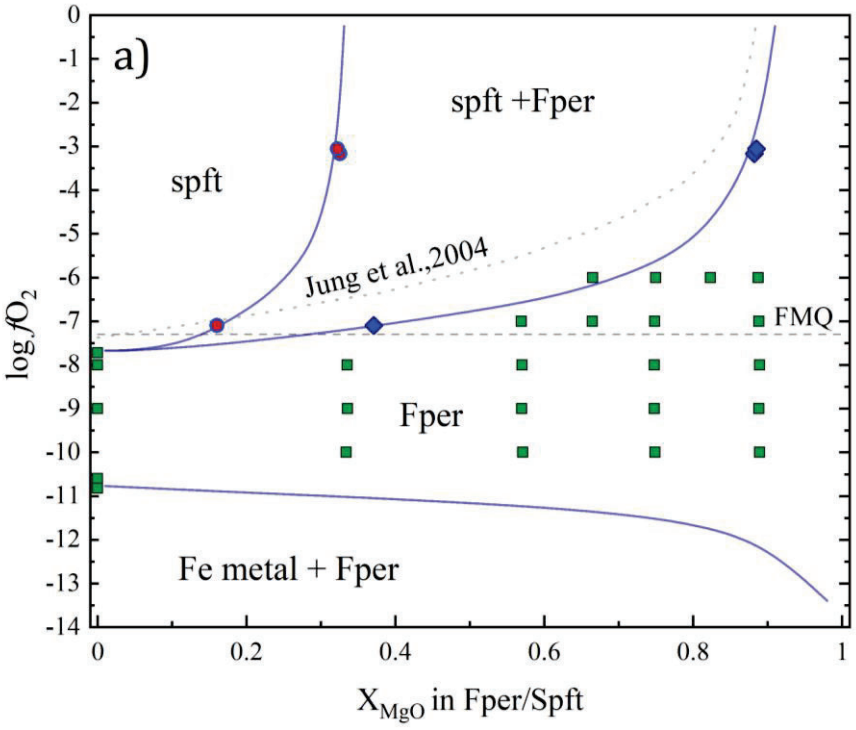

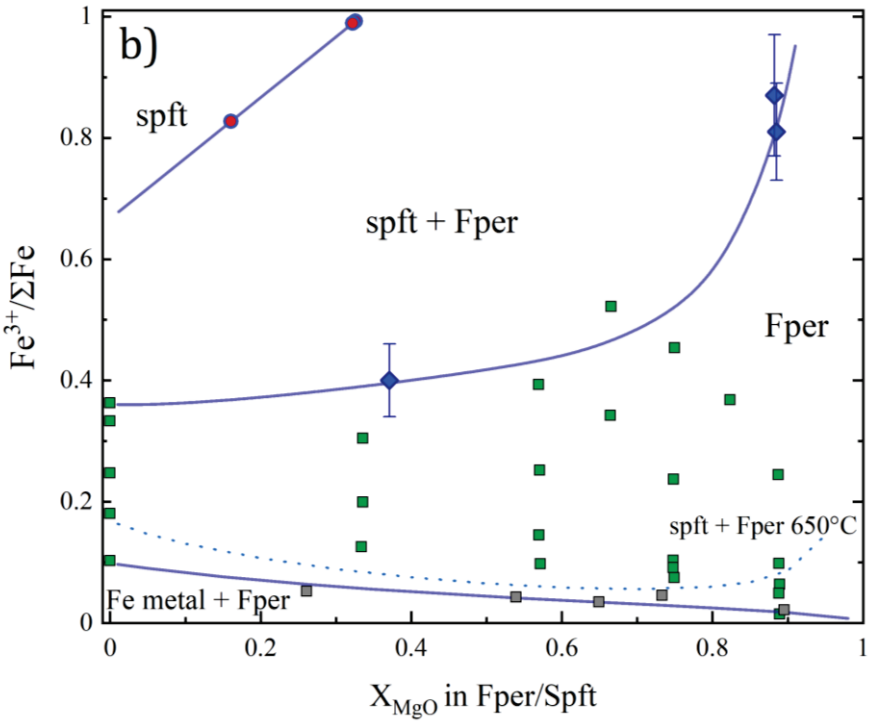

Figure 4.11: **a)** The fO_2 of spft, fper and Fe metal stability fields are plotted as a function of X_{MgO} in either fper or spft at 1300 °C. The experimental coexisting compositions of spft (red symbols) and fper (blue symbols) are indicated. The fper curve calculated from the thermodynamic model of Jung et al. (2004) is also shown as are experimental data for fper stability from Speidel (1967; green symbols). **b)** A similar diagram showing the Fe^{3+}/Fe_{tot} ratios for the same phase boundary curves as in a). Experimental data from O'Neill et al. (2003, grey squares) indicate the Fe^{3+}/Fe_{tot} ratio of fper in equilibrium with Fe-metal. The dotted curve shows the Fe^{3+}/Fe_{tot} ratio of fper in equilibrium with spft calculated at 650 °C.

The alternative is to assume single site mixing (at the octahedral site) and account for the complexity in the mixing relations using a subregular solution model for the excess Gibbs free energy of mixing ($\Delta_m G^{ex}$). Hidayat et al. (2015) assumed mixing of FeO and $FeO_{1.5}$ components, for example, and were able to reproduce the 1 bar variation in wüstite composition with fO_2 using such a subregular solution model. Jung et al. (2004) also used a similar subregular FeO-$FeO_{1.5}$-MgO model for fper but we found that the parameters involving MgO in this model are inconsistent with our measurements and with those of O'Neill et al. (2003). The subregular model uses the expression (Jung et al. 2004):

$$\Delta_m G^{ex} = X_{FeO}X_{FeO_{1.5}}q^{00}_{FeO,FeO_{1.5}} + X_{FeO}X_{FeO_{1.5}}(1 - X_{FeO_{1.5}})q^{10}_{FeO,FeO_{1.5}} + X_{FeO}X_{MgO}q^{00}_{FeO,MgO} + \left(X_{FeO_{1.5}}\right)^2 X_{MgO}q^{10}_{FeO_{1.5},MgO} + X_{MgO}X_{FeO_{1.5}}\left(1 - X_{FeO_{1.5}}\right)^2 q^{02}_{FeO_{1.5},MgO} \quad (7)$$

where the q terms describe the non-ideal interaction between the indicated components. The expression employs the Toop-type approximation, where $FeO_{1.5}$ is the asymmetric component (Toop 1965; Pelton 2001). The activity coefficients are then calculated as here for FeO:

$$RTln\gamma^{fper}_{FeO} = \Delta_m G^{ex} - x_{FeO_{1.5}}\left(\frac{\delta\Delta_m G^{ex}}{\delta x_{FeO_{1.5}}}\right)_{MgO} - x_{MgO}\left(\frac{\delta\Delta_m G^{ex}}{\delta x_{MgO}}\right)_{FeO_{1.5}} \quad (8)$$

The q terms for FeO-$FeO_{1.5}$ mixing were taken from Hidayat et al. (2015) and for FeO-MgO were obtained from a least squares fit of the measurements of O'Neill et al. (2003) on the fO_2 of fper in equilibrium with iron metal. For each of our experimental data points we then calculated the fO_2 using equations (3) and (5) and, when spft was present, equation (6). We then refined the remaining two MgO-$FeO_{1.5}$ q terms to obtain the same calculated fO_2 for each of our experimental data points (Table A.4.3). Further constraints on the Fe^{3+}/Fe_{tot} ratio of fper at iron-metal saturation were taken from the measurements of O'Neill et al. (2003). Coexisting values of $X^{fper}_{FeO_{1.5}}$ and $X^{spft}_{Fe_3O_4}$ were calculated by simultaneously refining the Gibbs free energy expressions for the equilibria:

$$MgFe_2O_{4(spft)} + FeO_{(fper)} \leftrightarrow Fe_3O_{4(spft)} + MgO_{(fper)} \quad (9)$$

and

$$FeO_{(fper)} + 2FeO_{1.5(fper)} \leftrightarrow Fe_3O_{4(spft)} \quad (10)$$

The resulting model, shown in Figure 4.11a, is similar to that of Jung et al. (2004) but deviates to lower fO_2, to agree with the experiments and is in better agreement with the metal saturated fper Fe^{3+}/Fe_{tot} ratios of O'Neill et al. (2003).

The data of Speidel (1967) predict a larger fper field in some instances, but the fper field is only interpreted in these data through variations in the gradient of fO_2 versus Fe^{3+}/Fe_{tot} ratio and may not be accurate. Although the uncertainties on the fper Fe^{3+}/Fe_{tot} ratios determined in our study are large, the model is well constrained along the fper-spft equilibrium curve by the three independent

fO_2 equilibria (3,5,6), as only very narrow ranges of fper Fe^{3+}/Fe_{tot} ratio and MgO-$FeO_{1.5}$ *q* terms can give consistent fO_2 values. The agreement within the fper field between the experimental fO_2 and fper Fe^{3+}/Fe_{tot} ratios, on the other hand, starts to deviate at higher X_{MgO} values as shown in Figures 4.12 and Figure A.4.3. The agreement with our data and that of Speidel (1967) would improve if the predicted Fe^{3+}/Fe_{tot} ratios were lower towards lower fO_2 (Figure 4.12). It is not possible to improve this fit, however, without compromising the fit along the fper-spft equilibrium curve or the agreement with the metal saturated Fe^{3+}/Fe_{tot} ratios (O'Neill et al. 2003), even by increasing the number of MgO-$FeO_{1.5}$ terms in the activity composition relation. Inconsistencies can be clearly seen in the Speidel (1967) data at these conditions, however, because some $Fe^{3+}/\Sigma Fe$ ratios are at or even below the level of Fe-metal saturation in Figure 4.11b, whereas the oxygen fugacities of these data, shown in Figure 4.11a, are ~2 log units above metal saturation. Similarly, when we compare our results with many previous studies that used thermogravimetric or wet-chemical methods to determine the Fe^{3+}/Fe_{tot} ratios (Brynestad and Flood 1958; Katsura and Kimura 1965; Speidel 1967; Valet et al. 1975; Hilbrandt and Martin 1998) inconsistencies arise between the data sets, as already discussed by Jung et al. (2004), particularly at high X_{MgO} values where the proportion of $FeO_{1.5}$ drops to ≤ 1 wt%. Therefore, given the current uncertainties we can consider our model satisfactory. Any further improvement most likely requires a more sophisticated treatment of the configurational entropy, that may involve the use of multiple components to describe ferric iron speciation in fper and the ordering of vacancies. This, however, would likely require in situ information on site occupancies and the state of vacancy ordering in fper.

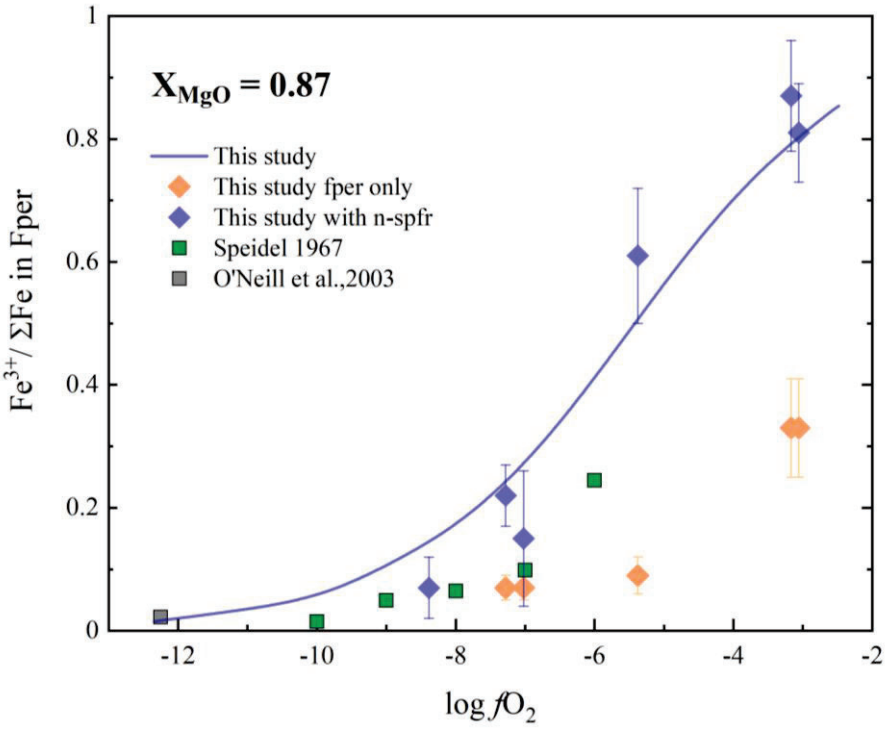

Figure 4.12: The fper Fe^{3+}/Fe_{tot} ratio versus the experimental oxygen fugacity plotted both for the Fe^{3+} measured only in the fper by MS (orange diamonds) and for the re-calculated values taking into account the contribution of the n-spft components (blue symbols). Data from previous experimental studies are also shown (Speidel 1967; O'Neill et al. 2003)

4.4 Discussion

Our results indicate that on quenching fper, at least from high-temperature experiments at room pressure, a coherent intergrowth of n-spft forms with grain sizes that increase with the fraction of n-spft exsolution and possibly also Fe-content, as has been observed previously in experimental (Longo et al. 2011) and natural samples (Wirth et al. 2014; Kaminsky et al. 2015). The range in grain sizes (Figure 4.7) is reflected in the Mössbauer spectra, which contain relaxed sextets with magnetic hyperfine fields that are shifted towards lower values. This relaxation with grain size has been observed in previous studies on n-spft (Gonser et al. 1968; Hartridge et al. 1997; Goya et al. 2003; Morup et al. 1976; Fock et al. 2018; Hah et al. 2021) with samples becoming superparamagnetic for grain sizes <10 nm. It is worth noting, however, that if there are

superparamagnetic domains in our samples they are not detectable in this instance with Mössbauer spectroscopy as they would overlap with the absorption from fper and presumably be included in the fper Fe^{3+}/Fe_{tot} ratio. The occurrence of n-spft exsolution makes measurements of the Fe^{3+}/Fe_{tot} ratios using Mössbauer spectroscopy more challenging as the iron-contents from fper must be combined with the contribution from the exsolution in order to obtain the original high temperature bulk Fe^{3+}/Fe_{tot} ratio (Longo et al. 2011; Nestola et al. 2016). The signal from the n-spft in the Mössbauer spectrum can be very subtle and could easily be missed particularly if spectra are only recorded over a velocity range from –5 to +5 mm/s, which is quite typical. In sample RPP2, for example, the n-spft component, which is hardly visible (Figure 4.4b), contributes more than half of the bulk ferric iron in the sample (Table 4.4). Having to recombine the Mössbauer signals in this way, however, raises the uncertainties on the Fe^{3+}/Fe_{tot} ratios significantly. One of the potential advantages of bulk, e.g. thermogravimetric analyses, is that the measurement of Fe is presumably not affected by such exsolution and if they could be demonstrated to be sufficiently precise, they may offer a better alternative to Mössbauer measurements, at least up to the fper-spft equilibrium curve. Mössbauer measurements at the fper-spft equilibrium curve have particularly large errors because the signals from the exsolved n-spft and the coexisting spinel phase cannot be resolve unequivocally, being based only on different line-widths of the sextet components. EELS measurements, using TEM, appear to be the only method with the spatial resolution to differentiate between the fper and spft coexisting phases, however a carefully fitting of the EELS patterns is necessary due to the complex contribution to the energy loss spectra of Fe^{2+} and Fe^{3+} occupying both tetrahedral and octahedral sites in the n-spft phase.

Electron diffraction images of fper grains containing n-spft exsolutions are significantly different depending on whether they were measured for the $(Mg_{0.15}Fe_{0.85})O$ or $(Mg_{0.80}Fe_{0.20})O$ bulk composition (Figure 4.3a and b). In the former case, the electron diffraction pattern, reported in the inset of Figure 4.3b, is very similar to those reported in the study performed on wüstite by

Andersson and Sletnes (1977), where satellite reflections around the *hk*0 fper reflections are present due to the existence of defect clusters with different degrees of periodicity (e.g. Welberry et al. 2014; Gavarri et al. 2018 and reference therein). Moreover, a clear peak attributed to the n-spft phase can be observed (Figure 4.3b inset) as it was in the wüstite patterns obtained by Andersson and Sletnes (1975), suggesting that growth of the 16:5 corner-sharing clusters (which is an element of the inverse spinel structure, Dimitrov et al. 1999; Hazen and Jaenloz 1984; Koch and Cohen 1969) to nm size produced the exsolution of the n-spft. Note that most of the fper grains of sample RPP10 analysed at the TEM show only exsolution of n-spft with no trace of satellite reflections (Figure 4.3c), suggesting that the defect clusters are a transient intermediate state toward the n-spft exsolutions. Fper inclusions from diamonds with $X_{MgO} = 0.345$ analysed by Wirth et al. (2014) contain spinel exsolutions with grain sizes in the 10-400 nm range and electron diffraction patterns consistent with a spinel structure exsolved from fper without the presence of satellite reflections. Also, as in the case of the samples obtained in this study (Figure 4.7), the spinel exsolutions have lattice spacings generally consistent with what would be expected for the magnetite-magnesioferrite solid solution.

For fper grains obtained from the $(Mg_{0.80}Fe_{0.20})O$ bulk composition, there is no trace of satellite reflections, and only well define n-spft peaks are present in the electron diffraction pattern (Figure 4.3a). Moreover, the n-spft and fper unit-cell axes follow the relationship $a_{fper} \cong \frac{1}{2} a_{n-spft}$ (Figure 4.3a, Figure 4.5, Figure 4.7), suggesting that growing of the defect clusters created by the presence of Fe^{3+} is even more favoured in this composition with respect to Fe-rich fper due to the similarity of the oxygen sublattices between host grain and exsolution. This similarity is likely driven by relaxation of local strains and results in fper having smaller and n-spft having larger unit-cell than expected for their compositions (Figure 4.7). Kaminsky et al. (2015) observed exsolutions in fper inclusions with $X_{MgO} = 0.773$, of what they termed Fe^{3+}-enriched clusters with

a reported composition of $Mg_{1.3}Fe_{1.8}O_4$, intermediate between fper and spft. Note, however, that they based their suggestion on Fe/(Fe+Mg) ratio estimated from EDX spectra collected from a cluster of ~ 10 nm size. The electron diffraction pattern, however, is consistent with a fper lattice superimposed with the lattice of a spft phase having the double unit-cell axis, as observed in our study.

As can be seen in Figure 4.11b, exsolution of n-spft occurs in fper having X_{MgO} = 0.87 when its Fe^{3+}/Fe_{tot} ratios are above 0.07. Using our model, we calculate that the fper-spft equilibrium curve is reached for this ratio at approximately 650 °C, shown by the dotted curve in Figure 4.11b. It seems plausible, therefore, that fast kinetics allow equilibrium exsolution of n-spft to occur down to this temperature. Previous studies also have reported the presence of exsolutions in fper samples having Fe^{3+}/Fe_{tot} ratio lower than 0.07 (Reichmann et al. 2000; Jacobsen et al. 2002; Longo et al. 2011). In the study of Jacobsen et al. (2002) some of the more Fe-rich samples have exsolved spft down to a fper Fe^{3+}/Fe_{tot} ratio of approximately 0.01 (Figure 4.10a), but these samples were cooled slowly inside the furnace over a period of several hours, which may have allowed exsolution to continue to grow even at lower temperatures. The predicted fper-spft equilibrium curve at 650 °C decreases steeply in Fe^{3+}/Fe_{tot} ratio for $1 < X_{MgO} < 0.80$ and then it increases again towards the wüstite end-member. This is consistent with the observation that wüstite samples contain magnetite exsolution when the Fe^{3+}/Fe_{tot} ratio is above approximately 0.25 (McCammon and Liu 1984). Samples from our study that were produced at the fper-spft equilibrium curve appear to have preserved larger amounts of ferric iron (~ 0.3) in fper (Figure 4.12) even after quenching, but given the large uncertainties on these measurements it is probably not justified to speculate why this might be.

The exsolution of spft does not appear to occur at high pressures (Dobson et al. 1998; Otsuka et al. 2010; Longo et al. 2011; Bataleva et al. 2019) at least to the same extent. At pressures of 5 GPa

Dobson et al. (1998) were able to quench fper with Fe^{3+}/Fe_{tot} ratios greater than 0.7 without any spft exsolution. This might be related to faster quench rates or slower rates of diffusion at high pressure and may well result from superparamagnetic behaviour due to a smaller grain size (< 10 nm) of the n-spft exsolution.

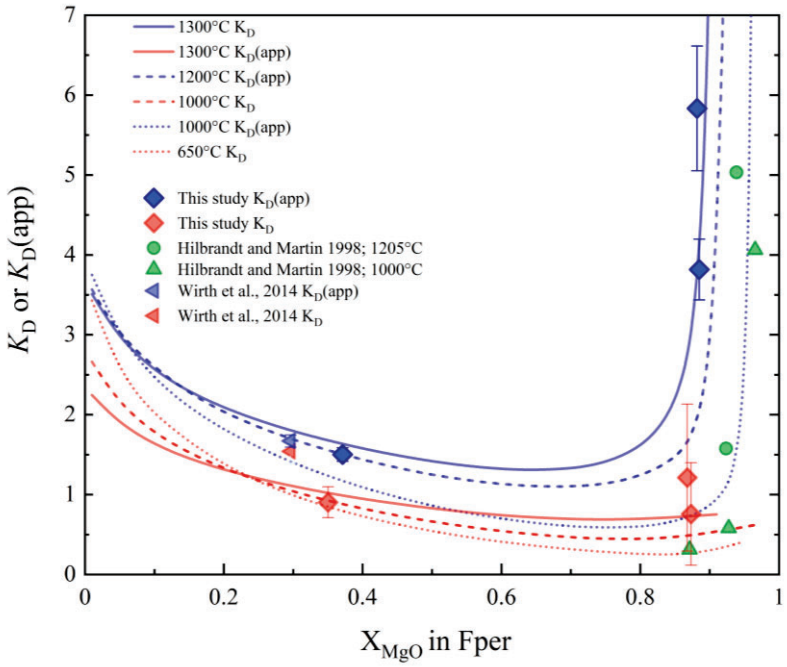

Figure 4.13: The fper-spft K_D(app) and molar Fe^{2+}-Mg exchange coefficient, $K_D=(Fe^{2+}/Mg)_{fper}/(Fe^{2+}/Mg)_{spft}$ calculated at different temperatures and compared to previous experimental measurements (Hilbrandt and Martin 1998) and values determined for a fper inclusion in diamond containing spft exsolution (Wirth et al. 2014).

In Figure 4.13 the molar Fe^{2+}-Mg exchange coefficient between fper and spft, i.e. $K_D=(Fe^{2+}/Mg)_{fper}/(Fe^{2+}/Mg)_{spft}$, has been calculated using the results of the model at 1300 °C and compared with the experimental data. As the only other experimental data on coexisting fper and spft comes from a study where the fper Fe^{3+}/Fe_{tot} ratio was not measured, the apparent exchange coefficient, $K_D(app)=([Fe^{2+}+Fe^{3+}]/Mg)_{fper}/(Fe^{2+}/Mg)_{spft}$, is also plotted. K_D(app) is more temperature dependent than K_D and is in reasonable agreement with the data of Hilbrandt and Martin (1998). Also plotted are values of K_D and K_D(app) for the fper with X_{MgO} = 0.345 present as inclusion in diamond in a sample studied by Wirth et al. (2014). To our knowledge this is the

only analysis of fper coexisting with spft in a natural sample. Some regions of exsolved spft in this sample are greater than 200 nm in at least two orthogonal directions. The K_D(app) value calculated for this sample is in excellent agreement with the model prediction. However, because the initial fper Fe^{3+}/Fe_{tot} ratio of this sample is only 0.078 the K_D value plots higher than the model curve. As can be seen in Figure 4.13, the model predicts that K_D is not temperature sensitive, so it is possible that the higher K_D in the natural sample results from exsolutions occurring at high pressures. If that is the case, the lack of temperature sensitivity suggests that K_D may provide a useful barometer, once calibrated. As shown in Figure 4.14, the partition coefficient, D, of Mn and Cr between fper and spft in the sample analysed by Wirth et al. (2014) are also in good agreement with the 1 bar experimental values obtained in this study. The Mn value in particular agrees well, and since there is a significant change in D_{Mn} with fper X_{MgO} in the experimental data, such partitioning might also be potentially used to place constraints on the conditions of exsolution and the nature of the initially exsolving phase.

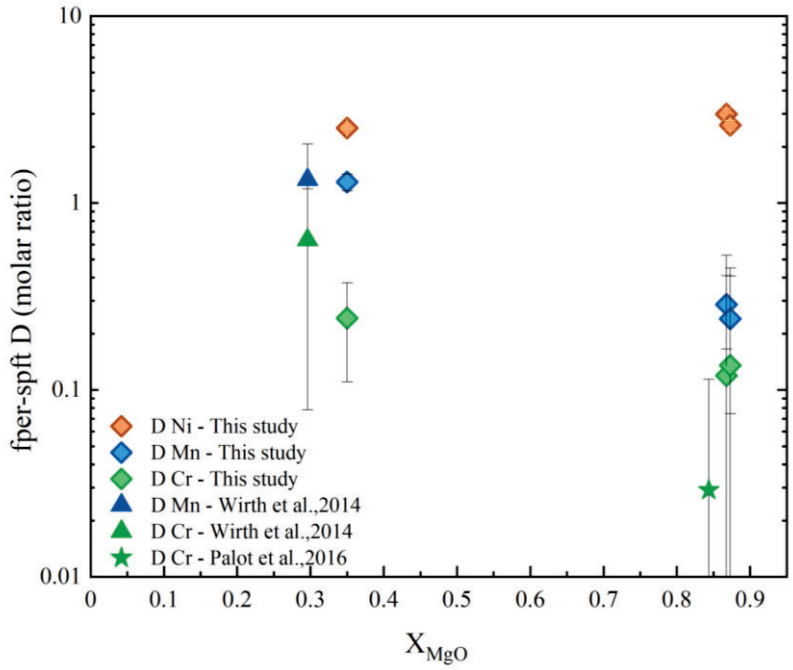

Figure 4.14: Fper- spft Partition coefficients (D) for manganese (Mn); nickel (Ni) and chromium (Cr) for samples RPP5, RPP6 and RPP11 are compared with values obtained for natural fper inclusions in diamonds containing spft exsolutions (Palot et al. 2016; Wirth et al. 2014).

Appendix Chapter 4

Table A.4.1: Chemical composition from the microprobe (EMP) measurements for all the phases in the recovered samples are here reported. Values are in element wt%.

Table A.4.2: Hyperfine parameters obtained from the fitting of the Mössbauer spectra collected for the samples investigated in this study

Table A.4.3: Thermodynamic parameters used for the thermodynamic model of the present study

Figure A.4.1: Fitting of the Fe L_3 electron energy-loss near-edge spectrum collected for fper in sample RPP6.

Figure A.4.2: Room temperature Mössbauer spectra for the samples investigated in this study

Figure A.4.3: Relationship between the experimental fO_2 and the Fe^{3+}/Fe_{tot} ratios for different compositions of fper

Table A.4.1: Chemical composition from the microprobe (EMP) measurements for all the phases in the recovered samples are here reported. Values are in element wt%.

sample	phase		Mg	Fe	Ni	Cr	Mn	Na	O	Pt	total
RPP1	**fper**	**Avg**	45.48	17.00	1.14	0.40	0.19	0.002	36.62	0.12	101.28
		stdv	0.26	0.08	0.03	0.02	0.02	0.003	0.34	0.16	0.49
	alloy	**Avg**	0.056	13.741	2.470	0.038	0.015	n.m.	83.963	0.018	100.321
		stdv	0.086	0.319	0.075	0.014	0.013		0.536	0.027	0.384
	c.p.f.u.		**Mg**	**Fe**	**Ni**	**Cr**	**Mn**	**Pt**	**Σcat**	**ΣOxy**	
	fper	**Avg**	0.848	0.138	0.009	0.004	0.002	0.000	1.00	1.04	
		stdv	0.0003	0.0002	0.0002	0.0002	0.0002				
	alloy	**Avg**	0.003	0.341	0.058	0.001	0.000	0.596	1.00	0.00	
		stdv	0.005	0.003	0.001	0.000	0.000	0.009			
RPP2	**fper**	**Avg**	45.01	17.01	1.12	0.38	0.20	0.01	37.25	0.16	101.35
		stdv	0.24	0.07	0.05	0.01	0.02	0.01	0.16	0.28	0.41
	alloy	**Avg**	0.052	10.162	1.016	0.037	0.013	n.m.	0.066	89.963	101.320
		stdv	0.073	0.276	0.041	0.013	0.015		0.092	0.629	0.544
	c.p.f.u.		**Mg**	**Fe**	**Ni**	**Cr**	**Mn**	**Pt**	**Σcat**	**ΣOxy**	
	alloy	**Avg**	0.847	0.139	0.009	0.003	0.002	0.000	1.00	1.06	
		stdv	0.0003	0.0002	0.0003	0.0001	0.0002				
			0.003	0.274	0.026	0.001	0.00	0.695	1.00	0.00	
			0.0044	0.0023	0.0006	0.0004	0.0004	0.0080			
RPP3	**fper**	**Avg**	45.155	16.601	1.044	0.394	0.177	0.002	38.213	0.072	101.867
		stdv	0.574	0.288	0.119	0.032	0.018	0.001	0.311	0.062	0.629
	alloy	**Avg**	0.061	5.369	0.388	0.033	0.023	n.m.	0.003	94.197	100.273
		stdv	0.068	0.430	0.044	0.015	0.021		0.007	0.836	0.450
	c.p.f.u.		**Mg**	**Fe**	**Ni**	**Cr**	**Mn**	**Pt**	**Σcat**	**ΣOxy**	
RPP3	**fper**	**Avg**	0.851	0.136	0.008	0.003	0.001	0.000	1.00	1.09	
		stdv	0.002	0.0004	0.0008	0.0002	0.0001	0.0004			
	alloy	**Avg**	0.004	0.163	0.011	0.001	0.001	0.891	1.00	0.00	
		stdv	0.005	0.008	0.001	0.0004	0.001	0.015			

Table A.4.1 continued

sample	phase		Mg	Fe	Ni	Cr	Mn	Na	O	Pt	total
RPP4	**fper**	**Avg**	46.023	16.012	1.040	0.345	0.252	0.004	37.542	0.021	101.238
		stdv	0.201	0.225	0.060	0.036	0.029	0.004	0.249	0.033	0.413
	alloy	**Avg**	0.099	9.780	0.853	0.031	0.050	n.m.	0.265	94.956	106.034
		stdv	0.114	0.249	0.084	0.014	0.037		0.150	1.150	1.380
	c.p.f.u.		**Mg**	**Fe**	**Ni**	**Cr**	**Mn**	**Pt**	**Σcat**	**ΣOxy**	
RPP4	**fper**	**Avg**	0.857	0.130	0.008	0.003	0.002	0.000	1.00	1.06	
		stdv	0.002	0.0010	0.0004	0.0003	0.0002				
	alloy	**Avg**	0.006	0.257	0.021	0.001	0.001	0.714	1.00	0.02	
		stdv	0.007	0.002	0.002	0.0004	0.001	0.009			
RPP5	**fper**	**Avg**	46.344	14.506	1.265	0.278	0.224	0.003	38.621	0.036	101.277
		stdv	*0.172*	*0.273*	*0.158*	*0.059*	*0.026*	*0.004*	*0.227*	*0.041*	*0.426*
	spft	**Avg**	11.656	52.962	0.283	1.562	0.524	0.006	31.279	0.042	98.315
		stdv	*0.134*	*0.806*	*0.059*	*0.595*	*0.042*	*0.007*	*0.509*	*0.046*	*0.745*
	alloy	**Avg**	0.032	1.824	0.149	0.027	0.020	n.m.	0.275	103.12	105.449
		stdv	*0.037*	*0.401*	*0.053*	*0.020*	*0.026*		*0.138*	*1.203*	*1.467*
	c.p.f.u.		**Mg**	**Fe**	**Ni**	**Cr**	**Mn**	**Pt**	**Σcat**	**ΣOxy**	
RPP5	**fper**	**Avg**	0.868	0.118	0.010	0.002	0.002	0.000	1.00	1.09	
		stdv	0.003	0.001	0.001	0.001	0.001				
	spft	**Avg**	0.977	1.932	0.010	0.061	0.019	0.00	3.00	3.99	
		stdv	0.011	0.014	0.002	0.021	0.001				
	alloy	**Avg**	0.002	0.058	0.004	0.001	0.001	0.934	1.00	0.03	
		stdv	0.003	0.011	0.001	0.001	0.001	0.016			
sample	**phase**		**Mg**	**Fe**	**Ni**	**Cr**	**Mn**	**Na**	**O**	**Pt**	**total**
RPP6	**fper**	**Avg**	46.718	14.135	1.026	0.265	0.196	0.002	38.183	0.031	100.572
		stdv	*0.320*	*0.130*	*0.062*	*0.018*	*0.033*	*0.004*	*0.258*	*0.033*	*0.552*
	spft	**Avg**	11.788	54.713	0.269	1.341	0.557	0.005	31.363	0.037	100.098
		stdv	*0.438*	*0.836*	*0.048*	*0.463*	*0.043*	*0.007*	*0.218*	*0.044*	*0.406*
	alloy	**Avg**	0.046	1.622	0.176	0.026	0.035	n.m.	0.344	99.664	101.924
		stdv	*0.042*	*0.415*	*0.042*	*0.011*	*0.042*		*0.060*	*0.768*	*0.620*

Table A.4.1 continued

	c.p.f.u.		Mg	Fe	Ni	Cr	Mn	Pt	Σcat	ΣOxy	
RPP6	**fper**	**Avg**	0.873	0.115	0.008	0.002	0.002	0.000	1.00	1.08	
		stdv	0.0010	0.0001	0.0004	0.0001	0.0003	*0.00*			
	spft	**Avg**	0.966	1.952	0.009	0.051	0.020	0.00	3.00	3.91	
		stdv	0.008	0.026	0.001	0.016	0.001				
	alloy	**Avg**	0.003	0.053	0.005	0.001	0.001	0.936	1.00	0.04	
		stdv	0.003	0.012	0.001	0.000	0.001	0.018			
sample	**phase**		**Mg**	**Fe**	**Ni**	**Cr**	**Mn**	**Na**	**O**	**Pt**	**total**
RPP9	**fper**	**Avg**	43.812	16.629	1.047	0.304	0.240	0.003	37.458	0.013	99.524
		stdv	0.441	0.362	0.054	0.022	0.038	0.004	0.347	0.036	0.581
	alloy	**Avg**	0.027	2.154	0.162	0.017	0.045	n.m.	0.326	98.670	101.412
		stdv	0.035	0.397	0.053	0.012	0.041		0.081	1.267	1.418
	c.p.f.u.		**Mg**	**Fe**	**Ni**	**Cr**	**Mn**	**Pt**	**Σcat**	**ΣOxy**	
RPP9	**fper**	**Avg**	0.847	0.140	0.008	0.003	0.002	0.000	1.00	1.10	
		stdv	0.002	0.001	0.0003	0.0002	0.0003				
	alloy	**Avg**	0.002	0.070	0.005	0.001	0.001	0.921	1.00	0.04	
		stdv	0.002	0.010	0.001	0.0004	0.001	0.016			
RPP10	**fper**	**Avg**	7.772	65.00	0.736	0.327	0.167	0.008	26.73	0.01	100.89
		stdv	0.084	0.44	0.026	0.011	0.019	0.011	0.308	0.03	0.2883
	alloy	**Avg**	0.00	15.80	4.50	0.01	0.002	n.m.	0.03	80.95	101.31
		stdv	0.00	0.97	0.06	0.01	0.004		0.04	0.62	0.54
	c.p.f.u.		**Mg**	**Fe**	**Ni**	**Cr**	**Mn**	**Pt**	**Σcat**	**ΣOxy**	
RPP10	**fper**	**Avg**	0.212	0.773	0.008	0.004	0.002	0.000	1.00	1.11	
		stdv	0.001	0.001	0.0002	0.0001	0.0002				
	alloy	**Avg**	0.000	0.365	0.099	0.000	0.000	0.535	1.00	0.00	
		stdv	0.000	0.012	0.001	0.0002	0.000	0.011			
RPP11	**fper**	**Avg**	13.673	56.41	1.63	0.119	0.211	0.006	29.49	0.03	101.54
		stdv	0.5481	0.6128	0.057	0.01	0.021	0.008	0.611	0.04	0.58
	spft	**Avg**	5.127	64.709	0.559	0.425	0.141	0.006	30.047	0.037	101.169
		stdv	0.056	0.135	0.026	0.052	0.016	0.011	0.170	0.043	0.273
	alloy	**Avg**	0.00	11.26	2.63	0.01	0.00	n.m.	0.03	88.97	102.92
		stdv	0.00	1.02	0.05	0.01	0.00		0.07	0.59	1.00

Table A.4.1 continued

	c.p.f.u.		Mg	Fe	Ni	Cr	Mn	Pt	Σcat	ΣOxy	
RPP11	**fper**	**Avg**	0.350	0.629	0.017	0.001	0.002	0.000	1.00	1.15	
		stdv	0.006	0.007	0.0002	0.0001	0.0002				
	spft	**Avg**	0.455	2.500	0.021	0.018	0.006	0.001	3.00	4.05	
		stdv	0.003	0.006	0.001	0.002	0.001				
	alloy	**Avg**	0.000	0.287	0.064	0.000	0.000	0.649	1.00	0.00	
		stdv	0.000	0.016	0.001	0.0003	0.000	0.016			
sample	**phase**		**Mg**	**Fe**	**Ni**	**Cr**	**Mn**	**Na**	**O**	**Pt**	**total**
RPP12	**fper**	**Avg**	8.123	63.538	0.906	0.447	0.167	0.006	26.94	0.02	100.3
		stdv	0.697	0.704	0.069	0.016	0.021	0.01	0.567	0.03	0.3811
	alloy	**Avg**	0.003	12.876	2.750	0.010	0.013	n.m.	0.103	84.873	100.633
		stdv	0.003	0.727	0.129	0.009	0.015		0.071	0.502	0.678
	c.p.f.u.		**Mg**	**Fe**	**Ni**	**Cr**	**Mn**	**Pt**	**Σcat**	**ΣOxy**	
RPP12	**fper**	**Avg**	0.223	0.759	0.010	0.006	0.002	0.000	1.00	1.12	
		stdv	0.012	0.013	0.0005	0.0000	0.0002				
	alloy	**Avg**	0.000	0.323	0.066	0.000	0.000	0.610	1.00	0.00	
		stdv	0.000	0.010	0.001	0.0002	0.000				

Notes : In the alloy measurements, Na was below the detector limit and therefore was not measured (n.m.). Abbreviations stand for: ferropericlase (Fper), spinel-structured ferrite (spft)

Table A.4.2: Hyperfine parameters obtained from the fitting of the Mössbauer spectra collected for the samples investigated in this study

Run	CS (mm/s)	QS (mm/s)	FWHM (mm/s)	Relative area (A)	BHF (T)	Site assignment	χ^2
RPP1	1.05 (1)	1.1 (8)	0.07 (3)	0.399	-	Fe^{2+} in Fper	0.89
	1.04 (1)	0.56 (4)	0.17 (1)	0.526	-	Fe^{2+} in Fper *	
	0.08 (3)	-	0.7 (1)	0.074	-	Fe^{3+} in Fper	
RPP2	1.04 (2)	0.59 (1)	0.47 (1)	0.775	-	Fe^{2+} in Fper	1.04
	0.16 (8)	-	0.83 (2)	0.057	-	Fe^{3+} in Fper	
	0.40 (9)	-0.04 (2)	1.3 (4)	0.123	43 (1)	n-spft	
	0.56 (12)	-0.18 (2)	0.56 (6)	0.044	37 (1)	n-spft	
RPP3	1.05 (1)	0.49 (1)	0.47 (2)	0.391	-	Fe^{2+} in Fper	0.96
	0.05	-	1.0 (1)	0.041	-	Fe^{3+} in Fper	
	0.31 (2)	0.02 (3)	0.57 (6)	0.210	46.4 (2)	n-spft	
	0.43 (5)	-0.02 (7)	0.91(2)	0.325	43.1 (6)	n-spft	
	0.50 (7)	0.35(2)	0.32(2)	0.034	36.9 (6)	n-spft	
RPP 4	1.04 (5)	1.0 (3)	0.73 (1)	0.440	-	Fe^{2+} in Fper	1.74
	1.05 (1)	0.52 (1)	0.39 (6)	0.409	-	Fe^{2+} in Fper	
	0.06 (2)	-	0.71 (5)	0.062	-	Fe^{3+} in Fper	
	0.28 (8)	-0.3(3)	1.5 (5)	0.089	43 (1)	n-spft	
RPP 5	1.07 (3)	0.25 (31)	0.6 (3)	0.077	-	Fe^{2+} Fper	2.82
	0.05	-	1.4 (7)	0.039	-	Fe^{3+} Fper	
	0.34 (2)	-0.01 (3)	1.3 (1)	0.471	38.5 (6)	n-spft	
	0.30 (1)	0.00 (2)	0.55 (9)	0.124	42.2 (3)	spft (S1)	
	0.29 (1)	0.01 (1)	0.60 (4)	0.289	45.2 (2)	spft (S1)	
RPP 6	1.04 (3)	0.00*	0.6 (3)	0.066	-	Fe^{2+} Fper	2.65
	0.11	-	1.3 (6)	0.033	-	Fe^{3+} Fper	
	0.33 (1)	-0.02 (2)	1.5 (1)	0.580	39.2 (6)	n-spft	
	0.30 (1)	-0.01 (2)	0.51 (7)	0.215	42.2 (2)	spft (S1)	
	0.29 (1)	0.01 (2)	0.62 (4)	0.106	45.1 (2)	spft (S1)	
RPP9	1.04 (2)	0.33 (2)	0.56	0.168	-	Fe^{2+} Fper	2.78
	0.03	-	1.0	0.022	-	Fe^{3+} Fper	
	0.30 (1)	0.00 (1)	0.55	0.295	46.3 (2)	n-spft	
	0.31 (1)	-0.01 (2)	0.48	0.114	44. (2)	n-spft	
	0.39 (2)	-0.04 (3)	1.1	0.402	41.(3)	n-spft	
RPP 10	0.98 (1)	0.84 (2)	0.65 (1)	0.583	-	Fe^{2+} Fper	1.25
	0.28	-	1.2 (3)	0.089	-	Fe^{3+} Fper	
	0.28 (1)	-0.01 (3)	0.35 (4)	0.148	48.8 (1)	n-spft	
	0.66 (3)	-0.02 (5)	0.76 (8)	0.180	45.8 (2)	$Fe^{2.5+}$ n-spft	

Table A.4.2 continued

RPP 11	1.03 (3)	0.88 (5)	0.60 (5)	0.087	-	Fe^{2+} Fper	1.15
	0.11	-	1.00	0.029	-	Fe^{3+} Fper	
	0.68 (5)	0.03 (8)	0.6 (1)	0.142	43.4 (5)	$Fe^{2.5+}$ n-spft	
	0.30 (1)	-0.01 (2)	0.40 (3)	0.376	48.7 (1)	spft (S1)	
	0.63 (4)	-0.05 (5)	0.8 (1)	0.366	46.4 (3)	spft (S2)	
RPP12	0.99 (2)	0.81	0.64 (3)	0.401		Fe^{2+} in Fper	0.85
	0.24	-	0.7 (2)	0.077		Fe^{3+} in Fper	
	0.48 (4)	-0.22	0.3 (2)	0.079	46.6 (3)	n-spft	
	0.28 (1)	0.01	0.32 (4)	0.195	48.9 (1)	n-spft	
	0.73 (6)	-0.01	0.7 (1)	0.249	45.5 (4)	$Fe^{2.5+}$ n-spft	

Table A.4.3: Thermodynamic parameters used for the thermodynamic model of the present study

Standard state data from Holland and Powell (2011)									
	$\Delta_f H$ **kJ/mol**	S **$JK^{-1}mol^{-1}$**	V_0 **J/bar**	a	b **($x10^5$)**	c	d	**Tc K**	**Smax J/K/mol**
MgO	-601.55	26.50	1.125	0.0605	0.0362	-535.8	-0.2992		
Magnetite	-1114.51	146.90	4.452	0.2625	-0.7205	-1926.2	-1.6557	848	35
Magnesioferrite	-1442.29	121.00	4.457	0.2705	-0.7505	-999.2	-2.0224	665	17
O_2	0	205.20	0	0.0483	-0.0691	499.2	-0.4207		
$Cp = a + bT + cT^{-2} + dT^{-0.5}$ ($kJK^{-1}mol^{-1}$)									
Standard state data from Hidyadt et al. (2015)									
G^{o}_{FeO}	$-285203.5 + 274.2455\,T - 49.19444\,T \ln T - 0.004678477\,T^2 + 297568.8\,T^{-1} + 574.4469 \ln T$								
$G^{o}_{FeO_{1.5}}$	$-523138.0 + 73.37019\,T - 26.96809\,T \ln T - 0.008835071\,T^2 + 1498519\,T^{-1} + 25471.09 \ln T$								
G^{o}_{Fe}	$-236.5 + 132.4156\,T - 24.6643\,T \ln T - 0.003758\,T^2 + 77359.0\,T^{-1} - 5.8927x10^{-8}T^3$								
fper mixing terms ($kJmol^{-1}$)									
$q^{00}_{FeO\text{-}FeO1.5}$	–59.412				**Hidyadt et al. (2015)**				
$q^{10}_{FeO\text{-}FeO1.5}$	42.677								
$q^{00}_{FeO\text{-}MgO}$	10.500				**This Study**				
$q^{10}_{FeO1.5\text{-}MgO}$	2.84-0.02092T								
$q^{20}_{FeO1.5\text{-}MgO}$	5.000								
Fe-Pt-Ni alloy mixing terms ($kJmol^{-1}$)									
W^{alloy}_{Fe-Pt}	-138.00				**Kessel et al. (2001)**				
W^{alloy}_{Pt-Fe}	-90.800								
W^{alloy}_{Ni-Pt}	-30.683				**Fu-Hsing et al. (1995)**				
W^{alloy}_{Pt-Ni}	-42.302								
W^{alloy}_{Fe-Ni}	-11.793				**Ono et al. (1977)**				
W^{alloy}_{Ni-Fe}	-3.071								
Spft $MgFe_2O_4$-Fe_3O_4 mixing terms ($kJmol^{-1}$)									
$W^{spfr}_{FeO-MgO}$	6.932				**Jamieson and Roeder (1984)**				
$W^{spfr}_{MgO-FeO}$	1.000								

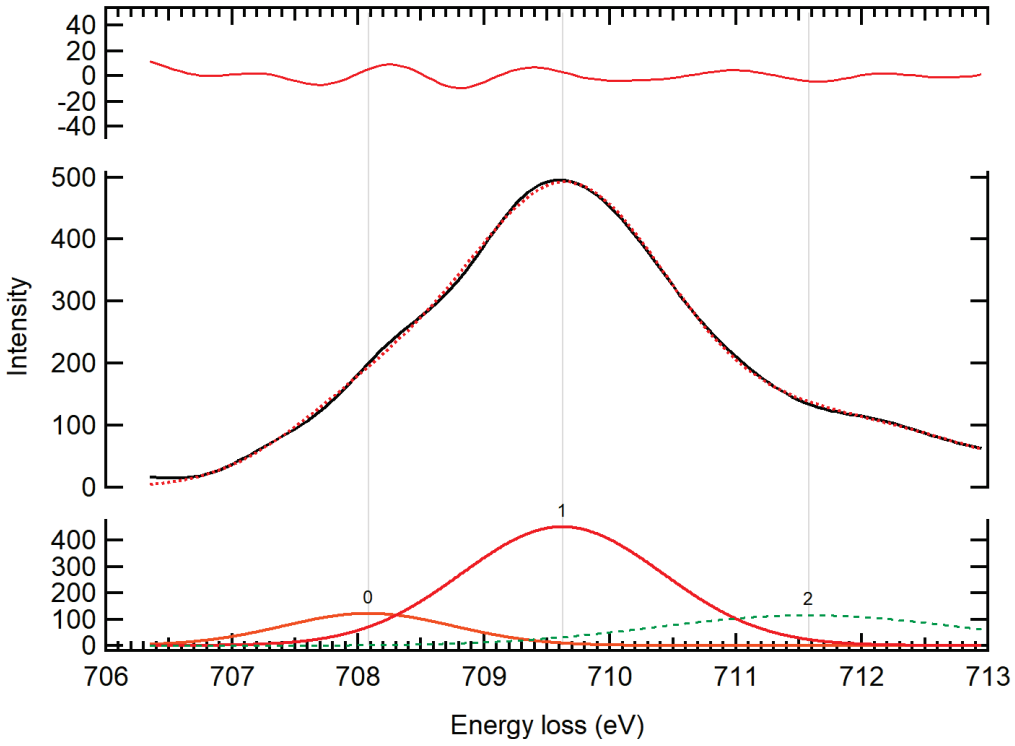

Figure A.4.1: Fe L_3 electron energy-loss near-edge spectrum collected for fper in sample RPP6. Due to the small amount of Fe in this sample, only two Gaussian peaks represent the signal of Fe^{3+} (red), and Fe^{2+} (orange) have been used to fit the spectrum. The green Gaussian peak is used to better fit the broad ELNES feature at higher energy and it is considered part of the background

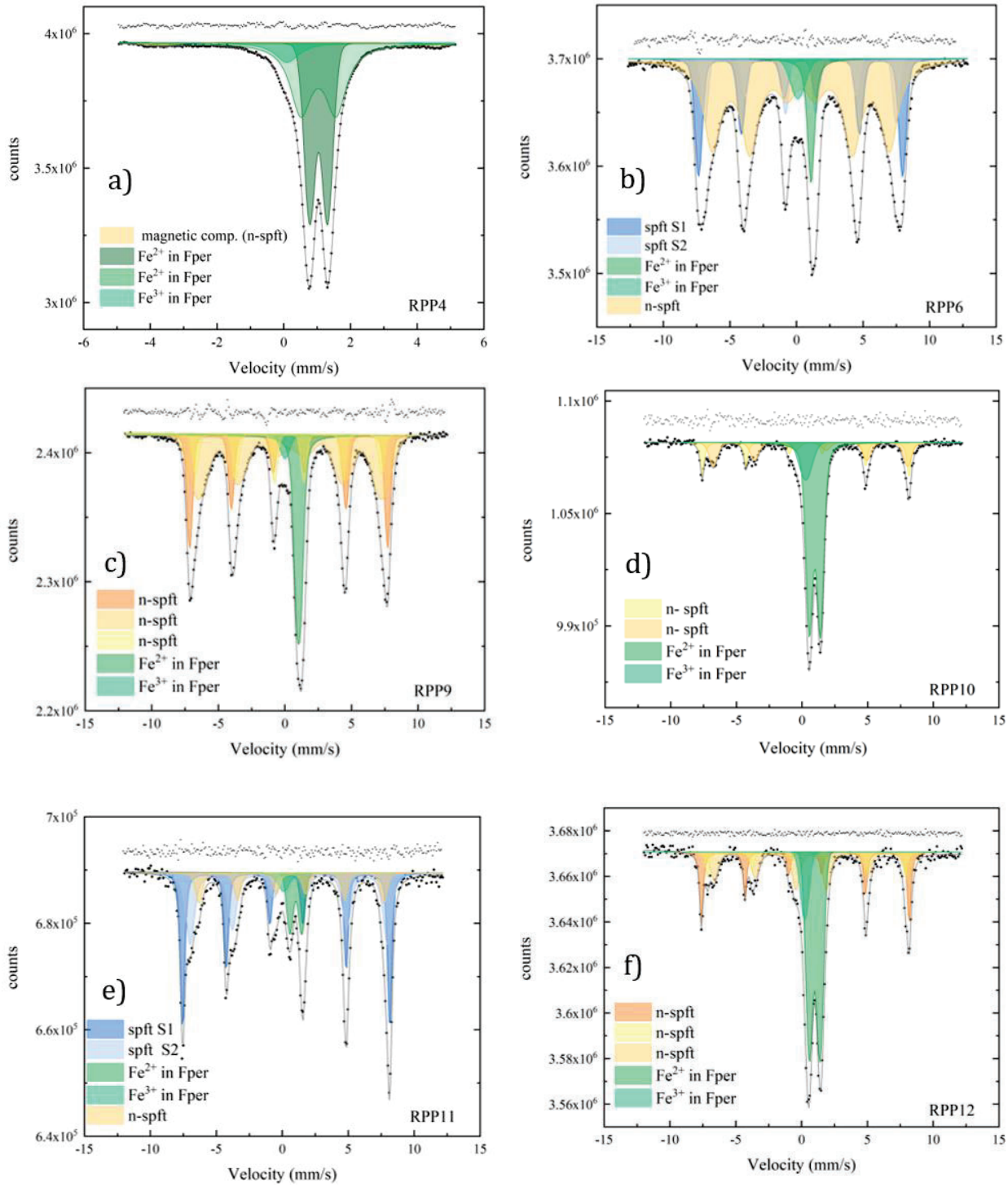

Figure A.4.2: Room pressure and temperature Mössbauer spectra for all the room pressure samples investigated in the present study. Spectra are shown in order from RPP1 to RPP12. In all spectra, the dark green doublet belongs to the ferrous iron and the light-green singlet to the ferric iron of fper. The dark blue and light blue fits of the magnetic sextet belong to S1 (Fe^{3+}) and S2 ($Fe^{2.5+}$), respectively of the spinel phase coexisting with fper. The yellow/orange sextets denotes the absorption of the n-spft component.

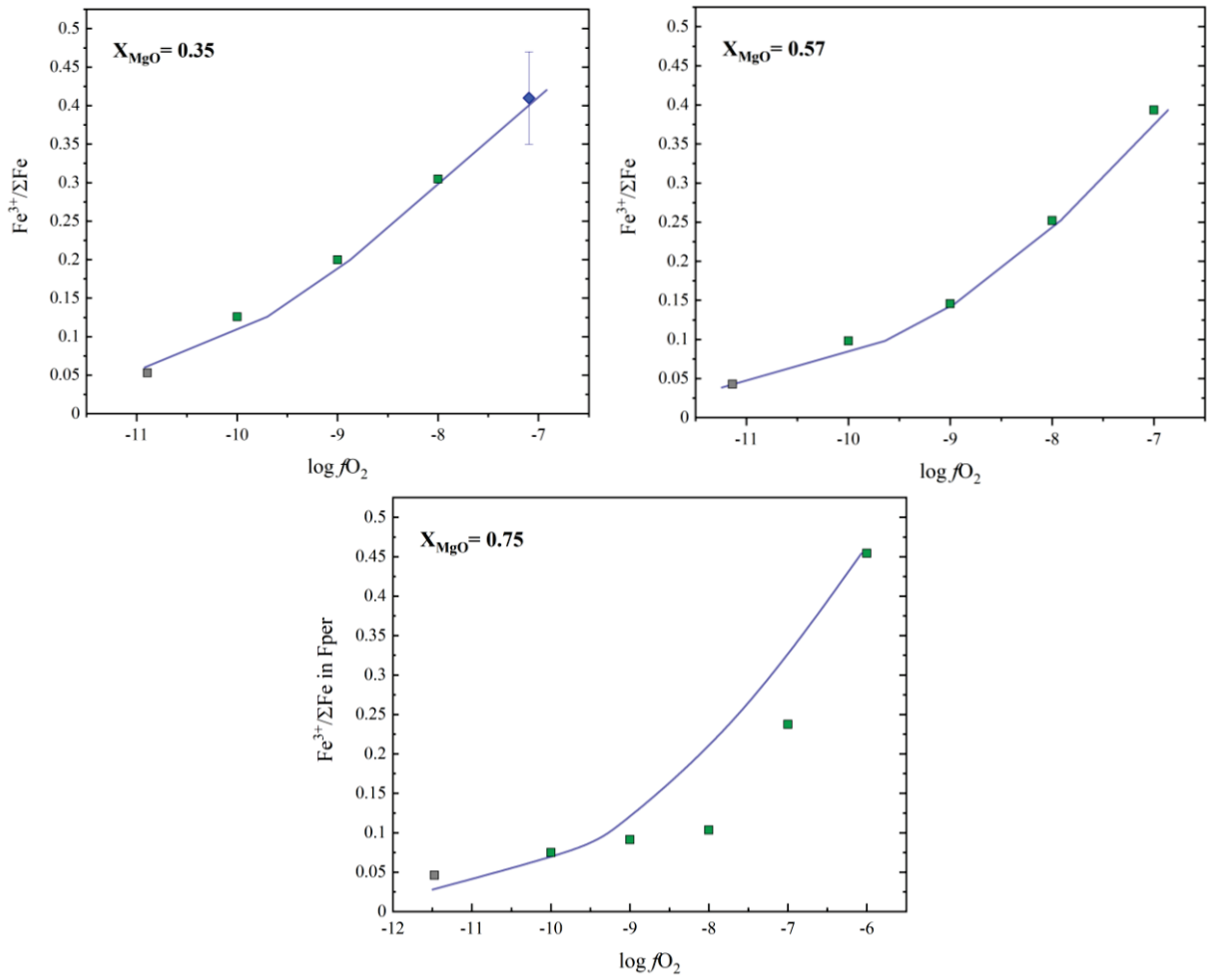

Figure A.4.3: Calibration of the thermodynamic model using the relationship between the experimental fO_2 and the Fe^{3+}/Fe_{tot} ratios for different compositions of fper expressed as X_{MgO}. Green squares: data from Spiedel (1967); gray squares data at Fe-metal saturation from O'Neill et al. (2003). The agreement within the fper field starts to deviate at higher X_{MgO} (see Figure 4.12 in main text.

5. High-pressure behaviour of the MgO-FeO-$FeO_{1.5}$ system

5.1 Introduction

Ferropericlase (fper) is likely to be the second most abundant mineral in the Earth's lower mantle and is also found as inclusions in super deep diamonds, which are proposed to originate at sub-lithospheric conditions. In fact, fper inclusions are used to identify super deep diamonds as such and, in many instances, it is argued that they originate in the lower mantle (Scott Smith et al. 1984; Harte and Hudson 2013; Kaminsky 2012; Kaminsky et al. 2009a, 2001; Stachel and Harris,2008; Hayman et al. 2005; Harte et al. 1999; Harte and Harris 1994; Wilding 1990; Davies et al. 2004, 1999; Stachel et al. 2000). A lower mantle origin assumes that the inclusions were formed in equilibrium with typical ultramafic mantle compositions, however, they could also form from silica-poor compositions at practically any depth in the diamond stability field (Gurney 1989; Stachel et al. 1998; Brey et al. 2004; Bulatov et al. 2019).

The magnesiowsütite-ferropericlase solid solution, which we refer to here for simplicity as fper, can also contain a significant fraction of Fe^{3+}, the incorporation of which is charge balanced through the creation of metal cation vacancies (V), resulting in non-stoichiometry that can be described by the formula $Mg_zFe^{2+}_{1-z-3x}Fe^{3+}_{2x}V_xO$. At room pressure the Fe^{3+}/Fe_{tot} ratio of fper varies strongly with oxygen fugacity (fO_2), reaching a minimum where fper is in equilibrium with iron metal (Srecec et al. 1987; O'Neill et al. 2003) and a maximum where it coexists with spinel

phases along the magnetite-magnesioferrite (Fe_3O_4-$MgFe_2O_4$) solid solution (Brynestad and Flood 1958; Katsura and Kimura 1964; Speidel 1967; Hilbrandt and Martin 1998). The Fe^{3+}/Fe_{tot} ratio of fper for a given composition appears to decrease, however, with pressure at a given oxygen fugacity, fO_2 (McCammon 1993; McCammon et al. 1998; Bolfan-Casanova et al. 2002; Frost and Langenhorst 2002; McCammon et al. 2004; Otsuka et al. 2010, 2013). Several studies have proposed using the Fe^{3+}/Fe_{tot} ratio of fper inclusions in diamonds to determine the fO_2 at which such inclusions, and presumably the diamonds, formed (Longo et al. 2011; Otsuka et al. 2013; Kaminsky et al. 2015). Otsuka et al. (2013) used the results of high-pressure experiments to calibrate an equation for the Fe^{3+} content of fper as a function of MgO content, pressure (P) temperature (T), and fO_2. The application of this equation to fper inclusions recovered from natural diamonds implies a very wide range of oxygen fugacities, covering over six log units, assuming P-T conditions of the top of the lower mantle (Kaminsky et al. 2015). This range extends well into the field where diamonds should be oxidised to carbonates (Stagno and Fei 2021). The equation of Otsuka et al. (2013) is also only calibrated using fper data with Mg/(Mg+Fe) > 0.5, so it cannot be applied to the full range of fper inclusion compositions, which stretch to Mg/(Mg+Fe) < 0.2 (Kaminsky 2012 and references therein).

Several studies also have noted that fper inclusions in diamonds can contain nano- to micro-sized exsolutions of magnetite-magnesioferrite spinel phases, here and after referred to as spft (Harte et al. 1999; Anzolini et al. 2019; Palot et al. 2016; Nimis et al.2019; Wirth et al. 2014; Kaminsky et al. 2015; Nestola et al. 2016; Kiseeva et al., 2022). Wirth et al. (2014), for example, found nano-meter scale coherent spft exsolutions in $(Mg_{0.35}Fe_{0.65})O$ diamond inclusions having composition, $(Mg_{0.42}Fe_{0.56}Mn_{0.02})[Fe_{1.94}Al_{0.03}Cr_{0.03}]O_4$. Those authors recognised that the exsolution of spft occurred at some point after the inclusion had been captured in the diamond and it lowered the Fe^{3+}/Fe_{tot} ratio of the recovered fper. The Fe^{3+}/Fe_{tot} ratio is quite often determined through Mössbauer spectroscopy, but given the lack of that information, the authors were able to

reconstruct the original fper Fe^{3+}/Fe_{tot} ratio from an estimate of the volume of the spft exsolution. In a similar way, Kaminsky et al. (2015) recalculated the Fe^{3+}/Fe_{tot} ratio measured by Mössbauer spectroscopy for fper inclusions found in several diamonds adding an average value of 0.021 to the obtained Mössbauer data to account for the presence of spft exsolutions which they refer to as "non-stoichiometric clusters". Spft exsolution from fper has also been observed in experiments, principally performed at room pressure and also in this case the bulk Fe^{3+}/Fe_{tot} ratio was calculated adding together the fper and spft Mössbauer contributions taking into account their relative abundance (Longo et al. 2011).

Aside from the necessity to correct fper Fe^{3+}/Fe_{tot} ratios for exsolved spft phases in order to obtain the Fe^{3+} content of ferropericlase at the conditions of formation, the question remains as to when these exsolutions occur and whether this reflects changes in *P* or *T*, or possibly even fO_2, after entrapment. To investigate the exsolution process, information is required on the conditions at which fper becomes saturated in Fe^{3+}, which is what causes the spft to form. The coexistence of two Fe^{2+}-Mg solid solutions, i.e. fper and spft, also raises the possibility of calibrating this cation exchange to provide information on the *P* or *T* of equilibration. However, although both fper and spft are well studied solid solutions, virtually nothing is known on how Fe and Mg partition between these phases.

There are further complications at pressures above 8 GPa where spft transforms to a range of newly discovered higher-pressure Fe-Mg-oxides (Lavina et al. 2011; Lavina and Meng 2015; Sinmyo et al. 2016; Ishii et al. 2018). There is evidence that some of these high-pressure phases may have also exsolved from fper inclusions in diamonds (Anzolini et al. 2020). Fe_4O_5 ($Fe_2^{2+}Fe_2^{3+}O_5$) is formed from an assemblage of $Fe_{1-x}O$ and Fe_3O_4 at pressures of 8 GPa (Woodland et al. 2012; Myhill et al. 2016) and forms a continuous solid solution to an $Mg_2^{2+}Fe_2^{3+}O_5$ end-member (Boffa Ballaran et al. 2015; Uenver-Thiele et al. 2017a). Fe_5O_6 ($Fe_3^{2+}Fe_2^{3+}O_6$) forms under similar

conditions but has only a limited solid solution with the Mg end member (Woodland et al. 2023). A $Mg_{0.87}Fe^{2+}_{4.13}Fe^{3+}_{4}O_{11}$ phase (Ishii et al. 2018) may have a limited stability field between 9 and 14 GPa (Woodland et al. 2023) but a Fe_7O_9 ($Fe^{2+}_{3}Fe^{3+}_{4}O_{9}$) phase (Sinmyo et al. 2016) is likely too oxidised to coexist with fper. Diamond anvil cell experiments by Hikosaka et al. (2019) indicate that Fe_4O_5 and Fe_5O_6 may remain stable to approximately 40 GPa although at pressures above 20 GPa a high-pressure structure of Fe_3O_4 is also stable (HP- Fe_3O_4; Uenver-Thiele et al. 2017b). A number of further iron-oxides and high pressure Fe_3O_4 phases have since been discovered at conditions compatible with the deeper lower mantle (Bykova et al. 2016; Khandarkhaeva et al. 2022). At pressures above the spft stability field, the upper fO_2 limit of fper stability will be marked by the formation of one of these Fe-Mg-oxides. Only phases that coexist with fper in this way are likely to have a chance of being stable in the mantle, the others are likely too oxidised, but there is currently little information to judge which phase this is likely to be for a given *P* and *T*.

In this study experiments have been performed up to pressures of 30 GPa, to determine the composition of fper, including its Fe^{3+}/Fe_{tot} ratio, at conditions where it coexists with spft, indicated hereafter as O4 phase, or higher-pressure Fe-Mg-oxides, mainly Fe_4O_5 and $Mg^{2+}_{2}Fe^{3+}_{2}O_{5}$, indicated hereafter as O5 phase. The formation of Pt-Fe alloy in the experiments was used to determine the fO_2 at the experimental *P*,*T* conditions. A thermodynamic model, an extension of the 1 bar model presented in Chapter 4, has been developed to fit the data set in order to calculate the fper stability field as a function of *P*, *T*, MgO content and fO_2. In addition, this model allows the compositions of coexisting phases to be determined. The experimental dataset also includes fper samples that did not coexist with other oxides that were used to calibrate the fper Fe^{3+}/Fe_{tot} at lower fO_2. With this model we explore the fper stability field, the fO_2 recorded by fper inclusions in diamonds and what this implies for their formation conditions and the conditions at which exsolved phases found in fper inclusions are formed.

5.2 Experimental procedures

5.2.1 Starting material

Starting materials were prepared from mixtures of Fe_2O_3 and MgO, plus the minor oxides NiO (1.3 wt%), Cr_2O_3 (0.5 wt%), MnO (0.2 wt%) and Na_2O (0.05 wt%) to reproduce natural Fper inclusion composition. Fe_2O_3 and MgO were presintered overnight at 1000 °C. The starting powders were then ground together and pressed into pellets that were first heated in a furnace to 500 °C to remove volatiles and then reduced for 48 hours in a gas mixing furnace at 1100 °C and at an fO_2 of 2 log units below the fayalite–magnetite–quartz (FMQ) buffer. The recovered fper powders were weighed and then further ground together with 5 to 20 wt. % Fe_2O_3 powder, previously fired at 1000 °C. The Fe_2O_3 extra amount was used to induce coexistence with spft or higher-pressure Fe-Mg-oxides. Additionally, 4 wt% PtO_2 powder was added to the starting materials to act as a sliding redox sensor (Woodland and O'Neill 1997; Kessel et al. 2001). Five ferropericlase starting materials with nominal stoichiometries $(Mg_{0.86}Fe_{0.14})O$, $(Mg_{0.50}Fe_{0.50})O$, $(Mg_{0.30}Fe_{0.70})O$, $(Mg_{0.05}Fe_{0.95})O$ and FeO were prepared (Table 5.1).

Table 5.1: Composition of the ferropericlase starting materials in wt%.

Ferropericlase stoichiometry		**Cr_2O_3**	**NiO**	**Na_2O**	**MnO**	**FeO**	**MgO**	**total**	**Added Fe_2O_3**	**Added PtO_2**
$(Mg_{0.86}Fe_{0.14})O$	(A)	0.50	1.30	0.05	0.20	13.71	84.24	100	20 or 10 wt%	4 wt%
$(Mg_{0.50}Fe_{0.50})O$	(B)	0.50	1.30	0.05	0.20	48.98	48.98	100	20 or 5 wt%	4 wt%
$(Mg_{0.30}Fe_{0.70})O$	(C)	0.50	1.30	0.05	0.20	68.57	29.39	100	20 wt%	4 wt%
$(Mg_{0.05}Fe_{0.95})O$	(D)	0.50	1.30	0.05	0.20	93.05	4.90	100	20 or 10 wt%	4 wt%
FeO	(E)	0.50	1.30	0.05	0.20	97.95	0	100	None or 5 wt%	4 wt%

Note: The amounts of hematite component and PtO_2 redox sensor are calculated relative to the weight of the ferropericlase composition to which it was added.

5.2.2 High pressure experiments

Most high *P-T* experiments were conducted using the 1000- and 5000-tonne 6-8 Kawai-type multianvil presses at pressures between 6 and 20 GPa using the high-pressure assemblies described in section 2.3.1. A single experiment was run at 30 GPa in the IRIS -15 Voggenreiter LPH 1500-840/200 press (Ishii et al.2016). A 5.7/1.5-type assembly was used with TF05 WC anvils. In this experiment, two samples with compositions $(Mg_{0.86}Fe_{0.14})O$ and FeO were placed respectively above and below the thermocouple junction. Each sample was 0.35 mm long and was placed inside a capsule of dense Al_2O_3 tube with inner and outer diameters of 0.25 mm and 0.6 mm respectively. The heater was comprised of 25 μm thick rhenium foil. The thermocouple was inserted longitudinally through the wall of the furnace with the junction located in the middle of the assembly (Ishii et al.2016). All experimental details are reported in Table 5.2.

5.3 Analytical methods

Recovered experimental runs were cut in half. Sample I1185 recovered from the 30GPa experiment was cut in half using an 0.08mm wire saw. One half was embedded in epoxy and polished for measurements with an electron microprobe analyser (EPMA), scanning electron microscope (SEM) and X-ray diffraction (XRD) analysis. The other half was polished to a thickness varying between 250 and 200 μm, depending on the iron content of the sample (Long et al. 1983) for in-house Mössbauer spectroscopy measurements (MS). Textural observations, preliminary phase identification and semi-quantitative chemical analyses of the recovered run products were performed using a scanning electron microscope (SEM) (ZEISS Gemini 1530) equipped with a field emission gun and energy-dispersive X-ray spectrometer (EDXS). Quantitative chemical compositions of the mineral phases were obtained using an electron microprobe analyser (EMPA, JEOL JXA 8200) operating at an acceleration voltage of 15 kV and

beam current of 15 nA. The Phi-rho-Z correction routine was applied for all analyses of this work. The standards employed were periclase (Mg), andradite (Fe), albite (Na), nickel oxide (Ni), $MnTiO_3$ (Mn), Cr_2O_3 (Cr) and Fe_2O_3 for O. Fe, Pt and Ni metal were used as standards for the analyses of the alloys. A minimum of 20 points were measured on each major phase in the sample. On the alloys, due to the reduced size, 5 to 10 points were collected. The focused beam had a size between 1-2 μm. Compositions and standard deviations of all phases are reported in Table A.5.1.

Table 5.2: Starting materials, experimental conditions and recovered run products of the high-pressure experiments, as determined by means of XRD and EMPA. Run duration was 5hrs heating plateu. The percentages show added hematite to the starting Fper composition.

sample	Start. comp.	P (GPa)	T(°C)	products	sample	Start. comp.	P (GPa)	T(°C)	products
S7029	A + 20%	6	1200	Fper + O_4 + Pt alloy	S7216-B	B + 20%	10	1400	Fper + Pt alloy + n-spft
Z2038	A + 20%	6	1600	Fper + Pt alloy + n-spft	S7216-A	B + 10%	10	1400	Fper + Pt alloy + n-spft
H5128	A + 20%	8	1200	Fper + Pt alloy + n-spft	Z1949-A	B + 20%	12	1200	Fper + Pt alloy + n-spft
S7004	A + 20%	8	1200	Fper + Pt alloy + n-spft	Z2122-B	B + 20%	16	1200	Fper + O_5 + Pt alloy
S7377	A + 20%	10	1200	Fper + O_4 + Pt alloy	Z2117-B	B + 20%	17	1200	Fper + O_5 + Pt alloy
S7180	A + 20%	10	1600	Fper + Pt alloy + n-spft	Z2115-B	B + 20%	20	1200	Fper + O_5 + Pt alloy
S7204	A + 20%	10	1800	Fper + Pt alloy + n-spft	Z2121-A	B + 20%	20	1600	Fper + O_5 + Pt alloy
Z1949-B	A + 20%	12	1200	Fper + Pt alloy+ n-spft	Z2151-A	B + 5%	20	1600	Fper + O_5 + Pt alloy
S7382	A + 20%	16	1200	Fper + O_5 + Pt alloy	Z2153-A	B +5%	20	1800	Fper + Pt alloy + n-spft
S7006	A + 20%	16	1200	Fper + O_5 + Pt alloy	H5189-A	C +20%	6	1200	Fper + Pt_3Fe + n-spft
S7016	A + 20%	20	1200	Fper + O_5 + Pt alloy	S7495-A	C + 20%	10	1200	Fper + O_4 + Pt alloy
Z2151-B	A + 20%	20	1600	Fper + O_5 + Pt alloy	H5190-A	C + 20%	16	1200	Fper + O_5 + Pt alloy
Z2153-B	A + 20%	20	1800	Fper + O_5 + Pt alloy	Z2077-A	C + 20%	16	1200	Fper + O_5 + Pt alloy
H4792	A + 20%	25	1200	Fper + O_5 + Pt alloy	H5189-B	D + 20%	6	1200	Fper + O_4+ [Fper + Spft] + Pt_3Fe
S7410	A + 20%	25	1000	Fper + O_5 + Pt alloy	S7509-A	D + 20%	6	1200	Fper + O_4+ [Fper + Spft] + Pt alloy
S7123-B	A + 10%	25	1400	Fper + small O_5 # + Pt alloy	S7604-A	D + 10%	10	1200	O_5 + [Fper+Spft] + Pt alloy
I1185-A	A + 20%	30	1200	Fper+ [Fper+O_4+?]+ Pt alloy	S7495-B	D + 20%	10	1200	O_6 + Pt_3Fe
S7470	B + 20%	6	1200	Fper + Pt alloy	Z2122-A	D + 20%	16	1200	O_6 + Pt_3Fe
H5164	B + 20%	6	1200	Fper + Pt alloy	Z2115-A	D + 20%	20	1200	O_6 + Pt_3Fe
S7510	B + 20%	6	1600	Fper + Pt_3Fe + n-spft	Z2077-B	D	16	1200	O_6 + Pt_3Fe
S7509-B	B + 20%	6	1200	Fper + Pt_3Fe + n-spft	H5190-B	D	16	1200	O_6 + Pt_3Fe
S7716-B	B + 5%	6	1200	Fper + Pt alloy + n-spft	Z2117-A	D + 20%	17	1200	O_6 + Pt_3Fe
Z2116	B + 20%	8	1200	Fper + Pt alloy + n-spft	Z2120-A	D + 20%	17	1200	O_6 + Pt_3Fe
S7691-A	B + 5%	8	1200	Fper + Pt alloy+ n-spft	S7716 A	E	6	1200	[FeO+Fe_3O_4] + Pt_3Fe
Z2155-B	B	8	1200	Fper + Pt alloy+ n-spft	S7691-B	E	8	1200	[FeO+Fe_3O_4] + Pt_3Fe
Z2155 A	B + 5%	8	1200	Fper + Pt_3Fe + n-spft	I1185-B	E	30	1200	FeO+ Fe_5O_6 + Pt alloy

Notes: * broad peaks in the X-ray patters of samples showing no macroscopic spinel phase, are fit with $(Mg,Fe)Fe_2O_4$ and called n-spft. Squared parentheses indicate back transformation products. # no O_5 detected in XRD; $O_4 = (Mg,Fe)Fe_2O_4$; $O_5 = (Mg,Fe)_2Fe_2O_5$; $O_6 = (Mg,Fe)_3Fe_2O_6$

Phase identification in the run products was performed with a Bruker D8 DISCOVER micro focused X-ray diffractometer (XRD) equipped with a two-dimensional solid-state detector (VANTEC500) and micro-focus Co-Ka radiation source (IμS) operated at 40 kV and 500 μA. The X-ray beam is collimated to a spot size of approximately 100 μm diameter by an IFG polycapillary X-ray mini-lens. Measurements were performed in a 2θ range between 25 and 85 for a total measurement time of 3600 s. The collected X-ray patterns were integrated using the DIFFRACEVA-V3.1 package and compared to the "Crystallography Open Data" database. Due to the focused beam being smaller than 100 μm, the diffraction patterns of most of the samples presents large spots instead of clear Debye rings (Figure A.5.1), due to the relative large dimensions of the fper grains (often larger than 10 μm) resulting in poor averaging statistics. Moreover, the very asymmetric shape of the reflections which cannot be properly fitted with Gaussian profiles has hindered a meaningful analysis of the grain size of n-spft as performed in Chapter 4, Section 4.3.4 and results in large uncertainties of the unit-cell lattice parameters (Table A.5.2) determined through full-pattern refinements using the general structure analysis system (GSAS) software package and the EXPGUI interface (Toby 2001; Larson, C.A. & von Dreele 2004).

Mössbauer analyses were performed on sections of recovered samples with a thickness between 250 and 200 μm. The dimensionless effective thickness of each sample was calculated to be roughly 5 mg Fe/cm^2 to avoid saturation effects. Data were acquired at room temperature (298K) in transmission mode on a constant acceleration Mössbauer spectrometer with a nominal 370 MBq ^{57}Co point source in a 12 μm thick Rh matrix. A piece of Ta foil drilled with a 1 mm diameter hole was used to select the area to be measured. Velocity scales were calibrated relative to 25 μm α-Fe foil. Spectra were collected using a velocity range of +5 to -5 mms^{-1} and +12 to – 12 mms^{-1} by moving the source relative to the sample in constant acceleration mode over 1-3 days. The wider

velocity scale was dictated by the presence of magnetically ordered Fe in the run products. The resulting spectra were then folded and fitted using a pseudo-Voigt line shape and a 1st order polynomial baseline with the MossA 1.01f software package (Prescher et al. 2012*)*. All fitted hyperfine parameters are reported in Table A.5.3.

Thin lamella for Trasmission Electron Microscopy (TEM) analysis of five selected samples (S7029, Z2151-B, Z2115-B, I1185-A and I1185-B) were prepared using a focused ion beam (FIB) milling machine (*FEI Scios* DualBeam milling) following the procedure described in Section 2.9. TEM measurements were carried out using a 200 kV analytical transmission electron microscope (ATEM, *FEI Titan G2 80-200 S/TEM*, *Philips CM20FEG*) equipped with an energy dispersive X-ray spectrometer (EDXS, *Brucker QUANTAX*) and an electron energy-loss spectrometer (EELS, *Gatan GIF Quantum® Model 963*). Energy dispersive X-ray spectroscopy (EDXS) maps have been collected on sample S7029 to identify the composition of some observed melt pockets around the grain boundaries in some of the investigated samples (Figure A.5.2) and to analyse the composition of back transformed grain of fper in sample I1185-A.

Electron energy-loss spectroscopy (EELS) was employed to determine the Fe^{3+}/Fe_{tot} ratio of the phases in the investigated lamellae. Up to four EELS spectra were collected for the fper grains of each sample. Moreover, for samples I1185-A and I1185-B EELS spectra were collected also for the Fe^{3+}-rich phase coexisting with fper, in order to constrain their stoichiometry. The collected EELS spectra were treated following the procedure detailed in Chapter 4, Section 4.2.6 and the resulting Fe^{3+}/Fe_{tot} ratios are reported in Table 5.3.

5.4 Results

5.4.1 Sample assemblages

Most of the recovered experiments contains either fper and Fe-Pt alloy or fper, Fe-Pt-alloy and an Fe^{3+}-rich phase (Table 5.2, Figure 5.1a,b,c).

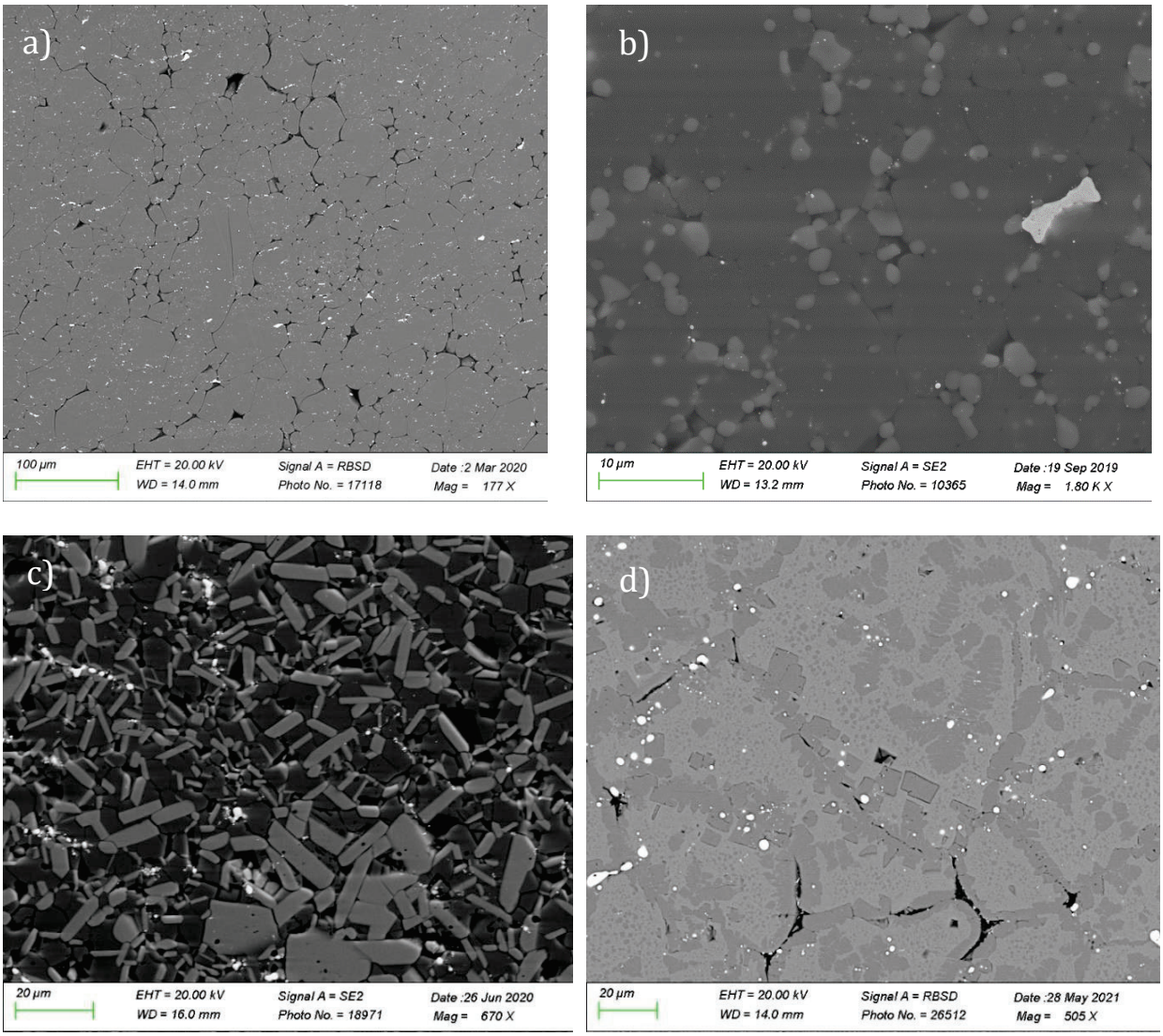

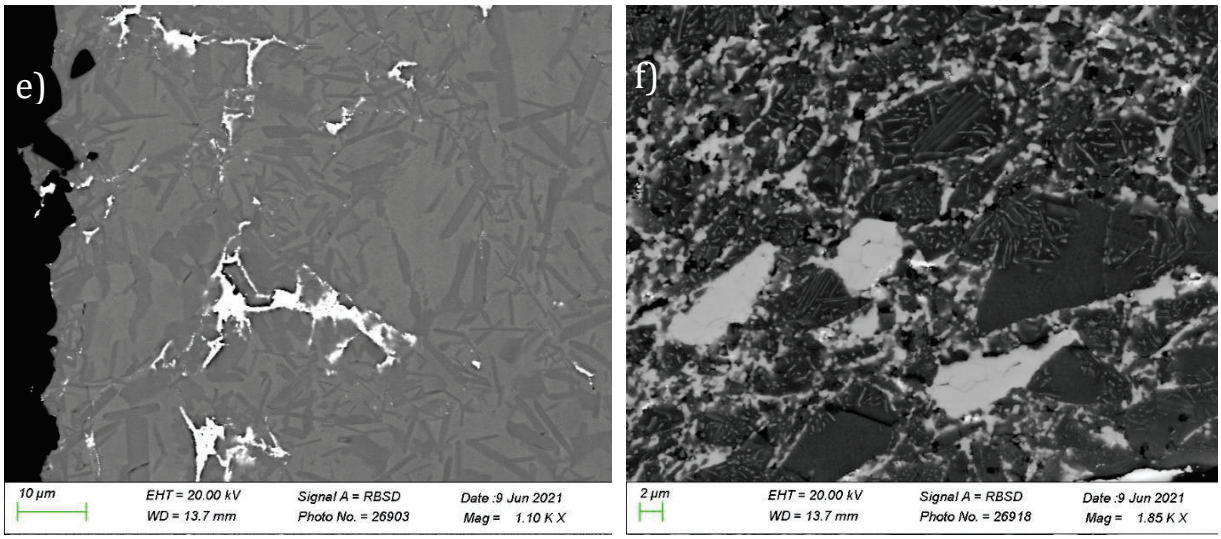

Figure 5.1: Backscattered SEM images of samples recovered from 1200 °C and various pressures. Grains of Pt-Fe alloy (white) can be seen dispersed through all samples. **a)** sample H5128 recovered from 8 GPa, showing only the presence of fper; **b)** sample S7029 recovered from 6 GPa showing clean regions of fper (dark) coexisting with smaller grains of spft (light); **c)** sample Z2077-A recovered from 16 GPa showing prismatic crystals of the O5 phase (light) with fper (dark); **d)** Mg-free sample S7716-A recovered from 6 GPa comprised of regions dominated by wüstite (light) and magnetite (dark) with a texture indicating a back transformation during quenching most likely from Fe_5O_6. Grain boundaries of larger pre-existing grains (~20 µm in diameter) are traced out mainly by magnetite crystals. Finer exsolution of magnetite can also be seen within the brighter areas; **e)** Mg-free sample I1185-B recovered from 30 GPa consists of dark elongate crystals of Fe_5O_6 coexisting with FeO; **f)** sample I1185-A recovered from 30 GPa dominated by a texture indicating a back transformation during quenching from an high-pressure Mg,Fe-oxide coexisting with fper.

In some experiments performed at low fO_2 or with high bulk Fe/(Fe+Mg) ratios an isoferroplatinum (Pt_3Fe) phase instead of the Pt-alloy was detected in the X-ray diffraction patterns. Some experiments were performed only in the fper field to get more accurate fper Fe^{3+}/Fe_{tot} determinations using Mössbauer spectroscopy. The diffraction patterns of most of the experiments in which only fper and Fe-Pt alloy were visible in the SEM images(Figure 5.1a), however, contain also broad peaks that can be indexed with a spinel-ferrite structure (Figure 5.2), suggesting the presence of spft exsolutions similar to what observed in samples synthetised at 1 atmosphere (Chapter 4). Such spinel reflections are even found in samples recovered from

pressures at which the spinel structure is not any more stable (Table 5.2; Figure 5.2) and their presence was confirmed by TEM analysis as described in the next section (5.4.2)

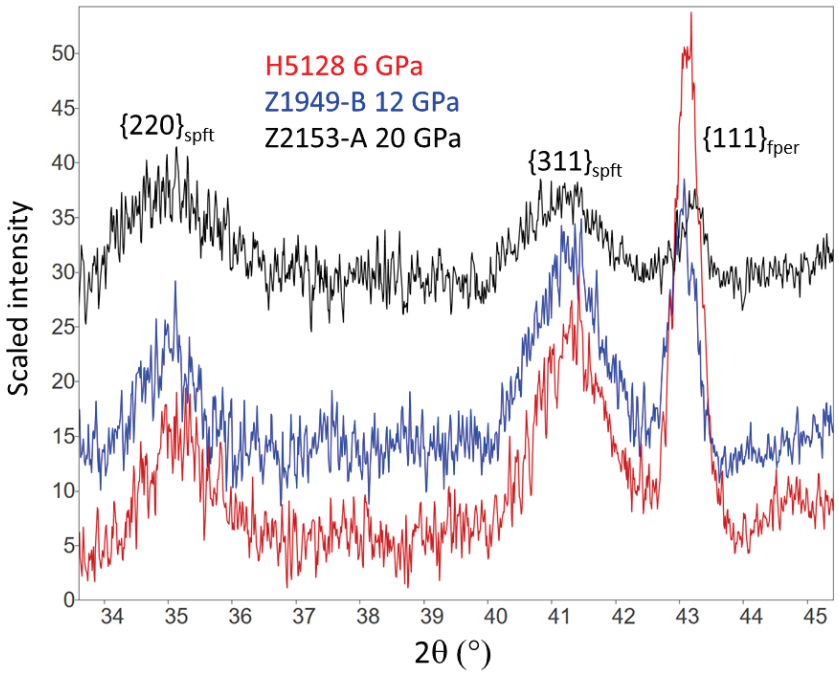

Figure 5.2: Details of the X-ray powder diffraction patterns collected for the samples recovered from experiments conducted at different pressures and at 1200 °C and containing only fper and Pt-Fe alloy. The broad peaks can be assigned to the {220} and {311} reflections of a spinel structure and are visible in all three samples, even that conducted at 20 GPa where the spinel phase is not anymore stable, although they appear broader than those observed for the other two samples, suggesting a smaller particle size. The intensity of the fper reflections is very different among the three samples due to spotty diffraction of the relatively larger fper grains which alter the final integrated intensity.

Experiments containing only fper and Fe-Pt alloy were generally repeated with more Fe_2O_3 added to the starting material until an additional Fe^{3+}-rich phase was formed. EPMA oxygen analyses (Table A.5.1) were used to check the stoichiometry of the Fe^{3+}-rich high *P* phases coexisting with fper. When the stoichiometry is calculated based on the correct total cation content the corresponding oxygen content is typically within 0.1 atoms of the expected value, whereas it is outside of this tolerance if an incorrect stoichiometry is chosen. Such stoichiometry has been then mostly confirmed by means of XRD. In one instance (S7123-B), the oxygen analysis was used to

identify a small amount of the O5 phase that did not appear in the XRD pattern. Oxygen analyses provide only qualitative information, however, on the Fe^{3+}/Fe_{tot} ratios of fper.

The recovered samples from experiments conducted using Fe-rich compositions (starting materials D and E, Table 5.1) appear different from experiments conducted using a Mg-rich bulk composition. Although the assemblages recovered from pressures below 10 GPa also consists of fper (which in the case of samples S7716-A and S7691-B is wüstite) and magnetite, as indicated from the XRD patterns, the texture of the fper grains suggests that a back transformation has occurred. This is particularly clear for the Mg-free samples (Figure 5.1d), where wüstite and magnetite appear to have exsolved from a pre-existing phase, the grain boundaries of which are picked out by grains of magnetite. Fine scale exsolution throughout the assemblage points to a rapid back transformation occurring, most likely, during *T* quenching, indicating very fast kinetics. This has been observed in previous studies (Woodland et al. 2012; Myhill et al. 2016; Woodland et al. 2023) and is possibly due to the proximity of the experimental conditions to the boundary between the $Fe_3^{2+}Fe_2^{3+}O_6$, indicated hereafter as O6, phase and the wüstite + magnetite field. The fine grained exsolution makes it difficult to identify the original phase, however, and the relict grain shapes are unlike the prismatic crystals of the O6 phase. In situ measurements are probably the only way to clarify these phase relations. Assemblages from the bulk composition D recovered from pressures higher than 10 GPa consists only of the O6 phase, whereas in the Mg-free sample I1185-B recovered from 30 GPa a mixture of FeO and Fe_5O_6 is present (Figure 5.1e). On the contrary the texture of the Mg-rich sample I1185-A recovered from 30 GPa is more complicated (Figure 5.1f). The majority of the sample consists of not well defined small grains which appear to be the result of a back transformation from an high-pressure precursor. Among this matrix the large fper crystals present large lamellae. There are also some large bright crystals whose stoichiometry determined by means of EMPA is that of the O4 (sp) phase. The XRD patterns of this sample is dominated by the Al_2O_3 capsule material and the few other diffraction peaks can all be

indexed by the fper unit-cell, therefore a more careful analysis of this sample has been performed using the TEM (see following section).

The nature of the Fe^{3+}- rich phase coexisting with fper varies depending on *P* and bulk composition as can be seen in Figure 5.3 for experiments run at 1200 °C, where the $Fe^{2+}/(Fe^{2+}+Mg)$ ratio derived for each recovered Fe^{3+}-rich phase according to its stoichiometry (Table A.5.1) is plotted. At 6 and 10 GPa, spft coexists with fper over a wide range of $Fe^{2+}/(Fe^{2+}+Mg)$ ratio. For $Fe^{2+}/(Fe^{2+}+Mg) = 1$, as already mentioned, the recovered assemblages recovered from at both 6 and 8 GPa have back transformed to wüstite and magnetite and are plotted with a different symbol.

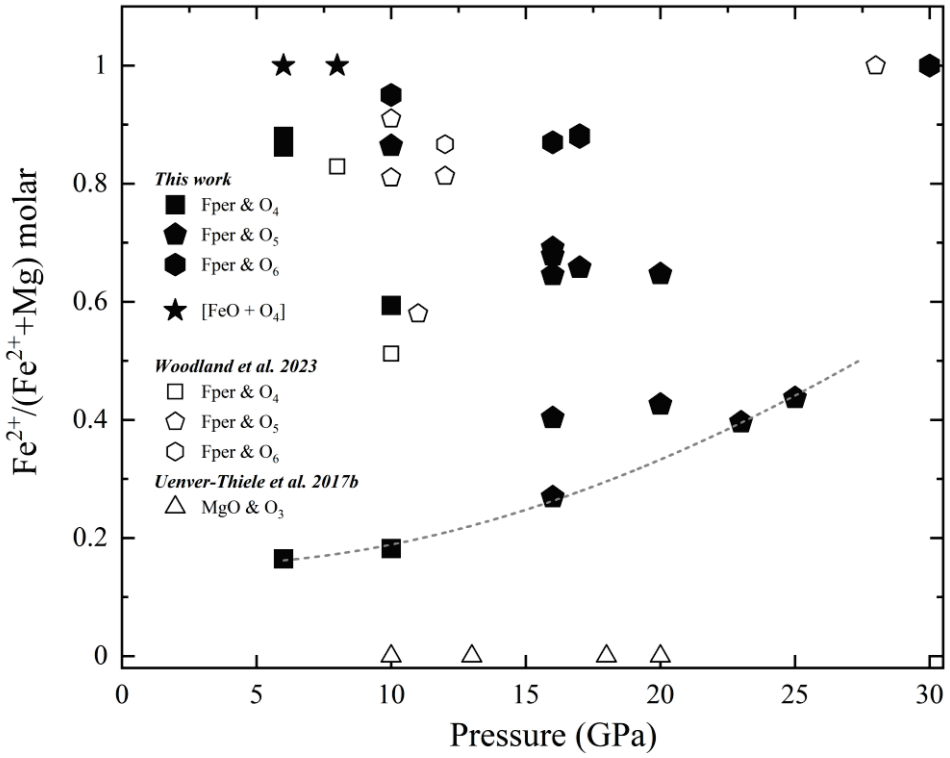

Figure 5.3: The $Fe^{2+}/(Fe^{2+}+Mg)$ ratio of Fe^{3+}-rich oxides coexisting with fper in experiments run at 1200 °C. Filled symbols are from this study and empty symbols are from Woodland et al. (2023) and Uenver-Thiele et al. (2017b). O4 represents $(Fe^{2+},Mg)Fe^{3+}{}_2O_4$; O5 represents the $(Fe^{2+},Mg)_2Fe^{3+}{}_2O_5$ phase, and O6 represents $(Fe^{2+},Mg)_3Fe^{3+}{}_2O_6$. [FeO+O4] indicates experiments conducted with the Mg-free starting material where a higher-pressure phase appears to have back transformed to an assemblage of wüstite and magnetite during quenching. MgO+O3 indicates where Uenver-Thiele et al., (2017b) found an assemblage of periclase + hematite. The dashed grey line marks compositions that were in equilibrium with fper having a Mg/(Mg+Fe) ratios of 0.8-0.9.

At P >10 GPa fper coexists with a O5 phase whose stability field is delimited at high $Fe^{2+}/(Fe^{2+}+Mg)$ ratio by the formation of the O6 phase and at lower ratio by the formation of periclase and hematite, as observed in the study of Uenver-Thiele et al. (2017b). The agreement with the study of Woodland et al. (2023) is very good except at 28 GPa, where their observation of Fe_4O_5 is at odds with Fe_5O_6 being found in this study at 30 GPa. As shown by Woodland et al. (2023), the transition between the O5 phase + Fe_xO field and the O6 field has a positive *P*-*T* slope and this inconsistency might be explained by differences in *T*, as at these conditions *T* uncertainties are of the order of 100 °C. That the O5 field extends to higher *T* at higher *P* is consistent with the observation from this study that the O5 phase is stable at least up to 1800°C at 20 GPa. However, the results of Woodland et al. (2023) also indicate that the O6 field expands towards lower $Fe^{2+}/(Fe^{2+}+Mg)$ ratio with increasing *T*. The grey dashed line in Figure 5.3 indicates compositions of Fe^{3+}-rich oxides in equilibrium with fper with an Fe/(Mg+Fe) of 0.2-0.1, showing that with increasing pressure more Fe^{2+} is partitioning into the high-*P* Fe^{3+}-rich oxide phases. This change in partitioning can be described using an apparent Fe-Mg exchange coefficient:

$$K_D(\text{app}) = ([Fe^{2+}+Fe^{3+}]/Mg)_{fper}/(Fe^{2+}/Mg)_{oxide} \quad (1)$$

which is defined using the total iron content of fper, due to the uncertainties of Fe^{3+}/Fe_{tot} determinations in this phase, as discussed later, but using the Fe^{2+} content of coexisting Fe^{3+}-rich oxides, as this can be determined from the stoichiometry of microprobe analyses. As shown later for a fper Mg/(Mg+Fe) > 0.5, K_D(app) is ~1 in the spft field at 1200 °C, whereas in the O5 field it is in the range 0.4 to 0.2.

5.4.2 TEM observations

TEM lamella were separated from five samples: S7029, Z2151-B, Z2115-B and I1185-A and I1185-B. Fper in samples synthetised at 6 and 20 GPa show a mottled appearance in bright field

(BF) images similarly to what observed in samples synthetised at room pressure (Chapter 4), suggesting the presence of nano-size exsolutions. High resolution imaging of sample S7029 (Figure 5.4a) allows to determine an average grain size of 10 – 12 nm for these exsolutions, moreover the electron diffraction pattern (inset in Figure 5.4a) taken from the same region can be indexed with both unit-cells of fper and a spinel ferrite phase, being the two topotaxial and following the relationship $a_{fper} \cong \frac{1}{2} a_{n-spft}$ as already observed for the Mg-rich samples described in Chapter 4, albeit the grain sizes of the exolutions observed in fper synthetised at room pressure in equilibrium with macroscopic spinel were much larger (i.e. at least 25-30 nm). The exsolutions present in the fper grains recovered from 20 GPa have even a smaller size, on the order of 1-5 nm (Figure 5.4b, note the different scale with respect to Figure 5.4a), independently from the starting composition of the experimental runs (composition A for sample Z2151-B, composition B for sample Z2115-B; Table 5.2) and from the temperature at which these samples have been annealed. The most interesting observation, however, is that such exsolutions appear to have a spinel structure topotaxial with the fper grains from which they have exsolved (inset in Figure 5.4b). The spinel reflections are very weak (note that the brightness of the image in figure 5.4b has been enhanced in order for the reflections to be seen), but they have been observed in fper grains of both samples recovered from 20 GPa. XRD diffraction patterns for these samples show only the presence of the O5 phase together with fper, likely due to the fact that the reflections belonging to the n-spft exsolution are very weak. However, broad reflections which can be attributed to a spinel structure have been observed for sample Z2153-A recovered from 20 GPa and 1800 °C. In this sample only fper and Pt-alloy are present and therefore there is no interference of a O5 phase. The fper grains of the Mg-free sample synthetised at 30 GPa also show very weak diffraction spots that can be indexed with a spinel structure (Figure 5.4c) suggesting that even in this sample topotaxial spinel exsolution occurred during quenching. Note that the image brightness has again been enhanced for clarity and as a consequence the diffraction spot of the spinel phase

appear much stronger than in reality. Unfortunately, due to the thickness of the specimen prepared for TEM analysis, it was not possible to obtain high-resolution images and therefore no information on the grain size of these exsolutions has been obtained. However, if the trend of n-spft grain size with pressure observed between room pressure and 20 GPa remains the same, the n-spft exsolution in fper at 30 GPa may be smaller than 1 nm.

The sample I1185-A synthetised at 30 GPa using a Mg-rich starting composition (Table 5.2), instead, appears completely different from all other samples. Two different areas can be seen in the BF image reported in Figure 5.4d similarly to what already observed in the SEM images (Figure 5.1f): one consists of fper crystals with large lamellae and the other consists of an assemblage of at least two and probably three phases which is likely the result of a back transformation. The electron diffraction pattern of the fper grain containing the large lamellae contains reflections belonging exclusively to the rock-salt structure of ferropericlase, suggesting that the lamellae grew incoherently with respect to fper in spite of their regular pattern. Unfortunately, it was not possible to find a lamella with an orientation which allowed to identify which phase it consisted of. In the back transformed assemblage it is possible to recognise some fper grains with no lamellae, referred to as [fper] in Figure 5.4d, which contains about 4 wt% less Fe (i.e. 6 wt% Fe in total, according to EDXS analyses) than those hosting the large lamellae (10% of Fe according to EDXS analyses). The thickness of the sample unfortunately did not allow for an accurate analysis of the other phases in the assemblages; however, EELS measurements were performed in this area as discussed at the end of the following paragraph.

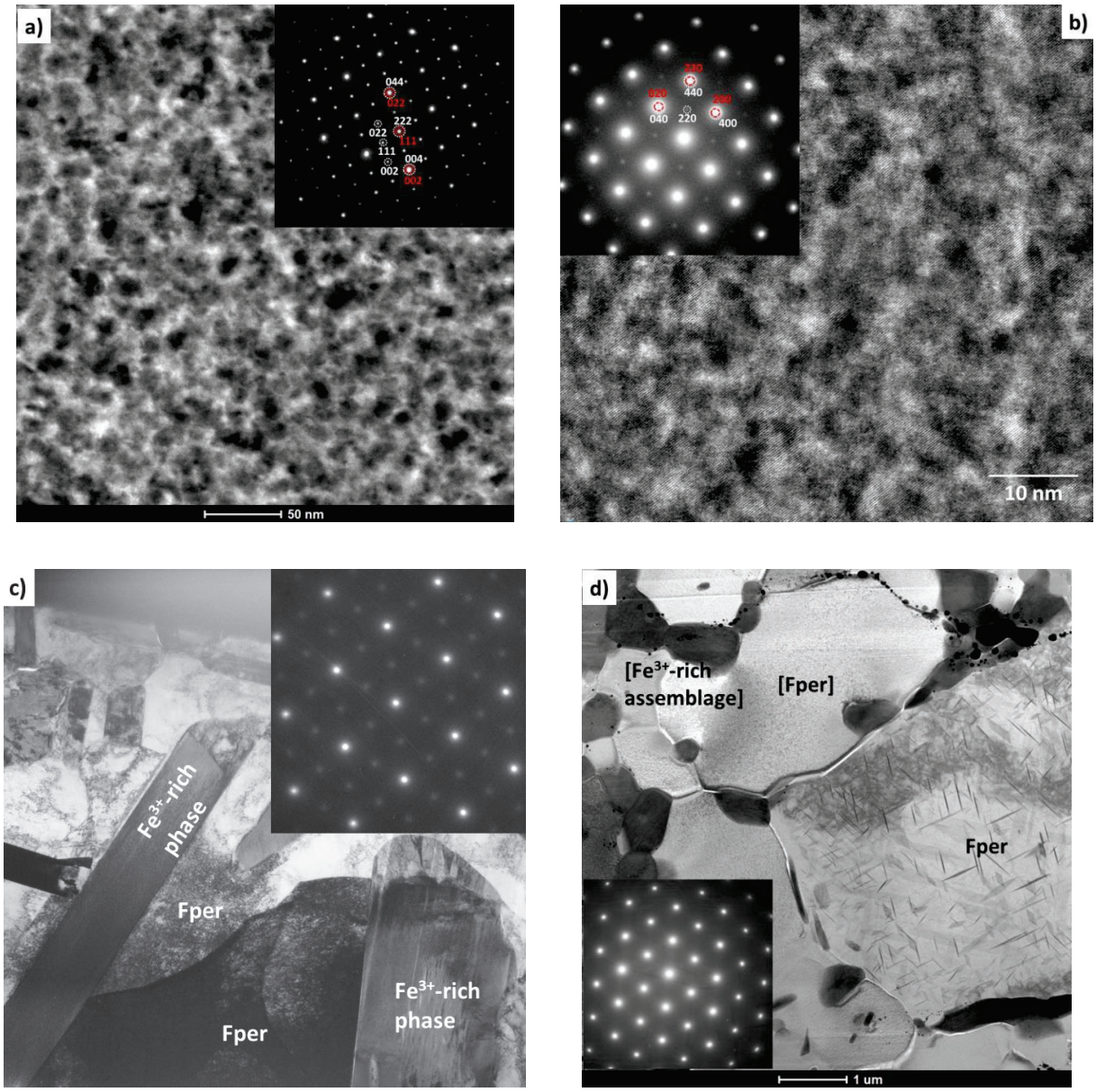

Figure 5.4: High-resolution STEM bright field images of fper grains from **a)** sample S7029 recovered from 6 GPa and **b)** sample Z2115-B recovered from 20 GPa with corresponding selected area electron diffraction patterns. Both fper grains show the presence of nm sized exsolutions. The corresponding electron diffraction patterns consist of both reciprocal lattices of fper (in red) and of the exsolution (in white) which can be indexed using the spinel structure (n-spft). Note that the grain size of the exsolution in sample Z2115-B is smaller (~5 nm) than that of the exsolution in sample S7029 (~10 nm). **c)** Bright field TEM image of the Mg-free sample I1185-B recovered from 30 GPa and selected area electron diffraction pattern taken from one of the fper grains. The depicted reciprocal lattice has the same orientation as that reported for sample S7029. Weak n-spft reflections are visible even in this sample. **d)** Bright field TEM image of sample I1185-A recovered from 30 GPa and selected area electron diffraction pattern taken from the fper grain containing the large lamellae which, however, do not appear in the electron diffraction pattern. The Fe^{3+}-rich assemblage is likely a back transformation of a high-pressure unquenchable phase

An example of EELS spectra collected for fper grains of all five samples are reported in Figure 5.5. The Fe L_3 edge of sample S7029 appears very broad as already observed for the fper samples synthetised at room pressure (Chapter 4) and has been fitted using the same procedure described in section 4.2.6, using four Gaussian profiles (see Figure 4.2). As pressure increases the L_3 edge maximum moves toward lower energies, suggesting an increase in Fe^{2+} content at the expense of Fe^{3+}. For these spectra the small Fe^{3+} signal at about 707.7 eV could not be resolved and therefore only three Gaussian profiles have been used for fitting the EELS signals. The resulting Fe^{3+}/Fe_{tot} ratios, calculated as average among the different EELS spectra collected for each sample are listed in Table 5.3. Note that the uncertainties reported represent only the standard deviation of the different measurements performed for each sample, however the real uncertainties are larger and may be on the order of at least 5%. The Fe^{3+} content in fper decreases with increasing pressure. The larger Fe^{3+}/Fe_{tot} ratio of sample Z2151-B with respect to sample Z2115-B (both samples have been recovered from 20 GPa) is likely due to its higher temperature of synthesis (1600 °C instead of 1200 °C for sample Z2115-B). For sample I1185-A the value reported in Table 5.3 is that obtained for the fper grains containing the large lamellae. An EELS spectrum was collected also for the [fper] grain visible in Figure 5.4d. The analysis of this spectrum reveals that not only this [fper] has a total Fe content smaller than the fper grains containing large lamellae, but also it has an Fe^{3+}/Fe_{tot} ratio of only 0.06 (3) further confirming that it likely resulted from a back transformation from an high-pressure precursor. The EELS spectrum collected in the region adjacent to [fper] (Figure 5.4d) suggests that the rest of the assemblage belonging to the Fe^{3+}-rich phase which coexisted with fper at 30 GPa and 1200 °C has an Fe^{3+}/Fe_{tot} ratio of ~ 0.5. However, such value is very likely an average value given that some part of this assemblage has the O4 stoichiometry according to the chemical analysis and therefore an Fe^{3+}/Fe_{tot} ratio closer to 1. At present it is therefore difficult to conclude what other phase is present in this assemblage and therefore to infer what high-pressure phase was present at the conditions of synthesis. The EELS

spectra collected for the Fe^{3+}-rich phase present in sample I1185-B (Figure 5.1e; Figure 5.4c) result in an Fe^{3+}/Fe_{tot} ratio of 0.41 (5) in agreement with the observation that this phase has the O6 stoichiometry.

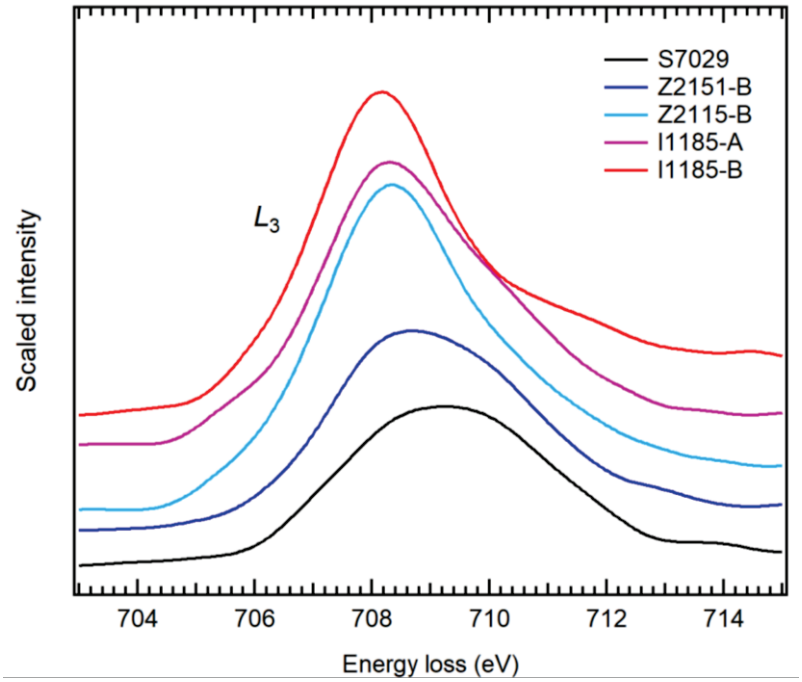

Figure 5.5: Example of Fe L3 edges collected for fper grains belonging to the five samples analysed in this study. The relative low signals of samples S7029, Z2151-B and I1185-A are due to the small iron contents present in these samples, ranging between 0.09 and 0.16 atoms per formula units. As pressure increases the maximum of the energy loss moves toward lower energies, suggesting that fper becomes more reduced at high-pressure.

5.4.3 Mössbauer spectroscopy Fe^{3+}/Fe_{tot} ratio determinations

Mössbauer spectra were collected for the majority of samples, many of which contained absorption from multiple phases. Fper was fitted with two sets of doublets for Fe^{2+} and a singlet for Fe^{3+}, all with Pseudo-Voight line shapes, as for the room pressure samples described in Chapter 4, Section 4.3.3 and as in previous studies (e.g. Dobson 1998; Mccammon et al. 1998; Otsuka et al. 2010, 2013). The obtained centre shift (CS) for the Fe^{2+} doublet (Table A.5.3) varied no more than 0.04

mm/s across all samples and agrees well with the typical value of 0.93 mm/s for the Fe^{2+} in octahedral site (Waychunas 1983; Dobson 1998; McCammon et al. 2004; Dyar et al. 2006; Otsuka et al. 2010; Nestola et al. 2016). For the majority of Mg-rich samples (synthetised from the bulk composition A and B) the Fe^{3+} CS values indicate tetrahedral site occupancy; however, for Fe-rich samples the CS values are more and more consistent with octahedral site occupancy (Table A.5.3; McCammon et al. 2004; Otsuka et al. 2010). The variation of the QS as a function of Cs for all samples investigated in this study are plotted together with literature data in Figure A.5.3.

Table 5.3: Fe^{3+}/Fe_{tot} ratio determined from Mössbauer spectroscopy and EELS

Sample	Fe^{3+}-rich phase	Fe^{3+}/Fe_{tot} in Fp	Fe^{3+}/Fe_{tot} with n-spft	EELS values
S7029	Spft	0.34 (4)		0.58 (6)
Z2038	n-spft	0.16 (5)	0.21 (8)	
H5128	n-spft	0.14 (5)	0.33 (8)	
S7004	n-spft	0.25 (6)	0.44 (11)	
S7377	Spft	0.26 (5)		
S7180	n-spft	0.22 (6)	0.63 (8)	
S7204	n-spft	0.20 (5)	0.46 (9)	
Z1949-B	n-spft	0.17(5)	0.50 (8)	
S7382	O_5 phase	0.15 (4)		
S7006	O_5 phase	0.24 (5)		
S7016	O_5 phase	0.11 (5)		
Z2151-B	O_5 phase	0.12 (5)		0.27 (1)
Z2153-B	O_5 phase	0.14 (6)		
H4792	O_5 phase	0.23 (5)		
S7410	O_5 phase	0.09 (3)		
S7123-B	O_5 phase	0.13 (5)		
I1185-A	[O_4]			0.15 (3)
S7470	Only Fper	0.11 (2)		
H5164	Only Fper	0.09 (2)		
S7510	n-spft*	0.13 (2)		
S7509-B	n-spft	0.12 (4)	0.34 (9)	
S7716-B	n-spft	0.12 (3)	0.41(8)	
Z2116	n-spft	0.15 (5)	0.40 (10)	
S7691-A	n-spft	0.09 (3)	0.28(7)	
Z2155-B	n-spft	0.11 (3)	0.34 (8)	
Z2155 A	n-spft	0.11 (2)	0.21(8)	
S7216-B	n-spft	0.13 (2)	0.36 (8)	
S7216-A	n-spft	0.13 (2)	0.37 (8)	
Z1949-A	n-spft	0.10 (2)	0.32 (8)	

Z2122-B	O_5 phase	0.13 (5)		
Z2117-B	O_5 phase	0.13 (5)		
Z2115-B	O_5 phase	0.15 (5)		0.16 (2)
Z2121-A	O_5 phase	0.18 (6)		
Z2151-A	O_5 phase	0.15 (5)		
Z2153-A	Only Fper	0.25 (2)		
H5189-A	n-spft	0.14 (3)	0.38 (10)	
S7495-A	Spft	0.12 (3)		
H5190-A	O_5 phase	0.14 (6)		
Z2077-A	O_5 phase	0.19 (5)		
H5189-B	Spft	0.13 (4)		
S7509-A	Spft	0.11 (4)		
S7604-A	Spft	0.08 (5)		
S7716 A	Spft	0.05 (3)		
S7691-B	Spft	0.07(3)		
I1185- B	O_6 phase			0.03 (1)
Note:* a very small magnetic signal is visible in the MS, indicating the presence of n-spft exsolution, but it cannot be fitted suggesting a limited amount of exsolved phase				

Many of the experiments performed below 12 GPa contained only fper and Fe-Pt alloy when observed at the SEM. The signal of Fe^0 in the alloy, expected as a singlet at CS values ranging between -0.65 and -0.11 (Preston et al.1962), was not observed in the present study, likely due to the low concentration of Fe in the alloy in the recovered experimental charges. However, all but two of the Mössbauer spectra contain magnetic sextets (Figure 5.6a) originating from n-spft exsolutions, as observed in the TEM samples. Such sextets have been fitted following the procedure described in details in Chapter 4, Section 4.3.3 and the results are reported in Table A.5.3. In order to obtain the Fe^{3+} content in fper at high-pressure and high-temperature, the fper Fe^{3+}/Fe_{tot} ratio needs, therefore, to be corrected taking into account the contribution of these exsolutions. To this end the valence state of the fitted sextets was considered following the procedure described in Chapter 4, Section 4.3.3. Corrected and uncorrected fper Fe^{3+}/Fe_{tot} ratios are reported in Table 5.3, while the fitted Mössbauer hyperfine parameters are reported in Table A.5.3. N-spft exsolutions are present also in fper grains coexisting with the O4 phase (Figure 5.4a), however, it was not possible to resolve the n-spft signals in the Mössbauer spectra, since these are dominated by the intense signal of the Spft phase (Figure 5.6b).

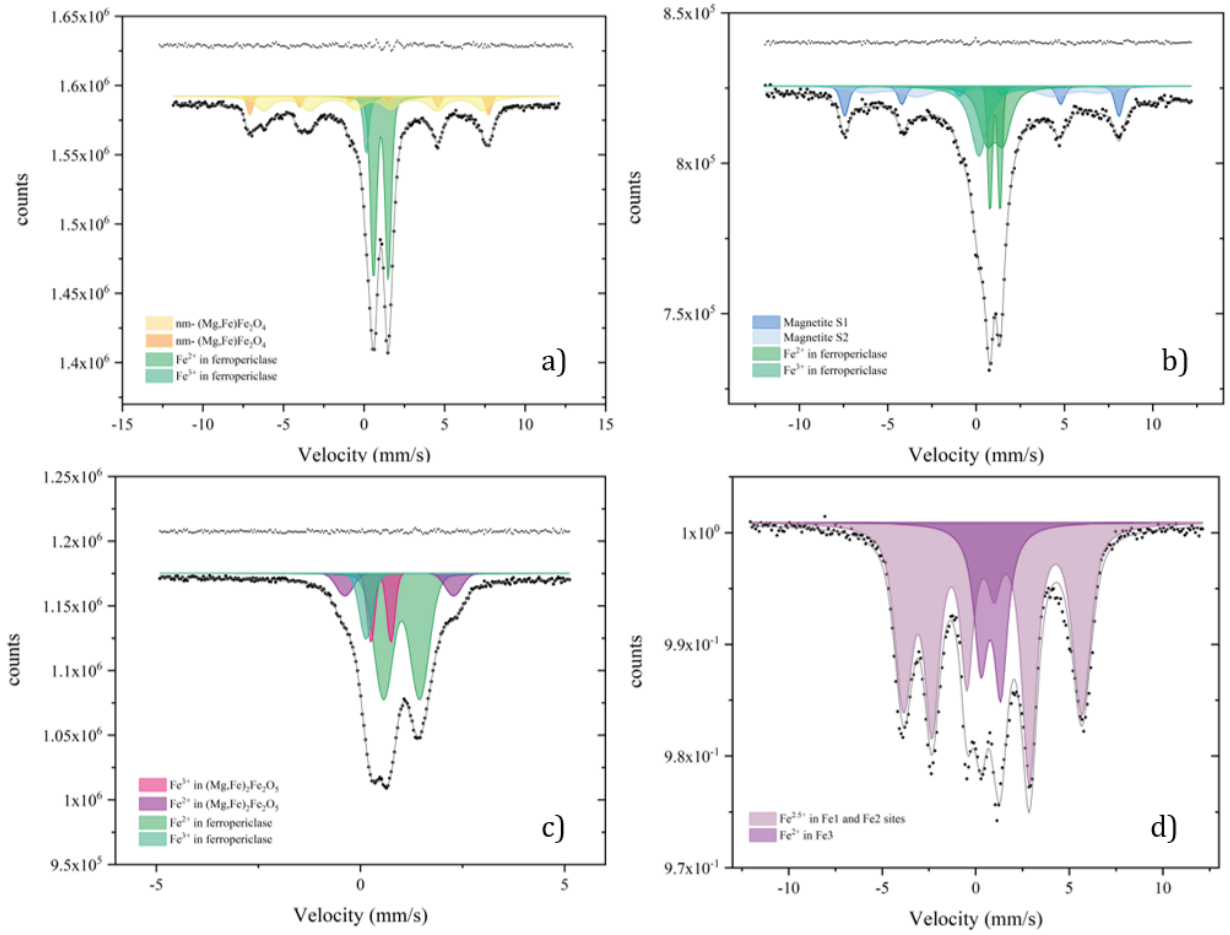

Figure 5.6: The two doublets of Fe^{2+} (green) and the singlet of Fe^{3+} (light green) of fper are present together with **a)** a broad magnetic sextet fitted with two contributions which can be assigned to a n-spft exsolution in sample S7509-B; with **b)** a well defined sextets also fitted with two contribution S1 and S2 (blue and light blue, respectively) which can be assigned to the coexisting spft phase for sample S7029; and with **c)** two doublets belonging to the O5 phase in sample Z2115-B. No fper is present in **d)** where the first fitted MS spectrum of the O6 phase is presented. In this spectrum a magnetic octet component (pink) is fitted to account for $Fe^{2.5+}$ in the octahedral sites, whereas the purple doublet represents Fe^{2+} in the trigonal prism of this oxide structure.

EELS measurements, which depend on the valence state of Fe present both in fper and in n-spft, show a higher Fe^{3+}/Fe_{tot} ratio for sample S7029 than that obtained from analysis of its Mössbauer, implying that a thorough characterisation of the fper grains is necessary to obtain accurate Fe^{3+} contents. Two samples, S7470 and H5164, synthetised at 6 GPa and 1200 °C, do not present any broad magnetic sextets originating from n-spft exsolution in fper. Their Fe^{3+}/Fe_{tot} ratio of 0.11 and

0.09, respectively, may mark the limit at which Fe^{3+} can be quenched into fper without causing exsolution, at least at these pressure and temperature conditions.

Samples synthetised at pressure above 12 GPa and containing the O5 phase have no magnetic component due to the presence of magnesium in the octahedral site, which likely interrupts the long-range magnetic ordering which has been reported for Fe_4O_5 (Ovsyannikov et al.2018). This phase was fitted with two quadrupole doublets (Figure 5.6c) corresponding to Fe^{2+} (CS= 0.93±3 mm/s; QS= 2.7±2 mm/s) and Fe^{3+} (CS= 0.49± 6 mm/s; QS= 0.51±3 mm/s) sites. The Fe^{3+} doublet of the O5 phase overlaps with the fper Fe^{3+} singlet resulting in large uncertainties in the fper Fe^{3+}/Fe_{tot} ratio particularly for samples with significant O5 contents. At pressures above 12 GPa, however, TEM SAED patterns indicate that n-spft exsolution still occurs in fper grains. The lack of a magnetic component in the Mössbauer spectra is most likely because the n-spft exsolution sizes are < 5 nm, as seen in Figure 5.4b. At these grain sizes there is a collapse in the magnetic ordering to a superparamagnetic state and the sextet contracts to a central doublet at room temperature (Hartridge et al. 1997; Goya et al. 2003; Morup et al. 1976; Fock et al. 2018; Hah et al. 2021) that then contributes to the fper Fe^{3+} intensity. The smaller grain size of the n-spft exsolution for samples synthetised at high pressures also might be the reason why the MS of sample Z2153-A recovered from 20 GPa and 1800 °C does not contain any magnetic signal in spite of the presence of spinel reflections in the XRD pattern (Figure 5.2).

The phase assemblage recovered from syntheses performed with the bulk composition $(Mg_{0.05}Fe_{0.95})O$ at pressures >10 GPa, resulted in an O_6 phase, with no coexisting fper. The MS spectrum in Figure 5.6d is the first reported for an O_6 oxide. The spectrum consists of two components: a magnetic octet corresponding to $Fe^{2.5+}$ at the Fe1 and Fe2 octahedral sites (CS = 0.65 mm/s), and a doublet corresponding to Fe^{2+} in the Fe3 trigonal prism (CS = 0.88 mm/s) of the Fe_5O_6 structure (Lavina and Meng 2015). In this case the presence of the less than 3 wt% of

Mg is not sufficient to alter the magnetic order. The obtained Fe^{3+}/Fe_{tot} of 38% is in quite good agreement with the 43% value calculated from the EPMA measurements.

5.4.4 Thermodynamic modelling

By fitting pressure dependent thermodynamic terms using the high *P* dataset, the room pressure model presented in Chapter 4 can be extended to allow the calculation of fper Fe^{3+}/Fe_{tot} at pressures consistent with at least the top of the lower mantle. Moreover, by incorporating the coexistence of spft and the O5 phase, additional constraints are added to the model and the conditions at which Fe^{3+}-rich oxides would exsolve from fper can be calculated. This allows the fO_2 stability field of fper to also be defined at high *P*-*T* conditions.

The model is constructed and refined as in Chapter 4. The fO_2 of each experiment is calculated using the composition of the Pt-Fe alloy and the equilibrium:

$$2Fe_{(Alloy)} + O_2 \leftrightarrow 2\ FeO_{(Fper)} \qquad (2)$$

Although the experiments also contain Ni, at high pressure conditions the amount of Ni entering the alloy is < 1 wt.% so the alloy is assumed to be a Pt-Fe binary, with activity composition relations taken from Kessel et al. (2001). Although room *P* and *T* unit-cell data for the Pt-Fe alloy (Gudmundson and Holloway 1993) imply a pressure dependent contribution to the excess Gibbs energy of mixing, $\Delta_m G^{ex}$, of approximately 80 J/kbar, the model is more consistent with the experimental data if this value is assumed to be zero. This assumption results in slightly higher oxygen fugacities that are, for example, 0.75 log units higher at 30 GPa. Although there is evidence for an isoferroplatinum (Pt_3Fe) phase being produced in some experiments, these were mainly at either very low fO_2 or in experiments with high Fe contents that are not crucial for the modelling. The Pt_3Fe phase was likely present also in the calibration experiments of Kessel et al. (2001) and it appears that this had no effect on the relationship between the fO_2 and the alloy composition.

The fper $\Delta_{\mathrm{m}}G^{\mathrm{ex}}$ is described with the subregular expression,

$$\Delta_{\mathrm{m}}G^{\mathrm{ex}} = X_{\mathrm{FeO}}X_{\mathrm{FeO_{1.5}}}q^{00}_{\mathrm{FeO,FeO_{1.5}}} + X_{\mathrm{FeO}}\mathrm{X}_{\mathrm{FeO_{1.5}}}(1 - X_{\mathrm{FeO_{1.5}}})q^{10}_{\mathrm{FeO,FeO_{1.5}}} + X_{\mathrm{FeO}}X_{\mathrm{MgO}}q^{00}_{\mathrm{FeO,MgO}} \quad (3)$$
$$+ (X_{\mathrm{FeO_{1.5}}})^2 X_{\mathrm{MgO}}\mathrm{q}^{10}_{\mathrm{FeO_{1.5},MgO}} + \mathrm{X}_{\mathrm{MgO}}X_{\mathrm{FeO_{1.5}}}(1 - X_{\mathrm{FeO_{1.5}}})^2 q^{02}_{\mathrm{FeO_{1.5},MgO}}$$

where the five non-ideal interaction parameters, q, have P dependent terms fitted to the experimental data. The activity coefficients are then calculated similarly to as here reported for example for FeO:

$$RT\ln\gamma^{\mathrm{Fper}}_{\mathrm{FeO}} = \Delta_{\mathrm{m}}G^{\mathrm{ex}} - X_{\mathrm{FeO_{1.5}}}\left(\frac{\delta\Delta_{\mathrm{m}}G^{\mathrm{ex}}}{\delta X_{\mathrm{FeO_{1.5}}}}\right)_{\mathrm{MgO}} - X_{\mathrm{MgO}}\left(\frac{\delta\Delta_{\mathrm{m}}G^{\mathrm{ex}}}{\delta X_{\mathrm{MgO}}}\right)_{\mathrm{FeO_{1.5}}} \quad (4)$$

Pressure dependencies of spft interaction parameters were also refined. Standard state Gibbs free energies of formation were determined using thermodynamic data from Holland and Powell (2011), Hidayat et al. (2015) and Myhill et al. (2015). Equation of state terms for MgO, FeO and Fe were refined using data from Tange et al. (2009), Campbell et al. (2009) and Dorogokupets et al. (2017). The room P and T volume (V_o) of the fper $FeO_{1.5}$ end-member was initially taken from McCammon and Liu (1984) but was allowed to vary in the refinement, as was the thermal expansion term for fper $FeO_{1.5}$.

The model was first refined using the experimental data on the composition of fper coexisting with spft up to 10 GPa by refining P dependent terms until model differences with experimental values of fper-spft K_D(app), fper Fe^{3+} and log fO_2 were minimized. The coexisting compositions are determined by the model at spft saturation using the equilibria:

$$MgFe_2O_{4(Spft)} + FeO_{(Fper)} \leftrightarrow Fe_3O_{4(Spft)} + MgO_{(Fper)}, \quad (5)$$

and

$$FeO_{(Fper)} + 2FeO_{1.5(Fper)} \leftrightarrow Fe_3O_{4(Spft)}, \quad (6)$$

In this way the fO_2 is also constrained independently in the model by the equilibria:

$$4FeO_{(Fper)} + O_2 \leftrightarrow 4FeO_{1.5(Fper)} \quad (7)$$

and

$$3FeO_{(Fper)} + 0.5O_2 \leftrightarrow Fe_3O_{4(Spft)} \quad (8)$$

and can be evaluated against the results obtained using equilibrium (2). Experiments containing only fper and Pt-Fe alloy were also used in the refinement by modelling the experimental fper composition using equations (2) and (7). The thermodynamic properties of spft end-members are very well established and for the magnesioferrite end-member are excellently constrained by the breakdown reaction to $MgO + Fe_2O_3$ determined by Uenver-Thiele et al. (2017) between 8 and 10 GPa.

In a second phase of the refinement coexisting fper and O5 phase compositions were modelled and compared with the experimental data using equilibria analogous to (5) and (6) but replacing spft components with those of the O5 phase. End-member properties for Fe_4O_5 were constrained from the phase relations of the reaction $4Fe_3O_4 = 2Fe_4O_5 + 2Fe_2O_3$ (Woodland et al. 2012) and for the $Mg_2Fe_2O_4$ endmember from the reaction $2MgO + Fe_2O_3 = Mg_2Fe_2O_5$ (Uenver-Thiele et al. 2017a;b). To obtain a better fit with the experimental Fe-Mg partitioning data it was necessary to push the Fe_3O_4 stability field to the upper limit in pressure defined by the phase relation uncertainties. Including the O5 phase in the model also allows an independent assessment of the experimental fO_2 to be obtained from the equilibrium:

$$4FeO_{(Fper)} + 0.5O_2 \leftrightarrow Fe_4O_{5(O5)} \quad (9)$$

No improvement in the model fit was obtained by including non-ideal Fe-Mg mixing terms for the O5 phase. The O6 phase was not included in the model because its stability field is limited and it would not provide further useful constraints. All standard state data and mixing terms are reported in Tables A.5.4 and A.5.5.

Only three of the five fper interaction parameters were found to require pressure dependent terms in the refinement, as reported in Table A.5.5. Of these $q^{00}_{\text{FeO-MgO}}$ was fixed at a value consistent with that determined by Frost (2003) using Fe-Mg partitioning between fper, garnet and ringwoodite. There is some trade-off between the pressure dependence of the fper interaction parameters and the V_0 of the fper $FeO_{1.5}$ component, however, the refinement that fitted the observations with the smallest interaction parameter pressure dependences was favoured.

Figure 5.7a shows calculations using the resulting thermodynamic model for the fO_2 at which fper is in equilibrium with spft at 6 GPa and the O5 phase at higher pressures. The model is compared with the experimental fO_2, determined with the Fe-Pt sliding redox sensor. Although the experiments at 30 GPa did not contain the O5 phase, the data of Woodland et al. (2023) indicate that the O5 stability field is relatively close to these experimental conditions and the Gibbs free energy differences between the O5 phase and the O6 and HP-$(Mg,Fe)Fe_2O_4$ phases are likely to be relatively small. The agreement between the experimental oxygen fugacities and those predicted by the model is very good. If excess molar volumes of mixing for the Fe-Pt alloy were used to determine a P dependence of the alloy, $\Delta_m G^{ex}$, then the calculated oxygen fugacities would decrease, which would cause greater deviation with the model. The model fO_2 values are actually well constrained by equilibria between fper and either spft or O5 phases, which most likely indicates that at the temperature of interest, the Fe-Pt excess molar volumes are much smaller than at room temperature, possibly due to invar effects (Liot and Hooley 2012).

As can be seen in Figure 5.7b, the model is able to consistently reproduce the Fe^{3+}/Fe_{tot} ratio of fper coexisting with either spft or the O5 phase between room pressure and 30 GPa. Mössbauer measurements at 6 GPa have large uncertainties due to overlaps between sextets originating from both n-spft exsolution and coexisting spft.

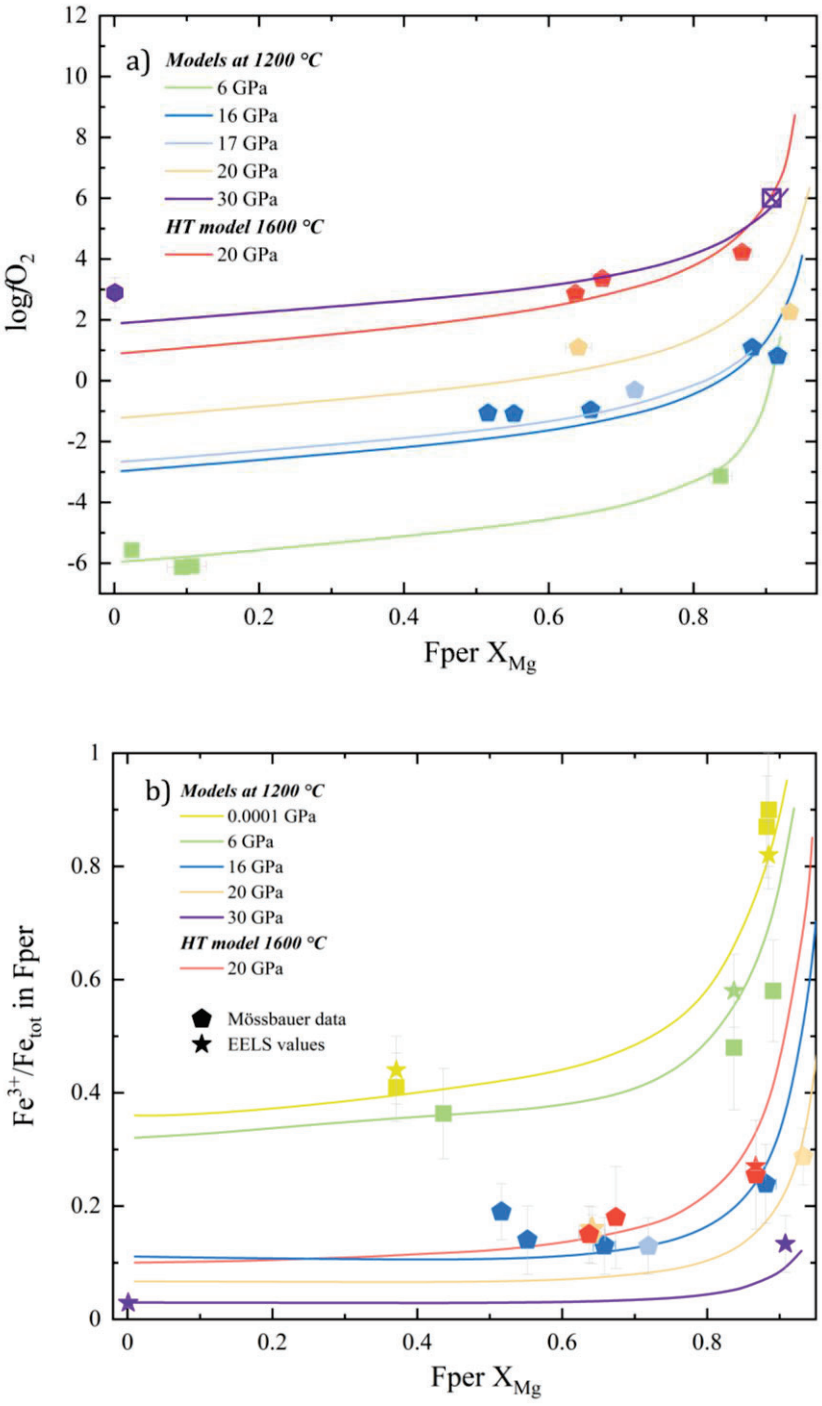

Figure 5.7: **a)** The fO_2 determined using the Fe-Pt alloy redox sensor for experiments where fper coexisted with spft (6 GPa; square symbols) and the O5 phase (16-20 GPa; pentagons). Solid curves are calculated for the same equilibria using the thermodynamic model. At 30 GPa the coexisting phases are O6 (hexagon) and an unquenchable (square with cross) phases, but the model assumes the O5 phase is present. **b)** The measured Fe^{3+}/Fe_{tot} ratios of fper coexisting with Fe^{3+}-rich oxides. Same symbols as in **a)**. Data are compared with the calculations from the thermodynamic model.

At higher pressures, however, the fper Mössbauer signal can be well resolved from the O5 pattern, even though the signals overlap to some extent (Figure 5.6c). There is good agreement with the model, except in a few instances where the proportion of the O5 phase in the sample is relatively high. EELS measurements are generally in good agreement with the model, except one measurement at 20 GPa and 1200 °C, where the measured Fe^{3+}/Fe_{tot} ratio is outside of the measurement uncertainties. The overall agreement between the measured fper Fe^{3+}/Fe_{tot} ratios and the thermodynamic model can be assessed in Figures 5.8a and 5.8b for experiments performed at pressures below and above 10 GPa respectively. A number of the experiments from below 10 GPa were performed at fO_2 conditions lower than the spft field, where Mössbauer spectra contain only signals from fper or from fper and exsolved n-spft. These samples are all in very good agreement with the model, whereas samples that also coexisted with macroscopic spft show a larger deviation. Similarly, in Figure 5.8b the three samples that show a greater deviation from the model contained a relatively large proportion of the O5 phase.

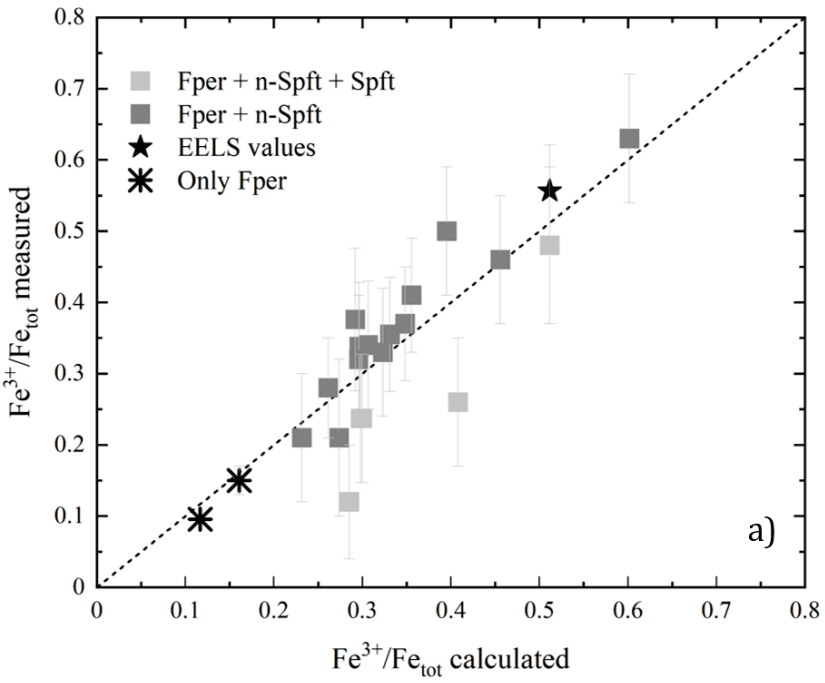

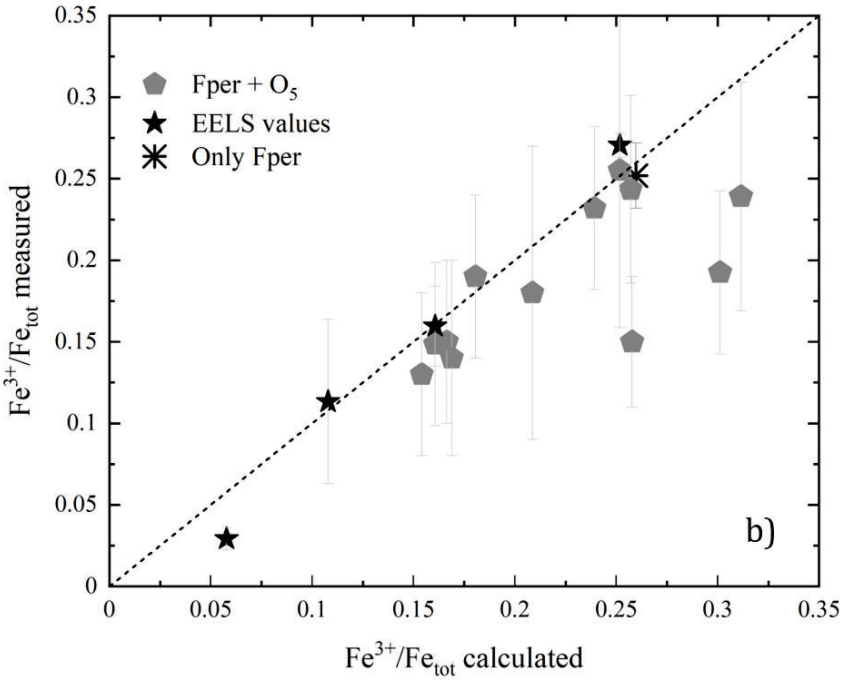

Figure 5.8: **a)** Comparison between measured fper Fe^{3+}/Fe_{tot} ratios and those calculated using the thermodynamic model at the experimentally determined fO_2, for experiments performed below 10 GPa. All measurements, other than those indicated as EELS, were made using Mössbauer spectroscopy. Many of these experiments were performed at oxygen fugacities below the spft stability field and therefore some Mössbauer spectra contain only fper and have the smallest uncertainties or contain fper and n-spft exsolution, where the Fe^{3+}/Fe_{tot} ratios have been recombined and the uncertainties are therefore slightly larger. Samples that also coexisted with macroscopic spft have the largest uncertainties. **b)** Same comparison as in **a)** this time made for experiments performed above 10 GPa, where the majority of samples coexist with the O5 phase.

Figure 5.9 shows experimental values of the fper-spft and fper-O5 K_D(app), as defined by equation (5), describing the Fe-Mg partitioning between the coexisting oxides. The model is in reasonable agreement with the experimental values over the entire pressure and temperature range. The K_D(app) uses the total Fe content of fper as measured by EPMA, so the m odel must reproduce the total Fe^{2+}+Fe^{3+} in fper in order to predict the correct value. This makes K_D(app) sensitive to the fper Fe^{3+}/Fe_{tot} ratio but not dependent on the uncertainties involved in its measurement. K_D(app) decreases with increasing pressure which means the coexisting Fe^{3+}- rich oxide becomes more Fe^{2+}-rich, as indicated by the dashed curve in Figure 5.3 for fper with X_{Mg} between 0.8-0.9.

Although there are some outliers in the experimental data, mainly caused by the difficulty in determining the fper Fe^{3+}/Fe_{tot} ratio, the experimentally determined fO_2, the fper Fe^{3+}/Fe_{tot} ratio and K_D(app) provide three independent constraints on the pressure dependent thermodynamic properties, that should, therefore, be well optimised in the model.

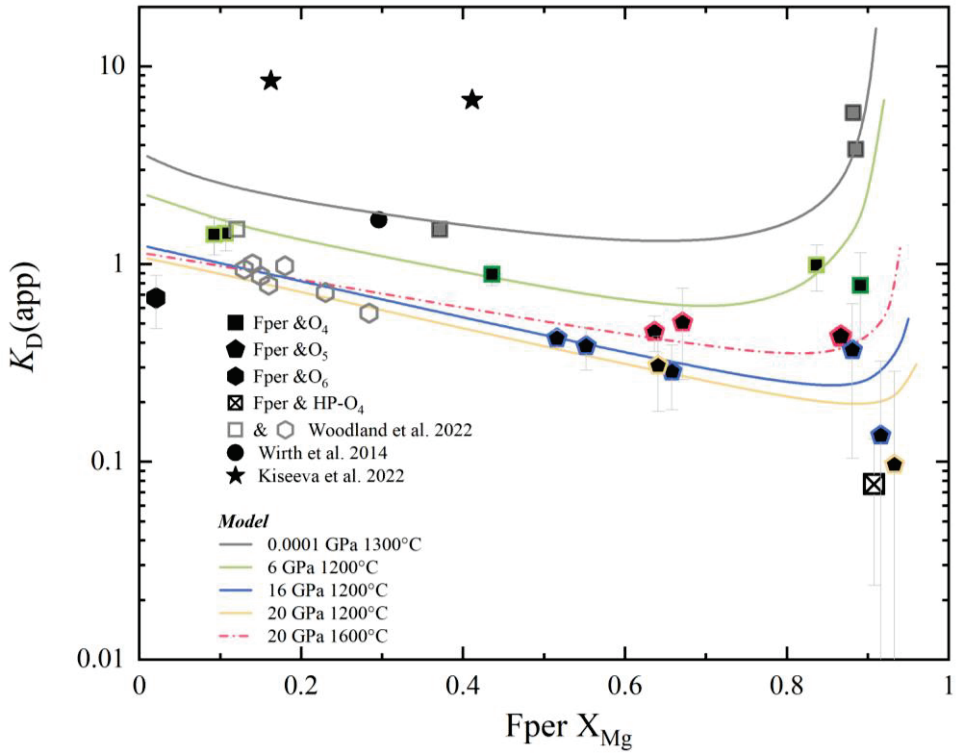

Figure 5.9: The apparent Fe-Mg distribution coefficient K_D(app), as defined in equation (1), for fper Fe-Mg exchange with coexisting Fe^{3+}-rich oxides. The data are from the conditions indicted by the colour coding of the thermodynamic model calculations (solid and dashed lines). The experimental value from Woodland et al. (2023) is from 1200 °C and 8 GPa. Data at 10 GPa are indicated by darker green squares but the model calculation is not pressure dependent at these conditions and is nearly coincident with the 6 GPa curve. The circle indicates an analysis from a fper inclusion in diamond showing spft exsolution (Wirth et al. 2014). The black stars indicate natural ferropericlase inclusion measured by Kiseeva et al. (2022).

5.4.5 Partitioning of Cr, Mn and Ni between fper and multi-valent Fe-oxides

Figure 5.10 shows partition coefficients for three minor elements between fper and coexisting Fe^{3+}-bearing oxides. For partitioning involving any particular phase there does not appear to be a strong change with either *P* or *T*. Mn shows one of the clearest overall trends with the MgO content of fper, caused likely by an increase in Mn valence state with increasing MgO, which corresponds to increasing fO_2. The O5 and O6 phases show strong differences in partitioning for Mn at low Mg-contents. There appears to be some tendency for higher D_{Cr} values for the O5 phase and particularly for the [O4] phase resulting from the back transformation of the unquenchable high-pressure precursor present in sample I1185-A at 30 GPa. This [O4] phase also has higher D_{Ni} values and to a lesser extent D_{Mn}.

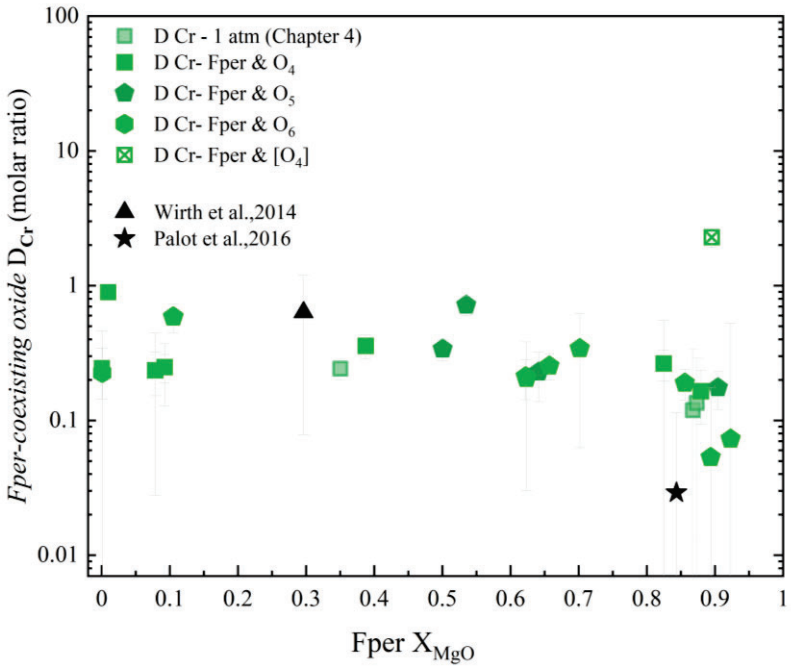

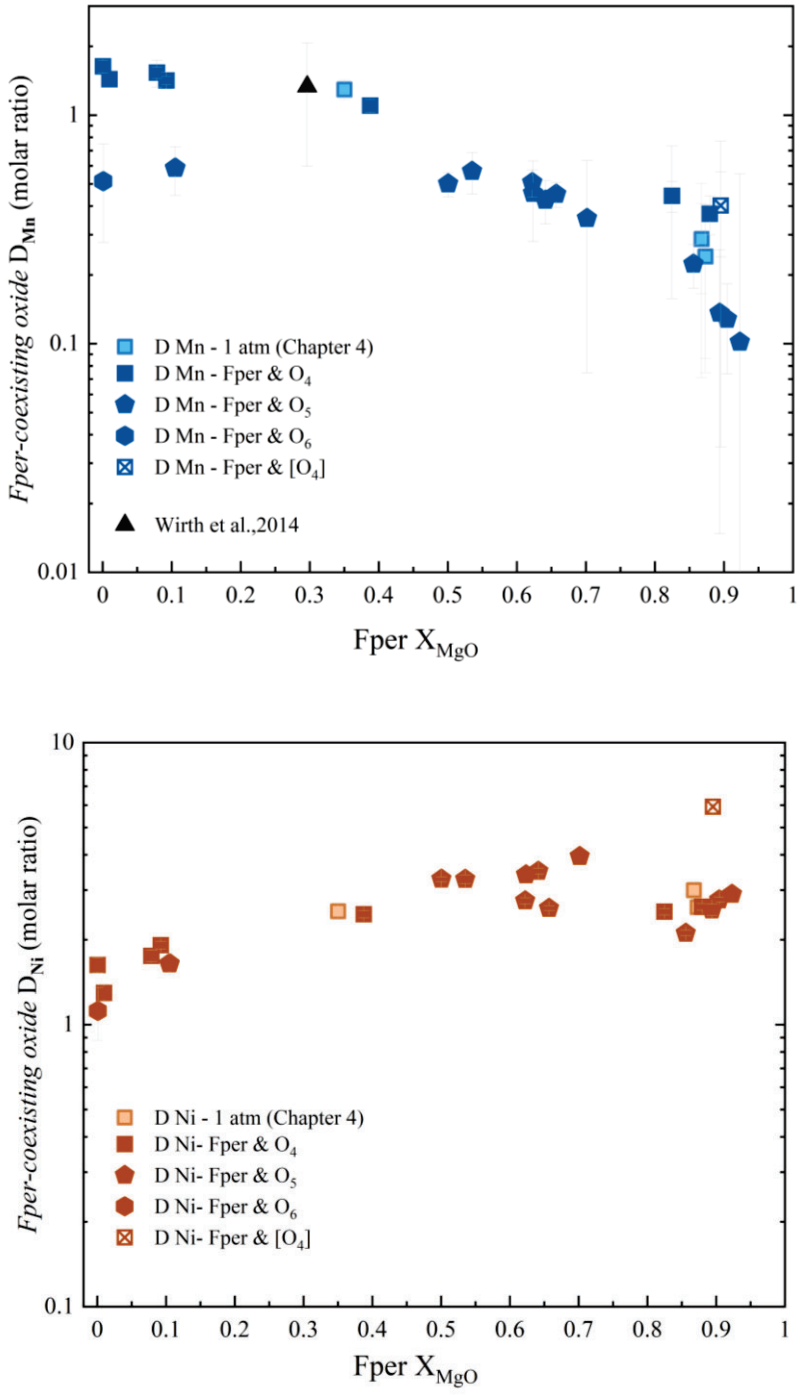

Figure 5.10: The partition coefficient, *D*, of a) Cr, b) Mn and c) Ni between fper and either spft, O5, O6 or [O4] phases. A comparison is made with natural samples where TEM measurements of spft exsolution within fper inclusions in diamonds have been analysed

5.5 Discussion

All samples examined using TEM, except sample I1185-A, showed a coherent topotaxial exsolution of nanocrystalline spft within the fper grains. Even at high pressures, the same n-spft exsolution formed during quenching. outside the stability field of the spinel-ferrite phase (Uenver-Thiele et al. 2017a,b; Woodland et al.2023). This suggests that the mechanism driving the exsolution is very likely similar to that acting at room pressure, implying that the Fe^{3+} atoms migrate to the interstitial tetrahedral sites of the fper structure during quenching giving rise to the formation of defect clusters (Dimitrov et al. 1999; Hazen and Jaenloz 1984; Koch and Cohen 1969) which rapidly grow to produce the n-spft coherent exsolutions. As the cubic oxygen sublattice is, in this case, only slightly altered, the formation of n-spft exsolution instead of high-pressure Fe,Mg-oxides has the advantage of minimising lattice strains at the grain boundary between fper and n-spft. The grain size of the n-spft exsolution appears to decrease with pressure, with samples recovered from 20 GPa having n-spft exsolution grain sizes as small as ~5 nm (Figure 5.4b). This is consistent with the very broad diffraction peaks assigned to a spinel phase in the XRD patterns for samples in which only fper was present (Figure 5.2). Even considering the large uncertainties, the unit-cell lattice parameters determined for n-spft appear much larger than those expected for compositions belonging to the magnesioferrite – magnetite solid solution and it might be due to a defect spinel structure. Given the small grain size, it is not surprising for such n-spft exsolution to have an enlarged unit-cell (Kurian and Mathew 2018), however another possible reason for this behaviour is related to the fact that such unit-cell fits better the oxygen sublattice of fper. Another important consequence of the n-spft small grain size is that this is consistent with a superparamagnetic behavior (Hartridge et al. 1997; Goya et al. 2003; Morup et al. 1976; Fock et al. 2018; Hah et al. 2021), which causes the n-spft magnetic signal to disappear from the Mössbauer spectra, as it collapses into a pattern that has hyperfine parameters really similar to the

ones of the Fe^{3+} component in fper. Mössbauer spectra of fper samples produced at 5 GPa and 1300 °C by Dobson et al. (1998) indicate Fe^{3+}/Fe_{tot} ratios of over 0.7 with no evidence of a magnetic signal. Such MS feature and large Fe^{3+}/Fe_{tot} ratio may be explained by n-spft having superparamagnetic behavior, with n-spft grain size smaller than observed in this study for similar pressures because of a faster multianvil quenching rate, as Dobson et al. (1998) used smaller 14 mm edge length octahedra. It is, however, difficult to reconcile the variation with Fe^{3+} content of the unit-cell axis of fper obtained in this and other studies with the unit-cell axis variation of the samples studied by Dobson et al. (1998) (Figure 5.11). As discussed in Chapter 4, Section 4.4, measuring the unit-cell lattice parameter of fper is not a convenient way to determine the Fe^{3+} content, given that the presence of n-spft exsolution may significantly change the effective fper chemical composition. It is, however, noticeable that all fper samples investigated in this study, as well as several fper measurements reported in the literature have significant lower molar volumes than samples with practically negligible Fe^{3+} content (Figure 5.11), except the data reported by Dobson et al. (1998) for which the change in volume is minimal in spite of the large Fe^{3+} variation among their fper samples. This may be due to the fact that in the mentioned study the authors used only the d-spacing of the 220 reflection for determining the unit-cell volume of fper which may result in much larger uncertainties in the calculated volume.

The molar volume of sample I1185-B , with composition E (Table 5.1), can be observed to plot really close to the stoichiometric FeO samples of Hentschel 1970 and Levin and Wagner 1966 (Figure 5.11) as expected from the EELS measurements (Table 5.3).

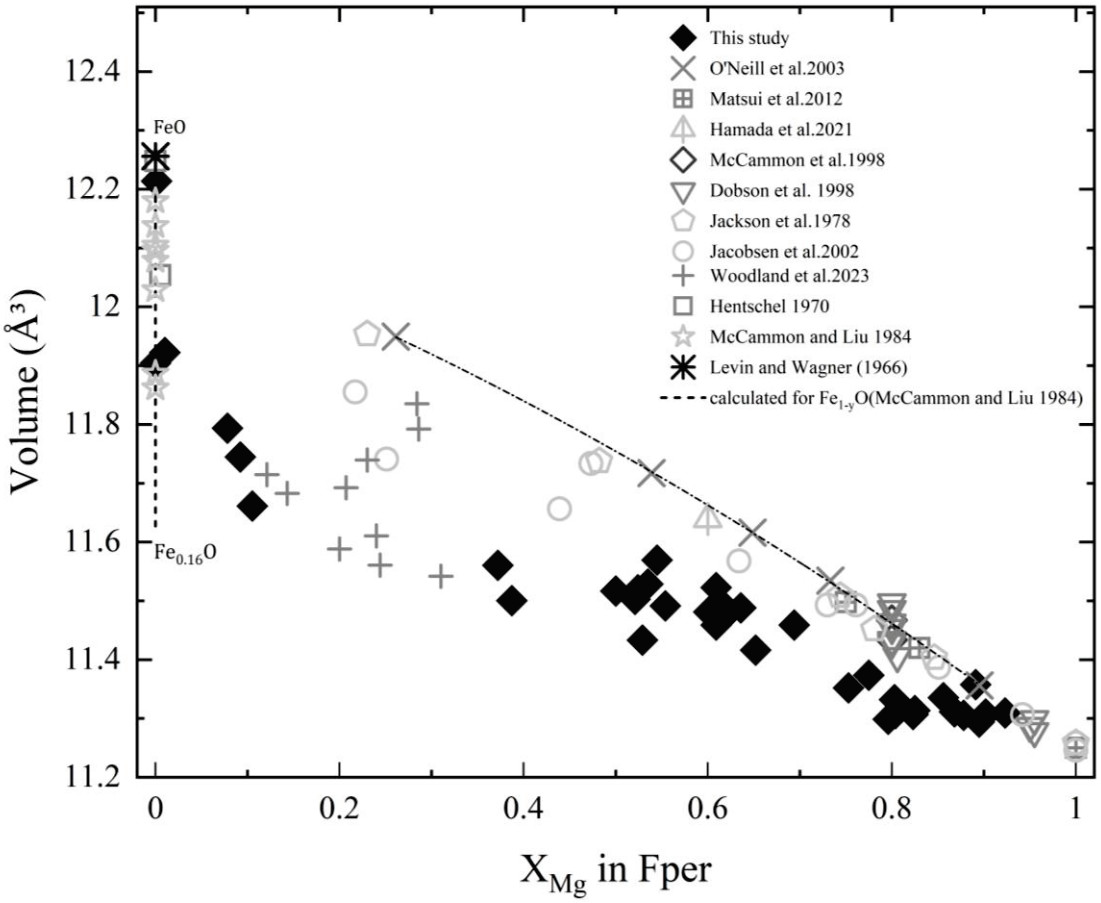

Figure 5.11: Fper molar volume as a function of MgO content, X_{MgO} for all fper samples investigated in this study and compared data reported in the literature.

Due to the migration of Fe^{3+} atoms on cooling, their site occupancy determined in quenched fper by means of MS may tell us very little about the speciation of Fe^{3+} at high temperatures. Moreover, since the only samples without n-spft exsolution were those having a Fe^{3+}/Fe_{tot} ratio smaller than 0.11 (Table 5.3), we can expect that exsolution may be a common feature even for fper samples with quite low Fe^{3+}/Fe_{tot} ratios, raising the question of whether fper physical property measurements made so far at room temperature may have been affected by the presence of this exsolved phase.

In figure 5.12 and 5.13 the log fO_2 and the fper Fe^{3+}/Fe_{tot} ratios that delimit the stability field of a $(Mg_{0.80}Fe_{0.20})O$ fper composition, i.e. close to that expected for the lower mantle, are shown respectively as a function of pressure at 1200 °C. Fper is still stable at oxygen fugacities above

and below the black curves but not with this composition. The fO_2 at which fper coexists with spft and the O5 phase can be seen to be broadly consistent with the $ReReO_2$ buffer for this composition at these conditions.

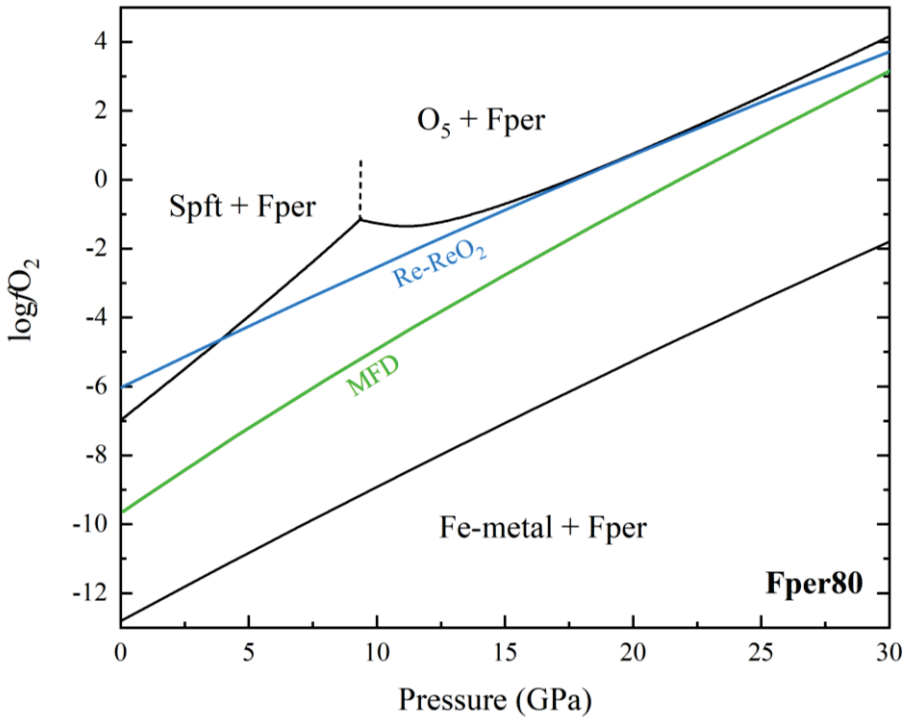

Figure 5.12: The solid black curves indicate the variation in log fO_2 at 1200 °C and conditions where $(Mg_{0.8}Fe_{0.2})O$ fper coexists with either spft or O5 or with iron metal, as indicated. Curves for the Re-ReO_2 oxygen buffer and the equilibrium between magnesite, fper and diamond (MFD) are also shown (see text for details).

In equilibrium with spft, the fper Fe^{3+}/Fe_{tot} ratio increases with pressure, but after the phase transformation to the O5 phase it decreases rapidly as the fper field contracts (Figure 5.13). In the top of the lower mantle the maximum fper Fe^{3+}/Fe_{tot} ratio at this temperature is calculated to be ~ 0.05. This upper limit to the fper Fe^{3+} content increases with temperature and with fper Mg content. At adiabatic temperatures at the top of the lower mantle (~ 1900 °C) the maximum fper Fe^{3+}/Fe_{tot} ratio for this composition increases to ~ 0.2, but this will decrease further with increasing pressure in the lower mantle.

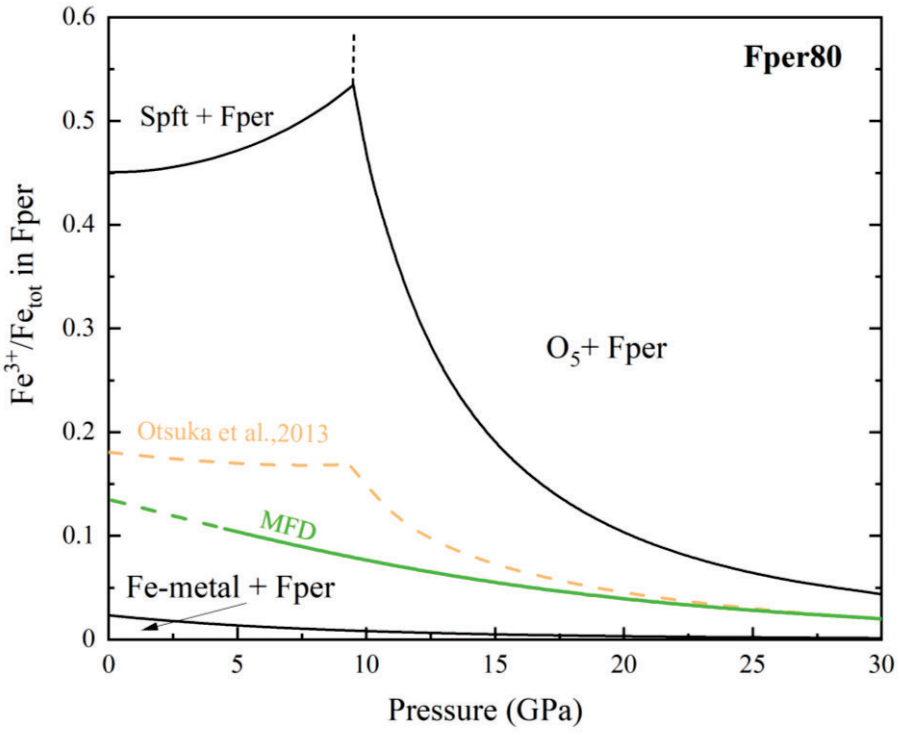

Figure 5.13: The fper Fe^{3+}/Fe_{tot} ratio is plotted at conditions where fper coexists with either spft or O5 or with iron metal as in Figure 5.10 (black curves) and along the MFD curve (green curve). The yellow dashed line shows the results of the model of Otsuka et al. (2013) calculated along the fper-spft and fper-O5 fO_2 curves shown in Figure 5.10.

5.5.1 Comparison with previous studies

Figure 5.13 shows how the high Fe^{3+}/Fe_{tot} ratios, observed for fper at room conditions (Brynestad and Flood 1958; Katsura and Kimura 1964; Speidel 1967) and moderate pressure (Dobson et al. 1998), evolve into the much lower values reported at higher pressures (McCammon et al. 1998; Bolfan-Casanova et al. 2002; Otsuka et al. 2010). In detail, however, there are a number of inconsistences with results from previous studies. Otsuka et al. (2010) made Mössbauer measurements on fper of approximately the same $(Mg_{0.8}Fe_{0.2})O$ composition produced at 5 and 15 GPa and 1400-2000 °C, buffered by assemblages of either Mo-MoO_2 or Re-ReO_2. At the Mo-MoO_2 buffer, which is ~1 log unit above the equilibrium with Fe-metal for this fper composition,

the fper Fe^{3+}/Fe_{tot} ratios of Otsuka et al. (2010) are in the range 0.008 to 0.03, which are within 1% of the values calculated in the thermodynamic model reported in this study.

However, the results reported for Re-ReO_2 experiments are much lower than those calculated in this study. At 5 GPa, for example, fper Fe^{3+}/Fe_{tot} ratios at conditions of the Re-ReO_2 buffer are reported to vary from 0.2 to 0.14 between 1400-2000 °C, whereas at the same conditions values of 0.39 to 0.32 are calculated from the model in this study. Bolfan-Casanova et al. (2002) also report Fe^{3+}/Fe_{tot} ratios for $(Mg_{0.93}Fe_{0.07})O$ fper at Re-ReO_2 buffer and 1200 °C, that decrease from 0.16 at 5 GPa to 0.01 at 25 GPa. In this study, however, the calculated values decrease from 0.37 to 0.05 over the same pressure range. Such low values, particularly at 5 GPa, are clearly also inconsistent with the fact that the fO_2 of the Re-ReO_2 buffer is close to the upper limit in fper stability (Figure 5.12) and that much higher Fe^{3+}/Fe_{tot} ratios have been reported at similar conditions, not only in this study but in that of Dobson et al. (1998). This underestimation of the fper Fe^{3+}/Fe_{tot} ratio could result from n-spft exsolution that went unnoticed in the Mössbauer spectra. However, in both Otsuka et al. (2010) and Bolfan-Casanova et al. (2002) quite large single crystals of fper, with dimensions of ~0.5 mm, were surrounded by buffering materials and used in the experiments. In order to reach equilibrium, solid state diffusion over large distances would have been required, and such assemblage is probably not effective at buffering the entire sample, particularly given that large amounts of oxidation were needed to reach Re-ReO_2 equilibrium. In this study, however, the spft or O5 phases were generally within 10 μm of the fper grains ensuring effective buffering. The analyses of these likely ineffectively buffered Re-ReO_2 fper samples were used to calibrate the model of Otsuka et al. (2013) for predicting the ferric iron content of fper as a function of composition, P, T and fO_2. As can be seen in Figure 5.13, this model significantly underestimates the ferric iron content of fper when it is employed at fO_2 conditions along the fper-spft and fper-O5 boundaries. Although the difference between the two models will improve towards lower oxygen fugacities, there is a tendency for the Otsuka et al. (2013) model to

overestimate the fO_2 calculated for a particular fper Fe^{3+}/Fe_{tot} ratio. Kaminsky et al. (2015), for example, used the equation of Otsuka et al. (2013) to calculate the fO_2 of fper inclusions in diamonds assuming conditions at the top of the lower mantle (25 GPa, 1687 °C), and obtained fO_2 values between +1 log unit and +8 log units above the iron-wüstite (IW) buffer. Instead, using the thermodynamic model determined in this study at the same conditions the inclusions fall in the range +2 to +5 log units above IW.

5.5.2 The upper oxygen fugacity limit of fper inclusions in diamonds

A number of fper inclusions in diamonds have been analysed in order to obtain their Fe^{3+}/Fe_{tot} ratios, resulting in a range between 0.02 and 0.12 (McCammon et al. 2004b; Otsuka et al. 2013; Kaminsky et al. 2015). Although the higher end of this range would be close to the limit of the fper stability field (Figure 5.13), it would still be possible for these compositions to have formed at the top of the lower mantle at adiabatic temperatures. However, this consideration pertains to the limit of the fper stability field with respect to the formation of the O5 phase or other higher-pressure oxides. As the fper inclusions would be in equilibrium with diamond as they formed, then the reaction:

$$MgO_{(fper)} + C_{(diamond)} + O_2 = MgCO_{3(magnesite)} \quad (10)$$

referred to with the acronym FDM, provides a further important limitation to the highest fO_2, and therefore the highest fper Fe^{3+}/Fe_{tot} ratio, at which the fper inclusions in diamonds could have formed. Above FDM, diamond and fper would react to form magnesite and if the temperature were high enough for magnesite to melt, then the resulting fO_2 would be close but still lower than FDM (Stagno and Frost 2010). However, although magnesite remains relatively iron poor in the

presence of iron bearing fper (Stagno et al. 2011), the Mg/(Mg+Fe) ratio of fper will affect the fO_2 of FDM. This can be accounted for by also considering the reaction:

$$FeO_{(fper)} + C_{(diamond)} + O_2 = FeCO_{3(siderite)} \quad (11)$$

Using a van Laar model for Fe-Mg interaction in the single site disordered carbonate solid solution, with the thermodynamic data reported in Table A.5.4, the $fO2$ of MFD, and the composition of the coexisting carbonate in the Fe-Mg-C-O system can be calculated as a function of the fper composition by solving Gibbs free energy expressions for equation (10) and (11) simultaneously.

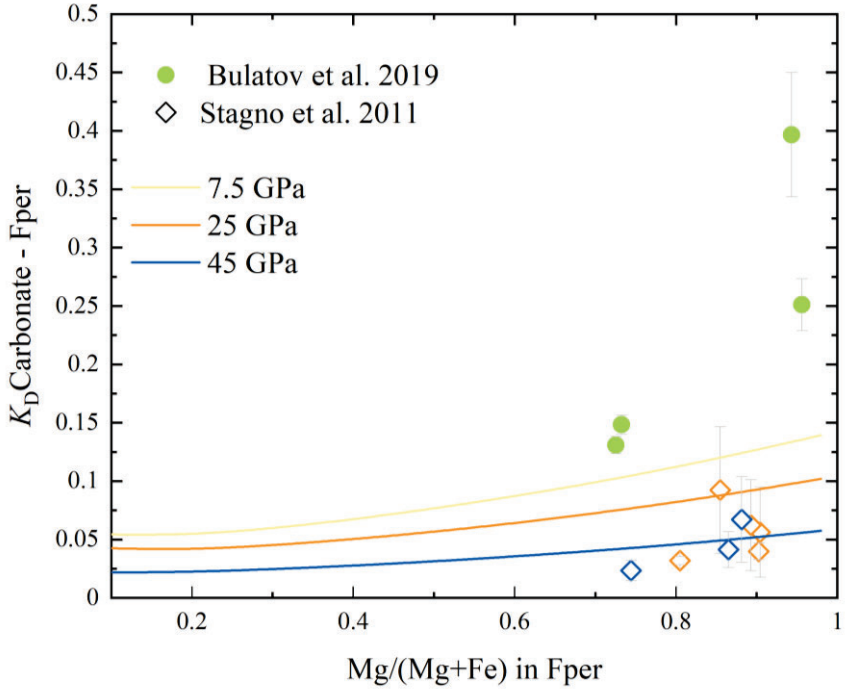

Figure 5.14: The carbonate-fper Fe-Mg distribution coefficient, K_D, as a function of the fper Mg/(Mg+Fe) ratio calculated at 1600 °C and different pressures. Stagno et al. (2011) data are from 25 and 45 GPa and 1500-1700 °C, while data from Bulatov et al. (2019) are from 7.5 and 10.5 GPa and 1550-1600 °C. In the latter study the carbonates also contain Ca.

This calculation can be tested against independent experimental data. Figure 5.14 shows the resulting carbonate-fper Fe-Mg distribution coefficient ($K_D=[Fe^{2+}/Mg]_{Carb}/[Fe^{2+}/Mg]_{Fper}$) calculated at 1600 °C and different pressures, which reproduces very well data from Stagno et al.

(2011) at 25 and 45 GPa and Bulatov et al. (2019) from 7.5 and 10.6 GPa. Carbonates from the study of Bulatov et al. (2019) also contained Ca, which likely explains the higher K_D values.

Using the thermodynamic model developed in this study, it is then possible to calculate the fper Fe^{3+}/Fe_{tot} ratio at conditions of the FDM buffer. These calculations are shown as a function of the fper Mg/(Mg+Fe) ratio in Figure 5.15, mainly for pressures and temperatures that are close to an adiabatic gradient in the Earth (Katsura 2022), except at 25 GPa, i.e. the top of the lower mantle, where the two temperatures (1200 °C and 1900 °C) are chosen to demonstrate the variation between plausible subduction and plume related temperatures. Dashed curves in Figure 5.15 also show the Fe^{3+}/Fe_{tot} ratio of fper in equilibrium with the O5 phase. The fO_2 of the FDM buffer increases with the Fe-content of fper, which also results in an increase in the fper Fe^{3+}/Fe_{tot} ratio. This is because more iron partitions into fper than the carbonate. Calcium would have the opposite effect and should, therefore, lower the fO_2 of FDM. The fper Fe^{3+}/Fe_{tot} ratio is again calculated to decrease with increasing pressure and also with temperature. Stagno et al. (2011) reported an EELS measurement of 0.02 (±5) for the Fe^{3+}/Fe_{tot} ratio of $(Mg_{0.85}Fe_{0.15})O$ fper buffered by FDM at 45 GPa and 1700 °C. This is consistent with the FDM thermodynamic model which predicts a ratio of 0.015 at the same conditions.

5.5.3 Comparison with fper inclusions in natural diamonds

In Figure 5.15, Fe^{3+}/Fe_{tot} ratios of fper inclusions in diamonds are plotted from three locations: the Juina kimberlites and São Luiz placer deposit in Brazil and the Kankan placer deposit in Guinea, West Africa (Kaminsky et al. 2015). TEM studies on samples from São Luiz and Juina have shown the presence of n-spft exsolution in several fper inclusion samples (Wirth et al. 2014; Kaminsky et al. 2015). Wirth et al. (2014) were able to analyse submicron regions of exsolved spft within a

fper inclusion and the K_D(app) calculated for this sample is shown in Figure 5.9 and appears to be quite consistent with equilibration between spft and fper at near room pressure conditions. It seems likely, therefore, given that decompression alone would bring fper inclusions further away from the spft exsolution boundary, that this exsolution occurs as the diamonds cool near the surface.

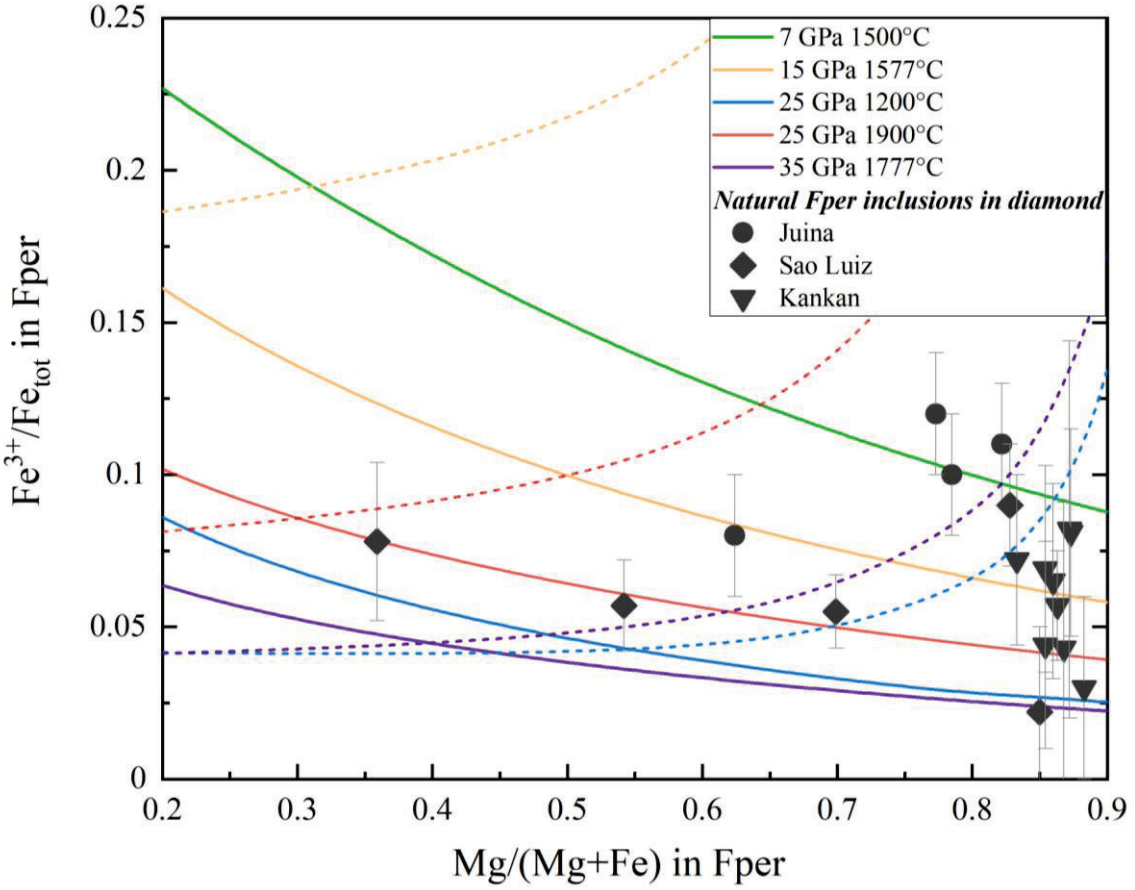

Figure 5.15: The Fe^{3+}/Fe_{tot} ratio in fper in equilibrium with diamond and Fe-Mg carbonate is calculated at the pressures and temperatures indicated (solid curves) and compared with Fe^{3+}/Fe_{tot} ratios reported for fper inclusions in natural diamonds (Kaminsky et al. 2015). Also plotted are Fe^{3+}/Fe_{tot} ratios of fper in equilibrium with the O5 phase (dashed curves). The fper inclusions cannot have formed at a particular set of *P*-*T* conditions if they plot above the corresponding solid (i.e. where diamond would not be stable) or dashed (where fper of that composition would not be stable) curves.

Wirth et al. (2014) recognised that this exsolution had occurred post entrapment and, therefore, corrected the original Mössbauer fper Fe^{3+}/Fe_{tot} measurement (McCammon et al. 1997) of

0.070(26), to account for the estimated 6–11 vol.% of exsolved spft phase and obtained a fper Fe^{3+}/Fe_{tot} ratio before exsolution of 0.11–0.14. Kaminsky et al. (2015) considered that the proportion of spft exsolution in fper inclusions could be generalised as being approximately 3.64 vol.% and from this value calculated that Mössbauer determinations of fper inclusion Fe^{3+}/Fe_{tot} ratios should be raised by 0.021. While this appears to be a conservative estimate of the exsolution effect, compared to that made by Wirth et al. (2014), values corrected in this way are plotted in Figure 5.15, under the proviso that they may be an underestimate.

If the diamonds in which the inclusions are found formed by reduction of carbonates, then the FDM curves in Figure 5.15 indicate the approximate *P* at which this must have occurred for the different inclusions. However, it is quite possible that the diamonds formed from reduction or oxidation of other types of carbon-bearing fluids or melts (Stagno et al. 2013), which would occur at oxygen fugacities lower than the FDM curves. Under these circumstances the FDM curves only indicate the maximum *P* at which the inclusions could have formed. For example, it is possible that four of the samples from São Luiz and about half of the samples from Kankan formed from carbonate at the top of the lower mantle, as they plot within error or below the FDM curve at 1900 °C and 25 GPa, and would also be consistent with adiabatic temperatures ~ 200 °C lower. Samples that plot above the FDM curve could not have formed at these conditions as diamond would react with fper to produce magnesite. However, if these samples were produced at oxygen fugacities below the FDM buffer then they could have been produced at practically any pressure up to 25 GPa. Only samples with Fe^{3+}/Fe_{tot} ratios < 0.03 could have formed in the lower mantle and this limiting Fe^{3+}/Fe_{tot} ratio value will drop further with increasing depth in the lower mantle. Furthermore, fper could not have formed above the dashed curves indicating the transformation to the O5 phase. For example, the samples from Junia and the most Fe-rich sample from São Luiz could not have formed at 25 GPa and 1200 °C, as the fper compositions would have broken down to the O5 phase. It is quite intriguing that these O5 phase boundaries cross the corresponding FDM

curves towards higher Fe-contents at pressures above 25 GPa. At these conditions the O5 field passes into the diamond stability field and it is, therefore, possible that the O5 phase could be captured as an inclusion in a diamond, if it were to form, for example, from carbonate reduction, at these conditions (Figure 5.15).

Many of the samples from Kankan have a maximum formation depth near the top of the transition zone. They could of course have been formed at depths shallower than this, but not deeper, as their ferric iron contents would be too high to be compatible with the diamond stability field. Lower than adiabatic temperatures would require fper to have even lower Fe^{3+}/Fe_{tot} ratios at the same depth. The three Mg-richer samples from Junia have a maximum possible depth of formation consistent with the base of the cratonic lithosphere.

One further constraint is provided by the fper Fe^{3+}/Fe_{tot} ratio when it is in equilibrium with Fe-rich metal, which defines an absolute lower limit to the fO_2 at which the inclusions could have formed. The model indicates that at the top of the diamond stability field at ~5 GPa fper Fe^{3+}/Fe_{tot} ratios in equilibrium with iron metal increase slightly from 0.01 to 0.04 as the fper Mg/(Mg+Fe) ratio decreases from 0.9 to 0.3. These Fe^{3+}/Fe_{tot} ratios decrease with pressure and are not particularly temperature sensitive. This indicates that only the two most reduced fper inclusions analysed so far could have formed in equilibrium with Fe-metal, the others must have been produced at higher fO_2.

The question arises as to how fper inclusions could be produced at depths shallower than the lower mantle, where in typical mantle peridotite they should react with pyroxene components to form olivine or its higher-pressure polymorphs. Several studies have proposed that this could occur through reduction of carbonates (Brey et al. 2004; Thomson et al. 2016; Bulatov et al. 2019; Bataleva et al. 2019). In fact, in a few isntances, the diamonds containing the fper inclusions also contain carbonates (McCammon et al. 2004). An appealing aspect of carbonate reduction is that it

provides a mechanism to explain the high Fe-contents of some fper inclusions (Bulatov et al. 2019). Fe partitions strongly into fper in equilibrium with solid and liquid carbonates (Bulatov et al. 2019). The model shown in Figure 5.14, for example, indicates that at 6 GPa and 1400 °C, fper with an Mg/(Mg+Fe) of 0.35 can be produced from partial reduction of a Ca-free carbonate with an Mg/(Mg+Fe) ratio of 0.93. The reduction itself could have been a response to an influx of reduced CH_4 or H_2 bearing fluids, as there is insufficient Fe^{2+} in mantle rocks to reduce the significant quantities of carbonate that would be required to produce a macroscopic diamond (Luth and Stachel 2014). The alternative scenario would be that the diamonds were produced from H_2O-dominated fluids or melts that are also Mg and Fe-rich (Kawamoto and Holloway 1997; Nakajima et al. 2019) and might potentially crystallise fper, especially if such melts went through several cycles of partial melting, migration and crystallisation, perhaps as a result of thermal perturbation due to the presence of a plume. Such H_2O-rich melts or fluid could form diamonds through the reaction: $CH_4+CO_2=2C+2H_2O$, which could even be driven by the dissolution of H_2O into nominally anhydrous minerals. The fluid or melt would have an fO_2 of at least 1 log unit below FDM (Stagno et al. 2010). For any set of conditions, this would lower the fper Fe^{3+}/Fe_{tot} ratio by approximately half the value indicated for FDM in Figure 5.15. This would imply that the majority of the natural inclusions would be consistent with formation in the cratonic lithosphere or at the top of the transition zone. However, the most Fe^{3+}-rich inclusions, mainly from Juina, are too oxidised to have formed through this mechanism, as, even at the graphite-diamond transition near 5 GPa, fper inclusions at 1 log unit below FDM would have Fe^{3+}/Fe_{tot} ratios in the range 0.05-0.07. These inclusions appear to be only consistent with formation from carbonates at or very near to cratonic lithosphere conditions.

Kisseeva et al. (2022) recently reported Fe^{3+}/Fe_{tot} ratios for five more fper inclusions in diamonds from São Luiz. Four of these had Fe^{3+}/Fe_{tot} ratios below detection limits, estimated to be 0.03, which means these inclusions could have been formed in the lower mantle. Single crystal X-ray

diffraction of one of these inclusions, with an Fe/(Fe+Mg) ratio of 0.81 indicates the presence of a coexisting spft single crystal, with the unit-cell axis aligned with that of fper. If this spft phase exsolved after capture from the fper, then based on the reported Mössbauer spectrum the combined original phase would have had an Fe^{3+}/Fe_{tot} ratio of approximately 0.5, which is far too high to correspond to a fper inclusion in a diamond under any conditions. This composition and oxidation state correspond, however, to the stoichiometry of the O6 phase, i.e. $(Mg_{0.33}Fe^{2+}_{0.67})_3\,Fe^{3+}_2O_6$. The comparatively high Mn content for this inclusion is also consistent with the low fper-O6 partition coefficient for Mn, shown in Figure 5.10b. The O6 phase was only observed experimentally in this study at $Fe^{2+}/(Mg+Fe^{2+})$ ratios >0.8 (Figure 5.3; Table 5.2), however, at 1400 °C and 10 GPa Woodland et al. (2023) reported an O6 with $Fe^{2+}/(Mg+Fe^{2+})$ ratio of 0.73, close to the value of 0.67 found for the diamond inclusion. If, towards higher temperatures, the O6 phase replaces O5, as the phase coexisting with fper at this relatively high Fe content and assuming that the O6 and O5 phases are similar at this composition given that the transition to the O5+fper field must be very close and K_D(app) for the O5 and O6 phases is near identical (Figure 5.9), than it is quite plausible that an O6 phase with this composition would be stable in the diamond stability field and could be trapped as an inclusion, as shown by the dashed curves in Figure 5.15 indicating the boundary with O5 stability. The minimum entrapment pressure can then be estimated for this inclusion using Figure 5.15 as being close to 25 GPa, at a temperature between 1200 °Cand 1900 °C. At 25 GPa and 1700 °C, for example, an O5 phase with an $Fe^{2+}/(Mg+Fe^{2+})$ of 0.67 could be in equilibrium with diamond. As shown in Figure 5.9 the K_D(app) for this inclusion is quite unlike that expected for fper-spft equilibrium, which might be explained as a result of both phases forming through a metastable breakdown of the O6 phase. It is interesting to note that if this O6 oxide formed by the reduction of carbonate, then although the O6 oxide has a high Fe^{3+} content, its stability at these conditions would not require especially oxidising conditions, other than those required for carbonate stability. The formation of the O6 phase would be an inevitable consequence

of the formation of a carbonate with a sufficiently high iron content and can be described by the reaction:

$$5FeCO_3 = Fe_5O_6 + 0.5C + 4.5CO_2 \quad (12)$$

where CO_2 would either be released or form more carbonate by reacting with other Mg or Ca bearing phases. Similar mechanisms involving either spft or other high-pressure oxides have been proposed as a diamond forming mechanisms in both experimental and natural samples (Boulard et al. 2012; Cerantola et al. 2017; Chen et al 2018). If the O6 phase formed at 25 GPa and 1700 °C, then employing the calculations shown in Figure 5.14, the coexisting carbonate would need to have an Fe/(Fe+Mg) ratio of only 0.09, although this value would be higher if the carbonate were Ca-bearing, and the fO_2 would be 3.5 log units above IW.

Appendix Chapter 5

Table A.5.1: Chemical composition for all the run products by means of EPMA. Data are reported in element wt% and c.p.f.u.

Table A.5.2: Unit-cell lattice parameters of the phase assemblages recovered in this study

Table A.5.3: Mössbauer parameters obtained from the fitting procedure of the Mössbauer spectra collected for the samples investigated in this study

Table A.5.4: Standard state thermodynamic terms used and refined in the present study

Table A.5.5: Thermodynamic mixing terms used for the thermodynamic model of this study

Figure A.5.1 : Example of collected diffraction data showing the presence of large spots in the samples rather than Debye rings.

Figure A.5.2: EDS elemental map performed on sample S7029

Figure A.5.3: Plot of CS (center shift) and QS (quadrupole splitting) for all the samples in the present work, together with the available literature.

Table A.5.1: Chemical composition for all the run products by means of EPMA. Data are reported in element wt% and c.p.f.u.

sample		Mg	Fe	Ni	Cr	Mn	O	Pt	total	Mg	Fe	Ni	Cr	Mn	Pt	Σoxy	Σcations
									S7029								
Fper	avg	42.99	19.58	1.00	0.27	0.19	37.07	0.20	101.36	0.823	0.163	0.008	0.002	0.002	0.000	1.08	1.0
	stdv	*0.82*	*0.79*	*0.03*	*0.03*	*0.01*	*0.22*	*0.18*	*0.20*	*0.016*	*0.007*	*0.000*	*0.000*	*0.000*	*0.000*		
O_4	avg	9.85	57.26	0.27	0.70	0.29	30.99	0.20	99.58	0.835	2.114	0.009	0.028	0.011	0.002	3.99	3.0
	stdv	*0.38*	*0.51*	*0.02*	*0.21*	*0.01*	*0.36*	*0.05*	*0.29*	*0.032*	*0.019*	*0.001*	*0.008*	*0.000*	*0.000*		
alloy	avg	0.11	4.80	0.22	0.02	0.02	0.14	96.34	101.41	0.008	0.146	0.006	0.001	0.001	0.848		1.0
	stdv	*0.06*	*0.19*	*0.03*	*0.01*	*0.01*	*0.10*	*0.44*	*0.50*	*0.004*	*0.006*	*0.001*	*0.000*	*0.000*	*0.004*		
									Z2038								
Fper	avg	39.20	26.05	0.01	0.01	0.06	36.22	0.02	101.69	0.775	0.224	0.000	0.000	0.000	0.000	1.09	1.0
	stdv	*0.62*	*0.78*	*0.02*	*0.01*	*0.04*	*0.28*	*0.03*	*0.32*	*0.012*	*0.007*	*0.000*	*0.000*	*0.000*	*0.000*		
alloy	avg	0.02	7.21	0.01	0.01	0.02	0.31	94.79	102.38	0.001	0.209	0.000	0.000	0.001	0.790		1.0
	stdv	*0.01*	*0.28*	*0.01*	*0.01*	*0.03*	*0.07*	*1.30*	*1.06*	*0.001*	*0.008*	*0.000*	*0.000*	*0.001*	*0.011*		
									H5128								
Fper	avg	37.23	27.97	0.01	0.01	0.06	35.27		101.84	0.753	0.246	0.000	0.000	0.001	0.000	1.08	1.0
	stdv	*0.43*	*0.22*	*0.02*	*0.01*	*0.03*	*0.34*		*0.58*	*0.009*	*0.002*	*0.000*	*0.000*	*0.000*	*0.000*		
alloy	avg	0.01	7.56	0.04	0.01	0.01	0.31	93.95	101.90	0.001	0.219	0.001	0.000	0.000	0.780		1.0
	stdv	*0.01*	*0.17*	*0.03*	*0.02*	*0.01*	*0.11*	*0.94*	*1.08*	*0.001*	*0.005*	*0.001*	*0.000*	*0.000*	*0.008*		
									S7004								
Fper	avg	41.36	22.08	0.97	0.33	0.20	0.100	37.07	0.17	*0.800*	*0.186*	0.008	0.003	0.002	0.000	0.98	1.0
	stdv	0.30	0.36	0.03	0.02	0.01	0.011	0.22	0.06	*0.003*	*0.003*	*0.000*	*0.000*	*0.000*	*0.000*		
alloy	avg	0.30	3.70	0.17	0.04	0.02	0.54	97.82	102.59	*0.028*	*0.113*	*0.005*	*0.001*	*0.001*	*0.860*		1.00
	stdv	0.43	0.36	0.03	0.02	0.01	0.48	0.47	1.24	*0.028*	*0.007*	*0.001*	*0.001*	*0.001*	*0.034*		
									S7377								
Fper	avg	47.67	13.54	1.13	0.22	0.17	38.18	0.14	101.11	0.878	0.109	0.009	0.002	0.001	0.000	1.07	1.0
	stdv	*0.65*	*0.83*	*0.07*	*0.04*	*0.01*	*0.29*	*0.07*	*0.64*	*0.012*	*0.007*	*0.001*	*0.000*	*0.000*	*0.000*		
O_4	avg	9.58	57.14	0.28	0.87	0.30	31.39	0.24	99.82	0.818	2.122	0.010	0.035	0.011	0.003	4.07	3.0
	stdv	*0.48*	*0.72*	*0.02*	*0.25*	*0.01*	*0.40*	*0.10*	*0.59*	*0.041*	*0.027*	*0.001*	*0.010*	*0.000*	*0.001*		
alloy	avg	0.08	4.34	0.14	0.05	0.02	0.31	96.62	101.57	0.005	0.134	0.004	0.002	0.001	0.862		1.0
	Stdv	*0.07*	*0.19*	*0.03*	*0.01*	*0.02*	*0.12*	*0.48*	*0.34*	*0.005*	*0.006*	*0.001*	*0.000*	*0.000*	*0.334*		
									S7180								
Fper	avg	40.71	22.30	0.94	0.34	0.19	36.37	0.01	101.24	0.796	0.190	0.008	0.003	0.002	0.000	1.08	1.0
	stdv	*0.15*	*0.17*	*0.05*	*0.01*	*0.02*	*0.20*	*0.02*	*0.40*	*0.003*	*0.001*	*0.000*	*0.000*	*0.000*	*0.000*		
alloy	avg	0.01	1.78	0.13	0.00	0.02	0.21	96.92	99.08	0.001	0.060	0.004	0.000	0.001	0.936		1.0
	stdv	*0.01*	*0.23*	*0.03*	*0.00*	*0.02*	*0.07*	*1.11*	*1.20*	*0.001*	*0.008*	*0.001*		*0.001*	*0.011*		

Table A.5.1

sample		Mg	Fe	Ni	Cr	Mn	O	Pt	total	Mg	Fe	Ni	Cr	Mn	Pt	Σoxy	Σcations
S7204																	
Fper	avg	41.76	20.44	0.89	0.34	0.20	36.51	0.09	100.48	0.813	0.173	0.007	0.003	0.002	0.000	1.08	1.0
	stdv	*0.31*	*0.46*	*0.05*	*0.02*	*0.04*	*0.22*	*0.24*	*0.43*	*0.006*	*0.004*	*0.000*	*0.000*	*0.000*	*0.000*		
alloy	avg	0.01	2.50	0.15	0.02	0.03	0.32	99.52	102.56	0.001	0.080	0.005	0.001	0.001	0.915		1.0
	stdv	*0.00*	*0.27*	*0.03*	*0.01*	*0.02*	*0.04*	*1.54*	*1.73*	*0.000*	*0.009*	*0.001*	*0.000*	*0.001*	*0.014*		
Z1949-B																	
Fper		70.22	28.45	1.22	0.48	0.27	100.76	*		0.804	0.183	0.008	0.003	0.002	0.000		1.0
		0.41	*0.17*	*0.07*	*0.02*	*0.03*	*0.31*			*0.005*	*0.001*	*0.000*	*0.000*	*0.000*	*0.000*		
alloy		0.31	4.95	0.18			0.55	95.27		0.021	0.149	0.005	0.000	0.000	0.845		1.0
		0.19	*0.40*	*0.02*			*0.20*	*1.07*		*0.013*	*0.012*	*0.001*			*0.009*		
S7382																	
Fper	avg	50.26	10.77	1.19	0.20	0.10	39.06	0.22	101.88	0.902	0.084	0.009	0.002	0.001	0.000	1.07	1.0
	stdv	*0.75*	*0.73*	*0.04*	*0.04*	*0.01*	*0.59*	*0.19*	*1.12*	*0.014*	*0.006*	*0.000*	*0.000*	*0.000*	*0.000*		
O_5	avg	10.85	56.76	0.28	0.76	0.51	30.29	0.30	99.82	1.194	2.717	0.013	0.039	0.025	0.004	5.06	4.0
	stdv	*0.60*	*0.55*	*0.02*	*0.08*	*0.02*	*0.32*	*0.09*	*0.52*	*0.066*	*0.026*	*0.001*	*0.004*	*0.001*	*0.000*		
alloy	avg	0.99	4.78	0.23	0.06	0.04	1.79	96.64	104.53	0.065	0.136	0.006	0.002	0.001	0.859		1.0
	stdv	*0.30*	*0.38*	*0.04*	*0.02*	*0.01*	*0.53*	*0.75*	*1.38*	*0.020*	*0.011*	*0.001*	*0.001*	*0.000*	*0.006*		
S7006																	
Fper	avg	47.18	14.81	1.11	0.17	0.14	0.12	37.60	0.19	0.868	0.119	0.008	0.001	0.001	0.000	1.05	1.0
	stdv	0.78	0.81	0.02	0.04	0.01	0.01	0.36	0.13	0.014	0.006	0.000	0.000	0.000	0.000		
O_5	avg	13.73	52.99	0.33	0.68	0.47	0.06	30.50	0.21	1.463	2.457	0.015	0.034	0.022	0.003	4.94	4.0
	stdv	0.84	0.60	0.02	0.12	0.01	0.02	0.33	0.09	0.089	0.028	0.001	0.006	0.001	0.000		
alloy	avg	0.11	4.28	0.16	0.04	0.03	0.27	97.09	104.00	0.007	0.132	0.005	0.001	0.001	0.854		1.0
	stdv	0.12	0.33	0.02	0.02	0.01	0.29	0.61	0.30	0.008	0.010	0.001	0.001	0.000	0.005		
S7016																	
Fper	avg	52.20	8.67	1.21	0.07	0.09	38.66	0.11	101.03	0.923	0.067	0.009	0.001	0.001	0.000	1.04	1.0
	stdv	*0.39*	*0.43*	*0.13*	*0.03*	*0.02*	*0.56*	*0.08*	*0.55*	*0.007*	*0.003*	*0.001*	*0.000*	*0.000*	*0.000*		
O_5	avg	10.39	57.66	0.27	0.64	0.55	30.26	0.20	100.81	1.149	2.774	0.012	0.033	0.027	0.003	5.08	4.0
	stdv	*0.68*	*0.81*	*0.03*	*0.21*	*0.03*	*0.53*	*0.17*	*0.75*	*0.075*	*0.039*	*0.001*	*0.011*	*0.001*	*0.000*		
alloy	avg	0.15	4.40	0.14	0.05	0.03	0.53	98.17	103.49	0.010	0.133	0.004	0.002	0.001	0.863		1.0
	stdv	*0.17*	*1.09*	*0.02*	*0.04*	*0.03*	*0.39*	*2.90*	*1.76*	*0.011*	*0.033*	*0.001*	*0.001*	*0.001*	*0.025*		
Z2151-B																	
Fper	avg	45.97	16.43	1.05	0.23	0.11	37.55	0.09	101.64	0.856	0.133	0.008	0.002	0.001	0.000	1.06	1.0
	stdv	*0.75*	*0.78*	*0.05*	*0.02*	*0.02*	*0.33*	*0.06*	*0.45*	*0.014*	*0.006*	*0.000*	*0.000*	*0.000*	*0.000*		
O_5	avg	13.89	53.00	0.35	0.86	0.33	31.31	0.21	100.80	1.474	2.448	0.015	0.043	0.016	0.003	5.05	4.0
	stdv	*0.20*	*0.38*	*0.02*	*0.04*	*0.02*	*0.38*	*0.11*	*0.40*	*0.022*	*0.018*	*0.001*	*0.002*	*0.001*	*0.000*		

Table A.5.1

sample		Mg	Fe	Ni	Cr	Mn	O	Pt	total	Mg	Fe	Ni	Cr	Mn	Pt	Σoxy	Σcations
alloy	avg	0.01	3.29	0.13	0.04	0.04	0.15	98.10	102.91	0.001	0.104	0.004	0.001	0.001	0.891		1.0
	stdv	*0.32*	*0.38*	*0.03*	*0.01*	*0.02*	*0.14*	*0.87*	*0.63*	*0.023*	*0.012*	*0.001*	*0.000*	*0.001*	*0.008*		
Z2153-B																	
Fper	avg	27.81	39.41	1.13	0.29	0.16	33.15	0.11	102.08	0.609	0.376	0.010	0.003	0.002	0.000	1.10	1.0
	stdv	*0.60*	*0.74*	*0.10*	*0.03*	*0.02*	*0.21*	*0.09*	*0.26*	*0.013*	*0.007*	*0.001*	*0.000*	*0.000*	*0.000*		
O_5	avg	8.05	61.08	0.35	0.80	0.23	29.59	0.20	100.74	0.905	2.990	0.016	0.042	0.012	0.003	5.06	4.0
	stdv	*0.11*	*0.22*	*0.02*	*0.04*	*0.02*	*0.32*	*0.23*	0.365	*0.012*	*0.011*	*0.001*	*0.002*	*0.001*	*0.000*		
alloy	avg	0.02	6.58	0.16	0.03	0.02	0.36	96.54	103.72	0.001	0.191	0.004	0.001	0.000	0.805		1.0
	stdv	*0.01*	*0.38*	*0.01*	*0.01*	*0.02*	*0.17*	*0.33*	*0.57*	*0.000*	*0.011*	*0.000*	*0.000*	*0.000*	*0.003*		
H4792																	
Fper	avg	49.52	12.20	1.20	0.09	0.11	38.44	0.15	101.69	0.891	0.096	0.009	0.001	0.001	0.000	1.05	1.0
	stdv	*0.45*	*0.56*	*0.07*	*0.02*	*0.01*	*0.30*	*0.13*	*0.37*	*0.008*	*0.004*	*0.000*	*0.000*	*0.000*	*0.000*		
O_5	avg	10.92	55.73	0.31	1.11	0.51	30.26	0.46	99.33	1.208	2.685	0.014	0.058	0.025	0.006	5.09	4.0
	stdv	*0.21*	*0.39*	*0.04*	*0.10*	*0.02*	*0.37*	*0.23*	*0.53*	*0.023*	*0.019*	*0.002*	*0.005*	*0.001*	*0.000*		
alloy	avg	0.15	3.52	0.15	0.03	0.01	0.38	97.65	101.88	0.010	0.110	0.004	0.001	0.000	0.885		1.0
	stdv	*0.23*	*0.52*	*0.04*	*0.04*	*0.01*	*0.31*	*0.80*	*0.31*	*0.017*	*0.016*	*0.001*	*0.001*	*0.000*	*0.007*		
S7410																	
Fper	avg	47.79	15.59	0.01	0.01	0.03	39.08	0.25	102.51	0.875	0.124	0.000	0.000	0.000	0.001	1.09	1.0
	stdv	0.63	0.73	0.01	0.01	0.01	0.23	0.26	0.30	0.011	0.006	0.000	0.000	0.000	0.000		
O_5	avg	3.70	67.89	0.01	0.01	0.15	28.94	0.36	101.06	0.443	3.541	0.000	0.001	0.008	0.005	5.07	4.0
	stdv	0.35	0.65	0.01	0.01	0.02	0.25	0.21	0.40	0.042	0.034	0.001	0.001	0.001	0.000		
alloy	avg		5.90	0.01			0.80	93.74	100.45	0.000	0.180	0.000	0.000	0.000	0.820		1.0
	stdv		0.29	0.01			0.13	0.45	0.24	0.000	0.009	0.000	0.000	0.000	0.133		
S7123-B																	
Fper	avg	43.45	20.93	0.01	0.01	0.05	36.84	0.08	101.50	0.825	0.173	0.000	0.000	0.000	0.000	1.06	1.0
	stdv	*0.30*	*0.40*	*0.02*	*0.01*	*0.03*	*0.18*	*0.08*	*0.31*	*0.006*	*0.003*	*0.000*	*0.000*	*0.000*	*0.000*		
O_5	avg	10.21	59.68	0.02	0.02	0.14	29.59	0.00	100.62	1.125	2.862	0.001	0.001	0.007	0.004	4.95	4.0
	stdv	*0.13*	*0.30*	*0.02*	*0.01*	*0.01*	*0.36*	*0.00*	*0.35*	*0.014*	*0.014*	*0.001*	*0.001*	*0.001*	*0.000*		
alloy	avg	0.03	3.31	0.00	0.00	0.02	0.04	98.05	102.17	0.002	0.105	0.000	0.000	0.001	0.894		1.0
	stdv	*0.69*	*0.72*	*0.05*	*0.02*	*0.01*	*0.15*	*1.11*	*0.71*	*0.051*	*0.023*			*0.000*	*0.010*		
I1185-A																	
Fper	avg	49.25	11.63	1.13	0.39	0.12	38.55	0.08	101.27	0.895	0.092	0.008	0.003	0.001	0.000	1.06	1.0
	stdv	*0.50*	*0.54*	*0.08*	*0.06*	*0.02*	*0.42*	*0.05*	*0.64*	*0.009*	*0.004*	*0.001*	*0.000*	*0.000*	*0.000*		
$[O_4]$	avg	4.71	64.61	0.11	0.10	0.18	29.56	0.14	99.70	0.428	2.554	0.004	0.004	0.007	0.002	4.08	3.0
	stdv	*0.73*	*0.96*	*0.02*	*0.04*	*0.04*	*0.58*	*0.10*	*1.00*	*0.066*	*0.038*	*0.001*	*0.002*	*0.002*	*0.000*		

Table A.5.1

sample		Mg	Fe	Ni	Cr	Mn	O	Pt	total	Mg	Fe	Ni	Cr	Mn	Pt	Σoxy	Σcations
alloy	avg	1.53	4.63	0.17	0.05	0.02	2.54	91.63	100.68	0.102	0.134	0.005	0.002	0.000	0.861		1.0
	stdv	*0.81*	*0.54*	*0.04*	*0.01*	*0.02*	*2.07*	*1.77*	*2.96*	*0.054*	*0.016*	*0.001*	*0.000*	*0.001*	*0.015*		
S7470																	
Fper	avg	24.30	45.19	0.74	0.30	0.29	31.53	0.10	102.51	0.545	0.441	0.007	0.003	0.003	0.000	1.07	1.0
	stdv	*0.73*	*0.92*	*0.04*	*0.02*	*0.02*	*0.24*	*0.04*	*0.14*	*0.016*	*0.009*	*0.000*	*0.000*	*0.000*	*0.000*		
alloy	avg	0.02	15.45	1.00	0.04	0.03	0.23	85.99	102.75	0.001	0.376	0.023	0.001	0.001	0.601		1.0
	stdv	*0.04*	*0.52*	*0.07*	*0.03*	*0.01*	*0.10*	*0.72*	*0.66*	*0.002*	*0.013*	*0.002*	*0.001*	*0.000*	*0.005*		
H5164																	
Fper	avg	35.54	31.96	0.42	0.44	0.24	34.10	0.10	102.83	0.711	0.278	0.003	0.004	0.002	0.000	1.04	1.0
	stdv	*3.15*	*4.28*	*0.08*	*0.09*	*0.04*	*1.00*	*0.06*	*0.34*	*0.063*	*0.037*	*0.001*	*0.001*	*0.000*	*0.000*		
alloy	avg	0.05	15.41	0.95	0.04	0.01	0.39	84.86	101.70	0.003	0.378	0.022	0.001	0.000	0.596		1.0
	stdv	*0.16*	*0.69*	*0.15*	*0.02*	*0.01*	*0.49*	*0.97*	*0.99*	*0.009*	*0.017*	*0.003*	*0.001*	*0.000*	*0.745*		
S7510																	
Fper	avg	28.65	39.55	0.48	0.37	0.28	32.56	0.03	102.04	0.618	0.371	0.004	0.004	0.003	0.000	1.07	1.0
	stdv	*0.52*	*0.62*	*0.05*	*0.03*	*0.04*	*0.21*	*0.04*	*0.28*	*0.011*	*0.006*	*0.000*	*0.000*	*0.000*	*0.000*		
alloy	avg	0.01	12.46	0.50	0.02	0.03	90.03	0.28	103.35	0.001	0.321	0.012	0.001	0.001	0.667		1.0
	stdv	*0.01*	*0.53*	*0.07*	*0.02*	*0.03*	*0.67*	*0.15*	*0.80*	*0.001*	*0.014*	*0.002*	*0.001*	*0.001*	*0.356*		
S7509-B																	
Fper	avg	23.30	45.74	0.83	0.30	0.30	31.56	0.03	102.43	0.529	0.452	0.008	0.003	0.003	0.000	1.09	1.0
	stdv	*0.30*	*0.36*	*0.07*	*0.02*	*0.04*	*0.22*	*0.05*	*0.32*	*0.007*	*0.004*	*0.001*	*0.000*	*0.000*	*0.000*		
alloy	avg	0.01	10.96	0.42	0.02	0.03	0.28	90.71	102.51	0.000	0.293	0.011	0.000	0.001	0.696		1.0
	stdv	*0.01*	*0.88*	*0.06*	*0.02*	*0.03*	*0.07*	*1.06*	*1.92*	*0.000*	*0.023*	*0.001*	*0.000*	*0.001*	*0.008*		
S7716-B																	
Fper	avg	27.53	39.14	0.85	0.38	0.18	34.11	0.16	102.34	0.609	0.377	0.008	0.004	0.002	0.000	1.15	1.0
	stdv	*0.58*	*0.61*	*0.05*	*0.02*	*0.02*	*0.32*	*0.21*	*0.43*	*0.013*	*0.006*	*0.000*	*0.000*	*0.000*	*0.000*		
alloy	avg	0.01	9.12	0.36	0.04	0.01	0.28	93.67	103.49	0.001	0.251	0.009	0.001	0.000	0.740		1.0
	stdv	*0.01*	*0.56*	*0.03*	*0.01*	*0.01*	*0.14*	*0.58*	*0.60*	*0.001*	*0.015*	*0.001*	*0.000*	*0.000*	*0.005*		
Z2116																	
Fper	avg	23.38	44.76	0.89	0.30	0.26	32.45	0.18	102.41	0.535	0.446	0.008	0.003	0.003	0.001	1.13	1.0
	stdv	0.24	0.19	0.03	0.02	0.02	0.28	0.12	0.24	0.005	0.002	0.000	0.000	0.000	0.000		
S7691-A																	
Fper	avg	25.98	42.36	1.00	0.26	0.28	31.46	0.08	101.59	0.576	0.409	0.009	0.003	0.003	0.000	1.06	1.0
	stdv	*0.42*	*0.40*	*0.04*	*0.10*	*0.09*	*0.23*	*0.09*	*0.27*	*0.009*	*0.004*	*0.000*	*0.001*	*0.001*	*0.000*		
alloy	avg	0.04	10.69	0.40	0.03	0.02	0.36	92.82	104.33	0.002	0.283	0.010	0.001	0.001	0.707		1.0
	stdv	*0.04*	*0.47*	*0.04*	*0.01*	*0.02*	*0.20*	*0.97*	*1.04*	*0.002*	*0.012*	*0.001*	*0.000*	*0.001*	*0.007*		

Table A.5.1 continued

sample		Mg	Fe	Ni	Cr	Mn	O	Pt	total	Mg	Fe	Ni	Cr	Mn	Pt	Σoxy	Σcations
									Z2155-B								
Fper	avg	26.41	40.81	0.97	0.37	0.17	33.31	0.16	102.20	0.589	0.396	0.009	0.004	0.002	0.000	1.13	1.0
	stdv	*0.40*	*0.47*	*0.05*	*0.01*	*0.02*	*0.32*	*0.12*	*0.37*	*0.009*	*0.005*	*0.000*	*0.000*	*0.000*	*0.000*		
alloy	avg	0.01	9.42	0.39	0.03	0.01	0.09	92.59	102.55	0.000	0.259	0.010	0.001	0.000	0.731		1.0
	stdv	*0.01*	*0.32*	*0.03*	*0.01*	*0.02*	*0.06*	*0.75*	*0.48*	*0.000*	*0.009*	*0.001*	*0.000*	*0.000*	*0.006*		
									Z2155-A								
Fper	avg	27.46	40.36	0.99	0.38	0.17	32.73	0.04	102.19	0.601	0.384	0.009	0.004	0.002	0.000	1.09	1.0
	stdv	*0.48*	*0.70*	*0.06*	*0.02*	*0.03*	*0.50*	*0.04*	*0.43*	*0.011*	*0.007*	*0.001*	*0.000*	*0.000*	*0.000*		
alloy	avg	0.01	11.06	0.49	0.03	0.01	0.08	91.50	103.32	0.000	0.293	0.012	0.001	0.000	0.695		1.0
	stdv	*0.01*	*0.51*	*0.08*	*0.02*	*0.02*	*0.03*	*1.44*	*1.39*	*0.000*	*0.014*	*0.002*	*0.000*	*0.001*	*0.011*		
									S7216-B								
Fper	avg	22.92	45.74	0.84	0.31	0.29	31.61	0.02	102.41	0.521	0.453	0.008	0.003	0.003	0.000	1.09	1.0
	stdv	*0.50*	*0.67*	*0.08*	*0.01*	*0.04*	*0.37*	*0.02*	*0.30*	*0.011*	*0.007*	*0.001*	*0.000*	*0.000*	*0.000*		
alloy	avg	0.00	7.84	0.20	0.01	0.01	0.01	95.61	103.99	0.000	0.221	0.005	0.000	0.000	0.773		1.0
	stdv	*0.00*	*0.53*	*0.04*	*0.01*	*0.02*	*0.02*	*1.57*	*1.14*	*0.000*	*0.015*	*0.001*	*0.000*	*0.001*	*0.013*		
									S7216-A								
Fper	avg	24.81	42.75	0.91	0.33	0.29	32.10	0.06	102.08	0.554	0.416	0.008	0.003	0.003	0.000	1.09	1.0
	stdv	*0.26*	*0.32*	*0.05*	*0.02*	*0.04*	*0.20*	*0.12*	*0.29*	*0.006*	*0.003*	*0.000*	*0.000*	*0.000*	*0.000*		
alloy	avg	0.01	7.42	0.19	0.01	0.02	0.46	98.05	106.19	0.001	0.208	0.005	0.000	0.001	0.787		1.0
	stdv	*0.01*	*0.54*	*0.05*	*0.01*	*0.03*	*0.12*	*1.48*	*1.35*	*0.001*	*0.015*	*0.001*	*0.000*	*0.001*	*0.012*		
									Z1949-A								
Fper	avg	38.73	59.51	1.14	0.44	0.37	100.80	*		0.524	0.451	0.008	0.003	0.003	0.000		1.0
	stdv	*0.37*	*0.53*	*0.08*	*0.02*	*0.02*	*0.58*			*0.005*	*0.004*	*0.001*	*0.000*	*0.000*	*0.000*		
alloy	avg	0.08	8.54	0.20		0.36	104.13			0.005	0.241	0.005	0.000	0.000	0.753		1.0
									Z2122-B								
Fper	avg	29.99	37.04	1.13	0.17	0.21	33.32	0.19	102.42	0.636	0.342	0.010	0.002	0.002	0.000	1.07	1.0
	stdv	*0.69*	*0.77*	*0.04*	*0.03*	*0.02*	*0.19*	*0.10*	*0.17*	*0.015*	*0.007*	*0.000*	*0.000*	*0.000*	*0.000*		
O_5	avg	6.18	64.25	0.24	0.54	0.37	28.27	0.32	100.26	0.710	3.214	0.011	0.029	0.019	0.005	4.94	4.0
	stdv	*0.31*	*0.73*	*0.03*	*0.09*	*0.03*	*0.33*	*0.24*	*0.64*	*0.036*	*0.037*	*0.001*	*0.005*	*0.001*	*0.000*		
alloy	avg	0.05	9.57	0.14	0.04	0.02	0.38	94.85	105.07	0.003	0.258	0.004	0.001	0.001	0.738		1.0
	stdv	*0.01*	*0.09*	*0.04*	*0.01*	*0.03*	*0.14*	*0.42*	*0.61*	*0.001*	*0.002*	*0.001*	*0.000*	*0.001*	*0.003*		
									Z2117-B								
Fper	avg	34.33	31.91	1.35	0.15	0.18	34.06	0.21	102.43	0.694	0.281	0.011	0.001	0.002	0.001	1.05	1.0
	stdv	*0.55*	*0.66*	*0.09*	*0.02*	*0.02*	*0.33*	*0.27*	*0.27*	*0.011*	*0.006*	*0.001*	*0.000*	*0.000*	*0.000*		
O_5	avg	5.97	65.32	0.24	0.30	0.35	28.21	0.22	100.70	0.685	3.258	0.012	0.016	0.018	0.003	4.91	4.0
	stdv	*0.37*	*0.68*	*0.03*	*0.08*	*0.03*	*0.23*	*0.19*	*0.45*	*0.042*	*0.034*	*0.001*	*0.004*	*0.001*	*0.000*		

Table A.5.1 continued

sample		Mg	Fe	Ni	Cr	Mn	O	Pt	total	Mg	Fe	Ni	Cr	Mn	Pt	Σoxy	Σcations
alloy	avg	0.95	6.97	0.13	0.00	0.01	0.05	97.07	104.35	0.059	0.232	0.003	0.000	0.000	0.764		1.0
	stdv	*0.24*	*0.91*	*0.03*	*0.01*	*0.03*	*0.01*	*0.81*	*1.00*	*0.015*	*0.025*	*0.001*	*0.001*	*0.001*	*0.006*		
Z2115-B																	
Fper	avg	28.75	38.43	1.11	0.17	0.21	32.92	0.46	101.94	0.618	0.359	0.010	0.002	0.002	0.001	1.07	1.0
	stdv	*0.85*	*0.84*	*0.04*	*0.02*	*0.02*	*0.25*	*0.69*	*0.51*	*0.018*	*0.008*	*0.000*	*0.000*	*0.000*	*0.000*		
O_5	avg	6.17	64.60	0.25	0.61	0.36	28.42	0.42	100.86	0.707	3.221	0.012	0.033	0.018	0.006	4.95	4.0
	stdv	*0.39*	*0.77*	*0.02*	*0.10*	*0.02*	*0.26*	*0.49*	*0.45*	*0.045*	*0.038*	*0.001*	*0.005*	*0.001*	*0.000*		
alloy	avg	0.08	8.11	0.12	0.07	0.02	0.49	94.74	103.65	0.005	0.228	0.003	0.002	0.001	0.769		1.0
	stdv	*0.09*	*1.22*	*0.03*	*0.08*	*0.02*	*0.25*	*1.31*	*2.53*	*0.006*	*0.034*	*0.001*	*0.002*	*0.001*	*0.011*		
Z2121-A																	
Fper	avg	31.06	35.72	1.19	0.17	0.21	33.76	0.19	102.46	0.652	0.326	0.010	0.002	0.002	0.001	1.08	1.0
	stdv	*0.42*	*0.39*	*0.06*	*0.02*	*0.02*	*0.31*	*0.14*	*0.21*	*0.009*	*0.004*	*0.000*	*0.000*	*0.000*	*0.000*		
O_5	avg	9.19	59.95	0.35	0.51	0.35	29.40	0.50	100.30	1.023	2.904	0.016	0.026	0.017	0.007	4.97	4.0
	stdv	*0.11*	*0.43*	*0.02*	*0.03*	*0.02*	*0.27*	*0.67*	*0.48*	*0.012*	*0.021*	*0.001*	*0.001*	*0.001*	*0.000*		
alloy	avg	0.01	5.87	0.13	0.03	0.02	0.26	99.37	105.69	0.001	0.170	0.004	0.001	0.001	0.826		1.0
	stdv	*0.01*	*0.56*	*0.02*	*0.01*	*0.00*	*0.19*	*0.63*	*0.87*	*0.001*	*0.016*	*0.000*	*0.000*	*0.000*	*0.005*		
Z2151-A																	
Fper	avg	28.85	38.70	1.12	0.27	0.16	32.17	0.13	101.58	0.622	0.363	0.010	0.003	0.002	0.000	1.05	1.0
	stdv	*0.40*	*0.48*	*0.05*	*0.02*	*0.02*	*0.25*	*0.25*	*0.39*	*0.009*	*0.005*	*0.000*	*0.000*	*0.000*	*0.000*		
O_5	avg	7.78	61.09	0.31	0.95	0.24	28.85	0.16	99.98	0.887	3.032	0.015	0.051	0.012	0.002	5.00	4.0
	stdv	*0.12*	*0.21*	*0.02*	*0.05*	*0.02*	*0.30*	*0.14*	*0.27*	*0.014*	*0.010*	*0.001*	*0.003*	*0.001*	*0.000*		
alloy	avg	0.05	7.01	0.17	0.04	0.01	0.34	95.80	103.32	0.003	0.202	0.005	0.001	0.000	0.794		1.0
	stdv	*0.04*	*0.55*	*0.03*	*0.01*	*0.02*	*0.25*	*0.70*	*0.59*	*0.003*	*0.016*	*0.001*	*0.000*	*0.000*	*0.006*		
Z2153-A																	
Fper	avg	41.00	21.67	0.97	0.34	0.13	37.35	0.13	101.61	0.803	0.185	0.008	0.003	0.001	0.000	1.11	1.0
	stdv	*0.35*	*0.14*	*0.03*	*0.01*	*0.02*	*0.41*	*0.16*	*0.57*	*0.007*	*0.001*	*0.000*	*0.000*	*0.000*	*0.000*		
alloy	avg	0.04	3.22	0.16	0.03	0.01	98.44	0.44	102.35	0.003	0.102	0.005	0.001	0.000	0.894		1.0
	stdv	*0.02*	*0.42*	*0.02*	*0.01*	*0.02*	*1.28*	*0.13*	*1.12*	*0.001*	*0.013*	*0.001*	*0.000*	*0.000*	*0.263*		
H5189-A																	
Fper	avg	14.85	56.22	0.81	0.40	0.10	29.51	0.13	102.07	0.372	0.613	0.008	0.005	0.001	0.000	1.12	1.0
	stdv	*0.16*	*0.36*	*0.04*	*0.03*	*0.03*	*0.30*	*0.40*	*0.31*	*0.004*	*0.004*	*0.000*	*0.000*	*0.000*	*0.000*		
alloy	avg	0.02	13.02	0.44	0.03	0.01	0.36	92.65	106.54	0.001	0.325	0.010	0.001	0.000	0.664		1.0
	stdv	*0.01*	*0.69*	*0.03*	*0.02*	*0.01*	*0.12*	*1.01*	*1.15*	*0.001*	*0.017*	*0.001*	*0.001*	*0.000*	*0.007*		

Table A.5.1 continued

sample		Mg	Fe	Ni	Cr	Mn	O	Pt	total	Mg	Fe	Ni	Cr	Mn	Pt	Σoxy	Σcations
S7495-A																	
Fper	avg	15.55	55.09	0.90	0.35	0.13	29.86	0.08	101.92	0.387	0.597	0.009	0.004	0.001	0.000	1.13	1.0
	stdv	*0.73*	*0.91*	*0.06*	*0.06*	*0.02*	*0.33*	*0.05*	*0.28*	*0.018*	*0.010*	*0.001*	*0.001*	*0.000*	*0.000*		
O_4	avg	4.58	65.89	0.31	0.83	0.10	29.49	0.12	101.24	0.406	2.543	0.011	0.035	0.004	0.001	3.97	3.0
	stdv	*0.13*	*0.49*	*0.02*	*0.24*	*0.02*	*0.30*	*0.09*	*0.28*	*0.011*	*0.019*	*0.001*	*0.010*	*0.001*	*0.001*		
alloy	avg	0.08	10.65	0.24	0.04	0.01	0.38	93.09	104.49	0.005	0.282	0.006	0.001	0.000	0.712		1.0
	stdv	*0.07*	*0.57*	*0.02*	*0.02*	*0.01*	*0.13*	*0.89*	*0.74*	*0.004*	*0.015*	*0.001*	*0.001*	*0.000*	*0.246*		
H5190-A																	
Fper	avg	23.66	45.58	1.39	0.20	0.11	31.45	0.18	102.40	0.535	0.448	0.013	0.002	0.001	0.000	1.08	1.0
	stdv	*0.41*	*0.34*	*0.03*	*0.02*	*0.01*	*0.15*	*0.15*	*0.40*	*0.009*	*0.003*	*0.000*	*0.000*	*0.000*	*0.000*		
O_5	avg	5.62	66.61	0.34	0.22	0.15	28.57	0.16	101.51	0.643	3.319	0.016	0.012	0.008	0.002	4.97	4.0
	stdv	*0.33*	*0.93*	*0.05*	*0.23*	*0.01*	*0.35*	*0.06*	*0.34*	*0.038*	*0.046*	*0.002*	*0.012*	*0.001*	*0.000*		
alloy	avg	0.14	10.14	0.25	0.03	0.01	0.15	93.41	104.13	0.008	0.271	0.006	0.001	0.000	0.723		1.0
	stdv	*0.14*	*0.47*	*0.02*	*0.02*	*0.01*	*0.17*	*1.47*	*1.25*	*0.008*	*0.012*	*0.001*	*0.001*	*0.000*	*0.011*		
Z2077-A																	
Fper	avg	21.69	48.25	1.22	0.22	0.10	31.13	0.11	102.61	0.500	0.484	0.012	0.002	0.001	0.000	1.09	1.0
	stdv	*0.40*	*0.33*	*0.04*	*0.02*	*0.02*	*0.18*	*0.08*	*0.16*	*0.009*	*0.003*	*0.000*	*0.000*	*0.000*	*0.000*		
O_5	avg	5.38	66.60	0.30	0.52	0.15	28.37	0.13	101.33	0.618	3.329	0.014	0.028	0.008	0.002	4.95	4.0
	stdv	*0.08*	*0.43*	*0.02*	*0.25*	*0.02*	*0.21*	*0.05*	*0.26*	*0.009*	*0.022*	*0.001*	*0.013*	*0.001*	*0.000*		
alloy	avg	0.01	9.95	0.22	0.04	0.00	0.12	92.72	103.05	0.000	0.271	0.006	0.001	0.000	0.724		1.0
	stdv	*0.01*	*0.82*	*0.02*	*0.01*	*0.00*	*0.11*	*0.66*	*0.48*	*0.000*	*0.022*	*0.000*	*0.000*	*0.000*	*0.005*		
H5189-B																	
Fper	avg	2.70	71.83	0.82	0.15	0.17	25.56	0.12	101.24	0.078	0.907	0.010	0.002	0.002	0.000	1.13	1.0
	stdv	*0.19*	*0.23*	*0.03*	*0.03*	*0.02*	*0.27*	*0.07*	*0.28*	*0.006*	*0.003*	*0.000*	*0.000*	*0.000*	*0.000*		
O_4	avg	1.30	70.58	0.44	0.62	0.10	28.21	0.12	101.26	0.120	2.831	0.017	0.027	0.004	0.001	3.95	3.0
	stdv	*0.03*	*0.09*	*0.04*	*0.07*	*0.02*	*0.13*	*0.06*	*0.15*	*0.003*	*0.004*	*0.001*	*0.003*	*0.001*	*0.000*		
alloy	avg	0.01	15.30	1.00	0.03	0.01	0.35	88.23	104.94	0.001	0.368	0.023	0.001	0.000	0.609		1.0
	stdv	*0.01*	*0.72*	*0.04*	*0.01*	*0.01*	*0.18*	*0.63*	*0.57*	*0.000*	*0.017*	*0.001*	*0.000*	*0.000*	*0.004*		
S7509-A																	
Fper	avg	3.20	71.11	0.76	0.19	0.16	25.83	0.13	101.25	0.092	0.893	0.009	0.003	0.002	0.000	1.13	1.0
	stdv	*0.19*	*0.41*	*0.04*	*0.02*	*0.02*	*0.43*	*0.10*	*0.29*	*0.006*	*0.005*	*0.000*	*0.000*	*0.000*	*0.000*		
O_4	avg	1.50	70.33	0.38	0.72	0.11	28.25	0.12	101.29	0.138	2.810	0.014	0.031	0.004	0.001	3.95	3.0
	stdv	*0.03*	*0.12*	*0.02*	*0.06*	*0.01*	*0.21*	*0.05*	*0.25*	*0.003*	*0.005*	*0.001*	*0.003*	*0.000*	*0.000*		
alloy	avg	0.02	14.91	0.70	0.04	0.01	0.39	88.17	104.25	0.001	0.364	0.016	0.001	0.000	0.619		1.0
	stdv	*0.02*	*0.47*	*0.06*	*0.03*	*0.01*	*0.26*	*0.42*	*0.62*	*0.001*	*0.011*	*0.001*	*0.001*	*0.000*	*0.003*		

Table A.5.1 continued

sample		Mg	Fe	Ni	Cr	Mn	O	Pt	total	Mg	Fe	Ni	Cr	Mn	Pt	Σoxy	Σcations
									S7604-A								
Fper	avg	3.55	67.81	1.13	0.24	0.13	25.99	0.07	99.01	0.105	0.876	0.014	0.003	0.002	0.000	1.17	1.0
	stdv	*0.11*	*0.40*	*0.05*	*0.01*	*0.02*	*0.37*	*0.07*	*0.43*	*0.003*	*0.005*	*0.001*	*0.000*	*0.000*	*0.000*		
O_5	avg	2.23	68.97	0.67	0.40	0.19	26.61	0.07	99.15	0.272	3.660	0.034	0.023	0.010	0.001	4.94	4.0
	stdv	*0.16*	*0.12*	*0.10*	*0.05*	*0.02*	*0.31*	*0.07*	*0.25*	*0.020*	*0.006*	*0.005*	*0.003*	*0.001*	*0.000*		
alloy	avg	0.01	15.00	0.80	0.04	0.01	0.32	87.89	104.06	0.000	0.366	0.018	0.001	0.000	0.616		1.0
	stdv	*0.01*	*0.82*	*0.10*	*0.01*	*0.02*	*0.20*	*0.98*	*0.58*	*0.000*	*0.020*	*0.002*	*0.000*	*0.000*	*0.007*		
									S7495-B								
O_6	avg	2.32	70.89	0.80	0.36	0.13	26.88	0.12	101.52	0.344	4.570	0.049	0.025	0.009	0.001	*6.05*	*5.0*
	stdv	0.11	0.25	0.08	0.03	0.02	0.18	0.05	0.34	0.017	0.016	0.005	0.002	0.001	0.001		
									Z2122-A								
alloy	avg	0.13	14.20	0.94	0.04	0.01	0.44	86.68	102.43	0.007	0.353	0.022	0.001	0.000	0.616		1.0
	stdv	*0.08*	*0.77*	*0.07*	*0.00*	*0.01*	*0.05*	*2.89*	*3.46*	*0.004*	*0.019*	*0.002*	*0.000*	*0.000*	*0.074*		
O_6	avg	2.66	70.75	0.87	0.35	0.16	26.35	0.14	101.30	0.390	4.518	0.053	0.024	0.010	0.003	5.87	5.0
	stdv	*0.19*	*0.47*	*0.10*	*0.03*	*0.02*	*0.29*	*0.10*	*0.47*	*0.028*	*0.030*	*0.006*	*0.002*	*0.001*	*0.000*		
									Z2115-A								
alloy	avg	0.09	14.13	0.72	0.03	0.00	1.69	88.43	105.09	0.005	0.350	0.017	0.001	0.000	0.627		*1.0*
	stdv	0.07	0.54	0.07	0.02	0.00	1.02	0.83	0.70	0.000	0.013	0.002	0.000	0.000	0.377		
O_6	avg	2.67	69.46	0.87	0.34	0.16	26.42	0.19	100.13	0.398	4.507	0.054	0.024	0.011	0.004	*5.99*	*5.0*
	stdv	0.18	0.33	0.08	0.02	0.02	0.29	0.14	0.31	0.027	0.021	0.005	0.002	0.001	0.002		
									Z2077-B								
O_6	avg	2.31	70.97	0.74	0.36	0.13	26.52	0.15	101.18	0.342	4.576	0.045	0.025	0.009	0.003	5.97	*5.0*
	stdv	0.25	0.38	0.14	0.05	0.01	0.39	0.13	0.45	0.036	0.024	0.008	0.003	0.001	0.000		
									H5190-B								
alloy	avg	0.00	8.16	0.50	0.02	0.00	0.13	92.69	101.50	0.000	0.232	0.014	0.001	0.000	0.754		
	stdv	0.00	0.83	0.04	0.02	0.00	0.04	0.73	0.54	0.000	0.023	0.001	0.000	0.000	0.223		
O_6	avg	2.52	70.99	0.90	0.33	0.15	26.51	0.14	101.53	0.370	4.540	0.055	0.023	0.010	0.003	5.92	5.0
	stdv	0.18	0.35	0.10	0.04	0.01	0.22	0.09	0.24	0.026	0.023	0.006	0.003	0.001	0.000		
									Z2117-A								
Fper	avg	5.82	67.49	1.82	0.17	0.15	24.88	0.12	100.56	0.161	0.811	0.021	0.002	0.002	0.000	1.04	1.0
	stdv	*0.19*	*0.39*	*0.12*	*0.03*	*0.02*	*0.20*	*0.04*	*0.30*	*0.005*	*0.005*	*0.001*	*0.000*	*0.000*	*0.000*		
O_6	avg	2.40	71.28	0.84	0.33	0.16	26.10	0.19	101.31	0.353	4.557	0.051	0.023	0.010	0.003	5.82	5.0
	stdv	*0.20*	*0.36*	*0.06*	*0.06*	*0.02*	*0.16*	*0.13*	*0.21*	*0.029*	*0.023*	*0.003*	*0.004*	*0.001*	*0.000*		

Table A.5.1 continued

sample		Mg	Fe	Ni	Cr	Mn	O	Pt	total	Mg	Fe	Ni	Cr	Mn	Pt	Σoxy	Σcations
Z2120-A																	
Fper	avg	5.89	66.85	1.81	0.18	0.14	25.12	0.24	100.37	0.163	0.807	0.021	0.002	0.002	0.001	1.06	1.0
	stdv	*0.62*	*0.80*	*0.20*	*0.05*	*0.02*	*0.20*	*0.21*	*0.55*	*0.017*	*0.010*	*0.002*	*0.001*	*0.000*	*0.000*		
O_6	avg	2.42	70.05	0.84	0.34	0.16	26.24	0.16	100.23	0.362	4.547	0.052	0.024	0.010	0.003	5.95	5.0
	stdv	*0.19*	*0.37*	*0.08*	*0.08*	*0.01*	*0.21*	*0.12*	*0.27*	*0.029*	*0.024*	*0.005*	*0.006*	*0.001*	*0.000*		
S7716-A																	
Fper	avg	0.32	74.52	0.52	0.39	0.16	24.60	0.05	100.58	0.010	0.976	0.007	0.005	0.002	0.000	1.12	1.0
	stdv	*0.03*	*0.33*	*0.03*	*0.01*	*0.02*	*0.29*	*0.06*	*0.35*	*0.001*	*0.004*	*0.000*	*0.000*	*0.000*	*0.000*		
O_4	avg	0.23	71.52	0.39	0.42	0.11	27.88	0.06	0.00	0.022	2.939	0.015	0.018	0.004	0.001	4.00	3.0
	stdv	*0.03*	*0.20*	*0.03*	*0.01*	*0.02*	*0.18*	*0.07*	*0.00*	*0.002*	*0.008*	*0.001*	*0.001*	*0.001*	*0.000*		
alloy	avg	0.00	12.81	0.56	0.03	0.02	0.13	90.66	104.21	0.000	0.326	0.014	0.001	0.000	0.661		1.0
	stdv	*0.00*	*0.56*	*0.02*	*0.01*	*0.02*	*0.11*	*0.26*	*0.44*	*0.000*	*0.014*	*0.001*	*0.000*	*0.000*	*0.002*		
S7691-B																	
Fper	avg	0.01	75.18	0.67	0.32	0.18	23.65	0.03	100.08	0.000	0.984	0.008	0.004	0.002	0.000	1.08	1.0
	stdv	*0.01*	*0.32*	*0.05*	*0.06*	*0.02*	*0.34*	*0.03*	*0.49*	*0.000*	*0.004*	*0.001*	*0.001*	*0.000*	*0.000*		
O_4	avg	0.01	71.16	0.39	1.24	0.10	26.81	0.06	99.85	0.001	2.923	0.015	0.055	0.004	0.001	3.84	3.0
	stdv	*0.01*	*0.27*	*0.03*	*0.09*	*0.01*	*0.43*	*0.06*	*0.52*	*0.000*	*0.011*	*0.001*	*0.004*	*0.001*	*0.000*		
alloy	avg	0.01	15.00	0.80	0.04	0.01	0.32	87.89	104.06	0.000	0.366	0.018	0.001	0.000	0.614		1.0
	stdv	*0.01*	*0.82*	*0.10*	*0.01*	*0.02*	*0.20*	*0.98*	*0.58*	*0.000*	*0.020*	*0.002*	*0.000*	*0.000*	*0.007*		
I1185-B																	
Fper	avg	0.03	75.29	1.22	0.21	0.14	23.18	0.14	100.22	0.001	0.978	0.015	0.003	0.002	0.001	1.05	1.0
	stdv	*0.01*	*0.74*	*0.19*	*0.12*	*0.02*	*0.82*	*0.31*	*0.60*	*0.000*	*0.010*	*0.002*	*0.002*	*0.000*	*0.000*		
O_6	avg	0.01	73.04	0.63	0.55	0.16	25.58	0.15	100.13	0.002	4.904	0.040	0.039	0.011	0.003	5.99	5.0
	stdv	*0.01*	*0.53*	*0.13*	*0.08*	*0.02*	*0.46*	*0.35*	*0.29*	*0.001*	*0.036*	*0.008*	*0.006*	*0.002*	*0.000*		
alloy	avg	0.00	14.04	0.62	0.03	0.00	0.57	86.07	101.34	0.000	0.357	0.015	0.001	0.000	0.627		1.0
	stdv	*0.00*	*0.94*	*0.12*	*0.01*	*0.01*	*0.42*	*0.46*	*1.10*	*0.000*	*0.024*	*0.003*	*0.000*	*0.000*	*0.003*		

(*) the values for these 2 samples are reported in oxide wt% and not element wt%

Table A.5.2: Unit-cell lattice parameters of the phase assemblages recovered in this study

Sample	Phase	a,b,c (Å)	α,β,γ (°)	Volume (Å^3)
S7029	Fper	4.219	90.00	75.1
		0.001	0.00	0.1
	Pt alloy	3.910	90.00	59.8
		0.001	0.00	0.1
	Spft	8.394	90.00	591.5
		0.004	0.00	0.4
Z2038	Fper	4.227	90.00	75.6
		0.001	0.00	0.1
	n-spft	8.436	90.00	600.3
		0.011	0.00	0.9
	Pt alloy	3.890	90.00	58.8
		0.004	0.00	0.1
H5128	Fper	4.225	90.00	75.4
		0.001	0.00	0.1
	n-spft	8.409	90.00	594.6
		0.008	0.00	0.7
	Pt alloy	3.890	90.00	58.9
		0.003	0.00	0.1
S7004	Fper	4.218	90.00	75.1
		0.001	0.00	0.1
	n-spft	8.425	90.00	598.0
		0.004	0.00	0.4
	Pt alloy	3.923	90.00	60.4
		0.004	0.00	0.1
S7377	Fper	4.219	90.00	75.1
		0.001	0.00	0.1
	Spft	8.377	90.00	587.8
		0.004	0.00	0.4
	Pt alloy	3.914	90.00	59.9
		0.003	0.00	0.1
S7180	Fper	4.218	90.00	75.1
		0.001	0.00	0.1
	n-spft	8.419	90.00	596.7
		0.012	0.00	0.9
	Pt alloy	3.924	90.00	60.4
		0.003	0.00	0.1
S7204	Fper	4.251	90.00	76.8
		0.001	0.00	0.1
	n-spft	8.437	90.00	600.6
		0.004	0.00	0.4
	Pt alloy	3.918	90.00	60.1
		0.003	0.00	0.1
Z1949-B	Fper	4.219	90.00	75.1
		0.001	0.00	0.1
	n-spft	8.414	90.00	595.8
		0.005	0.00	0.7
	Pt alloy	3.914	90.00	60.0
		0.003	0.00	0.1
S7470	Fper	4.252	90.00	76.8
		0.001	0.00	0.1
	Pt alloy	3.751	90.00	52.8
		0.003	0.00	0.1
S7510	Fper	4.241	90.00	76.2
		0.001	0.00	0.1
	n-spft	8.365	90.00	585.4
		0.006	0.00	0.6

Table A.5.2 continued

Sample	Phase	a,b,c (Å)	α,β,γ (°)	Volume (Å^3)
S7510	Pt_3Fe	3.870	90.00	57.9
		0.003	0.00	0.1
S7509-B	Fper	4.235	90.00	75.9
		0.001	0.00	0.1
	n-spft	8.396	90.00	591.8
		0.004	0.00	0.5
	Pt_3Fe	3.867	90.00	57.8
		0.003	0.00	0.1
S7716-B	Fper	4.246	90.00	76.6
		0.001	0.00	0.1
	n-spft	8.444	90.00	602.1
		0.008	0.00	0.9
	Pt alloy	3.886	90.00	58.7
		0.003	0.00	0.1
Z2116	Fper	4.232	90.00	75.8
		0.001	0.00	0.1
	n-spft	8.413	90.00	595.5
		0.005	0.00	0.8
	Pt alloy	3.880	90.00	58.5
		0.002	0.00	0.1
Z2155-A	Fper	4.241	90.00	76.3
		0.001	0.00	0.1
	n-spft	8.427	90.00	598.5
		0.016	0.00	1.0.
	Pt_3Fe	3.873	90.00	58.1
		0.004	0.00	0.1
S7216-B	Fper	4.243	90.00	76.4
		0.001	0.00	0.1
	n-spft	8.462	90.00	605.9
		0.006	0.00	0.8
	Pt alloy	3.895	90.00	59.1
		0.004	0.00	0.1
S7216-A	Fper	4.242	90.00	76.3
		0.001	0.00	0.1
	n-spft	8.437	90.00	600.5
		0.006	0.00	0.7
	Pt alloy	3.897	90.00	59.2
		0.004	0.00	0.1
Z1949-A	Fper	4.245	90.00	76.5
		0.001	0.00	0.1
	n-spft	8.414	90.00	595.7
		0.005	0.00	0.6
	Pt alloy	3.889	90.00	58.8
		0.003	0.00	0.1
Z2153-A	Fper	4.222	90.00	75.3
		0.001	0.00	0.1
	n-spft	8.456	90.00	604.6
		0.008	0.00	0.9
	Pt alloy	3.929	90.00	60.6
		0.003	0.00	0.1
H5189-A	Fper	4.250	90.00	76.79
		0.002	0.00	0.1
	n-spft	8.413	90.00	595.5
		0.004	0.00	0.5
	Pt_3Fe	3.868	90.00	57.8
		0.003	0.00	0.1

Table A.5.2 continued

Sample	Phase	a,b,c (Å)	α,β,γ (°)	Volume (Å^3)
S7495-A	Fper	4.243	90.00	76.4
		0.002	0.00	0.1
	Spft	8.404	90.00	593.5
		0.009	0.00	0.9
	Pt alloy	3.886	90.00	58.7
		0.003	0.00	0.1
H5189-B	Fper	4.279	90.00	78.3
		0.001	0.00	0.1
	Spft	8.390	90.00	590.6
		0.006	0.00	0.7
	Pt_3Fe	3.859	90.00	57.5
		0.003	0.00	0.1
S7509-A	Fper	4.273	90.00	78.0
		0.002	0.00	0.1
	Spft	8.376	90.00	587.7
		0.005	0.00	0.7
	Pt_3Fe	3.854	90.00	57.3
		0.002	0.00	0.1
S7716 A	Fper	4.294	90.00	79.2
		0.001	0.00	0.1
	Spft	8.399	90.00	592.5
		0.004	0.00	0.5
	Pt_3Fe	3.871	90.00	58.0
		0.003	0.00	0.1
S7691-B	Fper	4.292	90.00	79.1
		0.001	0.00	0.1
	Spft	8.413	90.00	595.4
		0.004	0.00	0.5
	Pt_3Fe	3.862	90.00	57.6
		0.003	0.00	0.1

Table A.5.2 continued

Sample	Phase	a (Å)	b (Å)	c (Å)	α,β,γ (°)	Volume (Å^3)
S7604-A	Fper	4.263	= =	= =	90.00	77.5
		0.001			0.00	0.1
	O_5	2.890	9.828	12.430	90.00	353.7
		0.002	0.007	0.015	0.00	0.4
	Spft	8.394	= =	= =	90.00	591.5
		0.009			0.00	1.0
	Pt_3Fe	3.873	= =	= =	90.00	58.2
		0.003			0.00	0.1
S7495-B	O_6	2.903	9.844	15.241	90.00	435.5
		0.001	0.009	0.016	0.00	0.4
	Pt_3Fe	3.860	= =	= =	90.00	57.5
		0.003			0.00	0.1
S7382	Fper	4.219	= =	= =	90.00	75.1
		0.001			0.00	0.1
	O_5	2.900	9.755	12.537	90.00	354.6
		0.004	0.010	0.016	0.00	0.6
	Pt alloy	3.917	= =	= =	90.00	60.1
		0.002			0.00	0.1
S7006	Fper	4.220	= =	= =	90.00	75.1
		0.001			0.00	0.1
	O_5	2.900	9.774	12.542	90.00	355.5
		0.006	0.016	0.022	0.00	1.0
	Pt alloy	3.926	= =	= =	90.00	60.5
		0.002			0.00	0.1
S7016	Fper	4.219	= =	= =	90.00	75.1
		0.001			0.00	0.1
	O_5	2.818	10.180	12.358	90.00	354.5
		0.003	0.014	0.010	0.00	0.5
	Pt alloy	3.914	= =	= =	90.00	59.9
		0.002			0.00	0.1
Z2151-B	Fper	4.223	= =	= =	90.00	75.3
		0.001			0.00	0.1
	O_5	2.8956	9.781	12.556	90.00	355.6
		0.012	0.018	0.022	0.00	1.5
	Pt alloy	3.931	= =	= =	90.00	60.8
		0.003			0.00	0.1
Z2153-B	Fper	4.238	= =	= =	90.00	76.1
		0.001			0.00	0.1
	O_5	2.894	9.770	12.563	90.00	355.3
		0.011	0.022	0.025	0.00	1.0
	Pt alloy	3.914	= =	= =	90.00	60.0
		0.003			0.00	0.1
H4792	Fper	4.225	= =	= =	90.00	75.4
		0.001			0.00	0.1
	O_5	2.893	9.740	12.554	90.00	353.8
		0.005	0.014	0.012	0.00	0.8
	Pt alloy	3.923	= =	= =	90.00	60.4
		0.004			0.00	0.1
S7410	Fper	4.226	= =	= =	90.00	75.5
		0.001			0.00	0.1
	O_5	2.890	9.646	12.732	90.00	355.0
		0.009	0.013	0.016	0.00	0.9
	Pt alloy	3.925	= =	= =	90.00	60.5
		0.002			0.00	0.1

Table A.5.2 continued

Sample	Phase	a (Å)	b (Å)	c (Å)	α,β,γ (°)	Volume (Å^3)
S7123-B	Fper	4.220	= =	= =	90.00	75.1
		0.001			0.00	0.1
		3.920	= =	= =	90.00	60.2
	Pt alloy	0.002			0.00	0.1
I1185-A	Fpe	4.217	= =	= =	90.00	75.0
		0.005			0.00	0.5
Z2122-B	Fper	4.242	= =	= =	90.00	76.3
		0.001			0.00	0.1
	O_5	2.899	9.766	12.571	90.00	355.9
		0.002	0.012	0.009	0.00	0.6
	Pt alloy	3.892	= =	= =	90.00	58.93
		0.001			0.00	0.07
Z2117-B	Fper	4.238	= =	= =	90.00	76.1
		0.001			0.00	0.1
	O_5	2.900	9.765	12.532	90.00	354.9
		0.002	0.011	0.010	0.00	0.6
	Pt alloy	3.890	= =	= =	90.00	58.9
		0.003			0.00	0.1
Z2115-B	Fper	4.242	= =	= =	90.00	76.3
		0.001			0.00	0.1
	O_5	2.893	9.746	12.556	90.00	354.0
		0.003	0.017	0.012	0.00	0.7
	Pt alloy	3.895	= =	= =	90.00	59.1
		0.002			0.00	0.1
Z2121-A	Fper	4.233	= =	= =	90.00	75.8
		0.002			0.00	0.1
	O_5	2.896	9.741	12.559	90.00	354.8
		0.007	0.022	0.024	0.00	0.9
	Pt alloy	3.912	= =	= =	90.00	59.8
		0.002			0.00	0.1
Z2151-A	Fper	4.241	= =	= =	90.00	76.3
		0.001			0.00	0.1
	O_5	2.903	9.763	12.572	90.00	356.4
		0.004	0.017	0.015	0.00	0.9
	Pt alloy	3.913	= =	= =	90.00	59.9
		0.002			0.00	0.1
H5190-A	Fper	4.246	= =	= =	90.00	76.6
		0.001			0.00	0.1
	O_5	2.896	9.769	12.536	90.00	354.7
		0.002	0.007	0.005	0.00	0.6
	Pt alloy	3.888	= =	= =	90.00	58.8
		0.002			0.00	0.1
Z2077-A	Fper	4.245	= =	= =	90.00	76.5
		0.001			0.00	0.1
	O_5	2.892	9.742	12.488	90.00	351.8
		0.006	0.016	0.018	0.00	0.8
	Pt alloy	3.881	= =	= =	90.00	58.5
		0.003			0.00	0.1
Z2122-A	O_6	2.891	9.879	15.328	90.00	437.8
		0.003	0.005	0.009	0.00	0.4
	Pt_3Fe	3.856	= =	= =	90.00	57.3
		0.003			0.00	0.1
Z2115-A	O_6	2.891	9.873	15.325	90.00	437.4
		0.001	0.006	0.007	0.00	0.4
	Pt_3Fe	3.867	= =	= =	90.00	57.8
		0.003			0.00	0.1

Table A.5.2 continued

Sample	Phase	a (Å)	b (Å)	c (Å)	α,β,γ (°)	Volume (Å^3)
Z2077-B	O_6	2.901	9.820	15.292	90.00	435.7
		0.002	0.015	0.013	0.00	0.8
	Pt_3Fe	3.846	= =	= =	90.00	56.9
		0.003			0.00	0.1
H5190-B	O_6	2.894	9.878	15.289	90.00	437.0
		0.002	0.009	0.010	0.00	0.9
	Pt_3Fe	3.872	= =	= =	90.00	58.1
		0.003			0.00	0.1
Z2117-A	O_6	2.890	9.867	15.332	90.00	437.2
		0.002	0.006	0.008	0.00	0.5
	Pt_3Fe	3.855	= =	= =	90.00	57.3
		0.003			0.00	0.1
Z2120-A	O_6	2.882	9.874	15.306	90.00	435.6
		0.002	0.006	0.011	0.00	0.7
	Pt_3Fe	3.860	= =	= =	90.00	57.52
		0.001			0.00	0.08
I1185-B	FeO	4.329	= =	= =	90.00	81.1
		0.008			0.00	0.9

Table A.5.3: Mössbauer parameters obtained from the fitting procedure of the Mössbauer spectra collected for the samples investigated in this study

sample	CS (mm/s)	QS (mm/s)	FWHM (mm/s)	Rel. area	BHF (T)	Site assignment	χ^2
S7029	1.07(1)	0.57(12)	0.31(24)	0.15		Fe^{2+} in Fper	1.58
	1.07(1)	0.94(2.1)	1.04(57)	0.27		Fe^{2+} in Fper	
	0.16(6)		1.12(19)	0.22		Fe^{3+} in Fper	
	0.31(3)	0.03(6)	0.52(13)	0.15	48.1 (2)	spft (S1)	
	0.45(2)	-0.08(23)	2.04(61)	0.20	45.2(3)	spft (S2)	
Z2038	1.03(1)	0.59(1)	0.30(4)	0.51		Fe^{2+} in Fper	1.04
	0.99(3)	1.12(3)	0.5(2)	0.26		Fe^{2+} in Fper	
	0.09(1)		0.7(1)	0.15		Fe^{3+} in Fper	
	0.36(1)	0.00(1)	0.7(2)	0.07	41.2(7)	n-spft	
H5128	1.03(1)	1.0(7)	0.5(4)	0.26		Fe^{2+} in Fper	0.90
	1.04(1)	0.6(1)	0.3(1)	0.27		Fe^{2+} in Fper	
	0.1(0)		0.7(3)	0.09		Fe^{3+} in Fper	
	0.6(1)	0.1(1)	1.7(4)	0.26	39.3(2)	$Fe^{2.5+}$n-spft	
	0.4(1)	0.0(1)	0.7(2)	0.12	44.3(5)	n-spft	
S7004	1.26(1)	1.16(24)	0.46(23)	0.07		Fe^{2+} in Fper	1.02
	1.05(1)	0.58(7)	0.35(5)	0.26		Fe^{2+} in Fper	
	0.11(4)		0.62(7)	0.11		Fe^{3+} in Fper	
	0.33(5)	-0.01(9)	0.71(22)	0.09	44.6(4)	n-spft	
	0.44(7)	-0.04(10)	1.90(30)	0.48	38.7(9)	n-spft	
S7377	1.04(1)	0.58(5)	0.33(3)	0.21		Fe^{2+} in Fper	0.76
	1.18(11)	1.04(16)	0.74(11)	0.14		Fe^{2+} in Fper	
	0.12		0.67	0.12		Fe^{3+} in Fper	
	0.35(9)	-0.01(15)	1.3(5)	0.09	43.8(9)	spft (S1)	
	0.51(15)	0.07(18)	2.5(7)	0.44	41.0(3)	spft (S2)	
S7180	1.01(1)	0.64(04)	0.41(08)	0.27		Fe^{2+} in Fper	1.08
	0.09(1)		0.78(11)	0.08		Fe^{3+} in Fper	
	0.40(1)	-0.07(10)	2.11(21)	0.66	42.1(1)	n-spft	
S7204	1.04(1)	0.56(02)	0.31(05)	0.30		Fe^{2+} in Fper	0.81
	1.06(1)	1.15(59)	0.71(34)	0.20		Fe^{2+} in Fper	
	0.11(2)		0.71(7)	0.12		Fe^{3+} in Fper	
	0.52(3)	-0.002 (17)	4.61(4)	0.37	9.02 (13)**	n-spft	

** really broad contribution is visible in the spectrum, but given the ±5 velocity scale of data acquisition, it was only possible to fit with a really broad doublet.

Table A.5.3 continued

sample	CS (mm/s)	QS (mm/s)	FWHM (mm/s)	Rel. area	BHF (T)	Site assignment	χ^2
Z1949-B	1.13(1)	1.14(32)	0.64(33)	0.16		Fe^{2+} in Fper	1.17
	1.04(1)	0.58(3)	0.30(4)	0.26		Fe^{2+} in Fper	
	0.14(3)		0.64(9)	0.09		Fe^{3+} in Fper	
	0.43(5)	0.01(8)	1.90(22)	0.49	41.7(4)	n-spft	
S7382	0.93(2)	0.67(3)	0.36(6)	0.45		Fe^{2+} in Fper	1.27
	0.10(0)		0.50(14)	0.08		Fe^{3+} in Fper	
	0.93(0)	2.91(3)	0.39(5)	0.10		$^{VI}Fe^{2+}$ in O_5	
	0.50(1)	0.55(2)	0.31(3)	0.37		$^{VI}Fe^{3+}$ in O_5	
S7006	0.97(2)	0.61(3)	0.22(08)	0.37		Fe^{2+} in Fper	1.24
	0.16(3)		0.57(35)	0.12		Fe^{3+} in Fper	
	0.96(2)	2.86(3)	0.46(5)	0.12		$^{VI}Fe^{2+}$ in O_5	
	0.54(2)	0.5503)	0.33(4)	0.41		$^{VI}Fe^{3+}$ in O_5	
S7016	1.04(1)	0.54(2)	0.29(7)	0.39		Fe^{2+} in Fper	1.48
	0.23(4)		0.10(86)	0.05		Fe^{3+} in Fper	
	0.93(6)	2.30(38)	1.01(30)	0.10		$^{VI}Fe^{2+}$ in O_5	
	0.36(2)	0.49(2)	0.34(7)	0.45		$^{VI}Fe^{3+}$ in O_5	
Z2151-B	1.01(1)	0.59(26)	0.37(10)	0.40		Fe^{2+} in Fper	1.40
	0.16(0)		0.23(16)	0.05		Fe^{3+} in Fper	
	0.94(0)	2.41(75)	0.91(52)	0.09		$^{VI}Fe^{2+}$ in O_5	
	0.37(0)	0.52(23)	0.49(14)	0.45		$^{VI}Fe^{3+}$ in O_5	
Z2153-B	1.01(1)	0.78(50)	0.66(36)	0.31		Fe^{2+} in Fper	1.06
	0.14(5)		0.32(59)	0.05		Fe^{3+} in Fper	
	0.89(80)	1.49(42)	1.26(66)	0.59		$^{VI}Fe^{2+}$ in O_5	
	0.60(8)	0.35(33)	0.30(50)	0.04		$^{VI}Fe^{3+}$ in O_5	
H4792	1.06(1)	0.52(5)	0.30(9)	0.52		Fe^{2+} in Fper	1.06
	0.17(8)		0.64(78)	0.16		Fe^{3+} in Fper	
	0.90(4)	2.86(7)	0.36(11)	0.08		$^{VI}Fe^{2+}$ in O_5	
	0.39(2)	0.42(23)	0.25(30)	0.24		$^{VI}Fe^{3+}$ in O_5	
S7410	0.95(5)	0.73(14)	0.32(10)	0.58		Fe^{2+} in Fper	0.82
	0.04(0)		0.82(30)	0.06		Fe^{3+} in Fper	
	0.93(2)	2.85(4)	0.29(9)	0.13		$Fe^{2+\ VI}$ in O_5	
	0.56(6)	0.50(4)	0.23(11)	0.23		$Fe^{3+\ octa}$ in O_5	

Table A.5.3 continued

sample	CS (mm/s)	QS (mm/s)	FWHM (mm/s)	Rel. area	BHF (T)	Site assignment	χ^2
S7123-B[#]	1.05(1)	0.64(3)	0.41(10)	0.81		Fe^{2+} in Fper	0.99
	0.15(4)		0.55(40)	0.19		Fe^{3+} in Fper	
S7470	1.06(1)	0.88(1)	0.55(2)	0.85		Fe^{2+} in Fper	1.10
	0.13(2)		0.45(7)	0.15		Fe^{3+} in Fper	
H5164	1.04(1)	0.62(1)	0.23(2)	0.24		Fe^{2+} in Fper	0.91
	1.03(1)	0.98(1)	0.44(2)	0.66		Fe^{2+} in Fper	
	0.13(2)		0.40(7)	0.9		Fe^{3+} in Fper	
S7510	1.08(2)	0.73(7)	0.37(31)	0.30		Fe^{2+} in Fper	1.49
	1.03(9)	1.0(6)	0.65(10)	0.58		Fe^{2+} in Fper	
	0.19(23)		0.69(42)	0.12		Fe^{3+} in Fper	
S7509-B	1.05(1)	0.90(0)	0.44(2)	0.48		Fe^{2+} in Fper	1.02
	0.18(0)		0.44(10)	0.07		Fe^{3+} in Fper	
	0.31(3)	0.03(2)	0.45(9)	0.09	45.9(2)	n-spft	
	0.58(4)	-0.02(6)	1.11(18)	0.37	42.1(4)	$Fe^{2.5+}$ n-spft	
S7716-B	1.08(1)	0.82(3)	0.42(4)	0.40		Fe^{2+} in Fper	1.13
	0.23(8)		0.37(50)	0.05		Fe^{3+} in Fper	
	0.31(3)	0.07(5)	0.49(8)	0.16	47.9(2)	n-spft	
	0.60(4)	-0.05(7)	0.81(20)	0.39	43.9(3)	$Fe^{2.5+}$ n-spft	
Z2116	1.05(2)	0.72(5)	0.29(15)	0.09		Fe^{2+} in Fper	1.26
	1.03(2)	1.11(28)	0.66(12)	0.35		Fe^{2+} in Fper	
	0.10(0)		1.03(41)	0.07		Fe^{3+} in Fper	
	0.61(5)	0.01(5)	0.82(19)	0.27	43.6(3)	$Fe^{2.5+}$ n-spft	
	0.33(2)	0.01(3)	0.38(5)	0.15	48.6(1)	n-spft	
	0.39(3)	0.09(4)	0.37(12)	0.07	46.3(3)	n-spft	
S7691-A	1.04(1)	0.73(05)	0.35(5)	0.31		Fe^{2+} in Fper	0.90
	1.00(1)	1.33(17)	0.46(15)	0.22		Fe^{2+} in Fper	
	0.21(4)		0.84(66)	0.05		Fe^{3+} in Fper	
	0.28(6)	0.03(10)	0.51(15)	0.05	45.9(3)	n-spft	
	0.54(6)	-0.02(8)	1.47(29)	0.37	41.3(7)	$Fe^{2.5+}$ n-spft	

Table A.5.3 continued

sample	CS (mm/s)	QS (mm/s)	FWHM (mm/s)	Rel. area	BHF (T)	Site assignment	χ^2
Z2155-B	1.01(1)	1.42(9)	0.43(7)	0.18		Fe^{2+} in Fper	1.09
	1.03(1)	0.73(2)	0.36(3)	0.32		Fe^{2+} in Fper	
	0.15(8)		1.10(26)	0.06		Fe^{3+} in Fper	
	0.28(2)	0.01(2)	0.21(5)	0.12	46.6(1)	n-spft	
	0.66(4)	0.15(5)	0.83(7)	0.31	44.0(3)	$Fe^{2.5+}$ n-spft	
Z2155 A	1.03(1)	0.99(04)	0.51(39)	0.56		Fe^{2+} in Fper	1.49
	1.04(1)	0.64(14)	0.25(40)	0.20		Fe^{2+} in Fper	
	0.09(5)		0.45(23)	0.09		Fe^{3+} in Fper	
	0.30(0)	-0.32(10)	0.74(30)	0.15	42.3(6)	n-spft	
S7216-B	1.00(2)	0.68(8)	0.23(21)	0.11		Fe^{2+} in Fper	1.28
	0.98(2)	1.08(41)	0.54(17)	0.45		Fe^{2+} in Fper	
	0.08(6)		0.50(18)	0.08		Fe^{3+} in Fper	
	0.54(3)	0.02(4)	1.21(15)	0.27	41.0(4)	n-spft	
	0.30(3)	0.03(4)	0.56(8)	0.09	45.5(2)	n-spft	
S7216-A	1.03(1)	1.09(17)	0.58(87)	44.00		Fe^{2+} in Fper	1.02
	1.03(1)	0.66(41)	0.28(42)	9.75		Fe^{2+} in Fper	
	0.12(3)		0.40(19)	8.38		Fe^{3+} in Fper	
	0.48(4)	-0.01(7)	1.51(21)	37.87	42.1(3)	n-spft	
Z1949-A	1.03(3)	0.74(14)	0.32(37)	0.17		Fe^{2+} in Fper	1.02
	1.01(5)	1.13(91)	0.59(23)	0.43		Fe^{2+} in Fper	
	0.19(5)		0.56(28)	0.07		Fe^{3+} in Fper	
	0.45(5)	0.06(8)	1.76(21)	0.33	41.5(4)	n-spft	
Z2122-B	0.99(2)	0.89(4)	0.58(4)	0.63		Fe^{2+} in Fper	1.07
	0.10(0)		0.45(30)	0.09		Fe^{3+} in Fper	
	0.96(3)	2.71(9)	0.42(8)	0.09		$^{VI}Fe^{2+}$ in O_5	
	0.50(2)	0.51(5)	0.26(5)	0.19		$^{VI}Fe^{3+}$ in O_5	
Z2117-B	1.10(1)	0.66(15)	0.42(11)	0.49		Fe^{2+} in Fper	0.95
	0.26(6)		0.13(62)	0.07		Fe^{3+} in Fper	
	0.96(3)	2.68(7)	0.38(9)	0.11		$^{VI}Fe^{2+}$ in O_5	
	0.41(9)	0.42(6)	0.44(20)	0.34		$^{VI}Fe^{3+}$ in O_5	
Z2115-B	1.01(4)	0.88(8)	0.56(3)	0.65		Fe^{2+} in Fper	1.27
	0.14(8)		0.37(18)	0.11		Fe^{3+} in Fper	
	0.95(3)	2.66(10)	0.48(9)	0.09		$^{VI}Fe^{2+}$ in O_5	
	0.50(3)	0.49(7)	0.23(7)	0.14		$^{VI}Fe^{3+}$ in O_5	

Table A.5.3 continued

sample	CS (mm/s)	QS (mm/s)	FWHM (mm/s)	Rel. area	BHF (T)	Site assignment	χ^2
Z2121-A	0.92(5)	0.99(8)	0.59(14)	0.59		Fe^{2+} in Fper	0.89
	0.21(2)	0.73(51)		0.04		Fe^{3+} in Fper	
	0.88(4)	2.78(15)	0.38(17)	0.08		$^{VI}Fe^{2+}$ in O_5	
	0.46(2)	0.51(5)	0.59(14)	0.29		$^{VI}Fe^{3+}$ in O_5	
Z2151-A	1.00(1)	0.81(15)	0.50(14)	0.61		Fe^{2+} in Fper	1.11
	0.15(3)		0.36(17)	0.11		Fe^{3+} in Fper	
	0.87(7)	1.85(53)	1.02(14)	0.19		$^{VI}Fe^{2+}$ in O_5	
	0.52(3)	0.47(10)	0.23(12)	0.09		$^{VI}Fe^{3+}$ in O_5	
Z2153-A*	1.04(1)	0.98(49)	0.92(73)	0.47		Fe^{2+} in Fper	1.24
	1.03(1)	0.53(7)	0.27(25)	0.25		Fe^{2+} in Fper	
	0.15(1)		0.85(20)	0.27		Fe^{3+} in Fper	
H5189-A	1.04(1)	0.90(0)	0.58(2)	0.48		Fe^{2+} in Fper	1.27
	0.22(2)		0.55(9)	0.08		Fe^{3+} in Fper	
	0.60(6)	0.11(7)	0.51(18)	0.09	47.8(4)	n-spft	
	0.27(2)	-0.04(3)	0.32(5)	0.16	49.0(1)	n-spft	
	0.63(3)	0.07(5)	0.47(19)	0.19	44.0(1)	$Fe^{2.5+}$ n-spft	
S7495-A	1.01(1)	0.86(2)	0.45(2)	0.38		Fe^{2+} in Fper	1.73
	0.21(2)		0.41(9)	0.05		Fe^{3+} in Fper	
	0.35(1)	0.02(1)	0.29(3)	0.18	48.(1)	spft (S1)	
	0.58(4)	-0.09(7)	0.4(1)	0.11	46.3(3)	spft (S2)	
H5190-A	0.98(3)	0.90(15)	0.61(10)	0.46		Fe^{2+} in Fper	1.05
	0.10(0)		0.50(1)	0.07		Fe^{3+} in Fper	
	0.97(3)	2.73(7)	0.41(8)	0.13		$^{VI}Fe^{2+}$ in O_5	
	0.53(3)	0.54(10)	0.35(5)	0.33		$^{VI}Fe^{3+}$ in O_5	
Z2077-A	1.07(2)	0.74(42)	0.45(3)	0.50		Fe^{2+} in Fper	1.24
	0.27(2)		0.23(2)	0.12		Fe^{3+} in Fper	
	0.96(1)	2.70(2)	0.31(2)	0.09		$^{VI}Fe^{2+}$ in O_5	
	0.45(5)	0.52(59)	0.43(9)	0.29		$^{VI}Fe^{3+}$ in O_5	
H5189-B	0.98(3)	0.77(5)	0.52(5)	0.35		Fe^{2+} in Fper	1.46
	0.31(6)		0.5(2)	0.05		Fe^{3+} in Fper	
	0.28(3)	-0.02(4)	0.3(1)	0.26	49.1(2)	spft (S1)	
	0.67(2)	0.07(3)	0.5(1)	0.34	46.7(3)	spft (S2)	

Table A.5.3 continued

sample	CS (mm/s)	QS (mm/s)	FWHM (mm/s)	Rel. area	BHF (T)	Site assignment	χ^2
S7509-A	0.96(3)	0.78(6)	0.5(1)	0.30		Fe^{2+} in Fper	1.33
	0.24		0.4(2)	0.04		Fe^{3+} in Fper	
	0.28(3)	-0.01(3)	0.3(1)	0.29	48.9(2)	spft (S1)	
	0.69(3)	0.10(4)	0.5(1)	0.37	46.7(3)	spft (S2)	
S7716 A	0.96(2)	0.75(3)	0.51(4)	0.46		Fe^{2+} in Fper	1.33
	0.25		0.8(1)	0.03		Fe^{3+} in Fper	
	0.26(2)	0.05(4)	0.3(1)	0.14	49.3(1)	spft (S1)	
	0.66(2)	0.03(3)	0.3(1)	0.37	46.2(1)	spft (S2)	
S7691-B	0.95(1)	0.73(1)	0.42(1)	0.56		Fe^{2+} in Fper	0.96
	0.30(2)		0.2(2)	0.04		Fe^{3+} in Fper	
	0.28(1)	0.01(1)	0.14(4)	0.13	49.2(1)	spft (S1)	
	0.66(1)	0.01(1)	0.22(1)	0.27	46.0(1)	spft (S2)	

Notes:# This sample contains only few small grains of O5 whose signals are likely too weak to be seen in the Mössbauer spectra; *n-spft visible in XRD but no magnetic signal observed in the Mössbauer spectra

Table A.5.4: Standard state thermodynamic terms used and refined in the present study

Standard state data from Holland and Powell, (2011)												
	$\Delta_f H$ kJ/mol	S $JK^{-1}mol^{-1}$	a	b ($x10^5$)	c	d	Tc K	Smax J/K/mol	V_0 J/bar	α_0 ($x10^5$) K^{-1}	K_{T0} GPa	K′
MgO	-601.55	26.5	0.0605	0.0362	-535.8	-0.2992			1.125	3.11	*160*	3.95
Magnetite	-1114.51	146.9	0.2625	-0.7205	-1926.2	-1.6557	848	35	4.452	*3.6*	181	4.05
Magnesioferrite	-1442.29	121.0	0.2705	-0.7505	-999.2	-2.0224	665	17	*4.415*	*3.6*	*178.4*	*4*
Fe_4O_5	-1342.0	230.0	0.3069	0.1075	-3140.4	-1.4705			5.376	3.7	190	5
$Mg_2Fe_2O_5$	-2008.0	155.0	0.2849	0.0724	-3328.8	-1.256			5.305	2.38	171	4
$MgCO_3$	-110.93	65.5	0.1864	-0.3772	0	-1.8862			*2.803*	*4.0*	*96*	*5.41*
$FeCO_3$	-762.22	93.3	0.1788	-0.0309	625.43	-1.773			*2.943*	*3.0*	*120*	*4.07*
Diamond	2	2.38	0.0243	0.6272	-377.4	-0.2734			*0.342*	*2.67*	*444*	*4*
O_2	0	205.2	0.0483	-0.0691	499.2	-0.4207						
$Cp = a + bT + cT^{-2} + dT^{-0.5}$ ($kJK^{-1}mol^{-1}$)												
Standard state data from Hidyadt et al., (2015)												
G^{o}_{FeO}	$-285203.5 + 274.2455\ T - 49.19444T \ln T - 0.004678477\ T^2 + 297568.8\ T^{-1} + 574.4469 \ln T$								1.226	*4.0*	*147*	*4*
$G^{o}_{FeO_{1.5}}$	$-523138.0 + 73.37019\ T - 26.96809T \ln T - 0.008835071\ T^2 + 1498519\ T^{-1} + 25471.09 \ln T$								*1.602*	*4.9*	*140*	*4*
$G^{o}_{Fe(gamma)}$	$-236.5+132.4156\ T-24.6643T \ln T-0.003758\ T^2+77359.0\ T^{-1}-5.8927x10^{-8}T^3$								*0.695*	5.3	*146*	*5.3*

Table A.5.5: Thermodynamic mixing terms used for the thermodynamic model of this study

fper mixing terms (kJmol^{-1})		
$q^{00}_{\text{FeO-FeO1.5}}$	–59.412+0.01*P* (kbars)	Hidyadt et al. (2015)
$q^{10}_{\text{FeO-FeO1.5}}$	42.677	
$q^{00}_{\text{FeO-MgO}}$	10.500+0.01*P*	This Study
$q^{10}_{\text{FeO1.5-MgO}}$	-29.103	
$q^{20}_{\text{FeO1.5-MgO}}$	5.000+0.025*P*	
Fe-Pt-Ni alloy mixing terms (kJmol^{-1})		
W^{alloy}_{Fe-Pt}	-138.00	Kessel et al. (2001)
W^{alloy}_{Pt-Fe}	-90.800	
Spfr $MgFe_2O_4$-Fe_3O_4 mixing terms (kJmol^{-1})		
$W^{\text{spfr}}_{\text{FeO-MgO}}$	8+0.01*P* (kbar)	Jamieson and Roeder (1984)
$W^{\text{spfr}}_{\text{MgO-FeO}}$	0.01*P*	
Note values in italics have been changed from Holland and Powell (2011) either using more recent equation of state data (see text for details) or due to refinement in this study.		

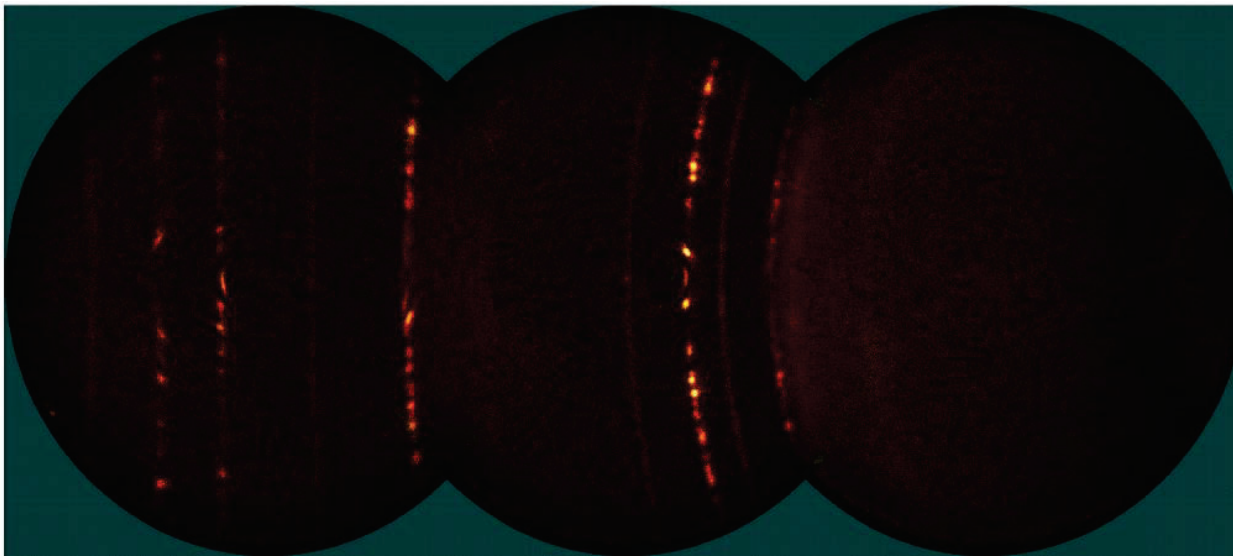

Figure A.5.1 : Example of one of the samples (Z1949-A) that present large spots instead of clear Debye rings from the measurements performed at the a Bruker D8 DISCOVER (see main text Section 5.3)

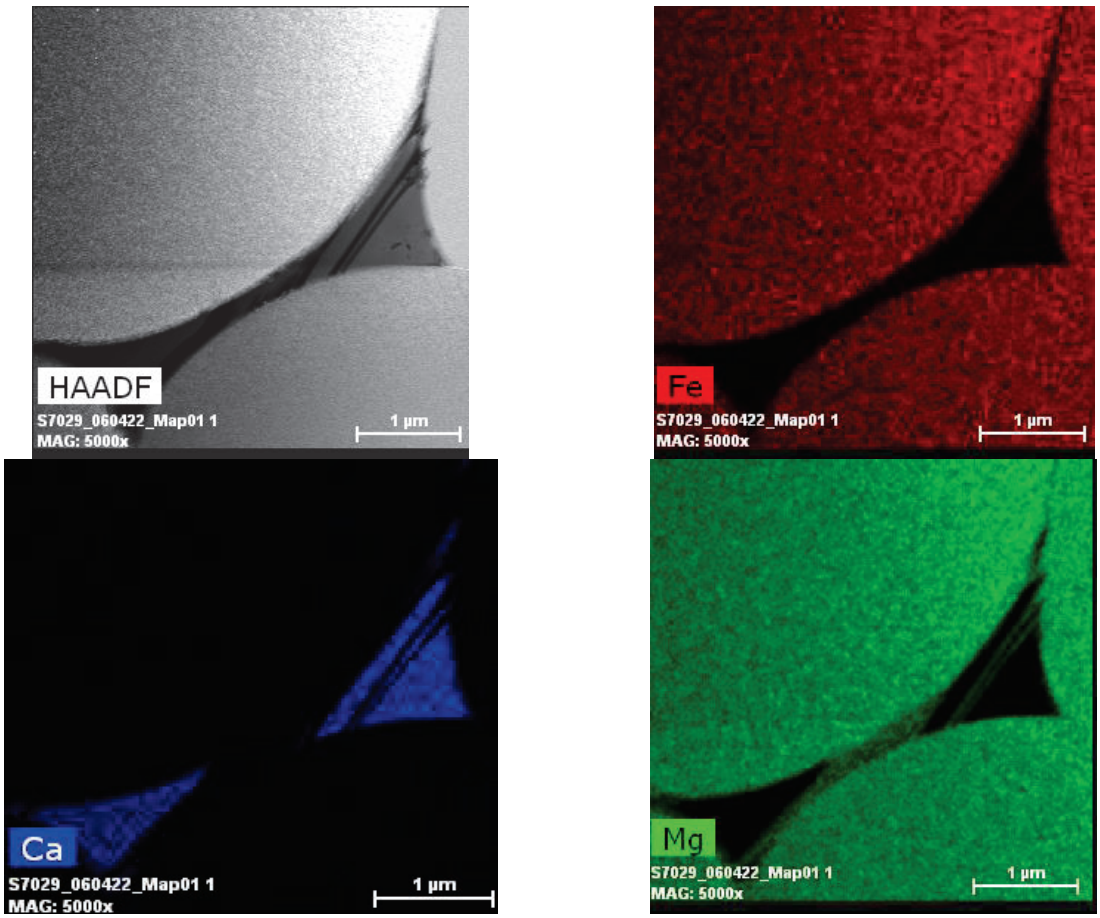

Figure A.5.2: Elemental map performed on sample S7029 allowed the identification of the small amount of melt in the sample to be a Ca-carbonate.

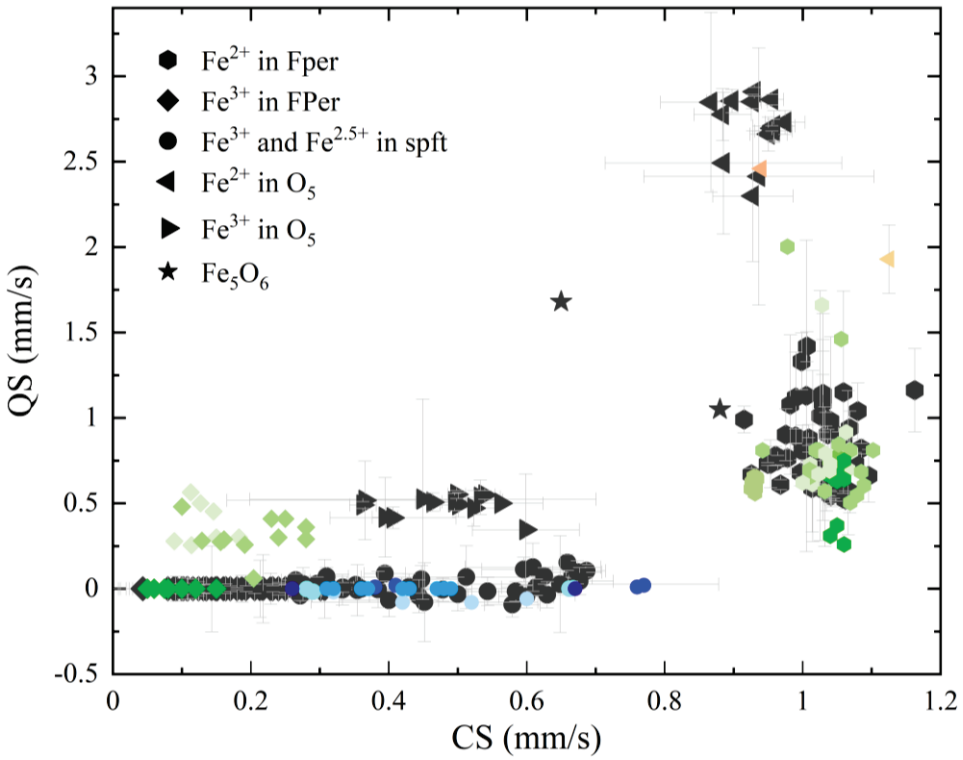

Figure A.5.3: Compilation of the available hyperfine parameters in the literature for fper [Nestola et al.2016; Otsuka et al.2010; Dominijanni MA; McCammon et al.2004; Dobson et al.1998]; spft [O'Neill et al.1992; Daniels and Rosenncwaig 1968; Lyubutin et al.2009; Shipilin et al.2015; Ilyengar et al.2014] is here compared with the valued obtained in the present work.

For the $Mg_2Fe_2O_5$, no data has been published, nonetheless data provided via personal communication by Kupenko I; and the published values from Ovsyannikov et al.2018 for Fe_4O_5 are plotted in orange. CS and QS of the magnetic component of the Fe4O5 end-member is not plotted here due to the absence of a mangetic component in the spectra from this work. No data on Fe5O6 is available to our knowledge.

6. The partitioning of nitrogen and its isotopes between hydrous minerals, diamond and nitrogen bearing fluids

6.1 Introduction

Tracing the deep Earth nitrogen (N) cycle requires an understanding of how N and its isotopes are partitioning during mantle melting, devolatilization and metasomatic processes. This is important, not only for understanding whether the mantle is a net sink or source for N but also for determining the origin of the N isotopic imbalance that exists between the mantle and surface reservoirs. While the depleted mantle has an $\delta^{15}N$ $[(^{15}N/^{14}N)_{sample}/(^{15}N/^{14}N)_{air}-1)\times1000]$ of -5 ± 2 ‰, surface reservoirs have $\delta^{15}N \geq 0$ and therefore cannot have been derived directly from the depleted mantle (Javoy et al. 1986; Cartigny 2005; Cartigny and Marty 2013; Cartigny et al. 2014). Subducted crust and sediment also have $\delta^{15}N > 0$ (Sigman et al. 2019; Ader et al 2006; Thomazo and Papineau 2013; Marty and Dauphas 2003), implying that this material has not significantly contributed to the depleted mantle. Further questions also arise concerning the origin of N in diamonds, which is one of the most N rich materials in the mantle. As the partitioning of N and fractionation of N isotopes during diamond formation is poorly understood, it is unclear whether differences in diamond N contents and $\delta^{15}N$ result from different source concentrations or from fractionation

mechanisms (Cartigny et al. 2001b; Cartigny et al. 2003; Mikhail et al. 2014; Cartigny and Marty 2013; Hogberg et al. 2016).

Some N is almost certainly recycled into the mantle. N initially present in organic matter in oceanic sediments becomes incorporated as ammonium (NH_4^+) in clay minerals, where it substitutes for K^+, during diagenesis. It is then passed on to micas such as biotite, muscovite and phengite during prograde metamorphism (Marty and Dauphas 2003; Li et al.2007; Busigny et al. 2011). Although experiments show that N is strongly partitioning into fluids and melts (Mallik et al. 2018; Förster et al. 2019; Li et al. 2013; Keppler et al. 2022), implying that most N may be recycled to the surface on short timescales, existing partition coefficients are limited in terms of mineralogy and *P*, *T* conditions, particularly given that the behaviour of N changes with fO_2 and probably also with water activity (Keppler et al. 2022). Furthermore, few studies have examined how N isotopes are partitioned during possible fractionation processes. The dearth of experimental data is in part due to the intrinsic difficulty in determining nitrogen concentrations and isotopic fractionations. Despite the advance in the utilization of secondary ion mass spectrometry (SIMS) and electron microprobe (EPMA) for these measurements, limitations to the accuracy of the obtained data are still present. The possibility of matrix effects due to change in composition between standard and samples, as well as the unknown effect of the nitrogen speciation on the efficiency of ionization and recombination reactions during SIMS data collection, still needs to be further investigated and precisely quantified. Moreover, the presence of water in the samples strongly affects the measurement of $^{15}N^{16}O^-$ in SIMS measurements leading to possible overestimation of the N concentration and preventing the precise acquisition of isotopic data on ^{15}N. Finally, collection of carbon and nitrogen isotopes in diamond by SIMS is not trivial. Recent analyses were performed on two laterally separated spots for C and N, respectively (e.g. Hauri et al. 2002; Palot et al. 2014; Petts et al. 2015; Gress et al. 2021) or, when measured on the same spot (Lai et al. 2022) the two elements would be collected one after the other, in which case the depth differences could be

problematic. A recent work from Ishida and co-authors have proposed the simultaneous determination of C and N in one analytical spot with high precision and spatial resolution (Ishida et al.2018, 2023) possibly leading to a new approach to $\delta^{13}C$, $\delta^{15}N$, and nitrogen mass fraction quantification in diamond.

In recent years, the electron microprobe (EPMA) has been widely used for in-situ nitrogen measurements of silicate and metallic phases (Bastin and Heijligers 1991; Li et al. 2015; von der Handt and Dalou 2016; von der Handt et al. 2019; Mosenfelder et al. 2019; Grewal et al. 2019; Nachlas et al. 2020). However, obtaining high-quality EPMA measurements of light elements such as N (along with B, C, O and F) is challenging mainly due to the fact that the detection limits for light elements is much higher than for other elements (Reed 2005). Moreover, the mobilization of N during measurements as well as the necessity for a precise background correction in oxygen bearing samples (von der Handt and Dalou 2016; von der Handt et al. 2019) presents additional challenges yet to be fully overcome.

To this day, the most utilized method for N isotope composition and mass fraction quantification is gas-source ion-ratio mass spectrometry (Cartigny and Marty 2013). These measurements are not exempt from analytical difficulties (e.g. isobaric interferences; Mo-N interaction during step-heating; complete liberation of lattice bound N) the main practical one being the amount of material necessary for obtaining good data quality (Boocock et al. 2020).

In order to obtain experimental charges for the analysis using mass spectrometry, we followed a novel approach which make use of glycine as the source of nitrogen in our experiments. Glycine is a naturally occurring amino acid observed not only in marine sediments but also in meteorites and comets (Altwegg et al.2016; Glavin et al. 2011; Koga et al. 2017: Hadraoui et al. 2019). For this reason, it represents a plausible nitrogen source in natural systems. Moreover, glycine has the advantage of being a small grained powder, that facilitates its weigh in and addition into

experimental charges as well as being an easily separable residue after the experiment. Other N-sources present some drawbacks such as causing strong reduction of the samples (e.g. Si_3N_4), or strong oxidation (e.g. NH_4OH) or introduce other elements in the system which may alter phase equilibria (e.g. NH_4Cl). Glycine imposes reducing conditions by leaving C in the capsule upon decomposition and, as it is present in excess, the N isotopic ratio between the starting material and the residue should be very similar.

The aim of the experiments planned for this study is to provide nitrogen partition coefficients between hydrous minerals and fluids at different *P-T-f*O_2 conditions that can shed light on the deep nitrogen cycle. Moreover, by achieving the synthesis of diamond from a metallic catalyst in absence of a diamond seed, we aim at determining the nitrogen partition coefficients as well as isotopic fractionation between diamond and the metallic melt.

6.2 Experimental methods

Starting materials for the high-pressure experiments were powdered natural minerals. A phlogopite, $KMg_3(AlSi_3O_{10})(F,OH)_2$, from North Burgess (Ontario, Canada), Kunipia-F, sodium bentonite containing 98-99 wt% montmorillonite $[(Na_{0.4}Ca_{0.03}K_{0.01})(Al_{1.6}Mg_{0.3}Fe_{0.1})Si_4O_{10}(OH)_2]$ (Nessa et al. 2007) and serpentinite samples as antigorite form Zermatt (CH) and a lizardite from Val Graveglia (IT) (Eberhard et al. 2022). The natural powders were analysed by means of EA-irMS and no significant N was detected (Table 6.2). Glycine ($C_4H_5NO_2$) was added to the experimental charges, which should breakdown at the experimental conditions to produce graphite and a NH_3 and N_2 bearing H_2O-rich fluid phase according to,

$$3C_2H_5NO_2 \rightarrow 6H_2O + NH_3 + 12C + N_2 \quad (1)$$

Fluid speciation calculations on glycine using the Deep Earth Water model of Huang & Sverjensky (2019) at 3 GPa and 500°C confirm the formation of subequal proportions of NH_3 and N_2, although

the N speciation is dependent on the actual experimental oxygen fugacity, which could be different to that imposed by the glycine itself.

All experiments were performed in a multianvil apparatus. For the hydrous mineral experiments starting materials were loaded as fine-grained powders into Au capsules of 4 mm diameter and 4 mm long. The glycine was loaded first, followed by a thin layer of SiO_2 and then the sample (see Chapter 2 paragraph 2.3.1.3). The capsule contained ~100 mg of total sample, including ~25 wt % glycine. The SiO_2 layer helped to separate the sample from the remaining glycine residue after the experiment, which was important for elemental analysis with isotope ratio mass spectrometry (EA-irMS). The experiments on hydrous minerals were performed at 3 GPa and 500°C.

In order to equilibrate diamond with glycine, diamonds were synthesised directly from graphite, without using seeds. A $Fe_{0.58}Ni_{0.30}S_{0.12}$ alloy composition catalyst (Zhimulev et al. 2012) was prepared from a mixture of metals and sulphur by grinding under ethanol in an agate mortar. MgO single crystal capsules of 3.6 mm outer- and 1.6 mm inner-diameter were used that were 1.5 mm deep and were closed with a 1 mm thick MgO single crystal lid. The capsule can contain approximately 25 mg of starting materials. A layer of glycine was placed at the bottom of the sample (~10 wt %) followed by a layer of metallic alloy catalyst and graphite powder in a 1:4 ratio by weight. The MgO capsule was then wrapped in a second capsule made of Pt-foil.

Table 6.1: Experimental conditions and run products

Run Nr.	P (GPa)	T (°C)	mineral	Duration	Run products
ES731	3	500	phlogopite	24 hrs	Phlogopite
ES373	3	500	antigorite	24 hrs	Antigorite
ES374	3	500	lizardite	24 hrs	Lizardite
ES375	3	500	montmorillonite	24 hrs	Tobelite
Z2045	13	1700	Fe-Ni-S + C	8 hrs	Fe-Ni-S melt + fper + diamonds

High pressure experiments were performed using multi-anvil presses at Tohoku University (TU) and the Bayerisches Geoinstitut (BGI). 25 mm edge length Cr_2O_3-doped MgO octahedral pressure

assemblies were compressed between tungsten carbide anvils with 15 mm corner truncations (25/15 assemblies). Stepped graphite heaters were employed at 3 GPa and a $LaCrO_3$ heater at 13 GPa. Type D thermocouples ($W_{97}Re_3$-$W_{75}Re_{25}$) were used. Experimental conditions and heating durations are shown in Table 6.1. The runs were quenched to room temperature within a few seconds by switching off the electrical power.

6.3 Analytical methods

Powder X-ray diffraction was performed on the recovered hydrous mineral samples using a Bruker D8 DISCOVER micro focused X-ray diffractometer equipped with a two-dimensional solid-state detector (VANTEC500) and micro-focus Co-Ka radiation source (IμS) operated at 40 kV and 500 μA. The powder recovered after the equilibration experiment of the montmorillonite samples, showed Tobelite (Higashi 1982) structure, consistent with the observation by Cedeño et al.2019 at similar P-T conditions in an NH_4-rich system. For the lizardite sample, the measured powder could be indexed with lizardite structure, with some minor peaks belonging to tobelite. The powders from sample ES373 on the other hand, showed considerable amount of tobelite together with the antigorite.

The sample capsule recovered from the diamond synthesis experiment was cut in half, embedded in epoxy resin and polished. Textural observations, preliminary phase identification and semi-quantitative chemical analyses of the recovered run product were performed using a scanning electron microscope (SEM; ZEISS Gemini 1530) equipped with a field emission gun and energy-dispersive X-ray spectrometer (EDXS).

6.3.1 Electron probe microanalysis (EPMA)

The metallic alloy catalyst in the diamond synthesis experiment was analysed with a JEOL JXA-8200 EPMA equipped with five wavelength-dispersive spectrometers at the Bayerisches Geoinstitut. Measurements were performed in wavelength-dispersive mode with a 15kV accelerating voltage and 15 nA beam current, 20s counting time on peak and 10s on background. The Phi-rho-Z correction routine was applied for all analyses of this work. The standards utilized for major element measurements were: FeS_2 for iron and sulphur, Ni metal for nickel and Fe_2O_3 for oxygen.

N concentrations were quantified using a LDE1 crystal. The N analyses were performed at 10 kV using a boron nitride standard. Samples were coated at the same time as the standard to avoid systematic error due to the absorption of N X-rays by C. Tests for N mobilization and surface damage indicated an optimal beam current of 20 nA, and counting times of 120 s on peak and 60 s on the background. Analyses were performed with a point beam. The quenched alloy separated into four phases with different contrasts in back scattered electron images. These phases were analysed individually, and the combined composition was determined using the programme Fiji – ImageJ (Schindelin et al. 2012) to estimate the volume fraction of the individual mineral phases (see Appendix 6.1).

6.3.2 Nitrogen measurements using elemental analyser isotope ratio mass spectrometry (EA-irMS)

The experimental charges from experiments on hydrous minerals as well as the starting minerals were analysed for both N concentration and isotopic ratio by means of an elemental analyser (Carlo Erba, EA1108) connected to a mass spectrometer (Finnigan Mat, MAT 252) at Tohoku University. For these analyses, the capsules were opened and the single phases carefully separated, weighted

and loaded into tin capsules. Approximately ten histidine ($C_6H_9N_3O_2$; $\delta^{15}N$= - 7.2‰) samples were run as standards to assess the machine bias. The analytical error was propagated from the reproducibility of the standard analyses (0.08‰, 1SD, n=8) and the nominal error of the irMS (0.2 ‰). After the standards, the tin capsules containing the glycine-residual and then the separated minerals from each experiment were measured, interspersed with blank measurements. The average peak area and δ-value of the blank measurement were used to correct the data for the blank contribution. Variations in the isotopic composition of nitrogen are expressed using the δ-notation in permil: $\delta^{15}N_{sample}$= $[(^{15}N/^{14}N)_{sample}/(^{15}N/^{14}N)_{standard}-1]$x 1000, where the standard is atmospheric N_2. The $(^{15}N/^{14}N)$air is defined as 3.6765×10^{-2} (Junk and Svec 1958). The resulting N concentrations and isotopic ratios are reported in Table 6.2, together with the calculated fractionation factor ($\Delta^{15}N= \delta^{15}N_{product} - \delta^{15}N_{glycine\ residual}$).

To obtain $\delta^{15}N$ ratios of sufficient accuracy using EA-irMS, sample N contents must be >50 µg, which is easily obtained from the 100 mg hydrous mineral samples given their N contents. The diamond sample on the other hand, which was < 10 mg as it was already cut in half, was considered to potentially have N contents which were too low to measure $\delta^{15}N$ ratios using this technique.

6.3.3 Diamond N-analyses using quadrupole mass spectrometry following stepwise combustion

Due to the small size of the recovered diamond material (sample Z2045) N concentration in this sample was obtained via stepwise combustion technique (Hashizume and Sugiura 1990; Yamamoto et al. 1998; Ishida et al. 2012), which allows N isotope measurements on samples containing at little as 100 mg of N. The diamond block was separated from the outer capsule and the main pool of quenched metallic alloy catalyst and placed in aqua regia to dissolve away any of the alloy from around or within the sample. The N concentration and isotopic ratio of the block was measured by the Balzer QMG420 quadrupole mass spectrometer at Ibaraki University, Japan,

following stepwise combustion in an oxygen atmosphere (Yamamoto et al., 1998).The applied procedure is based on the method described by Ishida et al. (2012). The platinum-wrapped sample was combusted in an oxygen atmosphere and heated in two temperature steps, first at 300°C to remove any surface contamination, subsequently at 1200°C for 90 minutes. The oxygen pressure during each analysis was approximately 4.0×10^2 Pa and the nitrogen contamination associated with the oxygen was less than 2.0×10^{-11} g. During the measurement the consumed amount of O_2 in the line was monitored and finally brought to zero. A second combustion cycle was performed at 1200°C to confirm that complete combustion had been achieved. The nitrogen from the diamond that was released upon combustion was finally converted into N_2 via the catalytic effect of the platinum. The amount of N_2 gas was quantified manometrically in the gas extraction line and purified cryogenically to then be measured by the mass spectrometer (Ishida et al. 2012; 2023). The C yield was 80.18 wt% as a result of periclase remaining within the sample, which should contain negligible amounts of N. The results are also reported in Table 6.2.

6.4 Results

The N contents of the mineral phases equilibrated with glycine at 3 GPa and 500°C are shown in figure 6.1a. All minerals show a substantial uptake of N even at the relatively low temperatures at which the hydrous minerals were equilibrated. None of the hydrous phases breakdown at these conditions except montmorillonite, which transforms to tobelite, an ammonium analogue of muscovite mica with the ideal formula $(NH_4)Al_2(AlSi_3)O_{10}(OH)_2$ (Cedeño et al., 2019).

The mineral samples were separated from the breakdown products of the glycine before EA-irMS analysis, which appeared in the recovered samples as a dark carbon rich-residue below the sample. This residue was not evident in the diamond synthesis experiment. The analysis of the residue showed that it also contained approximately 10 wt % N. This is slightly less than half of the N

content of the original glycine but implies that on quenching a N bearing material, potentially similar to glycine reformed. The glycine starting material was found to have a N content of 17.6 wt %, less than the ideal stoichiometry of 18.6 wt % but which could arise from adsorbed H_2O.

Table 6.2 : Nitrogen concentrations (N wt%) of starting materials and compositions and isotopic analysis ($\delta^{15}N$) of samples together with the calculated $\Delta^{15}N$. In each capsule, the glycine to mineral ratio was approximately 1:3 respectively.

	Starting minerals	**N wt%**		
	Phlogopite	0.01		
	Antigorite	-		
	Lizardite	0.01		
	montmorillonite	0.02		
Run number		**N wt%**	**$\delta^{15}N$ ‰**	$\Delta^{15}N$ **(min-gly)** ‰
	glycine	17.6 (2)	+ 2.1(2)	
ES375	glycine residual	9.99 (2)	+ 1.31 (20)	2.39
	tobelite	2.14 (2)	+ 3.70 (20)	
ES373	glycine residual	8.05 (2)	+ 2.35 (20)	2.83
	Antigorite	1.22 (2)	+ 5.19 (20)	
ES374	glycine residual	8.90 (2)	+ 2.48 (20)	2.97
	Lizardite	1.34 (2)	+ 5.44 (20)	
ES371	glycine residual	10.60 (2)	+ 2.06 (20)	2.03
	Phlogopite	0.35 (2)	+ 4.08 (20)	
Z2045	diamond	0.65*	- 0.3 (8)	
*was corrected to account for the missing 20wt%.				

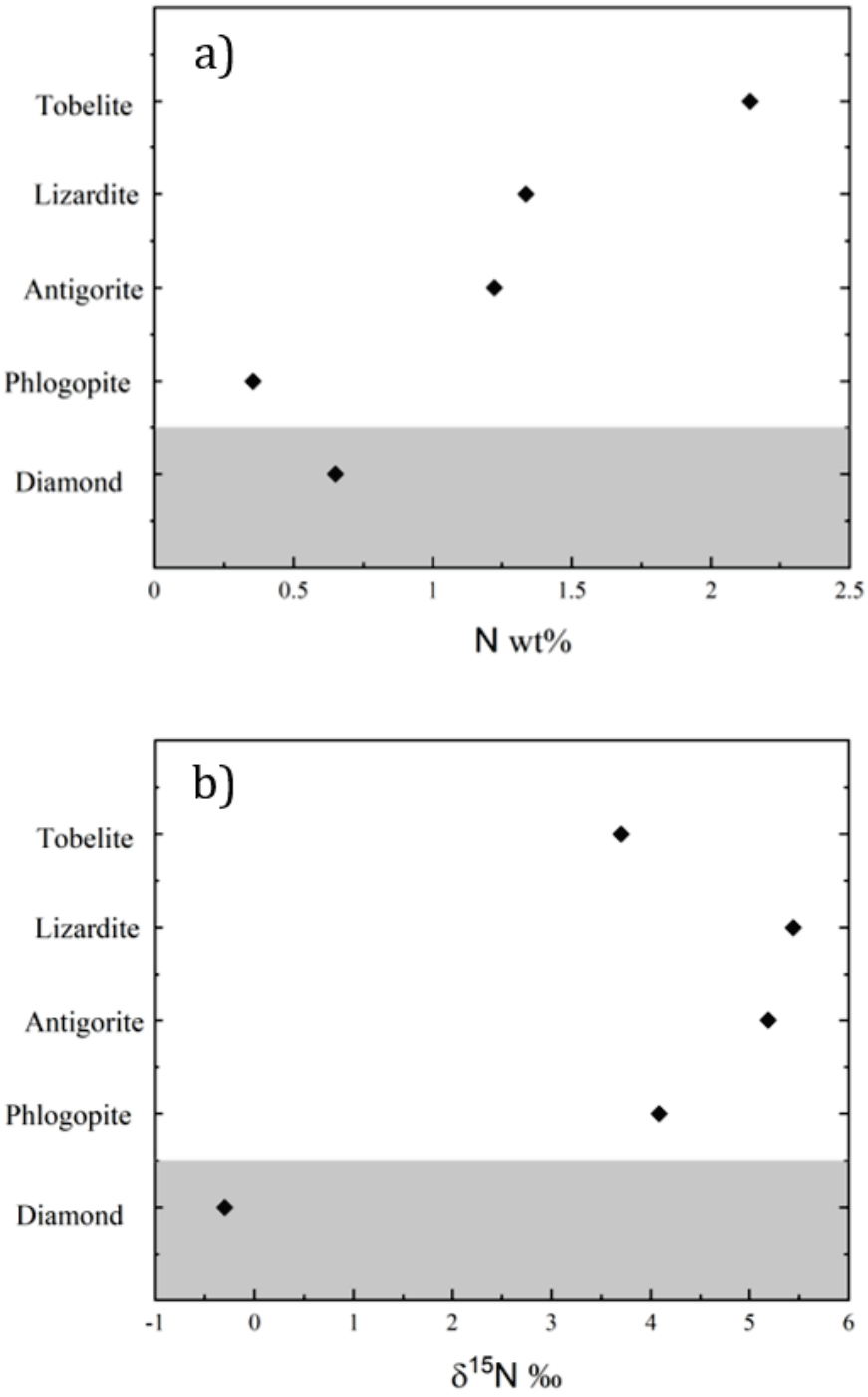

Figure 6.1: **a)** The nitrogen concentration and **b)** the $\delta^{15}N$ ratio for all minerals recovered from high-pressure experiments.

The measured $\delta^{15}N$ ratios of the recovered minerals are shown in figure 6.1b. The glycine starting material had a $\delta^{15}N$ ratio of +2.1(2), which means that all hydrous minerals became richer in ^{15}N, whereas diamond became poorer. For all the equilibration samples measured with the EA-irMS,

the glycine residue was measured as well for N concentration and isotopic signature, and can be observed to have a very similar $\delta^{15}N$ ratio as the original glycine. Only for tobelite did the $\delta^{15}N$ go down slightly to 1.31 ‰, which is probably due to the high N uptake of this mineral.

SEM images of the diamond synthesis experiment (Figure 6.2) show the single crystal MgO capsule containing an upper dark mass comprised of diamonds, mixed with some periclase, above a pool of quenched Fe-Ni-Pt-S alloy catalyst. Some Pt entered the catalyst through interaction of the alloy melt with the outer Pt capsule, although the Pt capsule remained intact. In the enlarged image (Figure 6.2b) of the main metallic alloy mass, different phases that quenched from the alloy melt can be observed in addition to euhedral diamonds. There is no evidence of a glycine residue but these euhedral diamonds most likely formed from the carbon in the residue from the N-source. Some periclase, and a more minor amount of metal alloy is observed to have entered the diamond mass during the experiment (Figure 6.2a). The periclase was probably drawn in from the capsule as a result of the volume change upon the graphite to diamond transition. Placing the separated diamond mass in aqua-regia should have removed the metallic alloy but the periclase remained, resulting in the measured C yield during the analysis of 80.18 wt%.

Four phases were characterised in the quenched alloy, a Ni-rich sulphide, an Fe-rich sulphide, an Ni-Fe-bearing alloy and a Pt-bearing alloy (see paragraph 6.6 at the end of the Chapter). The proportions and average analyses of these phases were used to determine the composition of the original liquid, which had the stoichiometry $Fe_{0.33}Ni_{0.28}Pt_{0.05}N_{0.02}S_{0.33}$. The Fe content is lower than in the starting metal as a result of oxidation that produced ferropericlase with the surrounding MgO capsule. This raised the S content of the metallic liquid but left the Ni content essentially unchanged. Interestingly, N can only be measured in the Pt-bearing alloy, which must have scavenged the N from the cooling liquid as it crystallised. It is of course also possible that more N was in the melt and was lost as the other non-N bearing phases crystallised. The surrounding MgO

has become ferropericlase with the composition $Mg_{0.93}Fe_{0.07}O$, from which an oxygen fugacity (fO_2) of -0.8 log units below the iron wüstite buffer ($\Delta IW = -0.8$) can be estimated for the experiment, assuming ideal mixing in the metal and a symmetric interaction parameter of 13 kJ/mol for Fe-Mg mixing in ferropericlase (Frost 2003).

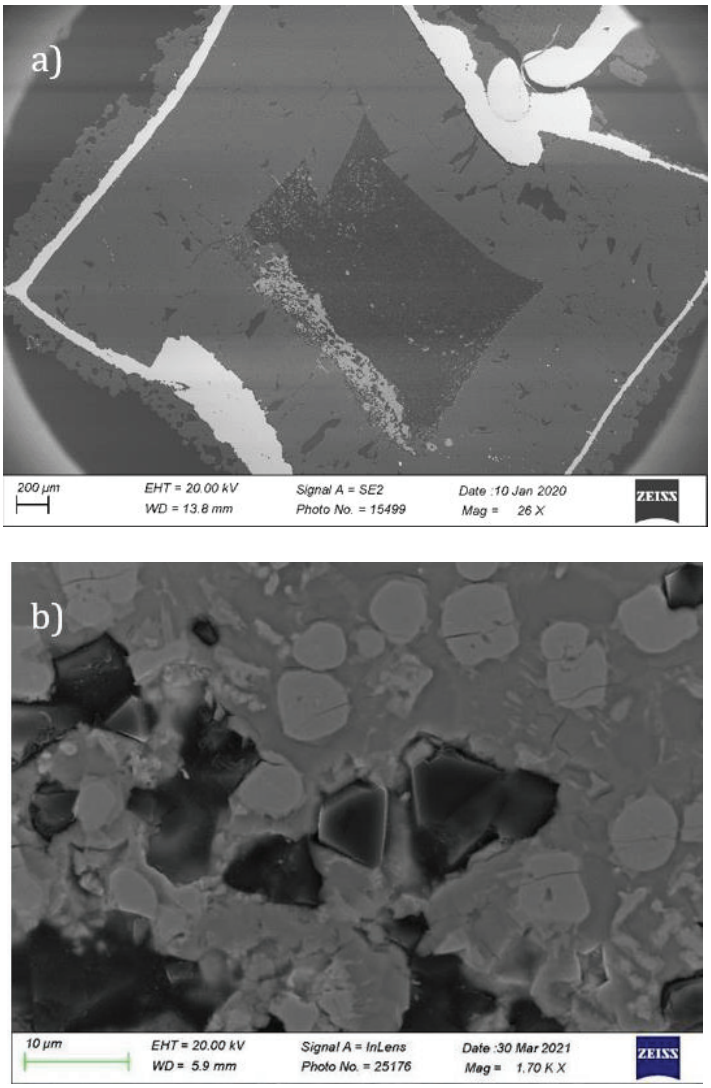

Figure 6.2: SEM images of sample Z2045. **(a)** The entire outer Pt foil and inner single crystal MgO capsule is shown with the thermocouple junction at the top. The inner slightly deformed MgO-single crystal capsule contains an assemblage of diamonds (darker material) interspersed with some lighter ferropericlase grains and a small amount of very bright Fe-Ni-Pt-S alloy quenched melt. A pool of Fe-Ni-Pt-S melt can be seen below the diamond material, which also contained some Pt contamination from the outer capsule. **(b)** Dark euhedral diamonds at the bottom of the capsule, that likely formed from the glycine residue, within the Fe-Ni-Pt-S melt pool. The melt contains rounded crystals of quenched Pt-Fe alloy.

6.5 Discussion

6.5.1 Hydrous mineral samples

The glycine starting material contained 17.6 wt % N and if it breaks down according to equation (1) the fluid should contain ~27 wt % N as N_2 and NH_3. Given the 1:3 mass ratio in which glycine was added to the hydrous mineral experiments, we expect a bulk composition with approximately 4.5 wt % N. This means that there was still significant N remaining in a coexisting fluid phase and even though the minerals contain quite high N contents, the N content of the fluid was probably at least ten times higher than in the minerals. As the fluid was not directly sampled, however, any estimate of the fluid-mineral partition coefficient based on mass balance would be highly uncertain.

As observed in the study of Cedeño et al. (2019), ammonium doped montmorillonite transforms to tobelite, an analogue of muscovite with NH_4^+ substituted into the interlayer, at temperatures above 350- 450°C between room pressure and 8 GPa. At the same experimental conditions, Cedeño et al. (2019) reported 0.74 wt % N in tobelite, compared to 2.14 wt % in this study, which probably reflects the difference in N contents of the starting materials of ~2 wt% versus ~4 wt %, respectively. Stoichiometric tobelite would contain 3.7 wt % N so there is likely still some nitrogen in the interlayer that was not accounted for. Natural biotite-phlogopite micas, which also host NH_4^+ in the interlayer site substituting for K^+, generally have the highest N contents in high grade metamorphic rocks (Honma and Itihara 1981), with values reported up to 0.3 wt % (Plessen et al. 2010). This highest value is in almost perfect agreement with the value of 0.35 wt % observed in this study for phlogopite. As it is difficult to imagine that such natural samples were exposed to fluids with similar N contents, it is possible that the experimental phlogopite did not reach equilibrium. Full replacement of K would result in an order of magnitude higher N concentration.

Lizardite and antigorite were also found to contain 1.2 and 1.3 wt % N respectively, which is surprising given that they do not have interlayer cations that can be replaced with NH_4^+ as for micas. For natural serpentinites, that were found to contain 5 to 45 ppm N (Pagé et al. 2018), it was proposed that N^{3-} might replace O^{2-} with charge compensation provided by Al^{3+} replacing Mg^{2+}. While there would be just enough Al in both the serpentine samples to accommodate this, it is extremely unlikely that such a major cation replacement could be accomplished under such conditions. It also seems unlikely that N would be stable in this form, compared to the fluid species. Some other mechanism, therefore, needs to be sought through further characterisation, such as molecular N_2 being trapped within the structure. It is also possible that, the presence of the tobelite in the X-ray analyses of these samples could explain where the nitrogen is stored, representing the possibility for the formation of a nitrogen-bearing additional phase in the serpentinite system. The limited data available does not allow to draw any conclusion on whether this is the case, but would open for the possibility of investigating this unprecedented mechanism of N-storage in serpentinites.

It is surprising, in general, that it is possible to substitute N to these extents given the timescale of only 1 day at 500 °C, although this may be facilitated by the relatively open phyllosilicate structures that probably allow rapid diffusion of N species along interlayers. One other possibility is whether the N is hosted in some other form, perhaps as a quenched organic residue, similar to the glycine residue found in each experiment. Figure 6.3 shows an experiment performed on montmorillonite at 3 GPa and a slightly higher temperature of 750 °C. It can be seen that the glycine residue remains at the base of the capsule and there is no indication for the presence of quenched glycine residues within the bulk of the sample material.

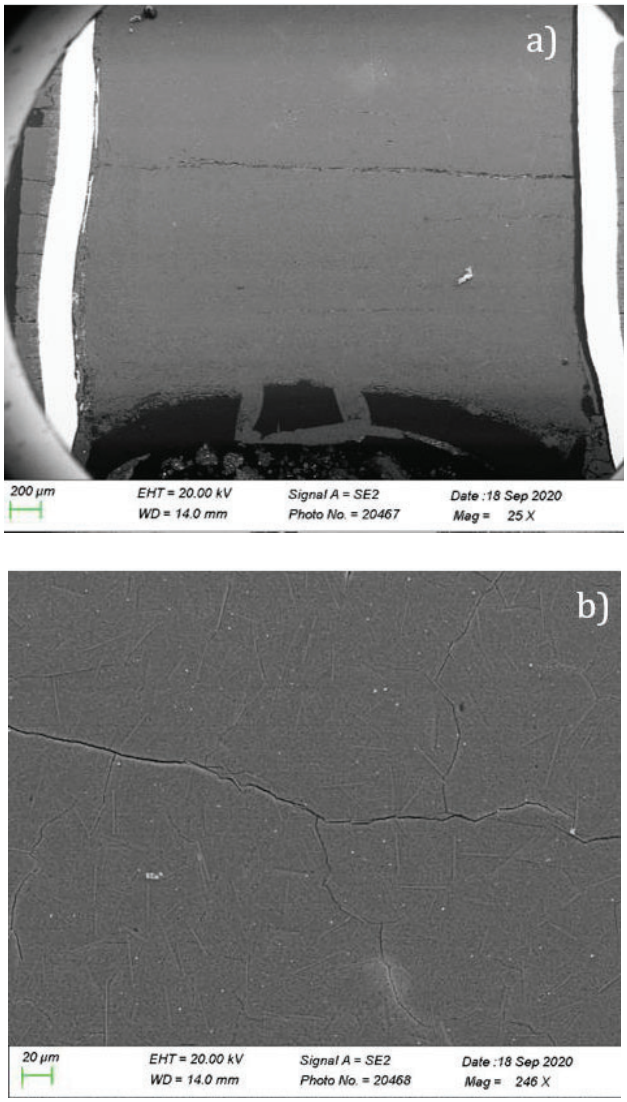

Figure 6.3: **a)** An experiment performed on montmorillonite at 3 GPa and 750 °C using a similar experimental arrangement to the experiment in Table 6.1. The dark residue from glycine can be seen below the sample but an enlargement of the sample material in **b)** shows no evidence for such material within the sample. Dark cracks that appear within the sample and between the sample and the wall of the bright Pt capsule in a) do not contain carbon rich residue.

The hydrous mineral samples all picked up isotopically heavy N in comparison to both the initial glycine starting material and the glycine residue analysed for each experiment.

In figure 6.4 the mineral-glycine fractionation factor ($\Delta^{15}N^{sample\text{-}gylcine} = \delta^{15}N^{sample} - \delta^{15}N^{glycine}$) is calculate using both the glycine starting material and the glycine residue analysed for each experiment. This is shown as a bar with the value calculated using the starting glycine at the top

of the bar and the value calculated from the glycine residue being the lower value. The range is a reasonable measure of the uncertainty, as apart from the tobelite experiment, mass balance indicates that the quenched glycine residue does not contain the entire fluid inventory of N.

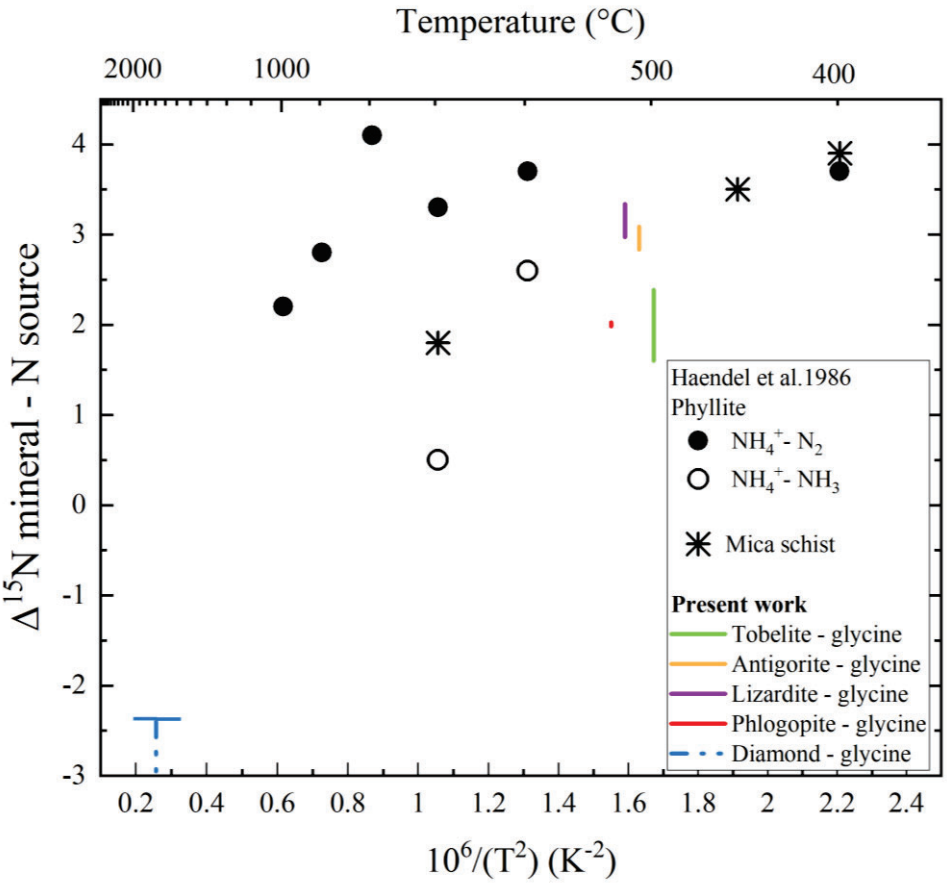

Figure 6.4: The ^{15}N fractionation factor between the mineral phases and the glycine source. The experimental results at 500 °C are spread in temperature for clarity. The bar for each sample indicates the fractionation factor assuming the δ^{15}N of the starting glycine material (top of the bar) and the δ^{15}N of the glycine residue (bottom of the bar). Data from Haendel et al. (1986) indicate Δ^{15}N rock-gas fractionation factors determined for phyllite and mica schist upon stepwise heating at ambient pressure (see text for details).

As shown in figure 6.4, the determined fractionation factors are in very good agreement with values determined by Haendel et al. (1986) at ambient pressure, based on the compositions of N-species in gases released from both natural phyllite and mica schist rock samples. N is likely hosted as NH_4^+ replacing K^+ in the mineral phases of these rocks. The measurements also differentiated

between fractionations involving N_2 and NH_3 species in the gas phases for phyllite at certain temperatures. While fractionation factors for tobelite and phlogopite are smaller than the values determined for mica-schist, the lizardite and antigorite values are in almost perfect agreement with the temperature trend. Although it is probably unlikely that N is present as NH_4^+ in the serpentinites, the higher fractionation factor may be also inconsistent with N being trapped in the structure as N_2.

It has been recognised that mineral phases in metamorphic rocks become progressively enriched in ^{15}N as the metamorphic grade increases and the N content decreases (Bebout and Fogel 1992; Mingram and Bräuer 2001). This is consistent with released NH_3 or N_2 preferentially removing ^{14}N, in line with the fractionation factors in figure 6.4. One possibility is that hydrous minerals, such as serpentine, could act as heavy nitrogen filters of N-bearing fluids originating through the breakdown of organic materials or other hydrous silicates in subduction zones. As in the current experiments, fluids passing through sections of hydrous minerals or in fact even contributing to forming hydrous minerals, would become shifted to towards lower values of $\delta^{15}N$. Heavy N will enter the hydrous minerals, although the majority of N would remain within saturating hydrous fluids. The initially subducted crust may have positive $\delta^{15}N$ values, but through exchange with hydrous minerals, the fluids emanating into the overlying lithosphere or mantle wedge could be shifted to progressively more negative values, and these fluids might potentially still be trapped in the upper mantle. Hydrous minerals breaking down beneath the arc would then release fluids with high $\delta^{15}N$ back to the surface.

A further area for future study would be to understand the nature of the N-rich glycine residual material, which could also potentially form a N host in subduction zones, as a breakdown product of organic material.

6.5.2 Nitrogen partitioning and isotopic fractionation in diamond

The determined diamond N content, 0.65 wt %, is high compared to previous studies on synthetic diamonds. Borzdov et al. (2002) synthesised diamonds containing 0.33 wt % N using an Fe_3N source at 7 GPa and Sokol et al. (2019) produced diamonds with up to 0.26 wt % N at 7.8 GPa in equilibrium with metallic Fe liquid containing ~4-5 wt % N. Both studies employed temperatures similar to this study. Natural diamond N contents are generally below 0.2 wt % (Stachel et al., 2022) but individual samples such as polycrystalline diamonds and those with eclogitic paragenesis can reach values near 0.4 wt % (Mikhail et al., 2014; Stachel et al., 2022) and metamorphic diamonds can contain much higher values (Xu et al. 2018).

In this study the diamonds were produced in equilibrium with an Fe-Ni-S bearing melt containing 0.47 wt % N. This value is similar to measurements made in metal-silicate equilibration experiments performed at a similar fO_2 by Speelmanns et al. (2019) and at similar sulphur contents by Grewal et al., (2019), although at lower pressures and temperatures. Based on the proportion of glycine added to the sample in this study, there should have been more N present in the bulk composition than found in either the diamond or the metallic phase, implying that there was an additional N bearing phase. Grewal et al. (2019) observed that the amount of N in Fe-metallic melt decreased as S was added, to the same level as found in this study, even though the N in the bulk composition remained constant, and the concentration in the coexisting silicate remained low, implying that the metal may have also coexisted with a saturating N-bearing phase. It is of course possible that the excess N escaped or partitioning into or through the Pt capsule. There was no glycine residue in the experiment as the carbon material from the residue seems to have transformed to diamonds found within the Fe-Ni-S melt.

Regardless of whether a coexisting fluid phase was present, a diamond-metal partition coefficient for N ($D^{diamond/metal}$) can be determined from the experiment, of 1.1 (3), by weight. In previous studies the metal-silicate partition coefficient ($D^{metal/silicate}$) for N was found to decrease slightly with temperature but not to be significantly affected by pressure or sulphur content and can be estimated to be at least 10 at the temperature and fO_2 (ΔIW = -0.8) conditions of this diamond synthesis (Speelmanns et al. 2019; Grewal et al. 2019; Shi et al. 2022). Combining these measurements, an estimate for $D^{diamond/silicate}$ can be made of 11, which based on the metal-silicate partitioning data is likely to be a minimum value, although is in good agreement with the range 4-16 determined by Palot et al., (2014) for superdeep diamonds from Kankan. That N is compatible in diamond makes sense considering the high concentrations found in diamonds compared to the low concentrations in the depleted mantle, which is likely < 0.3 ppm (Marty 2012).

Based on sector zonation and fractionation trends in diamonds, arguments have been made for both compatible and incompatible behaviour of N during diamond growth (Cartigny et al. 2001; Thomassot et al. 2007; Stachel et al. 2022). It has been proposed that compatibly may also depend on kinetics, with N being incompatible in equilibrium grown diamonds but compatible in rapidly grown samples (Cartigny et al. 2001; Stachel et al. 2022). Compatibility is likely to also dependent on the speciation of N in the growth medium (Mikhail and Howell 2016) and therefore also on fO_2 and f_{H_2O}. The sample from this study was grown relatively rapidly as the graphite diamond transition was significantly overstepped, the temperature was moderately high and a metallic catalyst was employed. It was also grown at an fO_2 that is lower than expected for lithospheric diamond formation (Stagno et al. 2013). However, the metal catalyst employed is close in composition to metallic melt phases found in sublithospheric CLIPPR diamonds implying that the fO_2 conditions may be quite comparable. Given the value of $D^{diamond/metal}$ obtained, the low N contents of these deep natural diamonds may result from low mantle N at these conditions rather

than changes in N-partitioning (Smith and Kopylova 2014), however, this could also be a result of very slow growth.

The $\Delta^{15}N^{diamond\text{-}gylcine}$ determined using the initial glycine $\delta^{15}N$, is -2.4 (10) ‰. As discussed previously, however, there were likely two phases coexisting with the diamond, metallic melt and a coexisting fluid phase, as a simple N mass balance indicates that not all the N was in the diamond and metallic melt. As it was not possible to measure $\delta^{15}N$ in the fluid or metal melt there is some uncertainty and the value determined using the initial glycine value provides only an upper bound to the possible fractionation factor. $\Delta^{15}N^{metal\text{-}silicate}$ was recently found to be near zero (Shi et al., 2022) at a similar fO_2 to the diamond synthesis experiment, however, so it is possible that if a fluid phase was present, the N isotope fractionation with the metal may not have been significant. If a mass balance is performed using the stating glycine proportion and assuming diamond coexisted with one other phase, or two phases with the same $\delta^{15}N$, then the $\Delta^{15}N^{diamond\text{-}gylcine}$ would be ~ -4 (1) ‰.

As shown in figure 6.5, the $\Delta^{15}N^{diamond\text{-}gylcine}$ value is quite consistent with the value determined by Petts et al. (2015), and if this is an upper bound, could also be consistent with the result of Palot et al. (2014), which was based on analyses of superdeep diamonds. Petts et al., (2015) also performed theoretical calculations of the N fractionation factor between the CN^- molecule, which was used as an analogue for N defects in diamond and different fluid species. Although the experimental value falls close to the NH_4^+ curve, Raman analyses on mafic silicate melts have shown no evidence for such melt species at similar fO_2 conditions (Dalou et al., 2019).

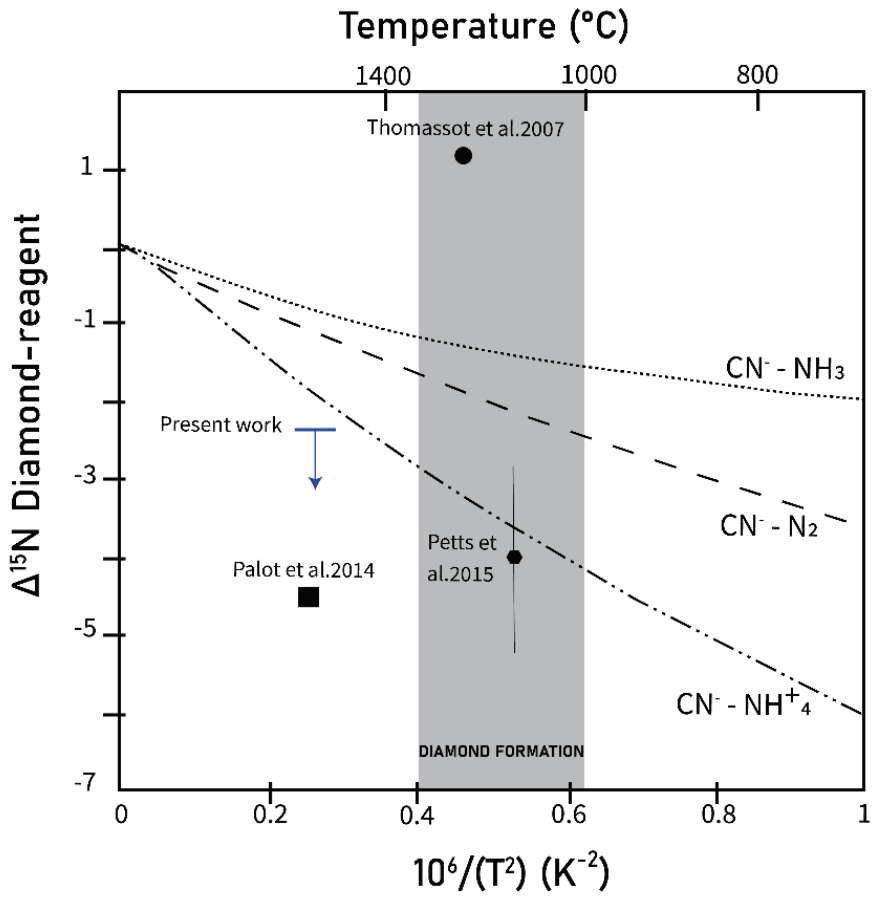

Figure 6.5: The $\Delta^{15}N^{diamond\text{-}gylcine}$ value determined in this study is shown as an upper bound based on the initial glycine $\delta^{15}N$. Several estimates are shown for fractionation factors based on analyses of natural diamonds. Theoretical calculations by Petts et al., (2015) are also shown assuming fractionation with different fluid species and using the CN^- molecule as an analogue for N in diamond.

6.6 Image analyses of the Fe-Ni-S melt of sample Z2045

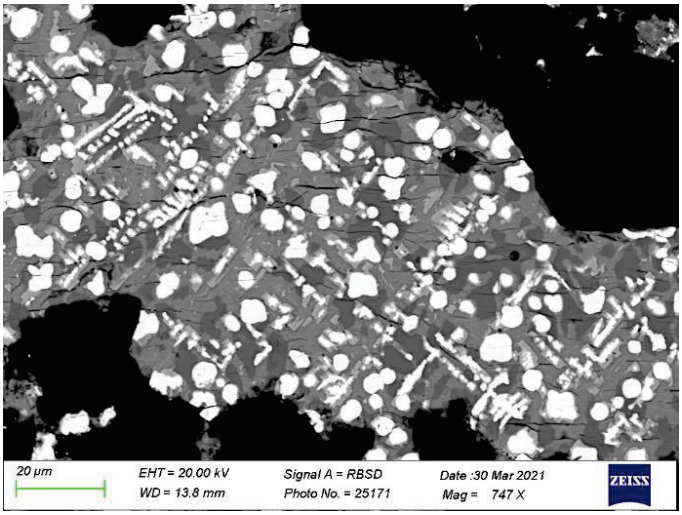

Total melt composition	
Fe	33.37 wt%
Ni	30.10 wt%
S	19.44 wt%
Pt	16.54 wt%
N	0.47 wt%
Total	99.83 wt%

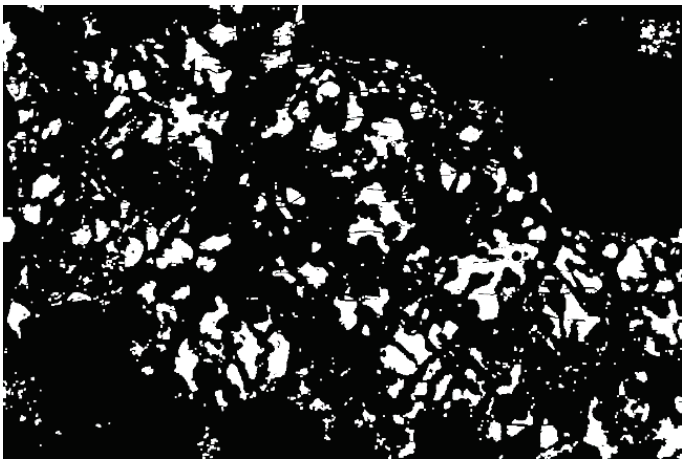

Phase 1 (20.28%)	
Fe	48.62 (1.2) wt%
Ni	14.8 (2) wt%
S	36.7 (6) wt%
Total	100 wt%

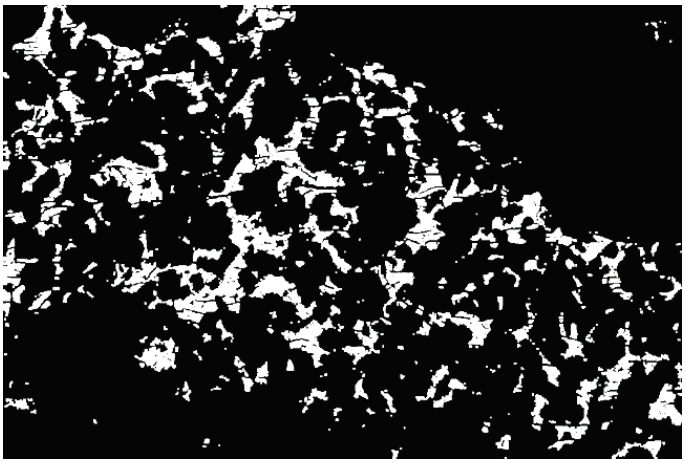

Phase 2 (19.80%)	
Fe	27.2 (1) wt%
Ni	52.6 (5) wt%
S	27.3 (7) wt%
Total	100 wt%

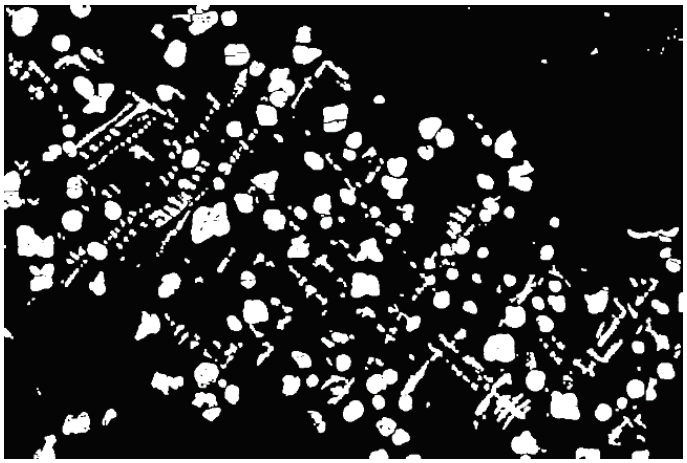

Phase 3 (16.74%)	
Fe	35 (1) wt%
Ni	8.34 (6) wt%
Pt	54.55 (3)
N	1.56 (3) wt%
Total	100 wt%

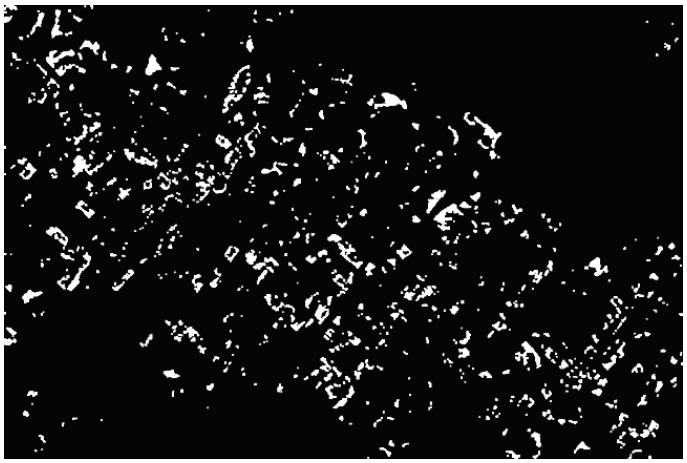

Phase 4 (10.09%)	
Fe	22.3 (6) wt%
Ni	66 (2) wt%
S	11.7 (8) wt%
Total	100 wt%

Appendix Chapter 6

A set of experiments was produced in order to test the applicability of a new data collection protocol for nitrogen measurements by means of EPMA. The ultimate scope is to obtain the partition coefficient (K_D) of nitrogen between hydrous minerals and melts and understand the effect of oxygen fugacity, pressure and temperature on nitrogen partitioning. In order to achieve this, hydrous aluminosilicate that are potentially main nitrogen carriers from the near-surface to the deep mantle (montmorillonite, phlogopite, phengite and serpentinites) are investigated here at sub-arc conditions.

This project has been carried out in collaboration with Dr. Eleanor R. Mare from the University of St. Andrews who provided the python code utilized for the processing of the EPMA data for the N concentration. Eleanor also has calibrated fundamental aspects of the data deconvolution (e.g. APF factor) that will be described in this section in order to better understand the data processing. Moreover, SIMS measurements have been performed at CRPG in collaboration with Evelyn Furi in order to compare such results with the in house EMPA analyses.

The challenges presented by the synthesis of the experimental charges, together with the complexity of the nitrogen concentration measurements in such phases resulted in data which rise several questions. In the following, an analysis of the problems encountered during collection and processing of data is presented, so to provide a basis for further work.

The protocol so far developed and tested is a powerful tool that provides the possibility of in-house nitrogen measurements.

Nonetheless, more work needs to be done in order to ensure the collection of the best data quality possible.

A.6.1. Sample preparation

The experimental charges needed for this investigation were of silicate minerals coexisting with a quenched glass from the partial melt. The starting materials utilized for the high-pressure experiments were the powdered natural minerals described in Chapter 6 (phlogopite, antigorite, lizardite , montmorillonite) and phengite from Dora Maira [$KAl_{1.5}(Mg,Fe)_{0.5}(Al_{0.5}Si_{3.5}O_{10})(OH)_2$] (kindly provided by Mattia Gilio). The nitrogen source chosen for these experiments is the same that was utilized in the experimental charges described in Chapter 6 : glycine ($C_4H_5NO_2$).

Two types of experiments were performed; partial melting experiments where the goal was to determine N partitioning between phases (set 1) and dehydration experiments, in which fluids released from serpentine dehydration where trapped in a layer of phlogopite (set 2). All experiments except one that was performed in a piston cylinder apparatus, were performed in a multianvil apparatus (Table A.6.1). In set 1, the experiments were performed at conditions required to obtain a coexisting partial melt for the montmorillonite (3 GPa 750-950 °C), phlogopite (2.5 GPa 1400 °C) and phengite (3 GPa 750 °C) samples, whereas, in set 2 antigorite and lizardite were run at the condition of initial dehydration (3 GPa, 650 °C). The majority of experiments were performed under the reducing conditions imposed by the graphite residue from the decomposition of glycine, whereas experiments on montmorillonite and phengite were also performed under oxidizing conditions provided by additional RuO_2. Further details on the experimental setup can be found in Chapter 2 , paragraph 2.3.1.3.

Table A.6.1: Details of the nitrogen partitioning experiments conditions. Both equilibration and partial melting experiments are shown here

Run Nr.	P (GPa)	T (°C)	mineral	N source	Duration (hrs)	buffer
Set 1: Partial melting experiments: reduced series						
S7544	3	650	phengite	glycine	1.5	C
S7558	3	750	phengite	glycine	2	C
S7471	3	750	montmorillonite	glycine	1.5	C
A1229	2.5	1400 (1hr) 1300 (2hrs)	phlogopite	glycine	3	C
Z2082	3	750	montmorillonite	glycine	3	RuO_2
Z2099	3	900	montmorillonite	glycine	3	RuO_2
S7564	3	750	phengite	glycine	2	RuO_2
Set 2: Dehydration experiments: reduced series						
V1182	3	650	Antigorite	glycine	48	C
V1183	3	650	Lizardite	glycine	48	C

Phase relations were investigated using the SEM (Figure A.6.1a) in order to ensure the coexistence of the mineral and glass phase in the experimental charges in set 1. The dehydration experiments involving lizardite and antigorite were loaded into a gold capsule together with phlogopite separated by a layer of diamond powder (Figure A.6.1b). Both samples underwent dehydration, to an assemblage of enstatite, forsterite and chlorite with accessory Fe-Cr spinel. The phlogopite layer in both capsules was unaltered.

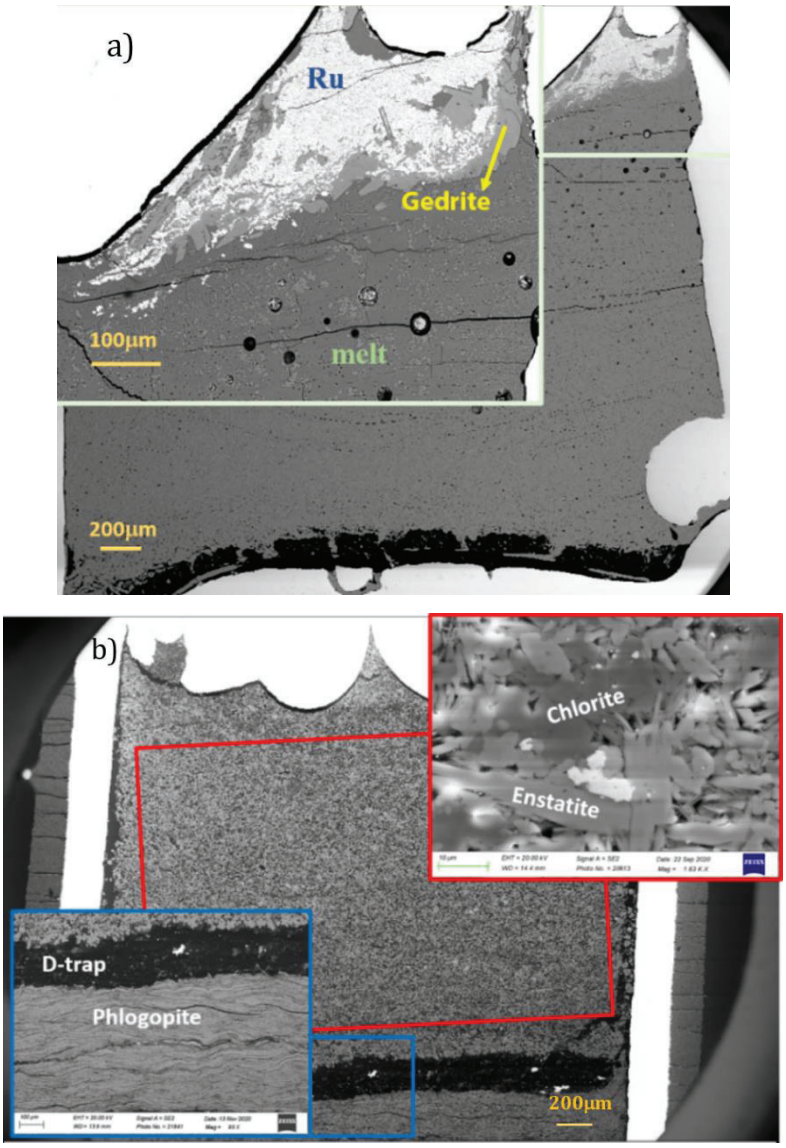

Figure A.6.1: Back scattered images of representative samples for the different sets: **(a)** sample Z2099 at 3GPa and 950°C. Crystals of gedrite are observed in coexistence with a recrystallized melt product and the Ru that was added as a redox buffer; **(b)** The lizardite sample (sample V1182 at 3 GPa 650°C) shows dehydration, to an assemblage of enstatite, forsterite and chlorite, plus some residual Fe-Cr spinel. The bottom layer of phlogopite appears unaltered.

A.6.2 Nitrogen measurement protocol at the EPMA

A JEOL JXA-8200 EPMA equipped with five wavelength-dispersive spectrometers at the Bayerisches Geoinstitut was used to determine the major element compositions of the synthesized samples. Measurements were performed in wavelength-dispersive mode with a 15kV accelerating

voltage and 15 nA beam current, 20s counting time on peak and 10s on background. The Phi-rho-Z correction routine was applied for all analyses of this work. Employed calibrants were diopside for Si and Ca, enstatite for Mg, spinel for Al, albite for Na and orthoclase for K. Iron- metal, Ti-metal, Ni-metal, Cr-metal, Mn-metal and Ru-metal were used as standards for Fe, Ti , Ni, Cr, Mn and Ru respectively.

The quantification of N with EPMA is considerably more challenging than conventional measurements due to several factors such as the relatively low fluorescence, possible material-specific peak shape and position, X-ray absorption by other components in the matrix and spectral interferences from higher-order lines of heavier elements (Reed 2005). In the present work, N concentrations were quantified using a LDE1 crystal. The N analyses were performed at 10 kV using a boron nitride (BN) primary standard. Samples were coated at the same time as the standard to avoid systematic error due to the absorption of N X-rays by C. Tests for N mobilization and surface damage indicated an optimal beam current of 20 nA, a defocussed beam of 20 μm, and counting times of 120 s on peak and 60s on the background.

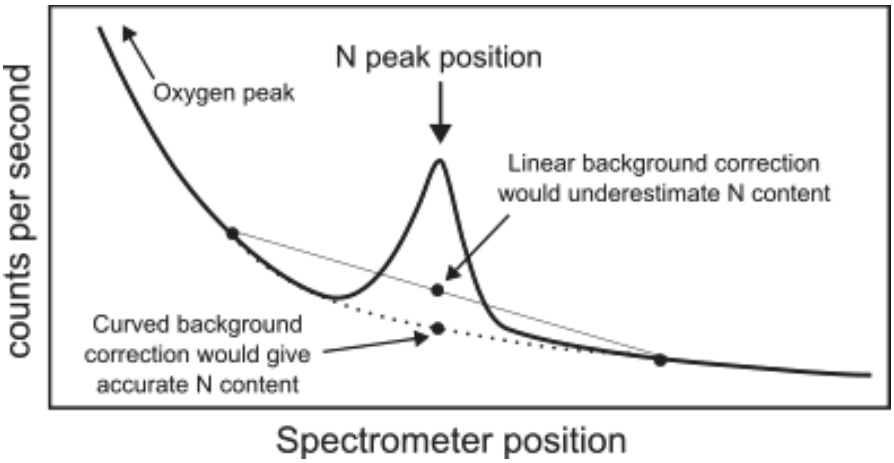

Figure A.6.2: Illustration showing the importance of correcting for background curvature when analysing N in oxides by EPMA. (E.Mare personal communication).

A procedure was developed to account for the curvature of the background around the N peak (Figure A.6.2). Although the primary standard, BN, has an almost linear background, oxygen-bearing samples exhibit a background with a strong curvature caused by the intense oxygen peak

at 524.9 eV (E Mare personal communication). To correct for this curvature, we followed a protocol illustrated in Figure A.6.3.

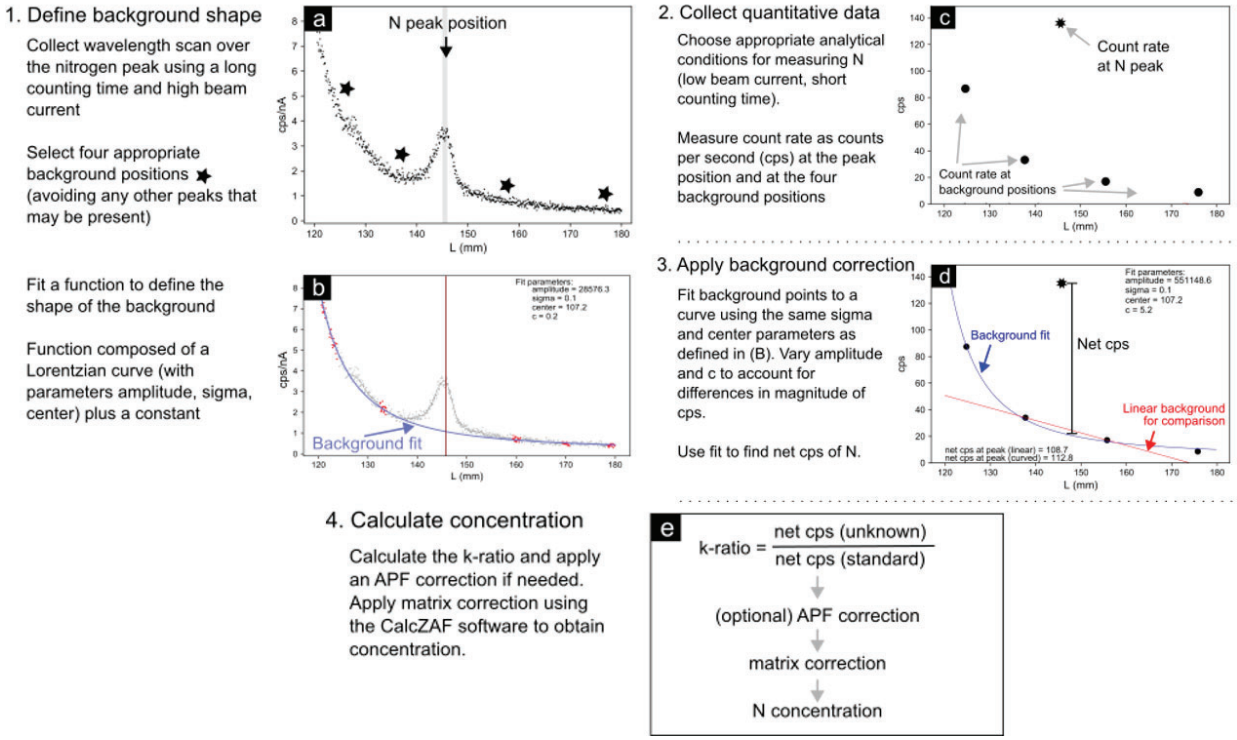

Figure A.6.3: Procedure for applying a curved background correction to N analyses by EPMA. The example shown here is an analysis of buddingtonite (E Mare personal communication). Panels a-d show counts per second (cps) against spectrometer position (L units in mm). Panel e shows the steps to go from background-corrected cps to concentration, where APF is the area-peak factor (see text).

In the first step the shape of the background is defined and suitable background positions for analysis are chosen. To do this, a wavelength scan is performed in the region around the N peak, conducted at a high beam current and with long counting times to obtain a sufficient signal-to-noise ratio to define the characteristics of the background fit (Figure A.6.3a). The background curvature was fit to a function composed of a Lorentzian curve plus a constant, to account for the continuum background (Figure A.6.3b). Although previous studies have used an exponential function to fit the background (von der Handt and Dalou 2016; von der Handt et al. 2019), a Lorentzian function was found to produce an overall better fit. The shape of the background was found to be the same throughout the samples analysed, as well as for the secondary standard. The

wavelength scan was then used to select four background analysis positions that avoided any secondary peaks (Figure A.6.3a). During quantitative analysis, count rates were measured at the N peak position (defined by the primary standard BN) and at the four background positions (Figure A.6.3c). The raw count rate at the N peak would normally be corrected for the background count rate at the same spectrometer position, using a simple linear background correction.

This would lead to an underestimate in the N content, however, as shown Figure A.6.2. Instead, we fit a curve to the four background measurements (Figure A.6.3d), using the fit parameters previously obtained from the wavelength scan (Figure A.6.3d). The parameters that define the shape of the background, i.e. the centre and width of the Lorentzian, are retained from the original fit to the wavelength scan **(**Figure A.6.3b**),** whereas the parameters that define the magnitude, i.e. the amplitude of the Lorentzian and the continuum background constant, are fitted in order to account for the lower beam current and counting time used in the analysis, compared to the original wavelength scan. With the four background points adequately fitted, the background count rate at the N peak position is obtained (Figure A.6.3d) and used to calculate the net N count rate and the k-ratio (the net N counts in the sample divided by net N counts in the standard; Figure A.6.3e). The N concentration was then obtained by applying a matrix correction to the k-ratio.

A further “area-peak factor” (APF) correction can in principle be made to account for differences in peak shape between samples and the standard (Bastin and Heijligers 1991). Differences in peak shape between different materials have been studied (E Mare personal communication) and are summarised in the next paragraph A.6.3.1. Nonetheless, based on the similarity between the height/area ratio of the BN standard and a range of other materials, no APF correction was applied.

Uncertainties and detection limits were determined using a Monte - Carlo approach. Standard deviations of each background measurement and the peak measurement were used to simulate 100 synthetic measurements. For each set of synthetic data (four background measurements and a peak

measurement), the fitting procedure shown in Figure A.6.3d was applied and a net cps was obtained. The standard deviation of these synthetic measurements of net cps is then used to find a relative standard deviation on the k-ratio. Given that the k-ratio is proportional to concentration (with the proportionality defined by the matrix correction), the relative standard deviation on the k-ratio is the same as the relative standard deviation on concentration. Further, the standard deviation of the background, obtained using this Monte - Carlo approach, was used to calculate detection limits. For each sample, a k-ratio was derived from a synthetic peak equivalent to three times the standard deviation of the background (Reed, 2005), and the matrix correction applied to find the detection limit in ppm. Commercial EPMA software does not have the functionality to implement a multi-point background, so these corrections are applied in post-processing. Raw data is extracted from the instrument, and the corrections are applied using a custom python module (Mare at al.in preparation) to produce a corrected k-ratio. The matrix correction is then applied using the CalcZAF software (www.probesoftware.com/Technical.html). In principle the matrix correction requires knowledge of the N valence state. Corrections assuming the full range of plausible valence states have been tested here and were found to be almost identical.

The detection limit for the measurements were about 1600 – 2600 ppm when counting for 10 s on the background, or 1000 to 1500 ppm when counting for 120 s on the background. Detection limits as defined here depend only on the beam current and the counting time of the background measurements. Beam current was kept low to avoid N mobilisation, but a long background counting time has no detrimental effect because background measurements are taken after the peak measurements.

A.6.2.1 Area-peak factor (APF) correction for nitrogen measurements by EPMA

In the following, a brief summary of the work done to assess the effect of varying peak shapes between sample and standard in EPMA analysis of nitrogen can be found. This work was done by E. Mare at the University of St Andrews using the EPMA lab at the University of St Andrews and the Australian National University Centre for Advanced Microscopy.

One challenge with light-element analysis by EPMA is the change in the shape of x-ray emission peaks between different materials. When measuring the concentration of an element by EPMA, we measure the intensity of the element's x-ray peak with respect to that of a standard of known concentration. However, concentration is proportional to the area, not the intensity, of the x-ray peak. Measuring the area of the peak is not practical, because it would require prohibitively long analysis times and likely cause beam damage to the sample. Instead, we measure the peak height (intensity), and assume that that the peak height/area ratio is equivalent between the sample and the standard. If we define the height/area ratio (HAR) of the unknown as

$$\mathrm{HAR_{unk}} = \frac{\mathrm{I_{unk}}}{\mathrm{A_{unk}}} \tag{2}$$

And the height/area ratio of the standard as

$$\mathrm{HAR_{std}} = \frac{\mathrm{I_{std}}}{\mathrm{A_{std}}} \tag{3}$$

where I is the intensity of the peak (the net counts per second after background correction) and A is the area of the peak, then the k-ratio, which is proportional to concentration, can be defined as:

$$\text{k-ratio} = \frac{\mathrm{I_{unk}}}{\mathrm{I_{std}}} = \frac{\mathrm{A_{unk}}}{\mathrm{A_{std}}} * \frac{\mathrm{HAR_{unk}}}{\mathrm{HAR_{std}}} \tag{4}$$

The assumption made in typical EPMA analysis is that the height/area ratios of standard and unknown are the same, so that the ratio $\frac{\mathrm{HAR_{unk}}}{\mathrm{HAR_{std}}}$ is equal to 1 and the k-ratio can be directly computed from intensity measurements. This assumption is reasonable for most elements that are routinely

analysed by EPMA, but not for light elements like nitrogen. There are several approaches to address this problem, but the one we focus on here is known as an 'area-peak factor' (APF) approach, pioneered by (Bastin & Heijligers, 1991). This involves quantifying the shape of the peak in both the standard and the unknown using wavelength scans. From this, the peak height/area ratio can be defined, and these values can be used to apply a correction factor to the k-ratio. We define the area-peak factor (APF) as the ratio of the height-area ratios of unknown and standard:

$$\mathrm{APF} = \frac{\mathrm{HAR_{unk}}}{\mathrm{HAR_{std}}} \tag{5}$$

The corrected k-ratio can then be calculated as:

$$\text{k-ratio (APF corrected)} = \frac{\mathrm{I_{unk}}/\mathrm{I_{std}}}{\mathrm{APF}} \tag{6}$$

A.6.2.2 Measuring the area-peak factor (APF)

It is quite challenging to get accurate measurements of the height-area ratios of unknown and standards. We can find the height-area ratio by obtaining wavelength scans over the peak, but long-duration scans at moderate or high beam currents are usually needed for sufficient signal-to-noise ratio. This becomes a problem in samples where N is readily mobilised by the beam. As the scan progresses through wavelengths, N will be increasingly mobilised and lost from the interaction volume, thereby distorting the recorded peak shape. To avoid this problem, many short-duration scans at low beam currents can be made over the N peak, each on a different spot, so that N mobilisation is minimised within each scan. Each scan is very noisy, but by averaging many of these scans the signal-to-noise ratio is improved.

We collected wavelength scans for four nitrides (GaN, Si_3N_4, AlN, BN) and two silicate samples (buddingtonite and a N-bearing glass). The nitrides were found to be very stable under the electron beam, so high currents (up to 150 nA) and scan durations of 25 minutes were used. The buddingtonite and glass were subject to N mobilisation effects, so these were treated carefully.

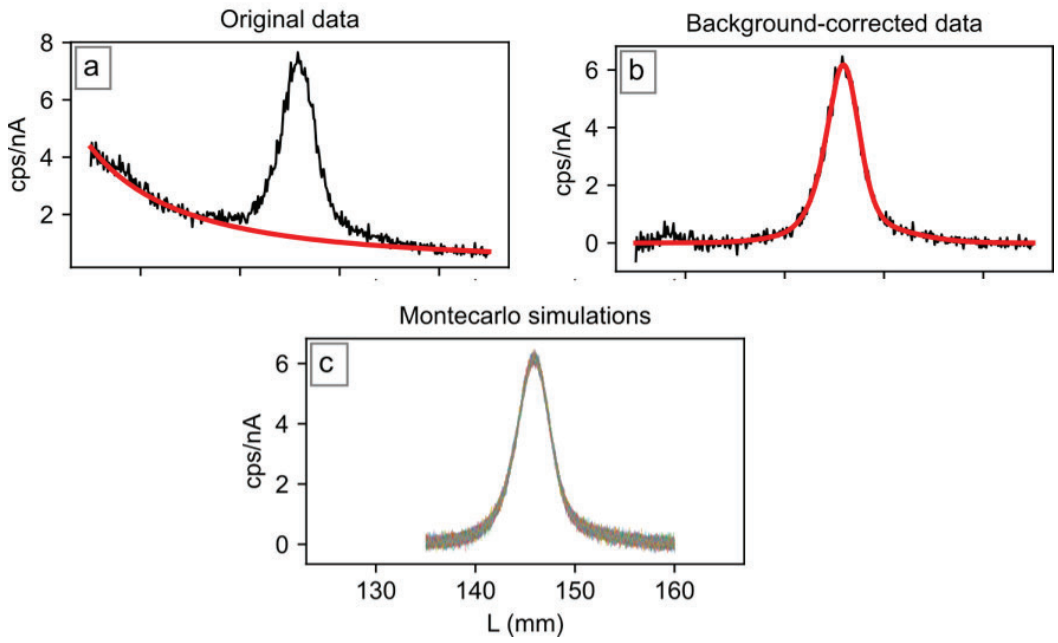

Figure A.6.4. Demonstration of the procedure for calculating the height/area ratio from a wavelength scan over the N peak in buddingtonite. **(a)** The background is fit to either a linear or Lorentzian curve (linear for nitrides, Lorentzian for oxides). **(b)** After subtraction of the background, the peak is fit using a combination of gaussians. Fit regions exclude any subsidiary peaks e.g. the small peak at around 129 mm. **(c)** Uncertainty on the height/area ratio (derived from the fit in B) is calculated using a monte-carlo simulation. The spectrum is simulated 100 times to obtain the standard deviation of the peak height and area.

Once the appropriate beam conditions (current and diameter of defocussed beam) were chosen, many individual one-minute scans over the N peak were obtained, each on different sample location, and these scans were averaged. The wavelength scans were then subject to a three-step process to obtain the height/area ratios:

1. Fit the background (using a linear function for the nitrides or a Lorentzian function plus a constant for the silicates) and subtract the fitted background from the spectrum (Figure A.6.4a)
2. Fit the peak to a combination of several gaussians (varied to obtain a good fit for each material), and obtain the height and area of the fitted curve (Figure A.6.4b)

3. Obtain uncertainties on the height/area ratio using a Monte - Carlo approach. This involves creating many synthetic spectra by adding appropriate noise to the fitted spectrum, and finding the standard deviation of peak heights and areas across all these synthetic spectra (Figure A.6.4c). Note than an alternative approach, involving repeatedly performing fits to synthetic spectra, yielded similar results but took much more computation time.

A comparison the peak shapes of all six materials can be seen in Figure A.6.5a. This figure shows the fits to each wavelength scan after background removal, normalised to constant area. The area-peak factor for each material relative to GaN is shown in Figure A.6.5b. Its notable that all area-peak factors are comparable across different spectrometers at two different laboratories.

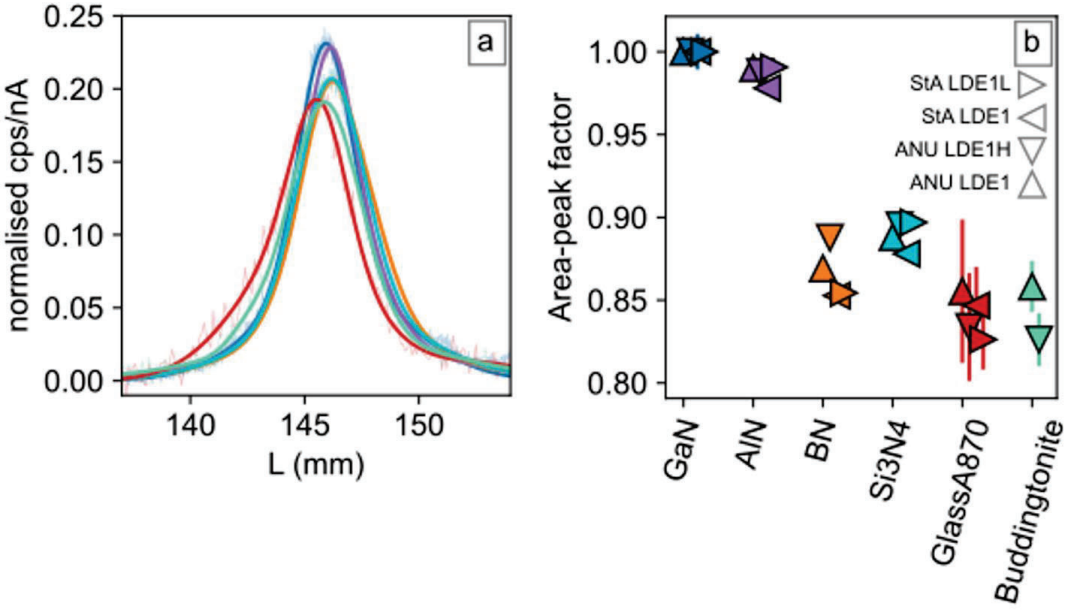

Figure A.6.5. **(a)** Shape of the N peak from wavelength scans on LDE1H at ANU in various materials after removing the background and normalising to constant area. The heights of each peak show variations in their relative height/area ratio with respect to one another. The position of the peak also shifts slightly between materials. **(b)** Area-peak factors for each material relative to GaN. Area peak factors are consistent across different instruments and crystals. Larger uncertainties on the buddingtonite and glass reflect the noisier spectra obtained for these samples.

Because the primary standard used in this thesis is BN, the APF values are calculated relative to BN in Table A.6.2. The silicate materials (glass and buddingtonite) both have only small APF values relative to BN, between 0.93-0.99. In practice, when the k-ratio is corrected this would result in a 1 to 7% increase in the k-ratio. Given that the analysis conducted in this thesis is using a different instrument again, we feel this small correction factor is not defined well enough to use and we instead do not apply an APF correction.

Table A.6.2:Area-peak factors obtained in this study, calculated relative to BN (rather than GaN as in Fig A.6.6 B).

Sample	ANU LDE1	ANU LDE1H	StA LDE1	StA LDE1L
GaN	1.150(9)	1.126(6)	1.173(13)	1.170(5)
AlN	1.139(3)	1.113(4)	1.147(4)	1.159(3)
BN	1.000(3)	1.000(2)	1.000(4)	1.000(2)
Si3N4	1.022(3)	1.008(1)	1.030(4)	1.050(5)
GlassA870	0.984(5)	0.939(37)	0.993(27)	0.967(21)
Buddingtonite	0.987(18)	0.931(18)	-	-

Numbers in parentheses are one standard deviation on the last digit, obtained using the Monte Carlo approach.

From Fig A.6.5a, it can also be seen that there are small differences in the peak position between different materials. If the N counts are collected at a spectrometer position defined by N in a nitride, it may be slightly off the centre of the N peak in a silicate. However, work to assess this concern has found it to be a small effect compared to the noise in the data for silicates such as buddingtonite, which only have a few percent N.

A.6.3 Tested Secondary standards

Two minerals were selected for testing as possible secondary standards for the nitrogen measurements at the EPMA and SIMS: buddingtonite and hyalophane. The buddingtonite utilized

in this work is an ammonium-endmember feldspar ($NH_4AlSi_3O_8$, 5.4 wt% N) that was synthesised in a double capsule using a piston cylinder apparatus at the Australian National University by A. Burnham. Stoichiometric proportions of $Al(OH)_3$ and SiO_2 were mixed and placed in an inner Pd capsule along with excess NH_4OH, and this capsule was placed in an Ag outer capsule containing additional NH_4OH and Fe metal powder. The sample was held at 0.5 GPa and 550 ºC for 3.5 days before quenching. The run product was confirmed to be buddingtonite by X-ray diffraction.

The hyalophane $(K,Ba)[Al(Si,Al)Si_2O_8]$ sample investigated, is a natural Ba-rich feldspar from Bosnia first described by Beran et al. (1992). Major element analyses were performed using the JEOL iSP100 Electron Probe Micro Analyser at the University of St Andrews. The acquisition was performed at 15 kV with a 20 micron spot diameter. The standards employed are wollastonite for Si, Corundum for Al, Celestine for Sr, Fe metal for Fe, Orthoclase for K, Barite for Ba and Jadeite for Na. Counting times were 30s on the peak and 15s on the background for Si, Al, K and Ba. For Sr and Fe 60s on the peak and 30 on the background were used. Sodium was acquired with 10s con the peak and 5 on the background. The major element composition in weight percent (wt%) of the hyalophane is this work is:

Table A.6.3: Major element composition of the hyalophane crystal utilized in the present work.

element	wt(%)
Si	22.86 (4)
Al	11.88 (4)
Sr	0.34 (1)
Fe	0.01 (1)
K	5.10 (3)
Ba	18.44 (11)
Na	1.13 (4)
O	40.26 (4)
Total:	100.03 (13)

A.6.3.1 Secondary EPMA standards and measurements with SIMS

In order to determine if the selected minerals could be used as secondary standard for the measurements performed in the present work, the N concentration in both samples was measured. Measurements were carried out at the electron probe microanalyzer (EPMA) and via secondary ion mass spectrometry (SIMS). The obtained results are presented hereafter.

Stoichiometric buddingtonite contains 5.4 wt% N, and previous EPMA measurements report values between 5.0 and 5.5 wt% N for synthetic samples (Förster et al. 2019; Harlov et al.2001; Pȍter et al.2007) and Beran et al. (1992) reported a value of 4 wt % for a natural sample. In the present work, a value of 4.4 (3) wt% was obtained. One reason for this apparently lower value may be that the synthesised crystals are typically only 5-20 microns big and as a defocussed beam was needed to avoid N mobilisation, it is challenging to ensure that the interaction volume is entirely within the boundaries of one crystal. Secondly, it is possible that some N mobilisation did occur during the analysis despite the care taken to avoid this by reducing the beam current, defocussing the beam, and shortening the counting time. SIMS analyses were performed on the same buddingtonite sample in the hope of using it as a standard but there was no detectable NO^- emission signal. It is therefore needed to further investigate the reason of these discrepancies, possibly by synthesising another buddingtonite batch in-house in hope of obtaining bigger grains and start the process again.

The hyalophane crystal is from the same batch of natural Ba-rich feldspar from Bosnia first described by Beran et al. (1992), who measured 0.12 wt% N using EPMA. Our measurements gave a value of 0.21(4) wt% N, which is higher than expected from the literature (Beran et al.1992; Mosenfelder et al. 2019). Although the background collected in the analysis was noisier than for other samples, monte-carlo simulations performed on the sample indicate +/- 10% uncertainty on

k_{raw} which is quite reasonable. Given the limited literature and the fact that this is a natural sample that might have a variable N content, the N value obtained in the present work may be reasonable. SIMS measurements performed on the hyalophane sample gave an apparent N concentration of only ~200ppm. This is a very low $^{14}N^{16}O^-$ signal is similar to the behaviour reported by Mosenfelder et al. (2019), who also observed an unexpectedly low $^{14}N^{16}O^-/^{30}Si^-$ signal when measuring their hyalophane crystal by SIMS. Mosenfelder and co-authors proposed this to be due to a strong matrix effect as well as the presence of BaO (~17wt%) in the structure. The high atomic mass of Ba appears to have a great effect for the Cs^+ beam analyses.

A.6.4 Nitrogen measurements by secondary ion mass spectrometry

Secondary ion mass spectrometry (SIMS) measurements of N in phases from partial melting (set 1) and dehydration (set 2) experiments were carried out using the CAMECA IMS 1280 HR2 at the Centre de Recherches Pétrographiques et Géochimiques (CRPG, Nancy). The samples for analysis were embedded in high-purity indium and coated with gold. The sample mounts were kept in the airlock of the instrument for at least 12 hours prior to the data acquisition to ensure removal of any adsorbed water. Analyses were performed under a pressure of approximately 2×10^{-9} Torr, using a Cs^+ primary ion beam operated at 10 keV with a current of 10 nA and a spot size of ~20 μm in diameter. Spot analyses of $^{14}N^{16}O^-$ and $^{15}N^{16}O^-$ were carried out in coexisting silicate melts and minerals in the experimental samples at a nominal mass resolution ($m/\Delta m$) of ~13,000 (see Füri et al.2018 for details). The $^{14}N^{16}O^-$ and $^{15}N^{16}O^-$ ion intensities were measured by ion counting on an electron multiplier (EM), together with the $^{30}Si^-$ and $^{16}O_2^-$ signals measured on a Faraday cup. Twenty-five cycles were collected for each analysis through the mass sequence $^{30}Si^-$ (3 s), $^{14}N^{16}O^-$ (6 s), $^{15}N^{16}O^-$ (20s), $^{16}O_2^-$ (4 s). The SIMS detection limit for N is ~1 ppm (Boulliung

et al. 2020). Nitrogen concentrations were obtained from the relationship between the secondary ion intensity ratios $^{14}N^{16}O^{-}/^{16}O_2^{-}$ or $^{14}N^{16}O^{-}/^{30}Si$ and the known nitrogen content (<1 to 3906 ppm) of nine synthetic basaltic glass calibrants (Figure A.6.6). This approach has been demonstrated to yield nitrogen concentrations in silicate glasses of variable compositions that are in excellent agreement with results from static mass spectrometry analyses (Boulliung et al. 2020) .

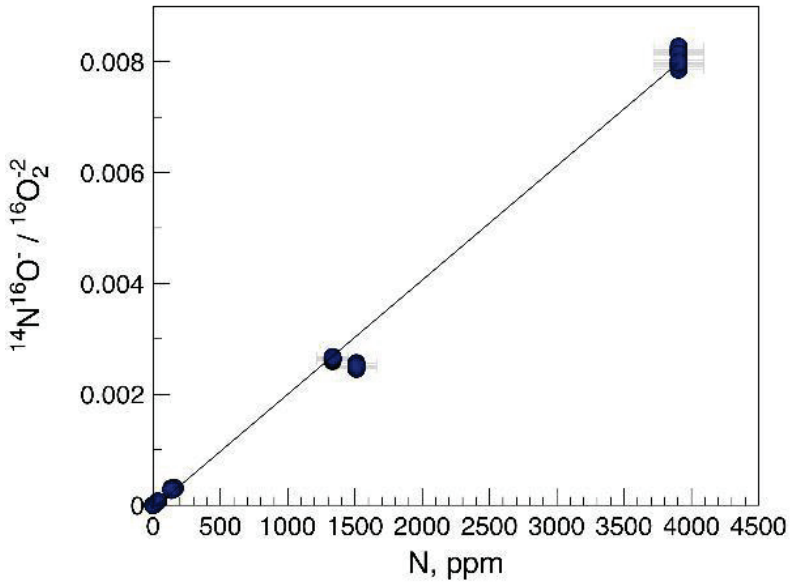

Figure A.6.6 : Representative calibration line obtained from fitting of the $^{14}N^{16}O^{-}/^{16}O_2^{-}$ ratio and the known N content of the calibrants measured every night during a 5-day measurement session. The data were regressed using IsoplotR (Vermeesch, 2018)

The presence of high amounts of water in many of the phases made it difficult to measure $^{15}N^{16}O$. To separate the $^{15}N^{16}O^{-}$ peak from $^{29}SiH_2^{-}$, the mass resolution needs to be ≥ 10,725 (Füri et al. 2018), whereas a mass resolution of 5550 is sufficient to resolve $^{14}N^{16}O^{-}$ from its neighbouring $^{28}SiH_2^{-}$ peak. The high intensities of the $^{29}SiH_2^{-}$ peak, as observable, for example, in sample S7471 (Figure A.6.7a), interfere with the $^{15}N^{16}O^{-}$ signal in many of the measurements, reducing the accuracy of isotope ratio measurements, leading to a possible over-estimation of the N concentration in those samples. Not all the samples were affected by this, as shown in Figure A.6.7b, where the $^{15}N^{16}O^{-}$ and $^{29}SiH_2^{-}$ peaks are suitably separated in a sample of V1183.

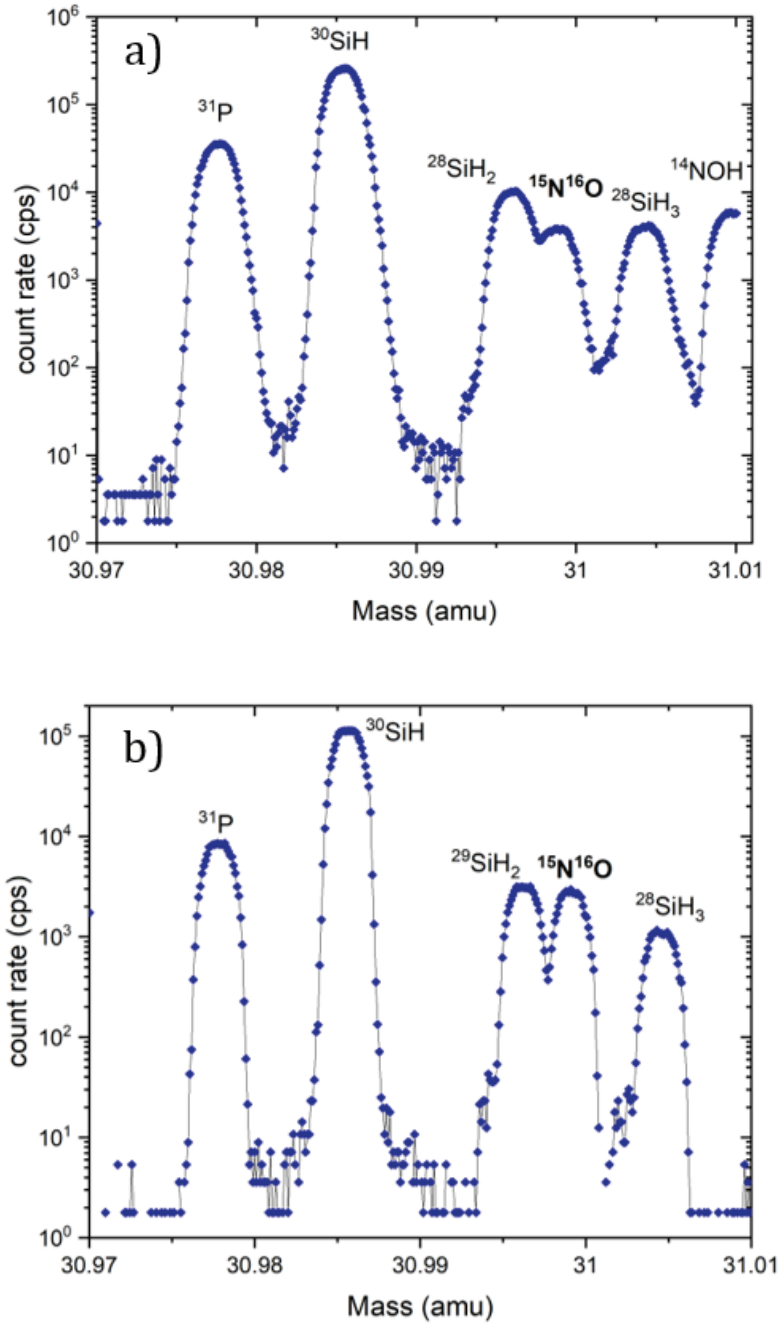

Figure A.6.7: High-resolution mass spectra at mass stations 31 on **(a)** sample S7471 obtained with a nominal mass resolution (m/Δm) of ~ 12995.**(b)** sample V1183 with (m/Δm) of 14294.

A.6.5 Nitrogen evaluation in the partial melting and dehydration experiments

The N concentrations for the phases in the experimental charges in this work measured both with EPMA and SIMS are reported in (Table A.6.4) and plotted in Figure A.6.8. Values are reported together with the detection limit obtained for the EPMA measurements.

Table A.6.4: Nitrogen concentration in weight percent (wt%) for the experimental charges determined both by means of EPMA measurements and SIMS. The detection limit in wt% calculated for the EPMA measurements is also reported. For SIMS, the detection limit was determined by Boulliung et al.2020 to be ~1 ppm.

Sample	EPMA N(wt %)	Detection limit (wt%)	SIMS N(wt %)
Z2099_min	0.05 (2)	0.09 (3)	0.04 (3)
Z2099_glass	0.11 (6)	0.06 (2)	0.10 (1)
S7471_min	1.9 (1)	0.10 (2)	1.4 (4)
S7471_glass	1.7 (2)	0.18 (4)	0.8 (1)
A1229_min	0.05 (2)	0.10 (2)	0.02 (2)
A1229_glass	0.05 (4)	0.09 (2)	0.03 (1)
S7558_min	0.06 (4)	0.14 (2)	0.03 (1)
S7558_glass	0.9(1)	0.14 (1)	0.5 (2)
V1182_min	0.4(1)	0.16 (3)	0.3 (2)
V1182_phlogopite	1.9 (1)	0.16 (2)	1.2 (3)
V1183_min_2	0.18 (8)	0.06 (1)	0.2 (1)
V1183_phlogopite	0.3 (2)	0.08(2)	0.2 (1)
S7564_min	0.04 (3)	0.02 (2)	0.01 (1)

The N concentration obtained on the same experimental charges both by means of SIMS and EPMA show good agreement for the low concentration phases (Figure A.6.8) up to about 0.4 wt%. The highest nitrogen concentration in the glass calibrants employed for these measurements is ~ 0.4 wt% (CB-2#1; Füri et al. 2018), but recent work by Boulliung et al. (2020) has shown that the

method pioneered by Füri et al. (2018) is reliable up to 0.6 wt% by comparing the SIMS measurements to bulk noble gas mass spectrometry. For higher N concentrations, the EPMA and SIMS results can be observed to deviate from the 1:1 line, with the SIMS results being consistently lower than the one from the microprobe. There are multiple reasons that could explain these discrepancies between the data, due to technical limitations of both analytical techniques. The possible reasons will be discussed here in detail.

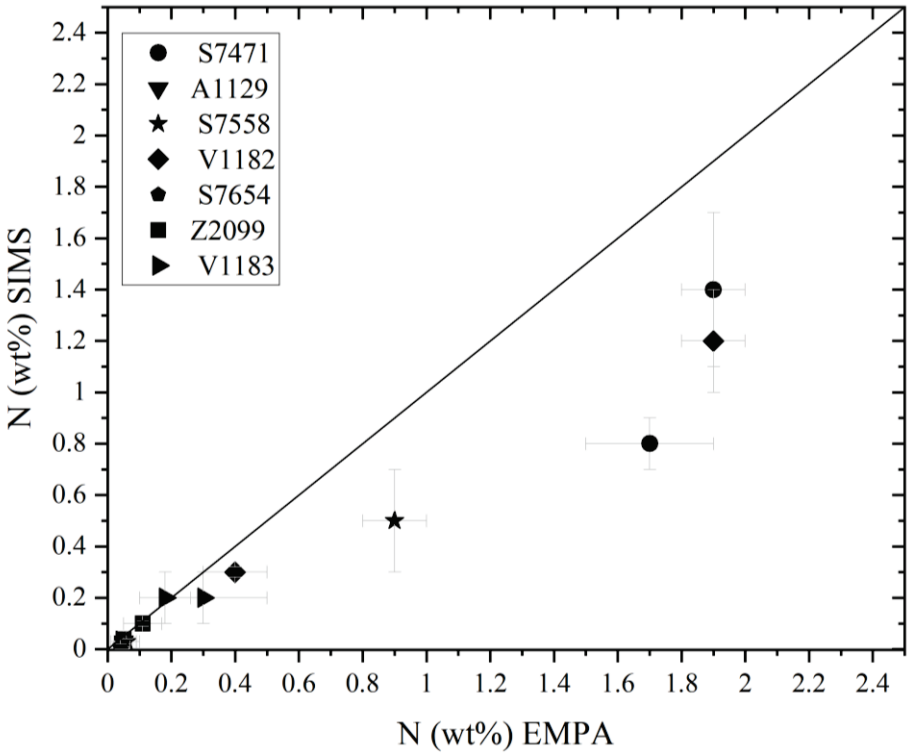

Figure A.6.8: Nitrogen concentration in wt% for the samples in the present work is here reported for the values obtained by means of secondary ion mass spectrometry (SIMS) and electron microprobe (EPMA) analyses. The 1:1 line is plotted as a solid line.

One of the major limitations of the SIMS technique is the matrix effect. It is difficult to assess to what extent this might affect the SIMS measurements since there is not much data available in the literature to properly quantify it, but previous work on other light elements has shown effects of both the structural environment (e.g. crystalline vs glass) and the bulk composition on SIMS analyses. For example, a decrease of the ion yields of the light elements with increasing (Fe+Mn)

content was reported in the work of Ottolini et al.2002 independently on the structure of the samples. Therefore, it is possible that the calibration of Füri et al. (2018) might underestimate the N concentration for samples with different structure and composition such as the ones in the present work (Boulliung et al 2020). Moreover, Mosenfelder et al.2019 suggested that the matrix effect leads to a reduced yield of the light element with an increase in molar mass of the matrix, an observation that agrees with previous work done on H analysis in zircon (Mosenfelder and Rossman 2014) and with instrumental mass fractionation of light and heavy isotope of O and H (Eiler et al.1997; Hauri et al.2006).

The observed underestimation for high N-concentration samples could also result from the ion collector used on the SIMS. To avoid oversaturating the EM with the high intensity secondary ion beam from the sample, high concentrations need to be acquired on the Faraday cup. For this reason, it is important to analyse the calibrants as well as the sample with the Faraday cup to make sure that the NO/O_2 ratio falls onto the same calibration line. During the data acquisition, we therefore measured one of the standards (CB-2# Füri et al.2018) on the FC. We observed that for this calibrant glass, the measurements yield a lower $^{14}N^{16}O^-$ signal on the FC (6.39E+04 cps) than on the electron multiplier (1.39E+05 cps). Consequently, high N contents were likely underestimated because the calibration line used in the present work was established on the EM.

On the other hand, the complexity of the EPMA nitrogen data evaluation is not to be underestimated. Our approach to correcting for the curvature of the background and the difference in peak shape between sample and standard relies on assumptions that may not be ideal. In particular, the peak shape and peak position is assumed to be the same between the sample and the standard, based on previous work (paragraph A.6.3.2) comparing N in silicate glasses and buddingtonite to BN. However, for the glasses and minerals measured in this study, quantifying

any difference in peak shape or position is impossible, because the low concentration of N in the samples would preclude obtaining wavelength scans with sufficient signal-to-noise ratio.

In addition, the quality of the major element data is also important in the quantification of N, because a matrix correction must be applied to obtain N concentration. The presence of water in the measured minerals or melts affects the EPMA measurement by yielding lower totals, but water by difference measurements are known to be unreliable (Hughes et al.2019). The matrix correction performed in the CalcZAF program does not allow for the calculation of water by difference when the N concentration is evaluated because of the software's inability to handle different cation to oxygen ratios for the same element. Moreover, the quality of the major elements data is important due to the fact that the calculated nitrogen concentration will be affected by it during the abovementioned matrix correction. It must be appreciated that these experiments where the achievement of the coexisting mineral phase with the glass resulting from its partial melt are extremely difficult. The final run products sometime present assemblages that have extremely fine grained or elongate crystals (e.g. S7471) and the melts show the presence of some bubbles possibly implying that some of the samples have been doped too highly in additional volatile components.

A.6.5.1 Partition coefficients

Mineral/melt partition coefficients (D_N) between silicate minerals and their partial melting products were calculated from the values in Table A.6.4. Partitioning is defined here as the wt.% ratio of nitrogen in either minerals or melts over fluid (e.g. D_N = mineral N (wt.%) / melt N (wt.%)), when the concentrations reflect an equilibrium distribution. The nitrogen partitioned into the minerals is therefore retained in the slab, while the N partitioned into the melt (or fluid) is expected to be lost to the mantle wedge and ultimately returned to the atmosphere. A recent work from Cannaò and co-authors has shown that a portion of the N fluxed into the mantle wedge may be

retained in secondary serpentinite that upon downward dragging of such materials, could play a role as N-rich reservoir int the upper mantle (Cannaò et al.2020). This is in good agreement with our results on the nitrogen retention capacity of the serpentinite (in the main text in Chapter 6).

To date, our understanding of the effect of fO_2 on the partitioning of nitrogen is still limited. What has been observed is that under oxidising conditions, the dominant N species are principally N_2 with minor contributions form N-O and C-N species (Roszkosz et al. 2006; Li et al.2015; Grewal et al. 2020). On the other hand, reducing conditions favour N-H species (e.g. NH_4) over N_2 (Mysen and Fogel, 2010; Li and Keppler, 2014; Li et al. 2015; Sokol et al. 2017; Mallik et al. 2018; Mosenfelder et al. 2019). Nitrogen compatibility is directly related to its speciation. N_2 is highly incompatible whereas ammonium is likely to be compatible in K-bearing minerals (Watenphul et al. 2009) and can dissolve as a trace component in potassium-absent phases (Li et al. 2013; Watenphul et al. 2010). What we observe in this study is that at reduced conditions, where the dominant N phase is expected to be NH_4, nitrogen still behaves incompatibly for the majority of the experiments, with the exception being the NH_4-phengite. This might suggest that N-concentration plays a role in the nitrogen partitioning. In Figure A.6.9, the partition coefficient values calculated for the present work are plotted together with the few literature data available for silicate mineral-melt partitioning (Förster et al. 2019; Yoshioka et al.2018, Keppler et al.2022, Jackson et al. 2021). Data for mineral - whole rock D_N produced by Toby Boocock (personal communication) have been added to this Figure. For these samples, the whole-rock is assumed to be an approximation for the bulk melt composition. The data appears scattered for phases such phlogopite (Förster et al. 2019), K-feldspar and biotite (Jackson et al. 2021; Boocock et al, in prep). The results reported from both Förster et al. 2019 and Jackson et al. 2021 are of experimental charges produced at a variety of P-T and fO_2 conditions that most likely explains the scatter in their results. Nonetheless, our results seem to be generally in good agreement with the literature and show that minerals such as NH^+_4-phengite and phlogopite, as well as biotite and K-feldspar

have the capacity to retain nitrogen. In a recent work by Yang and co-author on N-retention in K-feldspars, has shown that this mineral could be a potential carrier for nitrogen transport to the deep Earth (Yang et al.2022). These observation (Figure A.6.9) are interesting because, since the study by Honma and Itihara (1981) showing that N would partition preferentially into biotite, followed by muscovite and K-feldspar and lastly plagioclase and quartz, these data have been widely used as evidence that the presence of mica (i.e. biotite) controls the distribution of nitrogen in magmatic silicate systems (e.g. Busigny and Bebout, 2013; Halama et al. 2021; Johnson and Goldblatt, 2015). However, in Figure A.6.9 it can be observed that such a clear distinction cannot be drawn.

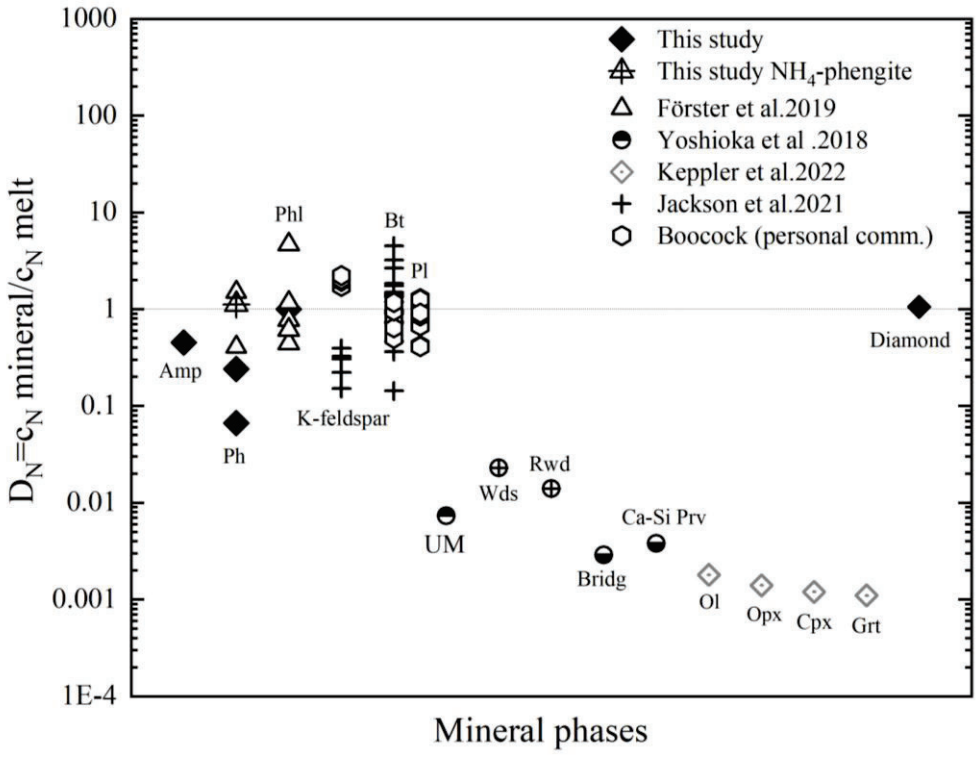

0

Figure A.6.9: Partition coefficients (D_N) between mineral and melt calculated for the present study are here plotted together with the available literature data. Mineral phases are : Amphibole (Amp); Phengite (Ph), Phlogopite (Phl); Botite (Bt); Plagioclase (Pl), wadsleyite (Wd); Ringwoodite (Rwd); Bridgmanite(Bridg); Calcium-Silicate Perovskite (Ca-Si Prv); Olivine (Ol); Orthpyroxene (Opx); Clinopyrozene (Cpx) and garnet (Grt). Note that for the Boocock samples the partition coefficient is between mineral and whole-rock.

Acknowledgments

This project has received funding from the European Union's Horizon 2020 research and innovation program under grant agreement No 871149. The EPMA work conducted by Eleanor Mare was funded by the Natural Environment Research Council award number NE/P012167/1, and a Carnegie Research Incentive Grant (reference RIG007794). EPMA nitrogen standards were provided by Colin Jackson and Antony Burnham. The authors acknowledge the instruments and expertise of Microscopy Australia at the Centre for Advanced Microscopy, Australian National University, a facility that is funded by the University and the Federal Government through NCRI.

Conclusions

This thesis focused on investigating the phase relations in the ferropericlase-spinel ferrite system by determining the maximum ferric iron content in ferropericlase at *P, T* and fO_2 conditions up to those where it coexists with either spinel or a high-pressure mixed-valence Fe and Mg oxide (e.g. Fe_4O_5 or Fe_5O_6). The following conclusions can be drawn:

1) For the first time, the compressibility of nearly pure magnesioferrite as well as of an intermediate $Mg_{0.5}Fe^{2+}_{0.5}Fe^{3+}_2O_4$ sample have been investigated using single crystal X-ray diffraction in a diamond anvil cell up to pressures comparable with the transition zone. Samples were produced in high-pressure synthesis experiments to promote a high level of cation ordering, with obtained inversion parameters larger than 0.83(5). The room pressure unit cell volumes, V_0, and bulk moduli, K_{T0}, could be adequately constrained using a 2nd order Birch-Murnaghan equation of state, which yields V_0 =588.97 (8) Å^3 and K_{T0} = 178.4(5) GPa for magnesioferrite and V_0 =590.21(5) Å^3 and K_{T0} = 188.0(6) GPa for the intermediate composition. As magnetite has K_{T0} = 180 (1) GPa (Gatta et al. 2007), this means the variation in K_{T0} across the magnetite-magnesioferrite solid solution is non-linear, in contrast to several other Fe-Mg spinels. The larger incompressibility of the intermediate composition compared to the two endmembers may be a peculiarity of the magnetite-magnesioferrite solid solution caused by an interruption of Fe^{2+}-Fe^{3+} electron hopping by Mg cations substituting in the octahedral site.

2) Experimental synthesis of ferropericlase with different compositions have been conducted up to 30 GPa in order to constrain the phase relations between ferropericlase with different Mg/(Mg+Fe) ratios and Fe3+-rich phases, i.e. spinel ferrite at low pressures and Fe,Mg-oxides with mixed valence at high-pressure. The majority of quenched ferropericlase samples contain nano-scale exsolutions of ferrite spinels, even when quenched at pressures where the spinel structure is not stable. Such exsolution are topotaxial with fper and likely results from the migration of Fe^{3+} atoms to the interstitial tetrahedral sites of the fper structure during quenching giving rise to the formation of defect clusters having the inverse spinel structure which rapidly grow to produce the n-spft coherent exsolutions. We show that for n-spft exsolutions >10 nm, it is possible to determine their contribution to the Mössbauer spectrum exploiting theier magnetic signal and reconstruct the high-temperature composition of fper, albeit with large uncertainties.

3) EELS measurements, using TEM, appear to be the only method with the spatial resolution to obtain an average Fe3+/Fetot ratio which take into account the presence of the spinel exsolved phase. However, a carefully fitting of the EELS patterns is necessary due to the complex contribution to the energy loss spectra of Fe^{2+} and Fe^{3+} occupying both tetrahedral and octahedral sites in the n-spft phase.

4) A thermodynamic model was constructed and refined by combining the results obtained from Mössbauer and EELS spectroscopy in order to describe the entire range of ferropericlase compositions in the system MgO-FeO-$FeO_{1.5}$. This model is capable to consistently reproduce the Fe^{3+}/Fe_{tot} ratio of ferropericlase coexisting with either spinel ferrite phase or the O_5 phase between room pressure and 30 GPa. The ferropericlase Fe^{3+}/Fe_{tot} ratio in equilibrium with spinel ferrite increases slightly with pressure. Above 10 GPa, however, after the phase transformation of spinel ferrite to the high-pressure

oxide, $[Fe^{2+}, Mg]_2Fe^{3+}{}_2O_5$, the Fe^{3+}/Fe_{tot} ratio declines rapidly. Comparison with previously proposed models show that these underestimate the Fe^{3+}/Fe_{tot} ratios at a given *P*, *T* and fO_2 conditions, likely due to the fact that n-spft exsolution were not taken into account in previous experimental works, because unnoticed.

5) The Fe-Mg partitioning K_D(app) between the coexisting oxides (e.g. fper-spft and fper-O_5) decreases with increasing pressure, implying that the Fe^{3+}-rich phases in equilibrium with ferropericlase become more Fe^{2+} rich with increasing pressure.

6) By defining the equilibrium between $(Mg, Fe)O_{Fper} + C_{diamond} = MgCO_{3\ mangesite}/FeCO_{3\ siderite}$ (with the acronym FDM), the fO_2 conditions of formation for fper inclusions in diamond have been constrained. The result in this work show that many of the natural diamond have a maximum formation depth near the top of the transition zone (or shallower). Only diamonds containing ferropericlase inclusion with Fe^{3+}/Fe_{tot} ratios < 0.03 could have formed in the lower mantle and this limiting Fe^{3+}/Fe_{tot} ratio value will decrease even further with increasing depth in the lower mantle. For Fe-rich ferropericlase, with Fe/(Fe+Mg) ratios > 0.5, the FMD curves intersect the equilibrium curves describing the equilibrium of ferropericlase with the O5 phase, implying that the O5 phase or the O6 phase (given the similarity between these two high-pressure oxides) may be entrapped in diamonds at lower mantle conditions.

7) The nitrogen (N) content and isotopic composition of several hydrous minerals and diamond have been measured, after equilibration at high pressures and temperatures with a fluid produced by the decomposition of glycine ($C_4H_5NO_2$). All phases show a relative enrichment in ^{15}N compared to the glycine starting material and its quenched residue but all contain less N than the coexisting fluid. Although it is generally assumed that N is substituted for interlayer K^+ cations in phyllosilicate minerals, this cannot be the case for

the serpentine minerals, which likely require another type of substitution mechanism. The passage of N-bearing fluids through lithologies containing hydrous minerals in subduction zones would remove ^{15}N from the fluid, causing N isotope fractionation in the mantle.

8) Diamonds were synthesised from graphite in the presence of an Fe-Ni-S catalyst and glycine at 13 GPa and 1700 °C. The partition coefficient for N (*D* diamond/metal) was determined to be 1.1(3), showing that N partitioned almost evenly between the diamond and the coexisting metallic catalyst. Moreover, the diamond became depleted in ^{15}N compared to the glycine starting material. As previous studies have shown N to be more compatible in Fe-Ni-S melts compared to silicate melts, this implies that N is most likely compatible during diamond growth processes, during which coexisting fluids should become progressively ^{15}N enriched.

Acknowledgments

First and foremost, I would like to thank my supervisors Tiziana Boffa Ballaran and Dan Frost for the endless support and patience during this whole journey. Tiziana, your advice, both on a professional and personal level, was always bringing me forward and kept me going. Sempre severa ma giusta, e te ne sono grata. Dan, thank you for putting up with the enormous amount of data I ended up producing and for guiding me through the incredibly complex world of thermodynamics.

I would like to thank Catherine McCammon for the productive chats and the always thoughtful advices. I am grateful to Alexander Kurnosov for his support with diamond anvil cell preparation and his positive attitude. Nobu-san and Dorothea Wiesner, without you all the TEM work would not have been possible, and I am really grateful for all your help. I want to thank Sami Mikhail and Eleanor Mare for the endless support and the indispensable help with the nitrogen measurements. Laura Uenver-Thiele, thank you for providing me the crystals and the starting material, but mostly for being a friend and helping me out every time I was struggling with our beloved ferropericlase- magnesioferrite system. Thank you to Evelyn Füri for the long days at the SIMS and for giving me the opportunity to collaborate with you. Last but not least I would like to thank Tony Withers , Gregor Golabek and Gerd Steinle-Neumann for helping me through the years and always being available for a chat.

This project would have been impossible without the technical support from Raphael Njul and Alexander Rother, on whom I could always count on for all sort of sample preparation, always perfect and right on time.

I am thankful to Heinz Fischer and Stefan Übelhack who prepared the best assemblies and equipped me with any type of tool I needed.

Thank you to Detlef Krause, Anke Potzel, Dorothea Wiesner and Ulrike Trenz for their support with the EPMA, SEM and in the chemistry lab. Many thanks to Petra Buchert, Janina Potzel and Anna Dinius who always helped me when I had bureaucratic difficulties.

I would like to thank all my friends at BGI Nicki, Lisa, Sumith, Serena, Marcel, Philipp and Remco who made my time here very enjoyable.

Barbara, thank you for keeping me together during this journey and being always available when I needed a chat.

I am very grateful to my family who always supported me during the last years.

Last but not least, I am beyond grateful to Jakob who has always been there for me during the good and bad times of this PhD with his endless support and encouragement.

References

Ader, M., Cartigny, P., Boudou, J. P., Oh, J. H., Petit, E., & Javoy, M. (2006). Nitrogen isotopic evolution of carbonaceous matter during metamorphism: Methodology and preliminary results.Chemical Geology,232(3-4), 152-169. doi:10.1016/j.chemgeo.2006.02.019

Akahama, Y., & Kawamura, H. (2006). Pressure calibration of diamond anvil Raman gauge to 310 GPa. Journal of Applied Physics, 100(4), 43516. https://doi.org/10.1063/1.2335683

Allaz, J. M., Williams, M. L., Jercinovic, M. J., Goemann, K., & Donovan, J. (2019). Multipoint background analysis: Gaining precision and accuracy in microprobe trace element analysis.Microscopy and Microanalysis,25(1), 30-46.

Altwegg, K., Balsiger, H., Bar-Nun, A., Berthelier, J. J., Bieler, A., Bochsler, P., & Wurz, P. (2016). Prebiotic chemicals—amino acid and phosphorus—in the coma of comet 67P/Churyumov-Gerasimenko. Science advances,2(5), e1600285. DOI: 10.1126/sciadv.1600285

Anderson, D. L., & Bass, J. D. (1984). Mineralogy and composition of the upper mantle. Geophysical Research Letters, 11(7), 637–640. https://doi.org/10.1029/GL011i007p00637

Andersson, B., & Sletnes, J. O. (1977). Decomposition and ordering in $Fe_{1-x}O$. Acta Crystallographica Section A: Crystal Physics, Diffraction, Theoretical and General Crystallography, 33(2), 268-276. https://doi.org/10.1107/S0567739477000680

Andrault, D., and Bolfan-Casanova, N. (2001) High-pressure phase transformations in the $MgFe_2O_4$ and Fe_2O_3-$MgSiO_3$ system. Physics and Chemistry of Minerals, 28, 211–217. https://doi.org/10.1007/s002690000149

Andreozzi, G.B., Bosi, F., and Garramone, F. (2001) Synthetic spinels in the $(Mg,Fe^{2+},Zn)(AI,Fe^{3+})_2O_4$ system. II. Preliminary chemical and structural data of hercynite and magnesioferrite samples. Periodico di Mineralogia, 70, 193–204.

Angel, R. J. (2003). Automated profile analysis for single-crystal diffraction data. Journal of Applied Crystallography, 36(2), 295-300. https://doi.org/10.1107/S0021889803001134

Angel, R. J. (2004). Absorption corrections for diamond-anvil pressure cells implemented in the software package Absorb6.0. Journal of Applied Crystallography,37(3), 486-492.https://doi.org/10.1107/S0021889804005229

Angel, R. J., Downs, R. T., & Finger, L. W. (2000). High-temperature–high-pressure diffractometry. Reviews in mineralogy and geochemistry, 41(1), 559-597. https://doi.org/10.2138/rmg.2000.41.16

Angel, R.J. (2000) Equations of state. High-temperature and high pressure crystal chemistry, MSA; Reviews in Mineralogy and Geochemistry; 41, 35–60. https://doi.org/10.2138/rmg.2000.41.2

Angel, R.J., and Finger, L.W. (2011) SINGLE: A program to control single-crystal diffractometers. Journal of Applied Crystallography, 44, 247–251. https://doi.org/10.1107/S0021889810042305

Angel, R.J., Bujak, M., Zhao, J., Gatta, G.D., and Jacobsen, S.D. (2007) Effective hydrostatic limits of pressure media for high-pressure crystallographic studies. Journal of Applied Crystallography, 40, 26–32. https://doi.org/10.1107/S0021889806045523

Antao, S., Hassan, I., Crichton, W.A., and Parise, J.B. (2005a) Effects of high pressure and high temperature on cation ordering in magnesioferrite, $MgFe_2O_4$, using in situ synchrotron X-ray powder diffraction up to 1430 K and 6 GPa. American Mineralogist, 90, 1500–1505. https://doi.org/10.2138/am.2005.1797

Antao, S.M., Hassan, I., and Parise, J.B. (2005b) Cation ordering in magnesioferrite, $MgFe_2O_4$, to 982°C using in situ synchrotron X-ray powder diffraction. American Mineralogist, 90, 219–228. https://doi.org/10.2138/am.2005.1559

Antic, B., Rodic, D., Nikolic, A.S., Kacarevic-Popovic, Z., and Karanovi, L. (2002) The change of crystal symmetry and cation ordering in Li-Mg ferrites. Journal of Alloys and Compounds, 336, 286–291. https://doi.org/10.1016/S0925-8388(01)01885-0

Anzolini, C., Marquardt, K., Stagno, V., Bindi, L., Frost, D.J., Pearson, D.G., Harris, J.W., Hemley, R.J., and Nestola, F. (2020) Evidence for complex iron oxides in the deep mantle from FeNi(Cu) inclusions in superdeep diamond. Proceedings of the National Academy of Sciences of the United States of America, 117, 21088–21094. https://doi.org/10.1073/pnas.2004269117

Anzolini, C., Nestola, F., Mazzucchelli, M.L., Alvaro, M., Nimis, P., Gianese, A., Morganti, S., Marone, F., Campione, M., Hutchison, M.T. and Harris, J.W. (2019). Depth of diamond formation obtained from single periclase inclusions. Geology,47(3), 219-222. https://doi.org/10.1130/G45605.1

B.E. Warren (1990). X-ray diffraction. Dover Publication, New York, pp. 258.

Badro, J., Fiquet, G., Guyot, F., Rueff, J. P., Struzhkin, V. V., Vanko, G., & Monaco, G. (2003). Iron partitioning in Earth's mantle: toward a deep lower mantle discontinuity.Science,300 (5620), 789-791. https://doi.org/10.1126/science.1081311

Ballhaus, C., & Frost, B. R. (1994). The generation of oxidized CO2-bearing basaltic melts from reduced CH_4-bearing upper mantle sources.Geochimica et Cosmochimica Acta, 58(22), 4931-4940. https://doi.org/10.1016/0016-7037(94)90222-4

Ballhaus, C., Berry, R. F., & Green, D. H. (1991). High pressure experimental calibration of the olivine-orthopyroxene-spinel oxygen geobarometer: implications for the oxidation state of the upper mantle.Contributions to Mineralogy and Petrology, 107, 27-40. https://doi.org/10.1007/BF00311183

Bancroft, G. M. (1973). Mössbauer spectroscopy: an introduction for inorganic chemists and geochemists. (John Wiley and Sons, Ed.).

Barin, I., & Platzki, G. (1989). Thermochemical data of pure substances (Vol. 304, No. 334, p. 1117). Weinheim: VCh. 10.1002/9783527619825

Bassett, W. A. (2009). High Pressure Research : An Diamond anvil cell , 50th birthday. High Pressure Research, 29(2), 163–186. https://doi.org/10.1080/08957950802597239

Bastin, G. F., & Heijligers, H. J. M. (1991). Quantitative electron probe microanalysis of nitrogen. Scanning, 13(5), 325-342.

Bataleva, Y. V., Palyanov, Y. N., Borzdov, Y. M., Kupriyanov, I. N., & Sokol, A. G. (2016). Synthesis of diamonds with mineral, fluid and melt inclusions. Lithos, 265, 292-303. https://doi.org/10.1016/j.lithos.2016.07.005

Bataleva, Y., Palyanov, Y., Borzdov, Y., & Bayukov, O. (2019). Processes and conditions of the origin for Fe^{3+}-bearing magnesiowüstite under lithospheric mantle pressures and temperatures. Minerals, 9(8), 474.DOI: 10.3390/min9080474

Bebout, G. E., & Fogel, M. L. (1992). Nitrogen-isotope compositions of metasedimentary rocks in the Catalina Schist, California: implications for metamorphic devolatilization history. Geochimica et Cosmochimica Acta, 56(7), 2839-2849. https://doi.org/10.1016/0016-7037(92)90363-N

Bebout, G. E., Banerjee, N. R., Izawa, M. R. M., Kobayashi, K., Lazzeri, K., Ranieri, L. A., & Nakamura, E. (2018). Nitrogen concentrations and isotopic compositions of seafloor-altered terrestrial basaltic glass: implications for astrobiology. Astrobiology, 18(3), 330-342.https://doi.org/10.1089/ast.2017.1708

Bebout, G. E., Fogel, M. L., & Cartigny, P. (2013). Nitrogen: Highly volatile yet surprisingly compatible. Elements, 9(5), 333-338. DOI: 10.2113/gselements.9.5.333

Bebout, G. E., Lazzeri, K. E., & Geiger, C. A. (2016). Pathways for nitrogen cycling in Earth's crust and upper mantle: A review and new results for microporous beryl and cordierite. American Mineralogist, 101(1), 7-24. https://doi.org/10.2138/am-2016-5363

Bekaert, D.V., Turner, S.J., Broadley, M.W., Barnes, J.D., Halldórsson, S.A., Labidi, J., Wade, J., Walowski, K.J. & Barry, P. H. (2021). Subduction-driven volatile recycling: A global mass balance. Annual Review of Earth and Planetary Sciences, 49, 37-70. https://doi.org/10.1146/annurev-earth-071620-055024

Beran, A., Armstrong, J., & Rossman, G. R. (1992). Infrared and electron microprobe analysis of ammonium ions in hyalophane feldspar. European Journal of Mineralogy, 4(4), 847-850.

Berry, A.J., Yaxley, G.M., Hanger, B.J., Woodland, A.B., de Jonge, M.D., Howard, D.L., Paterson, D. and Kamenetsky, V.S. (2013). Quantitative mapping of the oxidative effects of mantle metasomatism. Geology, 41(6), 683-686. https://doi.org/10.1130/G34119.1

Beyer, C., & Frost, D. J. (2017). The depth of sub-lithospheric diamond formation and the redistribution of carbon in the deep mantle. Earth and Planetary Science Letters, 461, 30-39.https://doi.org/10.1016/j.epsl.2016.12.017

Bhide, V.G., and Tambe, B.R. (1969) Investigation of the MgO:Fe system using the Mössbauer effect. Journal of Materials Science, 4, 955–961. https://doi.org/10.1007/BF00555310

Birch, F. (1947) Finite elastic strain of cubic crystals. Physical Review, 71, 809–824. https://doi.org/10.1103/PhysRev.71.809

Birch, F. (1947) Finite elastic strain of cubic crystals. Physical Review, 71, 809–824. https://doi.org/10.1103/PhysRev.71.809

Boehler, R., and De Hantsetters, K. (2004) New anvil designs in diamond-cells. High Pressure Research, 24, 391–396. https://doi.org/10.1080/08957950412331323924

Boffa Ballaran, T., Uenver-Thiele, L., & Woodland, A. B. (2015). Complete substitution of Fe2+ by Mg in Fe4O5: The crystal structure of the Mg2Fe2O5 end-member. American Mineralogist, 100(2-3), 628-632. https://doi.org/10.2138/am-2015-5138

Boiocchi, M., Caucia, F., Merli, M., Prella, D., & Ungaretti, L. (2001). Crystal-chemical reasons for the immiscibility of periclase and wustite under lithospheric P, T conditions. European Journal of Mineralogy, 13(5), 871-881.DOI: 10.1127/0935-1221/2001/0013/0871

Bolfan-Casanova, N., Mackwell, S., Keppler, H., McCammon, C., & Rubie, D. C. (2002). Pressure dependence of H solubility in magnesiowüstite up to 25 GPa: Implications for the storage of water in the Earth's lower mantle. Geophysical Research Letters, 29(10), 89-1. https://doi.org/10.1029/2001GL014457

Boocock, T. J., Mikhail, S., Prytulak, J., Di Rocco, T., & Stüeken, E. E. (2020). Nitrogen mass fraction and stable isotope ratios for fourteen geological reference materials: Evaluating the applicability of elemental analyser versus sealed tube combustion methods. Geostandards and Geoanalytical Research, 44(3), 537-551. DOI: https://doi.org/10.1111/ggr.12345

Borzdov, Y., Pal'yanov, Y., Kupriyanov, I., Gusev, V., Khokhryakov, A., Sokol, A., & Efremov, A. (2002). HPHT synthesis of diamond with high nitrogen content from an Fe3N–C system. Diamond and Related Materials, 11(11), 1863-1870. https://doi.org/10.1016/S0925-9635(02)00184-X

Bosi, F., Halenius, U., and Skogby, H. (2009) Crystal chemistry of the magnetite-ulvospinel series. American Mineralogist, 94, 181–189. https://doi.org/10.2138/am.2009.3002

Boulliung, J., Füri, E., Dalou, C., Tissandier, L., Zimmermann, L., & Marrocchi, Y. (2020). Oxygen fugacity and melt composition controls on nitrogen solubility in silicate melts. Geochimica et Cosmochimica Acta, 284, 120-133.

Boyd, S. R. (2001). Nitrogen in future biosphere studies. Chemical Geology, 176(1-4), 1-30. https://doi.org/10.1016/S0009-2541(00)00405-8

Brandon, A. D., & Draper, D. S. (1996). Constraints on the origin of the oxidation state of mantle overlying subduction zones: an example from Simcoe, Washington, USA. Geochimica et Cosmochimica Acta, 60(10), 1739-1749. https://doi.org/10.1016/0016-7037(96)00056-7

Brenker, F.E., Vincze, L., Vekemans, B., Nasdala, L., Stachel, T., Vollmer, C., Kersten, M., Somogyi, A., Adams, F., Joswig, W. and Harris, J.W.(2005). Detection of a Ca-rich lithology in the Earth's deep (> 300 km) convecting mantle. Earth and Planetary Science Letters, 236(3-4), 579-587. https://doi.org/10.1016/j.epsl.2005.05.021

Brenker, F.E., Vollmer, C., Vincze, L., Vekemans, B., Szymanski, A., Janssens, K., Szaloki, I., Nasdala, L., Joswig, W. and Kaminsky, F.(2007). Carbonates from the lower part of transition zone or even the lower mantle. Earth and Planetary Science Letters, 260(1-2), 1-9. https://doi.org/10.1016/j.epsl.2007.02.038

Brey, G. P., Bulatov, V., Girnis, A., Harris, J. W., & Stachel, T. (2004). Ferropericlase—a lower mantle phase in the upper mantle. Lithos, 77(1-4), 655-663. https://doi.org/10.1016/j.lithos.2004.03.013

Bruschini, E., Speziale, S., Andreozzi, G. B., Bosi, F., & Hålenius, U. (2015). The elasticity of MgAl2O4–MnAl2O4 spinels by Brillouin scattering and an empirical approach for bulk modulus prediction. American Mineralogist, 100(2-3), 644-651. https://doi.org/10.2138/am-2015-4993

Bruschini, E., Speziale, S., Bosi, F., & Andreozzi, G.B. (2018) Fe–Mg substitution in aluminate spinels: effects on elastic properties investigated by Brillouin scattering. Physics and Chemistry of Minerals, 45, 759–772. https://doi.org/10.1007/s00269-018-0960-3

Brynestad, J., and Flood, H. (1958) The Redox Equilibrium in Wüstite and Solid Solutions of Wüstite and Magnesium Oxide. Zeitschrift für Elektrochemie, 62, 953–958. https://doi.org/10.1002/bbpc.19580620905

Bulanova, G. P., Walter, M. J., Smith, C. B., Kohn, S. C., Armstrong, L. S., Blundy, J., & Gobbo, L. (2010). Mineral inclusions in sublithospheric diamonds from Collier 4 kimberlite pipe, Juina, Brazil: subducted protoliths, carbonated melts and primary kimberlite magmatism. Contributions to Mineralogy and Petrology, 160, 489-510.DOI: 10.1007/s00410-010-0490-6

Bulatov, V. K., Girnis, A. V., Brey, G. P., Woodland, A. B., & Höfer, H. E. (2019). Ferropericlase crystallization under upper mantle conditions. Contributions to Mineralogy and Petrology, 174, 1-14. https://doi.org/10.1007/s00410-019-1582-6

Bullen, K. E. (1942). The density variation of the Earth's central core. Bulletin of the Seismological Society of America, 32(1), 19-29. https://doi.org/10.1785/BSSA0320010019

Burgmann, W. (1975). The defect structure models for wüstite: A review. Metal Science, 9(1), 169-175. https://doi.org/10.1179/030634575790445107

Burns, R. G., & Solberg, T. C. (1990). 57Fe-bearing oxide, silicate, and aluminosilicate minerals: Crystal structure trends in Mossbauer spectra. 10.1021/bk-1990-0415.ch014

Busigny, V., & Bebout, G. E. (2013). Nitrogen in the silicate Earth: Speciation and isotopic behavior during mineral–fluid interactions. Elements, 9(5), 353-358.https://doi.org/10.2113/gselements.9.5.353

Busigny, V., Cartigny, P., & Philippot, P. (2011). Nitrogen isotopes in ophiolitic metagabbros: A re-evaluation of modern nitrogen fluxes in subduction zones and implication for the early Earth atmosphere. Geochimica et Cosmochimica Acta, 75(23), 7502-7521 doi:10.1016/j.gca.2011.09.049

Busigny, V., Cartigny, P., Laverne, C., Teagle, D., Bonifacie, M., & Agrinier, P. (2019). A re-assessment of the nitrogen geochemical behavior in upper oceanic crust from Hole 504B: Implications for subduction budget in Central America. Earth and Planetary Science Letters, 525, 115735.https://doi.org/10.1016/j.epsl.2019.115735

Busigny, V., Cartigny, P., Philippot, P., Ader, M., & Javoy, M. (2003). Massive recycling of nitrogen and other fluid-mobile elements (K, Rb, Cs, H) in a cold slab environment: evidence from HP to UHP oceanic metasediments of the Schistes Lustrés nappe (western Alps, Europe). Earth and Planetary Science Letters, 215(1-2), 27-42.https://doi.org/10.1016/S0012-821X(03)00453-9

Busigny, V., Laverne, C., & Bonifacie, M. (2005). Nitrogen content and isotopic composition of oceanic crust at a superfast spreading ridge: a profile in altered basalts from ODP Site 1256, Leg 206. Geochemistry, Geophysics, Geosystems, 6(12). https://doi.org/10.1029/2005GC001020

Bykova, E., Dubrovinsky, L., Dubrovinskaia, N., Bykov, M., McCammon, C., Ovsyannikov, S. V., Liermann, H.P., Kupenko, I., Chumakov, A.I., Rüffer, R., Hanfland, M & Prakapenka, V. (2016). Structural complexity of simple Fe2O3 at high pressures and temperatures. Nature Communications, 7(1), 10661. https://doi.org/10.1038/ncomms10661

Campbell, A. J., Danielson, L., Righter, K., Seagle, C. T., Wang, Y., & Prakapenka, V. B. (2009). High pressure effects on the iron–iron oxide and nickel–nickel oxide oxygen fugacity buffers. Earth and Planetary Science Letters, 286(3-4), 556-564. https://doi.org/10.1016/j.epsl.2009.07.022

Canil, D., & O'NEILL, H. S. C. (1996). Distribution of ferric iron in some upper-mantle assemblages. Journal of Petrology, 37(3), 609-635. https://doi.org/10.1093/petrology/37.3.609

Cannaò, E., Tiepolo, M., Bebout, G. E., & Scambelluri, M. (2020). Into the deep and beyond: Carbon and nitrogen subduction recycling in secondary peridotites. Earth and Planetary Science Letters, 543, 116328. https://doi.org/10.1016/j.epsl.2020.116328

Cartigny, P. (2005). Stable isotopes and the origin of diamond. Elements, 1(2), 79-84.https://doi.org/10.2113/gselements.1.2.79

Cartigny, P., & Marty, B. (2013). Nitrogen isotopes and mantle geodynamics: The emergence of life and the atmosphere–crust–mantle connection. Elements, 9(5), 359-366. https://doi.org/10.2113/gselements.9.5.359

Cartigny, P., Chinn, I., Viljoen, K. S., & Robinson, D. (2004). Early Proterozoic ultrahigh pressure metamorphism: evidence from microdiamonds. Science, 304(5672), 853-855.DOI: 10.1126/science.1094668

Cartigny, P., De Corte, K., Shatsky, V. S., Ader, M., De Paepe, P., Sobolev, N. V., & Javoy, M. (2001a). The origin and formation of metamorphic microdiamonds from the Kokchetav massif, Kazakhstan: a nitrogen and carbon isotopic study. Chemical Geology, 176(1-4), 265-281.https://doi.org/10.1016/S0009-2541(00)00407-1

Cartigny, P., Harris, J. W., & Javoy, M. (2001b). Diamond genesis, mantle fractionations and mantle nitrogen content: a study of δ13C–N concentrations in diamonds. Earth and Planetary Science Letters, 185(1-2), 85-98.https://doi.org/10.1016/S0012-821X(00)00357-5

Cartigny, P., Palot, M., Thomassot, E., & Harris, J. W. (2014). Diamond formation: a stable isotope perspective. Annual Review of Earth and Planetary Sciences, 42, 699-732. https://doi.org/10.1146/annurev-earth-042711-105259

Castellanos-Rubio, I., Rodrigo, I., Munshi, R., Arriortua, O., Garitaonandia, J. S., Martinez-Amesti, A., ... & Insausti, M. (2019). Outstanding heat loss via nano-octahedra above 20 nm in size: From wustite-rich nanoparticles to magnetite single-crystals. Nanoscale, 11(35), 16635-16649. DOI https://doi.org/10.1039/C9NR04970C

Catlow, C. R. A., & Fender, B. E. F. (1975). Calculations of defect clustering in Fe1-xO. Journal of Physics C: Solid State Physics, 8(20), 3267. DOI 10.1088/0022-3719/8/20/005

Cavé, L., Al, T., Loomer, D., Cogswell, S. and Weaver, L., 2006. A STEM/EELS method for mapping iron valence ratios in oxide minerals. Micron, 37(4), pp.301-309.

Cedeño, D. G., Conceicao, R. V., de Souza, M. R. W., Quinteiro, R. V. S., Carniel, L. C., Ketzer, J. M. M., ... & do Canto Bruzza, E. (2019). An experimental study on smectites as nitrogen conveyors in subduction zones. Applied Clay Science, 168, 409-420. https://doi.org/10.1016/j.clay.2018.11.006

Chen, M., Avarmaa, K., Klemettinen, L., O'Brien, H., Shi, J., Taskinen, P., ... & Jokilaakso, A. (2021). Precious Metal Distributions Between Copper Matte and Slag at High P SO 2 in WEEE Reprocessing. Metallurgical and Materials Transactions B, 52(2), 871-882.https://doi.org/10.1007/s11663-021-02059-z

Chepurov, A. I., Zhimulev, E. I., Sonin, V. M., Chepurov, A. A., & Pokhilenko, N. P. (2009, October). Crystallization of diamond in metal-sulfide melts. In Doklady Earth Sciences (Vol. 428, No. 1, p. 1139). Springer Nature BV.DOI: 10.1134/S1028334X09070228

Clark, R. C., & Reid, J. S. (1995). The analytical calculation of absorption in multifaceted crystals. Acta Crystallographica Section A: Foundations of Crystallography, 51(6), 887-897.https://doi.org/10.1107/S0108767395007367

Cline II, C. J., Faul, U. H., David, E. C., Berry, A. J., & Jackson, I. (2018). Redox-influenced seismic properties of upper-mantle olivine. Nature, 555(7696), 355-358. https://doi.org/10.1038/nature25764

Collerson, K. D., Williams, Q., Kamber, B. S., Omori, S., Arai, H., & Ohtani, E. (2010). Majoritic garnet: A new approach to pressure estimation of shock events in meteorites and the encapsulation of sub-lithospheric inclusions in diamond. Geochimica et Cosmochimica Acta, 74(20), 5939-5957. https://doi.org/10.1016/j.gca.2010.07.00 5939-5957

D'Haenens-Johansson, U. F., Butler, J. E., & Katrusha, A. N. (2022). Synthesis of diamonds and their identification. Reviews in Mineralogy and Geochemistry, 88(1), 689-753.https://doi.org/10.2138/rmg.2022.88.13

Dalou, C., Hirschmann, M. M., Jacobsen, S. D., & Le Losq, C. (2019). Raman spectroscopy study of COHN speciation in reduced basaltic glasses: Implications for reduced planetary mantles. Geochimica et Cosmochimica Acta, 265, 32-47.

Darken, L. S., & Gurry, R. W. (1945). The system iron-oxygen. I. The wüstite field and related equilibria. Journal of the American Chemical Society, 67(8), 1398-1412. https://doi.org/10.1021/ja01224a050

Dauphas, N., & Marty, B. (1999). Heavy nitrogen in carbonatites of the Kola Peninsula: A possible signature of the deep mantle. Science, 286(5449), 2488-2490. DOI: 10.1126/science.286.5449.2488

Davies, R. M., Griffin, W. L., O'Reilly, S. Y., & Doyle, B. J. (2004). Mineral inclusions and geochemical characteristics of microdiamonds from the DO27, A154, A21, A418, DO18, DD17 and Ranch Lake kimberlites at Lac de Gras, Slave Craton, Canada. Lithos, 77(1-4), 39-55.DOI: 10.1016/j.lithos.2004.04.016

Davies, R.M., Griffin, W.L., Pearson, N.J., Andrew, A.S., Doyle, B.J., O'Reilly, S.Y., 1999. Diamonds from the deep: pipe DO-27, Slave craton, Canada. In: Gurney, J.J., Gurney, J.L., Pascoe, M.D., Richardson, S.H. (Eds.), Proceedings of the VIIth International kimberlite Conference, J.B. Dawson volume. Red Roof Design, CapeTown, pp. 148–155.

Degterov, S. A., Pelton, A. D., Jak, E., & Hayes, P. C. (2001). Experimental study of phase equilibria and thermodynamic optimization of the Fe-Zn-O system. Metallurgical and Materials Transactions B, 32, 643-657. https://doi.org/10.1007/s11663-001-0119-2

Deines, P., Harris, J. W., & Gurney, J. J. (1991). The carbon isotopic composition and nitrogen content of lithospheric and asthenospheric diamonds from the Jagersfontein and Koffiefontein kimberlite, South Africa. Geochimica et Cosmochimica Acta, 55(9), 2615-2625.https://doi.org/10.1016/0016-7037(91)90377-H

Deines, P., Harris, J. W., & Gurney, J. J. (1993). Depth-related carbon isotope and nitrogen concentration variability in the mantle below the Orapa kimberlite, Botswana, Africa. Geochimica et Cosmochimica Acta, 57(12), 2781-2796. 10.1016/0016-7037(93)90390-I

Dewaele, A., Fiquet, G., Andrault, D., & Hausermann, D. (2000). P-V-T equation of state of periclase from synchrotron radiation measurements. Journal of Geophysical Research: Solid Earth, 105(B2), 2869-2877. https://doi.org/10.1029/1999JB900364

Dewaele, A., Torrent, M., Loubeyre, P., and Mezouar, M. (2008) Compression curves of transition metals in the Mbar range: Experiments and projector augmented-wave calculations. Physical Review B - Condensed Matter and Materials Physics, 78,104102-1–13. https://doi.org/10.1103/PhysRevB.78.104102

Dick, H.J.B., and Bullen, T. (1984) Chromian spinel as a petrogenetic indicator in abyssal and alpine-type peridotites and spatially associated lavas. Contributions to Mineralogy and Petrology, 86, 54–76. https://doi.org/10.1007/BF00373711

Dimitrov, D. V., Unruh, K., Hadjipanayis, G. C., Papaefthymiou, V., & Simopoulos, A. (1999). Ferrimagnetism and defect clusters in Fe 1− x O films. Physical Review B, 59(22), 14499. https://doi.org/10.1103/PhysRevB.59.14499

Dimitrov, D. V., Unruh, K., Hadjipanayis, G. C., Papaefthymiou, V., & Simopoulos, A. (2000). Defect clusters in Fe 1− x O and their ferrimagnetic properties. Journal of Applied Physics, 87(9), 7022-7024. https://doi.org/10.1063/1.372918

Dobson, D. P., Cohen, N. S., Pankhurst, Q. A., & Brodholt, J. P. (1998). A convenient method for measuring ferric iron in magnesiowu¨ stite (MgO-Fe1-xO). American Mineralogist, 83(7-8), 794-798. https://doi.org/10.2138/am-1998-7-811

Dobson, D. P., Richmond, N. C., & Brodholt, J. P. (1997). A high-temperature electrical conduction mechanism in the lower mantle phase (Mg, Fe) 1− x O. Science, 275(5307), 1779-1781.DOI: 10.1126/science.275.5307.1779

Donnelly, C. L., Stachel, T., Creighton, S., Muehlenbachs, K., & Whiteford, S. (2007). Diamonds and their mineral inclusions from the A154 South pipe, Diavik Diamond Mine, Northwest territories, Canada. Lithos, 98(1-4), 160-176.. 10.1016/j.lithos.2007.03.003

Dorogokupets, P. I. (2010). P–V–T equations of state of MgO and thermodynamics. Physics and Chemistry of Minerals, 37, 677-684. https://doi.org/10.1007/s00269-010-0367-2

Dorogokupets, P. I., Dymshits, A. M., Litasov, K. D., & Sokolova, T. S. (2017). Thermodynamics and equations of state of iron to 350 GPa and 6000 K. Scientific reports, 7(1), 41863. https://doi.org/10.1038/srep41863

Dubrovinskaia, N., Dubrovinsky, L., Caracas, R., & Hanfland, M. (2010). Diamond as a high pressure gauge up to 2.7 Mbar. Applied Physics Letters, 97(25), 251903.https://doi.org/10.1063/1.3529454

Dubrovinsky, L.S., Dubrovinskaia, N.A., McCammon, C., Rozenberg, G.K., Ahuja, R., Osorio-Guillen, J.M., Dmitriev, V., Weber, H.P., Le Bihan, T. & Johansson, B. (2003). The structure of the metallic high-pressure Fe3O4 polymorph: experimental and theoretical study. Journal of Physics: Condensed Matter, 15(45), 7697. 10.1088/0953-8984/15/45/009

Duffy, T. S., Hemley, R. J., & Mao, H. K. (1995). Equation of state and shear strength at multimegabar pressures: Magnesium oxide to 227 GPa. Physical Review Letters, 74(8), 1371. https://doi.org/10.1103/PhysRevLett.74.1371

Dyar, M. D., Agresti, D. G., Schaefer, M. W., Grant, C. A., & Sklute, E. C. (2006). Mössbauer spectroscopy of earth and planetary materials. Annu. Rev. Earth Planet. Sci., 34, 83-125. https://doi.org/10.1146/annurev.earth.34.031405.125049

Dyar, M. D., McGuire, A. V., & Mackwell, S. J. (1992). Fe3+/H+ and D/H in kaersutites—misleading indicators of mantle source fugacities. Geology, 20(6), 565-568. https://doi.org/10.1130/0091-7613(1992)020<0565:FHADHI>2.3.CO;2

Dziewonski, A. M., & Anderson, D. L. (1981). Preliminary reference Earth model. Phys. Earth Planet. Inter, 25, 297–356. https://doi.org/10.1016/0031-9201(81)90046-7

Eberhard, L., Thielmann, M., Eichheimer, P., Néri, A., Suzuki, A., Ohl, M., Fujita, W., Uesugi, K., Nakamura, M., Golabek, G.J. and Frost, D.J., 2022. A new method for determining fluid flux at high pressures applied to the dehydration of serpentinites. Geochemistry, Geophysics, Geosystems, 23(9), p.e2021GC010062.https://doi.org/10.1029/2021GC010062

Egerton, R. F. (2009). Electron energy-loss spectroscopy in the TEM. Reports on Progress in Physics, 72(1). https://doi.org/10.1088/0034-4885/72/1/016502

Egerton, R. F. (2011). Electron energy-loss spectroscopy in the electron microscope. Springer Science & Business Media. https://doi.org/10.1007/978-1-4757-5099-7

Egerton, R. F., & Malac, M. (2005). EELS in the TEM. Journal of Electron Spectroscopy and Related Phenomena, 143(2-3), 43-50.

Eggler, D. H.& Baker D.R. (1982). Reduced volatiles in the system CHO: Implications to mantle melting, fluid formation and diamond genesis. Advances in Earth and Planetary Science, 12, 237-250.

Eiler, J. M., Graham, C., & Valley, J. W. (1997). SIMS analysis of oxygen isotopes: matrix effects in complex minerals and glasses. Chemical Geology, 138(3-4), 221-244.https://doi.org/10.1016/S0009-2541(97)00015-6

Eugster, H. P. (1957). Heterogeneous reactions involving oxidation and reduction at high pressures and temperatures. The Journal of Chemical Physics, 26(6), 1761–1762. https://doi.org/10.1063/1.1743626

Evans, B. J., & Hafner, S. S. (1969). 57Fe hyperfine fields in magnetite (Fe3O4). Journal of Applied Physics, 40(3), 1411-1413. https://doi.org/10.1063/1.1657696

Fei, Y. (1996) Crystal chemistry of FeO at high pressure and temperature. In M.D. Dyar, C. McCammon, and M.W. Shaefer, Eds., Mineral Spectroscopy: A Tribute to Roger G. Burns, p. 243–254. Special Publication No. 5. The Geochemical Society, Houston

Fei, Y., Frost, D. J., Mao, H. K., Prewitt, C. T., & Haeusermann, D. (1999). In situ structure determination of the high-pressure phase of Fe3O4. American Mineralogist, 84(1-2), 203-206. https://doi.org/10.2138/am-1999-1-222

Finger, L.W., Hazen, R.M., and Hofmeister, A.M. (1986) High-Pressure crystal chemistry of spinel (MgAl2O4) and magnetite (Fe3O4): Comparisons with silicate spinels. Physics and Chemistry of Minerals, 13, 215–220. https://doi.org/10.1007/BF00308271

Finger, L.W., Hazen, R.M., and Hofmeister, A.M. (1986) High-Pressure crystal chemistry of spinel (MgAl2O4) and magnetite (Fe3O4): Comparisons with silicate spinels. Physics and Chemistry of Minerals, 13, 215–220. https://doi.org/10.1007/BF00308271

Fock, J., Hansen, M.F., Frandsen, C., and Mørup, S. (2018) On the interpretation of Mössbauer spectra of magnetic nanoparticles. Journal of Magnetism and Magnetic Materials, 445, 11–21.https://doi.org/10.1016/j.jmmm.2017.08.070

Foley, S. F. (2008). Rejuvenation and erosion of the cratonic lithosphere. Nature geoscience, 1(8), 503-510. https://doi.org/10.1038/ngeo261

Foley, S. F. (2011). A reappraisal of redox melting in the Earth's mantle as a function of tectonic setting and time. Journal of Petrology, 52(7-8), 1363-1391. https://doi.org/10.1093/petrology/egq061

Förster, M. W., Foley, S. F., Alard, O., & Buhre, S. (2019). Partitioning of nitrogen during melting and recycling in subduction zones and the evolution of atmospheric nitrogen. Chemical Geology, 525, 334-342. https://doi.org/10.1016/j.chemgeo.2019.07.042

Frost, B. R. (1991). Introduction To Oxygen Fugacity and its petrologic importance, 2, 1–9. https://doi.org/10.1515/9781501508684-004

Frost, D. J., & Langenhorst, F. (2002). The effect of Al2O3 on Fe–Mg partitioning between magnesiowüstite and magnesium silicate perovskite. Earth and Planetary Science Letters, 199(1-2), 227-241. https://doi.org/10.1016/S0012-821X(02)00558-7

Frost, D. J., & McCammon, C. A. (2008). The redox state of Earth's mantle. Annu. Rev. Earth Planet. Sci., 36, 389-420. https://doi.org/10.1146/annurev.earth.36.031207.124322

Frost, D. J., Liebske, C., Langenhorst, F., McCammon, C. A., Trønnes, R. G., & Rubie, D. C. (2004). Experimental evidence for the existence of iron-rich metal in the Earth's lower mantleNature, 428(6981), 409–412. https://doi.org/10.1038/nature02413

Frost, D. J., Mann, U., Asahara, Y., Rubie, D. C. (2008). The redox state of the mantle during and just after core formation. Philosophical Transactions of the Royal Society A: Mathematical, Physical and Engineering Sciences, 366(1883), 4315–4337. https://doi.org/10.1098/rsta.2008.0147

Füri, E., Deloule, E., & Dalou, C. (2018). Nitrogen abundance and isotope analysis of silicate glasses by secondary ionization mass spectrometry. Chemical Geology, 493, 327-337.

Gatta, G.D., Kantor, I., Boffa Ballaran, T., Dubrovinsky, L., and McCammon, C. (2007) Effect of non-hydrostatic conditions on the elastic behaviour of magnetite: An in situ single-crystal X-ray diffraction study. Physics and Chemistry of Minerals, 34, 627–635. https://doi.org/10.1007/s00269-007-0177-3

Gavarri, J. R., & Carel, C. (2017). A review about wüstite Fe 1-z O, pseudo-phases and defect clustering. arXiv preprint arXiv:1712.03741. https://doi.org/10.48550/arXiv.1712.03741

Gavarri, J. R., & Carel, C. (2019). The complex nonstoichiometry of wüstite Fe1-zO: review and comments. Progress in Solid State Chemistry, 53, 27-49.https://doi.org/10.1016/j.progsolidstchem.2018.10.001

Gerward, L., and Olsen, J.S. (1995) High-pressure studies of magnetite and magnesioferrite using synchrotron radiation. Applied Radiation and Isotopes, 46, 553–554.

Glavin, D. P., Callahan, M. P., Dworkin, J. P., & Elsila, J. E. (2010). The effects of parent body processes on amino acids in carbonaceous chondrites. Meteoritics & Planetary Science, 45(12), 1948-1972. https://doi.org/10.1111/j.1945-5100.2010.01132.x

Goldblatt, C., Claire, M. W., Lenton, T. M., Matthews, A. J., Watson, A. J., & Zahnle, K. J. (2009). Nitrogen-enhanced greenhouse warming on early Earth. Nature Geoscience, 2(12), 891-896.https://doi.org/10.1038/ngeo692

Goldstein, J., Newbury, D.E., Echlin, P., Joy, D.C., Lyman, C.E., Lifshin, E., Sawyer, L., and Michael, J.R. (2003) Quantitative X-Ray Analysis: The Basics. In Scanning Electron Microscopy and X-ray Microanalysis pp. 391–451

Gonser, U., Wiedersich, H., & Grant, R. W. (1968). Mössbauer studies on the superparamagnetic behavior of magnesioferrite precipitates. Journal of Applied Physics, 39(2), 1004-1005. https://doi.org/10.1063/1.1656143

Goya, G. F., Berquo, T. S., Fonseca, F. C., & Morales, M. P. (2003). Static and dynamic magnetic properties of spherical magnetite nanoparticles. Journal of applied physics, 94(5), 3520-3528. https://doi.org/10.1063/1.1599959

Greenberg, E., Rozenberg, G.K., Xu, W., Arielly, R., Pasternak, M.P., Melchior, A., Garbarino, G., and Dubrovinsky, L.S. (2009) On the compressibility of ferrite spinels: A high-pressure X-ray diffraction study of MFe2O4 (M=Mg, Co, Zn). High Pressure Research, 29, 764–779. https://doi.org/10.1080/08957950903424424

Greenwood, N. N., & Howe, A. T. (1972). Mössbauer studies of Fe 1–x O. Part I. The defect structure of quenched samples. Journal of the Chemical Society, Dalton Transactions, (1), 110-116. DOI: 10.1039/DT9720000110

Gress, M. U., Koornneef, J. M., Thomassot, E., Chinn, I. L., van Zuilen, K., & Davies, G. R. (2021). Sm-Nd isochron ages coupled with CN isotope data of eclogitic diamonds from Jwaneng, Botswana. Geochimica et Cosmochimica Acta, 293, 1-17.

Grewal, D. S., Dasgupta, R., & Farnell, A. (2020). The speciation of carbon, nitrogen, and water in magma oceans and its effect on volatile partitioning between major reservoirs of the Solar System rocky bodies. Geochimica et Cosmochimica Acta, 280, 281-301. https://doi.org/10.1016/j.gca.2020.04.023

Grewal, D. S., Dasgupta, R., Sun, C., Tsuno, K., & Costin, G. (2019). Delivery of carbon, nitrogen, and sulfur to the silicate Earth by a giant impact. Science Advances, 5(1), eaau3669. DOI: 10.1126/sciadv.aau3669

Gurney, J. J., Helmstaedt, H. H., Richardson, S. H., & Shirey, S. B. (2010). Diamonds through time. Economic Geology, 105(3), 689-712. https://doi.org/10.2113/gsecongeo.105.3.689

Gurney, J.J., (1989). Diamonds. In: Ross, J., et al. (Eds.), Kimberlites and Related Rocks. Spec. Publ.-Geol. Soc. Aust., vol. 14. Blackwell, Carlton, pp. 935–965.

Gütlich, P., Link, R., Trautwein, A. X. (1978). Mössbauer Spectroscopy and Transition Metal Chemistry–Inorganic Chemistry.

Haas, J. L., & Hemingway, B. S. (1992). Recommended standard electrochemical potentials and fugacities of oxygen for the solid buffers and thermodynamic data in the systems iron-silicon-oxygen, nickel-oxygen, and copper-oxygen. US Geological Survey. https://doi.org/10.3133/ofr92267

Haavik, C., Stølen, S., Fjellvåg, H., Hanfland, M., and Häusermann, D. (2000) Equation of state of magnetite and its high-pressure modification: Thermodynamics of the Fe-O system at high pressure. American Mineralogist, 85, 514–523. https://doi.org/10.2138/am-2000-0413

"Hadraoui, K., Cottin, H., Ivanovski, S. L., Zapf, P., Altwegg, K., Benilan, Y., ... & Zakharov, V. (2019). Distributed glycine in comet 67P/Churyumov-Gerasimenko. Astronomy & Astrophysics, 630, A32. https://doi.org/10.1051/0004-6361/201935018"

"Haendel, D., Mühle, K., Nitzsche, H. M., Stiehl, G., & Wand, U. (1986). Isotopic variations of the fixed nitrogen in metamorphic rocks. Geochimica et cosmochimica Acta, 50(5), 749-758.

10.1016/0016-7037(86)90351-0"

Haggerty, S. E. (1995). Upper mantle mineralogy stephen. J. Geodynamics, 3707(4), 331–364. https://doi.org/10.1016/0264-3707(95)00016-3

Hah, H. Y., Gray, S., Johnson, C. E., Johnson, J. A., Kolesnichenko, V., Kucheryavy, P., & Goloverda, G. (2021). Mössbauer spectroscopy of superparamagnetic Fe3O4 nanoparticles. Journal of Magnetism and Magnetic Materials, 539, 168382. https://doi.org/10.1016/j.jmmm.2021.168382

Halama, R., & Bebout, G. (2021). Earth's nitrogen and carbon cycles. Space Science Reviews, 217(3), 45.

Halama, R., Bebout, G. E., & Bea, F. (2021). Nitrogen loss and isotopic fractionation during granulite-facies metamorphism in the lower crust (Ivrea Zone, NW Italy). Chemical Geology, 584, 120475.https://doi.org/10.1016/j.chemgeo.2021.120475

Halama, R., Bebout, G. E., John, T., & Scambelluri, M. (2014). Nitrogen recycling in subducted mantle rocks and implications for the global nitrogen cycle. International Journal of Earth Sciences, 103(7), 2081-2099.

Halama, R., Bebout, G. E., John, T., & Scambelluri, M. (2014). Nitrogen recycling in subducted mantle rocks and implications for the global nitrogen cycle. International Journal of Earth Sciences, 103, 2081-2099.https://doi.org/10.1007/s00531-012-0782-3

Halama, R., Bebout, G. E., John, T., & Schenk, V. (2010). Nitrogen recycling in subducted oceanic lithosphere: the record in high-and ultrahigh-pressure metabasaltic rocks. Geochimica et Cosmochimica Acta, 74(5), 1636-1652.https://doi.org/10.1016/j.gca.2009.12.003

Hamada, M., Kamada, S., Ohtani, E., Sakamaki, T., Mitsui, T., Masuda, R., Hirao, N., Ohishi, Y. and Akasaka, M., 2021. Synchrotron Mössbauer spectroscopic and x-ray diffraction study of ferropericlase in the high-pressure range of the lower mantle region. Physical Review B, 103(17), 174108. DOI:https://doi.org/10.1103/PhysRevB.103.174108

Hansen, K. W., & Cutler, I. B. (1966). Electrical conductivity in Fe1-xO-MgO solid solutions. Journal of the American Ceramic Society, 49(2), 100-102. https://doi.org/10.1111/j.1151-2916.1966.tb13217.x

Harlov, D. E., Andrut, M., & Pöter, B. (2001). Characterisation of buddingtonite (NH4)[AlSi3O8] and ND4-buddingtonite (ND4)[AlSi3O8] using IR spectroscopy and Rietveld refinement of XRD spectra. Physics and Chemistry of Minerals, 28(3), 188-198.

Harris, J. W. (1992). Diamond geology. The properties of natural and synthetic diamond.

Harris, J., Hutchison, M. T., Hursthouse, M., Light, M., & Harte, B. (1997). A new tetragonal silicate mineral occurring as inclusions in lower-mantle diamonds. Nature, 387(6632), 486-488.https://doi.org/10.1038/387486a0

Harrison, H.R., and Aragon, R. (1978) Skull melter growth of magnetite (Fe3O4). Materials Research Bulletin., 13, 1097–1104. https://doi.org/10.1016/0025-5408(78)90195-2

Harte, B. (2010). Diamond formation in the deep mantle: the record of mineral inclusions and their distribution in relation to mantle dehydration zones. Mineralogical Magazine, 74(2), 189-215. DOI: 10.1180/minmag.2010.074.2.189

Harte, B., & Harris, J. W. (1994). Lower mantle mineral associations preserved in diamonds. Mineralogical Magazine, 58(1), 384-385 .DOI:10.1180/minmag.1994.58A.1.201

Harte, B., & Hudson, N. F. (2013). Mineral associations in diamonds from the lowermost upper mantle and uppermost lower mantle. In Proceedings of 10th International Kimberlite Conference: Volume One (pp. 235-253). Springer India. DOI: 10.1007/978-81-322-1170-9_15

Harte, B., & Richardson, S. (2012). Mineral inclusions in diamonds track the evolution of a Mesozoic subducted slab beneath West Gondwanaland. Gondwana Research, 21(1), 236-245. https://doi.org/10.1016/j.gr.2011.07.001

Harte, B., Harris, J.W., Hutchison, M.T., Watt, G.R., & Wilding, M.C. (1999) Lower mantle mineral associations in diamonds from São Luiz, Brazil. (E. Fei et al., Ed.) Mantle petrology: field observations and high pressure experimentation, a tribute to Francis R. (Joe) Boyd, 125–153. https://doi.org/10.1007/978-81-322-1170-9_15

Hartridge, A., Bhattacharya, A. K., Sengupta, M., Majumdar, C. K., Das, D., & Chintalapudi, S. N. (1997). Crystallite size dependence on the magnetic properties of nanocrystalline magnetite powders. Journal of magnetism and magnetic materials, 176(2-3), L89-L92. https://doi.org/10.1016/S0304-8853(97)01004-4

Hashizume, K., & Sugiura, N. (1990). Precise measurement of nitrogen isotopic composition using a quadrupole mass spectrometer. Journal of the Mass Spectrometry Society of Japan, 38(6), 269-286. https://doi.org/10.5702/massspec.38.269

Hauri, E. H., Wang, J., Pearson, D. G., & Bulanova, G. P. (2002). Microanalysis of δ13C, δ15N, and N abundances in diamonds by secondary ion mass spectrometry. Chemical Geology, 185(1-2), 149-163.doi:10.1016/s0009-2541(01)00400-4

Hayman, P. C., Kopylova, M. G., & Kaminsky, F. V. (2005). Lower mantle diamonds from Rio Soriso (Juina area, Mato Grosso, Brazil). Contributions to Mineralogy and Petrology, 149, 430-445. https://doi.org/10.1007/s00410-005-0657-8

Hazen, R. M. (1981). Systematic variation of bulk modulus of wüstite with stoichiometry. Carnegie Inst Wash Yearb, 80(27), 280.

Hazen, R. M., & Jeanloz, R. (1984). Wüstite (Fe1-x O): A review of its defect structure and physical properties. Reviews of Geophysics, 22(1), 37-46. https://doi.org/10.1029/RG022i001p00037

Hentschel, B. (1970). Stoichiometric FeO as metastable intermediate of the decomposition of wustite at 225 C. Zeitschrift für Naturforschung A, 25(12), 1996-1997. https://doi.org/10.1515/zna-1970-1241

Hernlund, J., Leinenweber, K., Locke, D., & Tyburczy, J. A. (2006). A numerical model for steady-state temperature distributions in solid-medium high-pressure cell assemblies. American Mineralogist, 91(2-3), 295-305.https://doi.org/10.2138/am.2006.1938

Hidayat, T., Shishin, D., Jak, E., and Decterov, S.A. (2015) Thermodynamic reevaluation of the Fe-O system. Calphad: Computer Coupling of Phase Diagrams and Thermochemistry, 48, 131–144.

Higashi, S. (1982). Tobelite, a new ammonium dioctahedral mica. Mineralogical Journal, 11(3), 138-146.https://doi.org/10.2465/minerj.11.138

Higo, Y., Inoue, T., Li, B., Irifune, T., and Liebermann, R.C. (2006) The effect of iron on the elastic properties of ringwoodite at high pressure. Physics of the Earth and Planetary Interiors, 159, 276–285. https://doi.org/10.1016/j.pepi.2006.08.004

Hikosaka, K., Sinmyo, R., Hirose, K., Ishii, T., & Ohishi, Y. (2019). The stability of Fe5O6 and Fe4O5 at high pressure and temperature. American Mineralogist, 104(9), 1356-1359. https://doi.org/10.2138/am-2019-7097

Hilbrandt, N., & Martin, M. (1998). High temperature point defect equilibria in iron-doped MgO: An in situ Fe-K XAFS study on the valence and site distribution of iron in (Mg1-xFex) O. Berichte der Bunsengesellschaft für physikalische Chemie, 102(12), 1747-1759. https://doi.org/10.1002/bbpc.19981021204

Hill, R.J., Craig, J.R., and Gibbs, G. V. (1979) Systematics of the Spinel Structure Type. Physics and Chemistry of Minerals, 4, 317–339. https://doi.org/10.1007/BF00307535

Hilton, D. R.; Fischer, T. P.; Marty, B. (2002). Noble Gases and Volatile Recycling at Subduction Zones. Reviews in Mineralogy and Geochemistry, 47(1), 319–370. doi:10.2138/rmg.2002.47.9

Hirose, K. (2002). Phase transitions in pyrolitic mantle around 670-km depth: Implications for upwelling of plumes from the lower mantle. Journal of Geophysical Research: Solid Earth, 107(B4), ECV-3. https://doi.org/10.1029/2001JB000597

Hirschmann, M. M. (2018). Comparative deep Earth volatile cycles: The case for C recycling from exosphere/mantle fractionation of major (H2O, C, N) volatiles and from H2O/Ce, CO2/Ba, and CO2/Nb exosphere ratios. Earth and Planetary Science Letters, 502, 262-273.https://doi.org/10.1016/j.epsl.2018.08.023

Hofer, F., Schmidt, F. P., Grogger, W., Kothleitner, G. (2016). Fundamentals of electron energy-loss spectroscopy. IOP Conference Series: Materials Science and Engineering, 109(1). https://doi.org/10.1088/1757-899X/109/1/012007

Hogberg, K., Stachel, T., & Stern, R. A. (2016). Carbon and nitrogen isotope systematics in diamond: different sensitivities to isotopic fractionation or a decoupled origin?. Lithos, 265, 16-30.https://doi.org/10.1016/j.lithos.2016.06.020

Holland, T. J. B., & Powell, R. (2011). An improved and extended internally consistent thermodynamic dataset for phases of petrological interest, involving a new equation of state for solids. Journal of metamorphic Geology, 29(3), 333-383. https://doi.org/10.1111/j.1525-1314.2010.00923.x

Holland, T. J., Hudson, N. F., Powell, R., & Harte, B. (2013). New thermodynamic models and calculated phase equilibria in NCFMAS for basic and ultrabasic compositions through the transition zone into the uppermost lower mantle. Journal of Petrology, 54(9), 1901-1920. https://doi.org/10.1093/petrology/egt035

Holloway, J. M., & Dahlgren, R. A. (2002). Nitrogen in rock: occurrences and biogeochemical implications. Global biogeochemical cycles, 16(4), 65-1. https://doi.org/10.1029/2002GB001862

Holloway, J. M., & Dahlgren, R. A. (2002). Nitrogen in rock: occurrences and biogeochemical implications. Global biogeochemical cycles, 16(4), 65-1.https://doi.org/10.1029/2002GB001862

Honma, H., & Itihara, Y. (1981). Distribution of ammonium in minerals of metamorphic and granitic rocks. Geochimica et Cosmochimica Acta, 45(6), 983-988.

Huang, E., & Bassett, W. A. (1986). Rapid determination of Fe3O4 phase diagram by synchrotron radiation. Journal of Geophysical Research: Solid Earth, 91(B5), 4697-4703. https://doi.org/10.1029/JB091iB05p04697

Huang, F., & Sverjensky, D. A. (2019). Extended Deep Earth Water Model for predicting major element mantle metasomatism. Geochimica et Cosmochimica Acta, 254, 192-230. https://doi.org/10.1016/j.gca.2019.03.027

Huang, F., & Sverjensky, D. A. (2019). Extended Deep Earth Water Model for predicting major element mantle metasomatism. Geochimica et Cosmochimica Acta, 254, 192-230.https://doi.org/10.1016/j.gca.2019.03.027

Hübschle, C.B., Sheldrick, G.M., and Dittrich, B. (2011) ShelXle : a Qt graphical user interface for SHELXL. Journal of Applied Crystallography, 44, 1281–1284. https://doi.org/10.1107/S0021889811043202

Hughes, E. C., Buse, B., Kearns, S. L., Blundy, J. D., Kilgour, G., & Mader, H. M. (2019). Low analytical totals in EPMA of hydrous silicate glass due to sub-surface charging: Obtaining accurate volatiles by difference. Chemical Geology, 505, 48-56.

Hutchison, M. T., Cartigny, P., & Harris, J. W. (1998, April). Carbon and nitrogen compositions and cathodoluminescence characteristics of transition zone and lower mantle diamonds from Sao Luiz, Brazil. In International Kimberlite Conference: Extended Abstracts (Vol. 7, pp. 336-338). DOI:https://doi.org/10.29173/ikc2727

Ibers, J.A., and Hamilton, W.C. (1974) International Tables for X-ray Crystallography: Revised and Supplementary Tables to Volumes 2 and 3. (J.A. Ibers & W.C. Hamilton, Eds.). Kynoch Press.

Irifune, T., Shinmei, T., McCammon, C. A., Miyajima, N., Rubie, D. C., & Frost, D. J. (2010). Iron partitioning and density changes of pyrolite in Earth's lower mantle. Science, 327(5962), 193-195. 10.1126/science.1181443

Ishida, A., Hashizume, K., & Kakegawa, T. (2012). Stepwise combustion analyses of distinct nitrogen isotopic compositions on Paleoproterozoic organic matter. Geochemical Journal, 46(3), 249-253.DOI: 10.2343/geochemj.1.0165

Ishida, A., Kitajima, K., Hashizume, K., Spicuzza, M.J., Zaitsev, A., Schulze, D.J. and Valley, J.W. (2023), Microscale Simultaneous Measurement of Carbon and Nitrogen Isotopes on Natural Diamond. Geostand Geoanal Res. Accepted Author Manuscript. https://doi.org/10.1111/ggr.12485

Ishida, A., Kitajima, K., Williford, K. H., Tuite, M. L., Kakegawa, T., & Valley, J. W. (2018). Simultaneous in situ analysis of carbon and nitrogen isotope ratios in organic matter by secondary ion mass spectrometry. Geostandards and Geoanalytical Research, 42(2), 189-203. https://doi.org/10.1111/ggr.12209

Ishii, T., Uenver-Thiele, L., Woodland, A. B., Alig, E., & Boffa Ballaran, T. (2018). Synthesis and crystal structure of Mg-bearing Fe9O11: New insight in the complexity of Fe-Mg oxides at conditions of the deep upper mantle. American Mineralogist: Journal of Earth and Planetary Materials, 103(11), 1873-1876. https://doi.org/10.2138/am-2018-6646

Ita, J., & Stixrude, L. (1992). Petrology, elasticity, and composition of the mantle transition zone. Journal of Geophysical Research: Solid Earth, 97(B5), 6849-6866. https://doi.org/10.1029/92JB00068

Jackson, C. R., Cottrell, E., & Andrews, B. (2021). Warm and oxidizing slabs limit ingassing efficiency of nitrogen to the mantle. Earth and Planetary Science Letters, 553, 116615. https://doi.org/10.1016/j.epsl.2020.116615

Jackson, I., Liebermann, R. C., & Ringwood, A. E. (1978). The elastic properties of (Mg x Fe 1− x) O solid solutions. Physics and Chemistry of Minerals, 3, 11-31. https://doi.org/10.1007/BF00357444

Jacobsen, S. D., Holl, C. M., Adams, K. A., Fischer, R. A., Martin, E. S., Bina, C. R., ... & Dera, P. (2008). Compression of single-crystal magnesium oxide to 118 GPa and a ruby pressure gauge for helium pressure media. American mineralogist, 93(11-12), 1823-1828.doi: 10.2138/am.2008.2988

Jacobsen, S. D., Reichmann, H. J., Spetzler, H. A., Mackwell, S. J., Smyth, J. R., Angel, R. J., & McCammon, C. A. (2002). Structure and elasticity of single-crystal (Mg, Fe) O and a new method of generating shear waves for gigahertz ultrasonic interferometry. Journal of Geophysical Research: Solid Earth, 107(B2), ECV-4. https://doi.org/10.1029/2001JB000490

Jamieson, H. E., & Roeder, P. L. (1984). The distribution of Mg and Fe2+ between olivine and spinel at 1300 C. American Mineralogist, 69(3-4), 283-291.

Jamieson, J. C. (1982). Pressure measurement at high temperature in X-ray diffraction studies: gold as a primary standard. High-pressure research in Geophysics, 27-48.

Janowski, J., Nowotny, J., & Rekas, M. (1989). Non-Stoichiometry and Defect Structure of FeO. Non-Stoichiometric Compounds: Surfaces, Grain Boundaries and Structural Defects, 115-121. DOI: 10.1007/978-94-009-0943-4_8

Javoy, M. (1997). The major volatile elements of the Earth: Their origin, behavior, and fate. Geophysical Research Letters, 24(2), 177-180. https://doi.org/10.1029/96GL03931

Javoy, M., Pineau, F., & Delorme, H. (1986). Carbon and nitrogen isotopes in the mantle. Chemical geology, 57(1-2), 41-62.https://doi.org/10.1016/0009-2541(86)90093-8

Javoy, M., Pineau, F., & Demaiffe, D. (1984). Nitrogen and carbon isotopic composition in the diamonds of Mbuji Mayi (Zaire). Earth and Planetary Science Letters, 68(3), 399-412.https://doi.org/10.1016/0012-821X(84)90125-0

Johnson, B., & Goldblatt, C. (2015). The nitrogen budget of Earth. Earth-Science Reviews, 148, 150-173.https://doi.org/10.1016/j.earscirev.2015.05.006

Jung, I. H., Decterov, S. A., & Pelton, A. D. (2004). Critical thermodynamic evaluation and optimization of the Fe–Mg–O system. Journal of Physics and Chemistry of Solids, 65(10), 1683-1695. https://doi.org/10.1016/j.jpcs.2004.04.005

Kaiser, W., & Bond, W. L. (1959). Nitrogen, a major impurity in common type I diamond. Physical Review, 115(4), 857.https://doi.org/10.1103/PhysRev.115.857

Kalska-Szostko, B., Zubowska, M., & Satuła, D. (2006). Studies of the magnetite nanoparticles by means of Mössbauer spectroscopy. Acta Physica Polonica A, 109(3), 365-369.

Kaminsky, F. (2012). Mineralogy of the lower mantle: A review of 'super-deep'mineral inclusions in diamond. Earth-Science Reviews, 110(1-4), 127-147. https://doi.org/10.1016/j.earscirev.2011.10.005

Kaminsky, F. V. (2017). The Earth's lower mantle. Composition and Structure. Cham: Springer Geology. DOI 10.1007/978-3-319-55684-0

Kaminsky, F. V. (2020). Basic problems concerning the composition of the Earth's lower mantle. Lithos, 364, 105515. https://doi.org/10.1016/j.lithos.2020.105515

Kaminsky, F. V., & Khachatryan, G. K. (2004). The relationship between the distribution of nitrogen impurity centres in diamond crystals and their internal structure and mechanism of growth. Lithos, 77(1-4), 255-271. https://doi.org/10.1016/j.lithos.2004.04.035

Kaminsky, F. V., Khachatryan, G. K., Andreazza, P., Araujo, D., & Griffin, W. L. (2009a). Super-deep diamonds from kimberlites in the Juina area, Mato Grosso State, Brazil. Lithos, 112, 833-842. https://doi.org/10.1016/j.lithos.2009.03.036

Kaminsky, F. V., Ryabchikov, I. D., McCammon, C. A., Longo, M., Abakumov, A. M., Turner, S., & Heidari, H. (2015). Oxidation potential in the Earth's lower mantle as recorded by

ferropericlase inclusions in diamond. Earth and Planetary Science Letters, 417, 49-56. 10.1016/j.epsl.2015.02.029

Kaminsky, F. V., Wirth, R., & Schreiber, A. (2013). Carbonatitic inclusions in deep mantle diamond from Juina, Brazil: new minerals in the carbonate-halide association. The Canadian Mineralogist, 51(5), 669-688. 10.3749/canmin.51.5.669

Kaminsky, F. V., Wirth, R., Schreiber, A. (2015b). A microinclusion of lower-mantle rock and other minerals and nitrogen lower-mantle inclusions in a diamond. Canadian Mineralogist, 53(1), 83–104. https://doi.org/10.3749/canmin.1400070

Kaminsky, F., Wirth, R., Matsyuk, S., Schreiber, A., Thomas, R. (2009b): Nyerereite and nahcolite inclusions in diamond: evidence for lower-mantle carbonatitic magmas. - Mineralogical Magazine, 73, 5, 797-816 DOI: 10.1180/minmag.2009.073.5.797

Kaminsky, F., Zakharchenko, O., Davies, R., Griffin, W., Khachatryan-Blinova, G., & Shiryaev, A. (2001). Superdeep diamonds from the Juina area, Mato Grosso state, Brazil. Contributions to Mineralogy and Petrology, 140, 734-753. https://doi.org/10.1007/s004100000221

Kantor, I., Prakapenka, V., Kantor, A., Dera, P., Kurnosov, A., Sinogeikin, S., and others (2012) BX90: A new diamond anvil cell design for X-ray diffraction and optical measurements. Review of scientific Instruments, 83, 125102. https://doi.org/10.1063/1.4768541

Kantor, I., Prakapenka, V., Kantor, A., Dera, P., Kurnosov, A., Sinogeikin, S., and others (2012) BX90: A new diamond anvil cell design for X-ray diffraction and optical measurements. Review of scientific Instruments, 83, 125102. https://doi.org/10.1063/1.4768541

Katsura, T. (2022). A revised adiabatic temperature profile for the mantle. Journal of Geophysical Research: Solid Earth, 127(2) https://doi.org/10.1029/2021JB023562

Katsura, T., & Kimura, S. (1965). Equilibria in the system FeO–Fe2O3–MgO at 1160° C. Bulletin of the Chemical Society of Japan, 38(10), 1664-1670.

Kelley, K. A., & Cottrell, E. (2009). Water and the oxidation state of subduction zone magmas. Science, 325(5940), 605-607. https://doi.org/10.1126/science.1174156

Kelly, J. F. (2000). Stable isotopes of carbon and nitrogen in the study of avian and mammalian trophic ecology. Canadian journal of zoology, 78(1), 1-27. https://doi.org/10.1139/z99-165

Kennett, B. L. N., & Engdahl, E. R. (1991). Traveltimes for global earthquake location and phase identification. Geophysical Journal International, 105, 429–465. https://doi.org/10.1111/j.1365-246X.1991.tb06724.x

Kennett, B. L. N., Engdahl, E. R., Buland, R. (1995). Constraints on seismic velocities in the Earth from traveltimes. Geophysical Journal International, 122(1), 108–124. https://doi.org/10.1111/j.1365-246X.1995.tb03540.x

Keppler, H., & Frost, D. J. (2005). Introduction to minerals under extreme conditions. https://doi.org/10.1180/EMU-notes.7.1

Keppler, H., Cialdella, L., Couffignal, F., & Wiedenbeck, M. (2022). The solubility of N2 in silicate melts and nitrogen partitioning between upper mantle minerals and basalt. Contributions to Mineralogy and Petrology, 177(8), 1-15. https://doi.org/10.1007/s00410-022-01948-z

Kerrich, R., Jia, Y., Manikyamba, C., & Naqvi, S. M. (2006). Secular variations of N-isotopes in terrestrial reservoirs and ore deposits. https://doi.org/10.1130/2006.1198(05)

Kessel, R., Beckett, J. R., & Stolper, E. M. (2001). Thermodynamic properties of the Pt-Fe system. American Mineralogist, 86(9), 1003-1014. 10.2138/am-2001-8-907

Kesson, S. E., & Gerald, J. F. (1992). Partitioning of MgO, FeO, NiO, MnO and Cr2O3 between magnesian silicate perovskite and magnesiowüstite: implications for the origin of inclusions in diamond and the composition of the lower mantle. Earth and Planetary Science Letters, 111(2-4), 229-240. https://doi.org/10.1016/0012-821X(92)90181-T

Kesson, S. E., Fitz Gerald, J. D., & Shelley, J. M. (1998). Mineralogy and dynamics of a pyrolite lower mantle. Nature, 393(6682), 252-255. 10.1038/30466

Khandarkhaeva, S., Fedotenko, T., Chariton, S., Bykova, E., Ovsyannikov, S.V., Glazyrin, K., Liermann, H.P., Prakapenka, V., Dubrovinskaia, N. & Dubrovinsky, L. (2021). Structural Diversity of Magnetite and Products of Its Decomposition at Extreme Conditions. Inorganic Chemistry, 61(2), 1091-1101. https://doi.org/10.1021/acs.inorgchem.1c03258

King, H.E.J., and Finger, L.W. (1979) Diffracted Beam Crystal Centering and Its Application to High-Pressure Crystallography. Journal of Applied Crystallography, 12, 374–378. https://doi.org/10.1107/S0021889879012723

Kiseeva, E.S., Korolev, N., Koemets, I., Zedgenizov, D.A., Unitt, R., McCammon, C., Aslandukova, A., Khandarkhaeva, S., Fedotenko, T., Glazyrin, K. and Bessas, D., (2022). Subduction-related oxidation of the sublithospheric mantle evidenced by ferropericlase and magnesiowüstite diamond inclusions. Nature Communications, 13(1), p.7517. https://doi.org/10.1038/s41467-022-35110-x

Kiseeva, E.S., Vasiukov, D.M., Wood, B.J., McCammon, C., Stachel, T., Bykov, M., Bykova, E., Chumakov, A., Cerantola, V., Harris, J.W. and Dubrovinsky, L. (2018). Oxidized iron in garnets from the mantle transition zone. Nature Geoscience, 11(2), 144-147.https://doi.org/10.1038/s41561-017-0055-7

Koch, F., & Cohen, J. B. (1969). The defect structure of Fe1− xO. Acta Crystallographica Section B: Structural Crystallography and Crystal Chemistry, 25(2), 275-287. https://doi.org/10.1107/S0567740869002111

Koga, T., & Naraoka, H. (2017). A new family of extraterrestrial amino acids in the Murchison meteorite. Scientific reports, 7(1), 636. https://doi.org/10.1038/s41598-017-00693-9

Kurian, J., & Mathew, M. J. (2018). Structural, magnetic and mossbauer studies of magnesium ferrite nanoparticles prepared by hydrothermal method. International Journal of nanoscience, 17(01n02), 1760001. https://doi.org/10.1142/S0219581X17600018

Kurian, J., & Mathew, M. J. (2018). Structural, magnetic and mossbauer studies of magnesium ferrite nanoparticles prepared by hydrothermal method. International Journal of nanoscience, 17(01n02), 1760001.https://doi.org/10.1142/S0219581X17600018

Kurnosov, A., Kantor, I., Boffa-Ballaran, T., Lindhardt, S., Dubrovinsky, L.,Kusnestov, A., Zehnder, B.H. (2008) A novel gas-loading system for mechanically closing of various types of diamond anvil cells. Review of scientific Instruments, 79, 045110. https://doi.org/10.1063/1.2902506

Kurnosov, A., Marquardt, H., Frost, D. J., Ballaran, T. B., & Ziberna, L. (2017). Evidence for a Fe3+-rich pyrolitic lower mantle from (Al, Fe)-bearing bridgmanite elasticity data. Nature, 543(7646), 543-546. https://doi.org/10.1038/nature21390

Labidi, J., & Young, E. D. (2022). The origin and dynamics of nitrogen in the Earth's mantle constrained by 15N15N in hydrothermal gases. Chemical Geology, 120709. https://doi.org/10.1016/j.chemgeo.2022.120709

Labidi, J., Barry, P.H., Bekaert, D.V., Broadley, M.W., Marty, B., Giunta, T., Warr, O., Sherwood Lollar, B., Fischer, T.P., Avice, G. , Caracausi, A. & Young, E. D. (2020). Hydrothermal 15N15N abundances constrain the origins of mantle nitrogen. Nature, 580(7803), 367-371. https://doi.org/10.1038/s41586-020-2173-4

Lai, M. Y., Stachel, T., Stern, R. A., Hardman, M. F., Pearson, D. G., & Harris, J. W. (2022). Formation of mixed paragenesis diamonds during multistage growth–Constraints from in situ δ13C–δ15N–[N] analyses of Koidu diamonds. Geochimica et Cosmochimica Acta, 323, 20-39 DOI:10.1016/j.gca.2022.02.020

Lak, A., Kranken, M., Ludwig, F., Kornowski, A., Eberbeck, D., Sievers, S., Litterst, F.J., Weller, H., and Schilling, M. (2013) Size dependent structural and magnetic properties of FeO–Fe 3 O 4 nanoparticles. Nanoscale, 5(24), 12286-12295 https://doi.org/10.1039/C3NR04562E

Larson, A.C. and Von Dreele, R.B. (2004) General Structure Analysis System (GSAS), Los Alamos National Laboratory Report LAUR 86-748

Larson, C.A. & von Dreele, R. (2004) General structure analysis system (GSAS), 86–748 p.

Lauterbach, S., McCammon, C. A., Van Aken, P., Langenhorst, F., & Seifert, F. (2000). Mössbauer and ELNES spectroscopy of (Mg, Fe)(Si, Al) O 3 perovskite: A highly oxidised component of the lower mantle. Contributions to Mineralogy and Petrology, 138, 17-26. https://doi.org/10.1007/PL00007658

Lavina, B., and Meng, Y. (2015) Unraveling the complexity of iron oxides at high pressure and temperature: Synthesis of Fe5O6. Science Advances, 1, 2–7. https://doi.org/10.1126/sciadv.1400260

Lavina, B., and Meng, Y. (2015) Unraveling the complexity of iron oxides at high pressure and temperature: Synthesis of Fe5O6. Science Advances, 1, 2–7. https://doi.org/10.1126/sciadv.1400260

Lavina, B., Dera, P., Kim, E., Meng, Y., Downs, R.T., Weck, P.F., Sutton, S.R. & Zhao, Y. (2011). Discovery of the recoverable high-pressure iron oxide Fe4O5. Proceedings of the National Academy of Sciences, 108(42), 17281-17285. 10.1073/pnas.1107573108

Lavina, B., Salviulo, G., and Della Giusta, A. (2002) Cation distribution and structure modelling of spinel solid solutions. Physics and Chemistry of Minerals, 29, 10–18. https://doi.org/10.1007/s002690100198

Lazor, P., Shebanova, O.N., and Annersten, H. (2004) High-pressure study of stability of magnetite by thermodynamic analysis and synchrotron X-ray diffraction. Journal of Geophysical Research: Solid Earth, 109, B05201. https://doi.org/10.1029/2003JB002600

Lebreton, C., & Hobbs, L. W. (1983). Defect structure of Fe1-xO. Radiation Effects, 74(1-4), 227-236. https://doi.org/10.1080/00337578308218416

Levin, R. L., & Wagner Jr, J. B. (1964). Lattice parameter measurements of undoped and chromium-doped wuestite (No. TID-20343). Northwestern Univ., Evanston, Ill. Technological Inst.

Levy, D., Diella, V., Dapiaggi, M., Sani, A., Gemmi, M., and Pavese, A. (2004) Equation of state, structural behaviour and phase diagram of synthetic MgFe2O4, as a function of pressure and temperature. Physics and Chemistry of Minerals, 31, 122–129. https://doi.org/10.1007/s00269-004-0380-4

Li, J., & Agee, C. B. (1996). Geochemistry of mantle–core differentiation at high pressure. Nature, 381(6584), 686-689. https://doi.org/10.1038/381686a0"

Li, K., Li, G. Y., Du, Y. F., Han, W., Zhang, J., Chen, L. H., ... & Li, L. (2021). Intraslab remobilization of nitrogen during early subduction facilitates deep nitrogen recycling: Insights from the blueschists in the Heilongjiang Complex in NE China. Chemical Geology, 583, 120474. https://doi.org/10.1016/j.chemgeo.2021.120474

Li, L., & Bebout, G. E. (2005). Carbon and nitrogen geochemistry of sediments in the Central American convergent margin: Insights regarding subduction input fluxes, diagenesis, and paleoproductivity. Journal of Geophysical Research: Solid Earth, 110(B11). https://doi.org/10.1029/2004JB003276

Li, L., Bebout, G. E., & Idleman, B. D. (2007). Nitrogen concentration and δ15N of altered oceanic crust obtained on ODP Legs 129 and 185: Insights into alteration-related nitrogen enrichment and the nitrogen subduction budget. Geochimica et Cosmochimica Acta, 71(9), 2344-2360.https://doi.org/10.1016/j.gca.2007.02.001

Li, Y., & Keppler, H. (2014). Nitrogen speciation in mantle and crustal fluids. Geochimica et Cosmochimica Acta, 129, 13-32.https://doi.org/10.1016/j.gca.2013.12.031

Li, Y., Huang, R., Wiedenbeck, M., & Keppler, H. (2015). Nitrogen distribution between aqueous fluids and silicate melts. Earth and Planetary Science Letters, 411, 218-228. https://doi.org/10.1016/j.epsl.2014.11.050

Li, Y., Wiedenbeck, M., Shcheka, S., & Keppler, H. (2013). Nitrogen solubility in upper mantle minerals. Earth and Planetary Science Letters, 377, 311-323. https://doi.org/10.1016/j.epsl.2013.07.013

Liot, F., & Hooley, C. A. (2012). Numerical Simulations of the Invar Effect in Fe-Ni, Fe-Pt, and Fe-Pd Ferromagnets. arXiv preprint arXiv:1208.2850. https://doi.org/10.48550/arXiv.1208.2850

Litvin, Y. A., Butvina, V. G., Bobrov, A. V., & Zharikov, V. A. (2002). The first synthesis of diamond in sulfide-carbon systems: the role of sulfides in diamond genesis. In Doklady earth sciences (Vol. 382, No. 1, pp. 40-43). Pleiades Publishing, Ltd.(Плеадес Паблишинг, Лтд).

Long, G. J., Cranshaw, T. E., & Longworth, G. (1983). The ideal Mössbauer effect absorber thickness. Mössbauer effect reference and data journal, 6(2), 42-49.

Longo, M., McCammon, C. A., & Jacobsen, S. D. (2011). Microanalysis of the iron oxidation state in (Mg, Fe) O and application to the study of microscale processes. Contributions to Mineralogy and Petrology, 162, 1249-1257. https://doi.org/10.1007/s00410-011-0649-9

Lu, F. H., Newhouse, M. L., & Dieckmann, R. (1995). Oxygen activity dependent dissolution of nickel from nickel oxide into platinum. Journal of Physics and Chemistry of Solids, 56(5), 715-724. https://doi.org/10.1016/0022-3697(95)80021-2

Luth, R. W. (1993). Diamonds, eclogites, and the oxidation state of the Earth's mantle. Science, 261(5117), 66-68. 10.1126/science. https://doi.org/261.5117.66

Luth, R. W., & Stachel, T. (2014). The buffering capacity of lithospheric mantle: implications for diamond formation. Contributions to Mineralogy and Petrology, 168, 1-12. https://doi.org/10.1007/s00410-014-1083-6

Mackwell, S., Bystricky, M., & Sproni, C. (2005). Fe–Mg interdiffusion in (Mg, Fe) O. Physics and chemistry of minerals, 32, 418-425. 10.1007/S00269-005-0013-6

Malaspina, N., Scambelluri, M., Poli, S., Van Roermund, H. L. M., & Langenhorst, F. (2010). The oxidation state of mantle wedge majoritic garnet websterites metasomatised by C-bearing subduction fluids. Earth and Planetary Science Letters, 298(3-4), 417-426. https://doi.org/10.1016/j.epsl.2010.08.022

Mallik, A., Li, Y., & Wiedenbeck, M. (2018). Nitrogen evolution within the Earth's atmosphere–mantle system assessed by recycling in subduction zones. Earth and Planetary Science Letters, 482, 556-566. https://doi.org/10.1016/j.epsl.2017.11.045

Mao, H.-K., Takahashi, T., Bassett, W.A., Kinsland, G.L., and Merrill, L. (1974) Isothermal compression of magnetite to 320 KB. Journal of Geophysical Research, 79, 1165–1170. https://doi.org/10.1029/JB079i008p01165

Marty, B. (2012). The origins and concentrations of water, carbon, nitrogen and noble gases on Earth. Earth and Planetary Science Letters, 313, 56-66. https://doi.org/10.1016/j.epsl.2011.10.040

Marty, B., & Dauphas, N. (2003). The nitrogen record of crust–mantle interaction and mantle convection from Archean to present. Earth and Planetary Science Letters, 206(3-4), 397-410.

Marty, B., & Dauphas, N. (2003). The nitrogen record of crust–mantle interaction and mantle convection from Archean to present. Earth and Planetary Science Letters, 206(3-4), 397-410. https://doi.org/10.1016/S0012-821X(02)01108-1

Matjuschkin, V., Woodland, A. B., Frost, D. J., & Yaxley, G. M. (2020). Reduced methane-bearing fluids as a source for diamond. Scientific Reports, 10(1), 6961. https://doi.org/10.1038/s41598-020-63518-2

Matsui, M., Ito, E., Yamazaki, D., Yoshino, T., Guo, X., Shan, S., Higo, Y. and Funakoshi, K.I. (2012). Static compression of (Mg0. 83, Fe0. 17) O and (Mg0. 75, Fe0. 25) O ferropericlase up to 58 GPa at 300, 700, and 1100 K. American Mineralogist, 97(1), 176-183.

Mc Dade, P., & Harris, J. W. (1998, April). Syngenetic inclusion bearing diamonds from Letseng-la-Terai, Lesotho. In International Kimberlite Conference: Extended Abstracts (Vol. 7, pp. 561-563).DOI: https://doi.org/10.29173/ikc2804

McCammon, C. (1993). Effect of pressure on the composition of the lower mantle end member FexO. Science, 259(5091), 66-68. https://doi.org/10.1126/science.259.5091.66

McCammon, C. (1995). Mössbauer spectroscopy of minerals. Mineral physics and crystallography: A handbook of physical constants, 2, 332.

McCammon, C. (1995). Mössbauer spectroscopy of minerals. Mineral physics and crystallography: A handbook of physical constants, 2, 332.

McCammon, C. (2005b). The paradox of mantle redox. Science, 308(5723), 807-808. DOI:10.1126/science.1110532

McCammon, C. (2021). Mössbauer Spectroscopy with High Spatial Resolution: Spotlight on Geoscience. Modern Mössbauer Spectroscopy: New Challenges Based on Cutting-Edge Techniques, 221-266. 10.1007/978-981-15-9422-9_5

McCammon, C. A, Hutchison, M., Harris, J. (1997b). Ferric iron content of mineral inclusions in diamonds from São Luiz: A view into the lower mantle. Science, 278(5337), 434–436. https://doi.org/10.1126/science.278.5337.434

McCammon, C. A. (1997a). Perovskite as a possible sink for ferric iron in the lower mantle. Nature, 387(6634), 694–696. https://doi.org/10.1038/42685

McCammon, C. A. (2000). Insights into phase transformations from Mössbauer spectroscopy. Reviews in Mineralogy and Geochemistry, 39(1), 241-264. https://doi.org/10.2138/rmg.2000.39.09

McCammon, C. A. (2001). Geophysics: Deep diamond mysteries. Science, 293(5531), 813–814. https://doi.org/10.1126/science.1063295

McCammon, C. A. (2005a). Mantle oxidation state and oxygen fugacity: Constraints on mantle chemistry, structure, and dynamics. Washington DC American Geophysical Union Geophysical Monograph Series, 160, 219-240. 10.1029/160GM14

McCammon, C. A., & Liu, L. G. (1984). The effects of pressure and temperature on nonstoichiometric wüstite, Fe x O: The iron-rich phase boundary. Physics and Chemistry of Minerals, 10, 106-113. https://doi.org/10.1007/BF00309644

McCammon, C. A., Beran, A., & Libowitzky, E. (2004). Mössbauer spectroscopy: applications. Spectroscopic methods in mineralogy, 6, 369-398.

McCammon, C. A., Stachel, T., & Harris, J. W. (2004b). Iron oxidation state in lower mantle mineral assemblages: II. Inclusions in diamonds from Kankan, Guinea. Earth and Planetary Science Letters, 222(2), 423-434.

McCammon, C. A., Stachel, T., Harris, J. W. (2004a). Iron oxidation state in lower mantle mineral assemblages. I. Empirical relations derived from high-pressure experiments. Earth and Planetary Science Letters, 222(2), 423–434. https://doi.org/10.1016/j.epsl.2004.03.019

McCammon, C., Peyronneau, J., & Poirier, J. P. (1998). Low ferric iron content of (Mg, Fe) O at high pressures and temperatures. Geophysical Research Letters, 25(10), 1589-1592. https://doi.org/10.1029/98GL01178

Mikhail, S., & Howell, D. (2016). Outlooks in Earth and Planetary Materials: Chemistry and Mineralogy of Earth's Mantle: A petrological assessment of diamond as a recorder of the mantle nitrogen cycle. American Mineralogist, 101(4), 780-787.DOI: 10.2138/am-2016-5464

Mikhail, S., Dobosi, G., Verchovsky, A. B., Kurat, G., & Jones, A. P. (2013). Peridotitic and websteritic diamondites provide new information regarding mantle melting and metasomatism induced through the subduction of crustal volatiles. Geochimica et Cosmochimica Acta, 107, 1-11.https://doi.org/10.1016/j.gca.2012.12.036

Mikhail, S., Verchovsky, A.B., Howell, D., Hutchison, M.T., Southworth, R., Thomson, A.R., Warburton, P., Jones, A.P. & Milledge, H. J. (2014a). Constraining the internal variability of the stable isotopes of carbon and nitrogen within mantle diamonds. Chemical Geology, 366, 14-23. https://doi.org/10.1016/j.chemgeo.2013.12.014

Miletich, R., Allan, D. R., Kuhs, W. F. (2000). High-Pressure Single-Crystal Techniques. Reviews in Mineralogy and Geochemistry, 41(1), 445–519. https://doi.org/10.2138/rmg.2000.41.14

Mingram, B., & Bräuer, K. (2001). Ammonium concentration and nitrogen isotope composition in metasedimentary rocks from different tectonometamorphic units of the European Variscan Belt. Geochimica et Cosmochimica Acta, 65(2), 273-287. https://doi.org/10.1016/S0016-7037(00)00517-2

Miyajima, N., Holzapfel, C., Asahara, Y., Dubrovinsky, L., Frost, D. J., Rubie, D. C., Drechsler, M., Niwa, K., Ichihara, M. Yagi, T. (2010). Combining FIB milling and conventional Argon ion milling techniques to prepare high-quality site-specific TEM samples for quantitative EELS analysis of oxygen in molten iron. Journal of Microscopy, 238(3), 200–209. https://doi.org/10.1111/j.1365-2818.2009.03341.x

Mørup, S., Topsøe, H., & Lipka, J. (1976). Modified theory for Mössbauer spectra of superparamagnetic particles: application to Fe3O4. Le Journal de Physique Colloques, 37(C6), C6-287. https://doi.org/10.1051/jphyscol:1976658

Mosenfelder, J. L., Von Der Handt, A., Füri, E., Dalou, C., Hervig, R. L., Rossman, G. R., & Hirschmann, M. M. (2019). Nitrogen incorporation in silicates and metals: Results from SIMS, EPMA, FTIR, and laser-extraction mass spectrometry. American Mineralogist: Journal of Earth and Planetary Materials, 104(1), 31-46. https://doi.org/10.2138/am-2019-6533

Mosenfelder, J., Rossman, G. R., & Johnson, E. A. Measurement of hydrogen in igneous feldspars by FTIR and SIMS: progress towards a quantitative geohygrometer.

Mössbauer, R. L. (1958). Kernresonanzfluoreszenz von Gammastrahlung in Ir191. Zeitschrift Ffir Physik, 151, 124–143.

Mukhopadhyay, B., Basu, S., & Holdaway, M. J. (1993). A discussion of Margules-type formulations for multicomponent solutions with a generalized approach. Geochimica et Cosmochimica Acta, 57(2), 277-283. https://doi.org/10.1016/0016-7037(93)90430-5

Murnaghan, F. D. (1937). Finite deformations of an elastic solid. American Journal of Mathematics, 59(2), 235-260.https://doi.org/10.2307/2371405

Myhill, R., Ojwang, D.O., Ziberna, L., Frost, D.J., Ballaran, T.B., and Miyajima, N. (2016) On the P–T–fO2 stability of Fe4O5, Fe5O6 and Fe4O5-rich solid solutions. Contributions to Mineralogy and Petrology, 171, 51. https://doi.org/10.1007/s00410-016-1258-4

Mysen, B. (2019). Nitrogen in the Earth: abundance and transport. Progress in Earth and Planetary Science, 6(1), 1-15. https://doi.org/10.1186/s40645-019-0286-x

Mysen, B. O., & Fogel, M. L. (2010). Nitrogen and hydrogen isotope compositions and solubility in silicate melts in equilibrium with reduced (N+ H)-bearing fluids at high pressure and temperature: Effects of melt structure. American Mineralogist, 95(7), 987-999.https://doi.org/10.2138/am.2010.3364

Nachlas, W., Baldwin, S., Thomas, J., & Ackerson, M. (2020). Investigation of N in Ammonium-bearing Silicates with Electron Probe Microanalysis (EPMA). Microscopy and Microanalysis, 26(S2), 42-43. 10.1017/S1431927620013203

Nakagiri, N., Manghnani, M.H., Ming, L.C., and Kimura, S. (1986) Crystal structure of magnetite under pressure. Physics and Chemistry of Minerals, 13, 238–244. https://doi.org/10.1007/BF00308275

Nakatsuka, A., Ueno, H., Nakayama, N., Mizota, T., and Maekawa, H. (2004) Single-crystal X-ray diffraction study of cation distribution in MgAl2O4-MgFe2O4 spinel solid solution. Physics and Chemistry of Minerals, 31, 278–287. https://doi.org/10.1007/s00269-004-0385-z

Navon, O., & Gurney, J. (1999). Formation of diamonds in the Earth's mantle. In Proceedings of the 7th International Kimberlite Conference (Vol. 2, pp. 584-604). Red Roof Designs Cape Town, South Africa.

Navon, O., Hutcheon, I. D., Rossman, G. R., & Wasserburg, G. J. (1988). Mantle-derived fluids in diamond micro-inclusions. Nature, 335, 784-789. https://doi.org/10.1038/335784a0

Nell, J., & Wood, B. J. (1991). High-temperature electrical measurements and thermodynamic properties of Fe3O4-FeCr2O4-MgCr2O4-FeAl2O4 spinels. American Mineralogist, 76(3-4), 405-426.

Nestola, F. (2017). Inclusions in super-deep diamonds: windows on the very deep Earth. Rendiconti Lincei, 28, 595-604.DOI 10.1007/s12210-017-0607-1

Nestola, F., Boffa Ballaran, T., Balic-Zunic, T., Princivalle, F., Secco, L., and Dal Negro, A. (2007) Comparative compressibility and structural behavior of spinel MgAl2O4 at high pressures: The independency on the degree of cation order. American Mineralogist, 92, 1838–1843. https://doi.org/10.2138/am.2007.2573

Nestola, F., Burnham, A.D., Peruzzo, L., Tauro, L., Alvaro, M., Walter, M.J., Gunter, M., Anzolini, C. and Kohn, S.C., 2016b. Tetragonal Almandine-Pyrope Phase, TAPP: finally a name for it, the new mineral jeffbenite. Mineralogical Magazine, 80(7), pp.1219-1232. https://doi.org/10.1180/minmag.2016.080.059

Nestola, F., Cerantola, V., Milani, S., Anzolini, C., McCammon, C., Novella, D., Kupenko, I., Chumakov, A., Rueffer, R. and Harris, J.W. (2016). Synchrotron Mössbauer Source technique for in situ measurement of iron-bearing inclusions in natural diamonds. Lithos, 265, 328-333. https://doi.org/10.1016/j.lithos.2016.06.016

Nestola, F., Korolev, N., Kopylova, M., Rotiroti, N., Pearson, D.G., Pamato, M.G., Alvaro, M., Peruzzo, L., Gurney, J.J., Moore, A.E. and Davidson, J. (2018). CaSiO3 perovskite in diamond indicates the recycling of oceanic crust into the lower mantle. Nature, 555(7695), 237-241. https://doi.org/10.1038/nature25972

Nestola, F., Periotto, B., Andreozzi, G.B., Bruschini, E., and Bosi, F. (2014) Pressure-volume equation of state for chromite and magnesiochromite: A single-crystal X-ray diffraction investigation. American Mineralogist, 99, 1248–1253. https://doi.org/10.2138/am.2014.4765

Nestola, F., Periotto, B., Anzolini, C., Andreozzi, G.B., Woodland, A.B., Lenaz, D., Alvaro, M., and Princivalle, F. (2015) Equation of state of hercynite, FeAl2O4, and high-pressure systematics of Mg-Fe-Cr-Al spinels . Mineralogical Magazine, 79, 285–294. https://doi.org/10.1180/minmag.2015.079.2.07

Nimis, P. (2022). Pressure and temperature data for diamonds. Reviews in Mineralogy and Geochemistry, 88(1), 533-565.https://doi.org/10.2138/rmg.2022.88.10

Nimis, P., Nestola, F., Schiazza, M., Reali, R., Agrosì, G., Mele, D., Tempesta, G., Howell, D., Hutchison, M.T. and Spiess, R. (2019). Fe-rich ferropericlase and magnesiowüstite inclusions reflecting diamond formation rather than ambient mantle. Geology, 47(1), 27-30. https://doi.org/10.1130/G45235.1

Nowotny, J., & Rekas, M. (1989). Defect Structure and Thermodynamic Properties of the Wustite Phase (Fe1-yO). Journal of the American Ceramic Society, 72(7), 1221-1228. https://doi.org/10.1111/j.1151-2916.1989.tb09711.x

Núñez-Valdez, M., Bruschini, E., Speziale, S., Bosi, F., Fregola, R.A., D'Ippolito, V., and Andreozzi, G.B. (2018) Reexploring the cation ordering and magnetic cation substitution effects on the elastic anisotropy of aluminum spinels. Journal of Applied Physics, 124, 175901. https://doi.org/10.1063/1.5050064

O'Neill, H.S.C., and Wall, V.J. (1987) The olivine - orthopyroxene - spinel oxygen geobarometer, the nickel precipitation curve, and the oxygen fugacity of the earth's upper mantle. Journal of Petrology, 28, 1169–1191. https://doi.org/10.1093/petrology/28.6.1169

O'Neill, H.S.C., Annersten, H., and Virgo, D. (1992) The temperature dependence of the cation distribution in magnesioferrite (MgFe2O4) from powder XRD structural refinements and Mossbauer spectroscopy. American Mineralogist, 77, 725–740.

Olsen, J.S., Gerward, L., Hinze, E., and Kremmler, J. (1994) High-pressure, high-temperature study of magnetite using synchrotron radiation. Materials Science Forum, 166–169, 577–582. https://doi.org/10.4028/www.scientific.net/MSF.166-169.577

O'Neill, H. S. C., Annersten, H., & Virgo, D. (1992). The temperature dependence of the cation distribution in magnesioferrite (MgFe2O4) from powder XRD structural refinements and Mössbauer spectroscopy. American Mineralogist, 77(7-8), 725-740.

O'Neill, H. S. C., Pownceby, M. I., & McCammon, C. A. (2003). The magnesiowüstite: iron equilibrium and its implications for the activity-composition relations of (Mg, Fe) 2 SiO 4 olivine solid solutions. Contributions to Mineralogy and Petrology, 146, 308-325. 10.1007/s00410-003-0496-4

O'Neill, H. St. c., and Wall, VI (1987) The olivine-orthopyroxene-spinel oxygen geobarometer, the nickel precipitation curve, and the oxygen fugacity of the Earth's upper mantle. Journal of Petrology, 28, 1169-1191. https://doi.org/10.1093/petrology/28.6.1169

Ono, K., Ueda, Y., Yamaguchi, A., & Moriyama, J. (1977). Thermodynamic study of Fe–Ni solid solution. Transactions of the Japan Institute of Metals, 18(9), 610-616. https://doi.org/10.2320/matertrans1960.18.610

Otsuka, K., Longo, M., McCammon, C. A., & Karato, S. I. (2013). Ferric iron content of ferropericlase as a function of composition, oxygen fugacity, temperature and pressure: Implications for redox conditions during diamond formation in the lower mantle. Earth and Planetary Science Letters, 365, 7-16. http://dx.doi.org/10.1016/j.epsl.2012.11.030

Otsuka, K., McCammon, C. A., & Karato, S. I. (2010). Tetrahedral occupancy of ferric iron in (Mg, Fe) O: Implications for point defects in the Earth's lower mantle. Physics of the Earth and Planetary Interiors, 180(3-4), 179-188. 10.1016/j.pepi.2009.10.005

Ottolini, L., Cámara, F., Hawthorne, F.C. and Stirling, J., (2002). SIMS matrix effects in the analysis of light elements in silicate minerals: Comparison with SREF and EPMA data. American Mineralogist, 87(10), pp.1477-1485.

Ottolini, L.P., Schingaro, E., Scordari, F., Mesto, E. and Lacalamita, M., (2010). The role of SIMS in the investigation of the complex crystal chemistry of mica minerals. In IOP Conference Series: Materials Science and Engineering (Vol. 7, No. 1, p. 012023). IOP Publishing.

Pagé, L., Hattori, K., & Guillot, S. (2018). Mantle wedge serpentinites: A transient reservoir of halogens, boron, and nitrogen for the deeper mantle. Geology, 46(10), 883-886. DOI: 10.1130/G45204.1

Pagé, L., Hattori, K., & Guillot, S. (2018). Mantle wedge serpentinites: A transient reservoir of halogens, boron, and nitrogen for the deeper mantle. Geology, 46(10), 883-886. https://doi.org/10.1130/G45204.1

Pal'yanov, Y. N., Sokol, A. G., & Sobolev, N. V. (2005). Experimental modeling of mantle diamond-forming processes. Russian Geology and Geophysics, 46(12), 1290-1303.

Paladino, A. E. (1960). Phase Equilibria in the Ferrite Region of the System FeO-MgO-Fe2O3. Journal of the American Ceramic Society, 43(4), 183-191. https://doi.org/10.1111/j.1151-2916.1960.tb12979.x

Palot, M., Cartigny, P., Harris, J. W., Kaminsky, F. V., & Stachel, T. (2012). Evidence for deep mantle convection and primordial heterogeneity from nitrogen and carbon stable isotopes in diamond. Earth and Planetary Science Letters, 357, 179-193. http://dx.doi.org/10.1016/j.epsl.2012.09.015

Palot, M., Jacobsen, S.D., Townsend, J.P., Nestola, F., Marquardt, K., Miyajima, N., Harris, J.W., Stachel, T., McCammon, C.A. and Pearson, D.G.. (2016). Evidence for H2O-bearing fluids in the lower mantle from diamond inclusion. Lithos, 265, 237-243. https://doi.org/10.1016/j.lithos.2016.06.023

Palot, M., Pearson, D. G., Stern, R. A., Stachel, T., & Harris, J. W. (2014). Isotopic constraints on the nature and circulation of deep mantle C–H–O–N fluids: Carbon and nitrogen systematics within ultra-deep diamonds from Kankan (Guinea). Geochimica et Cosmochimica Acta, 139, 26-46. https://doi.org/10.1016/j.gca.2014.04.027

Palya, A. P., Buick, I. S., & Bebout, G. E. (2011). Storage and mobility of nitrogen in the continental crust: Evidence from partially melted metasedimentary rocks, Mt. Stafford, Australia. Chemical Geology, 281(3-4), 211-226. https://doi.org/10.1016/j.chemgeo.2010.12.009

Palyanov, Y. N., Bataleva, Y. V., Sokol, A. G., Borzdov, Y. M., Kupriyanov, I. N., Reutsky, V. N., & Sobolev, N. V. (2013). Mantle–slab interaction and redox mechanism of diamond formation. Proceedings of the National Academy of Sciences, 110(51), 20408-20413. https://doi.org/10.1073/pnas.1313340110

"Palyanov, Y. N., Borzdov, Y. M., Bataleva, Y. V., Sokol, A. G., Palyanova, G. A., & Kupriyanov, I. N. (2007). Reducing role of sulfides and diamond formation in the Earth's mantle. Earth and Planetary Science Letters, 260(1-2), 242-256.

10.1016/j.epsl.2007.05.033"

"Palyanov, Y. N., Borzdov, Y. M., Khokhryakov, A. F., Kupriyanov, I. N., & Sobolev, N. V. (2006). Sulfide melts–graphite interaction at HPHT conditions: Implications for diamond genesis. Earth and Planetary Science Letters, 250(1-2), 269-280.

10.1016/j.epsl.2006.06.049"

Pamato, M. (2014) Single-crystal elasticity of Al-rich phases in the Earth's transition zone and lower mantle. PhD thesis, University of Bayreuth, pp. 194.

Pasternak, M. P., Nasu, S., Wada, K., & Endo, S. (1994). High-pressure phase of magnetite. Physical Review B, 50(9), 6446. https://doi.org/10.1103/PhysRevB.50.6446

Pearson, D.G., Brenker, F.E., Nestola, F., McNeill, J., Nasdala, L., Hutchison, M.T., Matveev, S., Mather, K., Silversmit, G., Schmitz, S. and Vekemans, B.. (2014). Hydrous mantle transition zone indicated by ringwoodite included within diamond. Nature, 507(7491), 221-224. https://doi.org/10.1038/nature13080

Pelton, A. D. (2001). A general "geometric" thermodynamic model for multicomponent solutions. Calphad, 25(2), 319-328. https://doi.org/10.1016/S0364-5916(01)00052-9

Pennycook, S. J., & Varela, M. (2011). New views of materials through aberration-corrected scanning transmission electron microscopy. Journal of electron microscopy, 60(suppl_1), S213-S223.https://doi.org/10.1093/jmicro/dfr030

Petts, D. C., Chacko, T., Stachel, T., Stern, R. A., & Heaman, L. M. (2015). A nitrogen isotope fractionation factor between diamond and its parental fluid derived from detailed SIMS analysis of a gem diamond and theoretical calculations. Chemical Geology, 410, 188-200. https://doi.org/10.1016/j.chemgeo.2015.06.020

Phillips, M. W., Popp, R. K., & Clowe, C. A. (1988). Structural adjustments accompanying oxidation-dehydrogenation in amphiboles. American Mineralogist, 73(5-6), 500-506.

Plessen, B., Harlov, D. E., Henry, D., & Guidotti, C. V. (2010). Ammonium loss and nitrogen isotopic fractionation in biotite as a function of metamorphic grade in metapelites from western Maine, USA. Geochimica et Cosmochimica Acta, 74(16), 4759-4771. DOI: 10.1016/j.gca.2010.05.021

Potapkin, V., Chumakov, A.I., Smirnov, G. V., Celse, J.P., Rüffer, R., McCammon, C., and Dubrovinsky, L. (2012) The 57Fe Synchrotron Mössbauer Source at the ESRF. Journal of Synchrotron Radiation, 19, 559–569. https://doi.org/10.1107/S0909049512015579

Potapkin, V., McCammon, C.A., Glazyrin, K., Kantor, A., Kupenko, I., Prescher, C., Sinmyo, R., Smirnov, G.V., Chumakov, A.I., Rüffer, R., and others (2013) Effect of iron oxidation state on the electrical condictivity of the Earth's lower mantle. Nature Communications, 4(1) 1427. https://doi.org/10.1038/ncomms2436

Pöter, B., Gottschalk, M., & Heinrich, W. (2004). Experimental determination of the ammonium partitioning among muscovite, K-feldspar, and aqueous chloride solutions. Lithos, 74(1-2), 67-90. https://doi.org/10.1016/j.lithos.2004.01.002

Pouyan, S., Bassett, W. A., & Lin-Gun, L. (1983). Experimental determination of the effects of pressure and temperature on the stoichiometry and phase relations of wüstite. Geochimica et cosmochimica Acta, 47(4), 773-778. https://doi.org/10.1016/0016-7037(83)90110-2

Prescher, C., McCammon, C. A., Dubrovinsky, L. (2012). MossA: A program for analyzing energy-domain Mössbauer spectra from conventional and synchrotron sources. Journal of Applied Crystallography, 45(2), 329–331. https://doi.org/10.1107/S0021889812004979

Prescher, C., McCammon, C., & Dubrovinsky, L. (2012). MossA: a program for analyzing energy-domain Mössbauer spectra from conventional and synchrotron sources. Journal of Applied Crystallography, 45(2), 329-331. 10.1107/S0021889812004979

Preston, R. S., Hanna, S. S., & Heberle, J. (1962). Mössbauer effect in metallic iron. Physical Review, 128(5), 2207.https://doi.org/10.1103/PhysRev.128.2207

Putnis, A. (1992). An introduction to mineral sciences. Cambridge University Press. https://doi.org/10.1017/CBO9781139170383

Rancourt, D. G., McDonald, A. M., Lalonde, A. E., & Ping, J. Y. (1993). Mössbauer absorber thicknesses for accurate site populations in Fe-bearing minerals. American Mineralogist, 78(1-2), 1-7.

Reed, S. J. B. (2005). Electron microprobe analysis and scanning electron microscopy in geology. Cambridge university press.https://doi.org/10.1017/CBO9780511610561

Reichmann, H. J., Jacobsen, S. D., Mackwell, S. J., & McCammon, C. A. (2000). Sound wave velocities and elastic constants for magnesiowüstite using gigahertz interferometry. Geophysical research letters, 27(6), 799-802. https://doi.org/10.1029/1999GL008411

Reichmann, H.J., and Jacobsen, S.D. (2004) High-pressure elasticity of a natural magnetite crystal. American Mineralogist, 89, 1061–1066. https://doi.org/10.2138/am-2004-0718

Richardson, S. H., Gurney, J. J., Erlank, A. J., & Harris, J. (1984). Origin of diamonds in old enriched mantle. Nature, 310(5974), 198-202. https://doi.org/10.1038/310198a0

Ringwood, A. E. (1962). A model for the upper mantle. Journal of Geophysical Research, 67(2), 857-867. https://doi.org/10.1029/JZ067i002p00857

Ringwood, A. E. (1991). Phase transformations and their bearing on the constitution and dynamics of the mantle. Geochimica et Cosmochimica Acta, 55(8), 2083-2110. https://doi.org/10.1016/0016-7037(91)90090-R

Robertson, R., Fox, J. J., & Martin, A. E. (1934). Two types of diamond. Philosophical Transactions of the Royal Society of London. Series A, Containing Papers of a Mathematical or Physical Character, 232(707-720), 463-535. https://doi.org/10.1098/rsta.1934.0013

Robinson, J.A.C., and Wood, B.J. (1998) The depth of the spinel to garnet transition at the peridotite solidus. Earth and Planetary Science Letters, 164, 277-284. https://doi.org/10.1016/S0012-821X(98)00213-1

Rohrbach, A., & Schmidt, M. W. (2011). Redox freezing and melting in the Earth's deep mantle resulting from carbon–iron redox coupling. Nature, 472(7342), 209-212. https://doi.org/10.1038/nature09899

Rohrbach, A., Ballhaus, C., Golla–Schindler, U., Ulmer, P., Kamenetsky, V. S., & Kuzmin, D. V. (2007). Metal saturation in the upper mantle. Nature, 449(7161), 456-458. http://dx.doi.org/10.1038/nature06183

Romanowicz, B. (2008). Using seismic waves to image Earth's internal structure. Nature, 451(7176), 266-268. 10.1038/nature06583

Rosenhauer, M., Woermann, E., Knecht, B., & Ulmer, C. G. (1977, September). The stability of graphite and diamond as a function of the oxygen fugasity in the mantle. In International Kimberlite Conference: Extended Abstracts (Vol. 2, pp. 285-287). https://doi.org/10.29173/ikc1023

Roskosz M., Mysen B. O. and Cody G. D. (2006) Dual speciation of nitrogen in silicate melts at high pressure and temperature: an experimental study. Geochim. Cosmochim. Acta 70(11), 2902–2918.

Roskosz, M., Bouhifd, M. A., Jephcoat, A. P., Marty, B., & Mysen, B. O. (2013). Nitrogen solubility in molten metal and silicate at high pressure and temperature. Geochimica et Cosmochimica Acta, 121, 15-28. https://doi.org/10.1016/j.gca.2013.07.007

Roskosz, M., Mysen, B. O., & Cody, G. D. (2006). Dual speciation of nitrogen in silicate melts at high pressure and temperature: an experimental study. Geochimica et Cosmochimica Acta, 70(11), 2902-2918. https://doi.org/10.1016/j.gca.2006.03.001

Roth, W. L. (1960). Defects in the crystal and magnetic structures of ferrous oxide. Acta Crystallographica, 13(2), 140-149.https://doi.org/10.1107/S0365110X60000297

Rozenberg, G.K., Amiel, Y., Xu, W.M., Pasternak, M.P., Jeanloz, R., Hanfland, M., and Taylor, R.D. (2007) Structural characterization of temperature- and pressure-induced inverse normal spinel transformation in magnetite. Physical Review B - Condensed Matter and Materials Physics, 75, 020102. https://doi.org/10.1103/PhysRevB.75.020102

Rüffer, R., and Chumakov, A.I. (1996) Nuclear Resonance Beamline at ESRF. Hyperfine Interactions, 97–98, 589–604. https://doi.org/10.1007/BF02150199

Rüffer, R., and Chumakov, A.I. (1996) Nuclear Resonance Beamline at ESRF. Hyperfine Interactions, 97–98, 589–604. https://doi.org/10.1007/BF02150199

Sano, Y., Takahata, N., Nishio, Y., Fischer, T. P., & Williams, S. N. (2001). Volcanic flux of nitrogen from the Earth. Chemical geology, 171(3-4), 263-271.10.1016/S0009-2541(00)00252-7

Sato, K., & Katsura, T. (2001). Sulfur: a new solvent-catalyst for diamond synthesis under high-pressure and high-temperature conditions. Journal of Crystal Growth, 223(1-2), 189-194.https://doi.org/10.1016/S0022-0248(01)00610-8

Scherrer, P. (1912). Bestimmung der inneren Struktur und der Größe von Kolloidteilchen mittels Röntgenstrahlen. In: Kolloidchemie Ein Lehrbuch. Chemische Technologie in Einzeldarstellungen. Springer, Berlin, Heidelberg. https://doi.org/10.1007/978-3-662-33915-2_7

"Schindelin, J., Arganda-Carreras, I., Frise, E., Kaynig, V., Longair, M., Pietzsch, T., Preibisch, S., Rueden, C., Saalfeld, S., Schmid, B. and Tinevez, J.Y., 2012. Fiji: an open-source platform for biological-image analysis. Nature methods, 9(7), pp.676-682.

https://doi.org/10.1038/nmeth.2019"

Schollenbruch, K., Woodland, A. B., Frost, D. J., & Langenhorst, F. (2009). Detecting the spinel–post-spinel transition in Fe3O4 by in situ electrical resistivity measurements. High Pressure Research, 29(4), 520-524. https://doi.org/10.1080/08957950903392092

Schollenbruch, K., Woodland, A. B., Frost, D. J., Wang, Y., Sanehira, T., & Langenhorst, F. (2011). In situ determination of the spinel–post-spinel transition in Fe3O4 at high pressure and temperature by synchrotron X-ray diffraction. American Mineralogist, 96(5-6), 820-827. https://doi.org/10.2138/am.2011.3642

Schweika, W., Hoser, A., Martin, M., & Carlsson, A. E. (1995). Defect structure of ferrous oxide Fe 1− x O. Physical Review B, 51(22), 15771. https://doi.org/10.1103/PhysRevB.51.15771

Sheldrick, G.M. (2008) A short history of SHELX. Acta crystallographica. Section A, Foundations of crystallography, 64, 112–122. https://doi.org/10.1107/S0108767307043930

Sheldrick, G.M. (2008) A short history of SHELX. Acta crystallographica. Section A, Foundations of crystallography, 64, 112–122. https://doi.org/10.1107/S0108767307043930

Shi, L., Lu, W., Kagoshima, T., Sano, Y., Gao, Z., Du, Z., ... & Li, Y. (2022). Nitrogen isotope evidence for Earth's heterogeneous accretion of volatiles. Nature Communications, 13(1), 4769. https://doi.org/10.1038/s41467-022-32516-5

Shirey, S. B., Cartigny, P., Frost, D. J., Keshav, S., Nestola, F., Nimis, P., ... & Walter, M. J. (2013). Diamonds and the geology of mantle carbon. Reviews in Mineralogy and Geochemistry, 75(1), 355-421.

Shirey, S., Smit, K., Pearson, D., Walter, M., Aulbach, S., Brenker, F., Bureau, H., Burnham, A., Cartigny, P., Chacko, T. and Frost, D. (2019). Diamonds and the mantle geodynamics of carbon. Deep Carbon. Past to present, 89-128. https://doi.org/10.1017/9781108677950

Shoemaker, D. P., & Bassi, G. (1970). On refinement of the crystal orientation matrix and lattice constants with diffractometer data. Acta Crystallographica Section A: Crystal Physics, Diffraction, Theoretical and General Crystallography, 26(1), 97-101.https://doi.org/10.1107/S0567739470000116

Sinmyo, R., Bykova, E., Ovsyannikov, S. V., McCammon, C., Kupenko, I., Ismailova, L., & Dubrovinsky, L. (2016). Discovery of Fe7O9: a new iron oxide with a complex monoclinic structure. Scientific Reports, 6(1), 1-7. 10.1038/srep32852

Smiltens, J. (1952) The Growing of Single Crystals of Magnetite. Journal of Chemical Physics, 20, 990–994. https://doi.org/10.1063/1.1700664

Smit, K. V., Shirey, S. B., Stern, R. A., Steele, A., & Wang, W. (2016). Diamond growth from C–H–N–O recycled fluids in the lithosphere: Evidence from CH4 micro-inclusions and δ13C–δ15N–N content in Marange mixed-habit diamonds. Lithos, 265, 68-81.doi:10.1016/j.lithos.2016.03.015

Smith, B. S., Danchin, R. V., Harris, J. W., & Stracke, K. J. (1984). Kimberlites near Orroroo, South Australia. In Developments in Petrology (Vol. 11, pp. 121-142). Elsevier. https://doi.org/10.1016/B978-0-444-42273-6.50017-1

Smith, E. M., & Kopylova, M. G. (2014). Implications of metallic iron for diamonds and nitrogen in the sublithospheric mantle. Canadian Journal of Earth Sciences, 51(5), 510-516.DOI: 10.1139/cjes-2013-0218

Smith, E. M., & Wang, W. (2016b). Fluid CH4 and H2 trapped around metallic inclusions in HPHT synthetic diamond. Diamond and Related Materials, 68, 10-12.https://doi.org/10.1016/j.diamond.2016.05.010

Smith, E. M., Shirey, S. B., Nestola, F., Bullock, E. S., Wang, J., Richardson, S. H., & Wang, W. (2016a). Large gem diamonds from metallic liquid in Earth's deep mantle. Science, 354(6318), 1403-1405.

Sobolev, N. V., Yefimova, E. S., & Koptil, V. (1998, April). Crystalline inclusioSobolev, N. V., Yefimova, E. S., & Koptil, V. I. (1999). Mineral inclusions in diamonds in the Northeast of the Yakutian diamondiferous province. Proceedings of the VIIth International Kimberlite Conference (Vol. 2, pp. 816–822). Cape Town: Red Roof Design.ns in diamonds in the northeast of the Yakutian diamondiferous province. In International Kimberlite Conference: Extended Abstracts (Vol. 7, pp. 832-834).

"Sokol, A.G., Palyanov, Y.N., Tomilenko, A.A., Bul'bak, T.A., Palyanova, G.A., 2017. Carbon and nitrogen speciation in nitrogen-rich C–O–H–N fluids at 5.5–7.8 GPa. Earth Planet. Sci. Lett. 460, 234–243

10.1016/j.epsl.2016.11.050"

Speelmanns, I. M., Schmidt, M. W., & Liebske, C. (2018). Nitrogen solubility in core materials. Geophysical Research Letters, 45(15), 7434-7443. https://doi.org/10.1029/2018GL079130

Speelmanns, I. M., Schmidt, M. W., & Liebske, C. (2019). The almost lithophile character of nitrogen during core formation. Earth and Planetary Science Letters, 510, 186-197. https://doi.org/10.1016/j.epsl.2019.01.004

Speelmanns, I. M., Schmidt, M. W., & Liebske, C. (2019). The almost lithophile character of nitrogen during core formation. Earth and Planetary Science Letters, 510, 186-197.https://doi.org/10.1016/j.epsl.2019.01.004

Speidel, D. H. (1967). Phase equilibria in the system MgO-FeO-Fe2O3: The 1300° C isothermal section and extrapolations to other temperatures. Journal of the American Ceramic Society, 50(5), 243-248. https://doi.org/10.1111/j.1151-2916.1967.tb15096.x

Speziale, S., Zha, C. S., Duffy, T. S., Hemley, R. J., & Mao, H. K. (2001). Quasi-hydrostatic compression of magnesium oxide to 52 GPa: Implications for the pressure-volume-temperature equation of state. Journal of Geophysical Research: Solid Earth, 106(B1), 515-528.doi:10.1029/2000JB900318.

Srečec, I., Ender, A., Woermann, E., Gans, W., Jacobsson, E., Eriksson, G., & Rosen, E. (1987). Activity-composition relations of the magnesiowüstite solid solution series in equilibrium with metallic iron in the temperature range 1050–1400 K. Physics and Chemistry of Minerals, 14, 492-498. 10.1007/BF00308284

Stachel, T., & Harris, J. W. (1997). Syngenetic inclusions in diamond from the Birim field (Ghana)–a deep peridotitic profile with a history of depletion and re-enrichment. Contributions to Mineralogy and Petrology, 127(4), 336-352.DOI: 10.1007/s004100050284

Stachel, T., & Harris, J. W. (2008). The origin of cratonic diamonds—constraints from mineral inclusions. Ore Geology Reviews, 34(1-2), 5-32. https://doi.org/10.1016/j.oregeorev.2007.05.002

Stachel, T., & Harris, J. W. (2009). Formation of diamond in the Earth's mantle. Journal of Physics: Condensed Matter, 21(36), 364206.DOI: 10.1088/0953-8984/21/36/364206

Stachel, T., & Luth, R. W. (2015). Diamond formation—Where, when and how?. Lithos, 220, 200-220.https://doi.org/10.1016/j.lithos.2015.01.028

Stachel, T., Brey, G. P., & Harris, J. W. (2005). Inclusions in sublithospheric diamonds: glimpses of deep Earth. Elements, 1(2), 73-78. https://doi.org/10.2113/gselements.1.2.73

Stachel, T., Cartigny, P., Chacko, T., & Pearson, D. G. (2022). Carbon and nitrogen in mantle-derived diamonds. Reviews in Mineralogy and Geochemistry, 88(1), 809-875. https://doi.org/10.2138/rmg.2022.88.15

Stachel, T., Harris, J. W., & Brey, G. P. (1998). Rare and unusual mineral inclusions in diamonds from Mwadui, Tanzania. Contributions to Mineralogy and Petrology, 132(1), 34-47. https://doi.org/10.1007/s004100050403

Stachel, T., Harris, J. W., Brey, G. P., & Joswig, W. (2000). Kankan diamonds (Guinea) II: lower mantle inclusion parageneses. Contributions to Mineralogy and Petrology, 140(1), 16-27. https://doi.org/10.1007/s004100000174

Stachel, T., Harris, J., Aulbach, S., & Deines, P. (2002). Kankan diamonds (Guinea) III: δ13C and nitrogen characteristics of deep diamonds. Contributions to Mineralogy and Petrology, 142(4), 465-475. https://doi.org/10.1007/s004100100297

Stagno, V. (2019). Carbon, carbides, carbonates and carbonatitic melts in the Earth's interior. Journal of the Geological Society, 176(2), 375-387. https://doi.org/10.1144/jgs2018-095

Stagno, V., & Fei, Y. (2020). The redox boundaries of Earth's interior. Elements: An International Magazine of Mineralogy, Geochemistry, and Petrology, 16(3), 167-172. 10.2138/gselements.16.3.167

Stagno, V., & Frost, D. J. (2010). Carbon speciation in the asthenosphere: Experimental measurements of the redox conditions at which carbonate-bearing melts coexist with graphite or diamond in peridotite assemblages. Earth and Planetary Science Letters, 300(1-2), 72-84. https://doi.org/10.1016/j.epsl.2010.09.038

Stagno, V., Ojwang, D. O., McCammon, C. A., & Frost, D. J. (2013). The oxidation state of the mantle and the extraction of carbon from Earth's interior. Nature, 493(7430), 84-88. DOI: 10.1038/nature11679

Stagno, V., Tange, Y., Miyajima, N., McCammon, C. A., Irifune, T., & Frost, D. J. (2011). The stability of magnesite in the transition zone and the lower mantle as function of oxygen fugacity. Geophysical Research Letters, 38(19). https://doi.org/10.1029/2011GL049560

Stixrude, L., & Lithgow-Bertelloni, C. (2005). Thermodynamics of mantle minerals—I. Physical properties. Geophysical Journal International, 162(2), 610-632.https://doi.org/10.1111/j.1365-246X.2005.02642.x

Stixrude, L., & Lithgow-Bertelloni, C. (2012). Geophysics of chemical heterogeneity in the mantle. Annual Review of Earth and Planetary Sciences, 40, 569-595. https://doi.org/10.1146/annurev.earth.36.031207.124244

Stolen, S., Glöckner, R., Gronvold, F., Atake, T., & Izumisawa, S. (1996). Heat capacity and thermodynamic properties of nearly stoichiometric wüstite from 13 to 450 K. American Mineralogist, 81(7-8), 973-981. https://doi.org/10.2138/am-1996-7-819

Tange, Y., Nishihara, Y., & Tsuchiya, T. (2009). Unified analyses for P-V-T equation of state of MgO: A solution for pressure-scale problems in high P-T experiments. Journal of Geophysical Research: Solid Earth, 114(B3). https://doi.org/10.1029/2008JB005813

Tappert, R., Foden, J., Stachel, T., Muehlenbachs, K., Tappert, M., & Wills, K. (2009a). Deep mantle diamonds from South Australia: A record of Pacific subduction at the Gondwanan margin. Geology, 37(1), 43-46. https://doi.org/10.1130/G25055A.1

Tappert, R., Foden, J., Stachel, T., Muehlenbachs, K., Tappert, M., & Wills, K. (2009b). The diamonds of south Australia. Lithos, 112, 806-821.. 10.1016/j.lithos.2009.04.029

Tappert, R., Stachel, T., Harris, J. W., Shimizu, N., & Brey, G. P. (2005). Mineral inclusions in diamonds from the Panda kimberlite, Slave Province, Canada. European Journal of Mineralogy, 17(3), 423-440. 10.1127/0935-1221/2005/0017-0423

Tatsumi, K., Muto, S., Nishida, I., & Rusz, J. (2010). Site-specific electronic configurations of Fe 3 d states by energy loss by channeled electrons. Applied Physics Letters, 96(20), 201911. https://doi.org/10.1063/1.3429593

Terwilliger, G. R., Bowen, H. K., & Gordon, R. S. (1970). Creep of Polycrystalline MgO and MgO-Fe2O3 Solid Solutions at High Temperatures. Journal of The American Ceramic Society, 53(5), 241-251. https://doi.org/10.1111/j.1151-2916.1970.tb12085.x

Thomassot, E., Cartigny, P., Harris, J. W., & Viljoen, K. F. (2007). Methane-related diamond crystallization in the Earth's mantle: stable isotope evidences from a single diamond-bearing xenolith. Earth and Planetary Science Letters, 257(3-4), 362-371. https://doi.org/10.1016/j.epsl.2007.02.020

Thomassot, E., Cartigny, P., Harris, J. W., Lorand, J. P., Rollion-Bard, C., & Chaussidon, M. (2009). Metasomatic diamond growth: A multi-isotope study (13C, 15N, 33S, 34S) of sulphide inclusions and their host diamonds from Jwaneng (Botswana). Earth and Planetary Science Letters, 282(1-4), 79-90.

Thomazo, C., & Papineau, D. (2013). Biogeochemical cycling of nitrogen on the early Earth. Elements, 9(5), 345-351. https://doi.org/10.2113/gselements.9.5.345

Thomson, A. R., Kohn, S. C., Prabhu, A., & Walter, M. J. (2021). Evaluating the formation pressure of diamond-hosted majoritic garnets: A machine learning majorite barometer. Journal of Geophysical Research: Solid Earth, 126(3), e2020JB020604. https://doi.org/10.1029/2020JB020604

Thomson, A. R., Walter, M. J., Kohn, S. C., & Brooker, R. A. (2016). Slab melting as a barrier to deep carbon subduction. Nature, 529(7584), 76-79. https://doi.org/10.1038/nature16174

Tichý, K. (1970). A least-squares method for the determination of the orientation matrix in single-crystal diffractometry. Acta Crystallographica Section A: Crystal Physics, Diffraction, Theoretical and General Crystallography, 26(2), 295-296.https://doi.org/10.1107/S0567739470000712

Toby, B. H. (2001). EXPGUI, a graphical user interface for GSAS. Journal of applied crystallography, 34(2), 210-213.https://doi.org/10.1107/S0021889801002242

Tolstikhin, I. N., & Marty, B. (1998). The evolution of terrestrial volatiles: a view from helium, neon, argon and nitrogen isotope modelling. Chemical Geology, 147(1-2), 27-52.https://doi.org/10.1016/S0009-2541(97)00170-8

Toop, G. W. (1965). Predicting ternary activities using binary data. Trans. TMS-AIME, 223, 850-855.

Tremper, R. T., Giddings, R. A., Hodge, J. D., & Gordon, R. S. (1974). Creep of Polycrystalline MgO-FeO-Fe2O3 Solid Solutions. Journal of the American Ceramic Society, 57(10), 421-428. https://doi.org/10.1111/j.1151-2916.1974.tb11373.x

Trots, D.M., Kurnosov, A., Vasylechko, L., Berkowski, M., Boffa-Ballaran, T., and Frost, D.J. (2011) Elasticity and equation of state of Li2B4O7. Physics and Chemistry of Minerals, 38, 561–567. https://doi.org/10.1007/s00269-011-0428-1

Tsuchiya, T., Tsuchiya, J., Dekura, H., & Ritterbex, S. (2020). Ab initio study on the lower mantle minerals. Annual Review of Earth and Planetary Sciences, 48, 99-119. https://doi.org/10.1146/annurev-earth-071719-055139

Tucker, J. M., & Mukhopadhyay, S. (2014). Evidence for multiple magma ocean outgassing and atmospheric loss episodes from mantle noble gases. Earth and Planetary Science Letters, 393, 254-265. https://doi.org/10.1016/j.epsl.2014.02.050

Turkin, A.I., and Drebushchak, V.A. (2005) Cation distribution in MgFe2O4 vs. pressure and temperature: Experiments in a “piston-cylinder” apparatus. American Mineralogist, 90, 764–767. https://doi.org/10.2138/am.2005.1714

Uenver-Thiele, L., Woodland, A.B., Boffa Ballaran, T., Miyajima, N., and Frost, D.J. (2017a) Phase relations of Fe-Mg spinels including new high-pressure post-spinel phases and implications for natural samples. American Mineralogist, 102, 2054–2064. https://doi.org/10.2138/am-2017-6119

Uenver-Thiele, L., Woodland, A.B., Boffa-Ballaran, T., Miyajima, N., and Frost, D.J. (2017b) Phase relations of MgFe2O4 at conditions of the deep upper mantle and transition zone. American Mineralogist, 102, 632–642.https://doi.org/10.2138/am-2017-5871

Uenver-Thiele, L., Woodland, A.B., Miyajima, N., Boffa-Ballaran, T., and Frost, D.J. (2018) Behaviour of Fe4O5–Mg2Fe2O5 solid solutions and their relation to coexisting Mg–Fe silicates and oxide phases. Contributions to Mineralogy and Petrology, 173, 1–16. https://doi.org/10.2138/am-2017-5871

Urakawa, S. (1991). Partitioning of Ni between magnesiowüstite and metal at high pressure: implications for core-mantle equilibrium. Earth and planetary science letters, 105(1-3), 293-313. https://doi.org/10.1016/0012-821X(91)90138-8

Valet, P. M., Pluschkell, W., & Engell, H. J. (1975). Equilibria between MgO-FeO-Fe2O3 solid-solutions and oxygen. Archiv für das Eisenhüttenwesen, 46(6), 383-388. https://doi.org/10.1002/srin.197503645

Vallet, P., & Carel, C. (1989). The Fe-O (iron-oxygen) phase diagram in the range of the nonstoichiometric monoxide and magnetite at the Fe-rich limit: reduction diagrams. Bulletin of Alloy Phase Diagrams, 10(3), 209-218. https://doi.org/10.1007/BF02877494

van Aken, P. A., & Liebscher, B. (2002). Quantification of ferrous/ferric ratios in minerals: new evaluation schemes of Fe L 23 electron energy-loss near-edge spectra. Physics and Chemistry of Minerals, 29, 188-200. 10.1007/s00269-001-0222-6

Van Aken, P. A., Liebscher, B., & Styrsa, V. J. (1998). Quantitative determination of iron oxidation states in minerals using Fe L 2, 3-edge electron energy-loss near-edge structure spectroscopy. Physics and Chemistry of Minerals, 25, 323-327. https://doi.org/10.1007/s002690050122

Van Rythoven, A. D., & Schulze, D. J. (2009). In-situ analysis of diamonds and their inclusions from the Diavik Mine, Northwest Territories, Canada: Mapping diamond growth. Lithos, 112, 870-879. 10.1016/j.lithos.2009.04.025

Vermeesch, P. (2018). IsoplotR: A free and open toolbox for geochronology. Geoscience Frontiers, 9(5), 1479-1493.

Volenik, K., Seberini, M., and Neid, J. (1975) A Mössbauer and X-ray diffraction study of nonstoichiometry in magnetite. Czechoslovak Journal of Physics, 25, 1063–1071. https://doi.org/10.1007/BF01597585

von der Handt, A., & Dalou, C. (2016). Quantitative EPMA of nitrogen in silicate glasses. Microscopy and Microanalysis, 22(S3), 1810-1811. 10.1017/S1431927616009892

von der Handt, A., Mosenfelder, J., Dalou, C., & Hirschmann, M. M. (2019). Recent Advances in the Analysis of Nitrogen by EPMA. Microscopy and Microanalysis, 25(S2), 2320-2321. doi:10.1017/S1431927619012339

W. Burgmann (1975) The Defect Structure Models for Wüstite: A Review,Metal Science, 9:1, 169-175, DOI: 10.1179/030634575790445107

Walker, D., Carpenter, M. A., & Hitch, C. M. (1990). Some simplifications to multianvil devices for high pressure experiments. American Mineralogist, 75(9-10), 1020-1028.

Walter, M.J., Bulanova, G.P., Armstrong, L.S., Keshav, S., Blundy, J.D., Gudfinnsson, G., Lord, O.T., Lennie, A.R., Clark, S.M., Smith, C.B. and Gobbo, L. (2008). Primary carbonatite melt

from deeply subducted oceanic crust. Nature, 454(7204), 622-625. https://doi.org/10.1038/nature07132

Walter, M.J., Kohn, S.C., Araujo, D., Bulanova, G.P., Smith, C.B., Gaillou, E., Wang, J., Steele, A. and Shirey, S.B., (2011). Deep mantle cycling of oceanic crust: evidence from diamonds and their mineral inclusions. Science, 334(6052), pp.54-57.DOI: 10.1126/science.1209300

Watenphul, A., Wunder, B., & Heinrich, W. (2009). High-pressure ammonium-bearing silicates: Implications for nitrogen and hydrogen storage in the Earth's mantle. American Mineralogist, 94, 283–292.

Watenphul, A., Wunder, B., Wirth, R., & Heinrich, W. (2010). Ammonium-bearing clinopyroxene: A potential nitrogen reservoir in the Earth's mantle. Chemical Geology, 270, 240–248.

Weir, C. E., Lippincott, E. R., Van Valkenburg, A., Bunting, E. N. (1959). Infrared studies in the 1- to 15-micron region to 30,000 atmospheres. Journal of Research of the National Bureau of Standards. Section A. Physics and Chemistry, 63,1. https://doi.org/10.6028/jres.063A.003

Welberry, T. R., & Christy, A. G. (1997). Defect distribution and the diffuse X-ray diffraction pattern of wüstite, Fe1− xO. Physics and Chemistry of Minerals, 24(1), 24-38.https://doi.org/10.1007/s002690050014

Welberry, T. R., Goossens, D. J., & Heerdegen, A. P. (2014). Local order in wüstite using a pair distribution function (PDF) approach. Mineralogical Magazine, 78(2), 373-385. https://doi.org/10.1180/minmag.2014.078.2.10

Wicks, J. K., & Duffy, T. S. (2016). Crystal structures of minerals in the lower mantle. Deep Earth: Physics and Chemistry of the Lower Mantle and Core, 69-87.

Wilburn, D.R., and Bassett, W.A. (1977) Isothermal compression of magnetite (Fe3O4) up to 70 kbar under hydrostatic conditions. High-temperature - High pressures, 9, 35–39

Wilding, M. C. (1990). Study of diamonds with syngenetic inclusions.

Wilding, M. C., Harte, B., & Harris, J. W. (1991, February). Evidence for a deep origin for Sao Luiz diamonds. In International Kimberlite Conference: Extended Abstracts (Vol. 5, pp. 456-458).https://doi.org/10.29173/ikc2603

Wirth, R., Dobrzhinetskaya, L., Harte, B., Schreiber, A., & Green, H. W. (2014). High-Fe (Mg, Fe) O inclusion in diamond apparently from the lowermost mantle. Earth and Planetary Science Letters, 404, 365-375. https://doi.org/10.1016/j.epsl.2014.08.010

Wirth, R., Kaminsky, F., Matsyuk, S., & Schreiber, A. (2009). Unusual micro-and nano-inclusions in diamonds from the Juina Area, Brazil. Earth and Planetary Science Letters, 286(1-2), 292-303.DOI: 10.1016/j.epsl.2009.06.043

Wirth, R., Vollmer, C., Brenker, F., Matsyuk, S., & Kaminsky, F. (2007). Inclusions of nanocrystalline hydrous aluminium silicate "Phase Egg" in superdeep diamonds from Juina (Mato Grosso State, Brazil). Earth and Planetary Science Letters, 259(3-4), 384-399.https://doi.org/10.1016/j.epsl.2007.04.041

Wirth, Richard. (2004). Focused Ion Beam (FIB): A novel technology for advanced application of micro- and nanoanalysis in geosciences and applied mineralogy. European Journal of Mineralogy, 16(6), 863–876. https://doi.org/10.1127/0935-1221/2004/0016-0863

Wiser, N. M., & Wood, B. J. (1991). Experimental determination of activities in Fe− Mg olivine at 1400 K. Contributions to Mineralogy and Petrology, 108(1-2), 146-153. https://doi.org/10.1007/BF00307333

Witte, K., Bodnar, W., Mix, T., Schell, N., Fulda, G., Woodcock, T. G., & Burkel, E. (2016). A detailed study on the transition from the blocked to the superparamagnetic state of reduction-precipitated iron oxide nanoparticles. Journal of Magnetism and Magnetic Materials, 403, 103-113. https://doi.org/10.1016/j.jmmm.2015.11.074

Wood, B. J., & Nell, J. (1991). High-temperature electrical conductivity of the lower-mantle phase (Mg, Fe) O. Nature, 351(6324), 309-311. https://doi.org/10.1038/351309a0

Wood, B. J., Bryndzia, L. T., & Johnson, K. E. (1990). Mantle oxidation state and its relationship to tectonic environment and fluid speciation. Science, 248(4953), 337-345.https://doi.org/10.1126/science.248.4953.337

Woodland, A. B., & O'Neill, H. S. C. (1997). Thermodynamic data for Fe-bearing phases obtained using noble metal alloys as redox sensors. Geochimica et Cosmochimica Acta, 61(20), 4359-4366. https://doi.org/10.1016/S0016-7037(97)00247-0

Woodland, A. B., Frost, D. J., Trots, D. M., Klimm, K., & Mezouar, M. (2012). In situ observation of the breakdown of magnetite (Fe3O4) to Fe4O5 and hematite at high pressures and temperatures. American Mineralogist, 97(10), 1808-1811. https://doi.org/10.2138/am.2012.4270

Woodland, A. B., Kornprobst, J., & Tabit, A. (2006). Ferric iron in orogenic lherzolite massifs and controls of oxygen fugacity in the upper mantle. Lithos, 89(1-2), 222-241. https://doi.org/10.1016/j.lithos.2005.12.014

Woodland, A. B., Uenver-Thiele, L., Boffa Ballaran, T., Miyajima, N., Rosbach, K., & Ishii, T. (2023). Stability of Fe5O6 and its relation to other Fe-Mg-oxides at high pressures and temperatures. American Mineralogist, 108(1), 140-149. https://doi.org/10.2138/am-2022-8370

Wordsworth, R. D. (2016). Atmospheric nitrogen evolution on Earth and Venus. Earth and Planetary Science Letters, 447, 103-111.https://doi.org/10.1016/j.epsl.2016.04.002

Xu, X., Cartigny, P., Yang, J., Dilek, Y., Xiong, F., & Guo, G. (2018). Fourier transform infrared spectroscopy data and carbon isotope characteristics of the ophiolite-hosted diamonds from the Luobusa ophiolite, Tibet, and Ray-Iz ophiolite, Polar Urals. Lithosphere, 10(1), 156-169. DOI: 10.1130/L625.1

Yagi, T., Sakai, T., Kadobayashi, H., & Irifune, T. (2020). high pressure generation techniques beyond the limit of conventional diamond anvils. High Pressure Research, 40(1), 148-161.https://doi.org/10.1080/08957959.2019.1704753

Yamamoto, T., Hashizume, K. O., MATSUDA, J. I., & Kase, T. (1998). Multiple nitrogen isotopic components coexisting in ureilites. Meteoritics & Planetary Science, 33(4), 857-870. https://doi.org/10.1111/j.1945-5100.1998.tb01692.x

Yamanaka, T., Kyono, A., Nakamoto, Y., Kharlamova, S., Struzhkin, V.V., Gramsch, S.A., Mao, H.K. & Hemley, R. J. (2015). New structure of high-pressure body-centered orthorhombic Fe2SiO4. American Mineralogist, 100(8-9), 1736-1743. https://doi.org/10.2138/am-2015-4744

Yang, Y., Huang, W., Qi, Z., & Xia, Q. (2022). Nitrogen retention in feldspar: Implications for nitrogen transport in subduction zones. Journal of Geophysical Research: Solid Earth, 127(5), e2021JB023347.

Yoshioka, T., Wiedenbeck, M., Shcheka, S., & Keppler, H. (2018). Nitrogen solubility in the deep mantle and the origin of Earth's primordial nitrogen budget. Earth and Planetary Science Letters, 488, 134-143.

Yoshioka, T., Wiedenbeck, M., Shcheka, S., & Keppler, H. (2018). Nitrogen solubility in the deep mantle and the origin of Earth's primordial nitrogen budget. Earth and Planetary Science Letters, 488, 134-143. https://doi.org/10.1016/j.epsl.2018.02.021

Zedgenizov, D. A., Kagi, H., Shatsky, V. S., & Ragozin, A. L. (2014). Local variations of carbon isotope composition in diamonds from Sao-Luis (Brazil): evidence for heterogenous carbon reservoir in sublithospheric mantle. Chemical Geology, 363, 114-124.. doi:10.1016/j.chemgeo.2013.10.033

Zedgenizov, D. A., Yefimova, E. S., Logvinova, A. M., Shatsky, V. S., & Sobolev, N. V. (2001, March). Ferropericlase inclusions in a diamond microcrystal from the Udachnaya kimberlite pipe, Yakutia. In DOKLADY EARTH SCIENCES C/C OF DOKLADY-AKADEMIIA NAUK (Vol. 377, pp. 319-321). INTERPERIODICA PUBLISHING.

Zerkle, A. L., & Mikhail, S. (2017). The geobiological nitrogen cycle: from microbes to the mantle. Geobiology, 15(3), 343-352. DOI: 10.1111/gbi.12228

Zhimulev, E. I., Chepurov, A. I., & Sobolev, N. V. (2018, December). Genesis of Diamond in Metal–Carbon and Metal–Sulfur–Carbon Melts: Evidence from Experimental Data. In Doklady Earth Sciences (Vol. 483, pp. 1473-1474). Pleiades Publishing. https://doi.org/10.1134/S1028334X18110247

Zhimulev, E. I., Chepurov, A. I., Sinyakova, E. F., Sonin, V. M., Chepurov, A. A., & Pokhilenko, N. P. (2012). Diamond crystallization in the Fe-Co-SC and Fe-Ni-SC systems and the role of sulfide-metal melts in the genesis of diamond. Geochemistry International, 50, 205-216.DOI: 10.1134/S0016702912030111

Zhimulev, E. I., Sonin, V. M., Mironov, A. M., & Chepurov, A. I. (2016). Effect of sulfur concentration on diamond crystallization in the Fe–C–S system at 5.3–5.5 GPa and 1300–1370 C. Geochemistry International, 54, 415-422.https://doi.org/10.1134/S0016702916050116

(Eidesstattliche) Versicherungen und Erklärungen

(§ 9 Satz 2 Nr. 3 PromO BayNAT)

Hiermit versichere ich eidesstattlich, dass ich die Arbeit selbstständig verfasst und keine anderen als die von mir angegebenen Quellen und Hilfsmittel benutzt habe (vgl. Art. 64 Abs. 1 Satz 6 BayHSchG).

(§ 9 Satz 2 Nr. 3 PromO BayNAT)

Hiermit erkläre ich, dass ich die Dissertation nicht bereits zur Erlangung eines akademischen Grades eingereicht habe und dass ich nicht bereits diese oder eine gleichartige Doktorprüfung endgültig nicht bestanden habe.

(§ 9 Satz 2 Nr. 4 PromO BayNAT)

Hiermit erkläre ich, dass ich Hilfe von gewerblichen Promotionsberatern bzw. -vermittlern oder ähnlichen Dienstleistern weder bisher in Anspruch genommen habe noch künftig in Anspruch nehmen werde.

(§ 9 Satz 2 Nr. 7 PromO BayNAT)

Hiermit erkläre ich mein Einverständnis, dass die elektronische Fassung meiner Dissertation unter Wahrung meiner Urheberrechte und des Datenschutzes einer gesonderten Überprüfung unterzogen werden kann.

(§ 9 Satz 2 Nr. 8 PromO BayNAT)

Hiermit erkläre ich mein Einverständnis, dass bei Verdacht wissenschaftlichen Fehlverhaltens Ermittlungen durch universitätsinterne Organe der wissenschaftlichen Selbstkontrolle stattfinden können.

……

Ort, Datum, Unterschrift